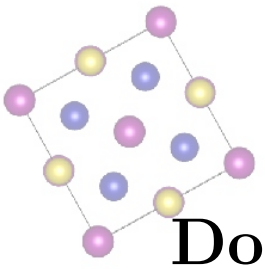

Doctoral Thesis

Magnetic investigations in the TEM: EMCD and DPC measurements on Heusler alloys towards interfacial properties and magnetic characterization of thin film systems

by

Daniela Ramermann

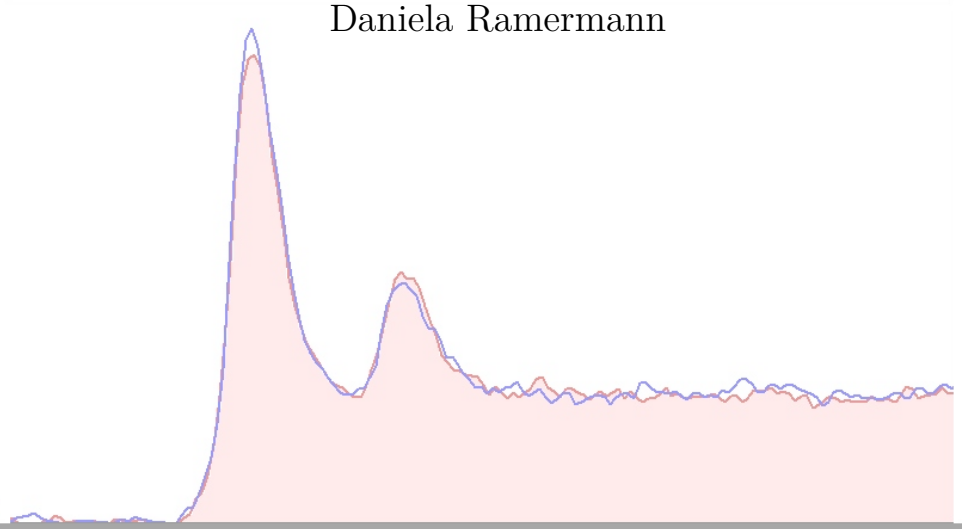

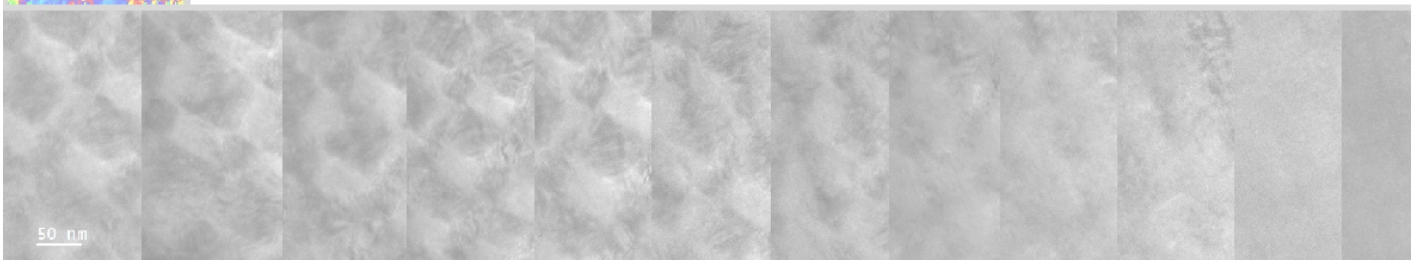

Doctoral Thesis

Magnetic investigations in the TEM: EMCD and DPC measurements on Heusler alloys towards interfacial properties and magnetic characterization of thin film systems

by

Daniela Ramermann

A Thesis Submitted to

Bielefeld University
Faculty of Physics

on December 16, 2020

Supervisor &	1st assessor:	Prof. Dr. Andreas Hütten
	2nd assessor:	Prof. Dr. Jürgen Schnack

„The light microscope opened the first gate to microcosm.
The electron microscope opened the second gate to microcosm.
What will we find opening the third gate?“

(Ernst Ruska)

„Wer konnte denn ahnen, dass sie dann gleich das ganze Buch liest?“

(Andreas Hütten)

Acknowledgements

I want to thank Prof. Andreas Hütten for his supervision of this thesis. He, Prof. Jürgen Schnack and Dr. Michael Czopnik did not give me up when I was a young student and helped me back on my path so I was able to finish my studies and was prepared well enough for being a researcher. To Michael also thank you for the fun we had in the years sharing an office on E5. During my work for this thesis I got computing power from Prof. Schnack and ideas and discussion, access to two modern electron microscopes and the necessary encouragement from Prof. Hütten, leading me to finishing my project with very interesting results.

Hanne Litschewsky, you have always been there, cheered me up and made the path to go look far easier than before, also thank you for all the nice chats we had. Your "little one" finally grew up!

Inga Ennen, it was a pleasure to share an office with you, there is no friendlier and more sensible colleague than you! I learned my first steps on the electron microscope from you and a lot of writing techniques, and you always helped along when I thought my data was not good.

My colleagues from D2: Andreas "Manni" Becker, Björn Büker and Martin Gottschalk deserve great thanks for preparing my samples according to my wishes, which sometimes were quite demanding. Thank you to Björn and Martin and sometimes Karsten Rott for cutting the lamellas thinner than thin and making a new one when I destroyed one with the electron beam. And to Manni for sputtering all I could dream of. To all of you thank you for the great company and all the nice and funny moments!

My TEM colleagues Yvonne Hannappel, Bernhard Kaltschmidt and Chris Taake, working with you and taming the new TEM was a pleasure!

Nadine Fokin provided me with freshly cooked nanoparticles and her and all other people from D2 I want to thank for their company, the discussions that gave a lot of new ideas for what else to try to investigate and in general the great atmosphere to work in.

Stefan Löffler and Michael Stöger-Pollach from USTEM Vienna kindly taught me how to measure and simulate EMCD and other TEM related tricks during my two visits in Vienna, without them parts of this work would not have been possible. Stefan provided the simulation tool "bw" and taught me a lot about the background of simulating EMCD.

The DAAD I want to thank for giving me the opportunity and the funding for research abroad at the University of Glasgow and Stephen McVitie, Trevor Almeida and Robert Webster from the Glasgow School of Physics and Astronomy for teaching me the art of magnetic DPC measurements on the TEM. I learned a lot on my visit and will keep it always in good memory! Without you all these results would not have been possible.

Science is food for the brain, music is food for the soul and also desperately needed, keeping company through good and bad times. I want to say thank you to the for me

most important musician Caroline Lavelle, for the great concerts I could attend and for your friendship. Also thank you to another for me very important musician Ally Storch for the music and concerts, the friendship and the help with the violin. And thank you to Sonia Anschütz for your music, friendship and getting along teaching me the violin at my grown age.

Last but not least: My family, among them my parents Birgitt and Rudolf, my sisters Jessica and Annika and all my friends, for always being supportive and patient throughout my work on this thesis, for providing enough chocolate to live on and bearing me hearing my music too loud.

Funding

The work in this thesis has been partly funded by:

DAAD "Kurzstipendium für Doktoranden" for a 5 month research visit at the University of Glasgow, School of Physics and Astronomy in the workgroup of Prof. Stephen McVitie from 1.10.2019 - 29.2.2020

Bielefelder Nachwuchsfonds "Abschlussstipendium für Promovierende" that funded me for the months after returning back to Germany to finish this project from 1.3.2020 - 30.11.2020.

Publications

Proximity-Induced Superconductivity and Quantum Interference in Topological Crystalline Insulator SnTe Thin-Film Devices
R. Klett, J. Schönle, A. Becker, D. Dyck, K. Borisov, K. Rott, D. Ramermann, B. Büker, J. Haskenhoff, J. Krieft, T. Hübner, O. Reimer, C. Shekhar, J.-M. Schmalhorst, A. Hütten, C. Felser, W. Wernsdorfer, and G. Reiss
Nano Letters (2018) American Chemical Society, doi: 10.1021/acs.nanolett.7b04870
https://doi.org/10.1021/acs.nanolett.7b04870

Participation in Conferences

DPG Frühjahrstagung, section condensed matter physics:

2018
MA 16.2 Talk "Electron microscopy: magnetic properties in another kind of light" D. Ramermann, I. Ennen, and A. Hütten

2019
MA 15.61 Poster "Heusler compound layer systems analysed with different HRTEM techniques"
D. Ramermann, A. Becker, I. Ennen, M. Gottschalk, B. Büker, and A. Hütten

MA 15.60 Poster "3D check board pattern formation of martensite/austenite domains in NiCoMnAl shape memory alloys"
A. Becker, D. Ramermann, M. Gottschalk, I. Ennen, B. Büker, T. Matalla-Wagner, A. Hütten, and G. Reiss

Thermag 2018: Poster "3D check board pattern formation of martensite/austenite domains in NiCoMnAl shape memory alloys"
A. Becker, D. Ramermann, M. Gottschalk, I. Ennen, T. Matalla-Wagner, A. Hütten, G. Reiss

Microscopy conference 2019: Poster "3D check board pattern formation in a NiCoMnAl shape memory Heusler alloy thin film system"
D. Ramermann, A. Becker, I. Ennen, B. Büker, M. Gottschalk, A. Hütten

EMAG conference 2020: Talk "On the magnetism of the Heusler Co_2FeSi influenced by adjacent iron layers investigated using DPC"
D. Ramermann, T. Almeida, R. Webster, A. Becker, S. McVitie, A. Hütten

Contents

1 Introduction **11**

2 Methods **13**
2.1 Electron microscopy . . . 13
2.2 Electron diffraction . . . 20
2.3 Electron energy loss spectroscopy (EELS) . . . 20
2.3.1 Electron scattering . . . 21
2.3.2 The inner shell and elemental quantification . . . 24
2.3.3 Measurement of specimen thickness . . . 26
2.4 Electron magnetic chiral dichroism (EMCD) . . . 26
2.5 Differential phase contrast and magnetic imaging . . . 29
2.6 Simulation (EMCD) . . . 33
2.7 Micromagnetic simulations . . . 34
2.8 Sample preparation . . . 36

3 Magnetic characterisation in the electron microscope: Results **39**
3.1 The choice of samples . . . 39
3.2 EMCD measurements on two different electron microscope types . . . 40
3.3 Evaluating EMCD measurements . . . 46
3.4 The thickness dependence of EMCD . . . 52
3.4.1 Simulation of the thickness dependence of EMCD in CoFe . . . 52
3.4.2 Measurement of the thickness dependence of EMCD on CoFe . . . 55
3.4.3 Conclusion for the measurement of the EMCD thickness dependence 61
3.5 Towards characterization of multilayer systems: Fe/Co_2FeSi/Fe . . . 68
3.5.1 Micromagnetic simulations . . . 81
3.5.2 EMCD measurements . . . 87
3.5.3 DPC measurements . . . 93
3.5.4 Conclusions for the Fe/Co_2FeSi/Fe system . . . 119
3.6 Towards characterization of multilayer systems: V/Co_2FeSi/V . . . 120
3.6.1 Micromagnetic simulations . . . 132
3.6.2 DPC measurements . . . 135
3.6.3 Altering of the specimen . . . 138
3.6.4 Conclusions for the V/Co_2FeSi/V system . . . 144
3.7 Towards characterization of multilayer systems: TMR Stack . . . 145
3.7.1 Chemical characterization of the Co_2MnSi/MgO interface . . . 152
3.7.2 Micromagnetic simulations . . . 158
3.7.3 EMCD measurements . . . 161
3.7.4 DPC measurements . . . 163
3.7.5 Conclusions for the TMR Stack . . . 170
3.8 The magnetic proximity effect . . . 171
3.8.1 Possibilities to measure the magnetic proximity effect using electron microscopy . . . 171
3.8.2 Sample design and properties . . . 172
3.8.3 DPC results . . . 180

3.8.4 EMCD results . . . 185
3.8.5 Conclusion for the V/Fe multilayer system with respect to the magnetic proximity effect . . . 189

4 The "Checkerboard"- an extraordinary sample 192
4.1 Structural properties . . . 197
4.1.1 Simulation of the crystal lattice and diffraction images . . . 197
4.1.2 Measurement of the crystal lattice and diffraction images . . . 202
4.1.3 Dark Field TEM . . . 214
4.1.4 Tomography of the checkerboard . . . 216
4.1.5 Stability over time . . . 219
4.2 Chemical properties . . . 223
4.3 Reproduction . . . 229
4.4 Temperature dependence: heating and cooling . . . 232
4.5 Magnetic properties: DPC and EMCD . . . 239
4.5.1 Differential phase contrast measurement of the magnetic properties of the checkerboard . . . 239
4.5.2 EMCD measurements on the checkerboard and comparison samples 245
4.6 Conclusion for the checkerboard . . . 247

5 Summary and Conclusion 249

6 Appendix 251
6.1 Additional information on the CoFe EMCD datasets . . . 251
6.2 Pixelated DPC datasets of the Fe/Co_2FeSi/Fe system . . . 259
6.3 Chemical results of the Fe/Co_2FeSi/Fe interfaces . . . 261
6.4 V/Co_2FeSi/V Peak shift data and Spectrum Image extracts . . . 262
6.4.1 Peak shifts of the overview dataset: . . . 262
6.4.2 Peak shifts of the MgO/V interface region: . . . 265
6.4.3 Peak shifts of the V/Co_2FeSi interface region: . . . 266
6.4.4 Peak shifts of the Co_2FeSi/V interface region: . . . 268
6.4.5 Spectrum image extracts of the interfacial regions . . . 270
6.5 Pixelated DPC datasets of the VCo_2FeSi/V specimen . . . 271
6.6 Thickness estimation of the TMR stack lamella: before and after 2nd thinning 275
6.7 Chemical analysis of the TMR stack . . . 279
6.8 Pixelated DPC of the TMR stack . . . 282
6.9 Additional structural information on the checkerboard . . . 285
6.10 Data of the checkerboard tomography series . . . 287
6.11 Checkerboard contrast plots . . . 293
6.12 Elemental maps of the checkerboard . . . 296
6.13 DM scripts for EMCD evaluation . . . 297
6.13.1 Script for automated EMCD data analysis: . . . 297
6.13.2 Setting the EMCD positions manually, working on front image . . . 307
6.13.3 Shifting one spectrum with respect to the other and calculate the difference . . . 314
6.13.4 Hook-Up Script for EMCD spectrum acquisition . . . 315
6.14 Mumax input scripts for the simulations . . . 315

6.14.1 Mumax input script for Fe/Co_2FeSi/Fe 315
6.14.2 Mumax input script for V/Co_2FeSi/V 316
6.14.3 Mumax input script for the TMR stack 318
6.15 QSTEM model examples 319
6.15.1 CFG file for austenite 319
6.15.2 CFG file for martensite 319
6.15.3 File for use with GBMaker to build a layer sandwich 323

1 Introduction

Magnetic materials have a wide range use in the modern world, from transformators to data storage and beyond. With their increasing use in for example thinfilm-sensor-systems in cars and machines [1] [2], data storage and processing technology [3] [4] and in biological and medical applications like magnetic nanoparticles helping with diagnosis [5] or in cancer therapy [6] they are a building block for modern technology. The requirements for such magnetic materials increase with the complexity of their applications. One class of materials subject to increased interest for various applications are Heusler alloys. Discovered in 1903 for their ability to show magnetic properties while none of the elements in their composition is magnetic the description of this class of materials broadened during the years with their applications [7]. Today full Heusler alloys are defined as a composition X_2YZ with X and Y being transition metals and Z is an element of the III.-V. main group of the elements. Important is that Heusler alloys are expected to be half metallic and able to achieve 100% spin polarization at room temperature and also large magnetic moments due to effects in their electron and spin configuration which makes them highly interesting materials for not only electronical applications but even more for spintronic applications [7].
But also the magnetism of well known materials like iron can still be responsible for interesting effects at very small scales [8] [9]. Investigating magnetism on these small scales is difficult as a certain amount/volume of the sample is needed for most investigation methods. The direct look at the nanoscale is only allowed by techniques based on the interactions of small particles with the sample like electron or ion microscopy.

The transmission electron microscope (TEM) has turned out to be a versatile analytic instrument. It is not only capable of visualizing the atomic structure and measure structural properties of a sample, it can also provide chemical and magnetic information in combination with the high spatial resolution and observe the change of sample properties in-situ. A combination of the possible investigation methods in the TEM can be conducted in the same measurement session and provide a comprehensive characterization the specimen. Therefore the TEM can be established as a tool for sophisticated investigations on (magnetic) materials which can lead to tailored nanomaterials with highly suitable tuned properties for their applications.

This thesis is the attempt to use the possibilities of the TEM including two methods for measuring magnetic properties in greater details: EMCD and DPC.
The specimen are created in a way that information on the small scale behaviour can be obtained in a set of different situations to collect some more puzzle pieces on the magnetic behaviour on Heusler alloys with an emphasis on interfacial properties.
First the EMCD method is evaluated on known samples like CoFe and magnetite to compare the used microscope types and to proof the thickness dependence of this technique. The main part are investigations of layered magnetic thin film samples where the magnetic Heusler Co_2FeSi forms a layer between two magnetic iron layers and two nonmagnetic vanadium layers and the behaviour is investigated with respect to the interfaces and the other chemical, structural and magnetic properties of the sample. More challenging is the following characterization of the TMR stack consisting of the Heusler Co_2MnSi where the atoms that form the interface are of great influence for the electronic and spincaloritronic

properties.
Another small scale influence of importance for the devices that become constantly smaller is the magnetic proximity effect of a neighbouring magnetic material into a nonmagnetic material of a special electron and spin configuration. The presence of such proximity effects is measured on a specially tailored iron/vanadium multilayer sample.

Research is not always working in the known and extending it step by step but also getting surprised by the unexpected and unknown. A shape memory alloy based on the quaternary full Heusler NiCoMnAl shows unexpected and novel structural behaviour - the checkerboard - and is investigated using the many methods the electron microscope can offer. Therefore the journey begins now with the electron microscope.

2 Methods

The investigations in this thesis use mainly electron microscopy to obtain information about the samples. This chapter gives an overview and the theoretical background for the electron microscope and the methods of Electron energy loss Magnetic Chiral Dichroism (EMCD), Differential Phase Contrast (DPC), the related simulation techniques and the sample preparation via sputter deposition and Focused Ion Beam (FIB) devices.

2.1 Electron microscopy

Optical microscopes are limited in their resolution by the wavelength of the light used. Visible light has a wavelength from $\approx 380 - 780$ nm, whereas the wavelength of electrons depends on their (relativistic) momentum:

$$\lambda = \frac{h}{\sqrt{2m_0eV(1 + \frac{eV}{2m_0c^2})}} \tag{2.1}$$

with V potential difference, m electron mass, h Planck´s constant, e electron charge, c velocity of light. After progress in the development of electromagnetic lenses in 1931 Ernst Ruska together with engineer Max Knoll built the first prototype of an electron microscope [10]. The scientific electron microscopes of today are still based on Ruska´s prototype, although many improvements have been made.
Often used acceleration voltages are in the range of $\approx 80 - 300$ keV, for special purposes the whole range of $\mathcal{O}(100$ eV) to $\mathcal{O}(1$ MeV) are used. The microscopes used in this work operate at 200 keV.
The high voltage is generated in a high voltage tank filled with SF_6 gas to prevent flashovers and fed into the electron gun. Modern microscopes have either a (Schottky) field emission gun (FEG) consisting of a tungsten tip coated with zirconium oxide, where thermionic emission into a Wehnelt cylinder (electrostatic lens) gives an already prefocused electron beam, or a cold FEG, where electrons are tunnelling out of a very sharp tungsten tip in a high electric field. The temperature of operation is much lower($\sim$ 1800 K for a FEG, $\sim$ 300 K for a cold FEG) and only the electric field is necessary for the extraction. [11] The cold FEG extracts electrons from an even smaller region of the tip, providing a higher coherence in the beam and better energy resolution.
Leaving the electron gun the electrons are going through an accelerator tube accelerating them to operation energy into the condenser lens system, consisting of two condenser lenses, the condenser apertures and a condenser mini-lens. Below is the goniometer with the specimen holder, the objective lens and mini-lens and it´s aperture and then the selected area aperture. After the objective lens system are several intermediate and projection lenses, the viewing chamber and depending on the given setup a range of detectors and (CCD) cameras, those for bright field detection are installed directly at the bottom. A post column energy filter might be installed, or in the column below the selected area aperture an in-column omega shaped energy filter. The whole microscope setup is on a damping chassis in a room where only very small vibrations, environmental changes and external magnetic or electric fields are present since any of these would have huge effects on the experiments.
The TEM itself can be operated in two main modes: TEM mode and scanning mode. In TEM mode the beam illuminates a certain section of the sample and the magnified

image can be seen on the viewing screen or the camera. The electron can also be treated as a wave, so the image also contains phase information and especially at high resolution simulations recalculating the exit wave are necessary for interpretation of the images. In TEM image mode the the projection system is focused on the first image plane, in TEM diffraction mode it is focused on the back focal plane of the objective lens, making the diffracted image visible in the first image plane. The TEM dark field mode combines both techniques by using an aperture so only the scattered/diffracted electrons contribute to the image, even a selection of some certain diffraction planes is possible by only allowing electrons from the selected diffraction spot through the aperture. In the resulting image only structures containing those diffraction planes are shown bright, everything else including the background is dark.
In scanning mode the beam is focused into a small probe and rastered across the sample using scanning coils. For every point one or more detectors convert the amount of electrons they detect into a signal strength giving one pixel of the resulting image. The focusing into a probe also means scanning transmission electron microscopy (STEM) is a diffraction technique. Several types of detectors are used in scanning mode: the bright field (BF) detector detects the transmitted beam intensity and is sensitive to mass-thickness contrast and diffraction contrast.

Dark field detectors omit the transmitted beam and are in most cases of an annular shape around the beam centre: annular dark field (ADF) and high angle annular dark field (HAADF) detectors, which are more sensitive to contrast obtained from a difference in the atomic number ($\sim Z^2$).

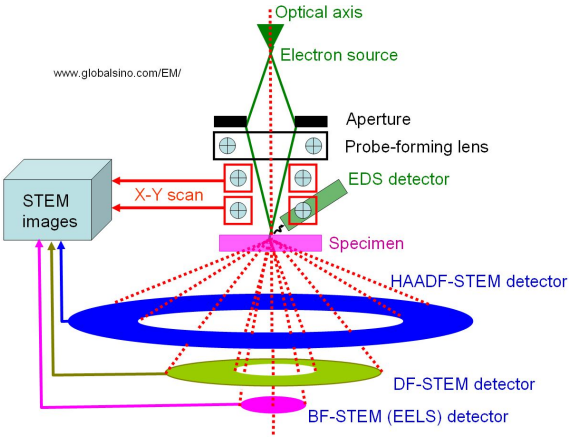

Figure 2: A selection of STEM detectors [13].

Differential phase contrast (DPC) uses segmented detectors to detect beam shifts caused by electric or magnetic fields. Forms arise from dividing the detector in halves, quarters, 8- or 16-fold segmented detectors or pixelated direct electron detectors. The latter are able to detect smaller beam shifts and record the disk of the transmitted beam in full.

The electron beam interacts with the sample also in a way that electrons are knocked out of the atom. Electrons from a higher energy atomic shell fill the gap and emit a X-ray photon with a characteristic energy for this transition. This allows for energy-dispersive X-ray spectroscopy (EDX) measuring the elemental composition of the sample: X-ray photons are detected here with a silicon drift detector containing silicon of very high purity. An incoming photon causes ionization and hence charge, which drifts in a small transversal field towards a collection electrode. In TEM mode the elemental composition of the whole illuminated area is measured, combined with the position information of the scanning mode elemental mappings are possible.

Inelastic scattering of the beam electrons with the sample lead to an element-specific energy loss of the electrons that can also be detected (EELS). Using an electrical prism ($\approx 90°$ bend of a post column or Ω shaped in-colum energy filter) the incident beam is spread with respect to the energy loss of it´s electrons. This method is also sensitive to specimen thickness, phonon and plasmon excitations and even oxidation states and different bound states of a material.

Overview of the TEMs used for this work:

	Jeol JEM-2200FS (Bielefeld)	Jeol ARM200F (Paderborn) ARM200cF (Glasgow)
Acceleration voltage	80-200 kV	30-200 kV (P), 60-200 kV (G)
Gun	ZrO/W(100) Schottky FEG	Cold FEG
Aberration correction	—	ASCOR Cs corrector up to 5th order
TEM point resolution (200 kV)	0.23 nm	0.19 nm
STEM point resolution (200 kV)		0.08 nm
Energy resolution	$\leq$ 0.80 eV FWHM (ZLP)	$\leq$ 0.30 eV FWHM (ZLP)
Pole piece	HR	UHR
Camera	Gatan OneView 4k $\times$ 4k CMOS	Gatan OneView 4k $\times$ 4k CMOS
Energy Filter	In-column Filter EFTEM in TEM mode	Post-column Gatan GIF Quantum ER [14] Dual EELS + EFTEM
EDS	Jeol SDD (60 mm^2) STEM EDX map possible (JEOL)	Jeol SDD (60 mm^2) Gatan DigiScan EELS+EDX map
STEM detectors	BF, DF	BF, ABF, DF, HAADF
Magnetic TEM	LowMag Lorentz mode ($\leq$ 50) k mag	Lorentz lens (Glasgow)
Magnetic STEM	—	8 segment DPC detector (Paderborn) 8 segment DPC detector (Glasgow) Medipix Merlin3 256 $\times$ 256 pixelated direct electron detector (Glasgow) Lorentz STEM mode (Glasgow)
Sample holders	Single tilt older Analytic double tilt holder Tomography holder Cryo-transfer system & holder by Fischione Heating holder(up to 1000° C)	Single tilt holder Analytic double tilt holder Wide-angle holder

Table 1: Overview of the electron microscopes used for this work [12] [15].

The electron microscope provides the environment to bring the electrons in a state where they can act as probes to investigate materials in various ways by their multiple possible interactions. These possible interactions of an electron with the specimen are the following:
Backscattered electrons collide with an atom of the specimen and are scattered elastically at about 180° angles. *Secondary electrons* are produced when incident beam electrons get close enough to transfer a small part of their energy to a specimen-atom-electron, which gets ionized and its electron leaves with a very small kinetic energy ($\sim$ 5 eV) and is called

secondary electron. One incident electron can cause many secondary electrons as there is only a very low energy loss and path change. *Auger electrons* occur if the incident beam electron excites an atom and instead of emitting an x-ray the atom emits an electron, the Auger electron. Its energy is characteristic for the transition and therefore for the element and allows chemical analysis of the surface as the mean free path of Auger electrons is very short. *Characteristic x-rays* are emitted when an excited core shell state in the specimen de-excites by emitting the energy difference to the lower state as an x-ray photon. These photons are characteristic for the element and allow chemical analysis. *Bremsstrahlung* originates from inelastic scattering of a beam electron leading to the emission of an x-ray photon. The energy spectrum of these photons is continuous up to the beam energy. *Light* that contains the *visible spectrum* is mostly emitted from transitions between energy states within or between the free electron and valence band. This is called cathodoluminescence. Also the sample is *heated* by the electron beam caused by energy transfer via scattering.
Most important for TEM analyses are elastic and inelastic scattering. Most of the beam electrons will pass the specimen without losing energy. *Elastic scattering* in the TEM takes the form of Rutherford scattering, where the incident beam electron interacts with the coulomb potential of the specimen´s atoms: nuclei and electrons.
Inelastic scattering leads to an energy loss of the beam electron, which is used to excite specimen electrons to higher energy states. The energy needed for such a transition depends on the element and the specific transition, this makes chemical analysis possible via collecting the energy loss spectrum.
Important in the TEM are only the following three types of interactions: Characteristic x-rays (EDX), elastic (diffraction techniques) and inelastic (energy loss spectroscopy) interactions, the others, like cathodoluminescence for example, are used in very specialized instruments.
It is important to note that the interactions of the beam with the specimen take place in the *electron interaction volume*, the size of it is increasing with the incident beam energy, decreasing as a function of atomic weight and the shape and symmetry is depending on the tilt of the specimen [17]. A schematic view of the interaction volume is shown in fig. 4.

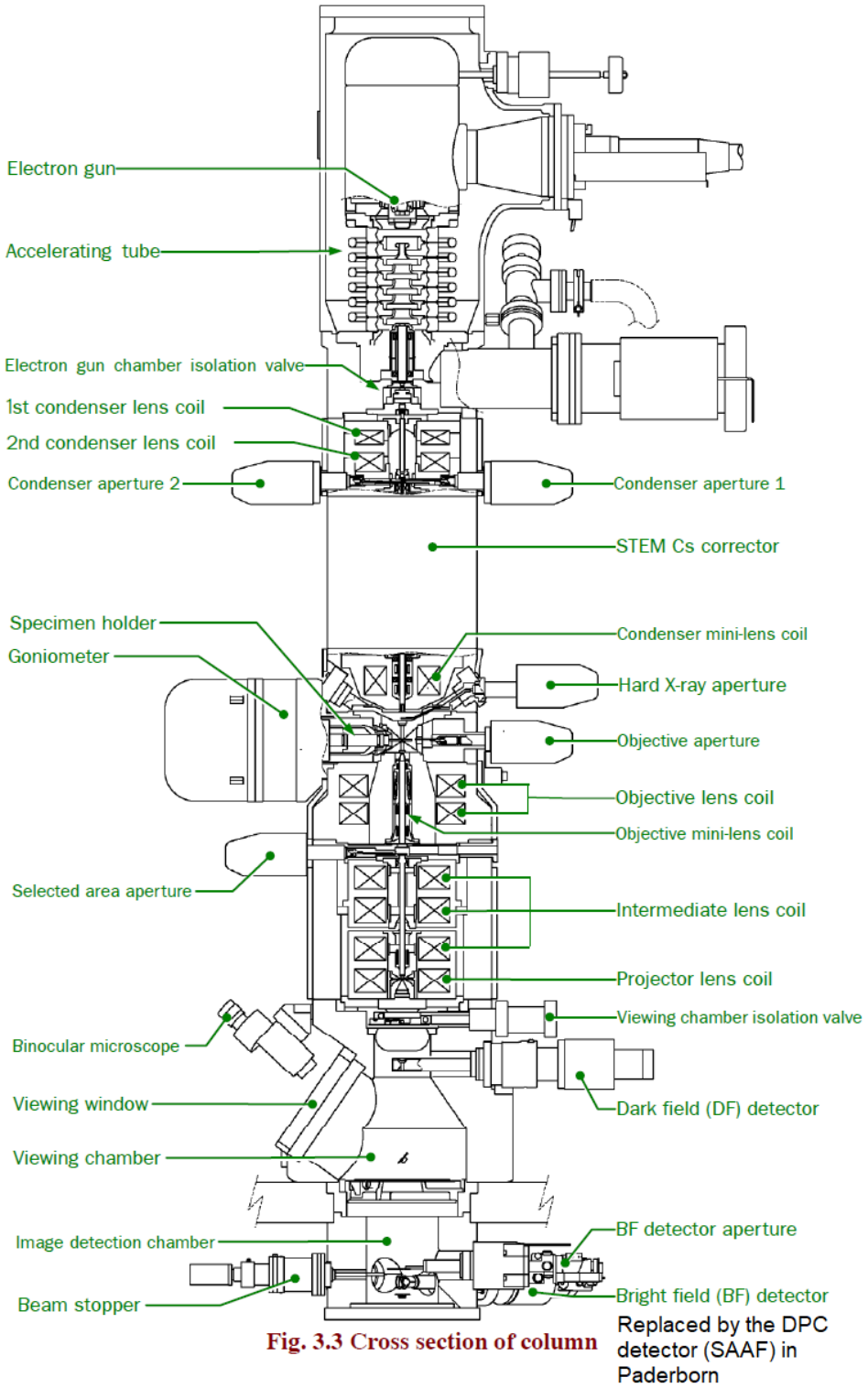

Figure 1: Schematic drawing of the Jeol JEM ARM200F representing the most-used type of TEM in this thesis. The post-column filter is not shown here. [12] with black annotations added by the author of this thesis.

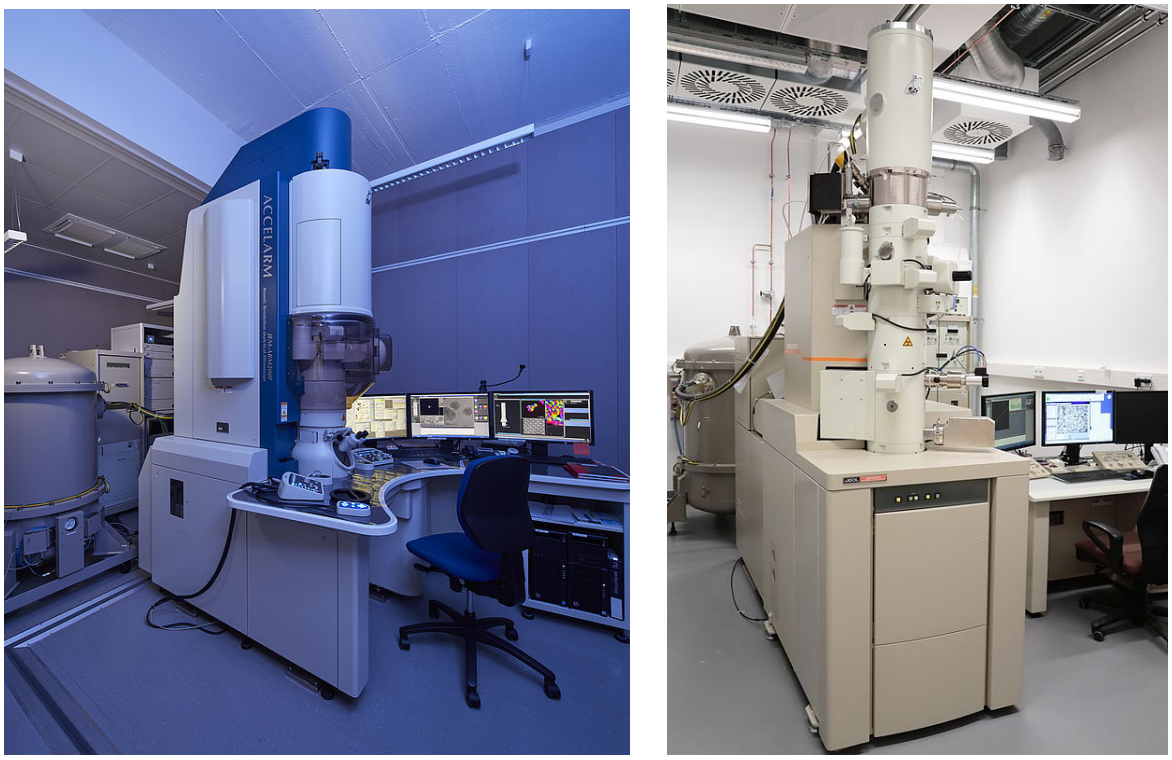

Figure 3: The used analytical transmission electron microscopes Jeol ARM 200F (Paderborn, left) [16] and the Jeol JEM-2200FS (Bielefeld, right).

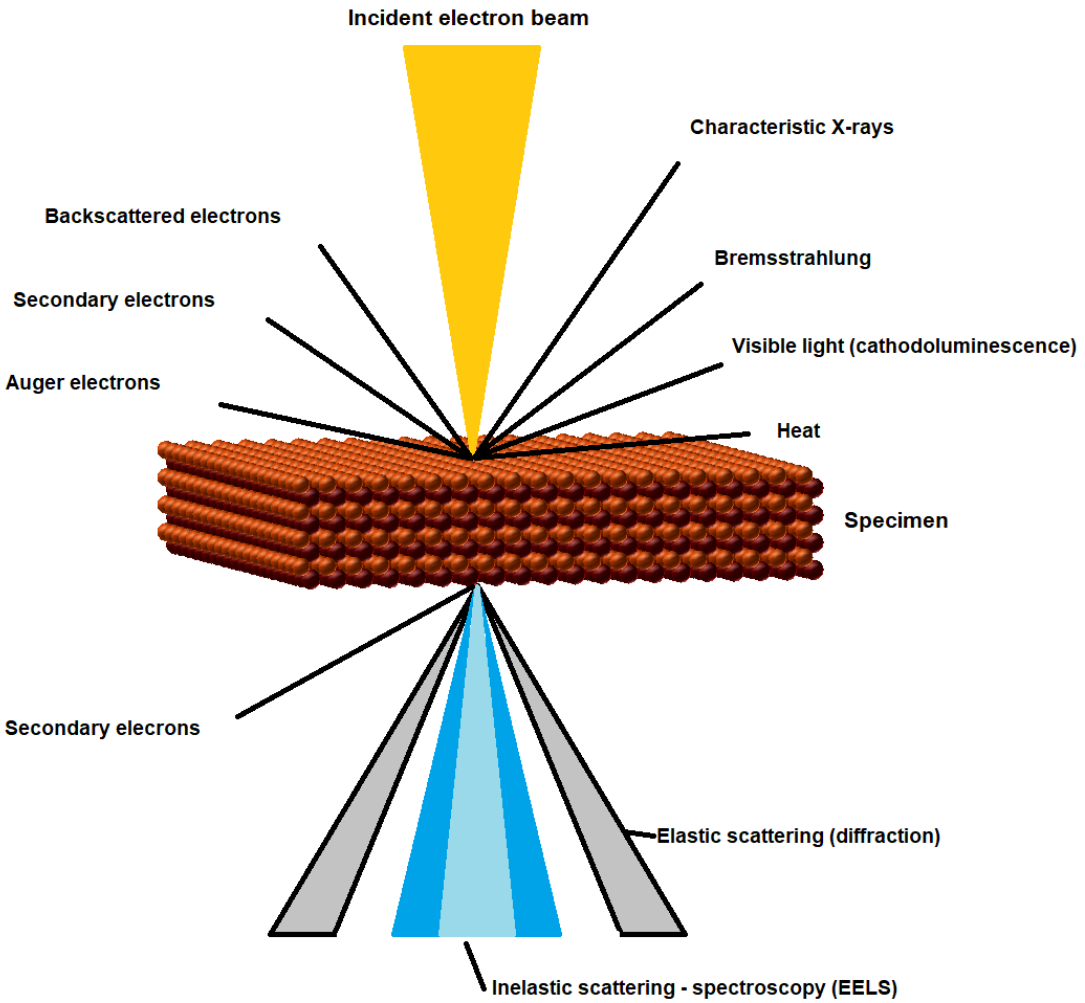

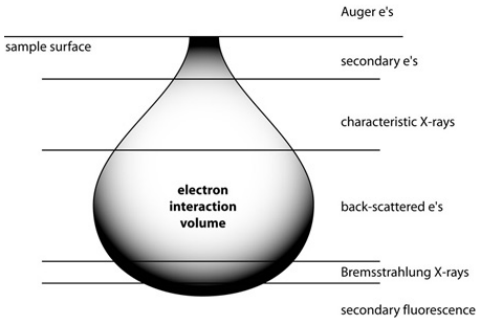

Figure 4: Electron-specimen interactions, based on [18], below a schematic of the interqaction volume taken from [17].

2.2 Electron diffraction

Diffraction on a crystal lattice is subject of Bragg´s law:

$$n \cdot \lambda = 2d \sin \Theta_B \tag{2.2}$$

with d the distance between the lattice planes, Θ_B the Bragg angle for constructive interference, n an integer number and the wavelength λ can be assigned according to eq. 2.1 because electrons can be treated as particles and as waves. Rewriting Bragg´s law as

$$\frac{2 \sin \Theta_B}{\lambda} = \frac{n}{d} = |\mathbf{K}|$$

gives the vector $\mathbf{K}$ that is reciprocally related to the distance d. This leads to the definition of the reciprocal lattice [19]: A lattice vector is defined as

$$\mathbf{r}_n = n_1\mathbf{a} + n_2\mathbf{b} + n_3\mathbf{c} \tag{2.3}$$

with n_i integers and the vectors $\mathbf{a}, \mathbf{b}, \mathbf{c}$ representing translations of the unit cell in real space. A vector of the reciprocal lattice can therefore be defined as

$$\mathbf{r}^* = m_1\mathbf{a}^* + m_2\mathbf{b}^* + m_3\mathbf{c}^* \tag{2.4}$$

with m_i again integers and $\mathbf{a}^*, \mathbf{b}^*, \mathbf{c}^*$ unit cell translations in reciprocal space. The relation

$$\mathbf{a}^* \cdot \mathbf{a} = \mathbf{b}^* \cdot \mathbf{b} = \mathbf{c}^* \cdot \mathbf{c} = 1 \tag{2.5}$$

where $\cdot$ denotes the scalar product defines the length of these vectors.
The vector $\mathbf{g}_{hkl} = h\mathbf{a}^* + k\mathbf{b}^* + l\mathbf{c}^*$ is the vector normal to the plane (hkl) that cuts the a, b and c axes at $1/a$, $1/b$ and $1/c$ with the hkl values being integers and called the Miller indices.
The Laue condition is an alternative formulation of the Bragg condition to describe diffraction on crystals in terms of the reciprocal lattice. It reads: Constructive interference is given only if the change of the wave-vector corresponds to a reciprocal lattice vector

$$\mathbf{k} - \mathbf{k}' = \mathbf{K} \quad \Leftrightarrow \quad \Delta\mathbf{k} = \mathbf{K} \tag{2.6}$$

with $\mathbf{k}$ vector of the incident wave, $\mathbf{k}'$ vector of the scattered wave and $\mathbf{K}$ the reciprocal lattice vector. The Ewald sphere construction (fig.5) shows the Laue condition: The radius of the Ewald sphere is $1/\lambda$, only where a reciprocal lattice point lies on the sphere the condition for diffraction is fulfilled. The other sphere with radius $2/\lambda$ marks the limit for vectors fulfilling the Laue condition, vectors outside the circle cannot lead to diffraction.

2.3 Electron energy loss spectroscopy (EELS)

Electron energy loss spectroscopy (EELS) uses the energy loss the beam electrons undergo in scattering to obtain information about the chemical properties of the specimen, among these are the type and quantity and information about the bonding of the atoms present.

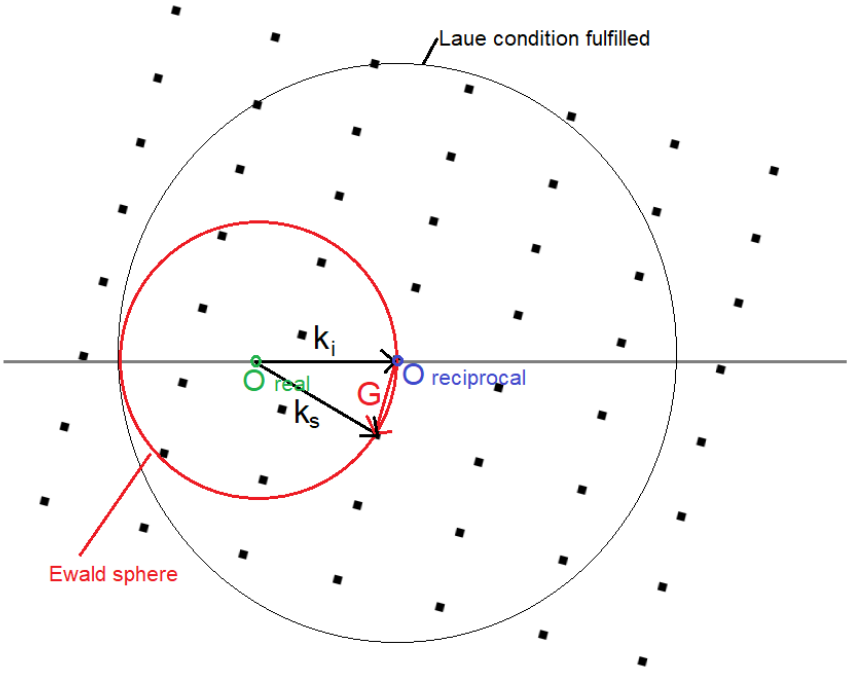

Figure 5: Ewald sphere construction, the Ewald sphere is shown in red, the part of the reciprocal lattice where the Laue condition is fulfilled shown by the black circle. Three points of the reciprocal lattice are on or nearly on the Ewald sphere and take part in diffraction.

2.3.1 Electron scattering

Elastic scattering means any energy loss to the specimen can not be detected experimentally [20], which means for the electron microscope, where the energy resolution is ~ 0.1 eV every effect with an energy range below this threshold will be treated as elastic.
EELS results of interactions of the electron beam with the specimen atoms on the Coulomb potential of the atoms. Electron repopulation leads to emittance of a characteristic X-ray photon which is collected in EDX measurements, this is a secondary decay event. EELS is the primary event and yields the highest amount of information [21]. The incident beam electrons are relativistic, therefore the Dirac equation describes the interaction including a term for the electromagnetic interaction

$$(i\gamma^{\mu} - m)\psi x = \frac{e}{\hbar c} A(x)\psi(x) \tag{2.7}$$

with i the imaginary unit, m the mass, e the electron charge, c the speed of light, $\hbar = h/2\pi$ the reduced Planck constant. Treating the potential $A^{\mu}\gamma_{\mu}$ according to classical physics the solution reads

$$\psi(x) = \psi_0(x) + \frac{e}{\hbar c} \int d^4y S_F(x-y) A(y)\psi(y) \tag{2.8}$$

with ψ_0 the free solution and $S_F(x-x')$ the Feynman propagator. In the lowest order the S-matrix reads

$$S_{\mathrm{fi}} = \delta_{\mathrm{fi}} - \frac{ie}{\hbar c}\int d^4\bar{x}\psi_{\mathrm{f}}(x)A(x)\psi_{\mathrm{i}}(x) \tag{2.9}$$

where i denotes the initial state and f the final state. For a Coulomb potential $A_0(x) = -\frac{Ze}{4\pi} \mid x \mid$ the Integration can be carried out, for obtaining a physical value the square of the final state $\mid S_{\mathrm{fi}} \mid^2$ leads to the Mott cross section formula

$$\frac{d\sigma}{d\Omega} = \left(\frac{ZZ'e^2}{4\pi\varepsilon_0}\right)^2 \cdot \frac{E^2}{(qc)^4} \cdot [1-\beta^2\sin^2(\theta/2)] \tag{2.10}$$

with θ the angle between the momentum of the ingoing particle and the outgoing particle and $\beta = v/c$ the relation of the velocity v to the velocity of light c, Ze and $Z'e$ the charges of particle and scattering center, ε_0 the vacuum permeability, $E^2 = (pc)^2 + (mc^2)^2$ the relativistic total energy, p the momentum, $q = 2\gamma mv\sin(\theta/s)$ the momentum transfer with γ the Lorentz factor. $\frac{d\sigma}{d\Omega}$ is the differential cross section, a quantity describing the probability of being scattered for a particle by the scattering center which is here the electron from the incident beam with a specimen atom.
For $\beta \to 0$ the Mott scattering formula translates into the Rutherford scattering formula which describes the interaction of charged particles on a charged scattering center for nonrelativistic particles:

$$\frac{d\sigma}{d\Omega} = \left(\frac{1}{4\pi\varepsilon_0}\frac{ZZ'e^2}{4E_0}\right)^2 \frac{1}{\sin^4(\theta/2)} \tag{2.11}$$

The Rutherford model works well for lighter elements at large scattering angles but at small scattering angles the scattering is overestimated, integration over all angles results in an indefinite cross section [20] which does not work with the probability interpretation of the cross section. Introducing screening effects on the nuclear field caused by the electron shell by a Wentzel/Yukawa ansatz with a nucleus potential dependent from the distance from the nucleus like

$$\phi(r) = \frac{Ze}{4\pi\varepsilon_0 r} \cdot \exp(-\frac{r}{r_0}) \tag{2.12}$$

with r_0 the screening radius, which has been estimated to $r_0 = a_0 Z^{-1/3}$ by Lenz [22]. The atomic potential is the important part to achieve greater accuracy of the description which methods like Hartree-Fock and Hartree-Slater, the Dirac based Mott cross sections, the Born approximation for $Z < 137$ and partial wave approaches provide [20].
Diffraction effects in elastic scattering occur because the waves are scattered on a regular lattice of atoms. The phase difference between waves is considered by the introduction of a structure factor $F(\Theta)$ [20]

$$F(\Theta) = \sum_j f_j(\Theta)\exp(i\mathbf{q}\cdot\mathbf{r}_j) \tag{2.13}$$

r_j the coordinate and f_j the scattering amplitude of atom j with the sum carried out over all atoms j, $\mathbf{q}\cdot\mathbf{r}_j$ the phase factor. Rewriting the sum in leads to

$$F(\Theta) \propto \int V(r)\exp(-\mathbf{q}\cdot\mathbf{r})d\tau \tag{2.14}$$

which shows the relation of the structure factor to the Fourier transform of the lattice potential. "The intensity scattered in a direction Θ relative to the incident beam is $|F(\Theta)|^2$ and peaks at values of Θ for which the scattered waves are in phase with one another." [20] Also reflection can occur from atomic planes of the spacing d depending on the unit cell structure, Bragg reflection occurs for an angle between the incident and the diffracted beam corresponding to a Bragg angle Θ_B defined by eq. 2.2.

Inelastic scattering causes shell electrons to be excited into higher energy states where the angle dependence has been modelled in an atomic model approach by Lenz to

$$\frac{d\sigma_i}{d\Omega} = \frac{4\gamma^2 Z}{a_0^2 q^4}\Big\{1 - \frac{1}{[1+(qr_0)^2]^2}\Big\} \tag{2.15}$$

with the approximation $q^2 = k_0^2(\Theta + \bar{\Theta}_E^2)$. In eq.2.15 the first term is the Rutherford cross section and the second part an inelastic form factor [20].
The Bethe theory approach describes inelastic scattering of electrons by an atom via describing every shell electron by a transition between the wavefunctions from the initial state ψ_0 to the final state ψ_n. The cross section is given using the first order Born approximation which is the lowest order term in perturbation theory. The differential cross section is given by

$$\frac{d\sigma_n}{d\Omega} = \left(\frac{4\gamma^2}{a_0^2 q^4}\right)\frac{k_1}{k_0} \mid \varepsilon_n(q) \mid^2 \tag{2.16}$$

with the first term again the Rutherford cross section, the second term based on the wavevectors of the incident electron before ($\mathbf{k}_0$) and after scattering ($\mathbf{k}_1$) and the third term is the inelastic form factor, "the square of the absolute value of a transition matrix element defined by" [20]

$$\varepsilon_n = \int \Psi_n^* \sum_j \exp(i\mathbf{q}\cdot\mathbf{r}_j)\Psi_0 d\tau = \left\langle \Psi_n \left| \sum_j \exp(i\mathbf{q}\cdot\mathbf{r}_j) \right| \Psi_0 \right\rangle \tag{2.17}$$

The energy dependence of scattering in combination with the angular dependence are described by a double-differential cross section

$$\frac{d^2\sigma}{d\Omega dE} = \frac{4\gamma^2 R}{Eq^2}\frac{k_1}{k_0}\frac{df}{dE}(q,E) \tag{2.18}$$

where for the angular dependence a relation between the scattering vector q and the scattering angle Θ needs to be established. Approximating $\mathbf{q}$ by the components $k_0\Theta$ and $k_0\Theta_E$ gives $q^2 \approx k_0^2(\Theta^2 + \Theta_E^2)$ so the double-differential cross section reads now

$$\frac{d^2\sigma}{d\Omega dE} \approx \frac{4\gamma^2 R}{Ek_0^2}\left(\frac{1}{\Theta^2+\Theta_E^2}\right)\frac{df}{dE} = \frac{8a_0^2R^2}{Em_0v^2}\left(\frac{1}{\Theta^2+\Theta_E^2}\right)\frac{df}{dE} \tag{2.19}$$

The Bethe theory describes process originating from inner shells well, for outer shell scattering the chemical bonds play also a role, this can be described by treating the scattered electron and the solid by a dielectric response function description [20]. A comprehensive description of scattering effects in EELS and their descriptions can be found in [20].

2.3.2 The inner shell and elemental quantification

In EELS spectroscopy of the inner shell gives access to information about "the empty local density of states above the Fermi level" [21] for each investigated atomic species, which also affects the shape of the edge [21]. Discrete inner shell states are excited into states above the Fermi level, the energy loss of the incident electrons is recorded into a spectrum which shows mostly discrete peaks for the atomic species of the specimen.
Plural scattering in the specimen occurs if the beam electrons scatter more than once while crossing the specimen, this leads to an added and shifted energy loss and therefore needs consideration. The probability of plural scattering is more likely if the specimen thickness exceeds the mean free path in the material, therefore a thickness (far) below 1 mfp is desirable for eels measurements. The presence of plural scattering leads to a signature in the low loss region and also on every elemental edge that needs to be treated by deconvolution before further processing.
The shape of the elemental edges follow rules of thumb, where K-shell edges are of hydrogenic shape, L-shell edges show are rounded to hydrogenic shape with "white lines" at onset, M-shell edges show a delayed onset, N- and O-shells vary in shape but appear as a kind of peak [21] (fig.6). Near the edge onset a fine structure of the edge can be

Figure 6 **Schematic illustration of K, L, M, N and O edge shapes; the "white lines" sometimes detected on L and M shells are shown as shaded peaks at the edge onsets. In all sketches the background shape has been omitted for clarity.**

Figure 6: Schematic drawing of the edge shapes taken from [21].

observed (ELNES) which results from solid state effects and can give information about the chemical state and other solid state properties [23] [24] [25].

For elemental quantification the integral of the edge needs to be measured. The background of the edge has to be subtracted with a suitable background model, common is a power law for the background $J(E) = Ae^{-r}$ with A the scaling constant and r the exponent determining the behaviour of the slope. The fit window for the background subtraction needs to be placed before the edge onset without overlapping with other edges. If edges overlap, a deconvolution method is necessary [20]. Other models are 2nd order polynomial, 1st order log-polynomial or atan-based models.
The integral of the background subtracted edge is corresponding "to the number of electrons which have lost energy due to the excitation of that particular shell" [21]. This is an intensity I_k which results from the incident electron beam intensity I_0(measurable by the

integral of the zero loss peak) by

$$I_k = I_0(t/\lambda_k) = NI_0\sigma_k \tag{2.20}$$

with N the number of atoms per unit area, σ_k the cross section for ionization of the $k-$th edge and λ_k the mean free path for the scattering event. In a microscope the recording of the scattering is limited by an angle β, also the energy range Δ that can be recorded is limited. Therefore the integral of the core-loss edge reads

$$I_k^1(\beta, \Delta) = NI_0\sigma_k(\beta, \Delta) \tag{2.21}$$

with $\sigma_k(\beta, \Delta)$ a partial cross section in dependence of β and Δ that can be obtained from measurements or calculated using a suitable model. If the integral covers a large enough energy window including a significant part of the fine structure oscillations the cross section can be calculated using an atomic model or for better accuracy the Hartree-Slater method based on molecular orbital calculations can be used [26].
Eq. 2.21 is valid only approximately when elastic scattering and plasmon excitation are included. The core loss integral including these effects and plural scattering reads

$$I_k(\beta, \Delta) \approx NI(\beta, \Delta)\sigma_k(\beta, \Delta) \tag{2.22}$$

with the low-loss intensity $I(\beta, \Delta)$ integrated up to the threshold energy loss Δ.
The atomic ratio of two elements is then given by

$$\frac{N_a}{N_b} = \frac{I_{ka}(\beta, \Delta)}{I_{jb}(\beta, \Delta)} \frac{\sigma_{jb}(\beta, \Delta)}{\sigma_{ka}(\beta, \Delta)} \tag{2.23}$$

It is possible to use edges of different shell index but for a similar edge shape the plural scattering effects are more comparable which leads to smaller deviation. Removing plural scattering by deconvolution allows the use of

$$\frac{N_a}{N_b} = \frac{I^l_{ka}(\beta, \Delta_a)}{I^l_{jb}(\beta, \Delta_b)} \frac{\sigma_{jb}(\beta, \Delta_b)}{\sigma_{ka}(\beta, \Delta_a)} \tag{2.24}$$

which allows to use a different energy window $\Delta_a \neq \Delta_b$ for each edge [20].

The Gatan GMS software used for evaluation in this work uses an approach based on MLS fitting [20]: Multiple least squares fitting is used to improve the result in cases where the background extrapolation fails for noisy data, weak core loss edges barely above the background and very close edges. The procedure of fitting takes into account both the background and the ionization edge(s) by fitting the total spectral intensity to an expression of the form

$$F(E) = Ae^{-r} + \sum\nolimits_n B_n S_n(E) \tag{2.25}$$

with the first term taking care of the background on a pre-edge window, $S_n(E)$ correspond to reference spectra for the core-loss of the element of interest which can be obtained from external standards or from data of the analysed sample using the Mendis method [27] and B_n are the coefficients resulting from minimizing $\sum_i (J_i - F_i)^2$ for i the data channels [28] [29] or resulting from a maximum likelihood estimation [30].

For quantification the coefficients B_n are used to derive atomic ratios of the elements, the $S_i(E)$ is measured for each element from a standard specimen and the atomic ratio of two elements a and b are calculated

$$\frac{N_a}{N_b} = \frac{B_a}{B_b} \frac{I_{ka}(\beta, \Delta)}{I_{kb}(\beta, \Delta)} \frac{\sigma_{kb}(\beta, \Delta)}{\sigma_{ka}(\beta, \Delta)} \tag{2.26}$$

with $I_{ka}(\beta, \Delta)$ and $I_{kb}(\beta, \Delta)$ integrals of the standard core-loss spectra, $\sigma_{ka}(\beta, \Delta)$ and $\sigma_{kb}(\beta, \Delta)$ partial cross sections depending on the collection angle β [20].
Improvements by Gatan engineers [31] split the spectrum in sub-regions containing a core-loss edge or overlapping edges and for every sub-region a multiple linear least squares fit is performed with a single background computed together with calculated or experimental cross-sections. Also the ELNES is determined and the region results are combined for an overall quantification.

2.3.3 Measurement of specimen thickness

The most common method is the log-ratio method where a low-loss spectrum is recorded. The integral of the zero-loss peak I_0 is compared to the total integral of the spectrum I_t. The thickness t is obtained by using the Poisson statistics of inelastic scattering

$$t/\lambda = -\ln \frac{I_0}{I_t} = \ln \frac{I_t}{I_0} \tag{2.27}$$

with t/λ the mean free path [20].
In the case of EFTEM it can be considered as recording a spectrum on every pixel of the image and selecting the zero-loss by the slit in the energy filter which is adjusted so only the zero-loss part can pass and two images are recorded: The unfiltered image and the elastic image that contains only the zero-loss part. Then I_0 is the filtered intensity and I_t the total (unfiltered) intensity.
For an accurate thickness estimation the integration limits have to be set carefully, the zero loss can be separated on the left anywhere where the signal approaches zero and on the right on the first minimum, the total spectrum has to be recorded until an energy when the contribution becomes negligible, which extends to higher energies for specimen containing heavier elements, also an extrapolation is possible [20]. The accuracy is $\approx 10\%$. Especially for a strongly limiting aperture ($\beta < 20$ mrad) the calculated mean free path can only be considered as an effective mean free path $\lambda(\beta)$ because electrons of higher scattering angles are removed from the spectrum [20].
The background arising from the instrumentation has to be subtracted from the data before processing, in the case of a CCD camera a dark image of the same exposure is acquired and subtracted automatically after the acquisition [20].
If the thickness in mean free path (mfp) is measured, the mean free path of the electrons in the specific material has to be determined to obtain the absolute thickness. A variety of methods and lists of materials exist [20], used in this work is mainly the Malis method [32].

2.4 Electron magnetic chiral dichroism (EMCD)

EMCD has been proposed by Schattschneider in 2003 as an analogon to XMCD [33] [34], which needs a synchrotron to measure, in a standard TEM [35]. A TEM is more common

and accessible and it has the advantage of a higher possible resolution, enabling the possibility for magnetic measurements up to the nanometer scale [36] or even atomic resolution [37].
Dichroism is the dependence of the absorption behaviour of a material on the polarization of the incoming photon in interaction with the anisotropic electronic structure which can exist naturally in a material or can be induced magnetically, with circular dichroism being the dependence on the helicity of the photon.
The EMCD effect can be described in the following way: An electron-induced virtual photon excites a core electron to an empty state above the Fermi level (EELS). In this interaction of photon and electron the symmetry is broken by magnetism, this depends on the helicity of the photon. The corresponding X-ray pendant XMCD is measured in large synchrotron facilities where the polarization of the X-rays can be controlled. In the TEM the electron gun (field emission gun) emits coherent electrons, but in interaction with the lattice of a crystalline specimen the electrons become chiral, so the specimen itself is acting as a beam splitter [38] and kind of sorts the electrons to left handed and right handed ones. Elastic scattering leads to diffraction, and in the diffraction plane EELS spectra are recorded on positions where electrons of different chirality arrive, the EMCD detector positions. If the magnetic moment of the specimen has broken the symmetry between the different chiralities these spectra are not equal anymore and the difference shows a dichroic effect. This allows access to the spin to orbit magnetic moment of an element in the specimen by use of the theoretical approach via sum rules in the evaluation [39].

EMCD can be described by using an analogon to XMCD - starting with the similarity between the near edge structures of XANES and ELNES [40]: The double differential cross section for ELNES is given by

$$\frac{\partial^2\sigma}{\partial E\partial\Omega} \propto \sum_{i,f} \frac{1}{q^2} \left|\langle f \left|\vec{\varepsilon_q} \cdot \vec{R}\right| i\rangle\right|^2 \delta(E_i - E_f + E) \tag{2.28}$$

where $\vec{\varepsilon_q} = \vec{q}/q$ and $\vec{q} = \mathbf{q} = \mathbf{k} - \mathbf{k}'$ the wave vector transfer, $\vec{R}$ the quantum mechanical position operator, $|i\rangle$ and $|f\rangle$ the electron initial and final state with their energies E_i and E_f.
In the XMCD case it is the XANES absorption cross section

$$\sigma \propto \omega \sum_{i,f} \left|\langle f \left|\vec{\varepsilon} \cdot \vec{R}\right| i\rangle\right|^2 \delta(E_i - E_f + E) \tag{2.29}$$

with ω the photon radial frequency and $\vec{\varepsilon}$ the polarization vector, which is formally equivalent to the inelastic electron scattering direction of momentum transfer $\vec{\varepsilon_q}$. In both cases an electric field $\vec{E}$ influences the electrons of the specimen atom: in the X-ray case the oscillating field of the photon and in the electron case the electric field of the electrically charged electron.
The electric field of a circularly polarized photon has a polarization vector $\vec{\varepsilon} \pm i \cdot \vec{\varepsilon}'$ ($\vec{\varepsilon} \perp \vec{\varepsilon}'$) and the electron pendant is the momentum transfer $\vec{q} + i \cdot \vec{q}'$ ($\vec{q} \perp \vec{q}'$). In the photon case i corresponds to a phase shift of $\pm\pi/2$ between the two perpendicular polarization states, in the electron case i corresponds to a phase shift of $\pm\pi/2$ between the perpendicular electron field components so the electron plane waves are shifted by $\pm\lambda/4$ corresponding to a phase difference of $\pm k\lambda/4 = \pm\pi/2$.

To excite an electron from a ground state (assumption: s to p state) into an excited state the frequency of the rotating electric field in the photon will be the resonance frequency corresponding to the excited state. The final p state can be described by $|l = 1, m = \pm 1\rangle$ which describes the orbital of a rotating final state with $\Delta m = \pm 1$. Introducing time dependence gives $\Psi \propto e^{i\omega t} e^{\pm\phi} = e^{i(\omega t \pm \phi)}$, a wave function where ϕ is a spherical coordinate system the azimuthal angle corresponding to a propagating wave in the angle ϕ.
The electron counterpart of the chiral transitions are described by the mixed dynamic form factor (MDFF) in inelastic electron scattering, which can be defined as

$$S(\vec{q}, \vec{q}', E) = \sum_{i,f} \langle f \left| \vec{q} \cdot \vec{R} \right| i \rangle \langle i \left| \vec{q}' \cdot \vec{R} \right| f \rangle \delta(E_i - E_f + E) \tag{2.30}$$

which reduces to the general dynamic form factor (DFF) $S(\vec{q}, E)$ for $\vec{q} = \vec{q}'$:

$$S(\vec{q}, \vec{q}', E) = \sum_{i,f} \left| \langle f \left| \vec{q} \cdot \vec{R} \right| i \rangle \right|^2 \delta(E_i - E_f + E) \tag{2.31}$$

For a momentum transfer $\vec{q} + i\vec{q}'$ follows for the cross section

$$\sigma^{\pm} := \frac{\partial^2 \sigma}{\partial E \partial \Omega} \propto \left(\frac{1}{q^4} S(\vec{q}, E) + \frac{1}{q'4} S(\vec{q}', E) \mp \frac{1}{q^2 q'2} 2\Im[S(\vec{q}, \vec{q}', E)] \right) \tag{2.32}$$

with $2\Im[S(\vec{q}, \vec{q}', E)] \propto \vec{q} \times \vec{q}'$ [35] [40] The last term is proportional to the vector product of $\vec{q}$ and $\vec{q}'$ and therefore is dependent on the helicity of the excitation. It is an interference term that would vanish if the two electron waves would be treated separately.
"The dichroic signal is defined as the spectral difference observable when the helicity is reversed." [40] A measurement of the dichroic signal needs two measurements with each using one of the two signs in eq. 2.32, by subtracting one measurement from the other the first terms cancel and only the interference term contributes. The percentage of the average dichroic signal is given by

$$\frac{\Delta\sigma}{\sigma} := 2 \cdot \frac{\sigma^+ - \sigma^-}{\sigma^+ + \sigma^-} \tag{2.33}$$

of which a variation has been used in this thesis.

The denoted approach is intended to give the idea of EMCD, detailed calculations can be found in [41] and [42]. The thickness dependence of the dichroic signal results from a thickness and eigenvalue dependent function in the more detailed final expression of the double differential scattering cross section [41]

$$\frac{\partial^2 \sigma}{\partial E \partial \Omega} = \sum_{\mathbf{ghg'h'}} \frac{1}{N_{\mathbf{u}}} \sum_{\mathbf{u}} \frac{S_{\mathbf{u}}(\mathbf{q}, \mathbf{q}', E)}{q^2 q'^2} e^{i(\mathbf{q}-\mathbf{q}')\cdot\mathbf{u}} \times \sum_{jlj'l'} Y^{jlj'l'}_{\mathbf{ghg'h'}} T_{jlj'l'}(t) \tag{2.34}$$

$$Y^{jlj'l'}_{\mathbf{ghg'h'}} = C^{(j)*}_{\mathbf{g}} C^{(j)}_{\mathbf{0}} D^{(l)}_{\mathbf{0}} D^{(l)*}_{\mathbf{h}} \times C^{(j')}_{\mathbf{0}} C^{(j')*}_{\mathbf{g'}} D^{(l')}_{\mathbf{0}} D^{(l')*}_{\mathbf{h'}} \tag{2.35}$$

With the function $T_{jlj'l'}(t)$ the thickness and eigenvalue dependent function corresponding to the Pendellösung:

$$T_{jlj'l'}(t) = e^{i[(\gamma^{(j)} - \gamma^{(j')}) + (\gamma^{(l)} - \gamma^{(l')}]\frac{t}{2}} \frac{\sin \Delta \frac{t}{2}}{\Delta \frac{t}{2}} \tag{2.36}$$

the $\frac{\sin x}{x}$ part corresponds to the Pendellösung and thickness t and the previous terms are a modulation depending on the eigenvalues.
The Pendellösung appears in the dynamical theory of diffraction where multiple scattering effects are considered. The thickness plays a role in how often the primary diffracted beam is scattered and again the scattered beams, which can lead up to extinction. In the simplest case, an ideal two beam case [20] intensity is shifted between the forward diffracted beam and the Bragg diffracted beam intensity because the Bragg diffracted beam also fulfils the Bragg condition and from it intensity is shifted away and back into the primary forward diffracted beam, the intensity goes between the beams like a pendulum, a "Pendel". The intensity result depends on where series of interchanging diffraction ends and this affects EMCD since it works with different scattering vectors corresponding to selected diffracted beams. In TEM images the Pendellösung appears as intensity fringes.

2.5 Differential phase contrast and magnetic imaging

Lorentz microscopy makes use of the Lorentz force effecting moving charges in a magnetic field. This is also the case for the electrons in the electron beam of the microscope moving in the field of a magnetic specimen and can be used to gain knowledge about the specimen magnetism. To achieve this, external magnetic fields must be kept from influencing the specimen, in non-specialized microscopes this is achieved by switching the objective lens off before inserting the specimen and doing all imaging in this obj-off mode. Specialized microscopes have an additional Lorentz lens below the objective lens of which the field is shielded from influencing the specimen by design [43] (permalloy shielding) and field geometry. This is designed to mostly affect only the electron beam and thus the imaging quality and allows higher magnifications and better image quality.

The acting Lorentz force on a moving electron is given by

$$\mathbf{F} = q(\mathbf{E} + v \times \mathbf{B}) = -e(\mathbf{E} + \mathbf{v} \times \mathbf{B})$$

with the charge q equal to the electron charge e and $\mathbf{F}$ the force the electron experiences, $\mathbf{v}$ the electron velocity, $\mathbf{B}$ the magnetic field strength and $\mathbf{E}$ the electric field strength. In a TEM, $\mathbf{E}$ is normally zero, giving $\mathbf{F} - e(\mathbf{v} \times \mathbf{B})$ where $\mathbf{F}$ is normal to $\mathbf{v}$ and $\mathbf{B}$ because of the vector product. Only in-plane magnetic components are detectable, the component parallel to the electron beam leads to no deflection because the vector product equals zero. If $\mathbf{B}$ changes its sign, the force acts in the opposite direction.
The Fresnel mode makes use of the deflection of the beam electrons depending on the magnetization direction to make domain walls visible (fig.7). The magnetization direction on both sides of the domain wall points into different directions. This deflects the beam electrons also in different directions from the domain wall, under parallel illumination in defocus mode the domain wall is shown by either high (region of overlapping electron beams, both deflected towards the domain wall) or low contrast (region of reduced electron density because the beams are deflected away from the domain wall). Bright lines appear if the electrons are deflected towards the domain wall, dark lines if they are deflected away.

The contrast is inverted by inverting the direction of the magnetic fields in the specimen and between overfocus to underfocus. It is possible to do quantitative analysis of magnetic

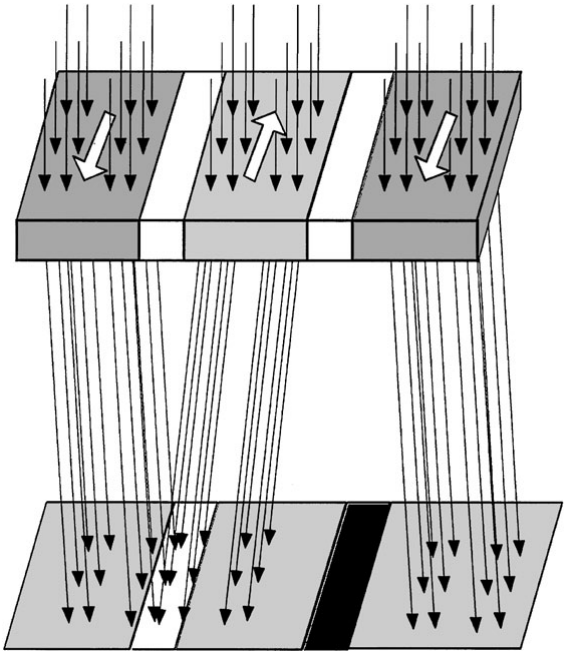

Figure 7: Generation of magnetic contrast in Fresnel Lorentz TEM images from interaction of the beam electrons with the magnetic induction in the specimen. Image taken from [43].

Fresnel images [44] [45] [46] but in this work it is used only on qualitative terms to check for magnetism in the specimen by applying an external field that magnetizes the specimen in both directions.

The application of Lorentz microscopy in scanning mode allows high resolutions and more detailed analysis by using different kinds of detectors. This is the Lorentz STEM or differential phase contrast measurement.
Non-ionised atoms and combination of atoms to matter are considered electrically neutral, although local electric fields can occur and the mean inner potential V_0, which is the sum of the Coulomb potential over all atoms of the crystal lattice, has effects on the electron beam. $V(r)$ can be expressed by a Fourier series, V_0 is defined as the mean inner potential [47]. Using DPC techniques it is possible to map potential and charge density at atomic resolution [48]. Measuring magnetic quantities adds the interaction with a magnetic field $\mathbf{B}$ which is the curl of the magnetic vector potential $\nabla \times \mathbf{A} = \mathbf{B}$. Adding an external field gives another magnetic vector potential, therefore magnetic observations in general need a space free from external magnetic fields (objective lens switched off).
In scanning mode the electron beam forms a probe that is rastered across the specimen, its deflection caused by the magnetic induction of the specimen due to the Lorentz force. The deflection along a direction represented by the unit vector $\hat{\mathbf{n}}$ is given by

$$\beta = \frac{e\lambda}{h} \int_{-\infty}^{\infty} (\mathbf{B} \times \hat{\mathbf{n}}) dl \tag{2.37}$$

with β the deflection angle, e the charge of the electron, λ the wavelength of the electron (at the chosen acceleration energy), $\mathbf{B}$ the vector of the magnetic induction at a point in

space and h Planck's constant [49]. The magnetic induction consists of the magnetization M (local) and the magnetic field strength H (extends over the space): $B = \mu_0(\mathbf{H} + \mathbf{M})$ with μ_0 the vacuum permeability. The magnetic field strength can be evaluated using magnetostatic calculations.
Due to the vector product only the induction perpendicular to the electron trajectory causes deflection, induction parallel to the beam results in a zero in the vector product. The integral in eq. 2.37 can be difficult to evaluate depending on the sample geometry because it is evaluated along the whole electron path. For a thin film this reduces to the distance the electron beam crosses in the specimen, which is the specimen thickness. This simplifies the equation to

$$\beta = \frac{e\lambda}{h}(\mathbf{B} \times \hat{\mathbf{n}})t \tag{2.38}$$

with t the specimen thickness, which can still differ between two points on the surface of the specimen. For specimen with non-uniform thickness it can be approximated by a function $t(x, y)$ and further simplified by keeping one coordinate constant resulting in $t(x)$, so the final used form of the equation reads

$$\beta = \frac{e\lambda}{h}B \cdot t(x) \tag{2.39}$$

The same result can be obtained by a quantum mechanical wave approach using the Aharonov-Bohm effect [50] with the given phase of the wave of

$$\phi = -\frac{e}{h}\int_{-\infty}^{\infty}(\mathbf{A} \cdot \hat{\mathbf{n}})dl \tag{2.40}$$

with $\mathbf{A}$ the magnetic vector potential. Applying the two-dimensional gradient operator $\nabla_\perp$ gives

$$\nabla_\perp\phi = -\frac{e}{h}\int_{-\infty}^{\infty}(\mathbf{B} \cdot \hat{\mathbf{n}})dl \tag{2.41}$$

using the well known substitution $\mathbf{B} = \nabla \times \mathbf{A}$. The right hand side is equivalent to eq.2.37 up to a constant factor. It is important to note that because of $\mathbf{B} = \nabla \times \mathbf{A}$ a deflection occurs because of interaction of the beam electrons with the rotation of the magnetic vector potential.

The segmented DPC measurements are performed using an annular segmented detector with four inner and four outer segments. To obtain the magnetic signal, the difference signals of opposite elements of the outer ring is used to map the deflection angle. This can be converted to the integrated in-plane component of the magnetic induction using eq. 2.39. Using an annular segmented detector form instead of the conventional solid quadrant detector has advantages in control of the accessible information and can reveal finer magnetic detail [51].
To obtain a deflection angle from the intensity differences the difference signal, for example $s_1 - s_3$ is divided by the total intensity calculated from the sum of all eight segments $S = \sum_{i=1}^{8} s_i$ and $\beta = ((\alpha \cdot \pi)/(2 \cdot \sqrt{2})) \cdot (s_1 - s_3)/S$ with α the parameter of the convergence angle of the probe that depends on the used aperture, which needs to be measured in the microscope. The same is carried out with the signal from $s_2 - s_4$ and the results are two

deflection maps perpendicular to each other. Normalization on a region known to show zero deflection like the vacuum or the substrate is possible after converting from intensity to deflection angle by using a region of interest and subtracting the mean value of this ROI from the difference signal.

For pixelated DPC the beam disc is recorded on a pixelated detector (here: array of 256×256 pixels, Medipix3 detector [52] [53]) for every scanned pixel. The shift can be followed by finding the circle of the disc in every image and calculating the shift from a zero point, this has been adapted in a Python script using fpd [54] by D. McGrouther and G. Paterson. [55]
First the center of the diffraction pattern is found using a Hough transform [56] after applying an edge filter. The Hough transform creates a parameter space that contains for every point in the image that lies on an edge all possible parameters of the figure to be found, in the case of a circle every point in the parameter space corresponds to a circle (center and radius) possibly matching to the point of interest in the image. Clustering in the parameter space indicates the most probable parameters, the highest value is best representation of the geometric figure to be found. The search in the parameter space can be accelerated by various methods [57].
From here on there are two possibilities for further evaluation, center of mass and phase correlation. Center of mass analyses the mass center of the intensity in the found circle, which can shift due to diffraction effects and indicate untrue beam deflections. Therefore the phase correlation process has been used, which "produces images which are more sensitive to the disc shape than to its intensity and is thus effective in reducing the influence of diffraction contrast." [55] A reference image is created using a matching algorithm, it acts as a representative for the image of the bright field disc. For magnetic measurements images of a section that is of uniform thickness and contains no magnetic signal should be supplied. The phase correlation algorithm follows, using fast fourier transforms where the phase information is isolated from the FFT cross-correlogram. It allows to calculate the relative translation between two images [58], with one image being the reference image calculated before, the shifts of the BF-disc images can be obtained. It works with two input images g_a and g_b which are filtered to reduce edge effcts using for example a Hamming filter [59]. The 2D discrete fourier transforms $\mathbf{G}_a = \mathcal{F}\{g_a\}$ and $\mathbf{G}_b = \mathcal{F}\{g_b\}$ are calculated of both images, then the cross power spectrum by taking the complex conjugate of $\mathcal{F}\{g_b\}$ and elementwise multiplication of the fourier transforms, afterwards normalizing the product elementwise:

$$R = \frac{\mathbf{G}_a \circ \mathbf{G}_b^*}{|\mathbf{G}_a \circ \mathbf{G}_b^*|} \text{ entry wise: } \Rightarrow \; R_{jk} = \frac{G_{a,jk} \cdot G_{b,jk}^*}{|G_{a,jk} \cdot G_{b,jk}^*|} \tag{2.42}$$

with $\circ$ the Hadamard product. The inverse Fourier transform gives the normalized cross-correlation $r = \mathcal{F}^{-1}\{R\}$ and the location of the peak in r is given by

$$(\Delta x, \Delta y) = \arg\max_{(x,y)}\{r\} \tag{2.43}$$

With the peak location of the reference given, all shifts can be calculated depending on this image. Some appearing shifts are caused by descan, relicts of the scanning system of the STEM. These follow a distinct model and can therefore be removed using a RANSAC resampling algorithm [60]. Knowing the microscope parameters it is possible to calculate

the deflection angle from the shift distance and convert it into a map of the integrated magnetic induction. The advantage of phase correlation processing is the suppression of diffraction contrasts that shift the intensity inside the BF disc. To proof a signal as magnetic it is still necessary to switch the signal using a external magnetic field in both directions - or to exclude all other possible sources.

2.6 Simulation (EMCD)

For simulating the EMCD effect depending on the specimen thickness a software package developed by S. Löffler has been used [61]. It allows to calculate the EMCD effect which depends on specimen thickness and crystal orientation, described by the specimen tilt, and the position of the scattering centers in the diffraction plane (the "EMCD position") and therefore in the specimen itself [61]. It uses the density matrix in single inelastic scattering approximation
$\rho(\mathbf{R},\mathbf{R}') = \int G(\mathbf{R},\mathbf{X})G^*(\mathbf{R}',\mathbf{X}')T(\mathbf{X},\mathbf{X}')\rho_i(\mathbf{X},\mathbf{X}')d^3Xd^3X'$ for the probe with ρ_i density matrix of the incident electron, T scattering kernel (inelastic effects), G the Green function propagating the electron in the crystal potential, $\mathbf{X},\mathbf{X}'$ real space positions of scattering centers and $\mathbf{R},\mathbf{R}'$ "the real-space positions of interest which are typically located in the exit plane of the specimen." [61]. Electron propagation in the lattice is modelled by Bloch waves $\psi(\mathbf{R}) = \sum_j \varepsilon_j \sum_g C_g^j e^{i(k_j+g)\cdot\mathbf{R}}$ with $\mathbf{g}$ a reciprocal lattice vector, j Bloch wave index, C_g^j "determined from the (elastic) scattering behaviour of the lattice and $\mathbf{k}_j$ and ε_j and are determined from the boundary conditions" [61]. The scattering kernel can be rewritten to incorporate inelastic scattering using the mixed dynamic form factor (MDFF), where a single particle approximation that is simplified by only using dipole transitions in the first order Born approximation for one electron is used for evaluation [61]. The double differential scattering cross section (DDSC) is derived from the Born approximation and used to measure "the inelastically scattered electrons in a fixed energy interval dE in two distinct angular ranges $d\Omega$. From these two values σ_1, σ_2, the relative dichroic signal is computed by $(\sigma_1 - \sigma_2)/(\sigma_1 + \sigma_2)$" [61]. The influence of the sample thickness on the EMCD signal is calculated by integrating the DDSC under the assumption that in the crystal lattice every atom contributes to inelastic scattering as a scattering center over the z component of $\mathbf{X}$, the real space positions of the scattering center, and evaluate the DDSC at all atom positions of the unit cell [61]. The result for the integral gives

$$\sum_{\substack{j,j',l,l' \\ \mathbf{g},\mathbf{g}',\mathbf{h},\mathbf{h}'}} \varepsilon_j C_g^j(\tilde{\varepsilon}_l \tilde{C}_h^l) * (\varepsilon_{j'} C_{\mathbf{g}'}^{j'}) * \tilde{\varepsilon}_{l'} \tilde{C}_{\mathbf{h}'}^{l'} \frac{e^{2\pi i(\mathbf{Q}-\mathbf{Q}')_{z^d}-1}}{2\pi i(\mathbf{Q}-\mathbf{Q}')_z} e^{2\pi i d(\tilde{\gamma}_{l'}-\tilde{\gamma}_l)} \tag{2.44}$$

$$\cdot \frac{a(\mathbf{Q}\cdot\mathbf{Q}') + ib(\mathbf{Q}\times\mathbf{Q}')\cdot e_B}{Q^2Q'^2} \cdot \left[\sum_n e^{2\pi i(\mathbf{Q}-\mathbf{Q}')_x(\mathbf{u}_n)_x}\right]$$

The y coordinate has been omitted because EMCD is usually measured in a 3-beam case or systematic row. The complexity of this equation is $\mathcal{O}(N_{in}^2 M_{in}^2 N_{out}^2 M_{out}^2)$ (N number of Bloch waves, M number of included diffraction spots) because this equation can not be separated, but it does not need to be sampled in x and z direction which reduces the complexity more than the separation could. The equation 2.44 has to be evaluated for every data point in thickness map calculations.

The input file for the program is written in XML and requires only parameters accessible from experiment: crystal structure including atom positions, acceleration voltage and aperture size used on the microscope, crystal orientation, detector positions, center of the Laue circle, the x, z and d ranges, the inelastically scattering element, the energy loss (EELS edge) and the number of diffraction spots and Bloch waves [61].

2.7 Micromagnetic simulations

Micromagnetic simulations are needed to get an estimation of the sample´s magnetism and evaluate what can be seen in magnetic TEM images, helping to distinguish magnetic fields from other fields and phase shifting mechanisms. Here Mumax3 [62], an open-source micromagnetic simulation package that runs on graphics cards is used. It is written in the programming languages Go and CUDA(Nvidia´s programming interface for their graphics cards) and solves the Landau-Lifshitz equation using a **finite-difference method**.
The space in 2D or 3D is discretized in orthorhombic cells where quantities depending on the volume are located in the center of the cell and interactions between cells on the face. "MuMax3 calculates the evolution of the reduced magnetization $\vec{\mathbf{m}}(\vec{\mathbf{r}}, t)$, which has unit length." [62] The material can be defined in regions each having its own set of parameters. In each cell the starting magnetization can be set randomly or according to an external field, the system then is evolved or relaxed into its lowest energy state by precession of the basic magnets according to the Landau-Lifshitz-Gilbert equation in response to torques. The torque is defined as the time derivative of the magnetization:

$$\frac{\partial \overrightarrow{\mathbf{m}}}{\partial t} = \vec{\tau} \tag{2.45}$$

The used form for the Landau-Lifshitz-torque in Mumax is [62]

$$\vec{\tau}_{LL} = \gamma_{LL} \frac{1}{1+\alpha^2} \left(\overrightarrow{\mathbf{m}} \times \overrightarrow{\mathbf{B}}_{eff} + \alpha \left(\overrightarrow{\mathbf{m}} \times \left(\overrightarrow{\mathbf{m}} \times \overrightarrow{\mathbf{B}}_{eff} \right) \right) \right) \tag{2.46}$$

with γ_{LL} the gyromagnetic ratio, α a dimensionless damping parameter and $\vec{\mathbf{B}}_{eff}$ the effective magnetic field [Tesla] composed of an *externally applied field*, a *magnetostatic field*, a *Heisenberg exchange field* over the 6 nearest neighbour cells in 3D, a *Dzyaloshinskii-Moriya interaction* "for thin films with out-of-plane symmetry breaking" [62], a *magneto-crystalline anisotropy field* and a *thermal field* [62].
Other torque-contributions are the Zhang-Li spin-transfer torque (applicable for electrical currents) and the Slonczewski spin-transfer torque for spin-polarized current which can modify the magnetic orientation of a thin film layer:

$$\vec{\tau}_{SL} = \beta \frac{\epsilon - \alpha\epsilon'}{1+\alpha^2} \left(\overrightarrow{\mathbf{m}} \times (\overrightarrow{\mathbf{m}_p} \times \overrightarrow{\mathbf{m}}) \right) - \beta \frac{\epsilon' - \alpha\epsilon}{1+\alpha^2} \overrightarrow{\mathbf{m}} \times \overrightarrow{\mathbf{m}}_p \tag{2.47}$$

$$\text{using} \quad \beta = \frac{j_z \hbar}{M_{sat} e d} \quad \text{and} \quad \epsilon = \frac{P(\vec{r}, t)\Lambda^2}{(\Lambda^2+1) + (\Lambda^2-1)(\overrightarrow{\mathbf{m}} \cdot \overrightarrow{\mathbf{m}}_p)} \tag{2.48}$$

"where j_z is the current density along the z axis, d is the free layer thickness, $\overrightarrow{\mathbf{m}}_p$ the fixed-layer magnetization, P the spin polarization, the Slonczewski Λ parameter characterizes

the spacer layer, and ϵ' is the secondary spin-torque parameter" [62].
Several explicit Runge-Kutta solvers are implemented: RK45 (Dormand-Prince), RK32 (Bogacki-Shampine), RK12 (Heun) which provide adaptive time step control according to a target error value and RK1 (Euler) [63].
Energy minimization for finding the energy minimum/equilibrium state of the system disables the precession term 2.46. After advancing in time until the total energy is comparable to the numerical noise floor. "We then begin monitoring the magnitude of the torque instead of the energy, since close to equilibrium the torque will decrease monotonically and is less noisy than the energy. So we advance further until the torque cuts into the noise floor as well. Each time that happens, we decrease MaxErr and continue further until MaxErr= 10^{-9}." [62]
Mumax can write distinct output files for the magnetization in x, y and z direction which can be processed with Gatan GMS3 for phase contrast simulations. These have been performed using two DM scripts written by M. Cushley and T. Waclawski at the University of Glasgow using the Mansuripur method [64] to calculate the phase modulation for Lorentz microscopy from the vector potential for a thin magnetic film.

Additionally the micromagnetic package MicroMagus [65] for quasistatic micromagnetic simulations has been used to obtain especially information about domain walls and the magnetic hysteresis of the samples. It evaluates the total magnetic free energy E_{tot} under given geometric and material parameters using the finite difference method. The contributions to the total free energy E_{tot} according to [65]

$$E_{\text{tot}} = E_{\text{ext}} + E_{\text{an}} + E_{\text{exch}} + E_{\text{dem}} \tag{2.49}$$

are the following together with their finite difference (FD) approximations:
The energy in the external magnetic field with the magnetization $\mathbf{M}_i$ of cell i and $\mathbf{m}_i = \frac{\mathbf{M}_i}{M_i}$, $\mathbf{H}_i$ the external field averaged over cell i and the cell volume ΔV_i

$$E_{\text{ext}} = -\int_V \mathbf{H}_{ext}(\mathbf{r}) \cdot \mathbf{M}(\mathbf{r}) \cdot dV \tag{2.50}$$

$$E_{\text{extFD}} = -\sum_i \mathbf{M}_i \cdot \mathbf{H}_i^{\text{ext}} \cdot \Delta V_i \tag{2.51}$$

The magnetocrystalline anisotropy with the $\mathbf{K}_i$ anisotropy constants in the uniaxial case with $\mathbf{n}_i$ the vector of the axis and the cubic case with the magnetic unit vector (p_x, p_y, p_z)

$$E_{\text{an}}^{\text{un}} = -\int_V K_1^{\text{un}}(\mathbf{r}) \cdot [\mathbf{m}(\mathbf{r}) \cdot \mathbf{n}(\mathbf{r})]^2 \cdot dV \tag{2.52}$$

$$\text{uniaxial} \quad E_{\text{anFD}}^{\text{un}} = \sum_i K_i^{un} \cdot \left[1 - (\mathbf{m}_i \mathbf{n}_i)^2\right] \cdot \Delta V_i \tag{2.53}$$

$$\text{cubic} \quad E_{\text{anFD}}^{\text{cub}} = \sum_i K_i^{cub} \cdot \left[p_{i,x}^2 p_{i,y}^2 + p_{i,x}^2 p_{i,z}^2 + p_{i,y}^2 p_{i,z}^2\right] \cdot \Delta V_i \tag{2.54}$$

The (isotropic) exchange stiffness with J_{ij} exchange coefficients, κ_{ij} the weakening of the exchange and α_{ij} the angle between $\mathbf{M}_i$ and $\mathbf{M}_j$

$$E_{\text{exch}} = \int_V A(\mathbf{r}) \cdot \left[(\nabla m_x)^2 + (\nabla m_y)^2 + (\nabla m_z)^2\right] \cdot dV \quad \text{exchange stiffness energy} \tag{2.55}$$

$$E_{\text{exch}}^{\text{il}} = -\int_S J_{\text{il}}^{12}(\mathbf{r}) \cdot (\mathbf{m}_1(\mathbf{r})\mathbf{m}_2(\mathbf{r})) \cdot dV \quad \text{interlayer exchange coupling (non-magnetic spacer layer)} \tag{2.56}$$

$$E_{\text{exchFD}} = \sum_{<i,j>} J_{ij}(\Delta V_i, \Delta V_j, \kappa_{ij}) \cdot \alpha_{ij}^2 \tag{2.57}$$

And the magnetodipolar interaction energy containing a stray field or demagnetizing field with $\hat{W}_{ij}$ the interaction coefficients between cells i and j

$$E_{\text{dem}} = -\frac{1}{2}\int_V \mathbf{M}(\mathbf{r}) \cdot \mathbf{H}_{\text{dem}}(\mathbf{r}) \cdot dV \quad \text{magnetodipolar interaction energy} \tag{2.58}$$

$$E_{\text{demFD}} = -\frac{1}{2}\sum_i \mathbf{M}_i \cdot \hat{W}_{ij}^{dem} \cdot \mathbf{M}_j \tag{2.59}$$

A hysteresis can be calculated by driving through the external field range and minimizing the free energy for each external field value.

2.8 Sample preparation

For investigation in a TEM/STEM a sample has to be electron transparent, this means usually the need of a thickness of below 100 nm, depending on the microscope´s acceleration voltage and the sample material. There are several methods to prepare a sample for the TEM, among them TEM grids, FIB lamellae, Ultramicrotomy, Chemical etching... used for this work are only TEM grids and FIB lamellae, so these will be covered in more detail.

A TEM grid is usually made of copper, nickel, gold, molybdenum, titanium, stainless steel or aluminum. The choice of material is dependent on the experimental conditions, for example the temperature as heating and cooling are possible in the TEM. Also specimen might react with certain grid materials, therefore a chemically inert material is needed. The TEM grid is 3.05 mm in diameter and has a mesh structure in all of its inner part except the outer border. Many different mesh sizes are available (100-1000 mesh) and the mesh number gives the number of mesh squares per inch and thus relates to the mesh hole size. This grid is coated with a very thin amorphous carbon or silicon monoxide film. Other possible coatings are a graphene monolayer, graphene oxide or polyvinyl formal resin.
The specimen for a grid is usually liquid or dissolved in a solvent. With a measuring pipette a small amount of the specimen (usually 2 μl) is transferred onto the grid which is held by tweezers. After a short waiting time the solvent is carefully drawn into a piece of blotting paper and the dried specimen ready to be put into the TEM.

A FIB lamella is used to prepare a thin specimen out of a greater amount of bulk

material. It is fabricated using a focused ion beam (FIB) device, which is a scanning electron microscope with an electron beam and an ion beam and a stage that can be moved and rotated in all three dimensions. Both electron and ion beam (here: Ga+ ions) can be operated at different voltages from 5 kV to 30 kV, also material deposition is possible with both electron and ion beam. For this the material (here: Pt) is connected to a precursor that is liquid but changes to gas form at temperatures not much higher than room temperature. After heating up the precursor this gas is run into a hollow needle which can be positioned near the deposition place. The majority of deposition occurs via low energy electron impact that decomposes the precursor [66] [67].
To cut a lamella, the sample is first covered with a rectangle ($\approx$ 10 μm $\times$ 2 μm) of Pt using the electron beam because it does less damage to the sample, and afterwards covered by more Pt deposited using the ion beam. Then above and below the deposited rectangle the sample material is milled away by the ion beam, afterwards also left and right of the rectangle with only a small support connecting the raw lamella to the rest of the sample. The raw lamella is then connected to a micromanipulator by Pt deposition, afterwards the support can be milled away. Now it can be positioned in a lamella holder and soldered to it using Pt deposition. For all the specimen used in this work the center of one of the two "M" structures of the holder is chosen. After the lamella is connected to the holder on both ends the micromanipulator is cut loose by ion milling and retracted. Now the raw lamella needs to be thinned to electron transparency, this is achieved by ion beam milling on both sides of the lamella with a higher ion energy ($\approx$ 30 kV) until the lamella is near to electron transparency, then a low energy ($\approx$ 5 kV or lower) is used to mill away material damaged by the higher energy milling and thinning further to receive a thickness in the relevant region of 50-100 nm, a good preparation can yield thicknesses as thin as 20 nm.

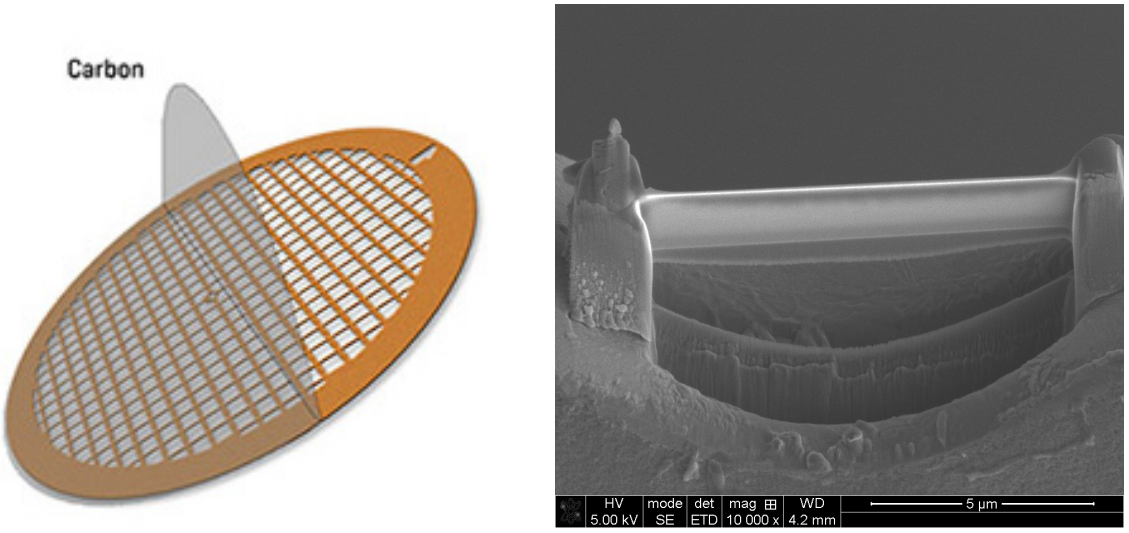

Figure 8: Left: TEM grid [68], right: FIB lamella in preparation courtesy to Björn Büker.

The samples themselves are produced by Co-sputter deposition on a substrate material. The substrate is chosen depending on its material and crystalline properties so the material to be sputtered on it without too much strain in the lattice or reactions that would cause formation of a different compound. A good match between the lattice means less than a

few percent difference in the lattice constants, matching between the lattice diagonal to the lattice constant is also possible and leads to growth rotated by 45°. The substrate is cleaned before by using an ultrasonic bath and additionally in the vacuum chamber by heating it up to high temperatures and letting it cool down to the targeted substrate temperature.
The sputter process itself is carried out by shooting accelerated positive ions (here: Ar) on a target of the desired material, the target material sputtered off by the momentum transfer of the impact is deposited on the substrate. The ion plasma can be generated in two ways: DC sputtering uses a diode circuit in a vacuum chamber where electrons are accelerated towards the anode and ionize gas atoms, the now positive ions are accelerated towards the cathode and generate secondary electrons there that are capable of ionizing more gas atoms. This can only be used for sputtering metals/conductors because otherwise the cathode would charge up. Non-metals/insulators can be sputtered by replacing the DC high voltage source by an AC voltage source. Using a magnetron sputter procedure increases the collision rate between electrons and sputter gas by guiding the electrons in a circular orbit above the cathode surface using tailored electromagnetic fields. For homogeneous deposition the substrate is moved relative to the cathode, here it is rotated onto its holder [69]. To prevent deposition of other than the desired elements the sputter sources are started minutes before the shutter to the substrate is opened. For protection of the sample against oxidation often a protection layer of for example MgO, Ru or Ta is applied on top of the sample. After the end of the sputtering process the sample can cool down slowly to room temperature, after cooling down the chamber is vented (mostly using inert gas like N_2 but also air is possible) and the sample lifted out.

3 Magnetic characterisation in the electron microscope: Results

3.1 The choice of samples

The first EMCD measurements were taken on standard samples: Magnetite star-shaped nanoparticles and polycrystalline cobalt-iron sputtered on a carbon-film TEM-grid. Of both samples the magnetism is relatively well understood and EMCD measurements have been performed by the Vienna group [70] [71] [72] [73].
The thickness dependence measurement had to be carried out on a sample that is not too complicated crystallographically so it is possible to simulate the EMCD effect dependent on the specimen thickness. (Crystalline) CoFe is such a system, crystallizing in the B2 structure.
Magnetic multilayer thin film systems are now frequently used in spintronics, for data storage and for sensoring applications. The interface between the layers is of great importance for their thermoelectric and magnetic properties. The TEM can in principle directly access the interface properties, so samples of thin film layer systems with special properties have been created.
The first layer system to be investigated consists of iron (50 nm) / Heusler Co_2FeSi (50 nm) / iron (50 nm) on MgO substrate. The Heusler itself has both interfaces to a magnetic material and the interactions at the interfaces are to be studied with the electron microscope. The huge layer thickness of 50 nm has been chosen to have enough area for easier tilting the specimen in EMCD (systematic row) condition in the TEM.
The second layer system made of Vanadium (50 nm) / Heusler Co_2FeSi (50 nm) / Vanadium (50 nm) on MgO substrate corresponds to the first system, but with interfaces to nonmagnetic material.
The third layer system is a functioning TMR stack made of Co_2MnSi (10 nm) / MgO (1.8 nm) / Co_2MnSi (15 nm) /MgO (3 nm) on MgO substrate. The thin layers make tilting in the microscope more challenging, so a second sample has been produced with increased layer thickness: MgO substrate / Co_2MnSi (40 nm) / MgO (20 nm) / Co_2MnSi (40 nm) /MgO (3 nm, protection). The layer thickness is important for the correct functioning of a TMR stack, especially the barrier needs to be thin enough to enable tunneling (the wave function reaches through the barrier and the probability for the electron to be there is > 0). The Co_2MnSi layers are of different thickness so they switch at different magnetic fields and both parallel and antiparallel configurations can be achieved.
The last layer system consists of layers of a magnetic and an nonmagnetic material. The idea is to measure the magnetic proximity effect [74] using a combination of DPC and EMCD. Since the magnetic layer magnetizes only the nearest up to $\sim$1.5 nm [75] of the nonmagnetic material, a verification of the proximity effect is challenging in the electron microscope. Inspired by the EMCD resolution increase in 2008 by Schattschneider et.al. [76] a layer system has been designed with alternating layers of vanadium and iron of these thicknesses: (Fe 5 nm / V 1 nm) x3 / (Fe 5 nm / V 4 nm) x3 / (Fe 5 nm / V 10 nm) x3 / Fe 5 nm / Pt 10 nm (capping for protection). The vanadium layers of 1 nm in between the iron layers should be fully magnetized due to the proximity effect, the 4 nm V layers should be approximately magnetized through the layers with a central dip in the center of each layer and the 10 nm vanadium layer should be magnetized in a way only the central $\approx$7 nm are nonmagnetic. The magnetization should give the same results with

opposite sign if the external magnetic field used to magnetize the iron is reversed.
The last choice of a sample happened during research because one out of a row of samples showed totally different properties in the TEM investigation: a very regular checkerboard pattern that could not have been expected. It has been investigated thoroughly with many methods in the TEM and also non-microscopy methods.

3.2 EMCD measurements on two different electron microscope types

The electron microscopes used for this work each have a different image filter. This has effects on the way EMCD can be measured in the specific setup.
On a microscope with a **post-column filter**, the specimen is tilted in EMCD condition (2 beam case, 3 beam case or systematic row condition) in diffraction mode. In TEM mode each of the 4 positions on the Thales circle can be selected, moving the diffraction pattern using the projective alignment in a way the desired position is aligned with the spectrometer entrance aperture. Then an EELS spectrum can be recorded. While using this method access to all EMCD positions is possible, the spectra of the positions are recorded consecutively. This brings the problem of altering the specimen because of electron beam damage and decreasing the material thickness, which also alters the EMCD conditions based on the thickness dependent Pendellösung. The intensity of consecutively recorded spectra can also vary and the noise level increase because of beam-sample interactions.
It is also possible to perform EMCD measurements in scanning mode of the microscope. Tilting the specimen can be done both in TEM mode or in scanning mode.
The microscope is switched to scanning mode using the smallest condenser aperture possible and a short camera length to obtain (nearly) distinct diffraction discs. The position of the row and discs on the image filter camera can be checked in EFTEM mode, where the same camera as for EELS is used. The row must be perpendicular to the energy axis of the spectrometer, which is usually adjusted in a way it goes horizontal across the center of the camera. So the row condition needs to be vertical, which can be adjusted by the intermediate (IL) and projection (PL) lenses in the lower column of the microscope up to $\approx 40-60^\circ$ depending on microscope and settings. If that is not sufficient, reinserting the specimen after changing its position in the holder or use of a rotational holder is necessary.
In scanning mode the diffraction EMCD condition is positioned on the spectrometer entrance aperture so that it is just out of the aperture or only a fraction of the diffraction disc electrons get in using the projection alignment. This ensures that two EMCD positions on their respective Thales circles get inside the spectrometer, but as less as possible electrons from the diffraction spots themselves because these electrons do not show circular dichroism and their intensity is high compared to the positions with high dichroism. Accessible are only EMCD positions on the same side of the diffraction row. The energy filter is set to the desired dispersion and the drift tube to the desired voltage to access the EELS edges of the specimen. Now it is possible to perform a linescan, sequence of points or spectrum image and use the capability of Digital Micrograph to add a "hook up" script to every point. The action from this script is performed either before or after the point. For getting the raw data containing both positions, the image must not be collapsed into a single spectrum, instead the camera is read out and the content saved as a normal 2D image. To get an activity to perform in the linescan that does not need the same camera to be read out another detector like for example the EDX detector is selected for the linescan,

but with a very short exposure time $\mathcal{O}(10^{-4} - 10^{-5})$ sec, as this signal is not needed for the EMCD measurement
Getting only one EMCD position into the entrance aperture would be possible, but the disadvantages from getting the measurements consecutively arise. Additionally the strength of STEM is performing many consecutive measurements, this for every EMCD position would add the obstacle of getting exactly the same beam positions on a increasingly damaged specimen area and repeat the line of measurements for at least a second position. The advantage of getting two positions at the same time is both measurements have similar intensity and similar noise, also the beam damage affects the specimen in a similar way over the measurement time.

On a microscope with an **in-column filter** the setup is slightly different: The main difference is that because of the position of the filter in the column only lenses above the filter have an effect on the way the electron beam enters the filter. The IL and PL lenses have no effect on the electrons entering the filter. So it is not possible to rotate the diffraction image, hence a rotational holder or turning the specimen by hand in the holder and tilting again to EMCD condition is necessary. The spectrometer entrance aperture can be selected from several sizes and can be moved so only the relevant position can enter the spectrometer, also the objective lens aperture can be used to select the parts of the beam. It is also in TEM mode possible to measure two EMCD positions (again restricted to the same side of the 3-beam-case or systematic row condition) in parallel, the same in scanning mode. The image filter is in EELS mode and the main camera below the filter records the image of the spectrum, which now can be evaluated further. Figure 10 shows a schematic drawing of recording EMCD data using an in-column filter. Another issue is the dependence on the chosen dispersion: the projection on the camera rotates and the shape changes, only the highest dispersions ($\approx 250 - 400$ μm/eV) have a width on the camera suitable for EMCD analysis, with decreasing value the dispersion becomes more a "line with pearls" on the camera with the "pearls" indicating the edges and the EMCD positions are separated by a few pixels only. A comparative view of the dispersion on both microscope types is shown in fig.9.

EMCD measurements in TEM mode have been performed on both the JEOL ARM200F

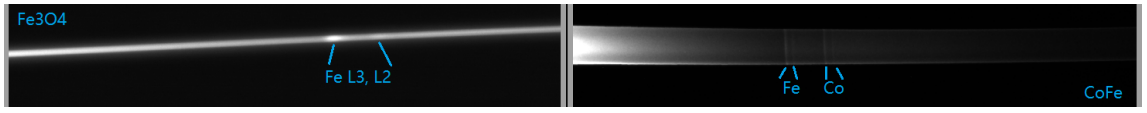

Figure 9: Left: dispersion of the TEM equipped with an in-column filter which rotates on the camera and becomes thinner with decreasing dispersion value. Right: dispersion of the post column filter Gatan Quantum ER which is projected onto the camera at the end of the spectrometer and does not rotate or change its behaviour depending on the chosen dispersion value. Both spectra are from EMCD measurements, in the case on the right the position of the diffraction discs and the EMCD positions in between are visible.

(post column filter) and the JEOL JEM-2200FS (in-column filter). The specimen investigated were the same: polycrystalline CoFe (10/20 nm) sputtered on a standard TEM grid (Cu with 25 nm amorphous carbon film, 400 mesh) and Magnetite Fe_3O_4 star-shaped

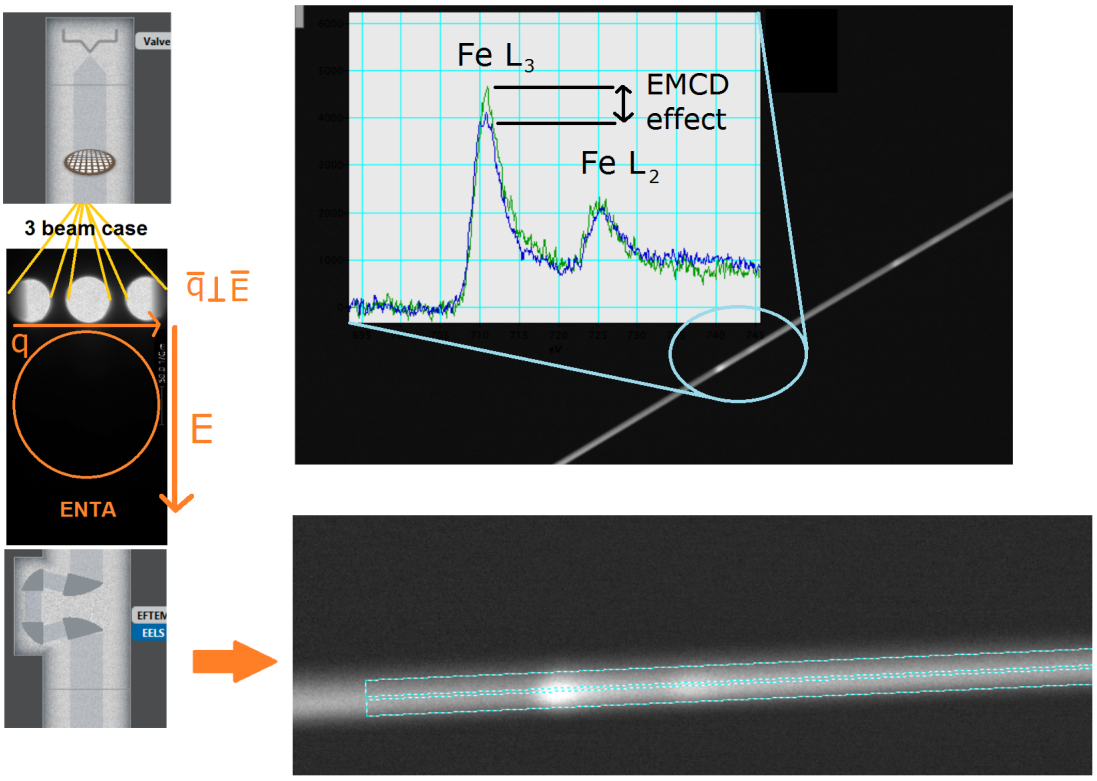

Figure 10: Schematic drawing of EMCD acquisition on an instrument with in-column filter. The electrons are emitted from the gun and pass the specimen, which is tilted into a 3 beam case as shown or systematic row condition. It needs to be adjusted/rotated in a way it lies perpendicular to the energy dispersive axis of the spectrometer/image filter. The entrance aperture (ENTA) of the spectrometer is placed on the diffracted spots such that the spots themselves do not pass the aperture, but the two EMCD positions do. The filter sorts these electrons by their energy and creates the spectrum, which can be viewed on the viewing screen or on the camera. Instead of letting the camera software collaps it into one spectrum and lose the position information, the whole camera image is recorded. Via the line profile tool spectra can be extracted and analysed.

nanoparticles fabricated by (Hamburg) on a standard TEM-grid (Cu with 25 nm amorphous carbon film, 400 mesh). The nanoparticle dispersion is pipetted onto the grid and then blotted and dried, so the nanoparticles are on the grid film with a minor amount of solvent. The advantage of polycrystalline films or nanoparticles is that always a grain or particle can be found in the right orientation for EMCD.

For the CoFe the measurements of the 20 nm specimen have been used since the 10 nm specimen has been very sensitive to beam damage with the needed longer exposure times: The second position data was far noisier with less counts, so the two position measurements were not obtained in similar conditions anymore. Often the beam has made a hole in the specimen, this happened also to the nanoparticles, they are $\approx 50-80$ nm in diameter and $\approx 10-20$ nm thick.

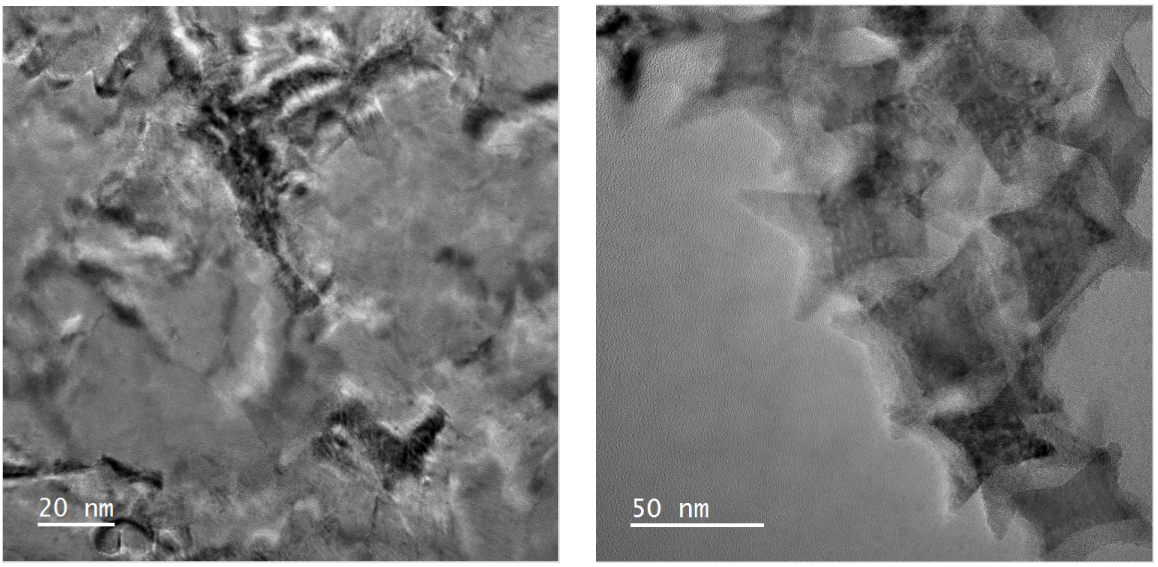

Figure 11: The specimen used in both types of microscope: polycrystalline CoFe (20 nm, left) and star-shaped Fe_3O_4 nanoparticles (right)

For each specimen three successful measurements have been obtained on each microscope.

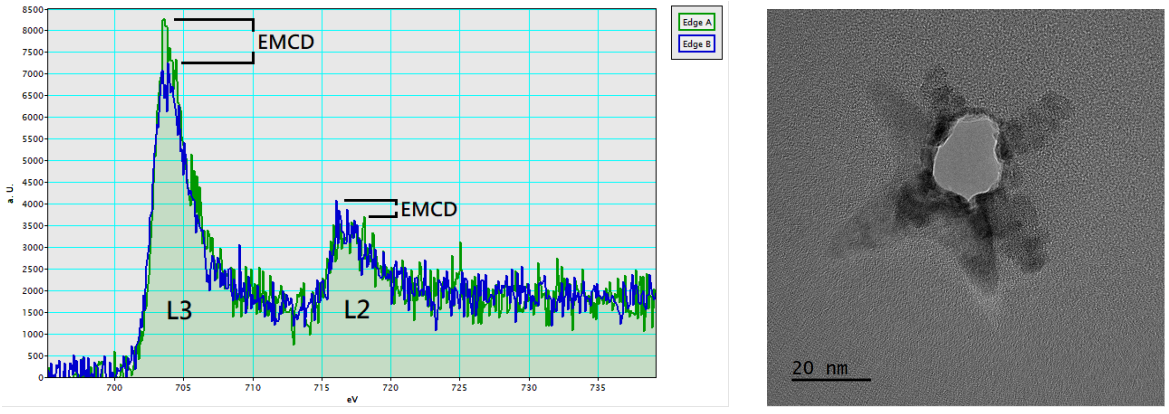

Figure 12: Result of an EMCD measurement: positive effect on the iron L3 edge and negative effect on the L2 edge (left). The beam shot through two overlaid Fe_3O_4 nanoparticles (right)

The following table (2) shows the results. The following microscope parameter have been used:
On the ARM 200F 200 keV acceleration voltage, magnification 200k, 5 mm spectrometer entrance aperture, 5 sec exposure time and dispersions of 0.025 eV and 0.1 eV per channel. On the 2200FS: 200 keV acceleration voltage, mag 200k, 10 μm selected area aperture, 10 sec exposure time and dispersion of 0.037 eV per channel. On this microscope the direction of the dispersion projected on the screen/camera rotates by changing the dispersion and the data is collected with the main camera, the Gatan OneView 4k x 4k.

Polycrystalline materials with crystallites of the size of nanoparticles and nanoparticles are only tilted and oriented with great difficulties and by the time one particular particle would have been tilted from a pole to a EMCD condition, the specimen in that place would be gone due to beam damage. Instead it is searched for a particle that already lies in the right orientation, this makes indexing of the used reflex difficult. For the measurements always those two diffraction reflexes are used that are closest to the transmitted beam, for CoFe these are the $(2,0,0)$ and $(\bar{2},0,0)$ reflexes or rotations of 90° of these, for Fe_3O_4 the $(2,2,0)$ and $(\bar{2},\bar{2},0)$ reflexes or rotations of these, for both materials the diffraction patterns are point symmetric for rotation by 90°. To obtain these results for the reflexes the FFT diffraction pattern of a HRTEM image of a crystalline part has been used and compared with a structural model of the material in JEMS [77]. This model has been tilted in the software from zone axis to a systematic row condition to calculate the excited reflexes. For the used materials the Hermann Mauguin space group is `P m -3 m` for the used CoFe and `F d -3 m` for the used Fe_3O_4.
Information on the expected results can be obtained from comparison with EMCD and XMCD measurements on CoFe and Fe_3O_4 from the literature. A measurement on FeCo [78] alloys shows for $Fe_{55}Co_{45}$ a notable signal only on the Fe L3 edge, data for Co is not shown there. This is not reproduced by the measurement in this thesis which shows also EMCD signal on the L2 edge, but the measurement uncertainty has only been calculated from the standard deviation of the three acquired values which allows for a large error on the measurement itself. Also effects of diffraction spots of other crystallites cannot be ruled out, it can not be made certain that only one grain is selected by the selected area aperture. For Fe_3O_4 XMCD measurements can be used for comparison although they do not consider the thickness dependence of EMCD via the Pendellösung. The form and sign of the effect should be comparable. The splitting in two peaks of the same sign on the Fe L3 edge [79] can not be observed. The Fe^{3+} peak is clearly visible in the very clean measurements from the ARM200F (fig.13). The noise level in the TEM measurements is too high to obtain detailed information on the L2 edge. For EMCD measurements the ARM200F is clearly advantageous over the JEM-2200FS because the measurement of EELS spectra is cleaner and less affected by the experimental conditions on a post-column filter.

ARM200F			2200FS		
Specimen	L3 edge	L2 edge		L3 Edge	L2 Edge
CoFe: Co	10.8%	1.1%		16.3%	13.1%
	10.1%	3.9%		5.1%	2.3%
	5.3%	3.1%		7.8%	4.3%
Result	$8.7 \pm 3.0\%$	$2.7 \pm 1.5\%$		$9.7 \pm 5.8\%$	$6.6 \pm 5.7\%$
CoFe: Fe	13.1%	9.6%		4.2%	8.6%
	6.5%	7.0%		3.3%	7.4%
	7.1%	21.2%		3.7%	2.2%
Result	$8.9 \pm 3.7\%$	$12.6 \pm 7.6\%$		$3.7 \pm 0.5\%$	$6.1 \pm 3.4\%$
Fe_3O_4: Fe	15.2%	7.2%		10.6%	4.8%
	12.7%	2.9%		2.8%	2.5%
	14.9%	4.2%		13.8%	2.6%
Result	$14.3 \pm 1.4\%$	$4.8 \pm 2.2\%$		$9.1 \pm 5.7\%$	$3.3 \pm 1.3\%$

Table 2: Measured relative EMCD effects on both microscopes for the specimen polycrystalline CoFe and Fe_3O_4 stars.

3.3 Evaluating EMCD measurements

Conventionally taken EMCD measurements are evaluated manually, obtaining an EELS spectrum on at least two complementary EMCD positions on the Thales circle(s). In the ideal case, where the specimen is not damaged and all conditions are the same on the positions except the interaction between the beam electrons of one chirality with the specimen compared to those electrons with the other chirality interacting with the specimen, this interaction only leads to the difference in the measured spectra: in the Fe_3O_4 sample on the L3 and L2 iron edges. In reality the counts drop with increasing beam damage on the specimen and other interactions occur, leading to more differences in the background of the spectra. If these increase, any effect maybe found cannot justified to be true and the measurement has to be discarded.

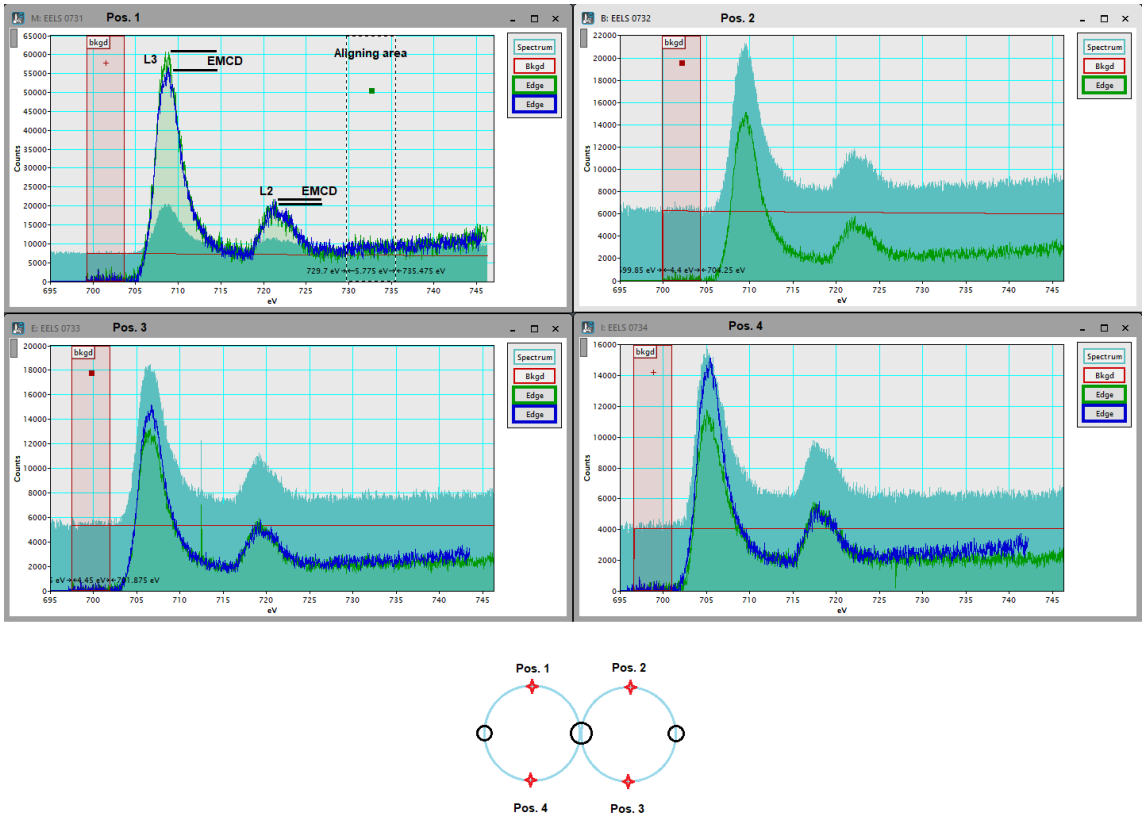

Figure 13: EMCD measurements on a Fe_3O_4 star-shaped nanoparticle on the 4 positions of the Thales circles as indicated in the schematic view below. Data recorded on the ARM200F. Pos. 2 was the starting point to determine the effect relative to pos.1, pos. 2 and pos. 4 which are shown in the overlay. In green: the EELS measurement of that position, in blue: the EELS measurement of pos. 2 as overlay. The red window has been used for background subtraction and in pos. 1 the aligning area is shown.

As for conventional EELS the background of the spectra needs to be subtracted using a suitable background model, for comparability the window before the edge is chosen of about the same width and position. The resulting spectra can be overlaid as it has been

done in figure 13 for pos. 2 over pos. 3 and pos. 4. Here nothing more needed to be done as the spectra were of the same height and the background after the edges stared to divert only at energies of several eV after both edges. The EMCD effect shows clearly in the difference in the L3 edge and the opposite sign effect in the L2 edge is barely visible. For pos. 1, which has been acquired as the first spectrum, there has been a difference in the number of counts between the spectra so one is shifted on the y-axis with respect to the other. This can be corrected by aligning both spectra "by integral" (GMS method), where a region of interest ("aligning area" in figure 13) indicates the region over which both spectra are integrated and then the whole spectra are multiplied by a factor resulting of the quotient of both integrals. This shifts both spectra and explains the higher number of counts as they are upscaled. It can be performed on a post-edge part of the spectra where they are only shifted in the y-axis relative to each other but do not differ in the shape of the post-edge background. From here evaluation like calculating the spin to orbit ratio of the magnetic moment can be done.

Spectra where both positions are acquired in parallel, like with an in-column filter microscope or in STEM mode, need to be evaluated in a slightly different way. Since this way of acquisition works only with EMCD positions on the same side of the 3 beam case or systematic row and involves two Thales circles, the spectrum needs to be recorded in a raw form on the camera that allows to find the EMCD positions and pull out a spectrum out of the raw data spectrum there. If the direction of the projected dispersion rotates with increasing dispersion on the camera, software needs to find the position of the spectrum data first. This has been programmed in Matlab by Chris Taake [80]: a linear function is fitted to the spectrum in the image, the slope of the spectrum is corrected as the tail often has a slight s-curved form due to not perfectly adjusted spectrometer lenses and the center of the spectrum is found by fitting a Gaussian function to it. Then the two positions are extracted at the same distance above and below the center via line profiles, converted into spectra and energy calibrated and subtracted, if necessary aligned on the background after the used edges. Otherwise this needs to be done manually, in the case of nonsymmetric raw spectra the human eye often produces better results. The spectra of the in-column filter microscope also have a different width on the camera depending on the chosen dispersion, the thinner spectrum of the lower dispersions makes evaluation more difficult and less accurate as more electrons of the central spot are included and spread across less pixels on the camera.

In STEM mode on a microscope with post column filter the choice of the dispersion has no effect on the way the spectrum is projected onto the camera, it is always a band of the same width in the center of the camera/detector. This setting is used for linescans to collect many datapoints of EMCD signal with high spatial resolution, as the step width can be set and the distance is only limited by the probe width. An example is shown in fig.14. The process of evaluation starts by determining the center of the stripe using a line profile across the stripe at the lower energies because it most likely shows the position of the central diffraction spot which has not been moved out of the aperture in total. Then a line profile is obtained from the likely EMCD positions a certain distance above and below the center, here labelled A and B. The integration width of the line profile should be as great as possible without including the central diffraction spot or regions from other diffraction spots. These line profiles, here shown below the image containing the spectrum, tend to be very noisy. Important for good results is the specimen quality, very thin and

clean specimen yield better results. Here the L3 edges of Fe and Co are visible and allows to calibrate the spectra by energy after converting them into EELS spectra in GMS, the L2 egdes are so noisy their position and shape can be determined only with difficulties. Manual evaluation uses background subtraction, overlay and if necessary aligning by integral again to obtain a preliminary result and see if there is any EMCD effect. If the data is very noisy, a Savitzky Golay spectral filter [81] can be useful: it reduces the noise at the cost of some of the peak height but this is applied to both spectra so it should have not a big effect on any notable EMCD effect. It can be used to determine if any effect might be visible and improve the signal to noise ratio. The error of the measurement can be determined via standard deviation of the remaining noise post-edge. The result for the single evaluated measurement is shown in fig.15, a very noisy dataset has been chosen to represent the reality better and to explain the arising challenges.

As the amount of data arising from linescans can be huge, evaluation by a program is needed. Such programs have been written in the scripting language of Digital Micrograph (Gatan) for the linescan data in this thesis. The program is intended to evaluate the raw data and return two overlaid spectra for further evolution in a different script. The scripts should work with every post-column filter data that is projected onto a 2k× 2k camera with the dispersion covering the central part in horizontal direction, some fine adjustments might be needed for systems other than Gatan Quantum ER. It is needed to write several scripts for different stages of the evaluation because control over the credibility of the evaluation is needed and can only be provided by human eyes as the raw data has very different "looks" depending on the actual measurement. The central diffraction spot might not be visible or boundary effects lead to faulty determination by the algorithm. The use of a trained AI could be a possible alternative in the future but this project has not been started yet.
The stages of evaluation are the following, with a spectrum extracted always over the whole image width:

- Reading in the data in a batch job imagewise, a linescan contained in one folder can be processed in a batch job
- Determine the region of the spectrum, this remains valid for all spectra from the same acquisition system
- Obtaining the crossprofile and evaluating it
- Finding the two positions for spectrum A and B and determining the quality of both spectra
- Making the spectra on the resulting coordinates
- Background subtraction on both spectra using a desired energy window
- Savitzky Golay filtering of both spectra in addition
- Returning the spectra and their difference in a profile image, also the Savitzky Golay filtered spectra and their difference

The first script exists in two versions already: for a notable maximum originating from the central diffraction spot and for a profile across the whole spectrum ("crossprofile") without notable features. The approach in the first case is to obtain a crossspectrum, find its maximum, search away from it for a minimum and take it as the y-coordinate for the center for one spectrum of 30 pixel width. The center for the other spectrum lies at the difference between center and the first spectrum to the other side from the center. The search for a minimum has turned out to be not very reliable as a plateau of approximately equal height appears in crossprofiles and the minimum is determined by the noise on it. Savitzky Golay filtering of the crossprofile has been built in to avoid this but succeeds only to a certain degree.
As a different way to determine the two spectrum positions it has been used that two good EMCD spectra should differ in nothing except the peak height on the edges. Post-edge the background should have exactly the same slope and height. So the two positions need to be found for which this is the case. If known, a center like a maximum or a reasonable position can be used to divide the whole image with the spectrum in two not necessarily equal regions for this search. All possible positions for the spectra are now tested systematically against each other (upper region against lower) by creating a spectrum in one region, creating one on the next possible y-value in the other region, lifting them on the same level by using a region pre-edge to normalize one spectrum to the other and using a post-edge region to determine its integral. If the difference of both integrals is smaller than a set value, the new value and both y-positions are stored and the next position is tested. Possible y-positions allow to integrate a lineprofile over 30 pixels and are still inside the area covered by the spectrum, which can be at maximum 200 pixels in y-direction but due to boundary effects 178 pixels are used. At the end the y-positions with the smallest possible integral difference indicate the most similar background and the found EMCD positions, which are returned. This always needs a check by the human eye to see if no extreme values on the boundaries had an effect and if the results are in accordance with the positions to be expected from the measurement settings.

A second script takes an overlay of two background subtracted spectra as input and allows to shift them to the left or right by a certain amount of channels to make sure the edges are on the correct position. Then the margins are cut off to have the same dataset/channel number size for both spectra because only images (GMS treats nearly all data as an image) of the same size can be subtracted. The difference of both spectra is calculated and the result displayed. This approach is needed because operations in GMS always run on the original dataset/image but not on the shifted one. Processing options exist that allow shifting in the display of the image, but this affects only the display of the image and not the underlying image data. Insufficient matching between both spectra can lead to faulty EMCD effects as is shown in fig.16.
The code can be found in Appendix 6.13, as basis for the input and batch routine a script by B. Schaffer [82] has been used, also parts of the Savitzky Golay spectral filter by D. Mitchell [81]. The EMCD application has been programmed by the author of this thesis.

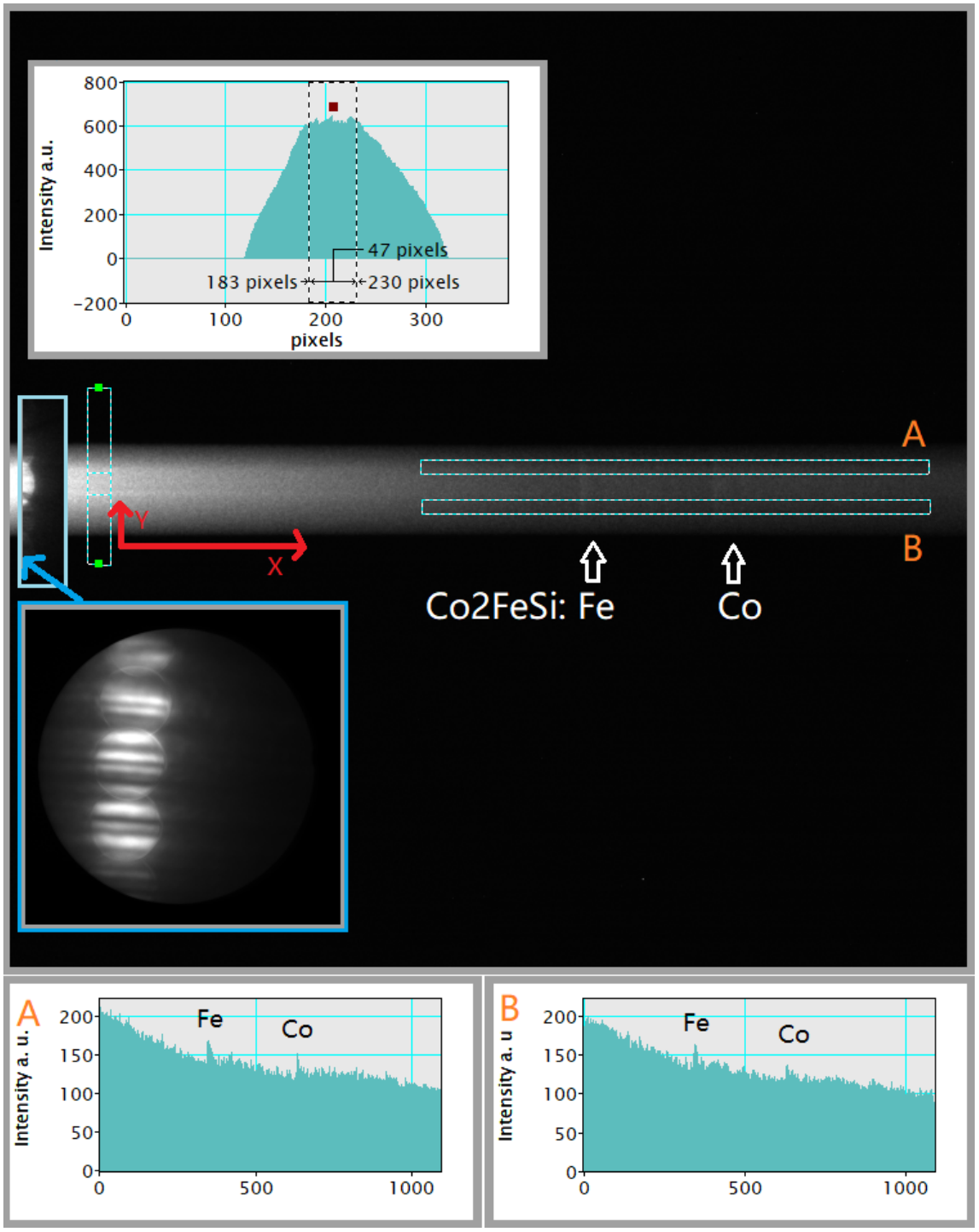

Figure 14: Evaluation of one EMCD measurement acquired in STEM mode using a post-column filter. The stripe of the spectrum contains also spatial resolved information. The systematic row as shown through the aperture (inlaid image, blue box) has been moved out of the aperture until only a small bit of the central diffraction spot is not blocked by the aperture but the two EMCD positions on their Thales circles still pass through (overlay at the left of the spectrum, light blue box). The profile across the spectrum to determine its center is shown above, the two line profiles on the EMCD positions on the spectrum and the resulting spectra below. The EELS Edges are barely visible but indicated by arrows.

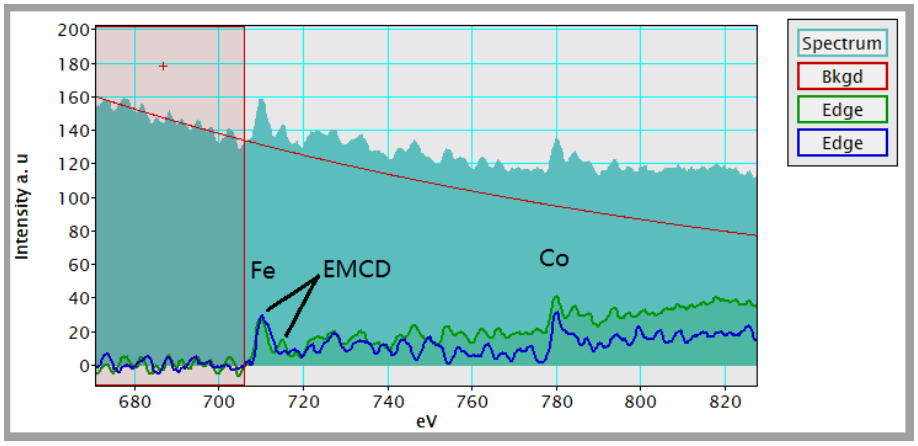

Figure 15: Evaluation of the two spectra from fig.14 on the Fe edge, the result has been filtered using the Savitzky Golay spectral filter. A small effect is visible but comparable to the noise. The window for the background subtraction is shown in red.

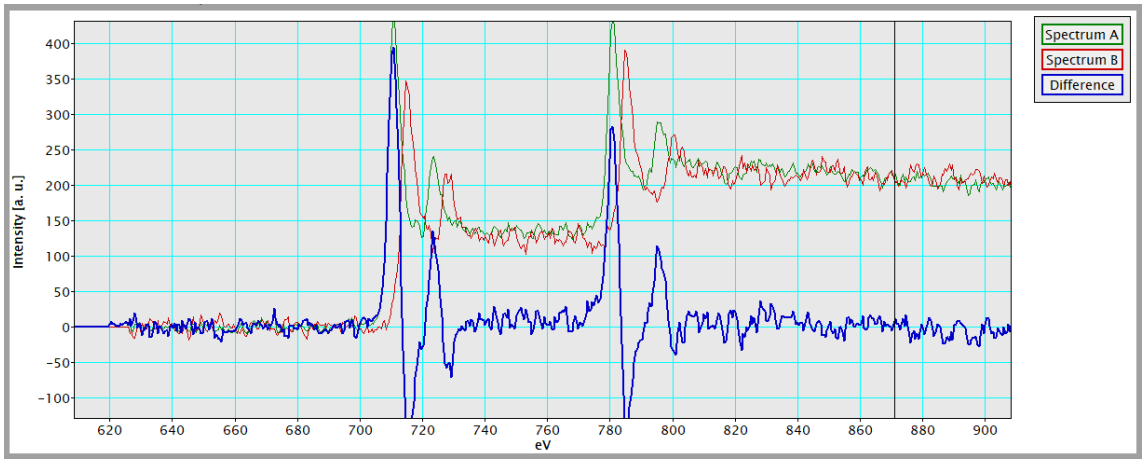

Figure 16: Wrong EMCD effect as a result of the subtraction of spectra not aligned well on the x-axis: Red and green are spectrum A and B with intentional misalignment and in blue their difference with huge up and down effects is shown.

3.4 The thickness dependence of EMCD

Unlike the x-ray pendant XMCD the EMCD effect is dependent on the specimen thickness due to the influence of the Pendellösung. This chapter aims to show this thickness dependence using several linescans on a specimen with varying known thickness from a well known material that can be simulated. This material has been chosen to be CoFe and a sample has been produced by Co-sputter deposition on MgO substrate that is grown highly epitaxial in the B2 structure. The sample has been sputtered by A. Becker and two FIB lamellas have been cut by K. Rott.

3.4.1 Simulation of the thickness dependence of EMCD in CoFe

To determine the theoretical magnitude of the EMCD effect depending on the specimen thickness a simulation using the tool "bw" by S. Löffler [61] has been carried out for the CoFe system. The input is given using a XML input file for the used configuration. It contains the crystal structure in the form of the unit cell with the lattice parameters $\gamma = \beta = \alpha = 90°$ and $a = b = c = 0.2857$ nm and the atom positions in fractional coordinates:

```
<atom element="Co" z="0" y="0" x="0"/>
<atom element="Fe" z="0.5" y="0.5" x="0.5"/>
```

To obtain a systematic row condition the Laue circle center has to be set so the excited reflexes form a systematic row. Depending on which reflexes form the systematic row a different Laue circle center has to be chosen. The possible reflexes for forming the used systematic row from the (0,0,1) zone axis in the TEM are the (2,0,0), (-2,0,0) reflexes and the (1,1,0), (-1,-1,0) reflexes, which correspond to a Laue circle center of (0,24,0) and (20,-20,0). The two detector positions on one side of the Thales circles have been used, an acceleration voltage of 200 kV, the thickness has been calculated in steps of 2 nm from 2 nm to 120 nm for both elements Fe and Co on the respective L3 edge (708 eV for Fe, 779 eV for Co). The ingoing beams are three (central diffraction disc and the two reflexes), the outgoing beams two (the two EMCD detector positions). The results are given as an intensity for each EMCD position from which the EMCD signal is calculated in the same way as in the experiment: $E_{\mathrm{EMCD}} = (A - B)/(A + B)$

The simulation results in fig.17 show the largest effect in the thinnest specimen parts ($\approx 18\%$ at 8 nm thickness) and the absolute value of the EMCD signal decreases with thickness. In the most accessible part between 15 nm and 60 nm up to $4 - 6\%$ EMCD effect can be expected. The effect of the Pendellösung is clear and the effect varies between its decreasing maximum value and zero. The sign can be reversed by interchanging the signals of the detector positions A and B. As for the following measurement only the overall magnitude of the EMCD effect has been considered, the absolute value of the simulation results used for comparison can be seen in fig.18. Since the result crosses the x-axis not far it is still comparable to the original result.

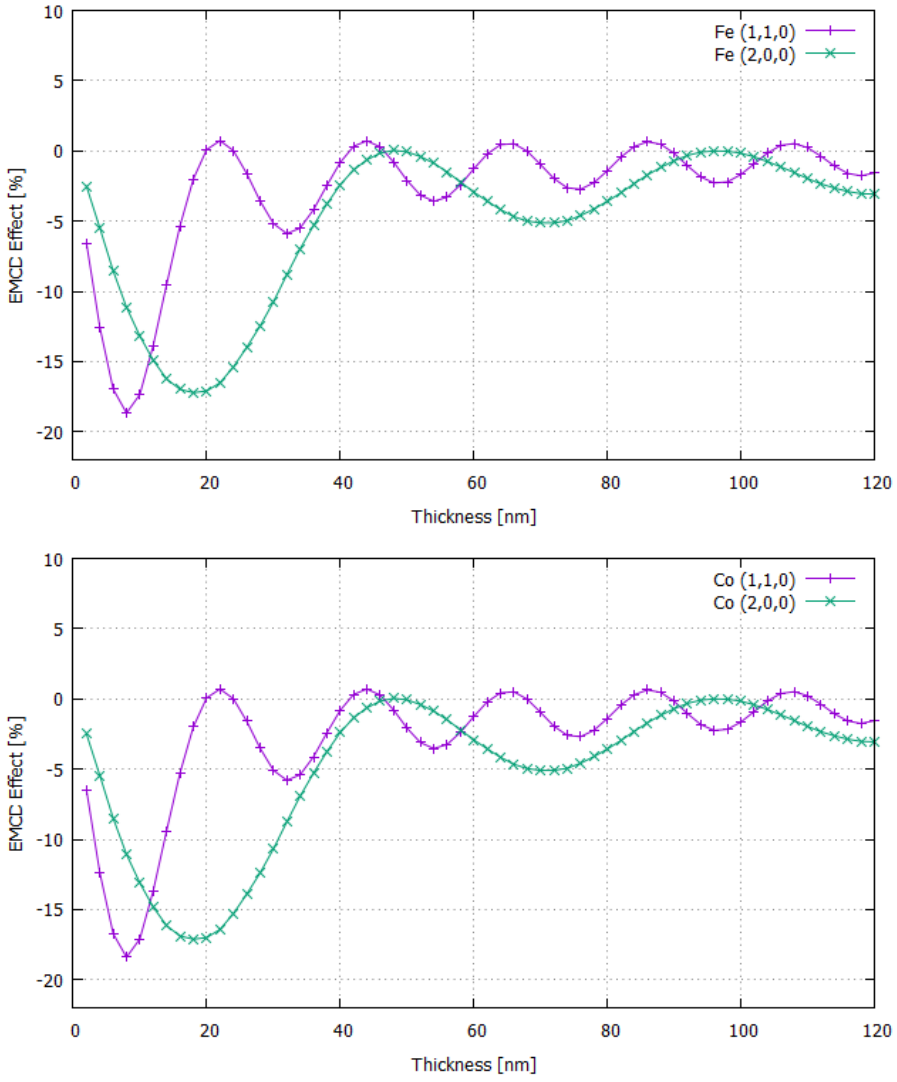

Figure 17: Simulation results for the thickness dependence of the EMCD signal of the cubic CoFe system calculated using "bw" [61] for the (1,1,0), (-1,-1,0) reflexes (purple) and the (2,0,0), (-2,0,0) reflexes (green) on the L3 edge for Fe (top) and Co (bottom). The influence of the Pendellösung is clearly visible.

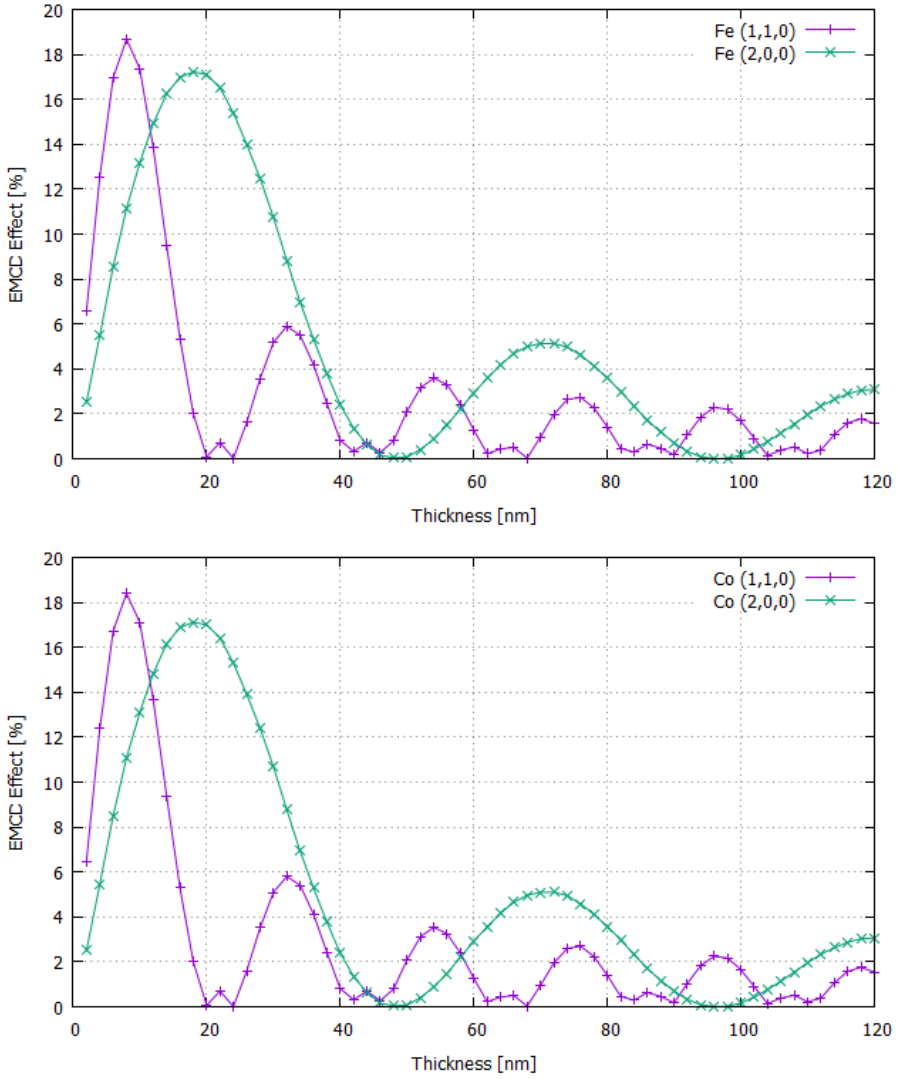

Figure 18: Absolute value of the CoFe EMCD simulation results for Fe (top) and Co (bottom). The result for the (1,1,0), (-1,-1,0) reflexes is shown in purple, the result for the (2,0,0), (-2,0,0) reflexes in green.

3.4.2 Measurement of the thickness dependence of EMCD on CoFe

To measure the thickness dependence a ≈ 280 nm thick layer of CoFe has been deposited by Co-sputter deposition at a temperature of 450° C at a base pressure of $< 5 \cdot 10^{-9}$ mbar, Argon flow 10 sccm, substrate rotation of 10 rpm on pre-cleaned (0,0,1) MgO substrate. After sputtering the sample cooled down to room temperature in the sputtering chamber. The resulting sample has been checked by XRD for crystallinity by A. Becker before the preparation of a FIB lamella. The FIB preparation has been carried out so that the resulting lamella shows a thickness gradient like a wedge: one end is thick, the other end as thin as possible (fig.19). Also towards the front the lamella becomes thinner due to the ion milling. Another polishing with low energy ions has been added to remove amorphized material. In fig.20 a HRTEM image and its FFT diffraction pattern is shown, the CoFe is grown epitaxial and no crystallites appear. The reflexes used for EMCD can be determined to be the (1,1,0), (-1,-1,0) or the (2,0,0), (-2,0,0) reflexes using JEMS [77] and tilting the virtual specimen in the program according to the values used in the TEM because only uncalibrated diffraction images have been recorded.
Comparison with the datasets ruled out the (2,0,0), (-2,0,0) reflexes because of no agreement between simulation and data.

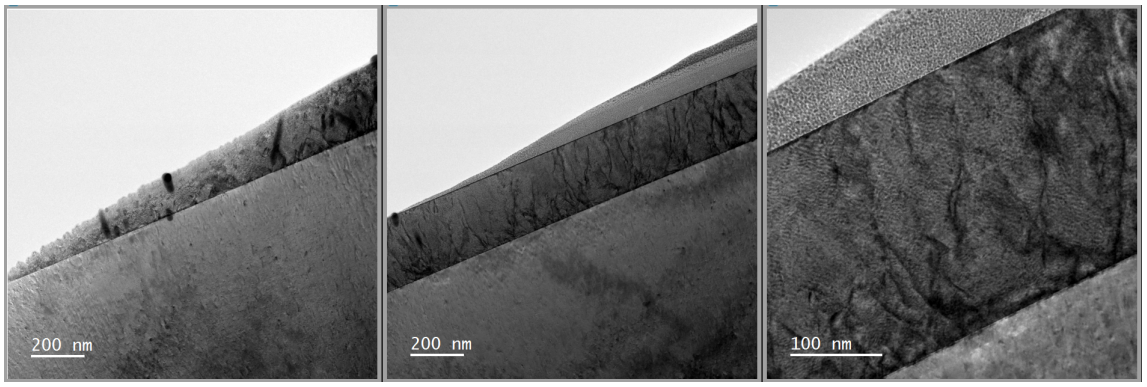

Figure 19: TEM images of parts of the wedge-form lamella, contamination stripes and dots on linescan areas visible in the left image. MgO substrate at the bottom of the image.

The EMCD measurements have been carried out on the ARM200F with post-column filter in STEM mode, the specimen has been tilted into systematic row condition in diffraction mode and the measurement parameters are the following: 200 kV, magnification 800kx, camera length 8 cm, 10 μm CL aperture to obtain separated diffraction discs, spot size 4C, 5 mm spectrometer entrance aperture, dispersion 0.5 eV/channel. The central diffraction disc has been moved out of the entrance aperture so only a small part of the disc and the two EMCD positions enter the spectrometer (fig.21). With this setting a set of six linescans consisting of 30-50 points have been recorded. The thickness of the lamella has been measured by EELS and EFTEM using the t/λ method after the EMCD

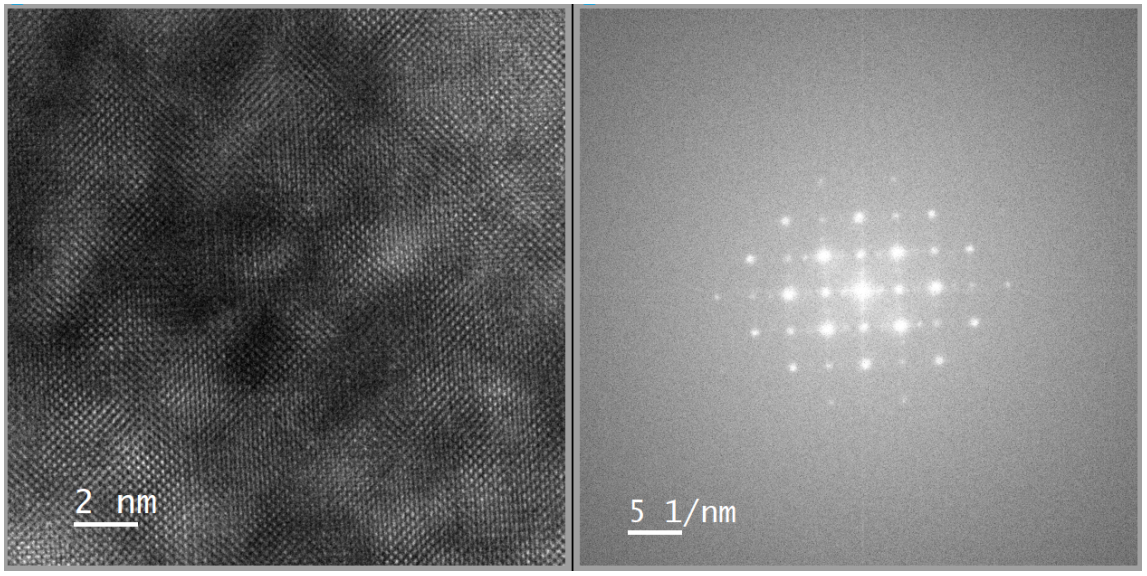

Figure 20: Left: HRTEM image of the CoFe specimen. Right: FFT diffraction image of this HRTEM image showing the CoFe to be of a cubic crystal structure matching the B2 structure in (0,0,1) zone axis.

measurements so the location of the linescans can be found in the thickness map and the thickness can be measured in a short distance parallel to the linescan. To reduce noise in this measurement the line profile used to measure the thickness in mean free path in the EFTEM thickness map integrates over 20-30 pixels. The thickness profiles for all used datasets and the linescan survey images can be found in Appendix 6.1. To assign the thickness to a measurement point the distance between two points on the linescan is measured and the mean thickness measured on points separated by this distance on the thickness profile after a smoothening low pass filter has been applied. For finding the specific regions the vacuum has been used as point of reference.
The thickness measured in mfp is converted into nm using the mean free path of Co (50%) Fe (50%) in the mean free path calculator of D. Mitchell [83] for $\beta = 15$ mrad: 96.42 nm.

The EMCD spectra on position A and B have been extracted after considering the properties of the data: if the central diffraction disc is visible as a stripe in the raw spectra and its position is stable or stable on significant parts of the linescan the spectra have been extracted using the DM script for evaluation on fixed positions for the whole linescan or for similar parts of a linescan separately. The evaluation scripts can be found in Appendix 6.13. To determine the data quality with respect to drift and descan the "crossprofile", a lineprofile obtained across the raw spectrum at a lower energy loss than the edge where EMCD is intended to be measured is used, the movement of the peak caused by the central beam disc shows in a varying position of the maximum of this crossprofile. For the set of six linescans used for this analysis the crossprofiles can also be found in Appendix 6.1. In the case of great variation the evaluation script using the permutation algorithm has been used. Datapoints without a clear position of the central beam disc or a position at the top or bottom margin of the raw spectrum have been discarded before processing the images containing the raw spectra because the extraction of the proper EMCD positions

is not possible there. Also spectra from the beginning or end of the linescan that do not include the Co and Fe edges have been discarded.

The first evaluation gives the spectra of position A and B background subtracted and overlaid and in addition both spectra overlaid without background subtraction in case the background subtraction did not succeed and for control of the slope of the post edge region. The overlaid spectra have been evaluated further manually which includes shifting one spectrum with respect to the other by up to 4-6 pixels to compensate the imperfect spectrometer alignment and aligning both spectra by integral on the post edge region to compensate for intensity differences. If an EMCD effect on the L3 edge has been visible (example in fig.22) it has been determined by measuring both peak heights and calculating the magnitude of the effect by $E_{EMCD} = (A - B)/(A + B)$ with A the peak height of spectrum A and B the peak height of spectrum B. For the measurement uncertainty the maximum of the noise N that remains pre-edge after background subtraction has been used and calculated similar to the EMCD effect: $E_u = N/(A + B)$. If no EMCD effect could be measured the datapoint has been discarded, this is unproblematic because all datapoints can be considered as single measurements on a certain thickness, the linescan is needed only to be able to relate the points to a thickness. If only on one of the elemental edges an EMCD effect could be measured, the other is set to zero without an assigned error. These points appear as points on the zero line without errorbars in the plots and are without a physical meaning because they can contain a hidden effect or none within the error and noise margins.

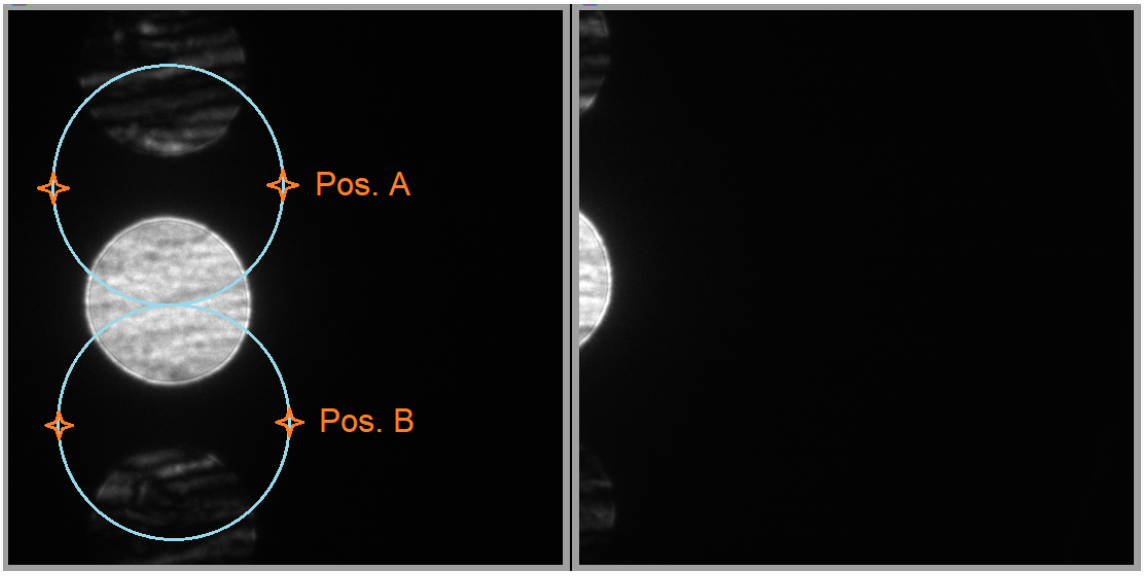

Figure 21: Left: The systematic row in STEM Mode on the spectrometer camera with drawn Thales circles. The orange stars mark the four EMCD positions, the two used positions are labelled with Pos. A and Pos. B. Right: the systematic row moved nearly out of the spectrometer entrance aperture ready for the linescan.

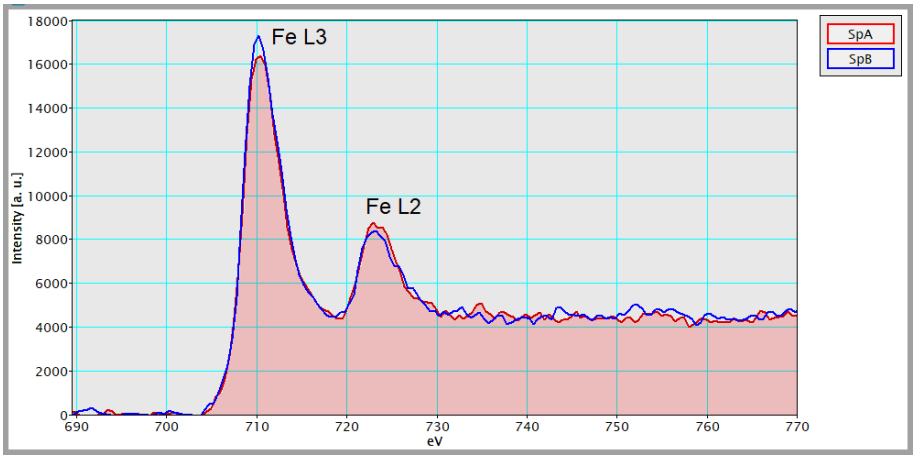

Figure 22: Example for a good measurement from the linescan data on the Fe L3 edge. The EMCD effect is clearly visible and exceeds the pre-edge noise, the effect on the L2 edge has the opposite sign.

The results are the datapoints of the magnitude of the EMCD effect plotted against the thickness. This has been done for all datasets together and then separately per dataset because the data is not comparable enough as it results from different linescans. The thickness estimation and the measurement settings add their error in a similar way on the same linescan but differ strongly between different linescans. The error in thickness estimation can be considered to be $\approx 5\%$ in EELS, so there is an uncertainty of ± 5 nm. Therefore the thickness has been shifted to up to ± 5 nm if a better matching of data and simulation could be achieved this way. Also evaluation has been done for both Fe and Co. A plot containing all the datasets and the simulation can be seen in fig.23 for Fe (top) and Co (bottom).

The mass of datapoints and large errorbars makes it difficult to overlook how well experiment and theory/simulation fit together. It is possible to state that there is some agreement, although in the thinnest part the effect magnitude does not reach the predicted value and there exist datapoints showing an EMCD effect higher than predicted. These occur rarely and can be treated as spikes in the statistics where they exceed the surrounding datapoints at similar thickness notably.
A lower EMCD effect than expected can be explained by the measurement geometry and the use of a specimen that is not a single crystal. The EMCD effect is measured in CBED mode with diffraction discs rather than diffraction spots because of the STEM EMCD setting. This is a possible measurement geometry according to [84] although the measured effect can be reduced. Also it can not be guaranteed that the region where the highest EMCD effect can be expected between the diffraction discs (a map can be found in [84] as an example) has been used for the measurement.
The spectrometer entrance aperture is used to separate which electrons can enter the spectrometer and it allows electrons from a certain region in the diffraction plane to enter. Also it is round and if the central beam of the systematic row does not hit towards the

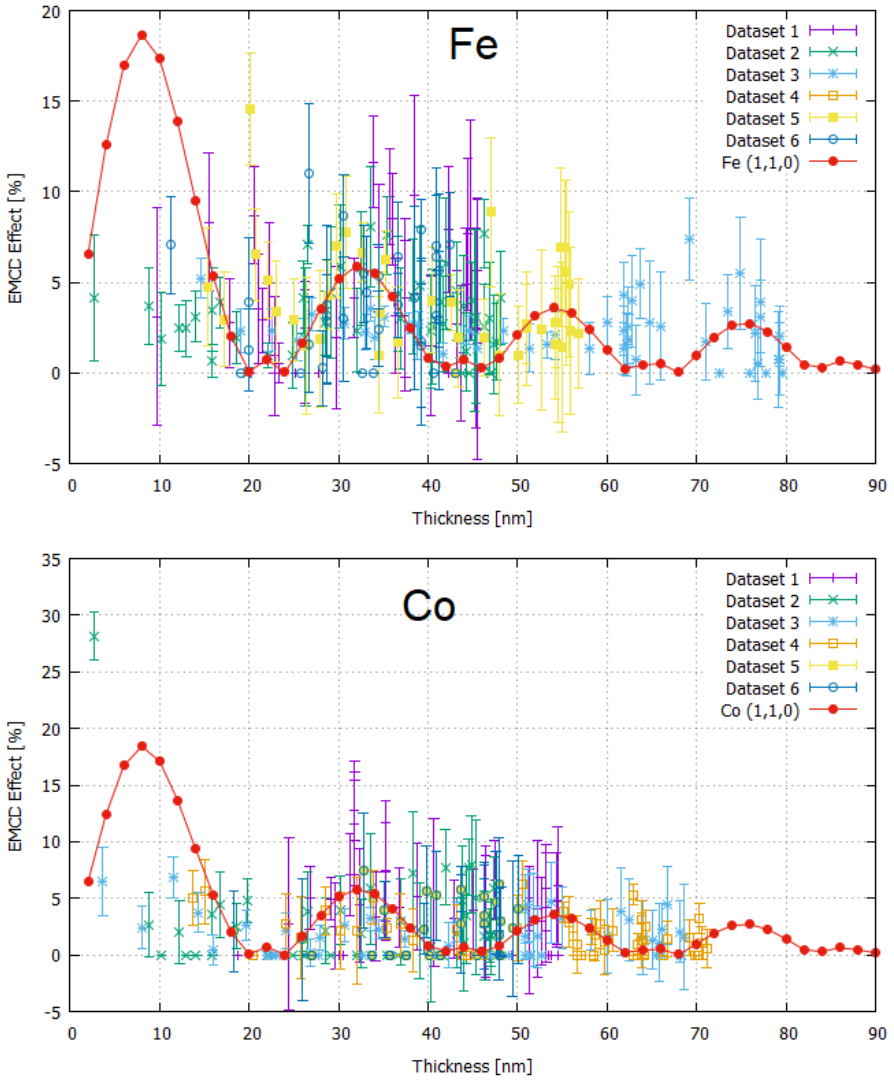

Figure 23: Combined data of all 6 linescans for Fe (top) and Co (bottom) for measuring the thickness dependence of the EMCD effect compared with simulation data for the (1,1,0) and (-1,-1,0) reflex (connected red points).

center geometrical effects limit the electrons that can enter and the two EMCD positions between the diffraction discs of the systematic row contain a different selection of electrons (fig.24).

Another effect is more apparent when looking at the datasets separately but can be seen also in the combined plot: Near the end of the linescan, which is also close to the CoFe/MgO substrate interface, higher effects than to be expected at the given thickness are measured again. It is reasonable to interpret this in the following way: because of the specimen tilt to obtain a systematic row diffraction condition the specimen is tilted so that only a part of the material crossed by the electron beam is CoFe, the other part

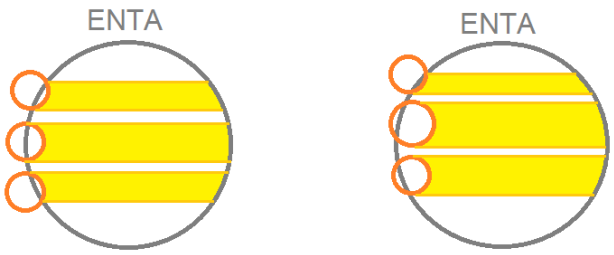

Figure 24: Geometric limitations resulting from the spectrometer entrance aperture (ENTA): The circular form introduces limitations, a shift of the systematic row (orange circles) up or down with respect to the aperture center causes a different amount of electrons and from different locations in the diffraction plane to enter the spectrometer (yellow marked regions). This can reduce or eliminate the measured EMCD effect.

is MgO. This would correspond to an EMCD effect magnitude of thinner material where the much weaker scattering MgO is not an obstruction for the electrons coming from the CoFe (fig.25). This is supported by the absolute count numbers of the raw data which decreases closer to the end of the linescan again while the thickness does not decrease.

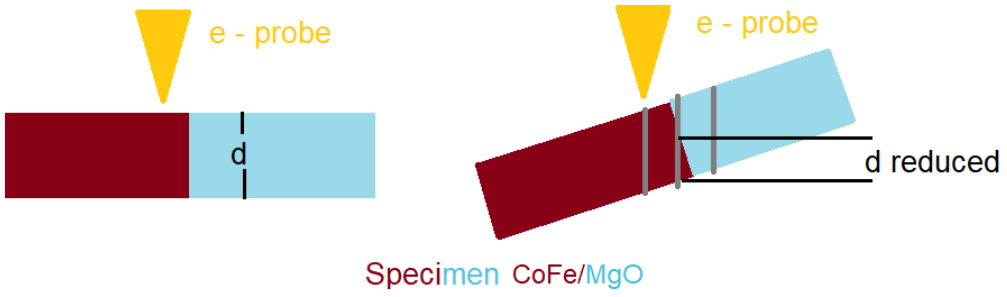

Figure 25: Schematic drawing of the reduction of the effective thickness contributing to the EMCD effect due to tilting the specimen to a systematic row condition.

The results are shown for each dataset separately for Fe in the figures 26 to 28 and for Co in the figures 29 to 31.
Most of the single datasets show only few datapoints in the low specimen thickness range < 15 nm because only 2 of 6 datasets have been measured on areas of this thickness and the agreement with the simulation is not very good there. The effect is less than a third of the expected value, which can be explained with a combination of the few counts and high noise in the spectra because of the very thin material crossed by the electron beam and with amorphisation and oxidation effects from the preparation and the handling on air. Additionally the t/λ method is not as reliable below ≈ 0.1 mfp, so the thickness estimation is less reliable there. At a thickness between 15 nm and 50 nm the data shows mostly large errorbars but is in agreement with the simulation. On the datapoints recorded at the end

of the linescan a clustering can be observed with the EMCD effect value partly exceeding the simulation data. Here the thickness has been obtained with the specimen tilted in zone axis and the EMCD measurement as described earlier on the specimen tilted in systematic row condition. Therefore the thickness measurements show a large thickness unaffected by the MgO substrate and the EMCD datapoints show a decreasing count rate that points to decreasing thickness and an EMCD effect in agreement with a lower thickness. Since this has been observed only after obtaining the data it is not possible to calculate this effect, the change in thickness could be calculated from the tilting angles and an EELS elemental map recorded both in zone axis and systematic row condition where the interface and in the case of tilting the material mix could be quantified.
Of the 6 datasets one is not in good agreement with the simulation, for Fe this is dataset 3 and for Co dataset 2. The other datasets show at least an overlap between the error margins and the simulation or especially in the case of smaller errorbars an EMCD effect below the simulation data but reproducing the slope.
The data for Co contains a lower number of datapoints because on more of the datapoints no EMCD effect could be measured.

3.4.3 Conclusion for the measurement of the EMCD thickness dependence

This measurement with the aim to show the thickness dependence of the EMCD effect on a CoFe wedge specimen shows an agreement of measurement and theory/simulation. It has to be considered that only datapoints obtained in the same measurement have similar effects and uncertainties on them and can be compared. The uncertainty is still high and the accurate thickness measurement of the specimen shows to be very important and either the measurements have to be obtained from regions far away from the interface to the substrate or the tilt has to be considered. Also in the EMCD measurement process some details need to be controlled with good accuracy, especially the position of the beam/central beam disc so descan, drift and deviation from the optimum position has to be avoided. The evaluation still needs care and a human eye because the signal is often on the noise level and a shift of a few pixels of the energy projection between the upper and the lower end of the spectrum occurs, a well trained artificial intelligence could be able to solve this.
To improve data quality a smaller number of measurements on a greater variation of thickness should reproduce the simulation better. But even though a lot of challenges have been on this measurement, at least an agreement between simulation and data could be achieved. The electron microscope is capable of measuring magnetic properties on a scale comparable to the beam diameter in scanning mode, which is of the order of nanometers. Very accurate measurements in a thickness regime where the Pendellösung predicts higher signal could even be used to determine a roughly predetermined thickness precisely.

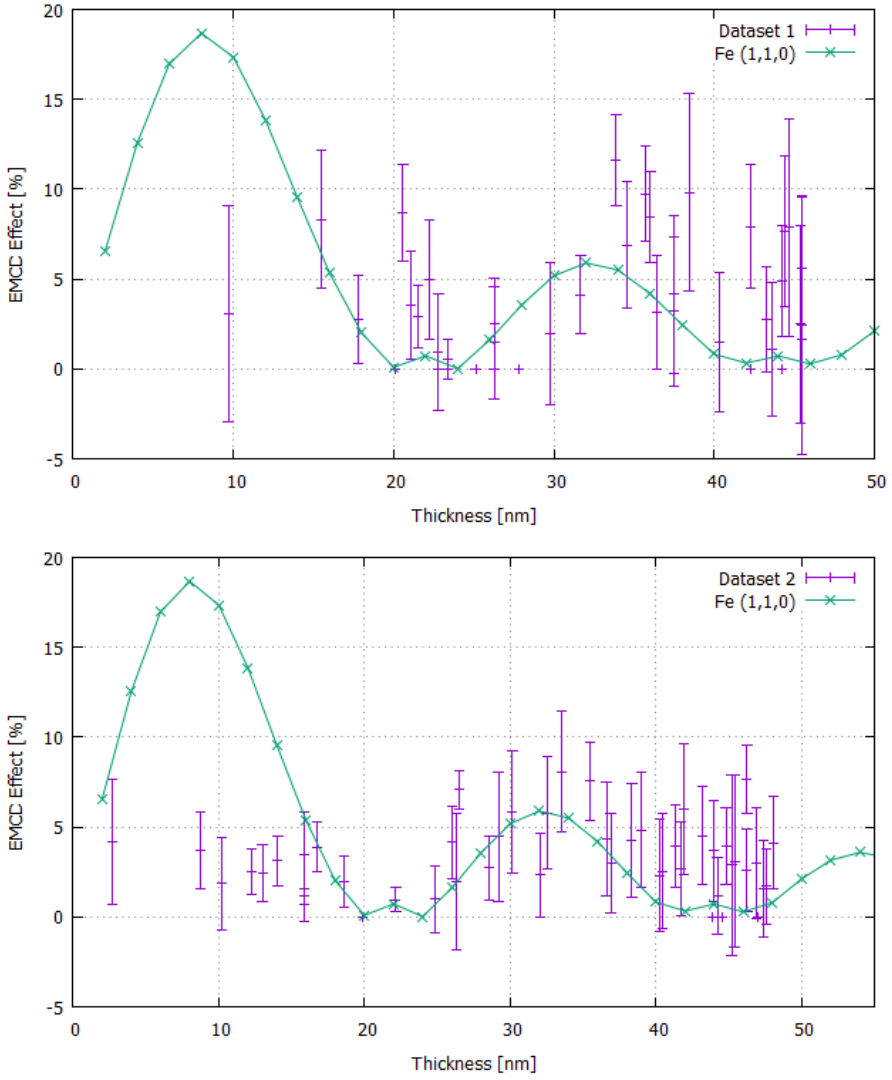

Figure 26: EMCD signal with respect to the specimen thickness for the Fe L3 edge: Dataset 1 (top) and 2 (bottom) compared with the simulation for Fe on the (1,1,0) and (-1,-1,0) reflexes.

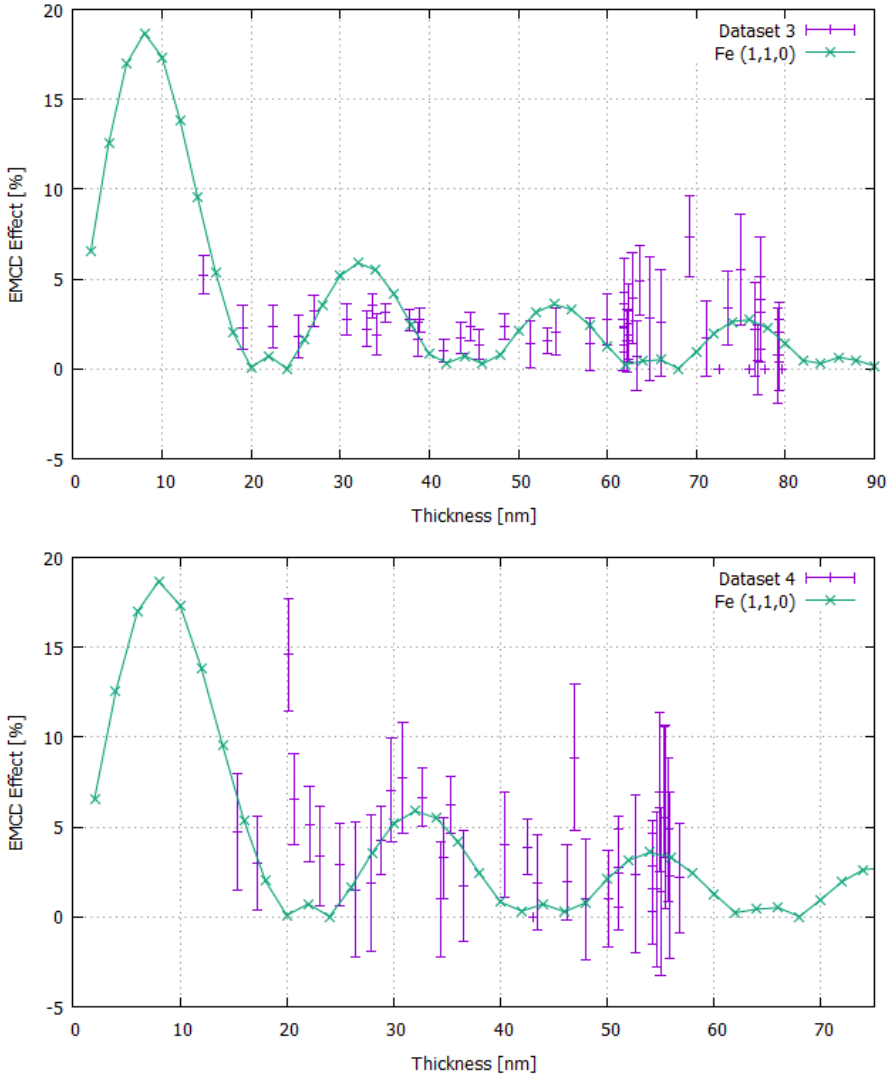

Figure 27: EMCD signal with respect to the specimen thickness for the Fe L3 edge: Dataset 3 (top) and 4 (bottom) compared with the simulation for Fe on the (1,1,0) and (-1,-1,0) reflexes.

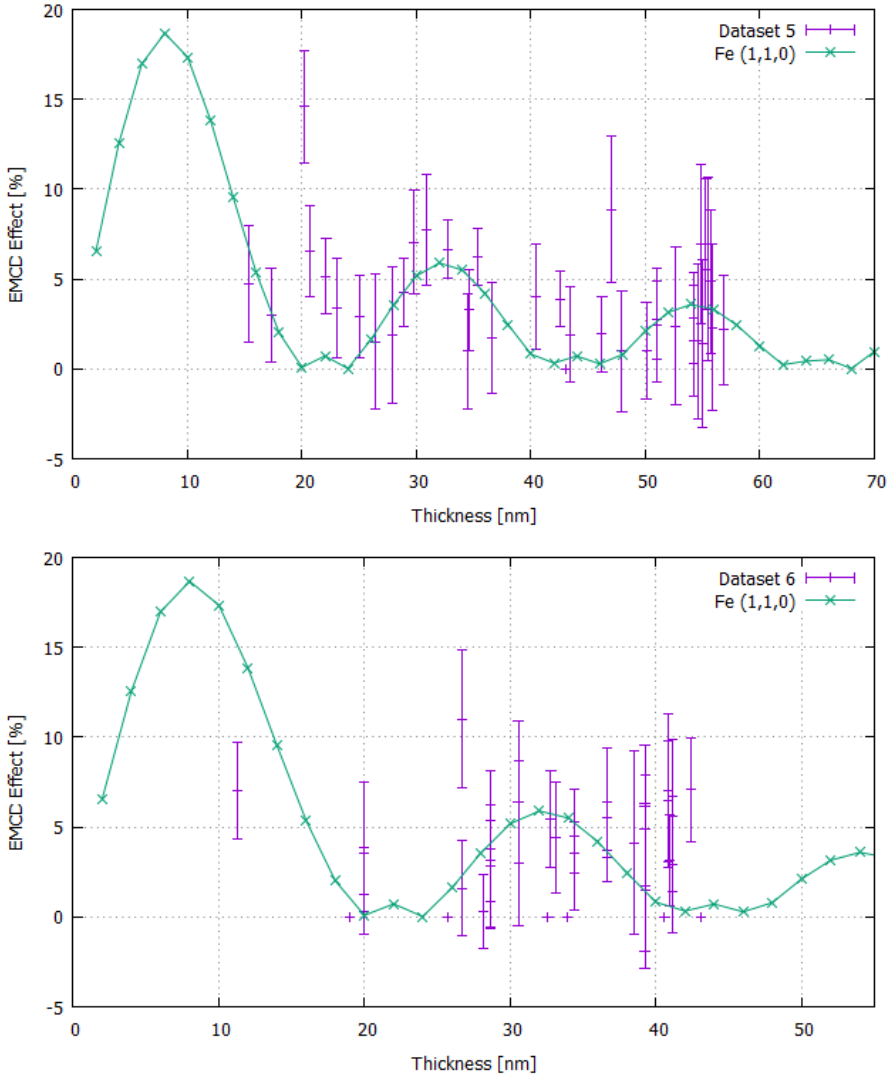

Figure 28: EMCD signal with respect to the specimen thickness for the Fe L3 edge: Dataset 5 (top) and 6 (bottom) compared with the simulation for Fe on the (1,1,0) and (-1,-1,0) reflexes.

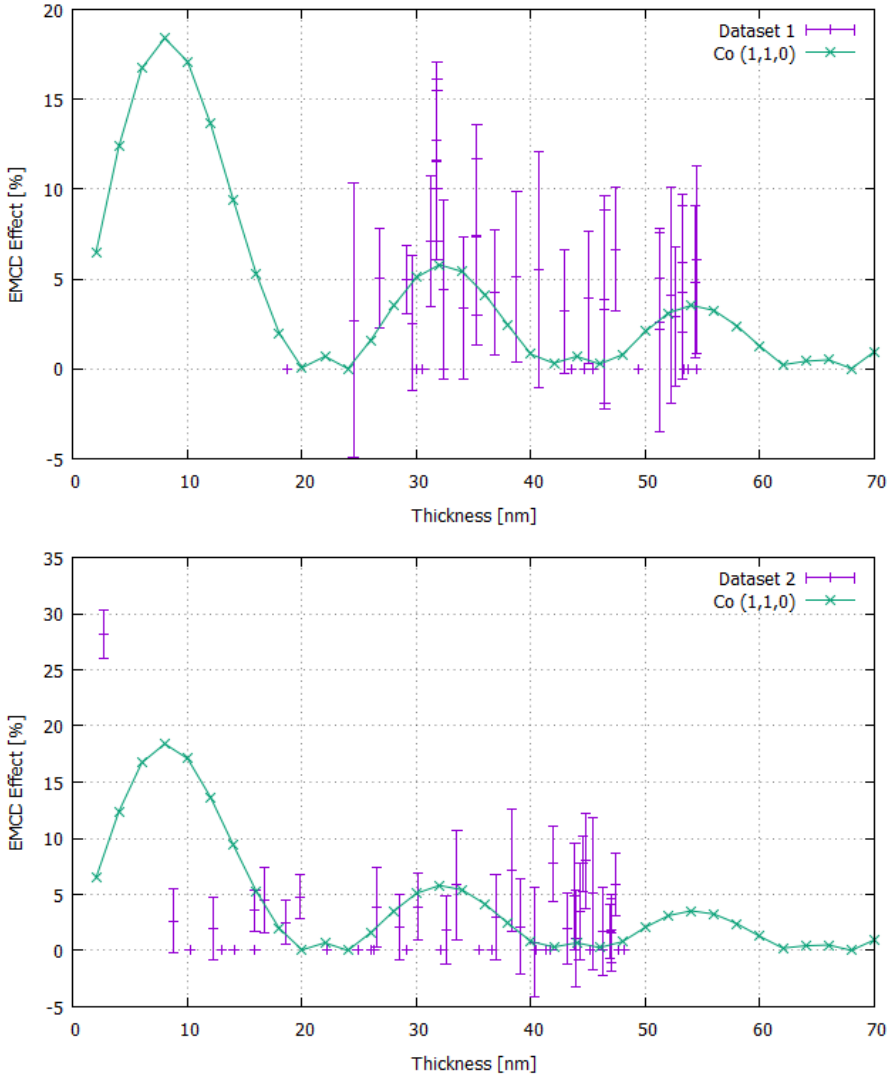

Figure 29: EMCD signal with respect to the specimen thickness for the Co L3 edge: Dataset 1 (top) and 2 (bottom) compared with the simulation for Co on the (1,1,0) and (-1,-1,0) reflexes.

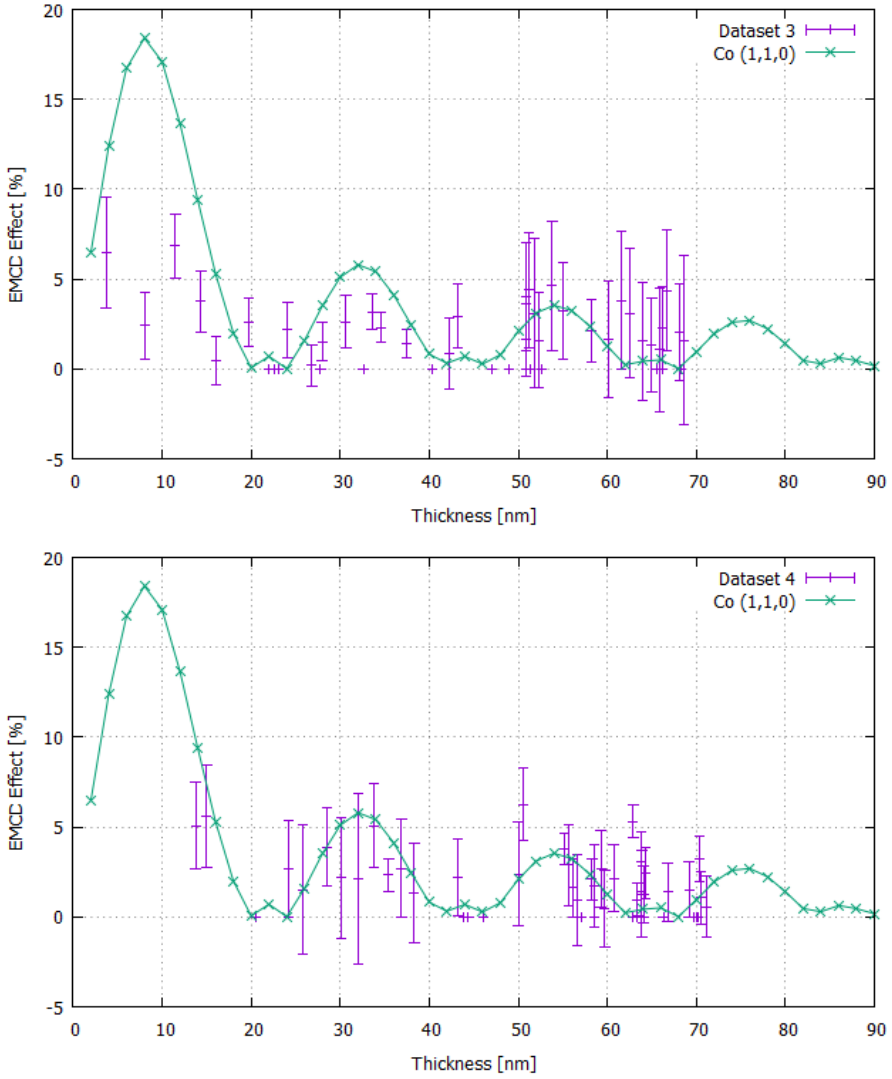

Figure 30: EMCD signal with respect to the specimen thickness for the Co L3 edge: Dataset 3 (top) and 4 (bottom) compared with the simulation for Co on the (1,1,0) and (-1,-1,0) reflexes.

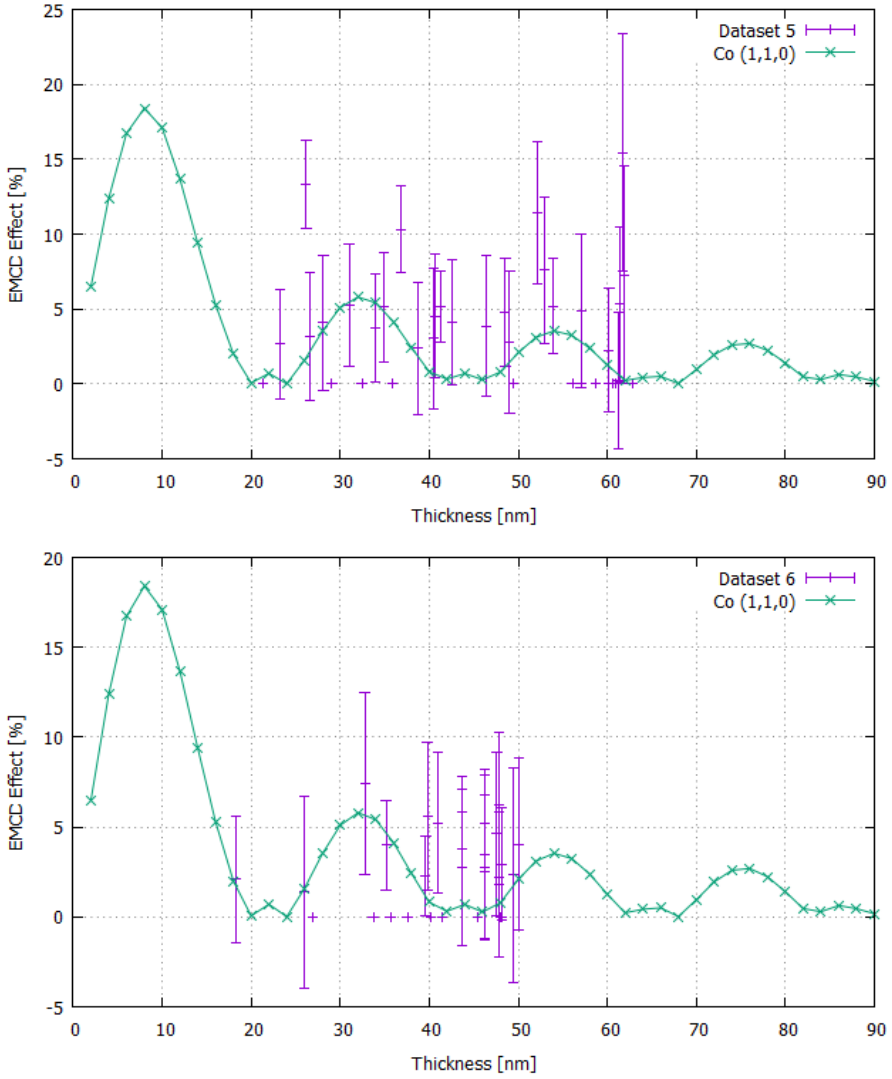

Figure 31: EMCD signal with respect to the specimen thickness for the Co L3 edge: Dataset 5 (top) and 6 (bottom) compared with the simulation for Co on the (1,1,0) and (-1,-1,0) reflexes.

3.5 Towards characterization of multilayer systems: Fe/Co_2FeSi/Fe

This multilayer system consists of layers of iron, the Heusler alloy Co_2FeSi and another iron layer, each intended to be 50 nm thick. It has been fabricated by Co-sputter deposition on MgO substrate by Andreas Becker under the following conditions: Sputter process at 450° C degrees at a base pressure of $< 5 \cdot 10^{-9}$ mbar with four sources Fe (DC-source), Si (RF-source), Co (DC-source) and MgO (RF-source, for protection on top of the layer system). After each layer a waiting time of 10 min has been kept. During sputtering the Argon flow has been set to 10 sccm, substrate rotation to 10 rpm. After sputtering cool down to room temperature in the sputtering chamber.
For pre-cleaning of the substrate before the sputtering process the substrate has been put into ultrasonic bath (10 min acetone, 10 min ethanol, 5 min DI Water), heated in the sputtering chamber to 700° C for 30 min followed by a cooling down to 450° C of 30 min. The TEM cross-section lamella has been cut using a FEI Helios FIB including a second ion beam milling after thinning at 5 kV to reduce beam damage on the specimen by Björn Büker.

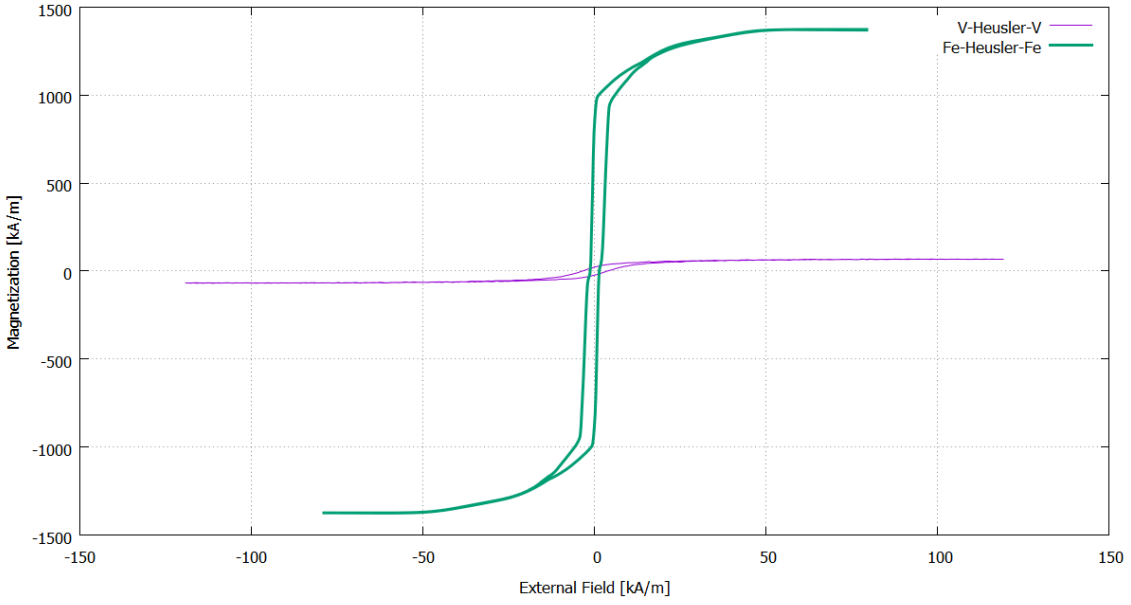

Figure 32: The AGM measurement of the Fe/Co_2FeSi/Fe layer system (green curve) and for comparison of the V/Co_2FeSi/V layer system (purple), the latter contains no other magnetic materials than the Heusler.

To obtain information about the magnetism of the sample, the original sample has been measured in the alternating gradient magnetometer (AGM) at room temperature. The magnetic active layer has an area of 12.25 mm^2 and a thickness of 157 nm. This gives a volume of $1.92325 \cdot 10^{-6}$ cm^3. The measurement is shown in fig.32 where for comparison also the measurement for the V/Co_2FeSi/V is shown, with the Heusler Co_2FeSi as the magnetically active part. But both samples have not been sputtered in the same session so it can not be concluded that both Co_2FeSi have the same properties as this is part of investigations. For now it is assumed:

The Fe clearly dominates the magnetic behaviour of the Co_2FeSi samples with a more than 20 times higher saturation magnetization of 1373 kA/m compared to 57.5 kA/m for the V/Co_2FeSi/V. This would correspond to a magnetic induction of 1.73 T (Fe/Co_2FeSi/Fe) and 0.072 T (V/Co_2FeSi/V). The hysteresis is narrow with a coercitivity of 1.3 kA/m. The remanence is measured to 840 kA/m.
Literature values are 1710 kA/m or 2.2 T for Fe [85] and $\approx$ 800 kA/m for Co_2FeSi at room temperature [86]. With these values and the layer dimensions taken into account a value of $1/3 \cdot 1710$ kA/m $+ 1/3 \cdot 800$ kA/m $+ 1/3 \cdot 1710$ kA/m $= 1407$ kA/m can be expected, the measured value is 98% of this expected value and thus in very good agreement. Possible reasons for the reduced value the V/Co_2FeSi/V shows are formation of different alloys, imperfections or defects in the sample which can reduce the (saturation) magnetization. With this agreement between expected and measured values it can be stated that the AGM measurement of the V/Co_2FeSi/V does not have the same or expected magnetic properties as a expected saturation magnetization of $\approx$ 800 kA/m is not in agreement with the measured value of 57.5 kA/m.
Measurement in the TEM shows a layer system of 157 ± 1.5 nm total thickness with the iron layer adjacent to the MgO measuring 50.0 ± 1.5 nm, the Heusler layer 56.4 ± 1.5 nm and the second iron layer $51.1 - 56.7 \pm 1.5$ nm with varying thickness because of surface roughness.

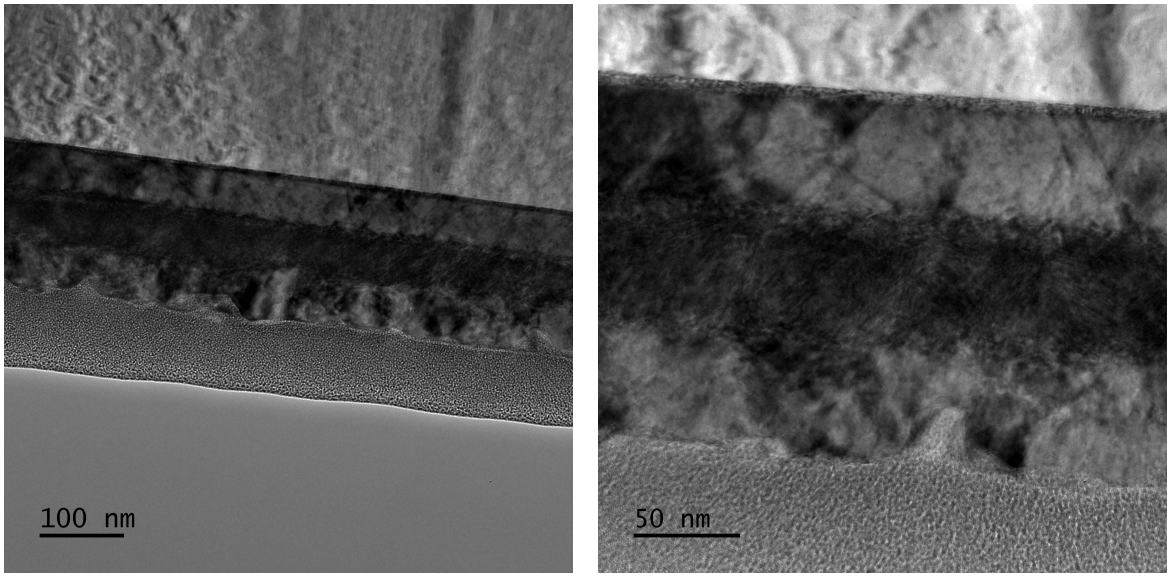

Figure 33: The (substrate on top of the image) MgO substrate/Fe/Co2FeSi/Fe/FIB Platinum layer system, images of the freshly cut lamella before it was sent to Glasgow courtesy to Inga Ennen.

To evaluate the thickness of the cross section an EELS zero loss map has been recorded on the ARM200cF (exposure time 0.0005 sec, 2.5 mm aperture, dispersion 0.5 eV/channel, STEM mag 600kx) and the relative thickness can be evaluated using the Malis t/λ method [32] implemented in a DM script by D. Mitchell [83]. The mean free path for 200 kV electrons can be calculated to:

63.84 nm for FIB-Platinum (assumption 80% Pt, 20% C)
83.65 nm for Iron
86.25 nm for Co2FeSi
111.9 nm for MgO
at an acceleration voltage of 200 kV and $\beta = 36$ mrad.

It can be assumed that the thickness is changing linearly over the layer system and only the FIB platinum might show different behaviour: to support this a line profile is taken of the thickness map in mfp (figure 35). It shows approximately linear behaviour over all layers, dropping off in the FIB platinum. The thickness was also estimated in each layer and multiplied by the mean free path of the specific elemental composition, this supports further the assumption that the thickness is a linear function on the iron and Heusler layers (figure 34).

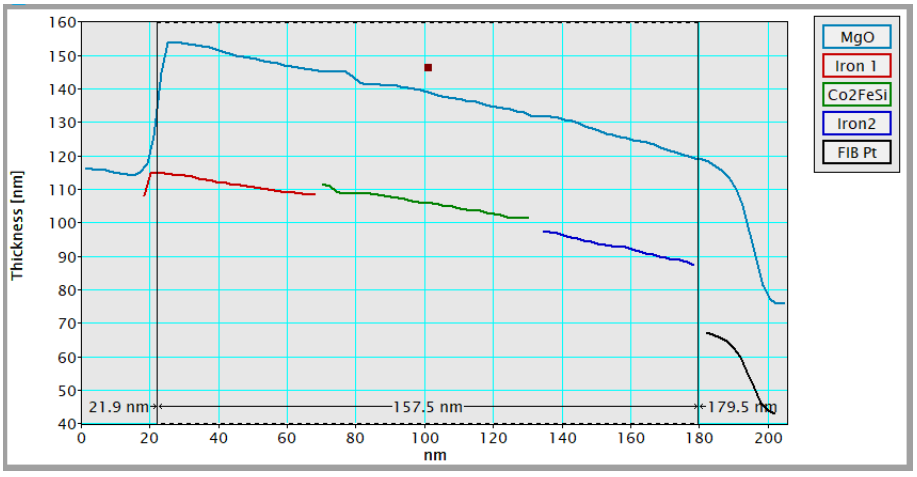

Figure 34: The line profile taken across the thickness map of the layer system in mean free path has been multiplied by the calculated mean free path for each chemical part. The thickness decreases in a approximately linear behaviour, justifying to fit a linear function to represent the thickness.

A linear function $f(x) = m \cdot x + b$ has been fitted to the Fe/Co_2FeSi/Fe part of the line profile to receive a function representing the thickness. To obtain consistent results when using this thickness function in the evaluation of the DPC data the starting point has been chosen to be the MgO/Fe interface. After length calibration in nm the fitted function representing the thickness reads

$$f(x) = -0.164289 \cdot x + 115.632 \tag{3.1}$$

for a thickness in nm and a goodness of fit statistic $\chi^2 = 0.4$. This fit quality measure is supplied by the used Gatan GMS 3 software and is based on the quadratic deviations between data and fit divided by the fit value of the point, therefore it depends also on the

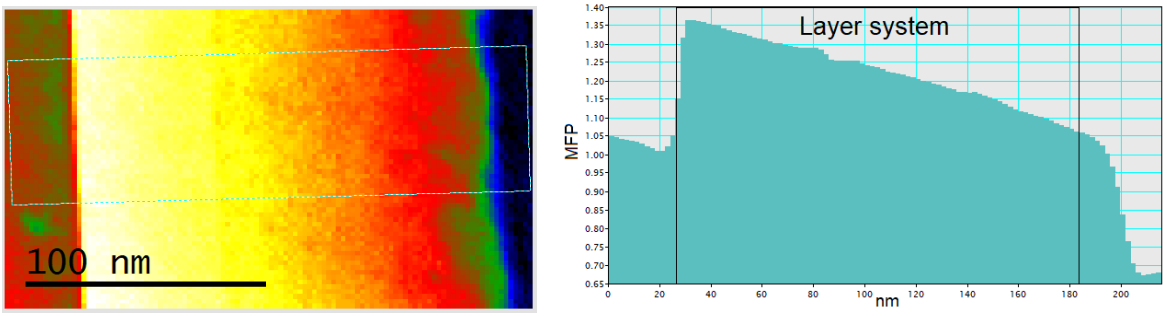

Figure 35: Thickness map of the lamella with MgO substrate on the left of the image (left) and the line profile taken from the indicated region (right, layer system marked).

units used. If the fit function is in good agreement with the relevant part of the thickness line profile the quality is considered well usable throughout this work, the error from the used EELS zero-loss based thickness estimation method is with about $7-10\%$ much larger than the fit quality determination suggests [87].

The chemical composition of the specimen has been evaluated using EELS on the ARM200cF equipped with a Gatan Quantum ER post column image filter. At a magnification of 600kx in scanning mode with a camera length of 20 cm a spectrum image of 62×110 pixels has been acquired with a dispersion of 0.5 eV per channel. The pixel time was 0.1 sec and the 2.5 mm spectrometer entrance aperture has been used. Accessible edges in the window from 250 eV to 1270 eV are oxygen K (532 eV), iron L_2 (721 eV), L_3 (708 eV), cobalt L_2 (794 eV), L_3 (779 eV) and carbon K (284 eV). Carbon is part of the precursor which contains the platinum used for deposition in the FIB. The major edges of silicon (K at 1839 eV, $L_{2,3}$ at 99 eV) and magnesium (K at 1305 eV, $L_{2,3}$ at 51 eV) are not accessible in the chosen energy window, the L-edges are in the low-loss region also superposed by phonons.
With the background-subtracted (power law) signal an elemental mapping has been performed for carbon, oxygen, iron and cobalt. A drift correction was applied to the corresponding HAADF image and the same correction used for each elemental mapping.

The interface between the oxygen from the MgO and the iron is very sharp with a width of $\approx 3.6 \pm 1.8$ nm equal to two pixels. The interface between Fe/Co_2FeSi is 9 ± 3.6 nm and the opposite interface between Co_2FeSi/Fe 18 ± 3.6 nm measured between cobalt and iron, the 2nd iron layer extends into half of the Co_2FeSi layer. The Co falls off from about the center of the Co_2FeSi layer leading to the assumption that the Co/Fe ratio is not $1 : 2$ as in Co_2FeSi but $1, x : 2 - x$ and Fe replaces Co to a certain amount in the lattice. The interface between the 2nd Fe layer and the FIB-Pt measures 5.4 ± 1.8 nm and can be considered very sharp. The Fe layer is not totally smooth and this roughness broadens the interface because of the summation over an area for the line profile. Especially apparent in the RGB overlay in fig.36 f) is that Fe has been introduced in the Co_2FeSi layer in a kind of grain in the upper part of the mapping. This has influence on the quantitative chemical composition, so another line profile has been obtained from a different region in the mapping. The result for comparison is shown in fig.37. Due to the drift correction no C is available, and in the O composition no change occurs so both are left out. No qualitative change can be observed, the amount of Fe is rising in the second half of the Co_2FeSi layer, the exclusion of the Fe-rich grain only smoothens the curve. Inside the layer the relation of Co_2FeSi is well matched with an amount of Co of $69.7 \pm 4.3\%$ and of Fe of $30.3 \pm 4.3\%$ (last third of layer excluded because of the above noted change in composition). Oxygen is only present in the MgO substrate and on the surface before the FIB-Pt has been applied, no oxidation of the layer system could be observed.
The chemically measured thickness of the layers is 50.5 nm (Fe1), 56 nm (Co_2FeSi), 50.5 nm (Fe2) measured on the chemical Fe/Co signals, the interfaces might smear it but the whole layer system is found to be 157 nm, this in consistent with the measurement from the TEM image.

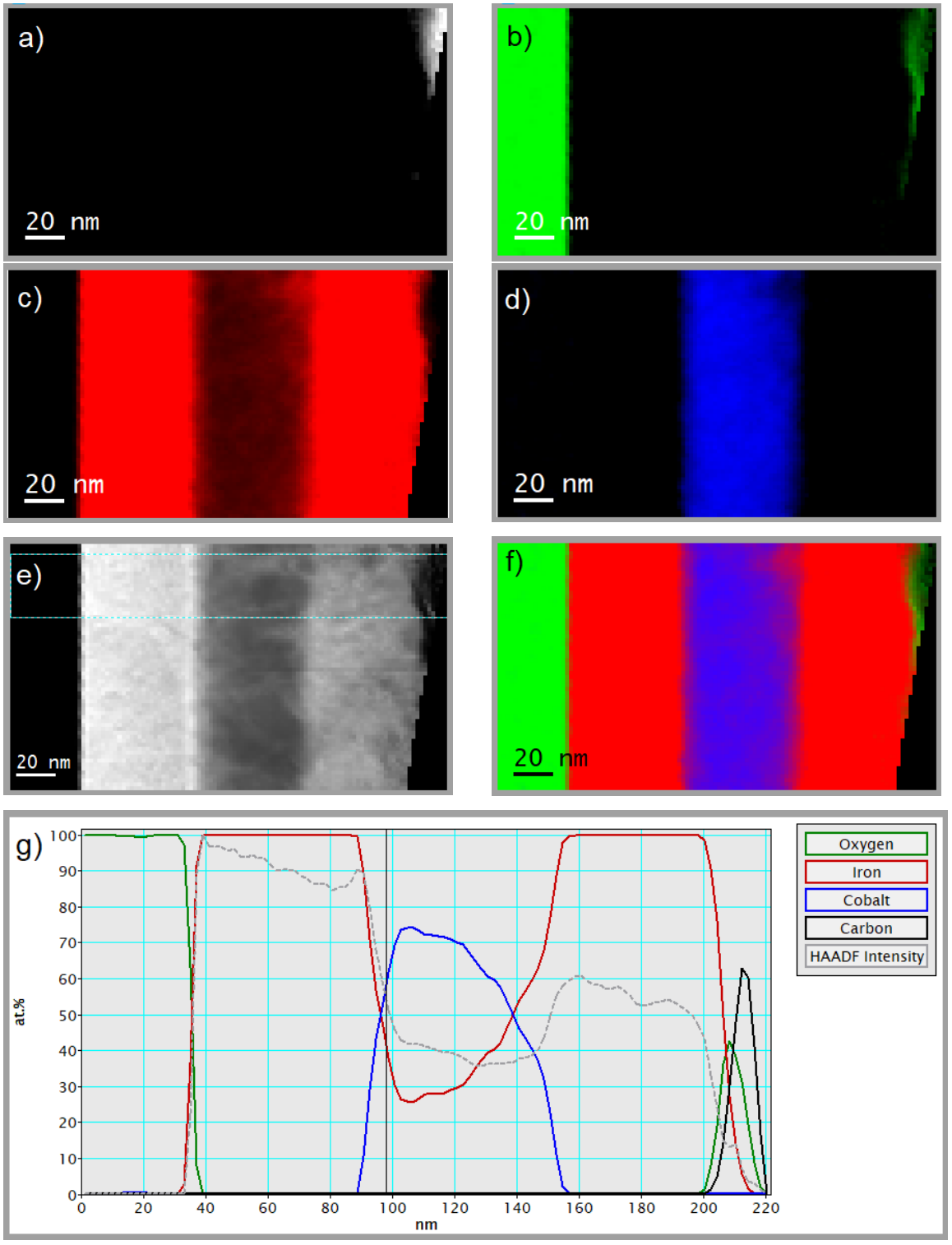

Figure 36: Drift corrected elemental maps for a) carbon, b) oxygen, c) iron and d) cobalt. The HAADF image in e) shows the layer system beginning with MgO from the left and the rectangle from where the line profile has been obtained and f) shows an overlay of oxygen (green), iron(red) and cobalt (blue). The missing part at the lower right edge results from post recording drift correction. In g) the quantitative elemental distribution across the layer system is shown with an overlay of the HAADF intensity to indicate the layer system.

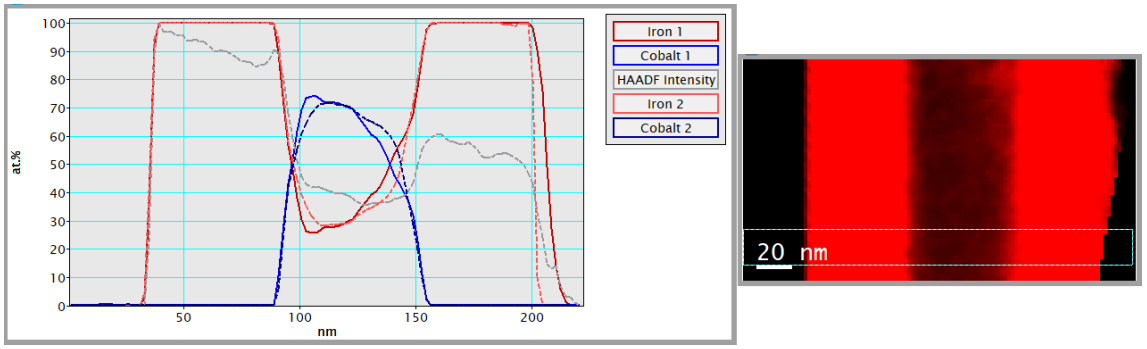

Figure 37: Left: Two line profiles of the Fe and Co composition in two different regions (numbered 1 and 2 in the legend) of the mapping overlaid, additionally the HAADF intensity profile is shown. The different decay of the Fe on the right occurs due to the drift correction that affects the second Fe layer in the second region. Right: Fe map with indicated region of the line profile.

The interface between the 1st Fe layer and the Co_2FeSi has been investigated more in detail for the interfacial properties. A spectrum image of 116×26 pixels has been recorded (dispersion 0.5 eV/channel, exposure time 0.1 sec, 2.5 mm aperture, magnification 2M, STEM camera length 20 cm) across the interface region. The data has been background subtracted and an elemental mapping been performed. The elements C and O could not be observed in this part of the specimen. The Fe and Co maps (fig.38) have been drift corrected and line profiles across the interface were obtained. In fig.38 d) they are shown with an overlay of the HAADF contrast image. Start and end of the interface region can be determined by the HAADF contrast as well as the profiles for Co and Fe. The whole interface region measures 12.5 nm, which contains two regions with different behaviour: in the left region with a width of 3.0 nm the iron drops rapidly to $\approx \frac{2}{5}$ of the former content while Co is rising. In the right region of 9.5 nm width the descent of the iron is less steep and the Co content raises to the final value for the alloy Co_2FeSi.
A simultaneous EELS and EDX measurement of all the interfaces of this specimen has been performed on the ARM200F in Paderborn. The results are shown in the Appendix 6.3. The quality of the layers is important for their magnetical properties, as for example

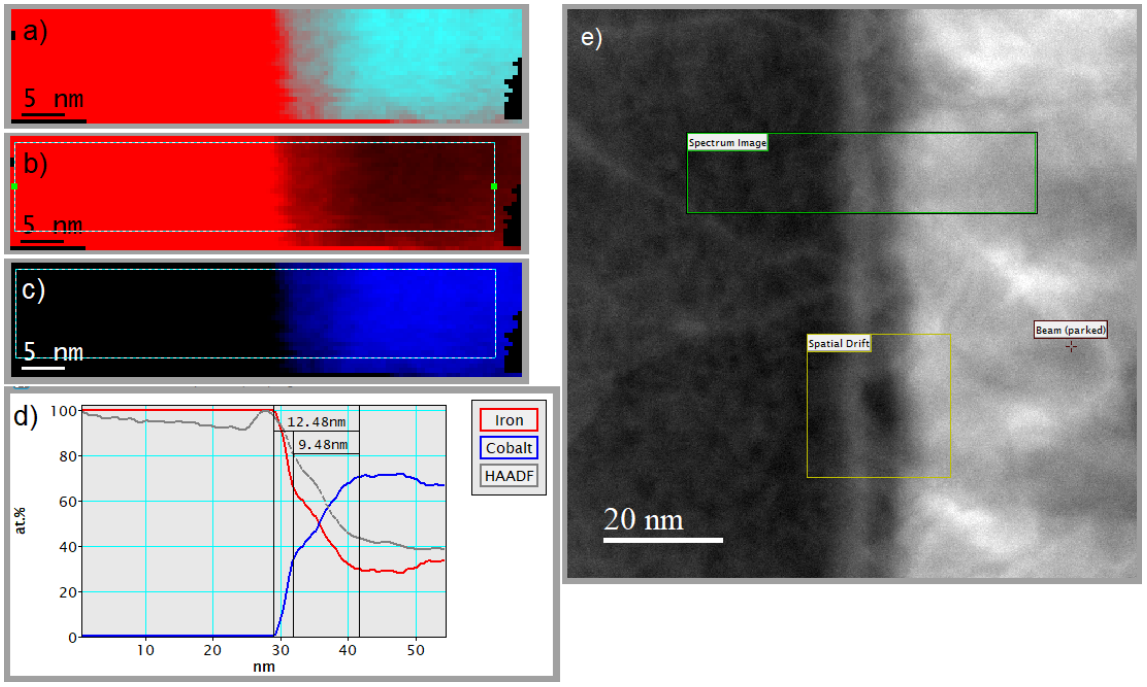

Figure 38: Drift corrected elemental maps for a) Fe/Co overlay, b) iron and c) cobalt, the drift correction failed in the bottom row of pixels. In d) the line profiles for Fe and Co as taken from the indicated region in the Fe map and an overlay of the HAADF contrast image are shown. The interface region is indicated and measured to be 12.48 nm in total and both interfacial regions are 3.00 nm and 9.48 nm. The STEM SI survey image with marked regions for the spectrum image and the drift correction is shown in e).

grains of different alloys would produce additional interfaces and magnetically different up to nonmagnetic regions in a layer. Diffusion can alter the interfaces in between the layers and introduce additional chemical compositions, roughness of a layer hinder the epitaxially

growth of the next layer. The quality of the layer system has been investigated by a peak shift mapping, high resolution HAADF and STEM of the interfaces and Single Precession Electron Diffraction (SPED).

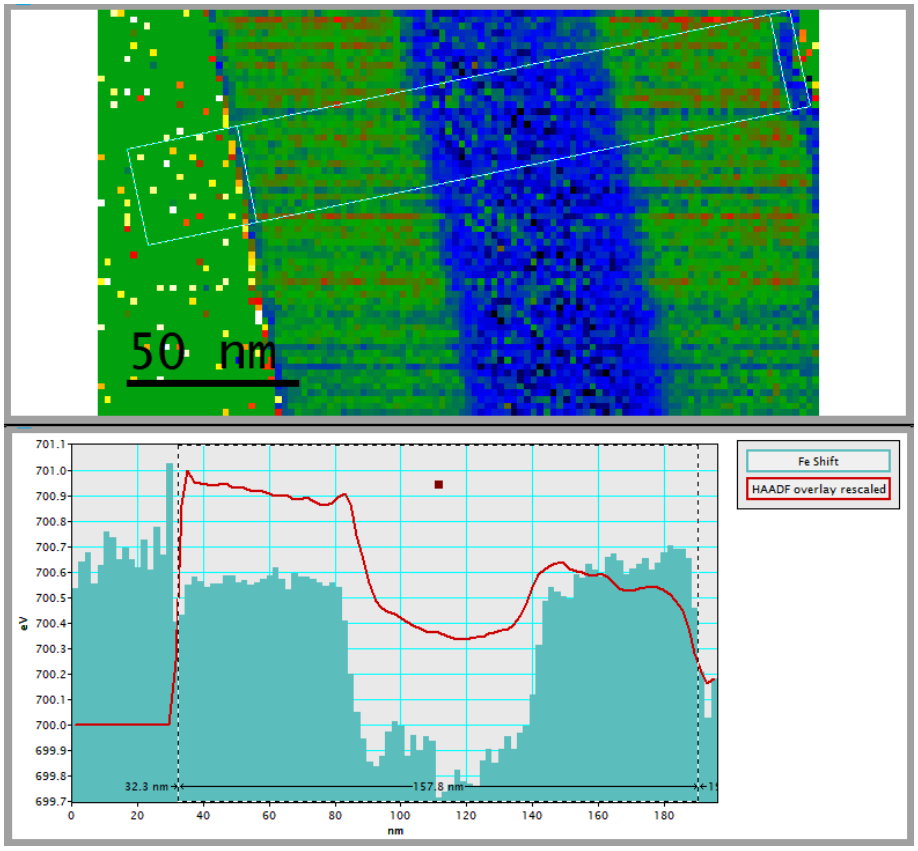

Figure 39: Peak shift mapping with line profile across the layer system, overlaid in the line profile with a rescaled HAADF contrast lineprofile of the same region.

The chemical shift of the Fe peak has been measured over the whole mapping (fig.39). The line profile taken of the peak shift across the layer system shows nearly no shift for the 1st Fe layer and slightly rising shift for the 2nd Fe layer. The value of the peaks do not center around the value of 708 eV for the Fe L3 edge because of an inherent energy shift in the spectrometer. Mean for the 1st Fe layer reads 700.57 ± 0.02 eV and for the 2nd layer 700.62 ± 0.06 eV. In the Heusler region the layer is separated in two regions, one region measures 19 nm in width and the Fe peak lies at 699.94 ± 0.06 eV then there is a very steep descent to 699.7 eV rising again to the level of the other region across 28.5 nm of the layer. The mean lies at 699.85 ± 0.09 eV which does not seem much different from the other region but qualitative there happens something different from the other region as there can be seen sudden shifting and a descent that does not occur in the other region. The line profile has been integrated over 15 pixels so local fluctuations are evened out.

The interface between Fe and MgO shows a 0.6 eV shift in the 3.6 nm interface region, followed by a 0.2 eV shift in the opposite direction for another 3.6 nm, from then on the 1st iron layer goes on. This can be interpreted as a shift in the chemical bonds as they react to the strain resuling from the mismatch in lattice constants of MgO and Fe (lattice parameter of MgO: 4.217 Angstrom, of α Fe 2.866 Angstrom, lattice mismatch 4.04% for a rotation angle of 45° between the lattices) and the first 3.6 ± 1.8 nm of the iron are under strain. The interfaces between iron and Co_2FeSi show similar changing in peak shift (width 5.4 ± 1.8 nm), it is not possible to distinguish the interfaces from each other, the change in the amount of iron in the Co_2FeSi/Fe interface is not visible in the peak shift of the interface itself.
Left of the interface seem to be very noisy shifts but they are not real shifts: There was no iron anymore, but on some datapoints the program was able to detect a very noisy peak, these show up in the mapping itself as mostly white and orange dots in between the uniformly green and by integrating over the part show as a signal. A threshold for the maximum shift has been set to 2.5 eV to cut off spurious and non-physical shifts resulting from non-accurate peak detection in the noise on the data but below this threshold wrong peaks can still be detected.

The dataset of the Fe/Co_2FeSi interface (fig. 40) has been evaluated for peak shifts. The dataset has been corrected for sample drift and for drift of the zero loss so only real chemical shifts remain. The width of the interface in peak shifts measures 9.0 ± 0.5 nm, this width measures the distance between (chemically) unstrained iron to unstrained Co_2FeSi.

HAADF images were also recorded as there are especially contrasts proportional to the atomic number visible due to the high scattering angle as well as grains in the layers. Fig.41 (left) shows a HAADF image of the whole layer system. In the line profile the layer widths can be measured as well as the interface widths. The 1st Fe layer measures 48.8 ± 0.8 nm, the Co_2FeSi layer 56.6 ± 0.8 nm and the 2nd Fe layer 50.8 ± 0.8 nm. Within the error margins this is consistent with the measurement in TEM mode and the total layer system thickness. The interfaces are measured to: 2.89 ± 0.5 nm for MgO/Fe, 7.44 ± 0.5 nm for Fe/Co_2FeSi, 7.85 ± 0.8 nm for Co_2FeSi/Fe and 4.13 ± 0.5 nm for Fe/FIB Pt. The 2nd Fe layer is not uniform, the intensity is falling uniformly for the left 27.7 ± 0.8 nm and uniform in the right part of the layer. Grains are measured to be 20-30 nm in the Fe layers and 15-20 nm in the Co_2FeSi layer. In the right image at the higher magnification of 2.5M the Fe/Co_2FeSi interface measures 5.94 ± 0.3 nm but there are many different contrasts so it is not possible to determine the beginning end end of the interface accurately, so only the part of the descent from starting signal to end signal has been measured. In figures 42 and 43 atomic resolution HAADF images of the MgO/Fe and Fe/Co_2FeSi interfaces are shown, improved by FFT filtering. The interface width can not be determined more accurately here because not all of the interface region fits into the scanned region in fig. 43. The MgO/Fe interface is measured to be 2.45 ± 0.3 nm.

In conclusion the MgO/Fe interface can be considered sharp without diffusion and introducing lattice strain only in the interface region because of the lattice mismatch of both compositions. The 1st Fe layer is chemically uniform and grown epitaxially. The

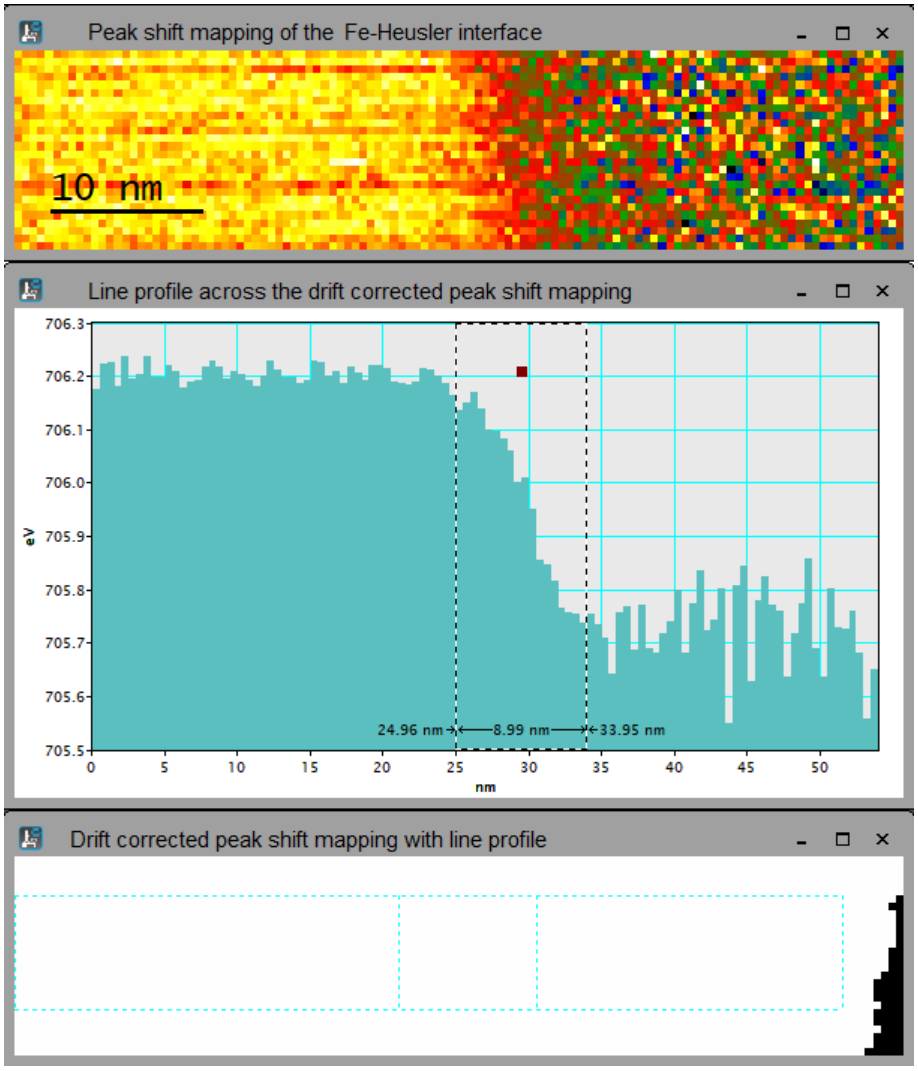

Figure 40: Peak shift mapping with line profile across the interface between the 1st Fe and the Co_2FeSi layer, the line profile has been taken from the drift corrected shift map as shown below.

Fe/Co_2FeSi is still sharp chemically with not much strain. The Heusler is divided in two parts approximately half of the layer, the first can be assumed to be pure Co_2FeSi, the second shows an continuous increase in iron and possibly created different alloys that contain Co and Fe in varying parts. The Co_2FeSi/Fe interface is in the HAADF and TEM visible as a rough interface but chemically the transition from Co_2FeSi which already contains Fe to pure Fe starts $\approx$ 20 nm from the Co_2FeSi/Fe interface and is probably caused by diffusion and the sputtering process of the second Fe layer.

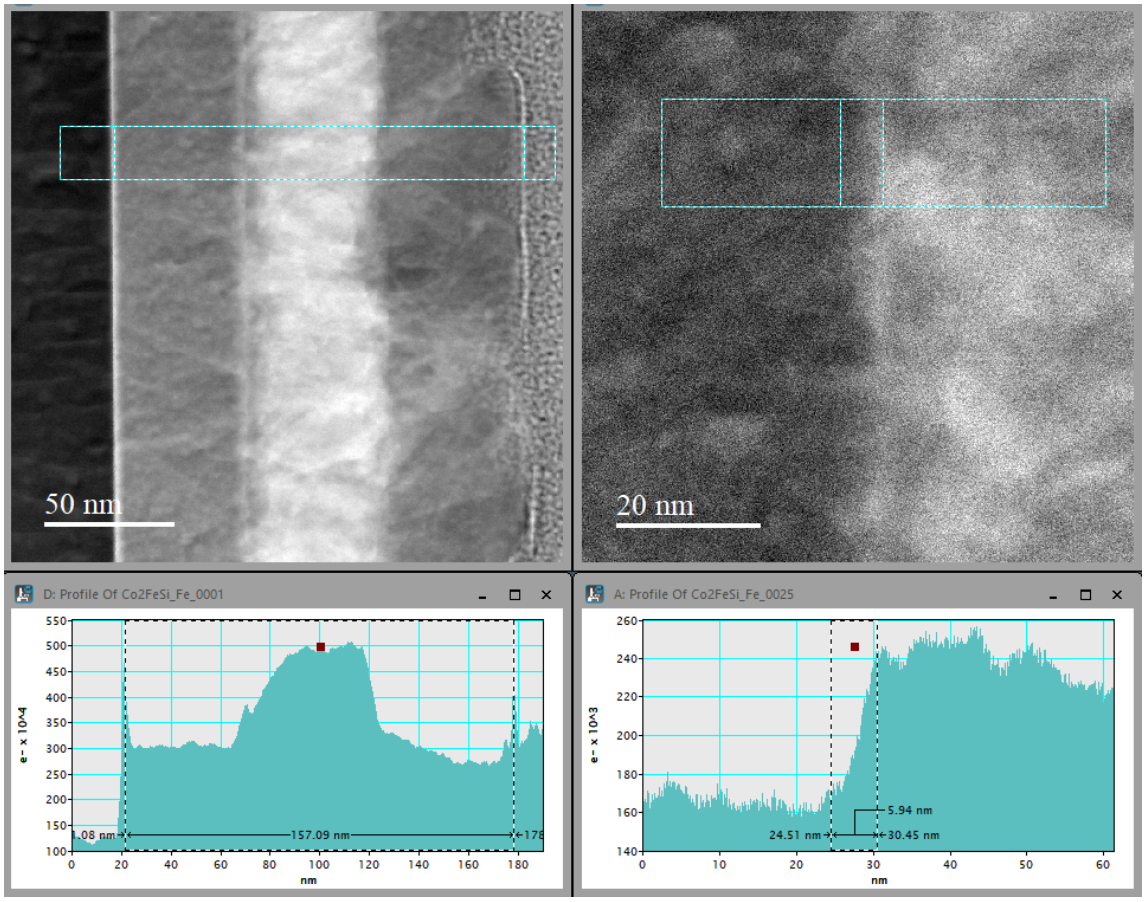

Figure 41: HAADF images of the whole layer system (left) and the Fe/Co_2FeSi interface (right). Below line profiles taken across the whole layer system and the interface.

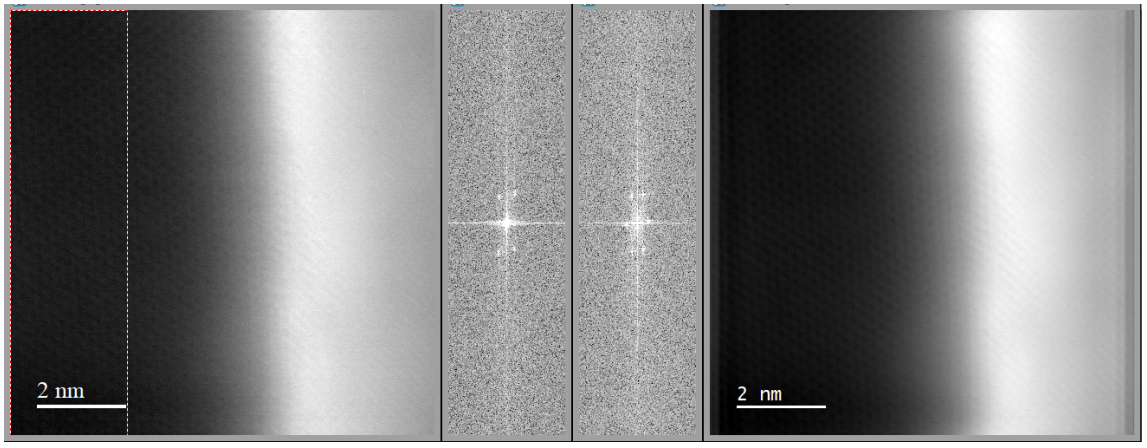

Figure 42: HAADF atomic resolution image of the MgO/Fe interface. Left original with ROI on it, in the center FFT images of this region on the left and on the right of the original image and on the right improved image by FFT, masking and adding both images.

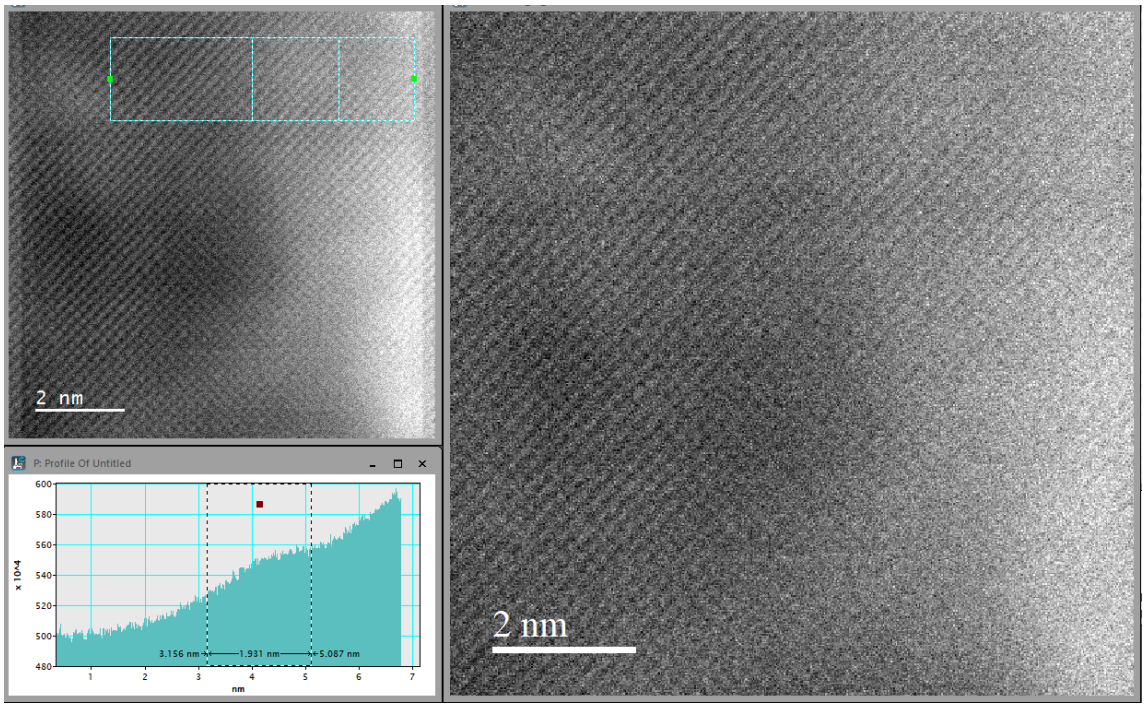

Figure 43: Right: HAADF atomic resolution image of the Fe/Co_2FeSi interface, left FFT filtering improved image with line profile across the interface (displayed below).

3.5.1 Micromagnetic simulations

For an overview of the magnetic properties that can be expected micromagnetic simulations with Mumax [62] have been performed. Further evaluation simulating DPC effects needs a thickness of the simulated sample of one layer, so the maximum possible thickness is the maximum cell length in this direction.
The mesh for the simulation has been set to $512 \times 512 \times 1$ cells with the cell size to be $5 \cdot 10^{-9} \times 5 \cdot 10^{-9} \times 10 \cdot 10^{-9}$ m. Three regions for the three active magnetic layers have been defined, each to be 50 nm (10 cells) wide in X-direction, 2560 nm (512 cells) in Y-direction and 10 nm (1 cell) thick.
For the material parameters the saturation magnetization Msat and the exchange stiffness Aex have been set. For iron is Msat=$1710 \cdot 10^3$ A/m [85] and Aex = $25 \cdot 10^{-12}$ J/m [85] and for Co_2FeSi the value of Msat=$881 \cdot 10^3$ A/m has been used, which is originally from a measurement of Co_2MnSi [88] but in still in agreement with Co_2FeSi values [86]. For the exchange stiffness Aex = $23.5 \cdot 10^{-12}$ J/m [89] has been used, also taken from Co_2MnSi which represents this kind of Heusler alloys as these simulations are to be taken as a guideline. No external Field has been applied in first simulations, in further simulations a field in x- and y-direction has been applied to have the sample magnetized in-plane. The whole system has been run through a hysteresis. The initial state has been set to random magnetization. The whole system is evolved to the minimum energy state by the `relax()` function. It is assumed here the minimum energy state has been found after relaxing the system, but it can not be confirmed as a saddle point, local minimum or very flat valley can be found instead. But it is a more robust method against divergence than the `minimize()` method which uses the conjugate gradient method [62]. The output can be imported into Gatan GMS for calculating the phase image that gives a sketch of what will be seen in DPC.

The simulation results for a relaxed sample are shown in fig.44. From random magnetization a magnetic field rising in 0.001 T steps to 0.1 T and back has been applied and at each step the energy has been minimized before changing the magnetic field. After the external magnetic field reached zero the state has been relaxed again. The magnetization in y-direction shows what to expect on a three layer sample that is magnetized in plane in this direction. The signal strength from the Co_2FeSi should be about half as strong as the one from the iron and hence be visible in DPC measurements.

In the microscope the objective lens has been switched on to a small value to tilt the specimen into the field and introduce an in-plane magnetization. This has been modelled by starting from a magnetic configuration with the iron layers magnetized parallel and antiparallel in y-direction and the Co_2FeSi starting from random magnetization. The 1st order uniaxial anisotropy constant has been added to the simulation and reads Ku1 = $4.81 \cdot 10^4$ J/m^3 for iron and Ku1 = $2.89 \cdot 10^3$ J/m^3 for Co_2FeSi. The magnetic field has been driven up to a very small value of 0.006 T and down again.

In the parallel magnetized layers case the result is qualitatively equivalent to the one shown in fig.44 and discussed above. If the starting configuration is magnetized antiparallel in y-direction in the iron layers, domain walls and regions of differently oriented magnetization

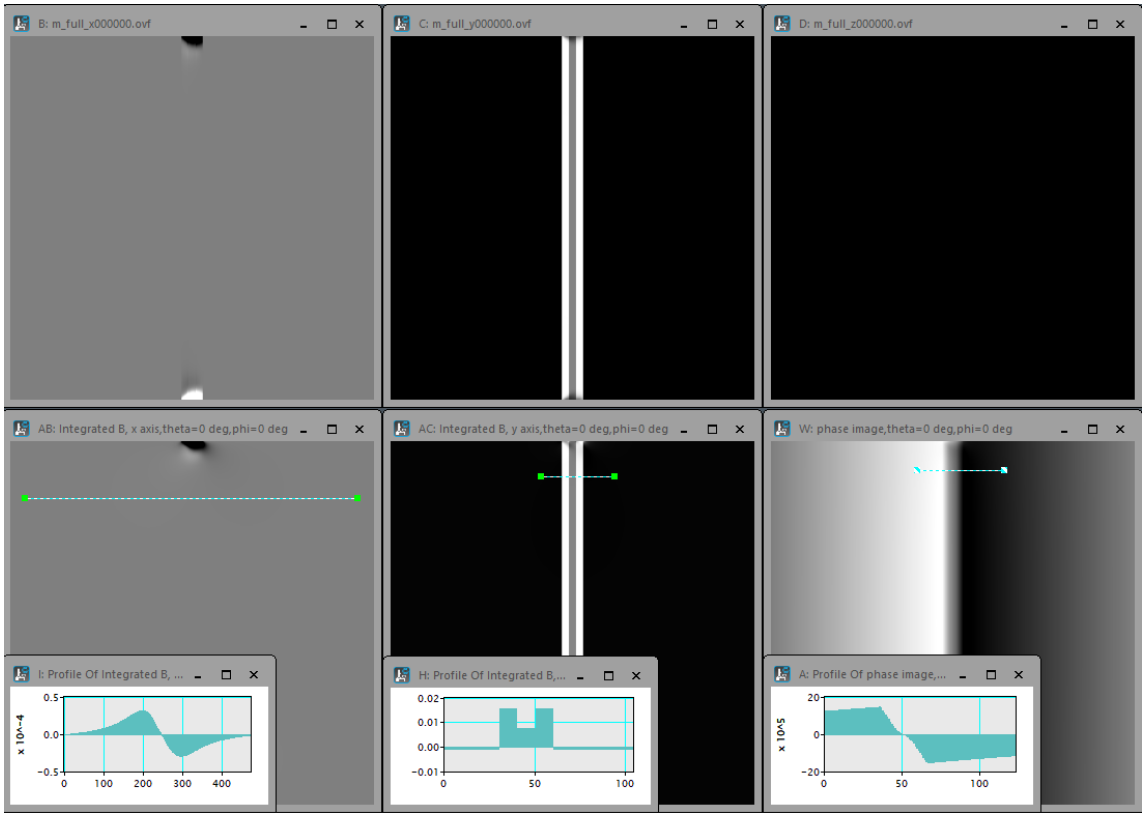

Figure 44: Simulated magnetization started with both iron layers magnetized parallel in y-direction for the x, y and z direction (upper row) and calculated integrated magnetization in x and y direction and the phase image (lower row).

are forming. The Co_2FeSi, which is a soft magnetic alloy, aligns itself according to the initial magnetization that formed from the random magnetization state in interaction with the iron magnetization. Several states are possible, with the whole Co_2FeSi being magnetized at whole like one of the iron layers, the outer parts of the Co_2FeSi each magnetized like the adjacent iron layer, the Co_2FeSi being nearly unmagnetized in y-direction and acting as a bridge to connect both iron layers magnetically and all possible states in between. The possible states are shown in the line profiles taken across the y magnetization in different positions that are in different states in fig.46. From the simulation the existence of domain walls can be expected with approximately one domain wall in 200 nm of the lamella length according to fig.45.

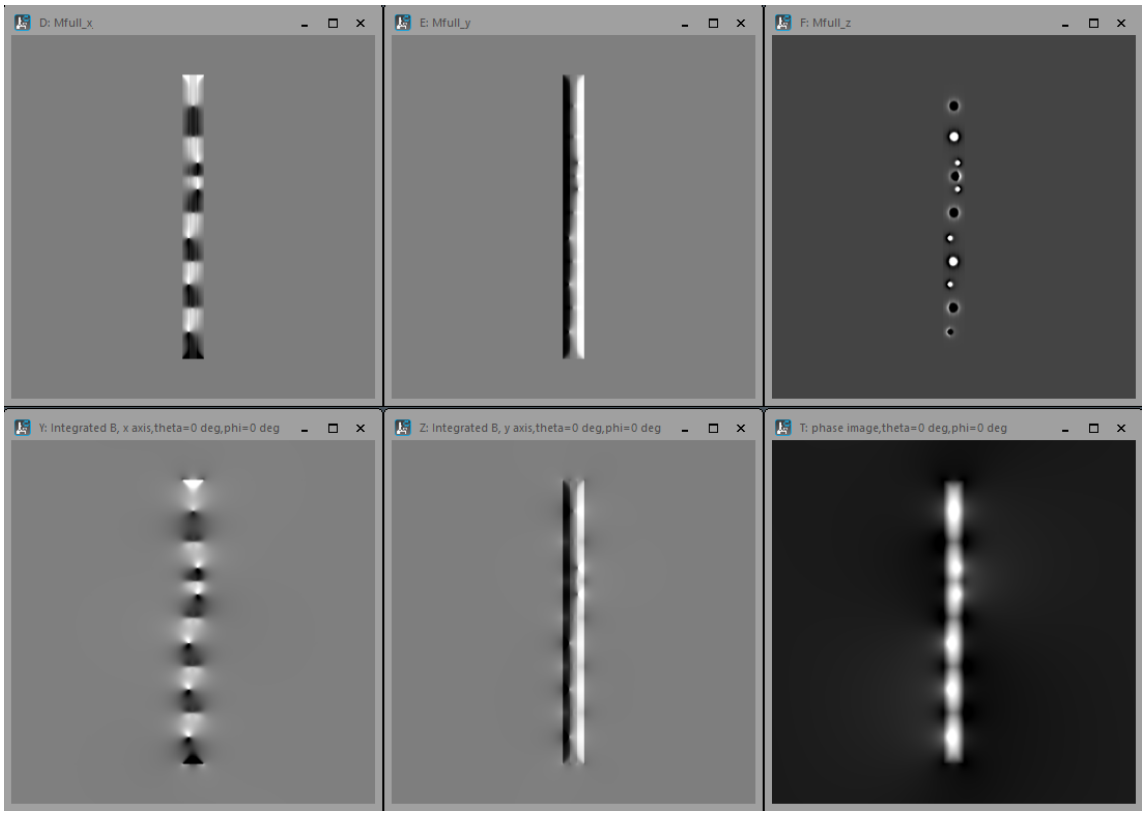

Figure 45: Simulated magnetization started with both iron layers magnetized antiparallel in y-direction for the x, y and z direction (upper row) and calculated integrated magnetization in x and y direction and the phase image for DPC (lower row).

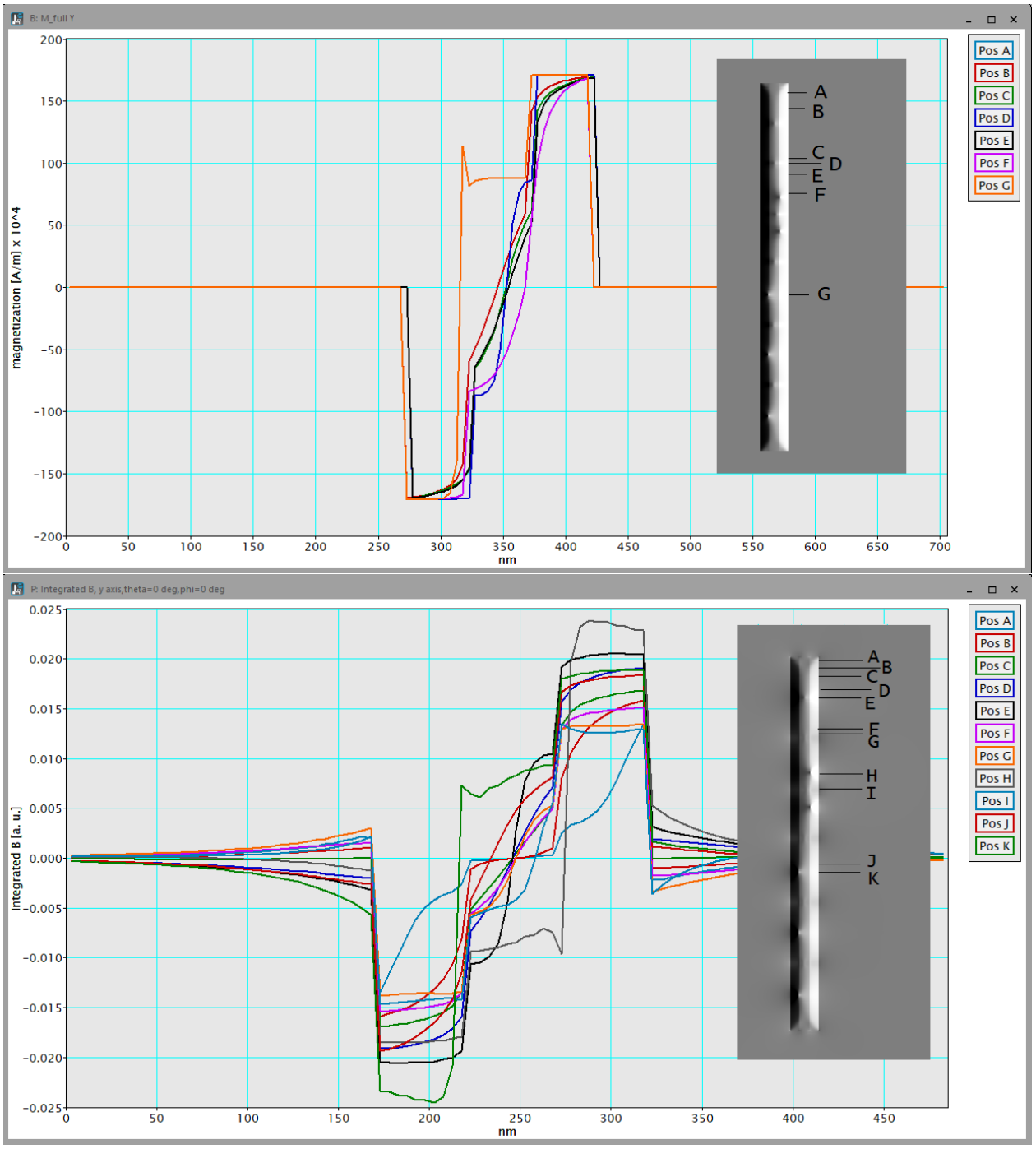

Figure 46: Top: Line profiles across the simulated magnetization in y-direction for an antiparallel iron state with included simulation result in the right part of the image. The y direction has been chosen as it resembles the view one gets in the electron microscope. The line profiles shown are taken on the position labelled with the respective letter. Bottom: Line profiles across the integrated magnetic induction calculated from the simulated magnetization, which is shown inside the image on the right. The line profiles are taken on the position indicated by the letter.

Additional micromagnetic simulations using Micromagus [65] have been supplied by A. Hütten. The system has been simplified to reduce the computing effort by modelling the layers with thinner subsystems: 50 nm Fe =8 nm + 8 nm + 8 nm + 8 nm + 8 nm + 8 nm + 2 nm and 56 nm Co_2FeSi = 15 nm + 15 nm + 15 nm + 11 nm with the layer thickness < demagnetization length. A hysteresis has been calculated by equilibrating the system in an external field of 0T $\rightarrow$ 0.5 T $\rightarrow$ 0.5 T $\rightarrow -0.5$ T $\rightarrow -0.5$ T $\rightarrow$ 0 T. The material parameters are the saturation magnetization of 1710 kA/m [85] for Fe and 800 kA/m [86] for Co_2FeSi, the anisotropy constant for Fe is $K_1 = 48$ kJ/m^3 $= 4.8 \cdot 10^5$ erg/cm^3, the exchange coupling $A = 21$ pJ/m$= 2.1 \cdot 10^{-6}$ erg/cm [85] which leads to the exchange length

$$l_{exch} = \sqrt{A/K} = 2.092 \cdot 10^{-6} \text{ cm}$$

,

$$L_{spm} = \frac{\left(\frac{220 \cdot T \cdot k_B S_i}{K S_i \cdot \pi}\right)^{(1/3)}}{1 \cdot 10^{-9}}$$

with $k_B S_i = 1.380649 \cdot 10^{-23}$ J/K, $KS_i = 48 \cdot 1000$ J/m^3 $\Rightarrow$ $L_{spm} = 18.432$ nm and demagnetization length

$$l_{dem} = \sqrt{(A/M_s)^2} = 8.474 \text{ nm}$$

and the damping parameter $\alpha = 0.0131$ [90]. For Co_2FeSi the parameters read exchange coupling $A = 31.5$ pJ/m$= 3.15 \cdot 10^{-6}$ erg/cm [91], $K_1 = 8960$ erg/cm^3 [86], the exchange length $l_{exch} = 187.5$ nm, the demagnetization length $l_{dem} = 17.411$ nm, $L_{spm} = 69.485$ nm and the damping parameter $\alpha = 0.04$ [91].

The simulation reproduces the measured hysteresis qualitatively with good agreement (fig.47), the saturation magnetization is in good agreement between AGM data and simulation, features of the measured hysteresis like the bend at ≈ 1000 kA/m are not well reproduced and the simulated coercitivity of 8.5 kA/m is ≈ 6 times as high as the measured coercitivity of 1.3 kA/m. The simulated remanence of 1280 kA/m is ≈ 1.5 times higher than the measured one of 840 kA/m. The domain wall thickness for Bloch walls in Fe is calculated to $\delta_{BW}^{\text{Fe}} = 65.71$ nm and in Co_2FeSi to $\delta_{BW}^{\text{Co}_2\text{FeSi}} = 589.05$ nm. From the observed magnetic states in the hysteresis appearance of magnetic domains and domain walls can be observed. The differences between simulation and measured values originate from the simulation being an idealized model and a magnetostatic calculation which does not reproduce the dynamic interactions inside the sample. Also the sample is in reality much more complex from the materials and crystallographic part, the simulation uses only a description of the model on a larger than atomic scale.
Guided by the simulations one can expect the appearance of domain walls, if their thickness is far below the calculated Bloch wall thickness Neel walls can be expected because they become energetically favourable over Bloch walls (fig.48 right). A switch of parts of the layer system or the full layer system caused by external fields can be expected in DPC measurements with a measurable remanent field.

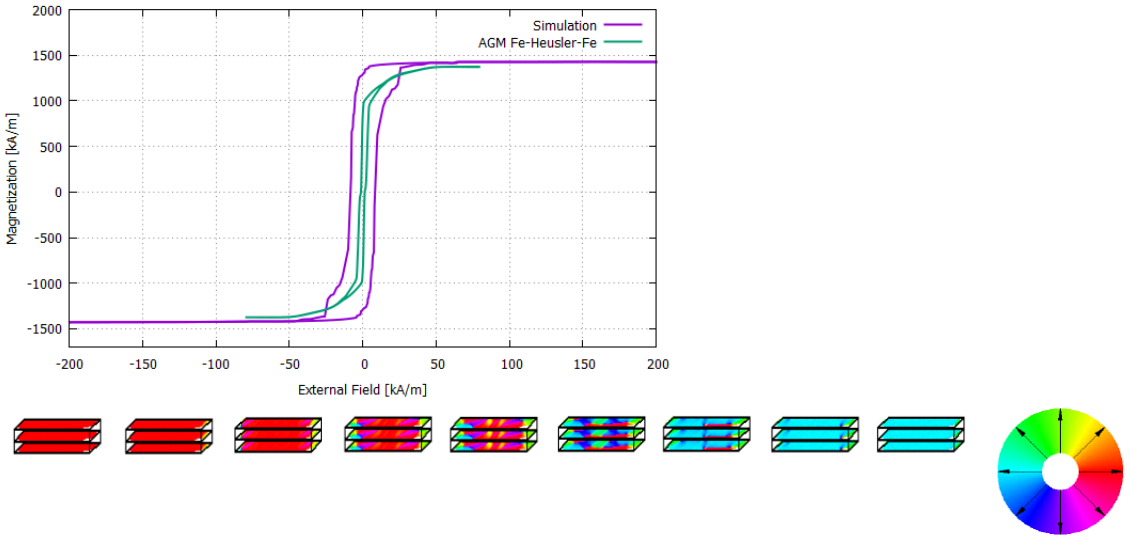

Figure 47: Top: The hysteresis simulated with Micromagus (purple) compared to the AGM measurement for the Fe/Co_2FeSi/Fe sample (green). The saturation magnetization is reproduced with good agreement, the sharp bend of the measured hysteresis at ≈ 1000 kA/m is not well reproduced, the coercitivity is broader and the remanence higher in the simulated data. Bottom: Intermediate states from the simulation depicting the change of the magnetic state and appearance of domains and domain walls, colour wheel for directions on the right. Simulation data courtesy to A. Hütten.

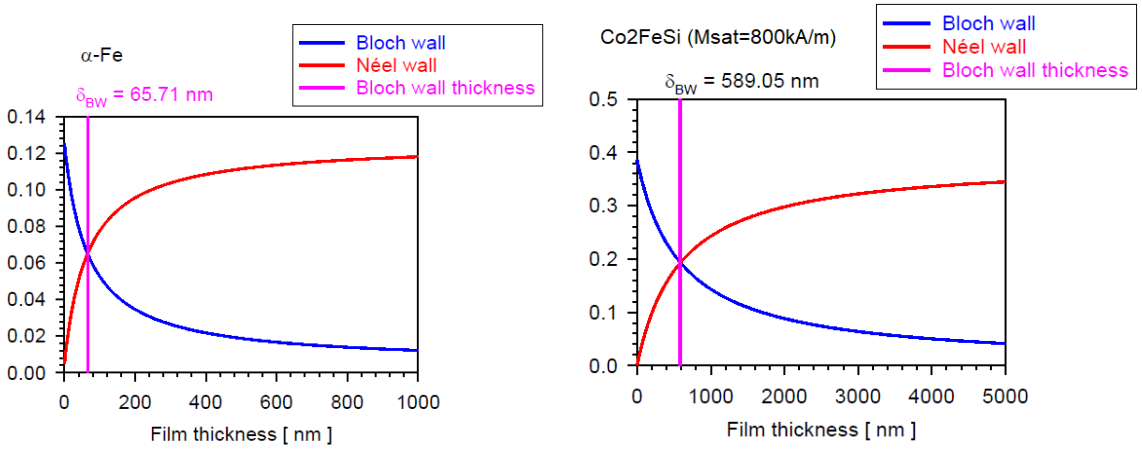

Figure 48: These graphics show the point where a Neel domain wall is energetically favoured over a Bloch wall and the calculated domain wall thickness corresponding to this point for both materials used in the layer system: Fe (left) and Co_2FeSi (right). Simulation and graphics courtesy to A. Hütten.

3.5.2 EMCD measurements

A set of EMCD linescans in STEM mode has been performed on the ARM200F. The acquisition parameters are 4 cm camera length and 10 μm aperture to obtain (nearly) separated diffraction discs, spot size 4C, magnification 500kx or 600kx, exposure 20 sec on the camera of the Gatan Quantum ER image filter. The drift tube voltage has been set to 500 V, the 5 mm entrance aperture has been used and a dispersion of 0.25 eV/channel (setting 1).
Due to low intensity in the spectra this has been changed to 6 cm camera length, 1eV/channel dispersion and 500 eV drift tube setting (setting 2). The specimen has been tilted to a systematic row condition on the layer system before such that the row lies nearly perpendicular to the dispersion on the spectrometer camera. Fine adjustment for perpendicularity has been done using the free lens control on the lower illumination system lenses PL and IL1,2. Then the systematic row has been moved on the camera so only a small part of the central beam and the two EMCD positions text to it enter the spectrometer (fig.49).
The diffraction reflexes used have been determined to be the (2,0,0) and (-2,0,0) reflexes using JEMS [77].
With this settings an EDX linescan has been acquired while having the spectrometer in

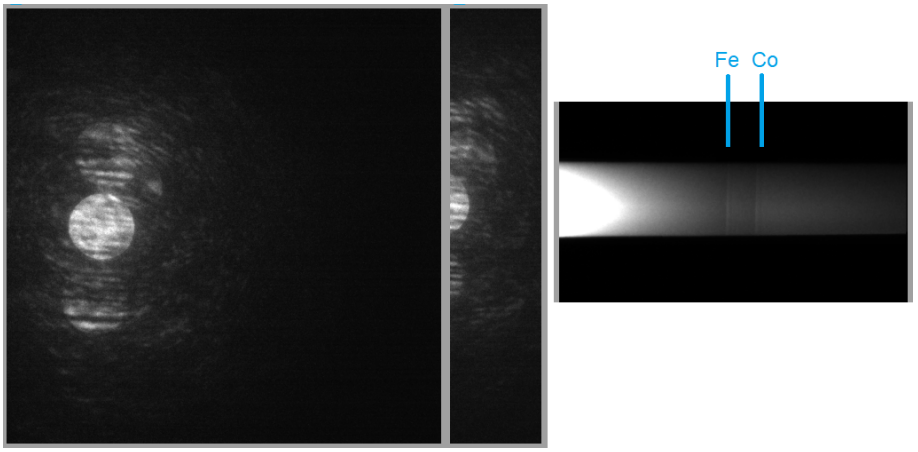

Figure 49: Position of the diffraction discs obtained using the 10μm condenser aperture in STEM mode on the spectrometer camera. They are moved out of the entrance aperture until only a small part of the discs including the EMCD positions can enter the spectrometer. A part of the resulting spectrum is shown on the right with both Fe and Co edge from the Co_2FeSi at a dispersion of 1 eV/channel.

EELS setting and reading out the camera before each pixel with the preset exposure time (Script in Appendix 6.13.4). The used microscope has no descan coils so the central beam moves with respect to the spectrometer entrance aperture. This has been taken care of in the script (Appendix 6.13) where the a search for the maximum on a lineprofile across the lower energy parts of the raw spectrum is obtained, smoothened via Savitzky Golay filtering and from there the maximum is obtained and acts as a divider for two regions in the raw spectrum from where the best EMCD positions are computed and extracted using lineprofiles integrating over 40 pixels.
Two linescans with setting 2 consisting of 16 pixels across the layer system have been

acquired. The EMCD effect on Fe and Co is known to have opposite sign on the L3 edge and L2 edge [41] [73], therefore only datapoints showing this have been taken into consideration for determining the effect. The spectra A and B are presented background subtracted and overlaid by the script. Then the script for shifting the spectra and aligning them on the post-edge background has been used. The shifts are between 0 and 4 pixels/channels. Measurements with a different decay in the post edge background cannot be aligned properly and are also discarded. The noise level is determined from the maximum of the fluctuations pre-edge after background subtraction, it is set in relation to the difference that gives the EMCD effect on each edge to determine the statistical measurement uncertainty. The magnitude of the EMCD effect in percent is shown in fig.50 for both datasets.

It has not been possible to extract a signal on all points of the linescan. The data is still very noisy, this explains the large errorbars. An example for a measurement showing an EMCD effect can be seen in fig.51. Where no effect could be observed the value has been set to zero and no error has been determined, this would have been possible from the noise level under the assumption that up to the noise level an effect could stay hidden. It can be stated that an EMCD effect could be be measured. The thickness dependence also has to be taken into account, the thickness has been measured by an EELS zero loss mapping and evaluated using the t/λ method. Thickness information is shown in fig.52 where it can be seen that the thickness ranges between ≈ 20 nm and ≈ 80 nm with a close to linear decay. The best region for measuring EMCD would be in the thinnest region, but there the lattice is not fully intact due to the FIB ion milling, the material is partly oxidized and the specimen contains only Fe there and is far away from the interface to the Co_2FeSi. The interface regions are ≈ 40 nm and ≈ 60 nm in thickness. These are the most interesting regions with respect to magnetic effects, although it is difficult to give reliable statements from the data shown in fig.50.
What can be stated is that in both datasets close to the interface at point 9 an EMCD effect on Fe is measured, also that the Co_2FeSi can be considered to be magnetic as both Fe and Co show EMCD effects, there needs to be a different explanation for the behaviour in DPC than the absence of ferromagnetism. The effect on Co is strong close to the interface at point 8, the Fe effect small there in both datasets.

The data from setting 1 looks different because of the different dispersion the electrons that would fit in one 1 eV wide channel now distribute over four 0.25 eV wide channels. There are less electrons per channel and increased noise (fig.53). The central beam does not move much during the linescan so the EMCD positions could be extracted on the same position in the spectra for all 16 points, integration width of the line profile again 40 pixels. The first datapoints have been obtained on very thin Fe but do not contain many electrons so no edge or EMCD effect could be extracted. From point 3 on the two EMCD spectra are of different quality with one containing more noise than the other. Only the Fe edge allows for a measurement, the Co edge is not extractable due to its shape and the noise. The thickness of the specimen is the same as for the setting 2 measurements but on a shifted region so the linescans do not overlap. In fig.54 the results are shown, the reduction of the Fe amount in the Co_2FeSi to 25% of the alloy is the reason no usable spectra could be extracted in this region. The errorbars are so large it is arguable if an effect has be measured or not, both presence and non presence of an EMCD effect are in agreement with this data.

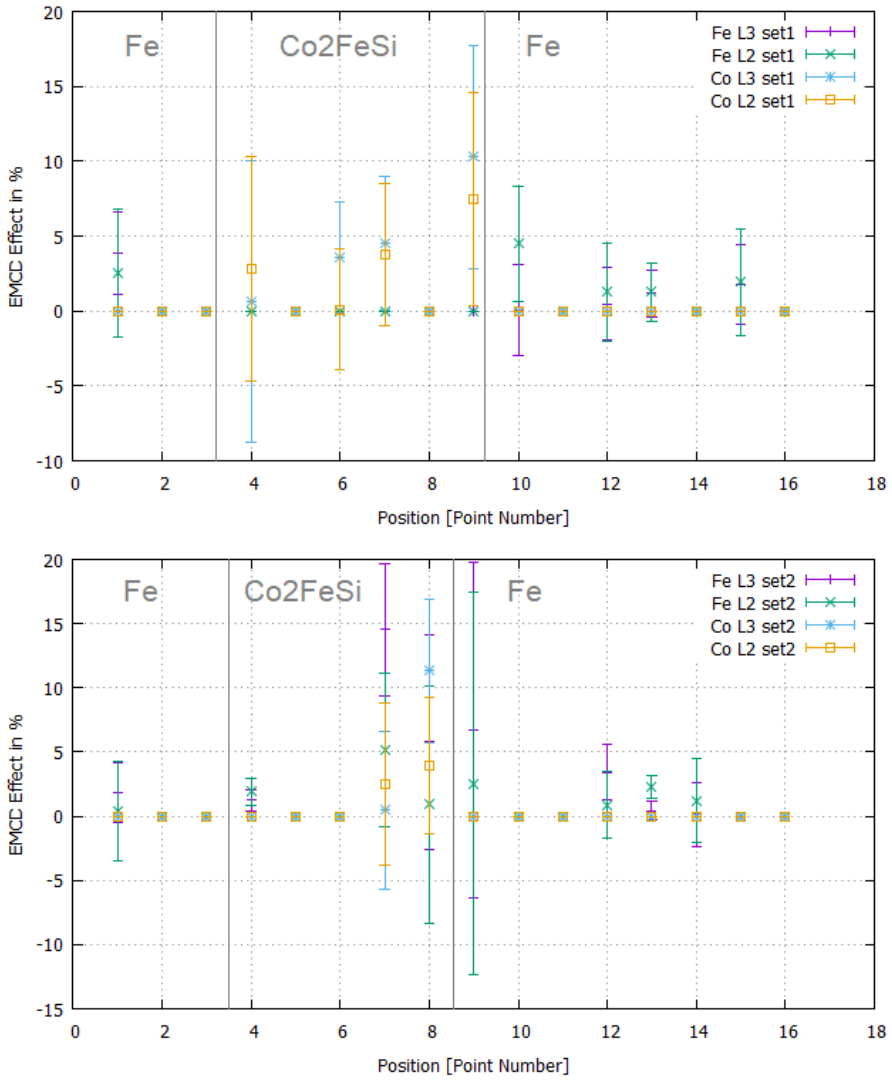

Figure 50: EMCD results for the two 16 point linescan datasets across the Fe/Co_2FeSi/Fe lamella. Start of the linescan has been on the thin Fe layer next to the vacuum, end on the Fe layer next to the MgO substrate, so the MgO substrate lies on the right of point 16.

To be able to obtain information on the interfaces using EMCD a set of linescans containing 5 points has been acquired across both interfaces with the parameters of setting 2. Two points are at maximum 5 nm apart so it can be assumed the thickness does not change notably. Before manual extraction of EMCD spectra the spectra containing only Fe and those containing both Fe and Co have been summed for each linescan to improve the signal to noise ratio. The EMCD effect of these two datapoints is determined from three linescans for each interface and shown in table 3. A high EMCD effect can be observed on the Co L3 edge, on the L2 edge a notable effect can be observed only for the Fe1/Co_2FeSi

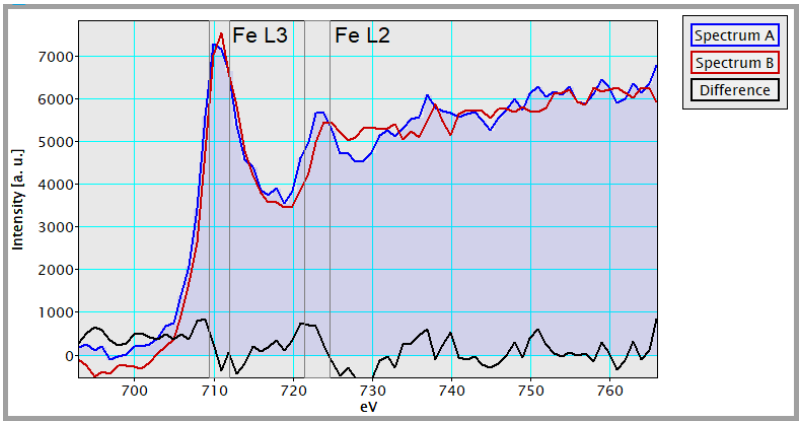

Figure 51: Example for a measurement point showing an EMCD effect on the Fe L3 and L2 edges. Noise on the data can lead to wrong effects that can be of the same magnitude as EMCD effects. Therefore the human eye has to look at the edges.

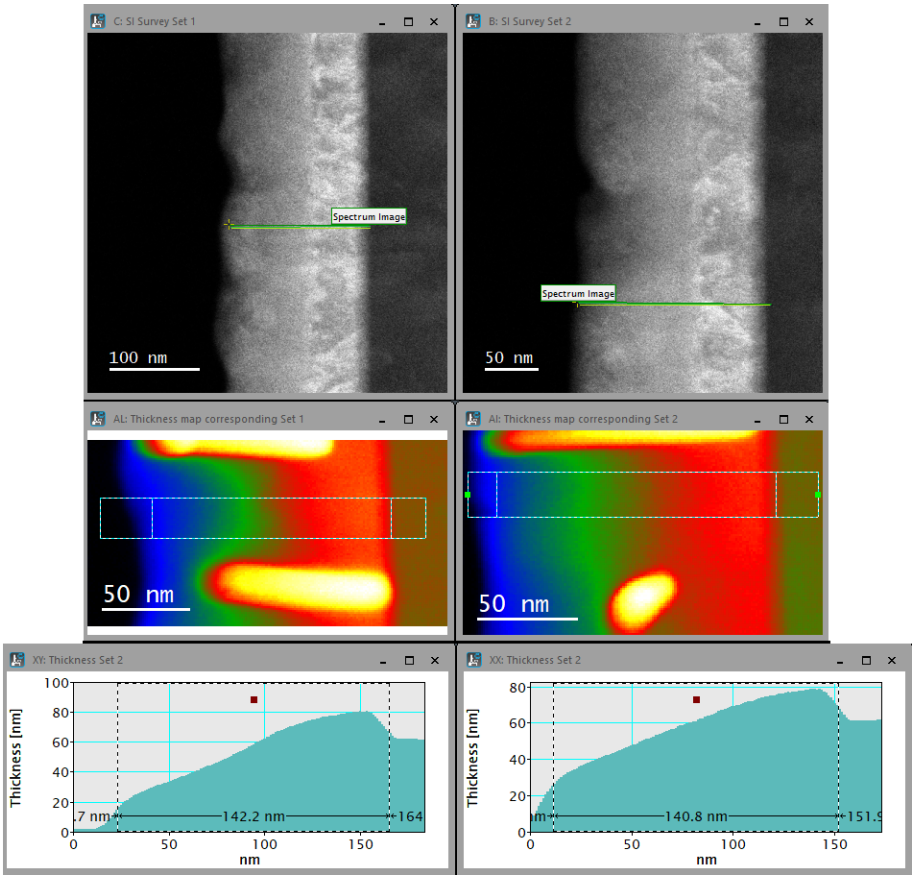

Figure 52: Thickness estimation for positions close to those used for EMCD measurements. The linescan position is highlighted in the thickness profile by a ROI.

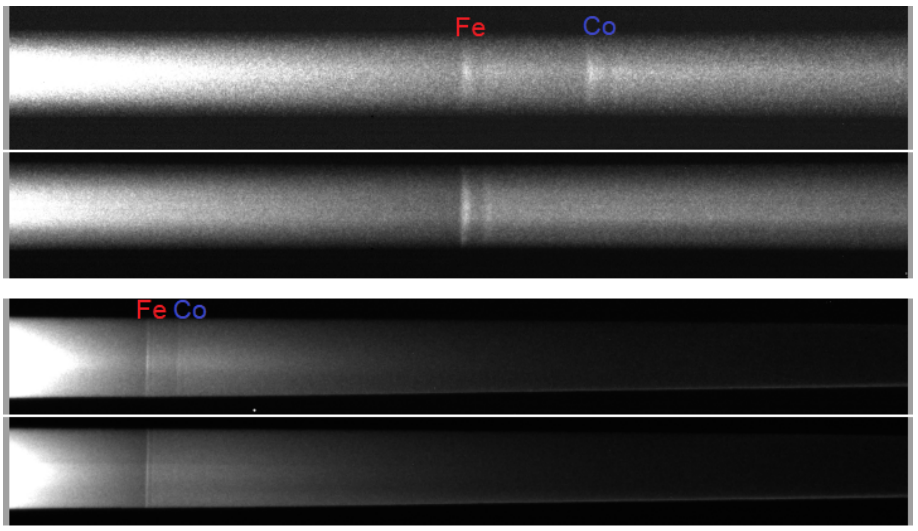

Figure 53: Comparison of the raw spectra for 0.25 eV/channel dispersion (top) and 1 eV/channel dispersion (bottom), each for one position on the Fe and one on the Co_2FeSi containing the Fe and Co edge. The Fe and Co edges are marked. The noise is reduced visibly by the 1 eV/channel dispersion.

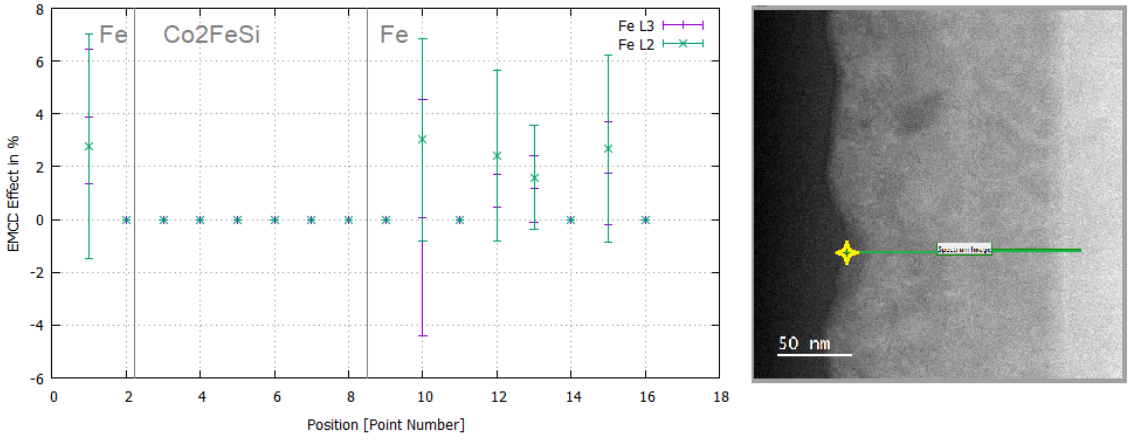

Figure 54: Left: EMCD result for the data acquired with setting 1 for Fe. The layers are marked with the vertical grey lines on the interfaces. Right: Survey image, start of linescan at the yellow point.

interface. On this interface the Fe in the Co_2FeSi tends to show a high signal and the neighbouring close to pure Fe only a low signal. On the Co_2FeSi/Fe2 interface the effect on the pure Fe L3 is slightly higher than on the Co_2FeSi. The measurements on the Co show high effects of $5-10\%$ on the L3 edge but also large uncertainties and smaller effects with larger uncertainties on the L2 edge. This results can give a hint that at the interface between Fe and Co_2FeSi the Co shows a notable magnetic moment. For more detailed interpretation the measurement uncertainties are too large.

Interface	Fe L3	Fe L2	Co L3	Co L2
Fe1/Co_2FeSi: Fe	$4.15 \pm 2.40\%$	$3.48 \pm 3.26\%$		
Fe1/Co_2FeSi: Co_2FeSi	$1.62 \pm 2.06\%$	$1.21 \pm 2.65\%$	$15.15 \pm 0.61\%$	$6.59 \pm 0.70\%$
Fe1/Co_2FeSi: Fe	$0.13 \pm 0.42\%$	$3.29 \pm 0.59\%$		
Fe1/Co_2FeSi: Co_2FeSi	$3.70 \pm 1.85\%$	$0.79 \pm 2.78\%$	$6.15 \pm 5.03\%$	$1.47 \pm 6.62\%$
Fe1/Co_2FeSi: Fe	$0.97 \pm 0.54\%$	$2.97 \pm 0.71\%$		
Fe1/Co_2FeSi: Co_2FeSi	$3.40 \pm 2.72\%$	$4.10 \pm 3.28\%$	$2.33 \pm 3.32\%$	$5.79 \pm 3.86\%$
Co_2FeSi/Fe2: Fe	$0.86 \pm 1.66\%$	$0.65 \pm 2.31\%$		
Co_2FeSi/Fe2: Co_2FeSi	$9.92 \pm 1.25\%$	$0.18 \pm 1.91\%$	$5.34 \pm 5.34\%$	$2.1.51 \pm 5.53\%$
Co_2FeSi/Fe2: Fe	$2.90 \pm 2.42\%$	$2.84 \pm 3.15\%$		
Co_2FeSi/Fe2: Co_2FeSi	$1.80 \pm 1.67\%$	$1.42 \pm 2.00\%$	$10.05 \pm 4.31\%$	$1.60 \pm 4.81\%$
Co_2FeSi/Fe2: Fe	$2.51 \pm 2.43\%$	$3.01 \pm 3.28\%$		
Co_2FeSi/Fe2: Co_2FeSi	$1.76 \pm 2.42\%$	$3.10 \pm 3.34\%$	$6.09 \pm 8.70\%$	$3.83 \pm 10.93\%$

Table 3: EMCD results for three linescans for each interface: Fe1/Co_2FeSi and Co_2FeSi/Fe2. On the Fe side only Fe could be measured, on the Co_2FeSi on the Fe and Co edges measurements have been obtained.

3.5.3 DPC measurements

In DPC many types of contrast resulting from structural, chemical or magnetic properties of the specimen are present, which makes interpretation of the results challenging. To be able to characterize what is seen the procedure goes stepwise from the known to the not-yet known about the specimen. For the DPC measurements where magnetic information is desired it goes from Lorentz microscopy with and without an applied magnetic field to segmented DPC measurements and then to pixelated DPC measurements. The latter are able to detect very small shifts of the beam disc.

In Lorentz microscopy an image of the specimen is taken at overfocus condition to minimize contrast differences (darker fringes, no additional bright fringes) while the amount of defocus makes magnetic information visible (chapter 2.5). To change the magnetism of the specimen the objective lens is switched on by a small amount using the free lens control. The magnetic field in z-direction has been measured in dependence of the current through the objective lens by the Glaswegian group with a Hall-probe specimen holder. For the following measurement the objective lens was excited to 10% which corresponds to a field in z-direction of $B_0 = 0.23$ T. The specimen is tilted 25° upwards or downwards into the field and then tilted back. The field on the specimen is $B_0 \cdot \sin 25° = 0.097$ T. Also a current of 5% of the objective lens has been used, corresponding to a field of $B_0 = 0.11$ T in z-direction and $B_0 \cdot \sin 25° = 0.046$ T on the specimen.
Tilting in both directions leads to magnetization of the specimen in both directions while nonmagnetic parts of the specimen should see no effect. The overlay of the intensity line profiles taken at the same place on both images show a change in parts of the specimen, mainly the iron layer next to the MgO substrate (fig. 55). The Heusler is scattering the electron beam very high and appears very dark in the image, this makes it difficult to detect any changes. The line profiles suggest a small change in the Heusler next to the MgO adjacent iron layer.

This qualitative measurement has been repeated on the ARM200cF in Glasgow at 200 keV in Fresnel mode (fig.56) with the objective lens excited to 0500 (microscope specific value) that corresponds to ≈ 0.1 T, Spot 2 and 150 μm CL aperture. Instead of zero a basic tilt of 5° has been used because of strong diffraction contrast at 0° which vanished at 5°. It turned out that the objective lens field managed to induce changes in the specimen between $-9.5°$ - $-10.7°$ and $19.5° - 20.5°$ so the specimen is mounted on the holder with a tilt of $\approx 5°$ and zero field on the specimen is therefore also at a tilt of $\approx 5°$. This is in accordance with the specimen contrast.
The induced change in the specimen as indicated by arrows in fig.56 is a magnetic signal because it changes with changing direction of the external magnetic field, with this knowledge segmented and pixelated DPC measurements are expected to give further insights into the magnetism of this thin film system.

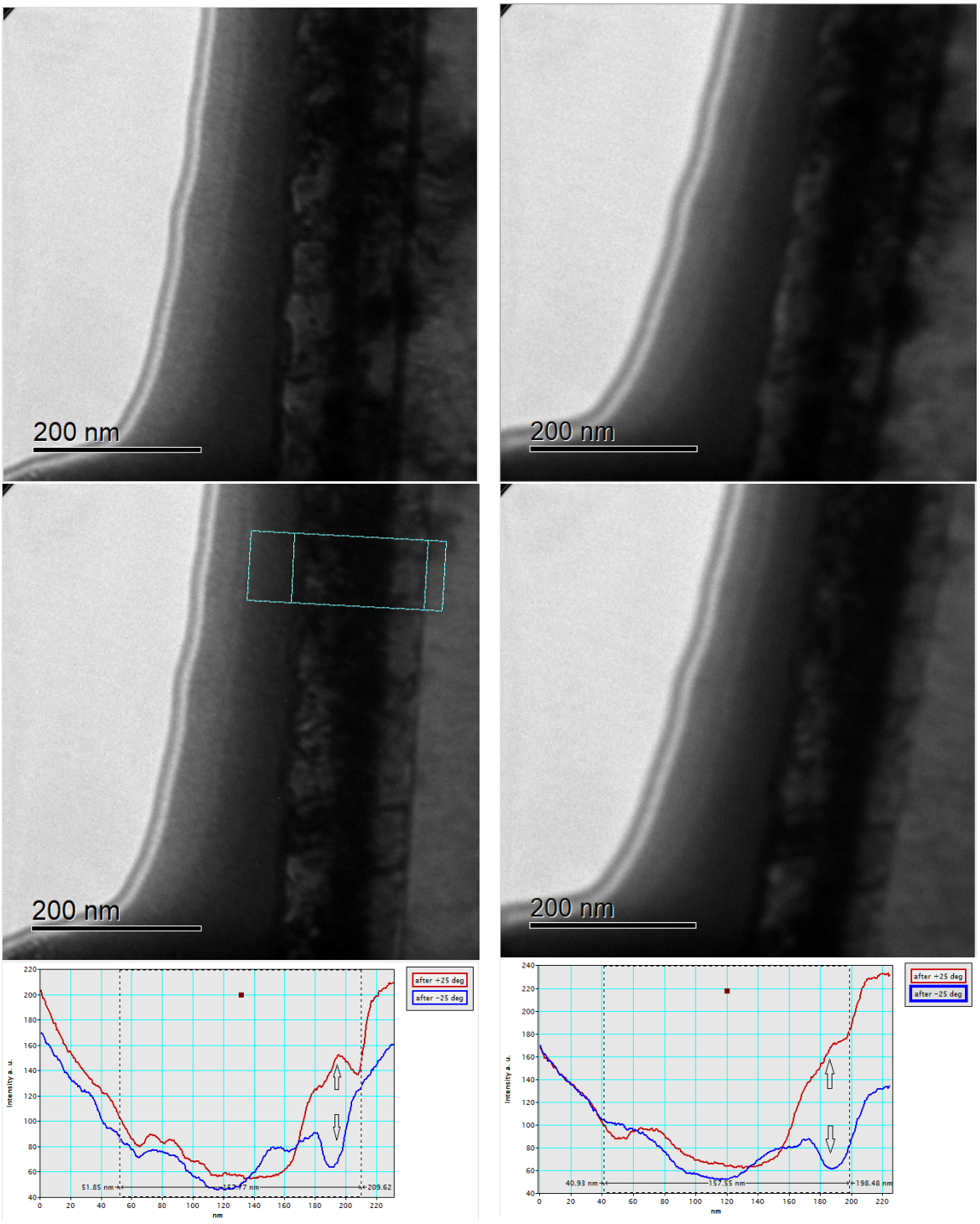

Figure 55: Left (up to down): images recorded in Lorentz mode on the FEI T20 microscope (Glasgow) after tilting to $+25°$ and after tilting to $-25°$ at 10% objective lens excitation. Right (up to down) at 5% objective lens excitation. Intensity profiles of both images are overlaid in the lowest figure. The region of interest markings show the beginning and end of the layer system. The MgO is on the right of the images, the FIB-Pt on the left.

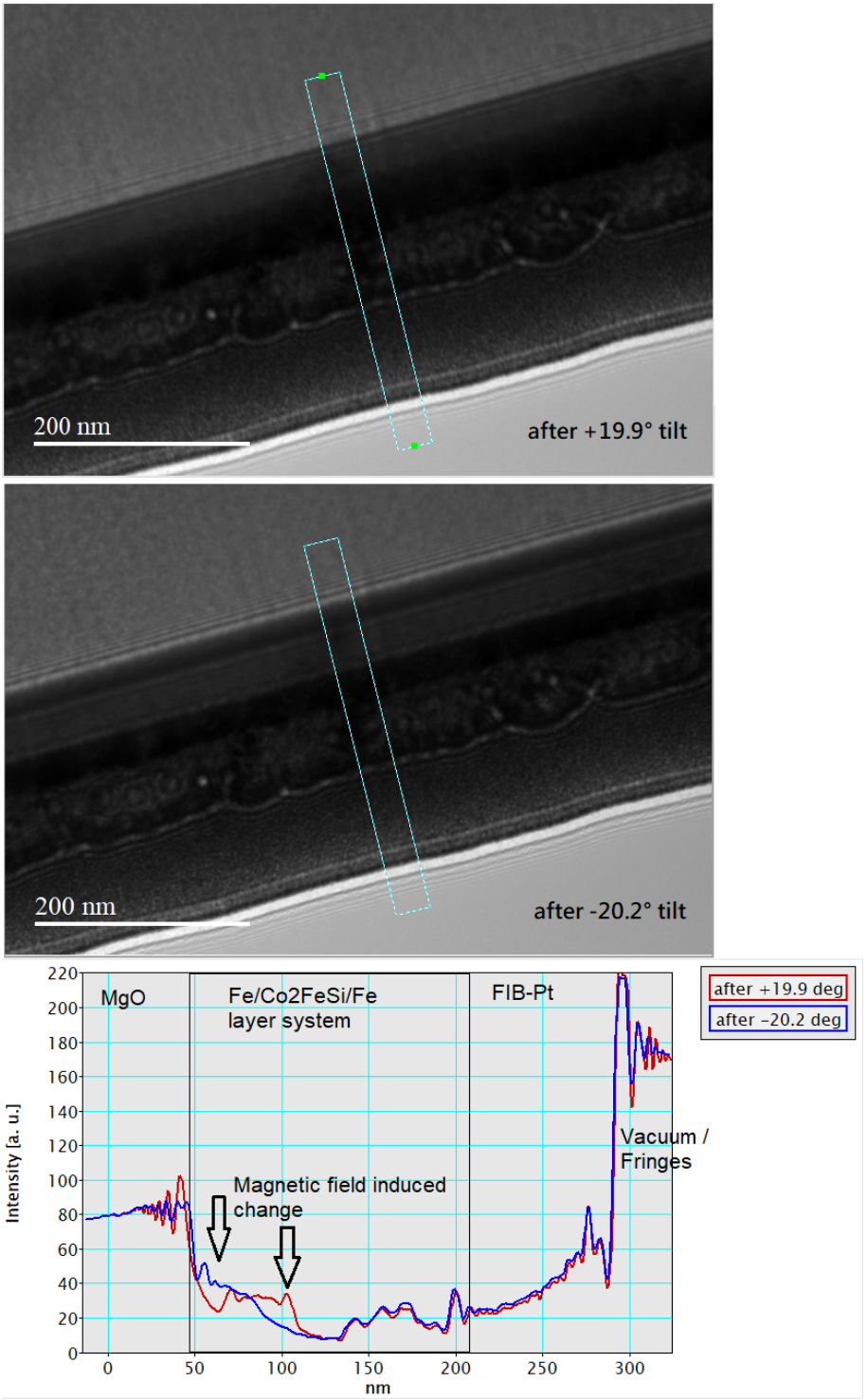

Figure 56: Tilting in Lorentz mode: ARM200cF results, the magnetic field induced specimen change is indicated by arrows. MgO on top of the image.

Segmented DPC has been performed on the ARM200cF in Glasgow using an 8-fold segmented detector that consists of an inner ring divided in 4 segments and an outer ring divided in 4 segments. Important for a good measurement is the centering of the beam on the detector, although it is possible to correct for small deflections afterwards. For having the specimen in a defined magnetized state the objective lens has been switched on to a value of 0500 (microscope specific value in the free lens control) which corresponds to a field of ≈ 0.1 T in z-direction. The specimen has been tilted into this field to angles between $+25°$ to $-25°$ giving an in-plane field of up to ± 0.0423 T. The possible magnetic states that have been achieved are shown in fig.57: Both iron layers magnetized in parallel in both possible directions, one iron layer magnetized antiparallel to the other and a mixture of both containing a domain wall. It has only been possible to achieve one of the two antiparallel configurations, possible reasons can be either the restricted tilting possibility in the TEM, which allows one layer to be effected more effectively by the objective lens field than the other layer or the layers differ in their magnetic properties and one layer can be switched by a lower external field than the other. The difference in magnetic properties is supported because the layers are not totally equal in thickness and structural properties, the Fe layer below the FIB-Pt is more grainy with a smaller grain size than the other Fe layer.

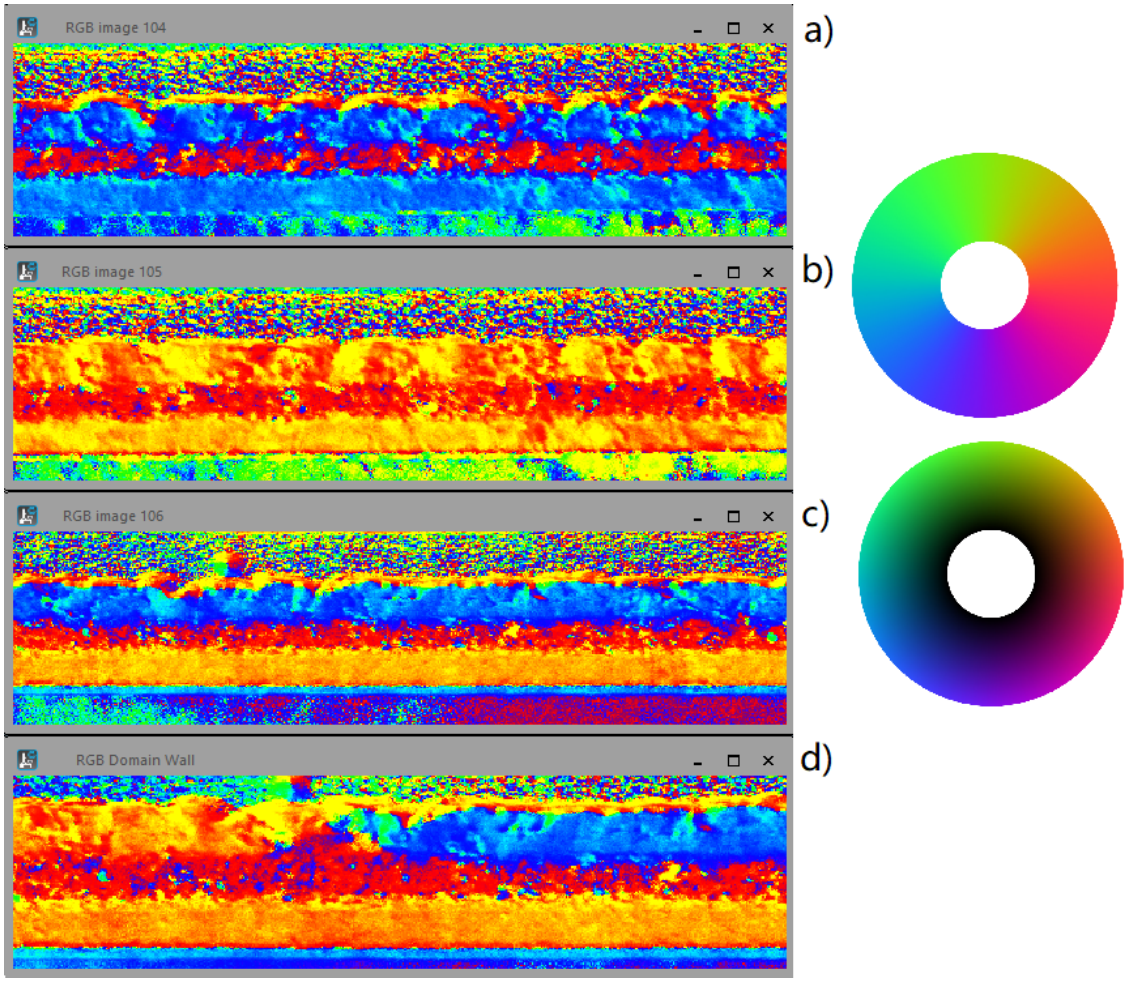

Figure 57: The possible magnetic configurations: a) both iron layers parallel in one direction, b) both layers parallel in the opposite direction, c) both iron layers antiparallel, d) domain wall, creating a transition from the parallel state to the antiparallel state. Layers from bottom to top: MgO, 1st Fe layer, Co_2FeSi, 2nd Fe layer, FIB Pt. In the FIB Pt one "ball" where a colour wheel is visible marks a beam parking position where the specimen has been damaged. On the right: colour wheels showing the colour code of the directions (upper wheel) and directions combined with the amount of deflection related to the strength of the magnetic induction (lower wheel). This color coding is used throughout this whole thesis.

Every detector segment records its own signal, also the output contains a sum signal of all segments and difference signals between opposite segments. But the same can be calculated from the eight segment signals and is done via a DM script which has been developed within this thesis combining several scripts provided by S. McVitie and his group for evaluating the four outer segments. A batch readin routine has been added, also a routine asking for the region for normalization, all the functions have been connected to each other. Normalization can be done on an area marked by a ROI, the mean signal of this region is subtracted from the difference images, correcting for any inherent deflection respective not centered beam. It is assumed that the MgO is non-magnetic and without other strong contrasts, therefore normalization is performed on the MgO area below the huge contrast of the MgO/Fe interface.
The calculated colour images show the direction and strength of the deflection. Which kind of contrast the source of this deflection is can not be answered, this needs further investigation: If the signal is of magnetic source, it can be changed by interaction with a magnetic field. This allows separating magnetic contrasts from all other contrast sources by introducing a small magnetic field that is strong enough to polarize the magnetic parts of the specimen. Changing the direction of polarization with changing the field direction makes the magnetic parts visible in the difference of the measurements.
To obtain the magnetic signal a point of orientation is needed and it is tried to have all magnetic signal or at least the magnetic signal of one important layer in one of the component images. These two images, deflection in x and y component, can be rotated by a 2D rotation matrix. A DM script has been written based on the rotation script provided by D. McGrouther [92] that does this rotation from 0° to 180° or a user-defined endpoint in steps of 1°. Similar to a line profile one of the component images is integrated across the layer system over an area specified by the user. In this line profile areas can be selected to be summed over. The absolute value of the contrast in this areas is minimised and the corresponding angle returned. This angle should be approximately the same for all datasets recorded under the same circumstances.
The contrast in the Fe layers should be minimized. For this specimen the angle to achieve this are between 58° and 62°. An example for a rotated dataset is shown in fig.58. The images show the deflection for the respective direction. With knowledge of the specimen thickness this can be converted into the integrated magnetic induction according to eq. 2.39.

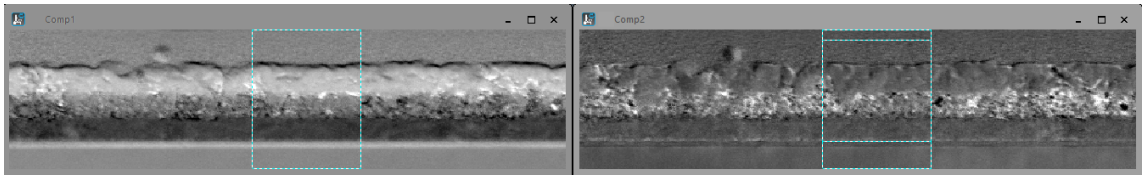

Figure 58: One dataset rotated, one component (Comp1, left) shows maximum contrast while the other component (Comp2, right) shows minimum possible contrast in the iron layers. A line profile is shown where the profiles which are then overlaid are taken.

Several datasets have been taken containing all three magnetic states and a domain wall. Of these the datasets 104, 105, 106, 107, 107a and 108 (107a is a separate dataset from 107) have been chosen because there is enough MgO in the image to do a normalization

without getting influences from the MgO/Fe interface and all magnetic states are at least once in them. On each high contrast image of these datasets a line profile has been taken on a region that is smooth with less visible grains, defects or other high contrasts. To check if the normalization is acceptable the MgO part of the line profile has to be approximately zero. The Signal in the FIB-Pt must be not much higher. The datasets including both components are shown in fig.59.

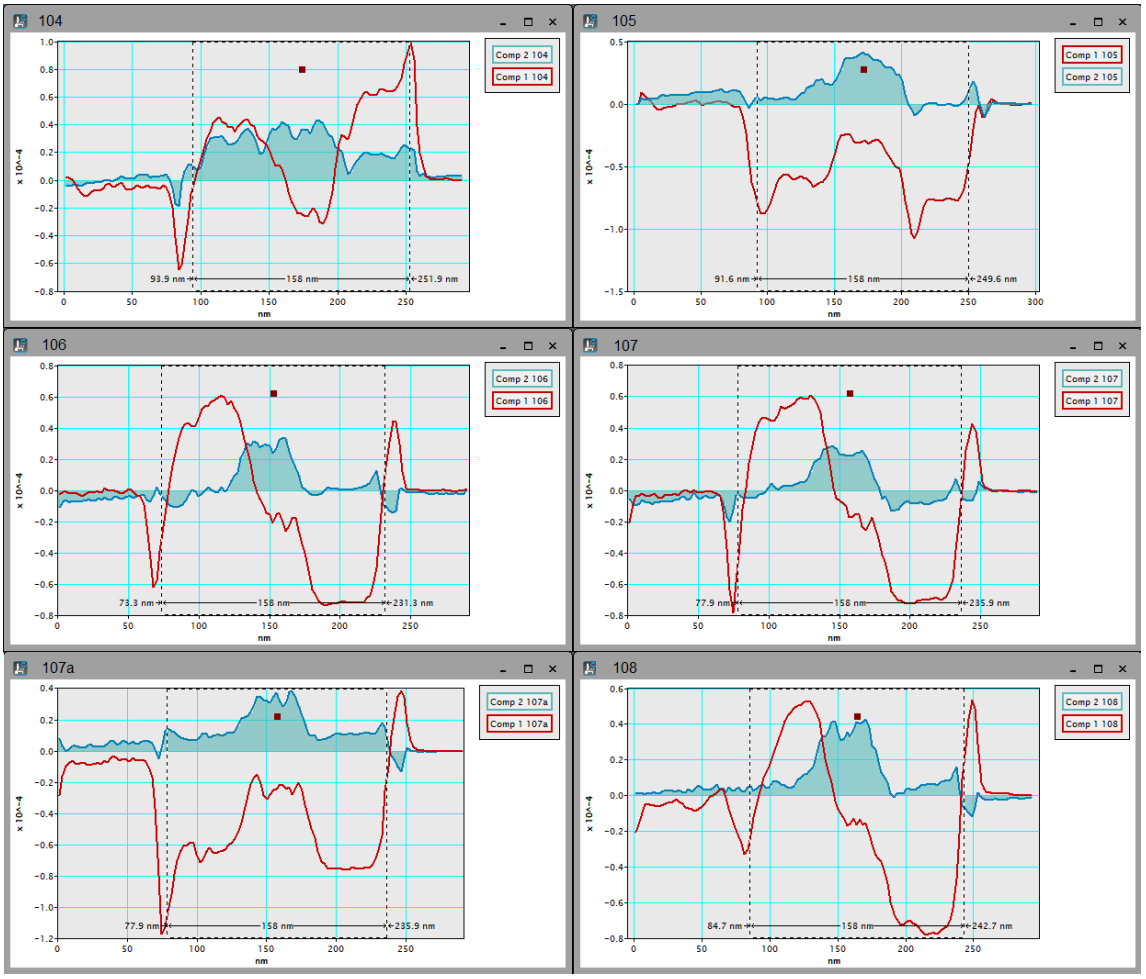

Figure 59: Lineprofiles across the chosen datasets 104, 105, 106, 107, 107a and 108: both components are shown. Comp1 contains the iron magnetism (red) and Comp2 probably contains magnetic signal from the Co_2FeSi (bluegreen). The deflection of the beam is shown in rad on the y-axis ($\mathcal{O}(10^{-4})$ rad). In the lineprofile from left to right: FIB-Pt, Layer system and MgO substrate. The deflection is there ≈ 0 so the normalization did work properly.

To be able to divide by the specimen thickness in the form of the thickness function (eq. 3.1), the starting point is set to the MgO/Fe interface. The following line profiles have been taken from the chosen datasets starting from this starting point across the layer system and then divided by the thickness function times the constant $c = \frac{e \cdot \lambda}{h}$ according to

eq. 2.39. The results are shown in fig.60. The different magnetic states can be observed and the magnetic induction ranges between $+0.95 \pm 0.14$ and -1.1 ± 0.14 Tesla for the iron layers. The error on this measurement is estimated by the mean offset of the FIB-Pt signal from zero.

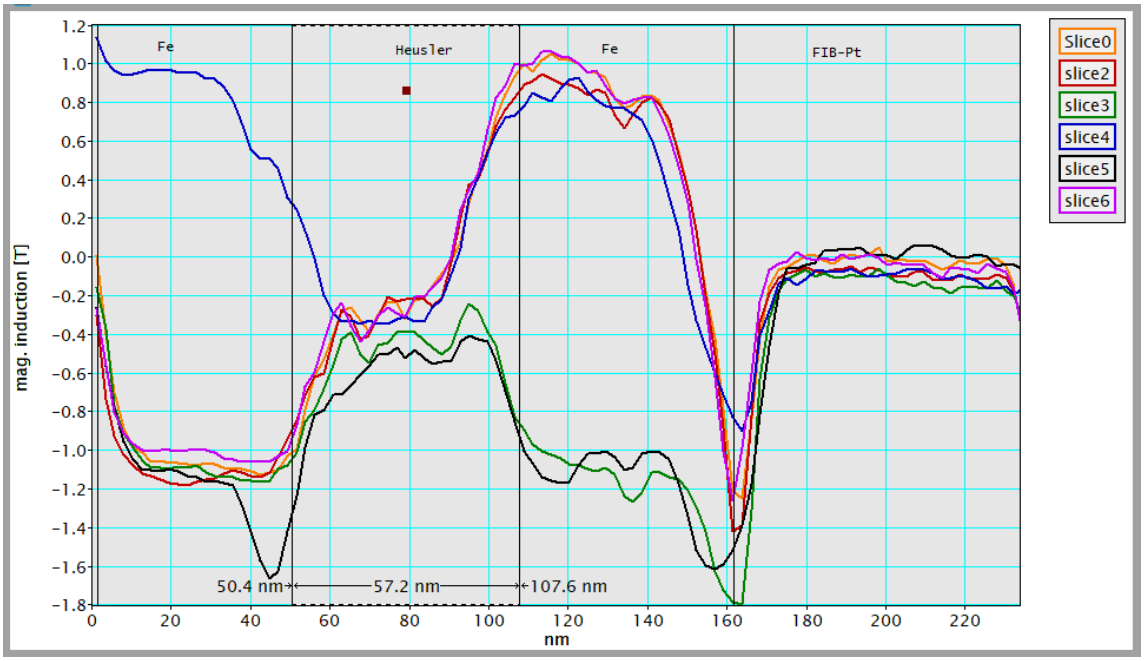

Figure 60: Results of the six datasets for the magnetic induction of the Fe/Co_2FeSi/Fe layer system. The layer system is marked as well as the Co_2FeSi layer in the center, measured to be 57.2 ± 2.3 nm here. In one dataset the iron is magnetized in parallel in one direction (blue), in two datasets in the opposite direction (green, black) and three datasets are in the only observed antiparallel state. Peaks in interface position result from the high contrast at the interfaces and is non-magnetic.

It can be assumed that the iron layers are magnetically saturated by the external objective lens field. The magnetic zero point then lies in between both directions and the magnetic induction of the iron can be determined to be half of the difference between both magnetic states. From the available states a number of datasets to relate to each other is possible. All possible combinations are shown in fig.61. The results for each iron layer are shown in tab.4. Within the error margins the magnetic induction is the same for both iron layers, averaging over only the center of the layer or the whole layer leads to a difference of ≈ 0.1 T for the absolute value of the magnetic induction. The magnetic zero point lies at -0.12 ± 0.06 T. The Co_2FeSi shows a in the central region a signal of -0.35 ± 0.1 T. This could lead to the conclusion that there is magnetic signal also from the Co_2FeSi. As it can be seen in fig.61 this signal could not be reversed like the one from the iron layers by the external magnetic field, so it is not a magnetic signal. Origin for contrast there might be the higher contrast from the Co_2FeSi that is not eliminated by rotating to minimum contrast in the iron layers.

In search for the magnetic properties of the Co_2FeSi it can be said that the magnetism

Datasets	Layer 1 (center)	Layer 2 (center)	Layer 1 (whole layer)	Layer 2 (whole layer)	magnetic zero
0 - 4	1.0 ± 0.03 T		0.90 ± 0.24 T		-0.08 ± 0.02 T
3 - 2		0.97 ± 0.04 T		0.90 ± 0.25 T	-0.15 ± 0.08 T
3 - 4	1.01 ± 0.03 T	0.96 ± 0.06 T	0.92 ± 0.23 T		-0.13 ± 0.05 T
4 - 2	1.05 ± 0.03 T		0.95 ± 0.22 T		-0.12 ± 0.08 T
5 - 2		0.92 ± 0.10 T		0.90 ± 0.22 T	-0.15 ± 0.06 T
6 - 3		1.02 ± 0.05 T		0.92 ± 0.32 T	-0.11 ± 0.07 T
6 - 4	0.96 ± 0.03 T		0.90 ± 0.19 T		-0.07 ± 0.03 T
Result	1.00 ± 0.03 T	0.97 ± 0.04 T	0.92 ± 0.22 T	0.89 ± 0.29 T	-0.12 ± 0.06 T

Table 4: Results for the magnetic induction for each layer calculated from the difference between the saturated iron layers in both directions. The values have been averaged over the central part of the line profile for each combination of datasets, interfaces are not taken into account. The right column shows the magnetic zero point determined from subtracting the layer signals from the signal in fig.61.

of the adjacent Fe layer is leaking into the Co_2FeSi as it can be seen in fig.60. It takes 9.2 ± 4.6 nm until the signal is fallen onto the Co_2FeSi niveau. This leaking signal is reversable under an external magnetic field and thus magnetic.

So far only one component has been analysed. For the Fe the magnetic signal has been rotated in the way it is contained in one component. The other component that results from the rotation contains signal perpendicular to the first component and is shown in fig.62. Here no reversals could be achieved so it needs further measurements to prove it is magnetic signal. The reason to treat it as a magnetic signal is that Co_2FeSi is a ferromagnetic alloy with a magnetization of 881 kA/m [88] (iron: 1710 kA/m). So a signal of approximately half of the strength of iron can be expected. For about half of the Co_2FeSi layer the composition suggests it is exactly Co_2FeSi, in the other half the rising amount of iron and the falling amount of Co gives way for the assumption of some of the Co atoms being replaced by Fe atoms. This can lead to the forming of other alloys that contain Co and Fe, like Fe_2CoSi, which is also a magnetic alloy [93].

The measured signal in the 2nd component gives 0.53 ± 0.08 T measured over the central part of the layer and 0.43 ± 0.10 T measured over the whole layer as marked in fig.62, which may take also interface effects into account. This is about half of the signal strength of the iron layers within the error margins and would match the expected. If this is a magnetic signal, it suggests that the Co_2FeSi is magnetized perpendicular to the iron layers regardless of their magnetization. A reason for this can be that Heusler alloys are soft magnetic materials and the objective lens field in z-direction was always on during the measurement. The specimen has been tilted into the field and back and the objective lens field always has influence on the material, superposed by the iron. Field components in z-direction cannot be measured by DPC as they cause no beam deflection. A superposition of these influences would lead to the Co_2FeSi being polarised in a direction between the iron layers and the objective lens field direction. The difference of the Co_2FeSi part from magnetic zero would then be the part in x-direction and the signal from the other component the part in y-direction. To determine direction and strength the process

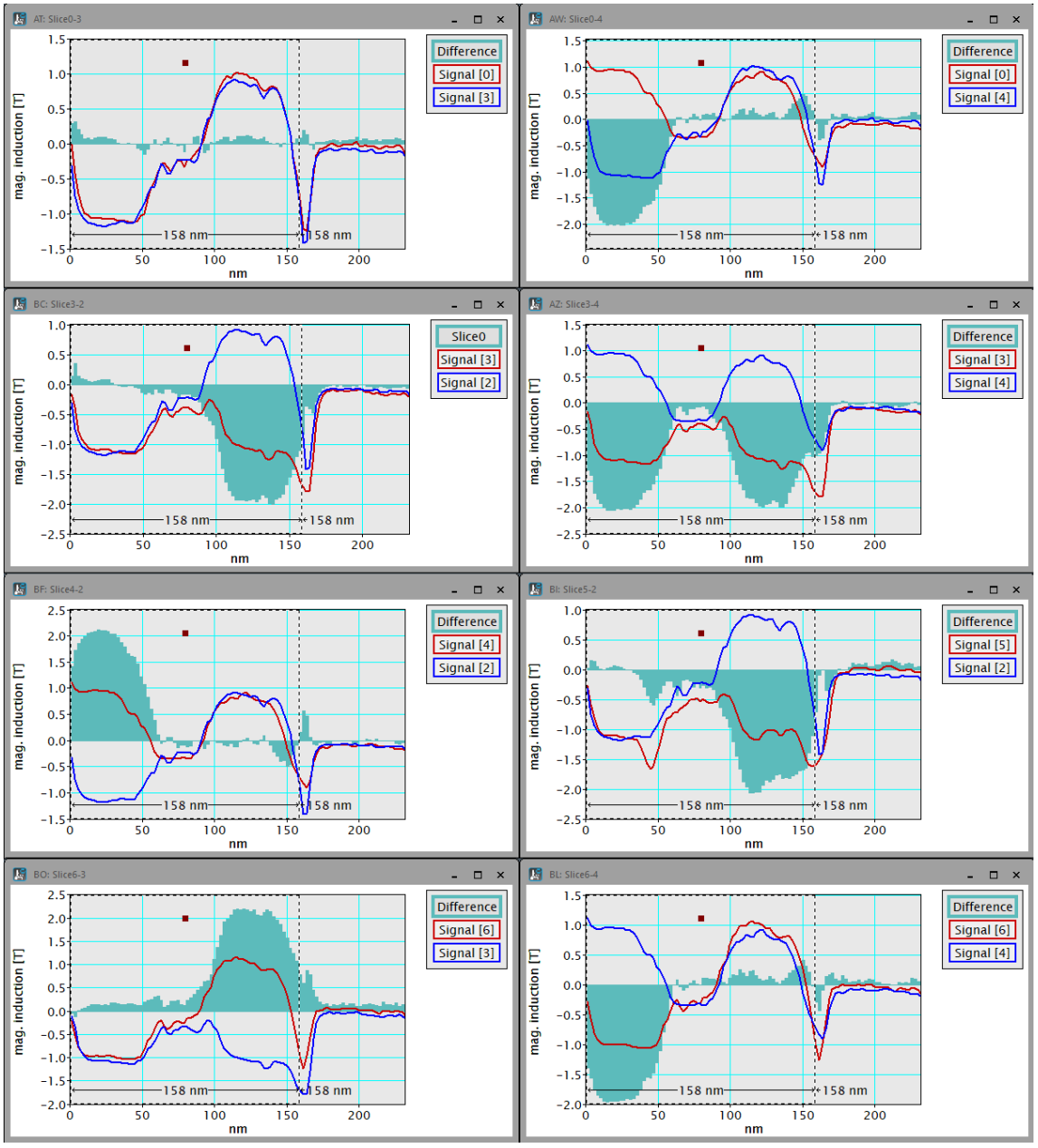

Figure 61: Differences of the datasets in all possible combinations that give a net signal. The difference of the two antiparallel states (top left) is shown to get an idea of the error margins that arise from the variability of measurements of the same magnetic state. The numbers of the datasets are those from fig.60. The difference is always shown in filled green, the two datasets in red and blue. The range of the layer system is marked by a ROI.

of rotating to minimum contrast and further evaluation is repeated with the Co_2FeSi region chosen to have minimum contrast on one and maximum contrast in the other component image and the angle of this condition gives the angle of the magnetic polarization of the Co_2FeSi relative to the iron. The results are shown in table 5.

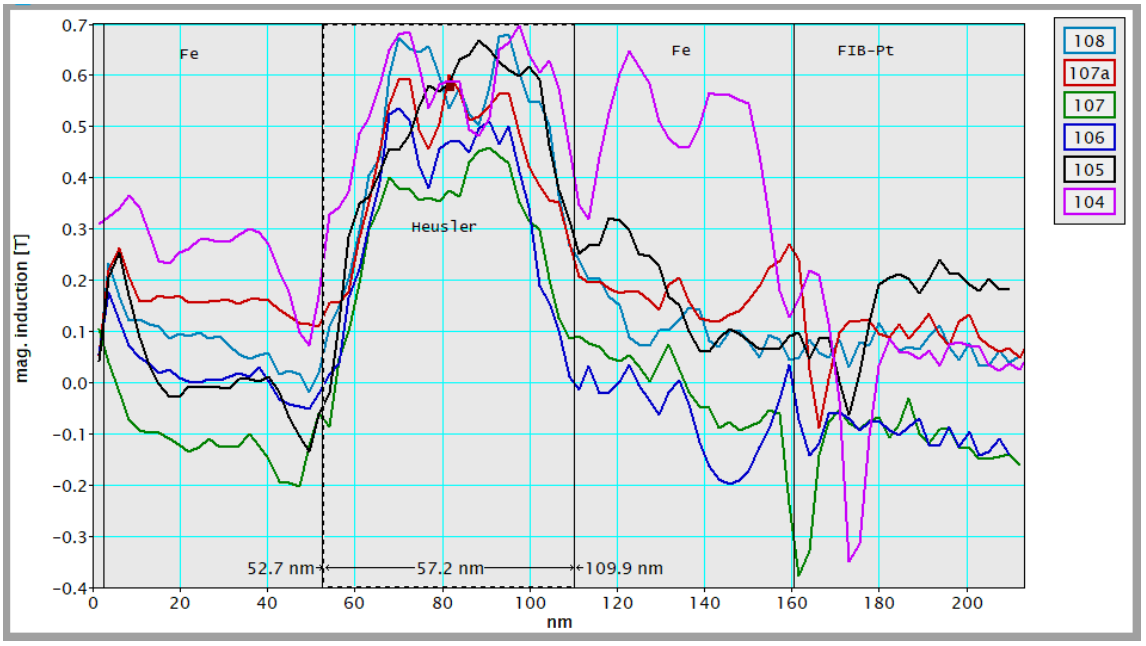

Figure 62: The magnetic induction inferred of the component perpendicular to the one from fig.60. The layer system is marked and the width of the Heusler layer shown. The signal in this part shows the Heusler being magnetized always in the same direction, perpendicular to the iron.

These results are far less stable than those obtained for the iron, where the experimental

Dataset:	104	105	106	107a	107	108
rotation angle:	155°	20°	143°	18°	177°	155°
magnetic state in the iron:	↓↓	↑↑	↑↓	↑↑	↑↓	↑↓
angle between iron and Co_2FeSi rotation angle:	100°	43°	85°	40°	119°	97°

Table 5: Rotation angles leading to minimum contrast in the Co_2FeSi layer for the used datasets along with the directional magnetic state of the iron.

conditions are not changing the angles also should not change. Here this can only be seen for dataset 105/107a which are both in the same magnetic state and have a similar angle for the Co_2FeSi. The dataset 104 has no second dataset to counterproof, so another dataset of the smaller recorded ones (256x64 pixels instead of 512x128 pixels) in the same magnetic state has been evaluated. There the rotation angle for the iron layers is 64° which is very close to the 58°-62° from the big datasets. For the Heusler layer the angle is 141° and the one from dataset 104 is 155°. For the antiparallel magnetized states the rotation angles returning minimum contrast read 143°, 177° and 155° and do not give a robust result. This might result from other contrasts being present in the Co_2FeSi from grains and high diffraction contrast.
The differences in rotation angles are shown in a schematic in fig. 63, where the magnetic iron states of "right" and "left" are drawn and assumed to be 180° apart in magnetization direction. The terms "right" and "left" are chosen because "up" and "down" would imply

a direction that is not in-plane of the specimen, which is not accessible by DPC. The rotation angle difference between Co_2FeSi and iron as shown in table 5 are drawn with respect to the specific iron magnetic state, e. g. 40° from the "right" defined state. For the antiparallel states both possibilities are shown in thinner lines as it is not possible to relate them to one of the iron magnetic directions.

From this schematic it can be deduced that it is difficult to tackle the magnetism of

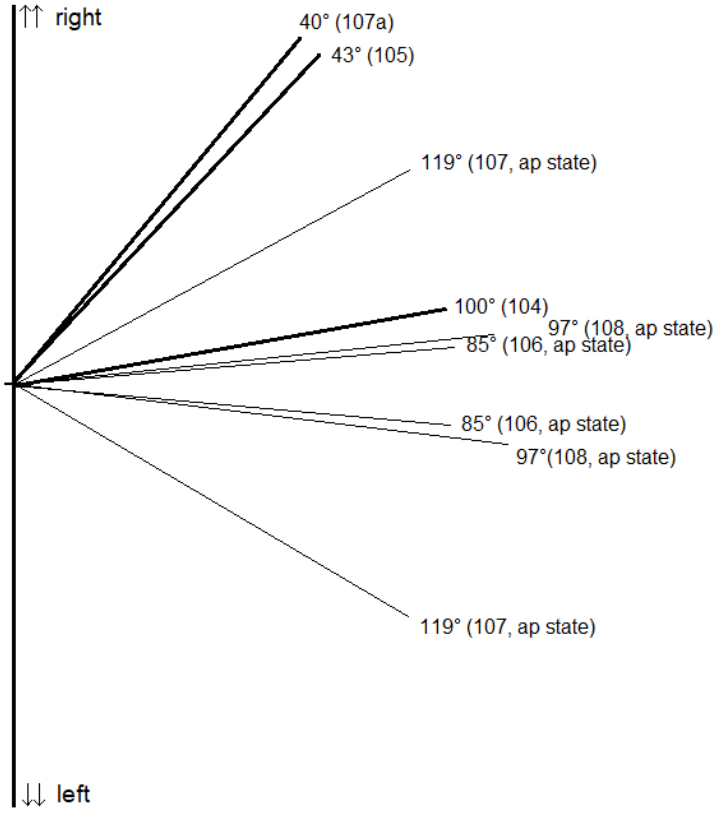

Figure 63: Schematic drawing of the magnetic iron states defined as "right" and "left" (180° apart) and the difference in Co_2FeSi rotation angle as shown in table 5. For the antiparallel iron magnetic states it is not possible to relate the Co_2FeSi rotation angle to one of the magnetic iron layers, so both possibilities are shown with a thinner line labelled also with "ap state". Behind the angle in degrees the dataset name is shown.

the Co_2FeSi, but it is always at least 40° rotated with respect to the iron, in many cases $\approx 90°$. Also only the layers as a whole are considered, the rotation for only parts of a layer resulting in an angle is the pixelwise processing that leads to the RGB colour image: from the component images comp1 and comp2 the direction of the (magnetic) contrast is calculated into an arctanimage via

$$\text{arctanimage} = \arctan(\text{comp1}/\text{comp2}) + 3.14159 \tag{3.2}$$

and assigning the results into colours. The value of π is added to avoid zero in the numerics. The colouring script has been provided by D. McGrouther (Glasgow). This

gives qualitative information about the specimen but it is not possible to get quantitative magnetic information out of this processing. Rotating and minimizing contrast pixelwise would be very prone to noise effects and because of the pixelwise difference in the rotation angle the advantage of taking lineprofiles and integrating over an area would get lost. The RGB images for all possible magnetic states of this data are shown in fig.57. It can be seen there that the Co_2FeSi is always in the same (yet proven to be) magnetic state regardless of the iron magnetic state. Also the Co_2FeSi appears thinner than to expect from the chemical analysis, showing already that the iron magnetism is influencing and leaking in the Co_2FeSi layer. One problem of these images is that also nonmagnetic contrasts lead to deflections and thus to colouring, which can be seen in the yellow/orange stripe next to the iron layers shown in blue.
A domain wall appears in the upper iron layer of dataset 115 (fig.57d) of which the properties are investigated in the following paragraph.

Appearance of domain walls happen in one of the iron layers at tilting angles close but below those sufficient to switch the magnetization of both iron layers, this happens after tilting to 15° (corresponding field in plane of 0.0258 T) and back to magnetic zero at 5°. The width of the domain wall has been measured using lineprofiles across the domain wall in two places to 9.5 ± 3.8 nm (fig.64). To determine the type of the domain wall the line profiles of both components are overlaid and it can be seen that both components are changing their sign indicating a rotation around an axis in the plane of the thin film making it a Neel type domain wall.

The domain wall state is useful for analysis as two magnetic states are present in the

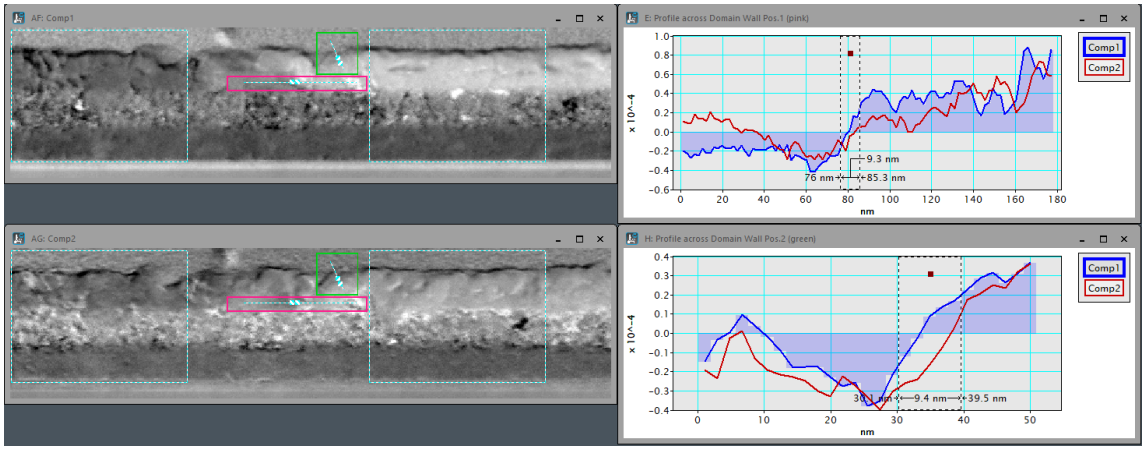

Figure 64: Component images of the domain wall. The region for the two lineprofiles, each shows both components overlaid, are surrounded by a pink rectangle and shown top right and by a green rectangle shown bottom right. Both measure the same width of 9.5 ± 3.8 nm for the domain wall. The light blue rectangles show the position of the line profiles used for further magnetic analysis of this specimen.

same dataset, so differences in experimental conditions are smaller than in comparisons between different datasets. The rotation angle is 55° for the parallel state and 57° for the

antiparallel state, so the mean value of 56° has been chosen for the whole dataset. After dividing by thickness the magnetic induction has been calculated for both components (fig.65). The results are shown in tab.6 and are comparable to those from the evaluation of the different datasets (tab.4).

Dataset	Layer 1 (center)	Layer 2 (center)	Layer 1 (whole layer)	Layer 2 (whole layer)
parallel	-1.08 ± 0.02 T	-1.03 ± 0.06 T	-1.04 ± 0.10 T	-1.01 ± 0.15 T
antiparallel	-1.15 ± 0.02 T	0.82 ± 0.11 T	-1.13 ± 0.07 T	0.78 ± 0.12 T
Magnetic zero		-0.11 ± 0.11 T		-0.12 ± 0.11 T
	Heusler (center)	Heusler (whole layer)		
parallel	0.46 ± 0.04 T	0.40 ± 0.11 T		
antiparallel	0.32 ± 0.9 T	0.26 ± 0.12 T		

Table 6: Magnetic induction from the domain wall dataset with a parallel magnetic state of both iron layers left of the domain wall and an antiparallel state right of the domain wall (fig.64). Each layer has been measured (Fe1, Co_2FeSi, Fe2) and the measurement integrated over the central layer part and over the whole layer as measured chemically, this contains also the interface regions. Magnetic zero has been calculated from the 2nd Fe layer that includes the domain wall and shows both magnetization directions.

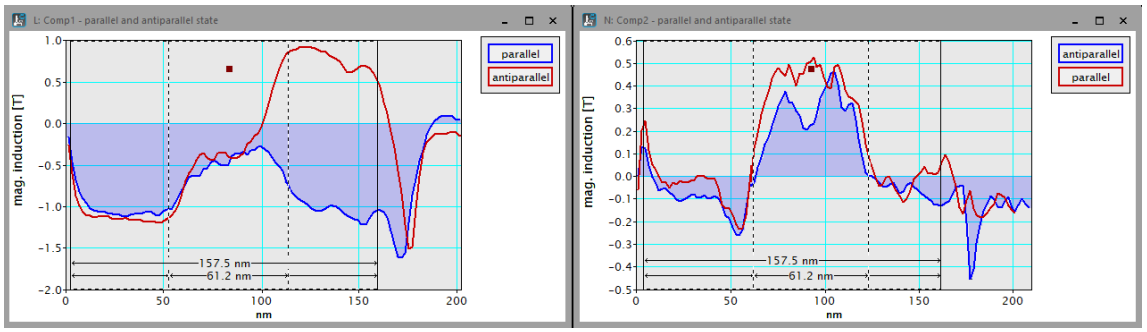

Figure 65: Results of the domain wall dataset for the magnetic induction after rotating to minimum contrast. The line profiles have been taken on the positions marked by rectangles in fig.64 and are overlaid for each component: Comp1 of the Fe layer system (left) and perpendicular component Comp2 (right). ROI are drawn to show the layer system and the Co_2FeSi layer.

Repeated DPC measurements have been conducted at the Paderborn TEM (Jeol ARM200F) in this setup: Measurement at objective lens off, tilting the specimen to the desired angle (±25°), switching the OL on to 0500, 10 sec waiting time, switch off, 10 sec waiting time, tilting back and recording a measurement. This should prevent an influence of the OL during tilting and magnetizing also the Co_2FeSi in in-plane direction. An external field zeroing setup or field measurement setup close to the specimen does not exist here. The results are less accurate as this microscope has no dedicated Lorentz lens and the STEM Lowmag mode needs very high camera lengths (1500 cm - 4000 cm) for the DPC detector (8-fold segmented Jeol SAAF) which leads to scan effects in the images. The used settings are Lowmag STEM, spot 1L, alpha 2, camera length 1500 cm. If the lenses are similar to the Glasgow ARM, which is the same model built a few years earlier, the lens value of 0500 corresponds to a magnetic field of ≈ 0.1 T. The outer four quadrants have been used for measurement and the beam has been centered as accurately as possible. The parallel state of the Fe layers in both directions has been measured twice.

In the colour image it can already be seen that it has been possible to switch the iron layers, the Heusler layer stays in the range of the blue/green colour scheme, which hints it is again not switched magnetically in this measurement. The FIB-Pt seems to show always blue colour but this is not switched and a normalization effect combined with the rapidly decreasing thickness in the FIB-Pt. The purple in dataset 4 results from a non-optimal normalization. Rotation by 177° separates the contrast in the Fe layers between the two components. Using line profiles integrating over 50 pixels across the components allow for comparison of the data (fig.67), it has been corrected for the specimen thickness using the thickness function (eq. 3.1).

Contrasts arising from a change in the mean inner potential at the layer boundaries are much higher in this data. The second component is intended to show the magnetic contrast, which is visible and reversed by the external field and comparable to the Glasgow result. The first component shows the signal perpendicular to the second component and the datasets 1 and 4 show a signal in the Fe layers, the opposite magnetized datasets 2 and 3 a signal that locates more towards the interfaces. This does not reproduce the signal of the component perpendicular to the Fe signal from Glasgow. If the rotation angle is not the most matching angle residual contrast leads to a residual signal in the other component and these signals can be related to those from the first component: the Fe magnetism and the MIP-change induced deflection on the interfaces. New and reversable information in the Co_2FeSi layer can not be found.

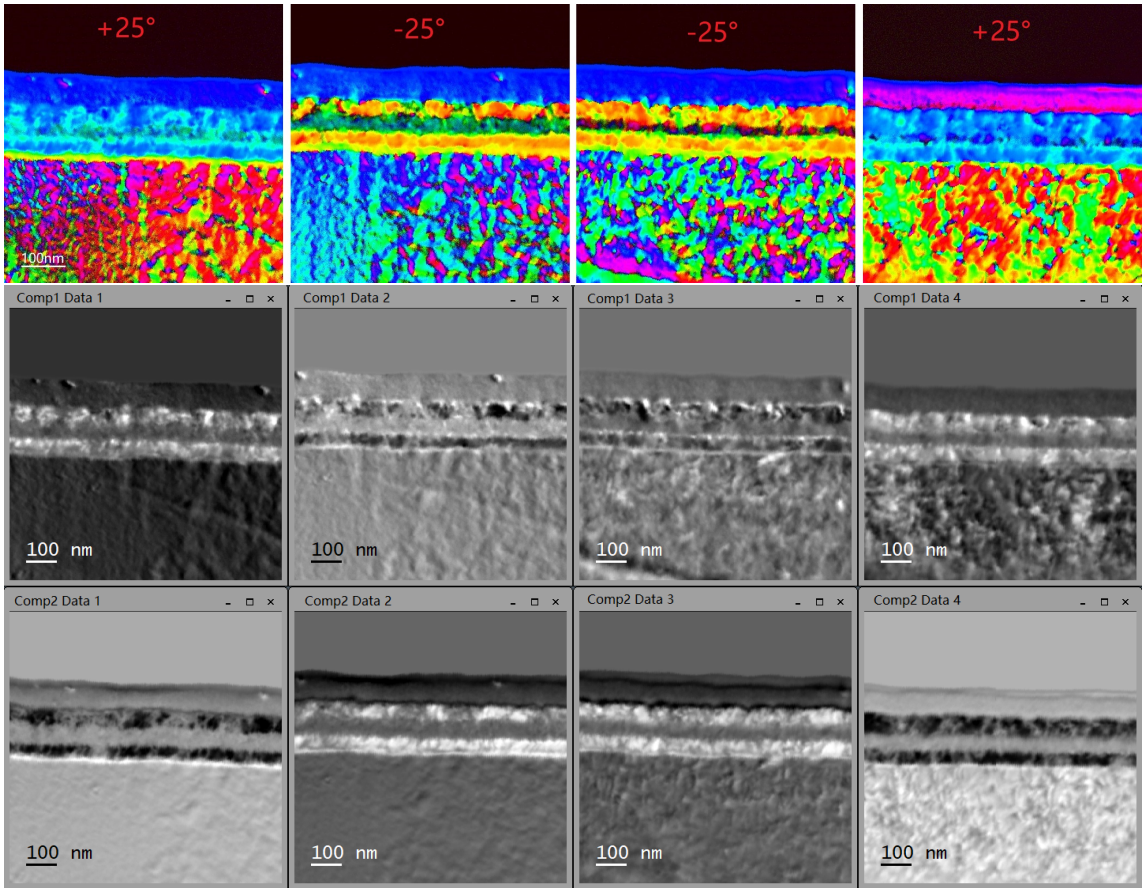

Figure 66: Results from the additional DPC measurements where care has been taken to avoid influence of the OL field on the specimen during tilting. For each tilting direction two datasets have been recorded, from left to right: dataset 1 to 4 with the top row showing the colour image from recording, the central row the first component and the bottom row the second component. These have been rotated by 177° to separate the contrast in the iron. The apparently differing contrast results from the software GMS using only relative contrasts in the display of images, the vacuum part for example is always zero but shown in different shades of grey in each component.

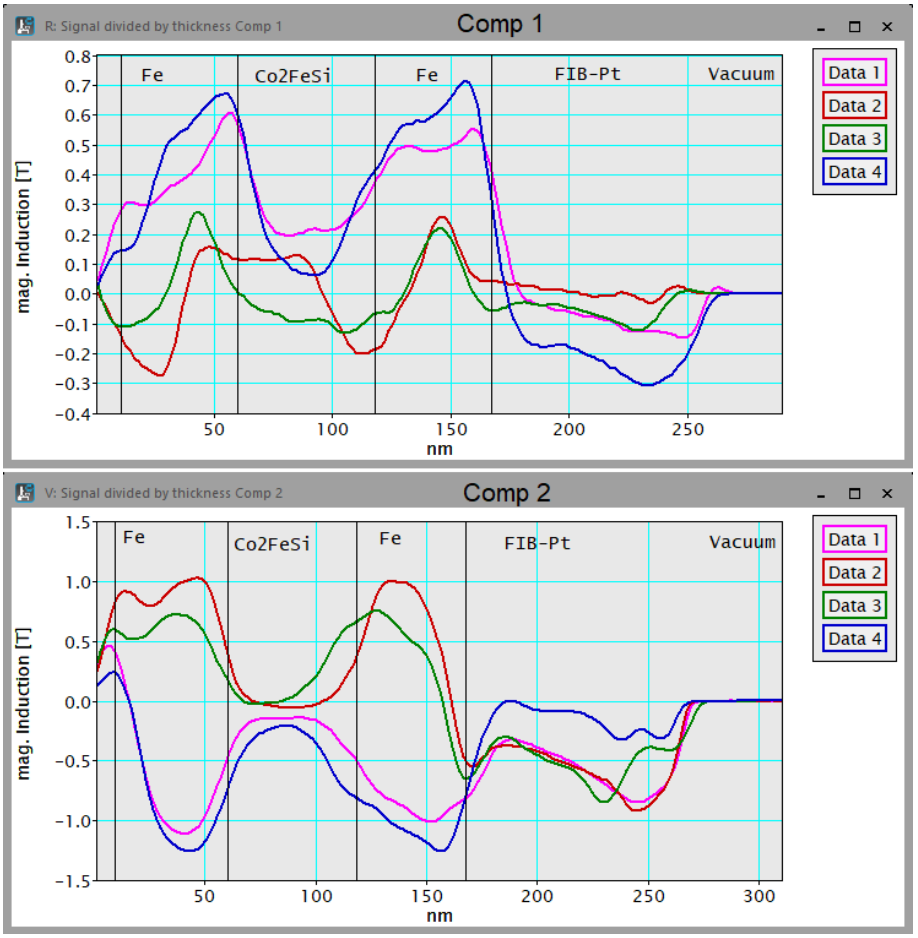

Figure 67: Results of the four segmented DPC measurements on the ARM200F in Paderborn with datasets 1 and 4 exposed to the external field in + tilting direction and datasets 2 and 3 in − tilting direction. Comp 2 contains the magnetic signal that shows to follow the external field direction, Comp 1 the signal perpendicular to Comp 1.

The influence of the mean inner potential (changes) on the contrasts seen in the DPC measurement is investigating by modelling the mean inner potentials (MIP) as they arise in the layer system: For MgO the MIP is 13.01 ± 0.08 V [94] [95], for Fe it is 22 V (partly from DFT calculations) [47] [96], for Co_2FeSi it is calculated from the elements of this compound:

$$2/4 \cdot V_0(\mathrm{Co}) + 1/4 \cdot V_0(\mathrm{Fe}) + 1/4 \cdot V_0(\mathrm{Si}) = 2/4 \cdot 29.5\ \mathrm{V} + 1/4 \cdot 22\ \mathrm{V} + 1/4 \cdot 9.26\ \mathrm{V} = 22.565\ \mathrm{V} \approx 22.6\ \mathrm{V}$$

with 9.26 ± 0.08 V for Si [95] and 29.5 V for pure Co [97]. For the FIB-Pt the value of pure Pt is assumed, 25 V [98]. These MIP are built into a layer system according to the measured dimensions. The derivative shows the change of the MIP and the contrasts that come up because of the change (fig.68). The model MIP also has been filtered by the Savitzky Golay spectral filter [81] that includes "moving a window across a 1D data set, in which a polynomial is fitted to the data. The fitted value at the midpoint of the window is substituted for the original data." [81]. This can also be considered as a mixture between differentiation and smoothening and gives a model which is more realistic because of the not totally sharp interfaces. Both modelling ways give qualitative the same result in the derivative, the one of the filtered model is broadened and less high because the interface is not as sharp. A huge contrast can be expected at the MgO/Fe interface because of the almost doubling in the MIP from MgO to Fe, small contrasts appear at the Fe/Co_2FeSi(negative) and the Co_2FeSi/Fe (positive) interfaces. In the DPC measurements

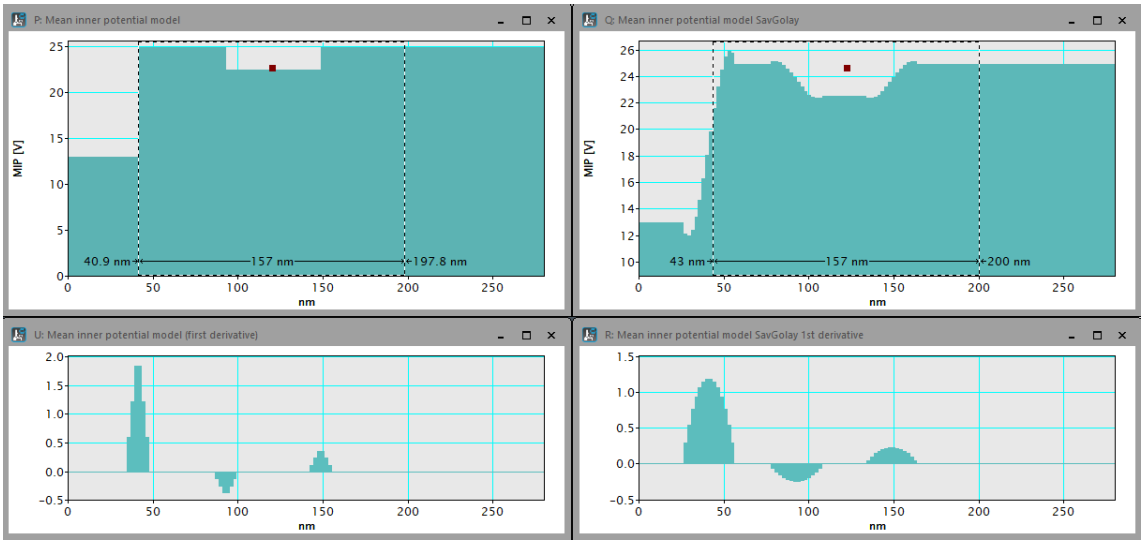

Figure 68: Mean inner potential model with layers of the same thickness as measured for this specimen (top left) and the 1st derivative of the MIP (bottom left). The MIP model has been smoothed by a Savitzky Golay filter (top right), which gives a derivative that is broader and less high in the peaks (bottom right).

the contrast from the MIP change at the MgO/Fe interface is clearly visible (fig69. At The Fe/Co_2FeSi interface the change in MIP is relatively small and the magnetic contrast exceeds it, this is similar for the other interface, Co_2FeSi/Fe, where a small dip in the same direction as the one for the MgO/Fe interface can be observed. At the Fe/FIB Pt interface there should be no contrast arising from the change in MIP. But as the iron layer has been

the surface before using the FIB to cut the lamella where the Pt has been deposited the contrast arising there is edge contrast.

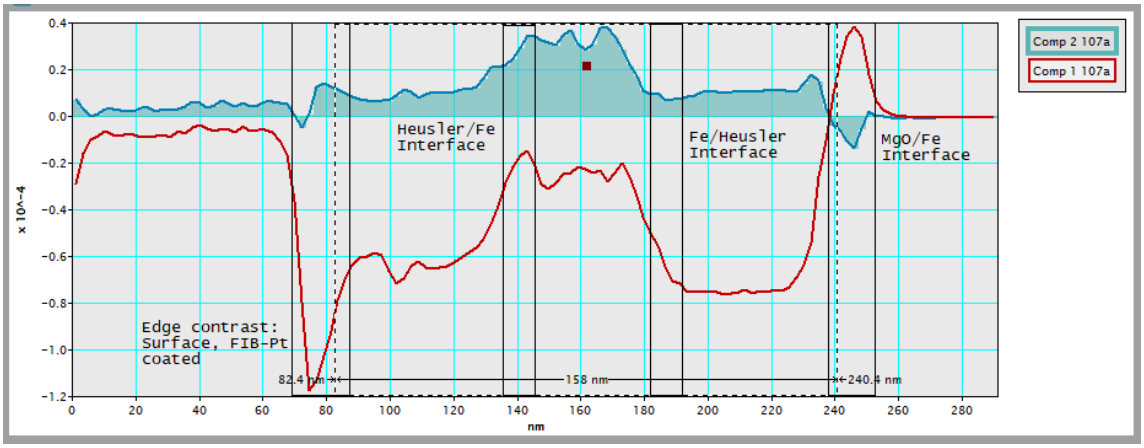

Figure 69: Dataset 107a (Fe layers magnetized in parallel) with one component (red) in the direction of the Fe magnetization and the other (blue) perpendicular. The contrasts at the interfaces are marked by rectangles, the one from the MIP change at the MgO/Fe interface are clearly visible, the others are small compared to the magnetic contrast of the iron. At the preliminary "end" of the layer system between Fe and FIB-Pt huge deflection by edge contrast can be found.

Appearance of a magnetic hysteresis can be shown only very limited using DPC because it can be detected if the external field is strong enough to switch the magnetization of the specimen, but a detailed measurement against a varying external field is not possible. Small reactions to the outer field that determine the form of the hysteresis can not be measured in the current setup, a sample design of many multilayers switching at different fields would allow to obtain more information. It has been tried to show the switching points and from which state the system emerged in fig.70. The system has always been tilted back to magnetic zero (5.6° tilt) for the DPC measurement. The iron layers are both switched at +25° or coming from +8.6° at +15° (this happened once) and for the other parallel state at -25°, earliest at -22°. The antiparallel state could be achieved by tilting to +8.6°. The domain wall has been achieved by first tilting to +8° and then to +15°. The corresponding field strengths are calculated from magnetic zero at -5.6°:

-25° → effective -19.4° ⇒ −0.033 T
-22° → effective -16.4° ⇒ −0.028 T
+8.6° → effective 14.2° ⇒ 0.024 T
+15° → effective 20.6° ⇒ 0.035 T
+25° → effective 30.6° ⇒ 0.051 T

To switch both layers a field of $0.033 - 0.035$ T is sufficient in both directions. A lower field of 0.024 T switches one Fe layer. Switching behaviour occurred within a field change corresponding to a tilt of one more degree around between effective 19° and 20° in the experiment which corresponds to a field change of 0.0016 T.

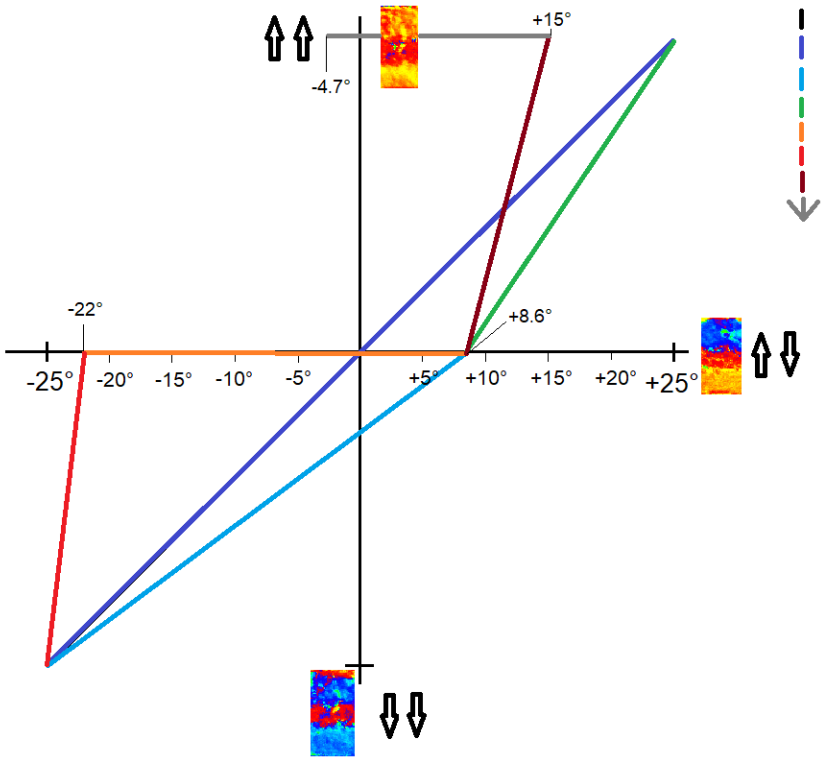

Figure 70: Magnetic hysteresis in DPC: Tilt series from 0° → -25° → +25° → (-25° → +8.6°) → -22° → -25° → (-25° → +8.6°) → +15° → -4.7°. Bracketed tilts were performed consecutively before the measurement. The line colours are intended to show the sequence as indicated in the coloured arrow top right. Each magnetic state is shown and the tilt angles that lead to the magnetic state.

Pixelated DPC has been performed in Glasgow on the ARM200cF using a Medipix3 CMOS detector with Merlin readout system [53] [99]. The detector consists of 256×256 pixels and is capable of single electron detection. For DPC or 4D STEM on every scanpoint the central disc or a greater section of the diffraction pattern is recorded. In the case of DPC it allows to follow beam shifts by following movements of the central disc. It has been corrected for descan effects and converted from beam shifts to magnetic induction. For this Fe/Co_2FeSi/Fe specimen one dataset for each parallel and the antiparallel state has been recorded and one of the domain wall. The resulting colour images are shown in fig.71. The single datasets can be found in Appendix 6.2. The data has been rotated by 80° during processing to achieve that one component image contains magnetic information parallel to the Fe magnetization direction and the other component information of perpendicular components. The final result (fig.72) shows that magnetic zero again is not at coordinate zero and the magnetism of the Fe reaches 12.8 ± 3.2 nm (Fe1)/16.0 ± 3.2 nm (Fe2) into the Co_2FeSi, consistent with the segmented DPC measurements. In the antiparallel state the central part of the Co_2FeSi has a bridge function where it changes nearly linear in the central Co_2FeSi part where no Fe influence remains. The magnetic induction has been measured, the results are shown in tab.7. Thee are two result lines because always one of the datasets can be compared with two others. It is again assumed that the Fe layers are fully saturated and the physical value for their magnetic induction is half of the difference. The final result is the mean of the two preliminary ones.

The layer adjacent to the MgO shows a higher magnetic induction with 1.17/1.14 T, the

Datasets	Layer 1 (center)	Layer 2 (center)	Layer 1 (whole layer)	Layer 2 (whole layer)
↓↓ 107	0.73 ± 0.05 T	1.00 ± 0.04 T	0.84 ± 0.29 T	0.78 ± 0.42 T
↑↓ 108	-1.55 ± 0.05 T	0.94 ± 0.09 T	-1.32 ± 0.37 T	0.88 ± 0.25 T
↑↑ 109	-1.66 ± 0.06 T	-1.16 ± 0.02 T	-1.54 ± 0.25 T	-1.16 ± 0.11 T
Result 1	1.14 ± 0.06 T	1.08 ± 0.07 T	1.08 ± 0.30 T	0.97 ± 0.26 T
Result 2	1.20 ± 0.06 T	1.05 ± 0.07 T	1.19 ± 0.30 T	1.02 ± 0.26 T
Result mag. Ind.	1.17 ± 0.09 T	1.07 ± 0.09 T	1.14 ± 0.36 T	1.0 ± 0.28 T

Table 7: Results for the Fe magnetic induction from pixelated DPC data (fig.72). Layer 1 is adjacent to the MgO, Layer 2 adjacent to the FIB-Pt.

other Fe layer reaches only 1.07/1.0 T (center/whole layer used for measurement), which is 91%/88% of the value of the first layer and can explain why the second layer always switches first. The errors of the measurement are high in the measurements using the whole layer because the variation on the edges of the layer are larger.

Magnetic zero can be determined to -0.25 ± 0.15 T which matches the measurement of the Co_2FeSi layer in the center with -0.16 ± 0.09 T (107) and -0.33 ± 0.06 T (109) giving the result -0.25 ± 0.15T. The antiparallel dataset is not considered because from the results in fig.72 it can be seen that there in the Co_2FeSi where no Fe influence remains the Co_2FeSi acts as a bridge between the antiparallel Fe parts with the material orienting on the nearest magnetic influence. So far no other magnetic signal could be obtained from the Co_2FeSi region. Looking at the other component from the pixelated DPC results (fig.72 bottom) shows no signal above the error margins. In both Fe layers a very small residual of ≈ 0.1 T can be seen, in between only noise. The result from the segmented DPC can

not be reproduced, the contrasts seen there can not be related to an actual deflection of the beam. This suggests that the Heusler Co_2FeSi is either non magnetic or shows a very softmagnetic behaviour and is influenced by the field of the objective lens which always points out of plane. No field zeroing measures have been performed and the residual field of the objective lens can have up to 0.015 T.
The extent of the Fe magnetism into the Co_2FeSi layer measures 12.8 ± 3.2 nm on both interfaces. So only the central two quarters of the layer are without magnetic influence from the Fe.

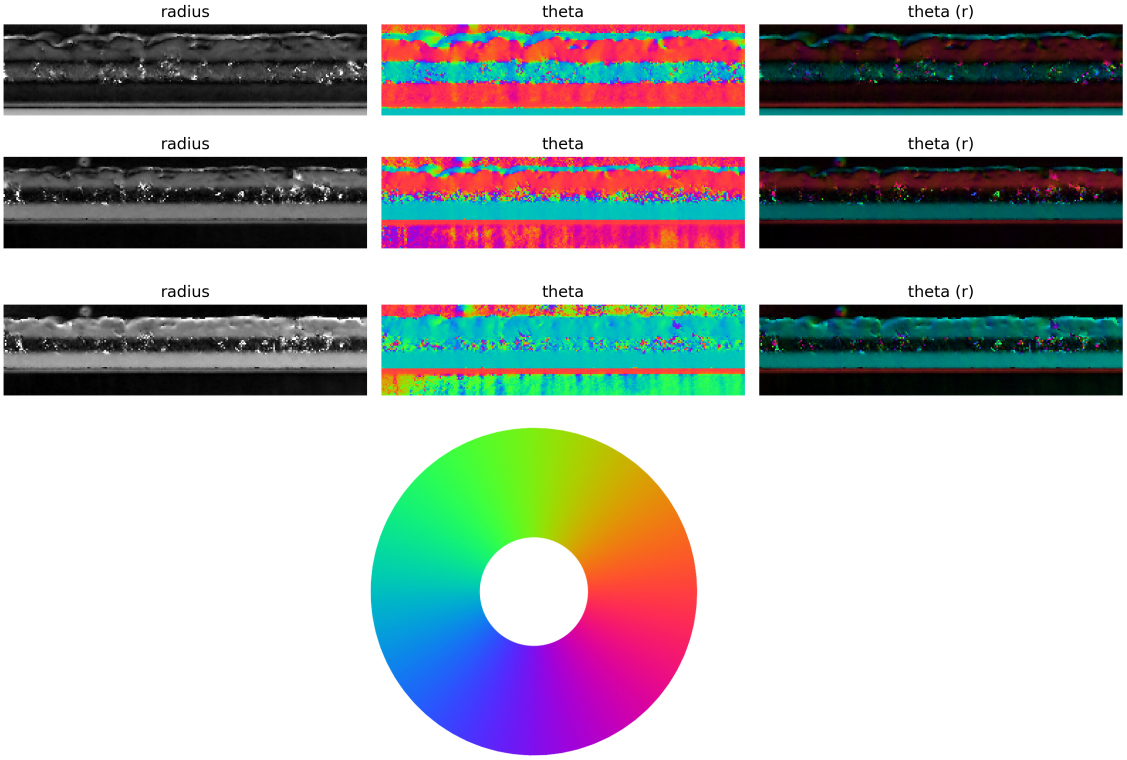

Figure 71: Pixelated DPC results for the " ↓↓ " (top) where the normalization did not succeed as there is nearly no MgO in the image and which results in an offset on the Co_2FeSi, the " ↑↓ "(center) and " ↑↑ "(bottom) datasets. The deflection information is shown as the deflection distance (radius), the deflection angle (theta) and the combination of both in a coloured image (theta(r)). The colourwheel below shows the directions. The center of the Co_2FeSi layer shows coloured pixels corresponding to many directions, this happens if the algorithm cannot find the circle of the diffraction disc properly.

The other measured dataset contains a domain wall in the Fe layer adjacent to the FIB-Pt and shows both parallel and antiparallel configuration in the same dataset, which minimizes errors resulting from changed measurement conditions. The resulting magnetic induction calculated from line profiles left and right of the domain wall and crossing the domain wall are shown in fig.74. In this more complicated situation the Co_2FeSi shows uniform magnetization in the data from the left which according to the angle image extends from the part of the second Fe layer that is magnetized in the opposite direction. The

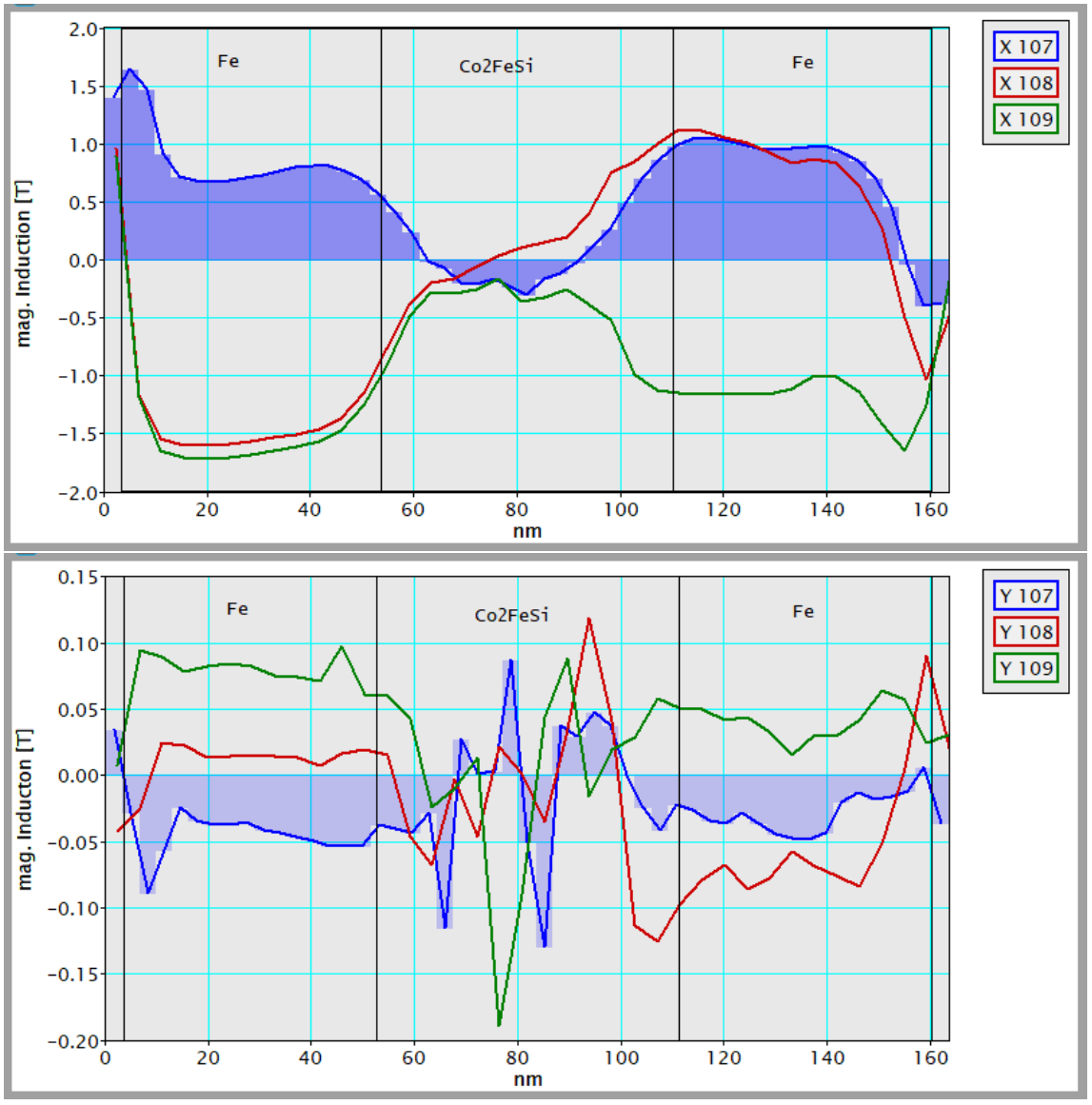

Figure 72: X (top) and Y (bottom) components of the two parallel and one antiparallel magnetized datasets. The Y components are on the noise level indicating that the rotation of the dataset by 80° is correct, the datasets still show their magnetic behaviour (parallel or antiparallel state). Magnetic zero is where the two parallel states meet.

domain wall lies tilted to $21.2 \pm 0.5°$ with respect to the layer system surface in the second Fe layer. It can be assumed that it follows grain boundaries or defects in the material. The magnetization direction changes by 180°. The slope in the center is determined by a linear fit $f(x) = m \cdot x + b$ resulting in $m = -0.108 \pm 0.010$ T. The points where this function crosses the horizontal lines defined by the average magnetic induction on both sides of the wall are determined from a plot according to the definition from [100] (fig.73 left). This has been done using gnuplot and calculate the intersection points. The upper

magnetic induction is measured to 0.58 T and the lower magnetic induction to -1.18 T as shown in fig.73 right. This gives a domain wall width of $\delta_{DW} = 14.9 \pm 2.4$ nm.
The Bloch wall thickness from the micromagnetic simulations has been calculated to $\delta_{BW} = 589.05$ nm, an order of magnitude higher, so a Neel type wall is expected here. The behaviour of both components is in agreement with a Neel type wall because both components show a rotation.

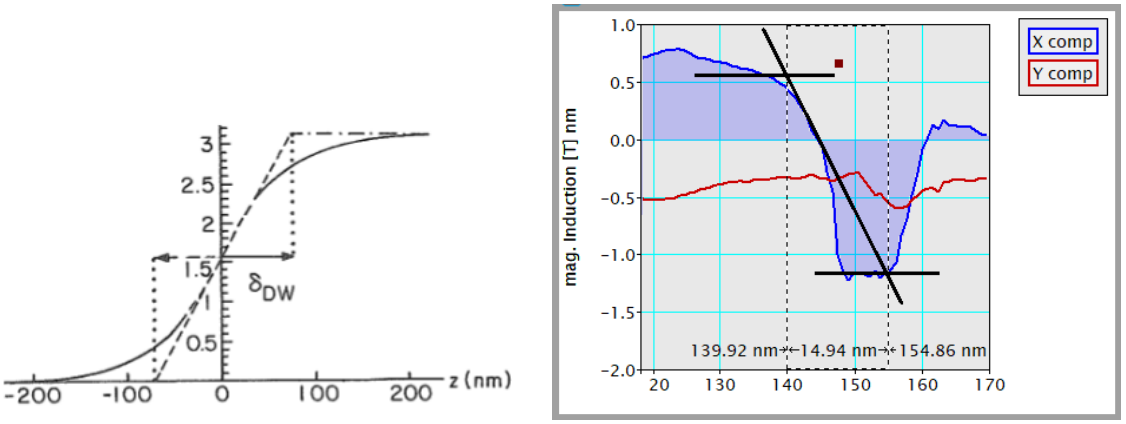

Figure 73: Left: Definition of the domain wall width δ_{DW} taken from [100]. Right: Measurement of the domain wall width on the pixelated DPC dataset from a lineprofile across the domain wall. This is an excerpt from the pixelated domain wall dataset shown in full in fig.74 bottom.

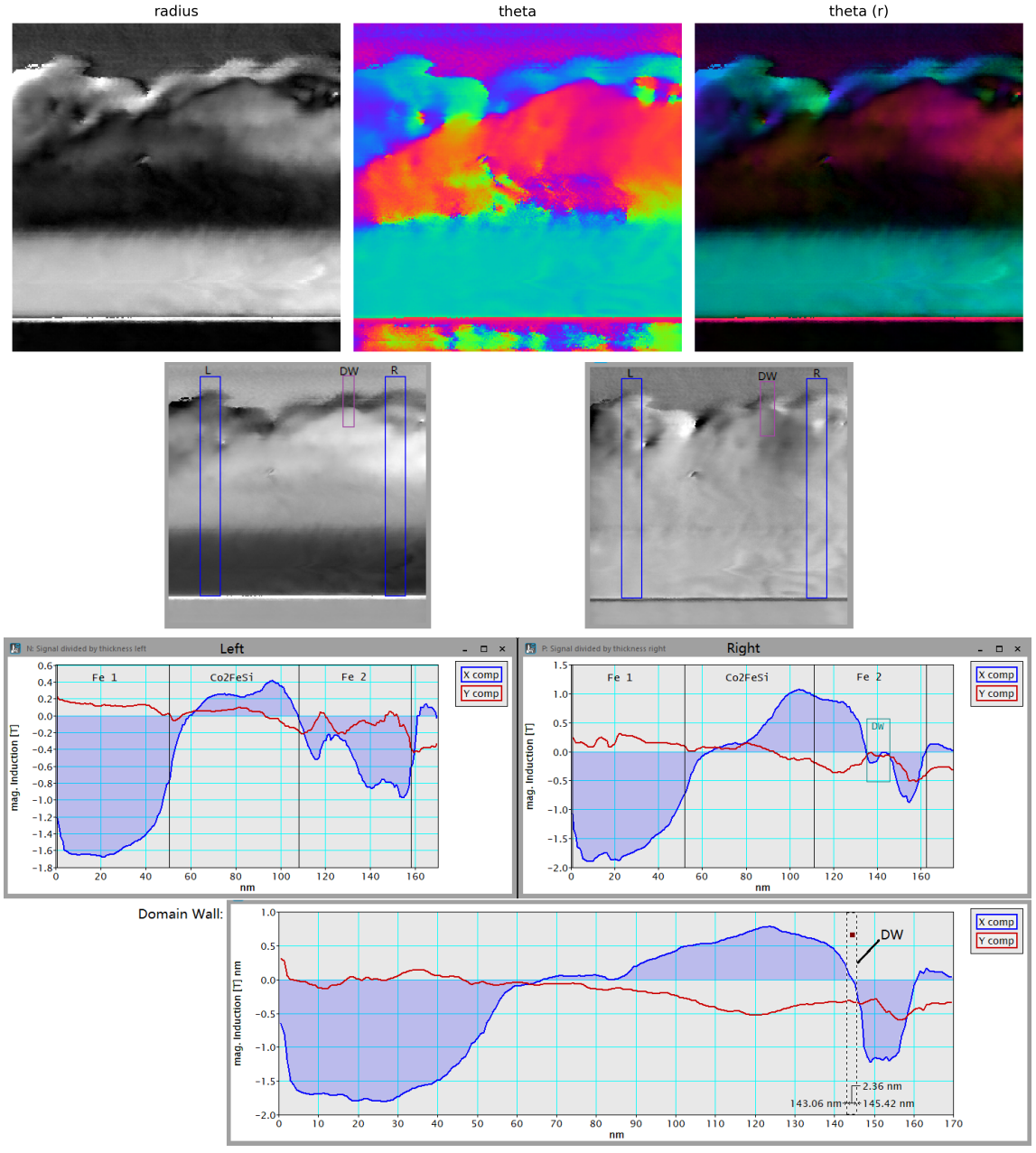

Figure 74: The domain wall: Top row: Strength (radius) and angle (theta) of the deflections, combined to an image in theta(r). Below: X and Y component with the positions of the extracted line profiles on the left and right side of the domain wall shown by blue rectangles, the position of the used part of the domain wall is shown by a purple rectangle. Both components of the magnetic induction are shown below for the left and right part and on the bottom for the line profile crossing the domain wall.

3.5.4 Conclusions for the Fe/Co_2FeSi/Fe system

The important results of the investigation of the Fe/Co_2FeSi/Fe layer system are the depth of the Fe influence in the Co_2FeSi of up to $\approx$ 13 nm, the very small or in z-direction pointing magnetism of the Co_2FeSi layer proving the material to show very soft-magnetic behaviour or very small magnetic induction and saturation magnetization. The Mumax simulations describe the iron magnetism with good agreement and the line profiles across the integrated induction show a majority of the cases where the Co_2FeSi is indeed acting more like a magnetic bridge than another magnetic layer. However this description is only valid for the antiparallel magnetized iron layers, in the parallel case according to all simulations the Co_2FeSi layer is expected to show a notable magnetic signal in the same direction as the iron which could not be observed in the TEM. In terms of magnetic behaviour the chemical interfaces between the layers lose their role, the notable difference in both Co_2FeSi/Fe interfaces does not appear in the magnetic data. With a change of materials from still ferromagnetic alloys to compositions that are not ferromagnetic anymore diffusion and formation of different alloys at the interface will probably show through to the magnetic properties. This information is important for all sensor applications consisting of sufficient thin layers as pinning effects can occur where they are or are not wanted. More information could be gathered in TEM measurements where a field-zeroing system is used and an external in-plane magnetic field can be applied. The behaviour of the iron is in accordance with its known properties.
Chemically the central Co_2FeSi layer is separated by the Co/Fe relation and by a change in a lattice constant. The most likely alloy Fe_2CoSi is also a soft magnetic full Heusler alloy and changes of the magnetic behaviour could not be observed.

3.6 Towards characterization of multilayer systems: V/Co_2FeSi/V

This multilayer system consists of three layers: Vanadium, the Heusler alloy Co2FeSi and another Vanadium layer. Each of these layers has been intended to be 50 nm thick, deposited by Co-sputter deposition at 450° C on MgO substrate by Andreas Becker under the following conditions: Sputter process at 450° C at a base pressure of $< 5 \cdot 10^{-9}$ mbar with targets used of V, Co, Fe, Si, and Mgo. Waiting time after each layer has been 10 min, other conditions were Argon flow 10 sccm and substrate rotation 10 rpm. After sputtering cool down to room temperature in the sputtering chamber. Pre-cleaning as for the Fe/Co_2FeSi/Fe sample: ultrasonic bath (10 min acetone, 10 min ethanol, 5 min DI Water) and heating to 700° C for 30 min followed by a cool down phase to 450° C of 30 min in the sputter chamber.

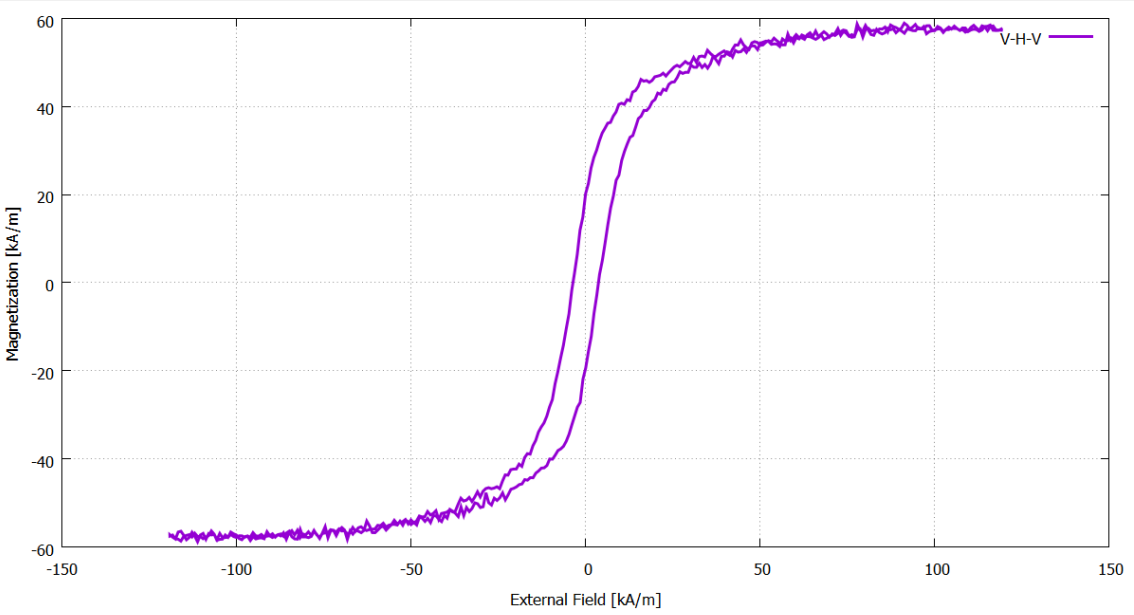

Figure 75: The AGM measurement of the V/Co_2FeSi/V sample with a saturation magnetization of 57.5 kA/m.

For information about the magnetization of the sample AGM measurements have been performed at room temperature. The magnetically active volume is given by an area of 13.6 mm^2 and a layer thickness of 58.6 nm, which is a result of the chemical analysis. So the volume is $7.9696 \cdot 10^{-7}$ cm^3. This measurement shown in fig.75. The saturation magnetization is measured to 57.5 kA/m and the hysteresis shows a coercivity of 3.6 kA/m. The remanence lies at 22.4 kA/m. According to this measurement it is a soft magnetic material, although less soft magnetic than the Fe/Co_2FeSi/Fe sample which has a coercivity of 1.3 kA/m.
The literature values for Co_2FeSi vary but are much higher than the measured values here: 1124 kA/m [101] (measured at 295 K) or 1250 kA/m [102] (measured at 373 K). Possible reasons for this deviation will be discussed after the other measurements at the end of this chapter.

A cross section TEM lamella has been cut using a FEI Helios Dual Beam FIB including the second ion beam milling after thinning at 5 kV by Björn Büker. The total thickness of the layer system is measured to be 160.2 nm where the layers are V (46.6 ± 1.2 nm), Co_2FeSi (58.6 ± 1.9 nm) and V (55.2 ± 3.9 nm) the large error originates from varying thickness due to surface roughness.

The thickness of the FIB lamella has been evaluated using EELS measurements on the

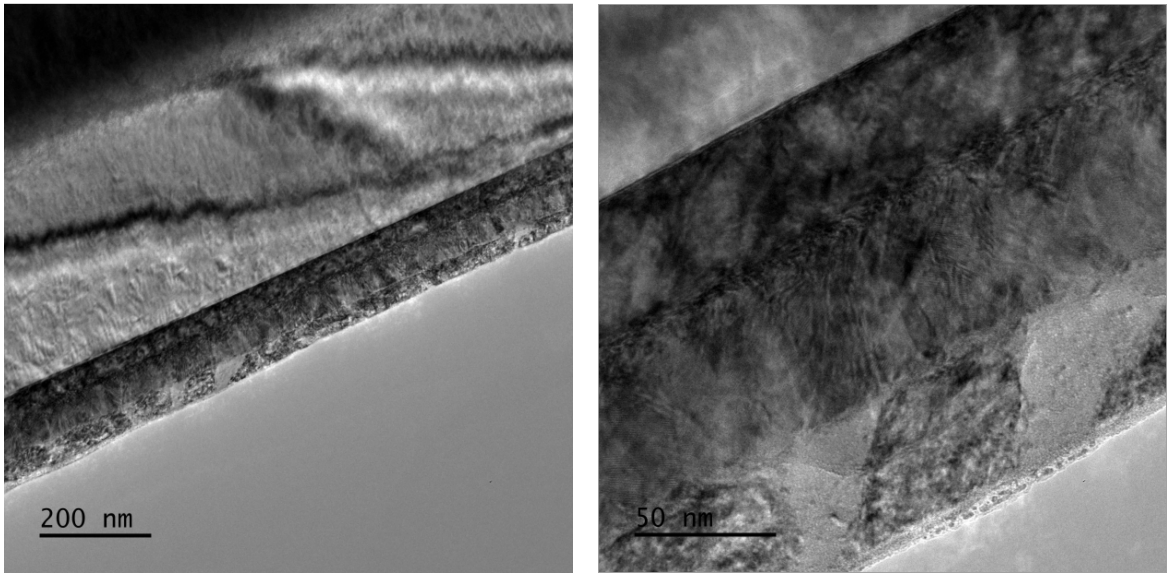

Figure 76: The MgO substrate/V/Co_2FeSi/V/FIB Platinum layer system (substrate on top of the image), images of the freshly cut lamella before it was sent to Glasgow courtesy to Inga Ennen.

ARM200F (Gatan Quantum GIF post column filter) also providing chemical data about this specimen.
A set of two zero loss EELS maps of 100x30 pixels each has been recorded on the ARM200F (exposure time 0.0001 sec/0.0005 sec, 5 mm aperture, dispersion 0.25 eV/channel, STEM mag 600kx). These have been converted into thickness maps using the t/λ method. Fig.77 and 78 show the two datasets taken for thickness estimation. Since drift has been a problem at recording these data, a post recording drift correction has been applied by correcting the corresponding STEM image on a high contrast linear feature and applying this correction also on the map (fig.77). Because in one dataset the interface MgO/V has been lost in this process, it could only be applied to one dataset, the other had to be used without drift correction (fig.78).

Across the layer system a line profile integrating over several pixels has been obtained. As a reference starting point the interface MgO/V has been chosen to cover the thickness in the whole layer system. To convert the relative thickness given in mean free path (mfp) the DM script [83] using the Malis method [32] has been used. It calculates the mean free path for 200 keV electrons at $\beta = 20.8333$ mrad to

94.91 nm for Vanadium
94.3 nm for Co_2FeSi (50% Co, 25% Fe, 25% Si)

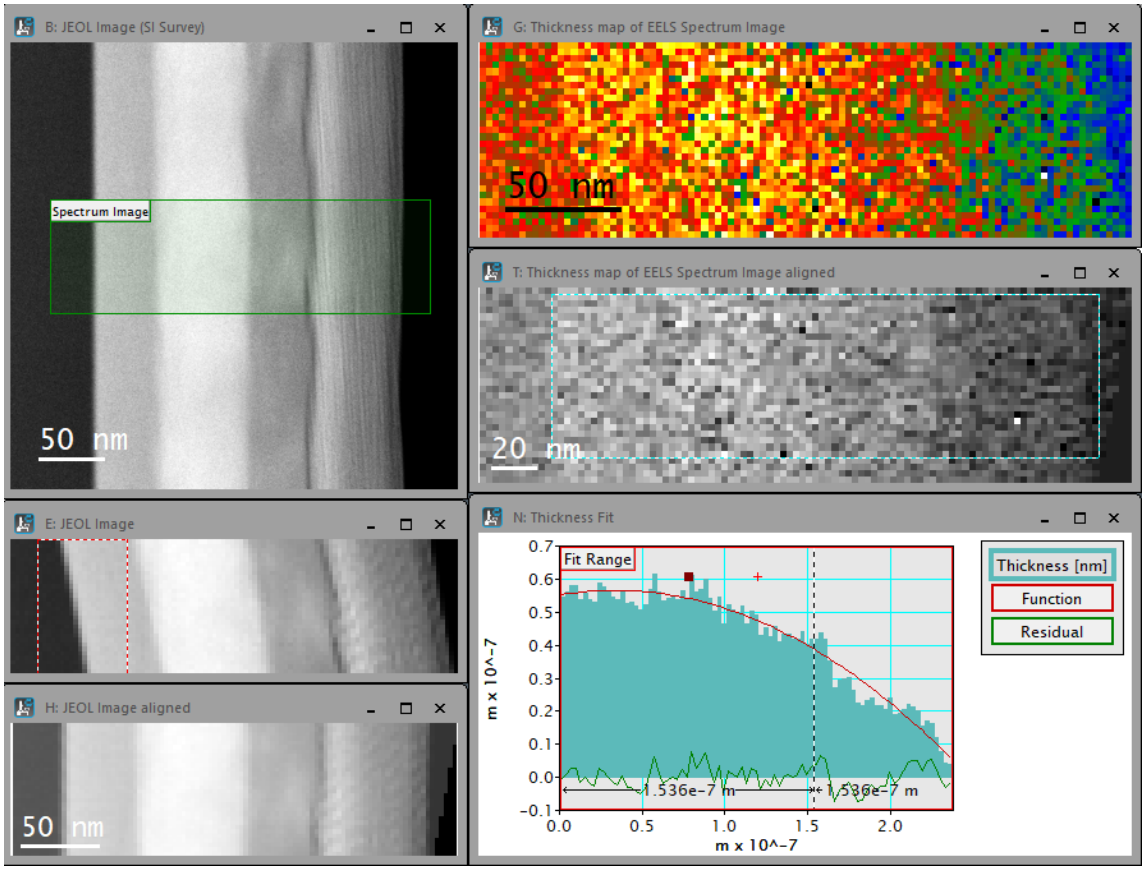

Figure 77: The first EELS zero loss mapping used for a thickness map. Left, top to bottom: STEM Survey image with area used for the map in green, Jeol ADF image used for drift correction and the drift corrected ADF image. Right, top to bottom: Thickness map with thickness in mfp colour coded, the thickness map drift corrected like the ADF image and area used for the line profile marked by a rectangle and the line profile of the thickness taken across the drift corrected thickness map. The distance and thickness are already given in meter and the layer system region has been used for a fit of a quadratic function which is also shown with the fit residuals.

These values are very close to each other and it can be assumed that the error margins in the datasets are much higher than the effects of the difference in mfp: The maximum difference between the two possible results is 0.4 nm and the standard deviation in an even and small part of the dataset is at 1.7 nm. So the mean value of 94.6 nm is used as the mfp for the whole layer system starting from the MgO/V interface.
The resulting thickness profiles show a curve suggesting not to use a linear function to fit but a quadratic one. This seems to match the data as can be seen in both datasets (fig.77 down right, fig.78 top right).

One fit has been performed on the first thickness map where drift correction has been possible, giving the result

$$f(x) = -0.00123851 \cdot x^2 + 0.0800272 \cdot x + 55.4809 \quad \chi^2 = 11.5$$

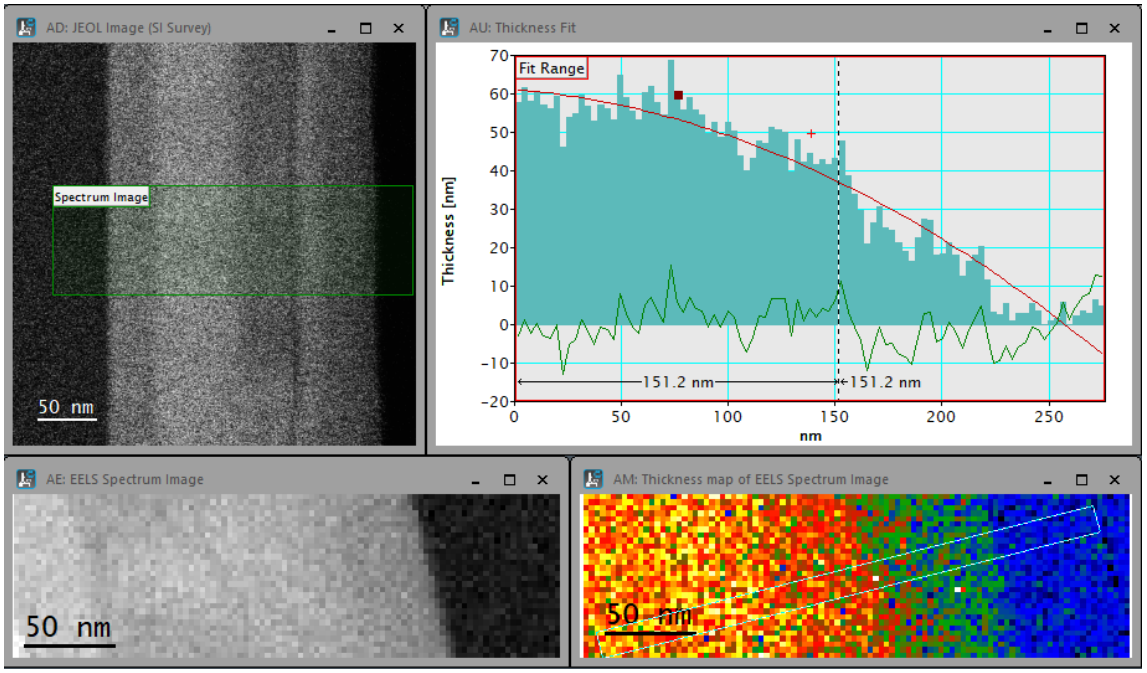

Figure 78: The second EELS mapping used for thickness estimation. Top left shows the survey image with the region for the mapping marked by a green rectangle, bottom left shows the spectrum image and bottom right the thickness map in mfp. With drift correction the interface MgO/V would be removed from the dataset so the line profile has been drawn perpendicular to the layer system as shown on the thickness map, starting point is the MgO/V interface. Top right: The line profile converted into thickness (in nm) with the fitted quadratic function and fit residuals.

Of the other set two fits have been performed on two different lineprofiles, giving

$$f(x) = -0.000745523 \cdot x^2 - 0.0484241 \cdot x + 61.1924 \quad \chi^2 = 31.8$$

and

$$f(x) = -0.000477023 \cdot x^2 - 0.11707 \cdot x + 62.2325 \quad \chi^2 = 26.7$$

The three fit results are shown in fig.79. The functions are reasonably similar, showing that the thickness of the lamella decreases from about 60 nm to 35-40 nm at the end of the layer system. The purple curve (2nd result) lies mostly in between the others and has been chosen for further evaluations to represent the thickness of the lamella for DPC. The translation in meters is the following:

$$f(x) = -7.45523 \cdot 10^{-13} \cdot x^2 - 4.84242 \cdot 10^{-11} \cdot x + 6.11924 \cdot 10^{-8} \tag{3.3}$$

The chemical composition has been evaluated spatially resolved by STEM EELS mappings and a linescan on the ARM200F equipped with a Gatan Quantum ER post column filter. At a magnification of 800kx (200 kV, camera length 80 cm, exposure 0.2 sec, 5 mm spectrometer entrance aperture, dispersion 0.5 eV, drift tube set to 300 V, gain normalized

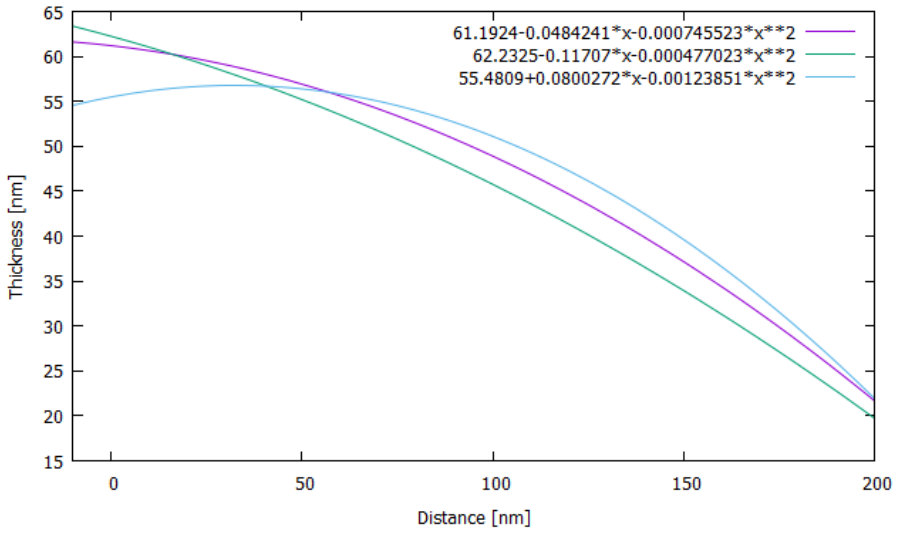

Figure 79: The three fit results for the thickness of the specimen across the lamella. Zero is set to be the interface between MgO and Vanadium.

and HQ dark correction) a 150x15 pixel spectrum image has been acquired, also a linescan of 230 pixels across the layer system (fig.80). Accessible edges in the recorded range of 200 eV-1224 eV are oxygen K (532 eV), vanadium L_2 (521 eV),L_3 (513 eV), iron L_2 (721 eV), L_3 (708 eV), cobalt L_2 (794 eV), L_3 (779 eV) and carbon K (284 eV). Carbon is part of the precursor which contains the platinum used for FIB deposition and can also contaminate the specimen under the electron beam.

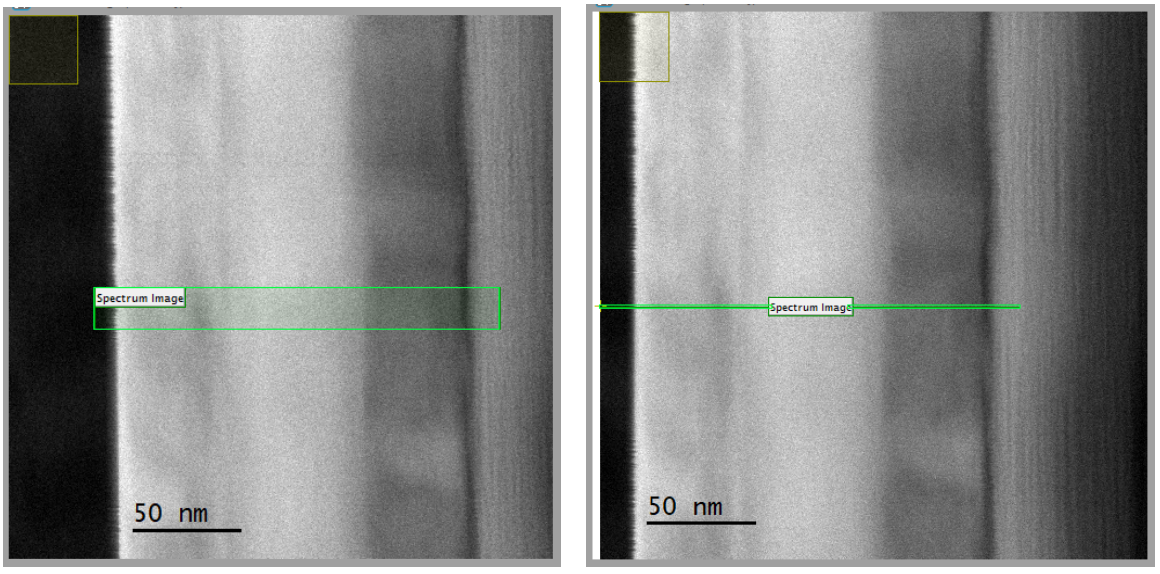

Figure 80: The survey images of the spectrum image and linescan, showing the position and size of the investigated area indicated by a green rectangle or line.

As in the Fe/Co_2FeSi/Fe specimen the edges of silicon and magnesium are not accessible. An elemental mapping has been performed on the spectrum image after background subtraction (power law). The result has been drift corrected (shown in fig. 81) and a line profile has been taken across the layer system integrating over 10 of the 15 available pixels. Also a background subtraction has been performed on the linescan data (power law). The elements C, O, Co, Fe and V have been found and chosen for evaluating the composition, the results are shown in fig.82. The vanadium seems to have diffused into the MgO, which contains $7.2 \pm 1.0\%$ V in the mapped part near the interface. On the V/Co_2FeSi interface the vanadium also diffused up to 14 nm into the Co_2FeSi falling from 34% to 0%. The iron starts higher at 39%, showing a small peak, and the cobalt lower than to be expected at 36% with the missing percentage being vanadium (25%). This might originate from starting the sputtering source for iron earlier and sputtering at a higher rate than the cobalt source, this evens out after a short time sputtering and the Co_2FeSi shows an iron/cobalt ratio of $67\%/33\% \approx 2:1$ compatible to Co_2FeSi. The interface Co_2FeSi/V again shows vanadium diffusion up to 15 nm into the Co_2FeSi from 0% to 34% when Fe and Co are ending. The V/Pt (FIB) interface shows a sharp interface with some mixing between C and V which probably results from the deposition of the Pt (with precursor containing C) by the ion beam. Also oxygen is present at the interface that results from contact with air after the sputter process and cooldown.

Between the linescan and the mapping is a difference in the amount of oxygen shown, in the linescan oxygen is present in the MgO substrate and the interface V/Pt ($9.8 \pm 6.2\%$) and $0.8 \pm 1.3\%$ are measured in the Co_2FeSi layer. In the mapping $\approx$ 60% oxygen is measured at the interface V/Pt but in this dataset no C has been measured which would change the relative percentage. In the Co_2FeSi layer $13.7 \pm 1.8\%$ oxygen are measured. The difference in both measuring methods is the beam rastering only across one line or a whole rectangle with neighbouring scan points being influenced by each other especially with contamination. Therefore the mapping suffers more from contamination which may contain oxygen and carbon but the latter is not being measured in the mapping.
The whole layer system is measured to a thickness of 162.3 ± 1.2 nm (map) with the 1st V layer measuring 52.5 ± 1.2 nm, the Co_2FeSi 58.6 ± 1.2 nm and the 2nd V layer 51.2 ± 1.2 nm respective for the linescan data 162.49 ± 0.82 nm for the whole layer system, 51.7 ± 0.82 nm for the 1st V layer, 60.73 ± 0.82 nm for the Co_2FeSi layer and 50.06 ± 0.82 nm for the 2nd V layer. Both measurements are consistent with each other within the error margins. The measured interface widths are shown in table 8.

Interface:	MgO/V	V/Co_2FeSi	Co_2FeSi/V	V/Pt (FIB)
Linescan	3.28 ± 0.82 nm	7.39 ± 0.82 nm	4.92 ± 0.82 nm	4.1 ± 0.82 nm
Mapping	3.7 ± 1.2 nm	7.3 ± 1.2 nm	4.9 ± 1.2 nm	4.9 ± 1.2 nm

Table 8: Measurement of the interface widths for both linescan and mapping. The results are consistent within the error margins.

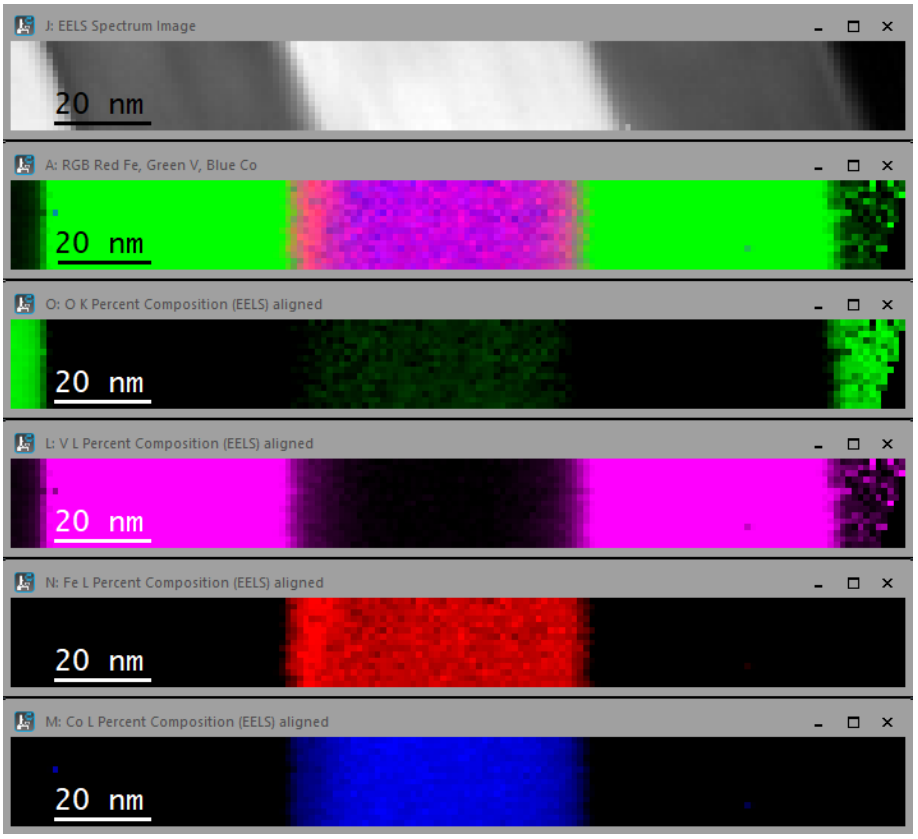

Figure 81: (Top to bottom) Spectrum image across the layer system, RGB overlay of the elemental maps for the elements Fe (red), V (green) and Co (blue) with the V/Co_2FeSi interface on the left showing an excess of Fe in the Co_2FeSi and drift corrected elemental maps for oxygen (green), vanadium (purple), iron (red) and cobalt (blue).

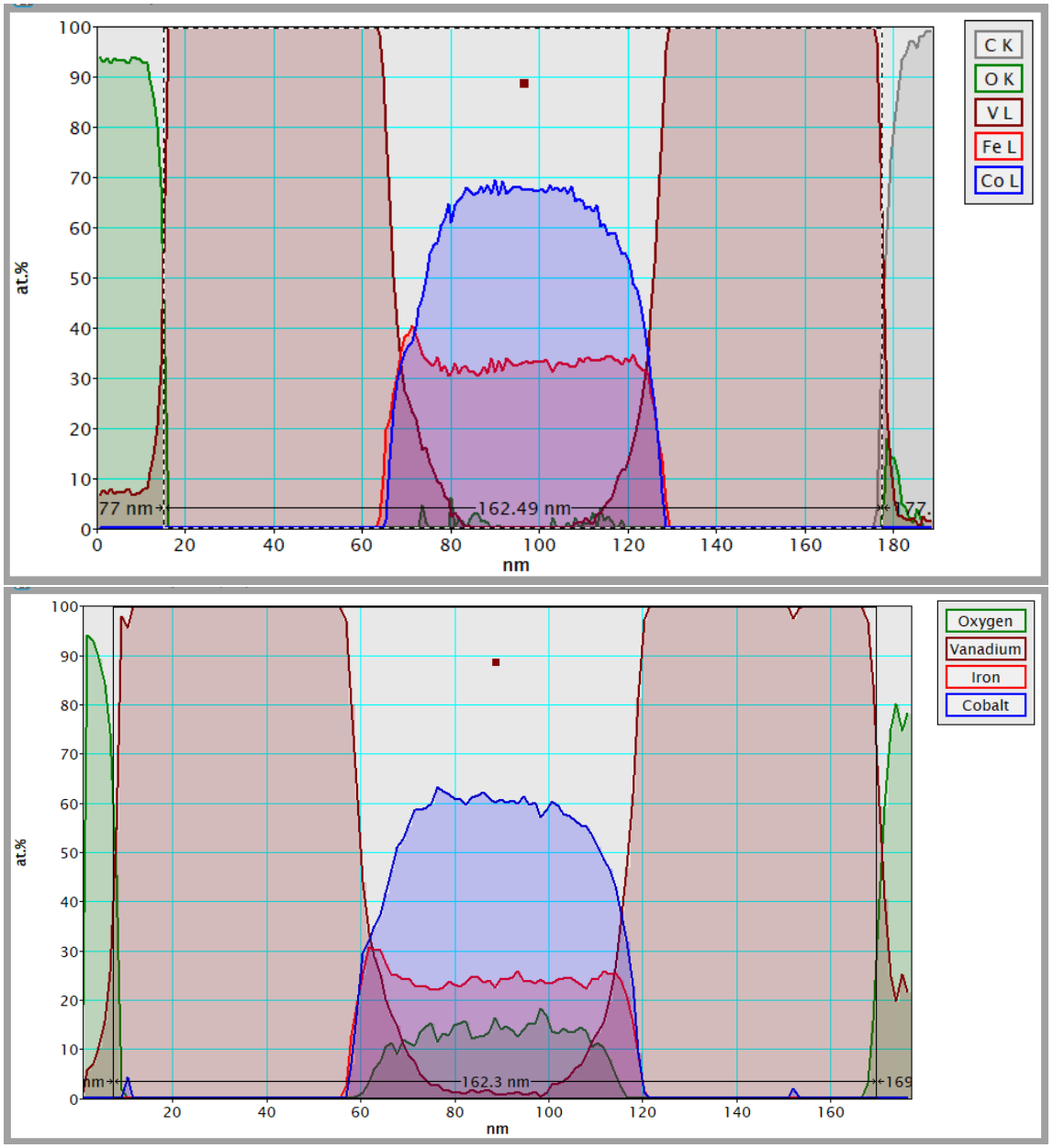

Figure 82: Elemental composition across the layer system measured by an EELS linescan (top) and EELS mapping (bottom). Qualitative and quantitative they give a similar result with the only notable difference being the different amount of oxygen in the Co_2FeSi layer.

More detailed chemical SI maps have been recorded of the three interfaces MgO/V, V/Co_2FeSi and Co_2FeSi/V. The areas chosen for the spectrum image are shown in fig.83 for all three interfaces and the results of the mappings are shown in fig.84. All maps have been drift corrected post acquisition and a line profile has been taken across the interface as indicated in the elemental maps. Depending on the elements involved in the interface and their EELS accessibility the elements that have been used for evaluation vary. For the MgO/V interface O and V have been investigated, also C as it shows contamination in the TEM. For the V/Co_2FeSi and Co_2FeSi/V interfaces Fe, Co and V have been investigated. The C map has been also evaluated but the result is very similar to the first result so the maps are not shown. Carbon contamination is negligible in this measurement.
The MgO/V interface results show a very sharp interface with a width of 2.8 ± 0.8 nm. According to the data a very small amount of vanadium is distributed evenly in the MgO which is measured to $1.9 \pm 0.3\%$. This is most likely a wrong result because in the spectrum image there is only the power law background and measurement noise (Appendix, fig.210). The C is measured to zero.
For the V/Co_2FeSi interface the width is measured to 13.8 ± 1.8 nm. Within the first 7.3 nm the V falls to $\approx 35\%$ and the Fe and Co rise to $\approx 30\%$ each. In the other half of the interfacial region Co is rising further to the plateau value of $79.4 \pm 2.3\%$ and Fe is falling slightly and reaches a plateau value of $15.9 \pm 2.2\%$. This does not match the relation of 2(Co):1(Fe) for Co_2FeSi and shows instead $\approx 5(Co) : 1(Fe)$, the excess of Co can lead to the formation of Co-rich alloys in the interface region. The appearance of up to 5.1% Co in the V layer far from the interface results from a few small pixels from the mapping where noise has been recognized as a Co signal. The V is falling slightly but does not reach zero in the area of measurement. A look at the spectrum image (Appendix, fig.211) shows the V reaches zero at 15.6 ± 1.8 nm from the interface center, but the V and O edges are very close (V: 513, 521 eV, O: 532 eV) and overlap. Some oxidation did occur to the specimen from air contact, the overall amount is negligible.
The width of the Co_2FeSi/V interface is measured to 7.9 ± 1.1 nm. This includes the descent of Co and Fe to $\approx$ zero and the rise of the V content to 100%. Before the interface the specimen consists of $75.2 \pm 1.8\%$ Co, $22.9 \pm 2.2\%$ Fe and a towards the interface increasing amount of V. The relation between Co and Fe is $\approx 3.3(Co) : 1(Fe)$. The small amount of V in the Co_2FeSi and of Co in the V is checked using the spectrum image (Appendix, fig.212), showing that V reaches zero 13.5 ± 1.1 nm from the interface center. The small Co contamination in the V results from local noise.
In conclusion the interfaces between Co_2FeSi and both V layers are not totally sharp, if the Co_2FeSi is sputtered on another material a small iron peak exists like in the Fe/Co_2FeSi/Fe specimen and the V tends to reach further into a material instead of forming sharp interfaces. The generation of the Co_2FeSi Heusler alloy is very likely only in the central part of the layer, towards the interfaces the composition varies and Co-rich alloys might have formed.

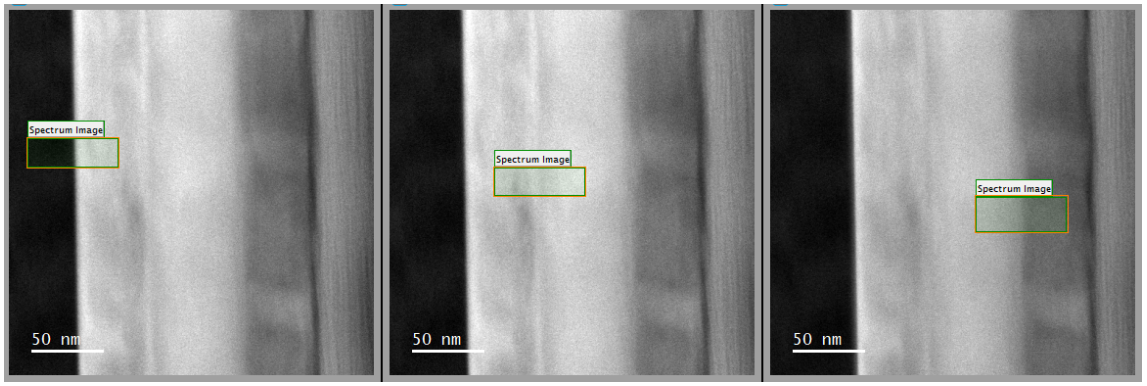

Figure 83: Survey STEM ADF images of the layer system with the area for the spectrum image on the interfaces shown by a green rectangle. Left: Interface MgO/V, center: Interface V/Co_2FeSi, right: Interface Co_2FeSi/V

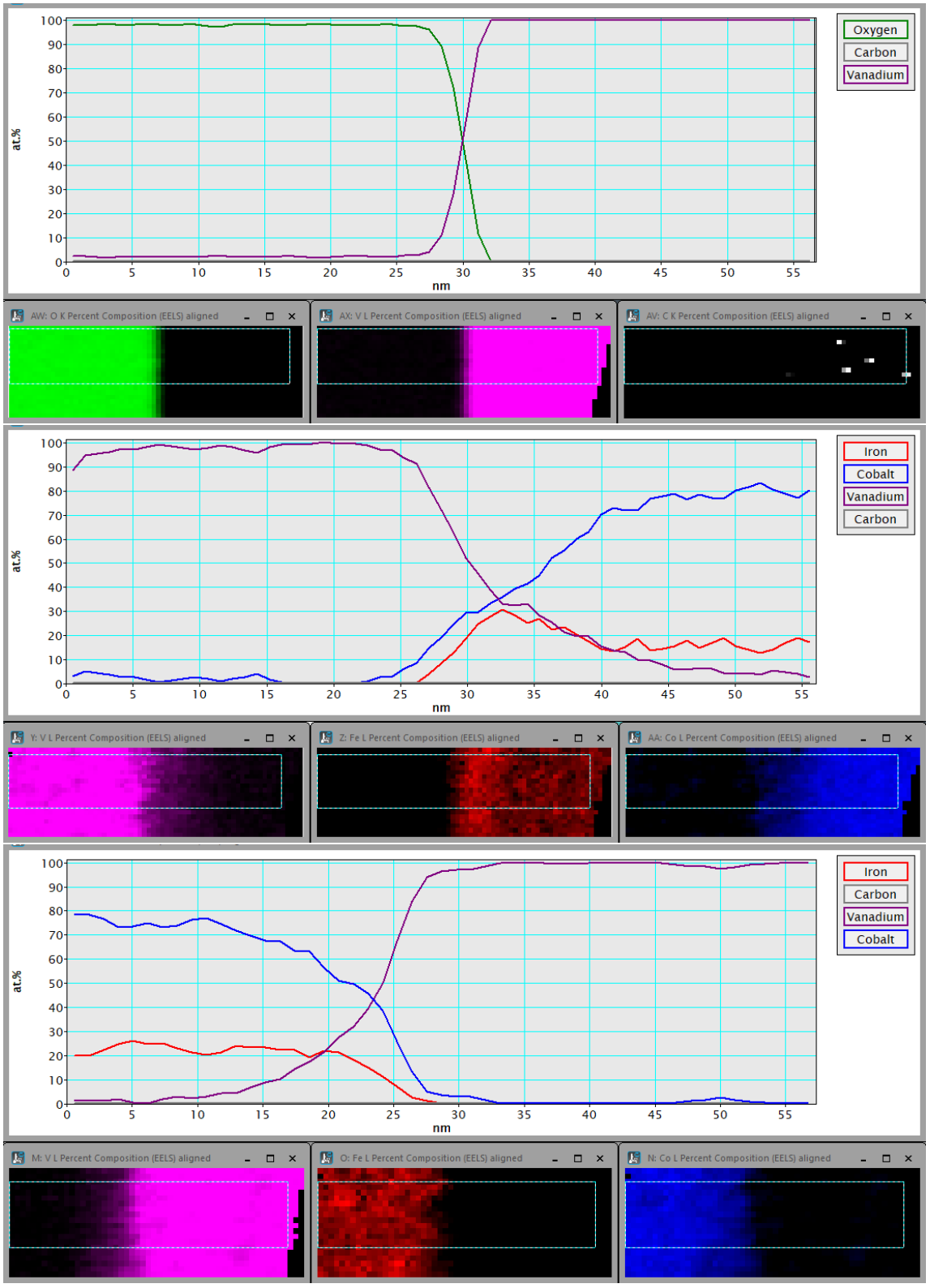

Figure 84: EELS results for the MgO/V (top), V/Co_2FeSi (center) and Co_2FeSi/V (bottom) interfaces along with the relevant elemental maps. The maps have been drift corrected post acquisition and the region rom where the line profile has been obtained it indicated by a rectangle.

Peak shift mappings help determining the quality of the layers and interfaces as different chemical bonding will lead to chemical shifts on the EELS elemental edges. Formation of a different alloy can be identified. Peak shift mappings have been created from the spectrum image for the vanadium, iron and cobalt peak by using the routine supplied with the "SI Tools" [103] with the method of fitting a Gaussian to the peak to determine the position. The datasets are noisy in the higher energy regions and other methods like taking the peak maximum as the peak position are very prone to errors. As the amount of an element diminishes in the interface regions the peak becomes harder to detect as a real peak and if the peak height is of the order of the noise it becomes impossible. To prevent such situations it is possible to define the "Relative Peak Intensity Threshold" as follows "This parameter is a measure of the height of the elemental edge above background divided the total intensity at the peak." [103] For evaluation of the datasets shown here it has been set to 0.15. The results of the peak shift mappings are drift corrected as the corresponding elemental maps and then a line profile is taken across the layer system to integrate over an area and reduce noise. Details of the data can be found in Appendix 6.4. Where the interface width can be measured it is shown in the following table 9:

Information about the quality of the interface region with respect to the central layer

Edge / Interface:	MgO/V	V/Co_2FeSi	Co_2FeSi/V)
V L3	3.71 ± 1.86 nm	9.18 ± 2.3 nm	4.5 ± 1.2 nm
V L2	smeared	4.59 ± 1.86 nm	6.7 ± 1.2 nm
Fe L3		noise	noise
Co L3		smeared	6.6 ± 2.4 nm
O K	2.79 ± 1.86 nm		

Table 9: Measurement of the interface widths from the peak shift mappings. Noise means no signal could be found in the data, smeared means the interface beginning/end could not be determined.

region is scarce in this data as the peak shifts are very noisy. It can be stated that the iron in the first ≈ 5 nm near the interface sees a chemical shift of $0.3 - 0.5$ eV. For cobalt no shifts can be determined. Vanadium shows more clear in the L3 edge a shift of $0.15 - 0.2$ eV in the $\approx 5 - 7$ nm wide interface region. Oxygen shows a change from $+0.05$ eV to -0.15 eV at the interface.

3.6.1 Micromagnetic simulations

As for the preceding sample micromagnetic simulations with Mumax [62] have been performed with the following settings: Mesh size $512 \times 512 \times 1$ cells with cell size of $5 \cdot 10^{-9} \times 5 \cdot 10^{-9} \times 10 \cdot 10^{-9}$ m. Three regions have been defined with the central region containing the active magnetic layer, each to be 50 nm (10 cells) wide in X-direction, 2560 nm (512 cells) in Y-direction and 10 nm (1 cell) thick.
For the material parameters the saturation magnetization Msat has been set to Co_2FeSi: Msat $= 881 \cdot 10^3$ A/m [88] [86] and the exchange stiffness to Aex $= 31.5 \cdot 10^{-12}$ J/m [104]. The simulation has been started from random magnetization with no external field applied and it is evolved to the minimum energy state by the `relax()` function. The output has been imported into Gatan GMS and the phase image has been calculated for DPC comparison. In fig.85 the magnetization is shown for the x, y and z direction.

Again the magnetization in y-direction shows what to expect in this layer system, an external field would change the magnetization to be homogeneous in the field direction which would be the y direction in the microscope. Without external field influence domain walls can appear. The signal strength of the magnetic signal in DPC measurements can be expected to be approximately half of the signal strength of iron, so the Co_2FeSi should be magnetically visible. No notable substructure can be seen from the simulation and the interfaces to the vanadium can be expected to be sharp with only stray fields extending into the vanadium.

Additional micromagnetic simulations using Micromagus [65] have been supplied by A. Hütten. The system has been divided in subsystems for reduced computing effort: 58 nm Co_2FeSi = 15 nm + 15 nm + 15 nm + 13 nm (layer thickness < demagnetization length). The hysteresis has been calculated from equilibrating the system in an external field of 0 T $\rightarrow$ 0.5 T $\rightarrow$ 0.5 T $\rightarrow$ -0.5 T $\rightarrow$ -0.5 T $\rightarrow$ 0 T. The material parameters are the saturation magnetization Msat=800 kA/m [86], the anisotropy constant $K1 = 8960$ erg/cm^3 [86], the exchange coupling $A = 31.5$ pJ/m$= 3.15 \cdot 10^{-6}$ erg/cm [91] and the damping parameter $\alpha = 0.04$ [91]. The exchange length is given by $l_{exch} = 187.5$ nm, the demagnetization length by $l_{dem} = 17.411$ nm and $L_{spm} = 69.485$ nm.
The results of the simulation are shown in fig.86. The hysteresis shows a much higher saturation magnetization than the AGM data, here it is the measured data that does not represent the value for the saturation magnetization that can be expected from literature [86]. Because of the small saturation magnetization of the data the remanence of 22.4 kA/m is also very small and differs from simulation value of 752 kA/m, the coercitivity measures 10.9 kA/m in the simulation and 3.6 kA/m in the measured data. The overall slope of both hystereses is comparable, the measured sample is not in agreement with the literature values. The Bloch wall thickness is simulated to $\delta_{BW} = 589.05$ nm in Co_2FeSi, this is much larger than the layer thickness of this sample. Therefore possibly apparing domain walls are expected to be of the Neel wall type. Since the AGM measurement differs so much from the expected magnetization only a small magnetic signal can be expected in the DPC measurements. The signal should be switchable by an external field but the caused beam deflection is possibly very weak.

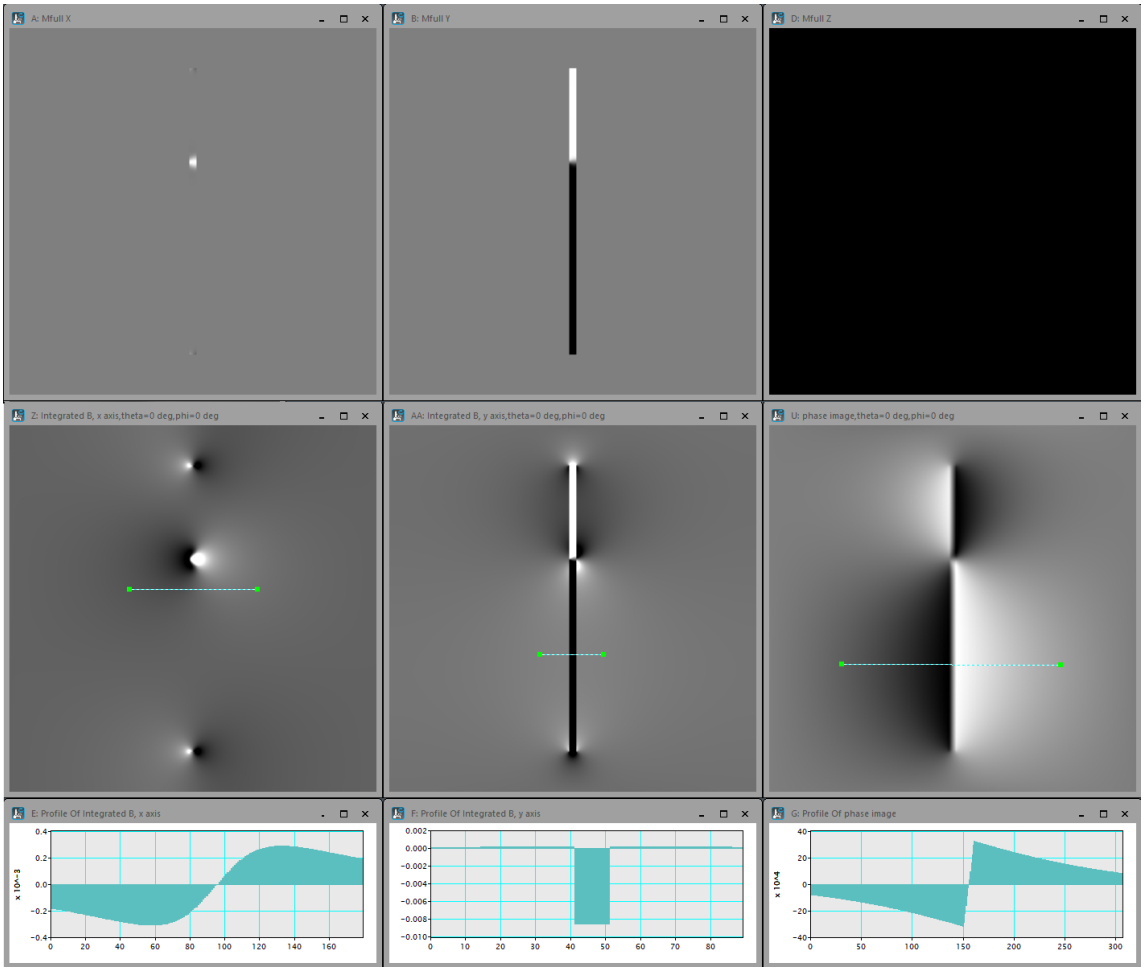

Figure 85: Top row: Simulated magnetization for the x, y and z direction started from random magnetization for the V/Co_2FeSi/V system. As V is nonmagnetic, only the central Heusler layer appears including a domain wall, in z-direction the simulated magnetization is $\mathcal{O}10^{-35} \approx 0$ //m. The central row shows the integrated magnetic induction along the x and y direction and the calculated phase image. In the bottom row lineprofiles give a first indication of the shape of the expected magnetic signals.

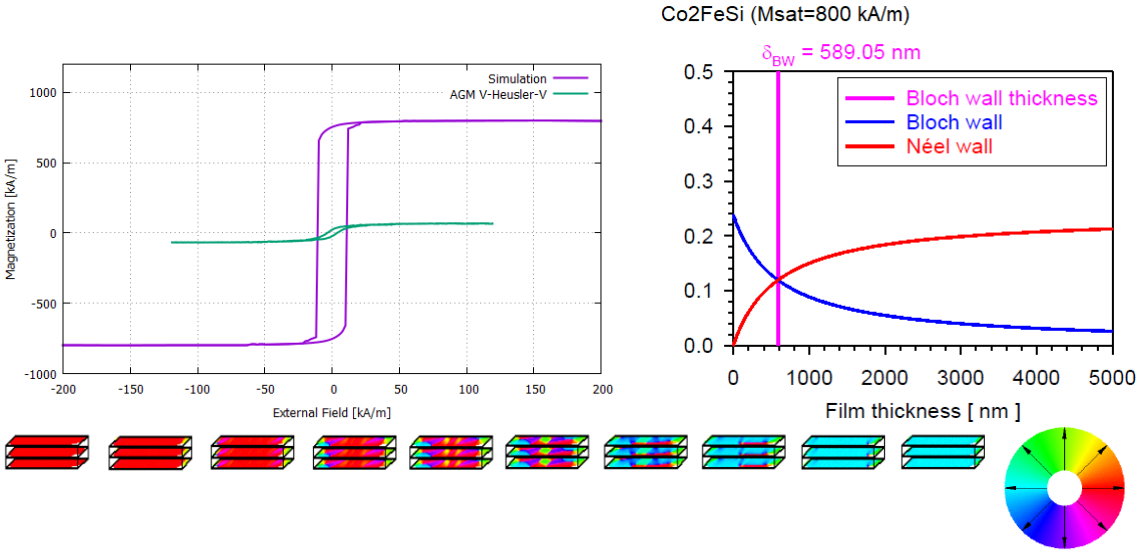

Figure 86: Left: Simulated hysteresis from Micromagus (purple) and AGM measured hysteresis (green) for the V/Co_2FeSi/V sample where Co_2FeSi is the only magnetically active layer. The shape of the hysteresis is reproduced in a qualitative way but with a notably much lower saturation magnetization in the measurement compared to the simulation data. The sharp bend of the measured hysteresis at $\approx$ 1000 kA/m is not well reproduced, the coercitivity is broader and the remanence higher in the simulated data. Right: Result for the Bloch wall thickness from the simulation. Bottom: Intermediate states from the simulation depicting the change of the magnetic state and appearance of domains and domain walls, colour wheel for directions on the right. Simulation courtesy to A. Hütten.

3.6.2 DPC measurements

On this specimen segmented and pixelated DPC measurements have been performed. Lorentz TEM microscopy has been omitted because only weak fields can be expected from the AGM measurements so methods of high sensitivity are needed. Three segmented DPC measurements have been obtained, at 0° and after +25° and −25° tilt with the objective lens set to 0500 / ≈ 0.1 T. The minimum contrast condition for the magnetic layer has been fulfilled for a rotation angle of 65° which is intended to separate the magnetic signal between the two perpendicular components. Normalization has been carried out on the MgO substrate. Line profiles have been taken across the layer system on both component images of the three datasets, to exclude defects and grain boundaries integration took place over 300 of 512 pixels. The signal has been divided by the thickness function eq. 3.3 to convert the deflections in magnetic induction. The results are shown in fig.87:

Both components show no reversable magnetic signal in one component, the spikes result

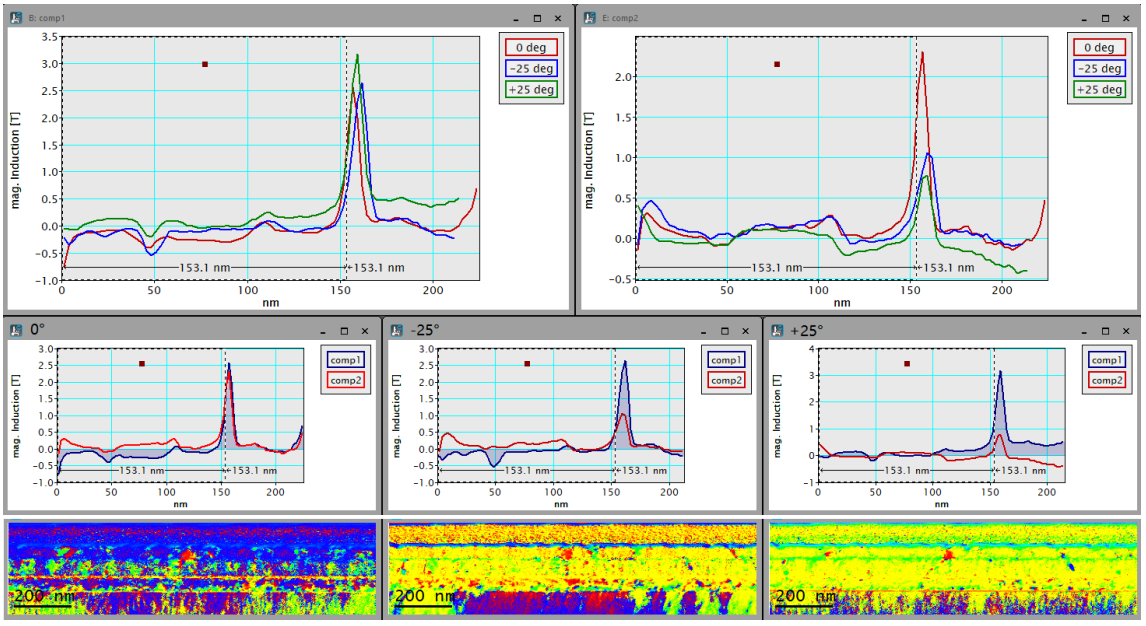

Figure 87: Results of the segmented DPC measurements for the V/Co_2FeSi/V specimen: Top left overlay of the lineprofiles across the component 1 image for all three datasets, top right for the component 2 image. No definite magnetic part of the signal that reacts to an external field could be found. Bottom: both components for each dataset and the corresponding colour image below.

from the change in the mean inner potential at the interfaces. The used unit of mag. induction [T] can therefore not be justified but is displayed to maintain consistence with the measurements on the other specimen. The colour images show the same colour only interrupted by noise or grain boundary signals in both the Co_2FeSi and the vanadium layers. The colour images are not processed for specimen thickness influence so the resulting colour is mainly a gradient in thickness. In conclusion no magnetic information can be gained from the segmented DPC data of this specimen.

The mean inner potential is modelled to explain the spikes in the DPC signal: The value for MgO is 13.01 ± 0.08 V [94] [95], Co_2FeSi is modelled again as for the Fe/Co_2FeSi/Fe specimen with a resulting MIP of ≈ 22.6 V, the value for V is 21.6 V (theoretical value $V_0(7)$ [47]). For the FIB-Pt the value of pure Pt can be assumed, 25 V [98], but as FIB-Pt contains a certain amount of C from the precursor a mix of 75%Pt 25%C with the MIP of C used being 14.94 V(theoretical value $V_0(5)$ [47]), which gives for the FIB-Pt $3/4 \cdot V_0(\mathrm{Pt}) + 1/4 \cdot V_0(\mathrm{C}) = 3/4 \cdot 25\ \mathrm{V} + 1/4 \cdot 14.94\ \mathrm{V} = 22.485 \approx 22.5$ V. A model profile is made of these MIPs according to the layer system dimensions, with and without a thin layer of a low-MIP material in the range of MgO or C ($\approx$ 14V) at the interface between V and FIB-Pt. This is intended to model the spike that can result from a large MIP change as well as edge effects. The derivative of the models shows the change of the MIP and the contrasts that result from the change. Fig.88 shows both model variants and their derivatives.

The calculated value of 21.6 V ($V_0(7)$ [47]) has been chosen instead of the $V_0(5)$ value

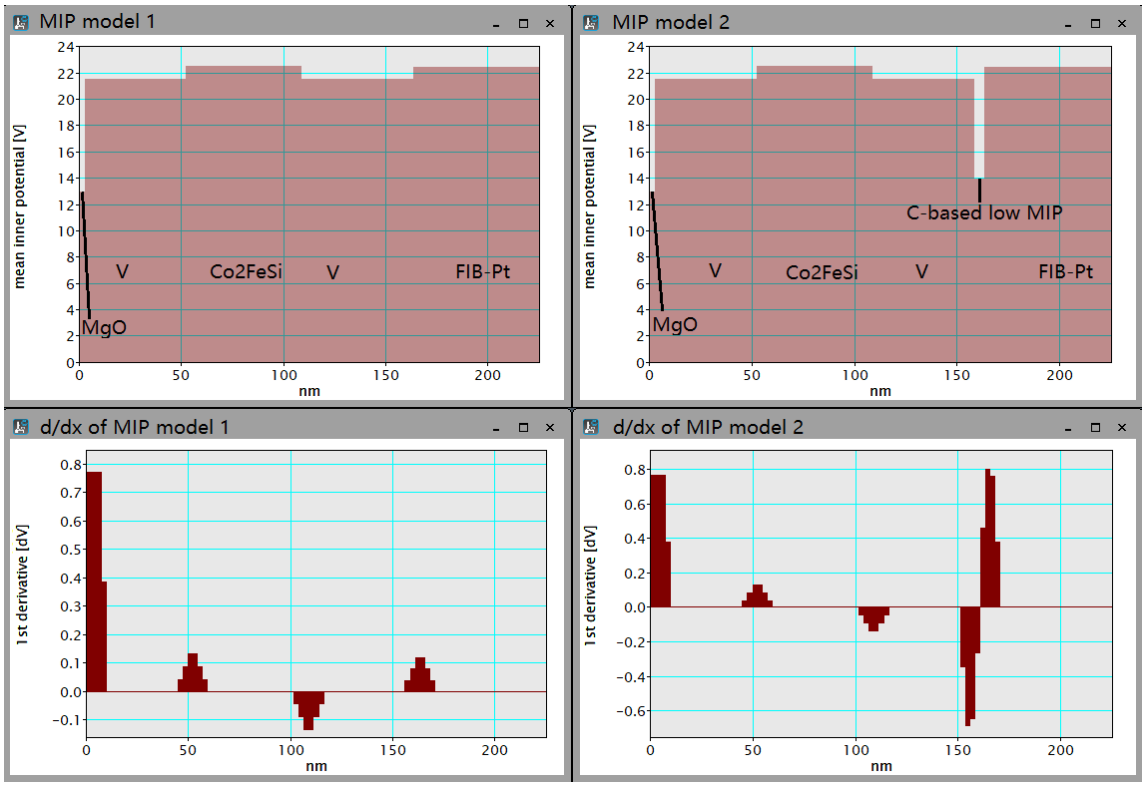

Figure 88: Models for the mean inner potential: without (left) and with added thin layer of low-MIP material (right). Bottom: derivatives of the MIP model.

because it is lower than the estimated MIP for Co_2FeSi, so the derivative (and peak) direction in the model matches the observation from the segmented DPC measurements on the MgO/V and the V/Co_2FeSi interface in fig.87. Most of the peaks can be explained qualitatively by the MIP model, on the V/FIB-Pt interface the former surface of the V

including surface oxidation most probably led to a more complicated situation than this model can explain. Also the values of the MIP are not always obtained from experiments and can be subject of discussion.

Pixelated DPC datasets have been obtained twice of both tilting directions. A detailed view of the datasets can be found in Appendix 6.5. They have been processed using the phase correlation processing instead of center of mass processing to follow the circle of the actual central diffraction spot. Drift correction has been applied using the RANSAC algorithm [60]. A circle has been found in nearly all pixels, reducing the noise pixels to only a few areas. Normalization has been carried out on the MgO substrate. The datasets have been acquired after the following tilts at 0° with an external magnetic field of ≈ 0.1 T:
101: +25°
102: -25°
103: -25°
104: +25°
The resulting X and Y components have been rotated to achieve minimum contrast in the Y component, this is intended to have the magnetic signal in the X component. The rotation angles to achieve this condition are 63° (101), 66° (102), 63° (103) and 61° (104) which are in good agreement to each other. Line profiles have been obtained with an integration width of 100 pixels (Appendix fig.213), starting on the MgO/V interface so the thickness function eq. 3.3 can be used for evaluation. The results for both components are shown in fig.89. The signal is dominated by nonmagnetic sources of beam deflection like the MIP, but as magnetic signal is reversable with the external field direction, possible magnetic signal can be seen in the Heusler part of the X component. Its strength can only be measured in the central part of the layer because MIP changes on the interfaces to the vanadium cause stronger beam deflections than the magnetism.

The results are the displayed in table 10. With the assumption that the magnetic layer

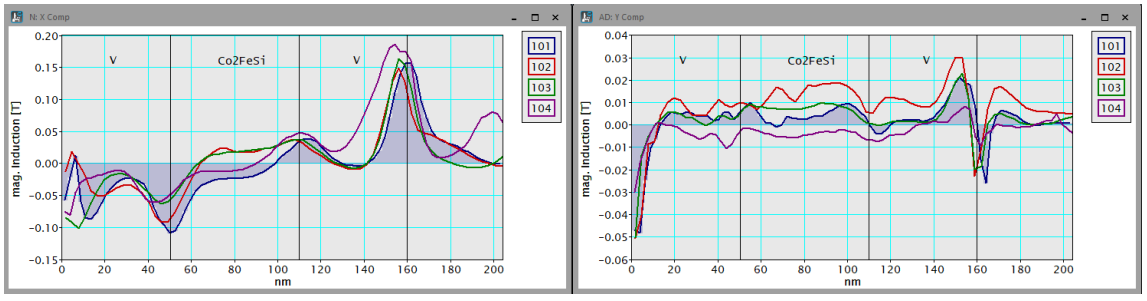

Figure 89: Results of the four datasets: X component containing possibly magnetic signal (left) and Y component obtained from the minimum contrast component (right).

is saturated by the external field in both directions, half of the difference signal between both directions gives the magnetic induction of the layer which results as the mean of the four possible difference values to 0.018 ± 0.004 T. This is a very weak magnetic signal but it could be reversed by the external field. The expected signal would be of about half the

Dataset	101	102	103	104
mag. Induction [T]	-0.023 ± 0.001 T	0.017 ± 0.001 T	0.020 ± 0.001 T	-0.011 ± 0.003 T
Difference results:	0.02 ± 0.001 T	0.022 ± 0.001 T	0.014 ± 0.003 T	0.016 ± 0.003 T

Table 10: Measured magnetic induction in the center of the Co_2FeSi layer for each of the datasets. For each magnetization direction there are two results, with the assumption the layer has been fully saturated half the difference gives the magnetic induction of the Co_2FeSi layer. The differences are shown in the 3rd row. From this data the magnetic induction is measured to 0.018 ± 0.004 T.

strength of iron, but the AGM result already shows a much smaller magnetic signal than expected.
Magnetic influence on the neighbouring layers could not be observed, V is a nonmagnetic material but there is the possibility of magnetic proximity effects introduced by an adjacent strong magnetic material. The magnetic results are overlaid by effects MIP-change that cause higher beam deflection than the magnetism, therefore information about the magnetism at the interfaces to the neighbouring layer is hard to obtain. From the data in fig.89 the magnetic part of the signal starts where the MIP induced deflection ends inside the Co_2FeSi layer, probable assumptions can be that the layer is magnetic until the interface or the magnetism drops down towards the interface.

3.6.3 Altering of the specimen

Over time an altering of the specimen of the V/Co_2FeSi/V system that lead to partial destruction of the layer system has been observed, this shall be described and investigated in this chapter. The first FIB lamella has been cut in Bielefeld and sent to Glasgow via mail. Before sending it it has been checked in the JEOL 2200FS TEM in Bielefeld if it is thin enough for further investigation and for obvious flaws in the layer system. All three layers were observable in the TEM image, but weeks later it has been investigated in Glasgow and the layer system could not be recognized properly anymore, especially the vanadium was everywhere an EELS mapping showed. A second lamella has been cut in Bielefeld, checked also to see if the sample itself changed over time with the result that the sample is still as intended and the lamella is ok. This one could be investigated properly in Glasgow in DPC and HAADF and has been carried back to Germany for the chemical measurements, which took place days after arrival with the results shown in fig.82. Further DPC measurements have been rescheduled because of the Covid pandemic and took place months later, when this lamella also had changed. Another EELS and additional HRTEM measurements have been conducted to show the difference and investigate what happened in the specimen. The EELS results after the altering are shown in fig.90 where linescans have been conducted across the layer system in two places of the lamella. The result is that the vanadium has extended in both layers, the layer adjacent to the MgO has been widened by 10 ± 2 nm, the other V layer more than doubled with a new width of 122 ± 10 nm (fig.91). In the center of this layer a notable amount of O is visible, approaching 40% of the elemental composition. This suggests that oxidation of the V took place and led to the volume increase. Additional O is not visible in the other V layer. The linescan near the end of the lamella crosses a round structure which is contamination from an earlier

investigation and consists mainly of carbon. Apart from this the results are comparable.

To access the structure of the layers, HRTEM images have been recorded (fig.94). Using FFT allows to measure structural parameters in a FFT diffraction image. The FIB-Pt is amorphous with small crystallites, the V layer below is mostly amorphous but shows one cubic crystal lattice, the Co_2FeSi layer is polycrystalline, the other V layer a mixture of amorphous and containing small crystallites. The transition to the MgO seems continuous in the TEM images although the EELS result shows there still is a clear separation. The crystal lattice of the MgO seems to have not changed much, the rings indicating the material being partly amorphous have been added during the change of the specimen, also the additional crystallites.
The V layer that shows the cubic lattice is analysed further to measure the lattice parameters. The distance between the center of the diffraction pattern and the mostly vertical diffraction spots is measured to 4.933 1/nm, the horizontal to 4.536 1/nm in the FFT image. The inverse transformation gives for the first parameter 0.2027 nm and for the second 0.2205 nm. FFT filtering by applying a mask and inverse fourier transforming it shows a lattice overlaid by a cloudy structure that presumably results from the amorphous part that has been covered by the mask (fig.92).

The possible compounds can consist of V, O, C and maybe Pt according to the chemical data and known composition. A search for compounds with a cubic crystal system and lattice parameter near the measured one results in vanadium oxides of which some are cubic and allow for the possibility of a partially intact V lattice which has the lattice parameter 2.592 Å [105]. The other possibility is the incomplete creation of vanadium oxide, a dataset of $O_{0.532}V$ with the lattice parameters $a = 2.94$ Å, $b = 2.94$ Å and $c = 3.5$ Å has been taken into account [106]. Analysis using the program suite JEMS [77] using the crystal parameters found a reasonably good match for the incomplete vanadium oxide with the strongest four excited reflexes being (002), $(00\bar{2})$, $(1\bar{1}0)$ and $(\bar{1}10)$ in accordance with the FFT diffraction pattern as shown in fig.93. It can be concluded that the altering of the specimen occurred due to incomplete oxidation of the vanadium with an oxygen part of up to 40% according to the EELS measurements: $O_{0.4}V$.
Another TEM investigation weeks later shows more advanced altering of this specimen, the V layers are not recognizable anymore. Therefore specimen like this one that are prone to alterations need to be investigated on a short timescale.

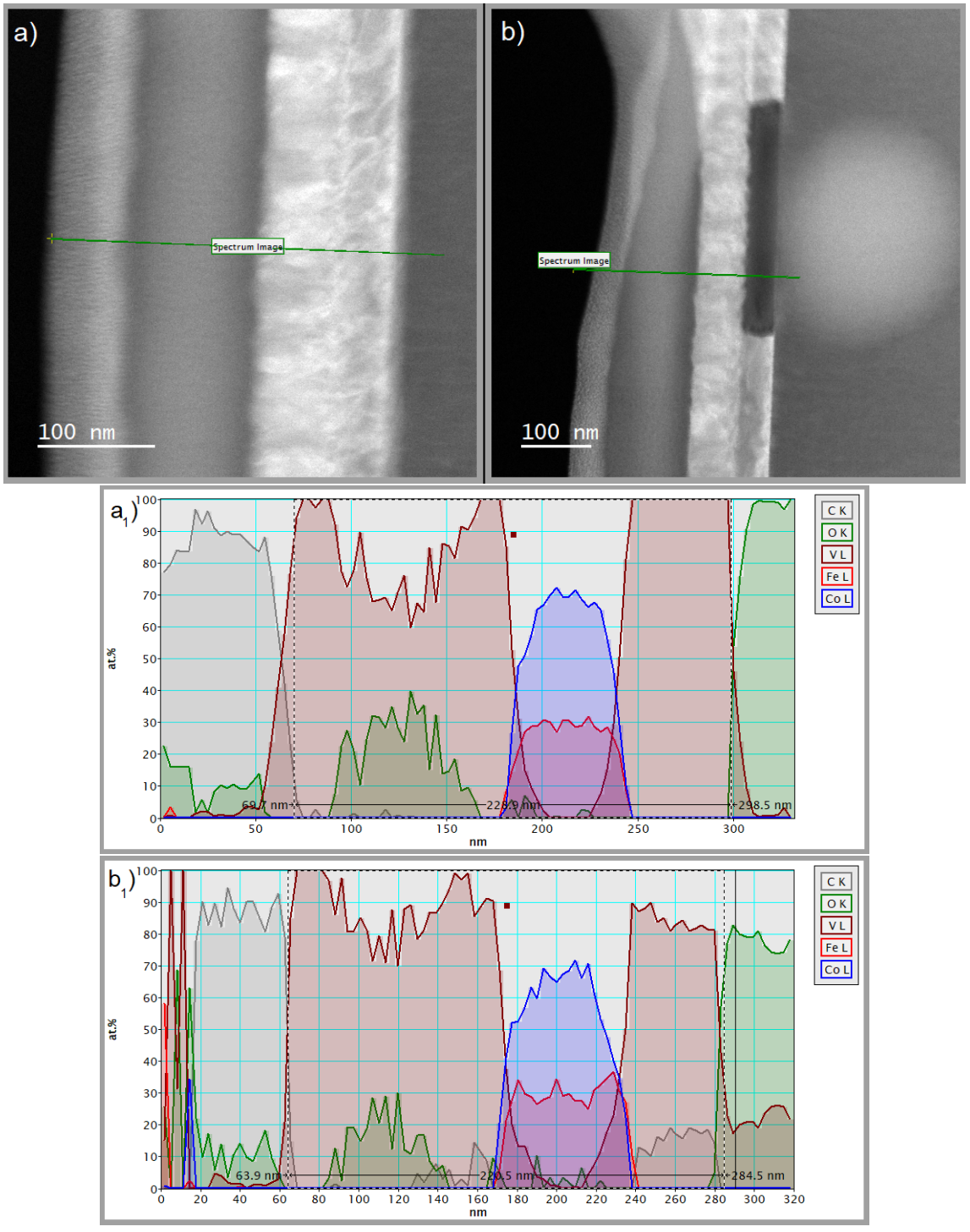

Figure 90: EELS linescans across the 2nd altered lamella, a) in the center of the lamella and b) on the thinnest end of the lamella. Below a_1) and b_1) show the corresponding elemental quantification, MgO substrate on the right.

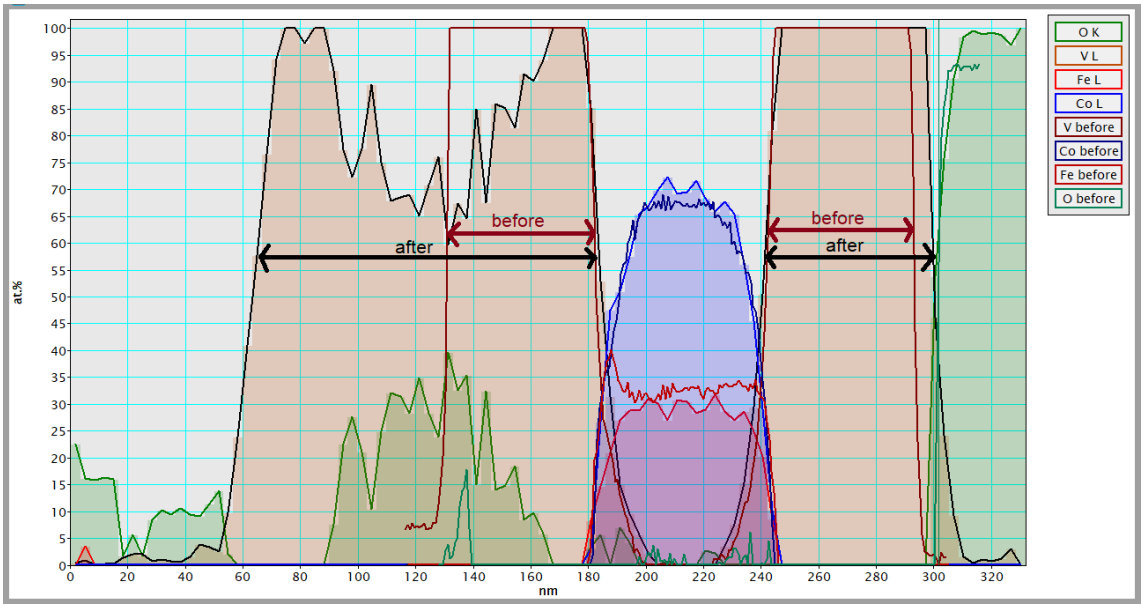

Figure 91: Overlay of EELS measurement from when the layer system was still intact (before) and after the change four months later. The Heusler layer (Co, Fe) does not show a notable difference but the V layers both broadened, one more than doubled its extent. Additional oxidation has occurred shown by the O data (green).

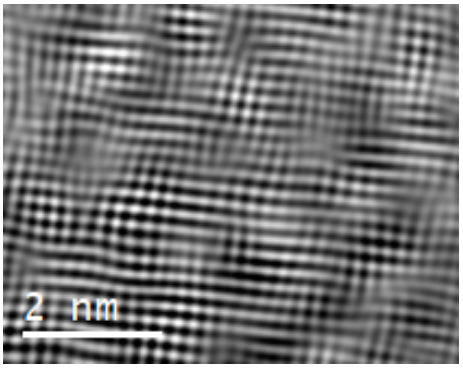

Figure 92: FFT filtered crystal structure from the V layer adjacent to the FIB-Pt.

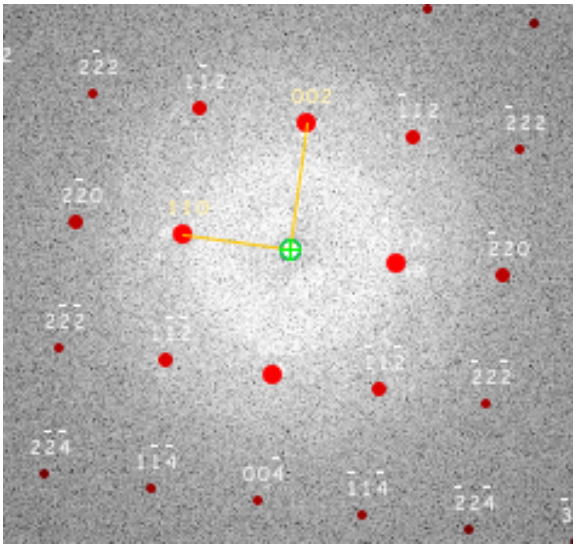

Figure 93: Indexing of reflexes of $O_{0.532}V$ using JEMS [77] overlaid with the FFT diffraction pattern showing a cubic lattice. The strongest four reflexes are the only ones appearing in the FFT.

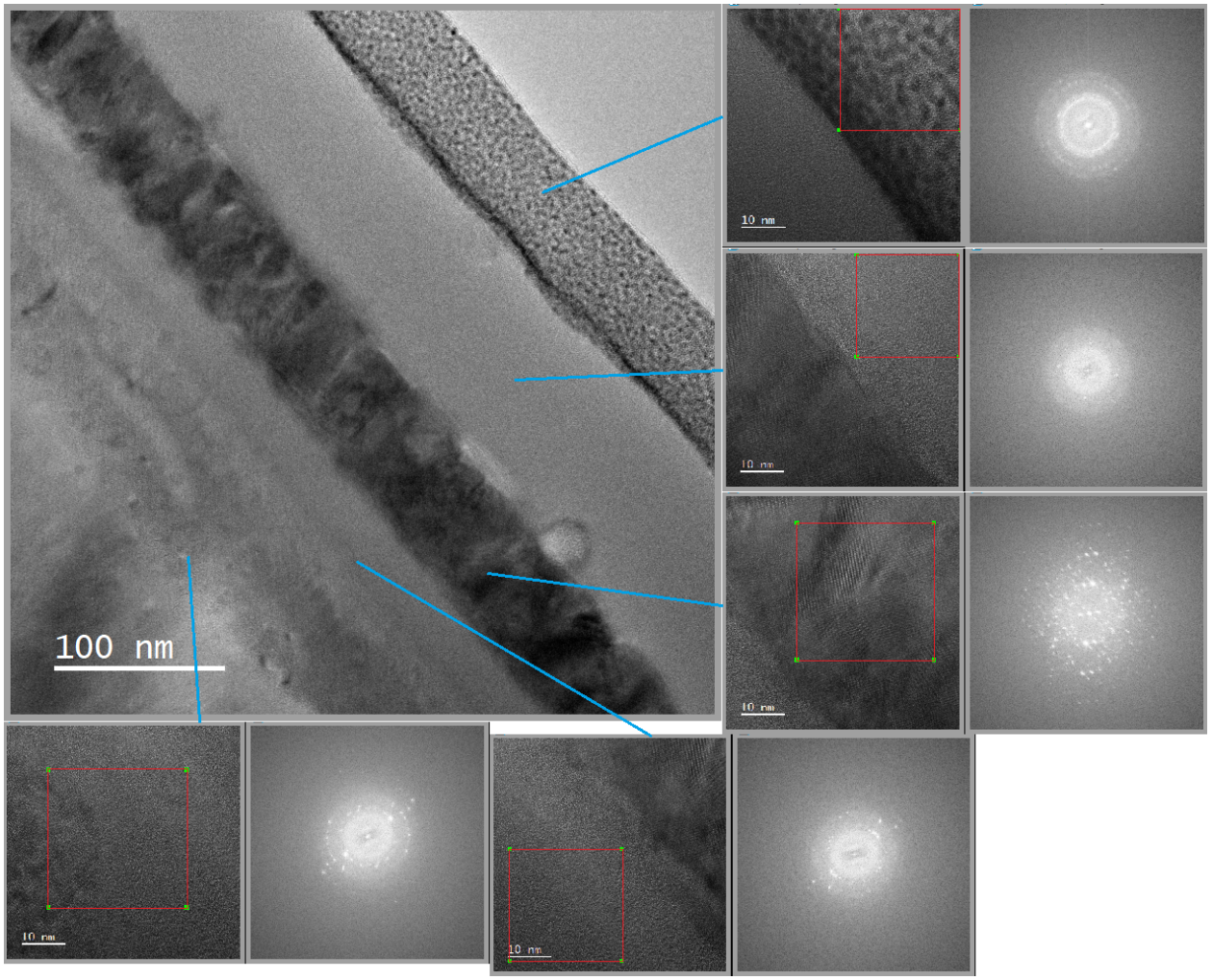

Figure 94: Overview image with an HRTEM image for every region and corresponding FFT diffraction images.

3.6.4 Conclusions for the V/Co_2FeSi/V system

The V/Co_2FeSi/V system did not show the expected magnetic behaviour, the hysteresis showed a very low saturation magnetization of 57.5 kA/m compared to simulations but also to literature values for Co_2FeSi which lie at about 20 times higher values (800 kA/m to 1250 kA/m) [86] [102]. A possible source for this behaviour is the intrusion of vanadium through the whole layer, from the interfaces a notable vanadium amount reaches in up to a quarter of the Co_2FeSi layer, in the central two quarters up to 5.1% vanadium is measured. Also the chemical proportions for Co_2FeSi are not met entirely so cobalt-rich alloys can form in those regions. All these alloys show different magnetic properties.
Over time the layer system is not stable, the vanadium is prone to oxidation and the layer extent and the composition change. These conclusions are valid for the system as it has been measured before the alterations took place.
In agreement with the low magnetization the measurement of the magnetic induction in the TEM has been challenging. The deflection is small and other effects like the MIP change exceed it. Segmented DPC did not show any signal that could be proven to be magnetic, but the more refined method of DPC using the pixelated detector Medipix3 with phase correlation processing afterwards is able to extract very weak magnetic signal. This demonstrates the strength of this method as by following the diffraction disc and the exclusion of descan artifacts a very fine tracking of its deflection is possible. The measured value for the magnetic induction is 0.018 ± 0.004 T which corresponds to a magnetization of 14 ± 3 kA/m which is of the same order as the measured remanence of 22.4 kA/m. Since the given measurement uncertainty is only statistical and systematic uncertainties could not be followed in total through the data acquisition and evaluation process agreement of these values can be expected. It has already proven pixelated detectors being superior over segmented systems when it comes to fine details/small variations in magnetism and small magnetic fields.
So even though this sample does not have the desired properties the measurements are in agreement and a notably small magnetic induction proved to be measurable with advanced DPC methods.

3.7 Towards characterization of multilayer systems: TMR Stack

The effect of tunneling magneto resistance (TMR) uses the spin of the electrons as another degree of freedom enabling applications of spintronics as well as electronics. A main device is the magnetic tunnel junction (MTJ) which are built of two ferromagnetic layers separated by a thin insulating tunneling barrier [107]. For applications the bottom ferromagnetic layer is pinned by an additional anti-ferromagnetic pinning layer [108]. The resistance of this MTJ is dependent on the orientation of the magnetization of the ferromagnetic layers: the tunneling magneto resistance is defined as TMR $= \frac{R_{ap}-R_p}{R_p}$ with $R_{ap} = R$ (antiparallel) and $R_p = R$ (parallel), usually $R_{ap} > R_p$. TMR is a transport property, high TMR is useful for any process in which fast but reliably distinguishing between two states is needed. To obtain huge TMR half-metallic ferromagnets have been found to play a major role because of their high spin polarization [109], half-metallic means the valence band is partially filled for electrons of one spin orientation with a gap for the other orientation, leading to be a conductor for only the first spin orientation [110]. "For small voltages the resistance is connected to the spin dependent density of states (DOS) at the Fermi level of the ferromagnets. Hence, the TMR value is also given by TMR $= \frac{2P_1P_2}{1-P_1P_2}$ [111] with the spin polarization $P_{1,2}$." [112]
Full Heusler alloys based on Co are promising materials as they are predicted to have high spin polarization up to 100% and a high Curie temperature making them usable over a broader temperature range [88]. High TMR effects and proven half-metallicity have been achieved experimentally for Co_2MnSi at low temperatures as well as at room temperature [113] [114] [115].
The material of the tunneling barrier also has a huge influence on the TMR properties of the system. Huge TMR effects have been obtained using (amorphous) Al-O [113] but also crystalline and amorphous MgO has been investigated, giving especially high TMR ratio at room temperature [116] [117]. Electronic and spincaloritronic properties of Co_2MnSi are predicted to depend on which atoms of the Co_2MnSi sit on the interface to the MgO [118], which will be investigated in chapter 3.7.1.
A MTJ made of Co_2MnSi and MgO has been created with the magnetic layers being of different thickness so they switch at different magnetic fields and thus both parallel and antiparallel state can be achieved.

This system has been prepared twice: one sample with increased layer thickness that is an advantage for tilting in EMCD conditions and one sample which is a fully functioning TMR stack with its thin layers and barrier. The thin TMR stack has been investigated with DPC in Glasgow (segmented and pixelated) and chemically in Paderborn, the thick version chemically and with EMCD and DPC in Paderborn, performing DPC measurements with the segmented detector system of JEOL.

The MTJ has been sputtered on MgO substrate with these layer thicknesses: Substrate MgO / Co_2MnSi (10 nm) / MgO (1.8 nm) / Co_2MnSi (15 nm) / MgO (3 nm, protection of surface). The thick version has been planned with substrate MgO / Co_2MnSi (40 nm) / MgO (20 nm) / Co_2MnSi (40 nm) / MgO (3 nm, protection). The Co-sputter deposition conditions are the equal to those for the Fe/Co_2FeSi and V/Co_2FeSi samples: Pre-cleaning in ultrasonic bath (10 min acetone, 10 min ethanol, 5 min DI Water), heating to 700° C for 30 min and cool down phase to 450° C of 30 min in the sputter chamber. Sputter

process at 450° C at a base pressure of $< 5 \cdot 10^{-9}$ mbar, targets used for Co, Mn, Si, and Mgo. Waiting time after each layer 10 min, Argon flow 10 sccm and substrate rotation 10 rpm.
Both samples have been measured in the AGM, the results are shown in fig.95.

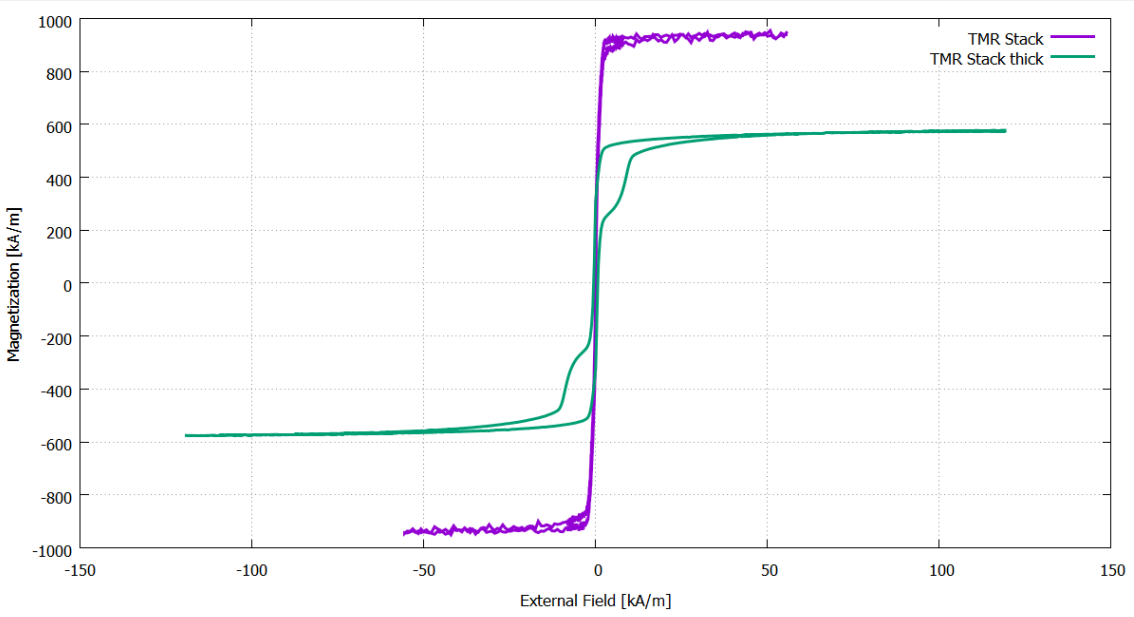

Figure 95: The AGM measurement of the two TMR stack samples, the TMR stack (purple) and the thick version of it (green).

The magnetically active volume has been determined from the layer thicknesses and sample areas: For the TMR stack the chemical layer thickness has been measured to 25.16 nm and the sample area measures 12.6 mm^2, resulting in a volume of $3.17 \cdot 10^{-7} cm^3$. For the thick sample the layer thickness is 80.8 nm and the sample area and 9.2 mm^2, so the volume calculates to $7.4336 \cdot 10^{-7}$ cm^3.
The layer thickness is the only difference between the two samples and it has a huge influence on the magnetic behaviour: The TMR stack switches very fast with a saturation magnetization of 936 kA/m, a very narrow coercitivity of 0.15 kA/m and a remanence of 229 kA/m. The theoretical magnetization at 0 K lies with 1018 kA/m [88] close to the measured value as the AGM measurements have been performed at room temperature. Another measurement gives 881 kA/m for the saturation magnetization [88], this lies below the AGM measurement here. The thick version of a TMR stack has a lower saturation magnetization of 572 kA/m more in agreement with [88], the coercitivity is more than four times as wide with a value of 0.69 kA/m and the remanence higher with 306 kA/m.
The shape of the hysteresis curve alters notably with the central part still narrow but at approximately half the saturation magnetization in both directions a bulge forms, driving the external field up in each direction leads to this behaviour which is an effect of the interaction between the external field and the in opposite direction magnetized thick layers.

The TEM cross section lamellas have been cut using a FEI Helios Dual Beam FIB including the second ion beam milling after thinning at 5 kV by Björn Büker. The main chemical analysis and DPC measurements will be carried out on the actual TMR stack, the EMCD measurements on both lamella with a check if the chemical composition and crystallinity is ok on the lamella from the thicker sample as well. The total thickness of the layer system measured on a TEM image is starting on substrate: 10.5 ± 0.4 nm (Co_2MnSi layer 1), 1.7 ± 0.4 nm (MgO barrier), 15.1 ± 0.4 nm (Co_2MnSi layer 2) and 3.2 ± 0.4 nm MgO (Protection layer). The thickness measured over the whole layer system is 29.8 ± 0.8 nm. The thickness of the layers is varying up to 0.5 nm for each layer. HRTEM images show an epitaxial growth and high crystallinity of the Co_2MnSi layers.

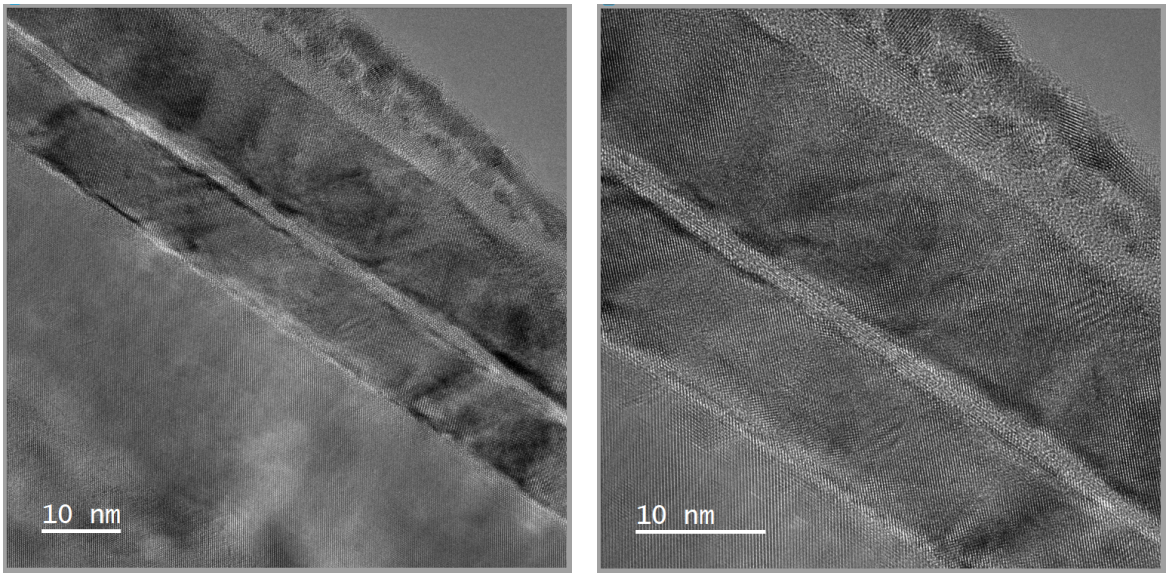

Figure 96: The MgO substrate/Co_2MnSi/MgO/Co_2MnSi/MgO/FIB Pt layer system, substrate on the bottom left of the image. These images have been recorded back in Paderborn after further thinning of the lamella. Due to the narrowness of the total layer system the overview image (left) has been recorded in HRTEM mode already, at higher magnification another HRTEM image has been recorded (right).

Thickness and chemical composition have been measured on the ARM200F in Paderborn (Gatan Quantum GIF post column filter). During the first measurement no sufficient EELS signal in the high loss region could be obtained and the lamella turned out to be too thick for that, so it has been thinned a second time by FIB milling and measured again. Both times the thinning has not been carried out uniformly so a gradient emerges over the length of the lamella, which is also indicated by the amount of FIB Pt present. In thinner parts of the lamella it is milled away and only the protection of MgO remains. In general a SI zero loss map has been acquired in places with a substantial amount of FIB Pt left and none left. Acquisition parameters are before the second thinning: (1) 0.001sec exposure, $\beta = 8.33$ mrad, 5 mm entrance aperture, 2.5M magnification, camera length 20 cm; (2) 0.0002 sec exposure, $\beta = 27.78$ mrad, 5 mm entrance aperture, 3M magnification, camera length 6 cm. After second thinning: (3) 0.001 sec exposure, $\beta = 8.33$ mrad, 5 mm

entrance aperture, 2.5M magnification, camera length 20 cm; (4) 0.0001 sec exposure, $\beta =$ 27.78 mrad, 5 mm entrance aperture, 1.5M magnification, camera length 6 cm.
For each of the four measurements a thickness function has been fitted, before the second thinning a linear function could be applied, after the second thinning the thickness profile of the lamella changed and a quadratic polynomial has been fitted. The detailed results in thickness estimation are shown in appendix 6.6. As a reference starting point the MgO substrate/Co_2MnSi has been chosen. A line profile has been obtained across the layer system in the thickness map, integrating over a wider area to avoid local effects. Area with visible contamination has been excluded. The whole dataset has been multiplied with the estimated mean free path value for Co_2MnSi and only the two Co_2MnSi layers have been taken into account for the fit. Before a check has been carried out if the thickness can be approximated with one function: the dataset has been multiplied by the mean free path value for both MgO and Co_2MnSi and the results are overlaid. The results for each material in the respective layer combined should be able to be fitted by a curve or linear function. The mean free path values are:
MgO: 116.4 nm ($\beta = 27.78°$)
Co_2MnSi: 90.18 nm ($\beta = 27.78°$)
MgO: 143.1 nm ($\beta = 8.333°$)
Co_2MnSi: 112.1 nm ($\beta = 8.333°$)
These values are calculated using the mean free path estimator of D. Mitchell [83] and the Malis [32] method. The different β angles arise of a changed camera length in STEM imaging. Before the second thinning the thickness profile could be fitted by a linear function, after the second thinning a quadratic function needed to be used. The MgO protection layer does protect the TMR stack also from the ion milling, if it is milled away, the layers are widely damaged, this results in the different thickness profile. The results are the following:

before 2nd thinning, thick part (TMR1):	$f(x) = -1.24887 \cdot x + 120.357$
before 2nd thinning, thin part (TMR2):	$f(x) = -1.0729 \cdot x + 56.6188$
after 2nd thinning, thick part (TMR3):	$f(x) = -0.0137211 \cdot x^2 + 0.0102797 \cdot x + 53.0034$
after 2nd thinning, thin part (TMR4):	$f(x) = -0.0653795 \cdot x^2 + 1.12328 \cdot x + 38.5144$

Table 11: Results for the fitted functions approximating the thickness of the TMR layer system with the substrate MgO/Co_2MnSi interface as starting point. Before the second thinning a linear function was sufficient, after a quadratic function is necessary to approximate the thickness. Distance on the x-axis has been measured in nm. The fit quality measures are $\chi^2 = 21.9$ (TMR1), $\chi^2 = 3.5$ (TMR2), $\chi^2 = 6.8$ (TMR3) and $\chi^2 = 7.4$ (TMR4).

The chemical composition has been measured with combined EELS and EDX simultaneous on the ARM200F (Gatan Quantum ER 465 GIF, JEOL SDD 60 mm^2 EDX detector). During the measurement there has been drift and contamination so all mapping results show a certain amount of carbon. Since this carbon contamination increases during the measurement, not the full mapping is used for determining the chemical composition. The drift has been corrected post-acquisition. Not all elements of the specimen are accessible

in EELS, only C, O, Mn and Co have edges in the region of ≈250 eV - 900 eV. The EDX measurement conducted in parallel is sensitive to all other elements but the short acquisition time limits the number of recorded signal. One EDX mapping that shows all elements is shown in fig.98, more details of the chemical composition is shown in Appendix 6.7. The C contamination makes a notable percentage of the whole composition so the percentage does not reach the expected values. The relation is correct for the used materials of MgO and Co_2MnSi: 1 : 1 and 2 : 1 : 1 within the error margins, because of the few counts the data is very noisy. The standard deviation is already at 5% and a systematic error because of drift and contamination is also added. For the chemical width of the layers the following values have been measured:
Co_2MnSi1: 9.9 ± 0.5 nm
MgO barrier: 2.0 ± 0.5 nm
Co_2MnSi2: 15.3 ± 0.5 nm
MgO protection layer: 3.0 ± 0.5 nm

HAADF images have been recorded for information about the grain size and quality of the layer system. Two are shown in fig.97 with a more detailed view in the left image and an overview image on the right. The grain size of the Co_2MnSi approaches the thickness of the respective layer at $\approx 10-15$ nm. The layers are mostly straight and of equal thickness with no notable diffusion, the MgO barrier without holes but of slightly varying thickness and shows small bends where the underlying Co_2MnSi layer locally decreases in thickness. The overview HAADF image shows altering of the MgO substrate ≈50 nm below the layer system (fig.97 right), this results probably from the pre-cleaning process.

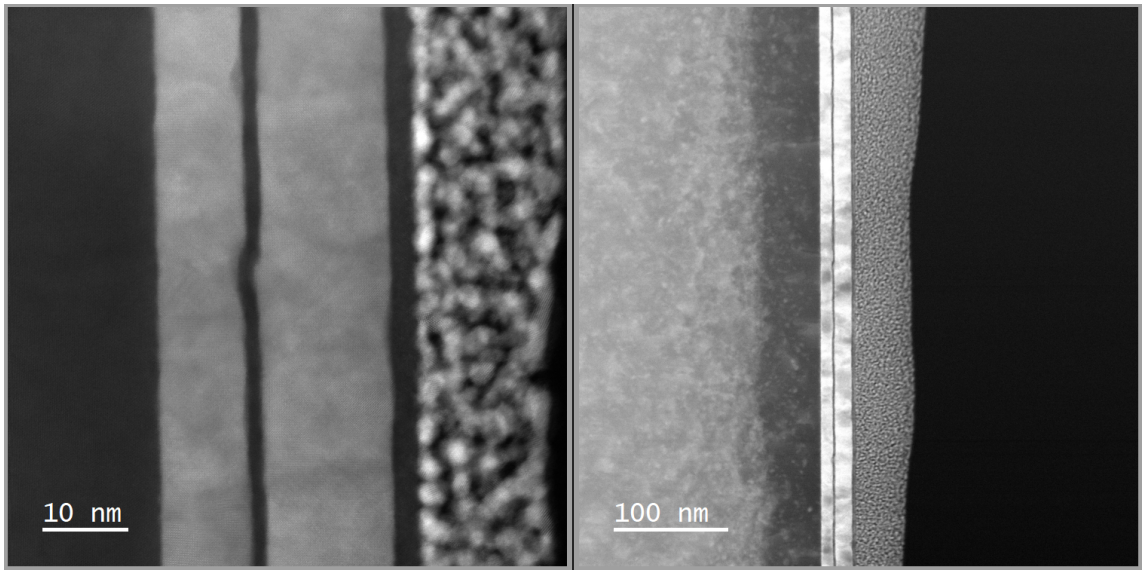

Figure 97: HAADF images of the TMR stack recorded on the ARM200F. The MgO substrate is on the left, the FIB-Pt on the right side of the images. Left: Close view of the layer system at 3M magnification, 8 cm camera length showing a bend in the MgO barrier layer and slightly varying thickness of this layer. Right: overview image of the layer system showing the grains in the Co_2MnSi layers at 400k magnification and 20 cm camera length. The MgO substrate below (left) of the layer system shows altering for ≈50 nm probably due to the pre-cleaning.

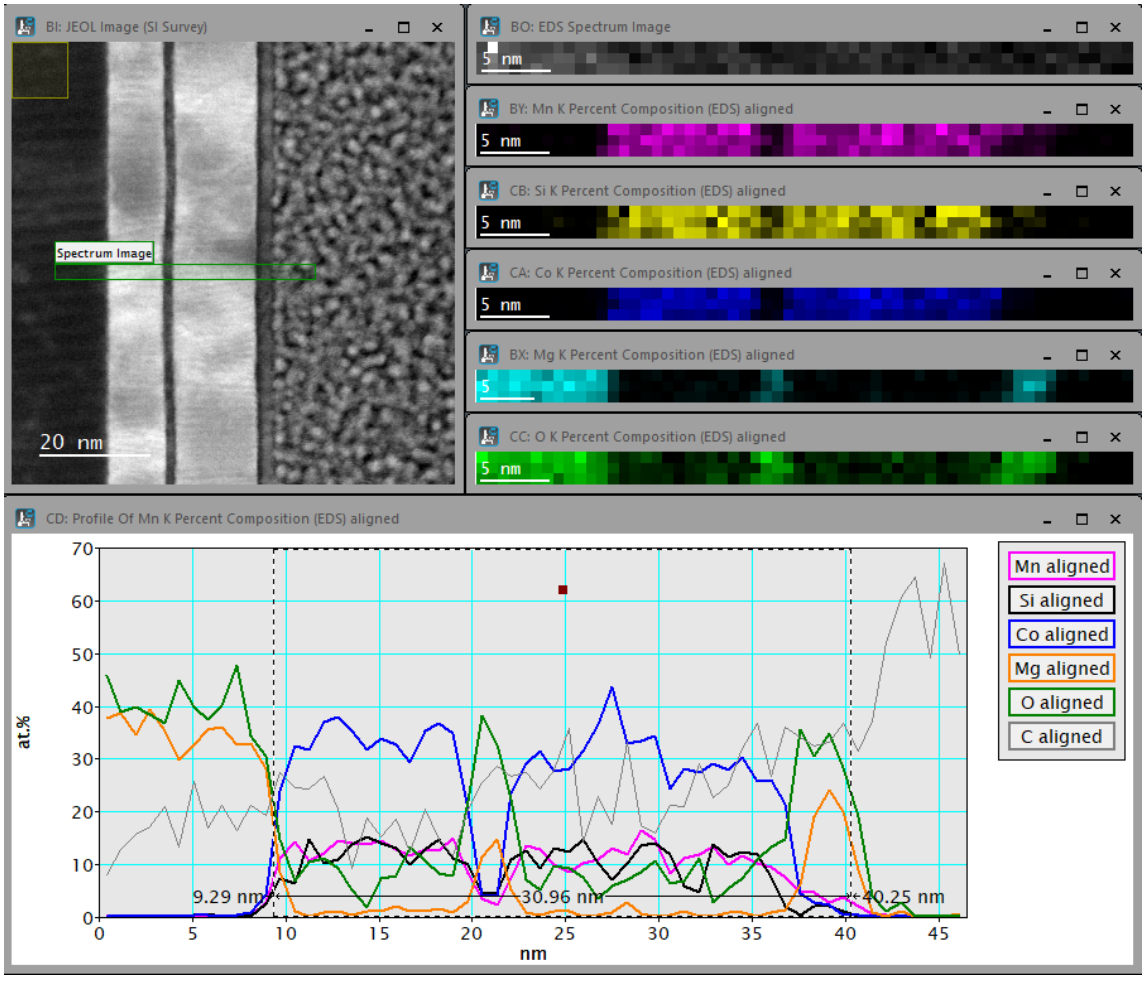

Figure 98: Results of an EDX mapping of the TMR stack in the thick part after thinning. The Survey image (top left) shows a notable amount of FIB-Pt in the right of the image. Due to drift and contamination only very small mappings have been possible, this one has only 3 rows and needed post-acquisition drift correction before summation was possible. Top right: the EDX mapping and elemental maps for the elements Mn, Si, Co, Mg and O. The layers can be resolved. Bottom: Percent composition for the elements with C contamination present all over the mapping, ranging between 10% and 25% and increasing further in the FIB-Pt. The relation resembles the intended composition with $\approx 1:1$ for Mg and O and $\approx 2:1:1$ for Co, Mn and Si.

3.7.1 Chemical characterization of the Co_2MnSi/MgO interface

The interface between the Co_2MnSi and the MgO barrier is important for the electronic transport and spincaloritronic properties of the system according to a theoretical approach by Geisler and Kratzer [118] which shows notably different behaviour of the MTJ with respect to the interface atoms, calculated for CoCo/O, MnSi/O and MnMn/O. It is therefore indicated to characterize the interface chemically and reveal which of the calculated models is correct to describe the Co_2MnSi/MgO system.
A thin specimen suitable for high-resolution STEM-EELS has been prepared by FIB milling by Björn Büker. The thinning process only partly succeeded because of the MgO layers that are much harder to mill away than the Co_2MnSi layers, due to scattering effects the Co_2MnSi is milled away or greatly damaged when the MgO is sufficiently thin. The thickness of the lamella on the thinnest usable part (lattice of the Co_2MnSi intact over at least several nm around the MgO) has been measured using EELS zero loss map and the t/λ method to 27 ± 6 nm. The different scattering properties of the materials make STEM imaging difficult due to high contrast differences. On the MgO barrier a few HAADF images of atomic resolution could be acquired, a better region for imaging has been found in the interface of the MgO substrate to the first Co_2MnSi layer.
The STEM images have been acquired on the ARM200F in Paderborn with the following parameters: 200 kV, 2048×2048 pixels at a dwell time of 10 μs, 4 cm camera length, magnification of 20-50M and the annular dark field detector used as HAADF detector covering a scattering angle of 140-550 mrad under the given conditions. To improve the image quality a FFT filtering has been used by applying a mask on the FFT diffraction image and transforming the masked area back. This increases the signal to noise ration in the images as can be seen in fig.99. Drift from the acquisition is still visible in the images, also a non uniform lattice that can result from non-uniform growth, bending of the specimen and strain.

The software JEMS [77] allows to use a model of a crystal to determine the atom positions in an image, additionally the line profile tool can be used to survey the interface region in search for atom positions. HAADF shows Z-contrast, atoms scatter differently according to their atomic weight so the peaks representing them are of different magnitude. Models with crystal parameters from MgO (COD 1000053, [119]) and Co_2MnSi (COD 1539797, [120]) from the crystallography open database [121] have been used, the .cif files can be imported into JEMS. A simulation of a HAADF STEM image with the given parameters has the result shown in fig.100 together with a line profile that has been drawn after importing the image in GMS to show the scattering behaviour of the given atoms. The crystal structure has been visualized using the program VESTA [122] and is shown in fig.101. In MgO the Mg atoms are orange and the O atoms green. In Co_2MnSi the Co atoms are blue, the Mn atoms purple and the Si atoms yellow. This colour coding continues through this chapter. The knowledge about the atoms and their brightness in the DF image (simulated with the parameters used in the microscope, which makes the annular dark field detector a HAADF detector) allows to identify the type of atoms in lineprofiles to determine which atoms form the interface.

These lineprofiles help to uncover if there are less scattering atoms because a smaller peak or a superposition peak structure showing a shoulder like behaviour appears in the

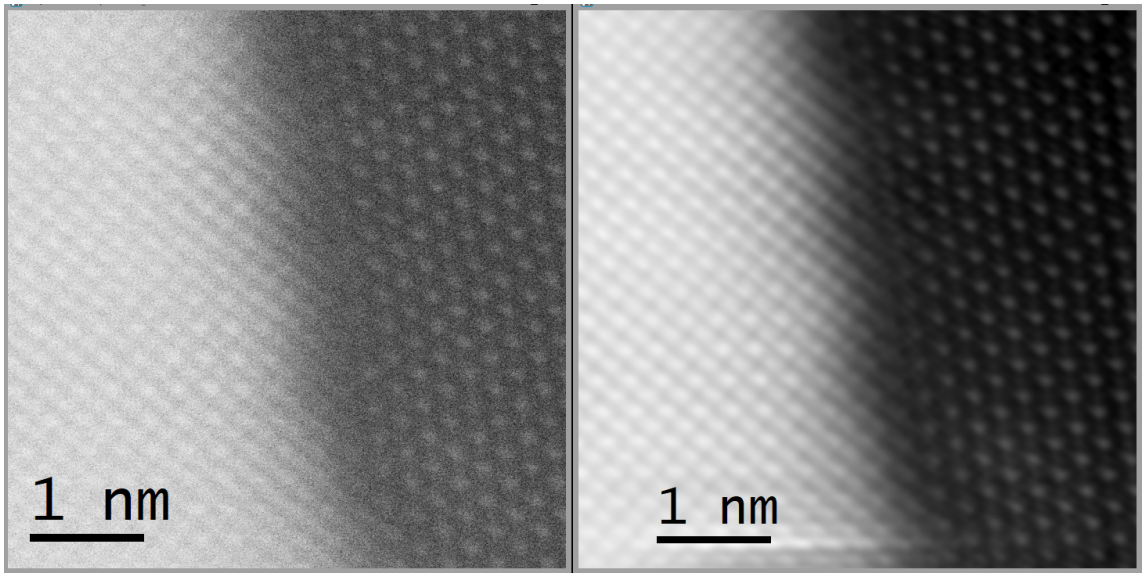

Figure 99: Left: Original STEM image of the Co_2MnSi/MgO interface. Right: FFT filtered image.

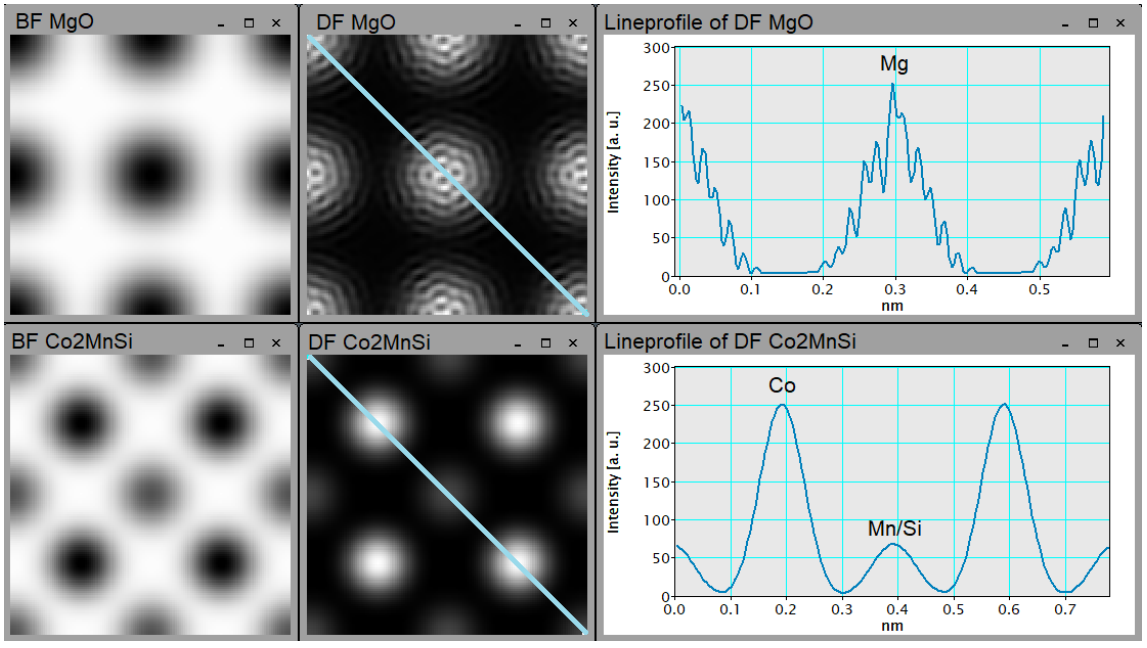

Figure 100: Top row: Simulated BF and DF image and a line profile drawn across the DF image for MgO. The dark/bright positions are Mg atoms on top of O atoms. Bottom row: Simulated BF and DF image and a line profile drawn across the DF image for Co_2MnSi. The darkest/brightest positions are the Co atoms, the others Mn or Si atoms, the atomic column consists of alternating Mn and Si.

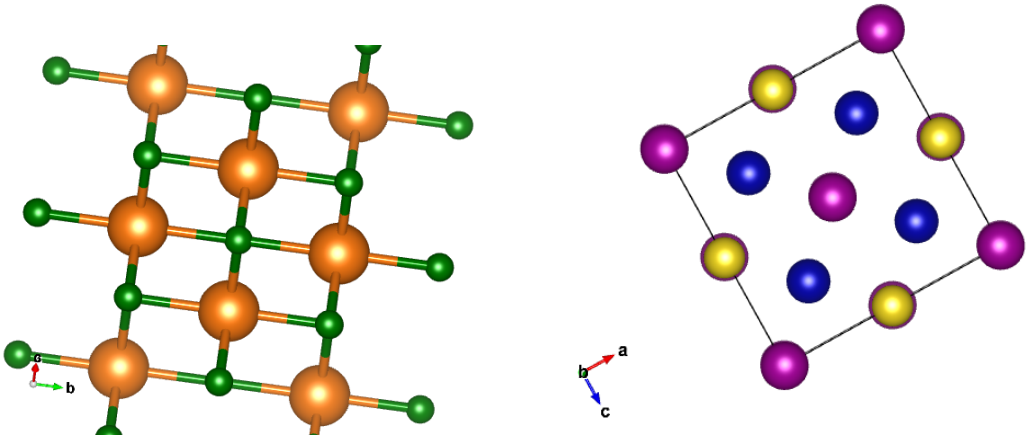

Figure 101: Visualized crystal structure of MgO (left) and Co_2MnSi (right), atom colours: Mg orange, O green, Co blue, Mn purple, Si yellow.

lineprofile. The oxygen in MgO can be observed using this method on the FFT filtered HRSTEM (fig.102).

The positions of Co and Mn,Si have been uncovered in a similar way by a lineprofile

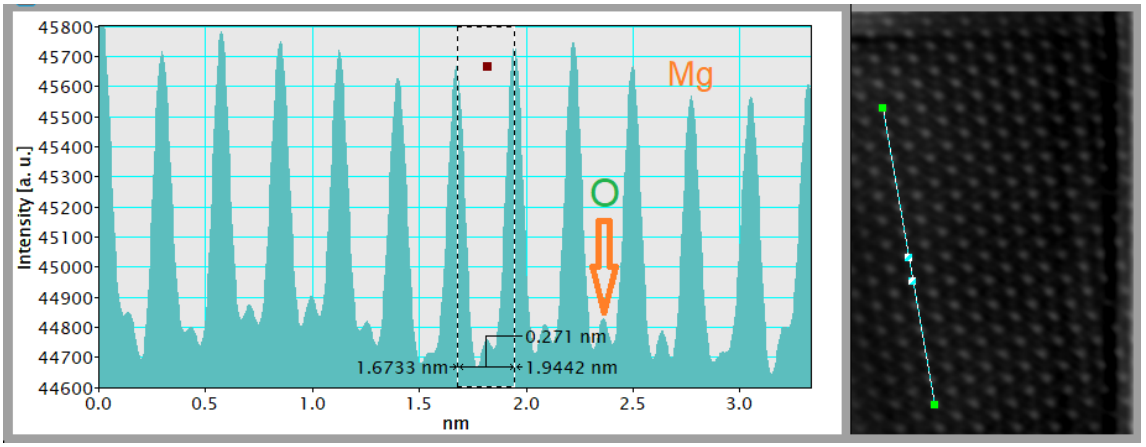

Figure 102: Lineprofile on the MgO part of the FFT filtered HRSTEM image showing the Mg atoms and in between the O atoms.

across a suitably chosen column of atoms with respect to the unit cell positions (fig.103). It is not possible to distinguish between Mn and Si atoms because of the orientation of the unit cell. The atom positions have been identified using peak height and the distance between two peaks until reaching the interface where not only the intensity is changing notably but it is not very clear which atoms form the interface. Careful measuring from known atoms on and under the assumption the MgO and V do not mix and form a clear interface on the scale of ≈10 atoms the interface region has been checked for appearing peaks that indicate an atom position. Between the Co atoms and the O of the MgO no other atoms have been found. Ongoing from the Mn/Si row another atom position after

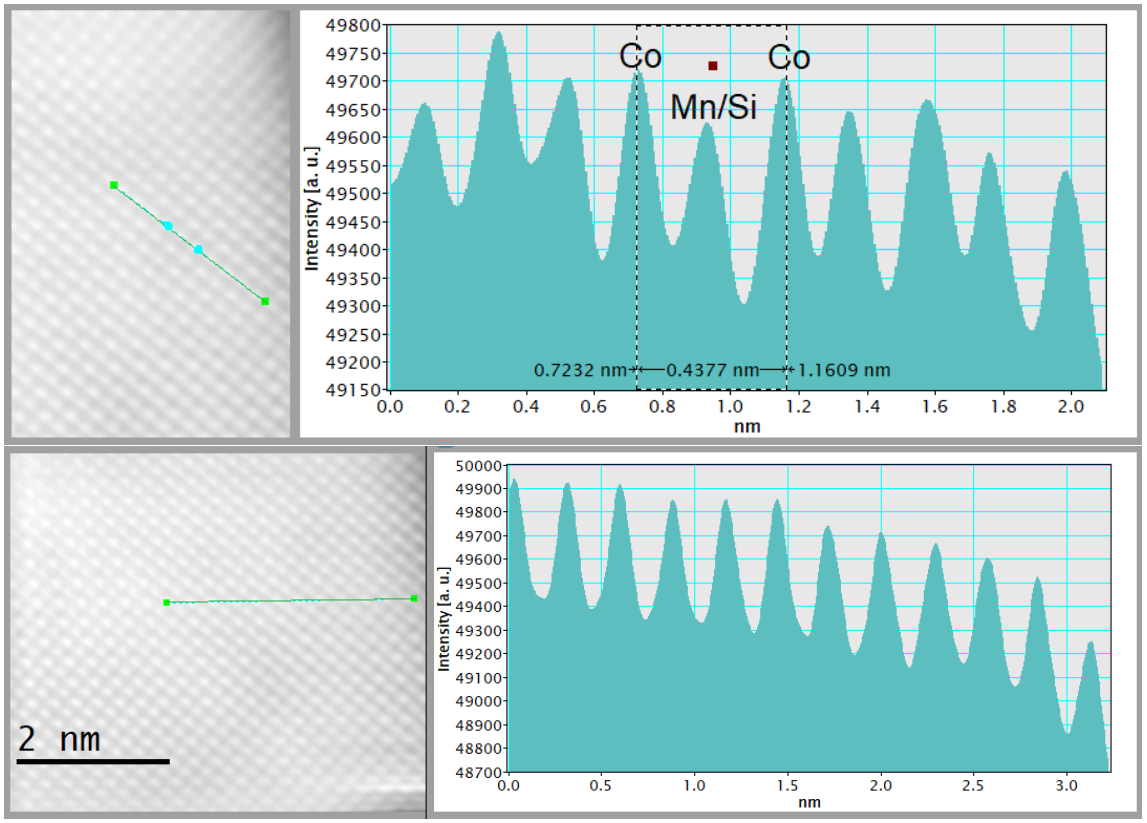

Figure 103: Lineprofile on the Co_2MnSi part of the FFT filtered HRSTEM image: Showing the Mn/Si atoms in between the Co atoms (top) and a row of Co atoms (bottom). There the intensity ceases towards the interface on the right side of the image and the lineprofile.

the last identified Co position could be found (fig.104) and it has been identified as another Mn/Si atom column. In two investigated FFT filtered HRSTEM images the atoms have been marked manually by a dot in the used colour code after identification which atoms form the final image and are therefore the result of this investigation (fig.105). Between the Co and the Mgo is a greater distance without any invisible atom in between, the Co binds to the O of the MgO. The Mn/Si forms alternating columns which bind to the Mg. The present bindings are therefore Co-O and MnSi-Mg. With respect to [118] the CoCo/O result is expected to agree with measurements.

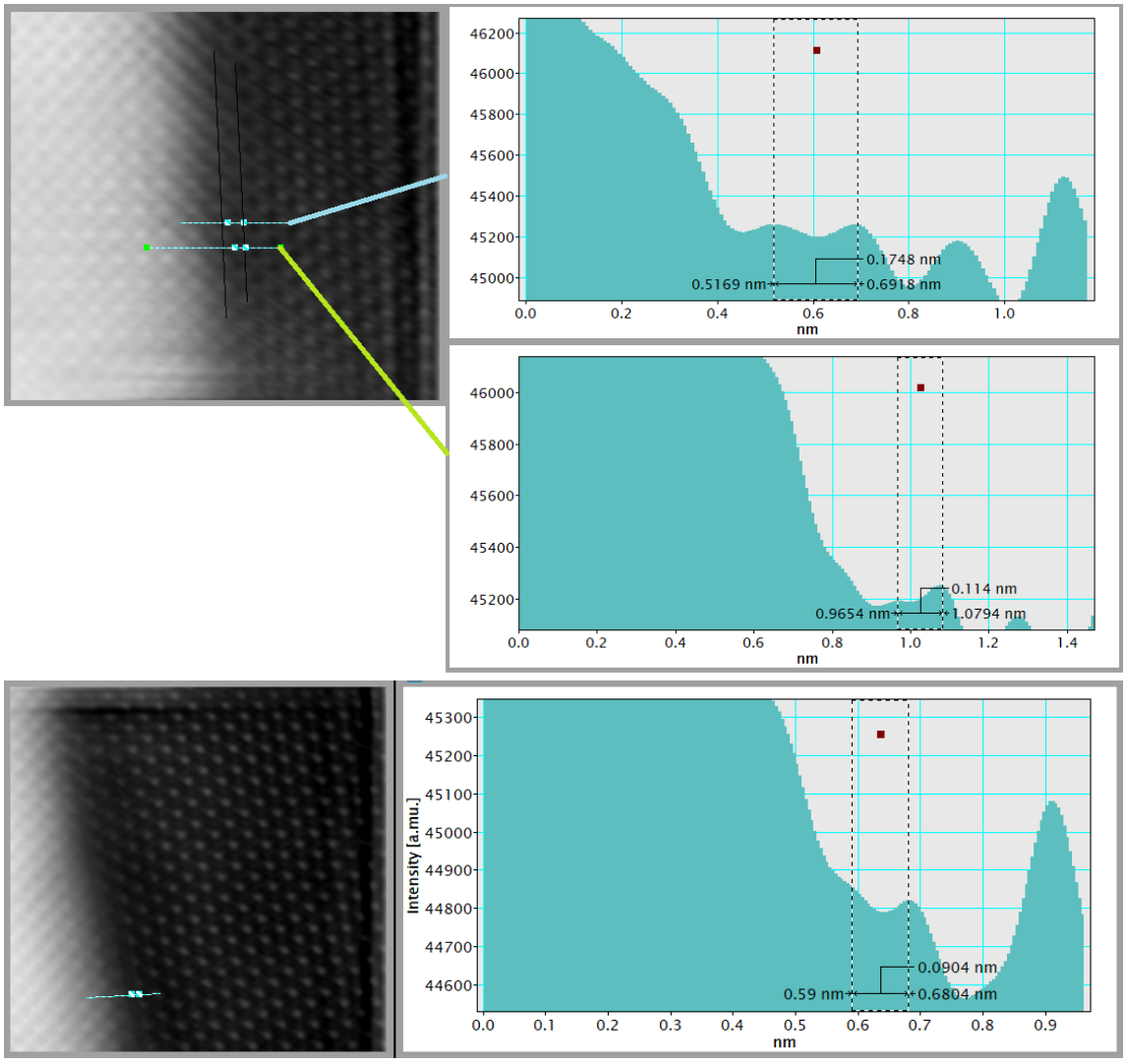

Figure 104: Lineprofiles on the interface region, on the left is a part of the FFT filtered image containing the interface region with the line profiles drawn on and the endpoints of the ROI indicated on the lineprofile. On the right are the lineprofiles with a ROI marking the important peaks. The intensity axis has been rescaled to show the important parts of the interface.

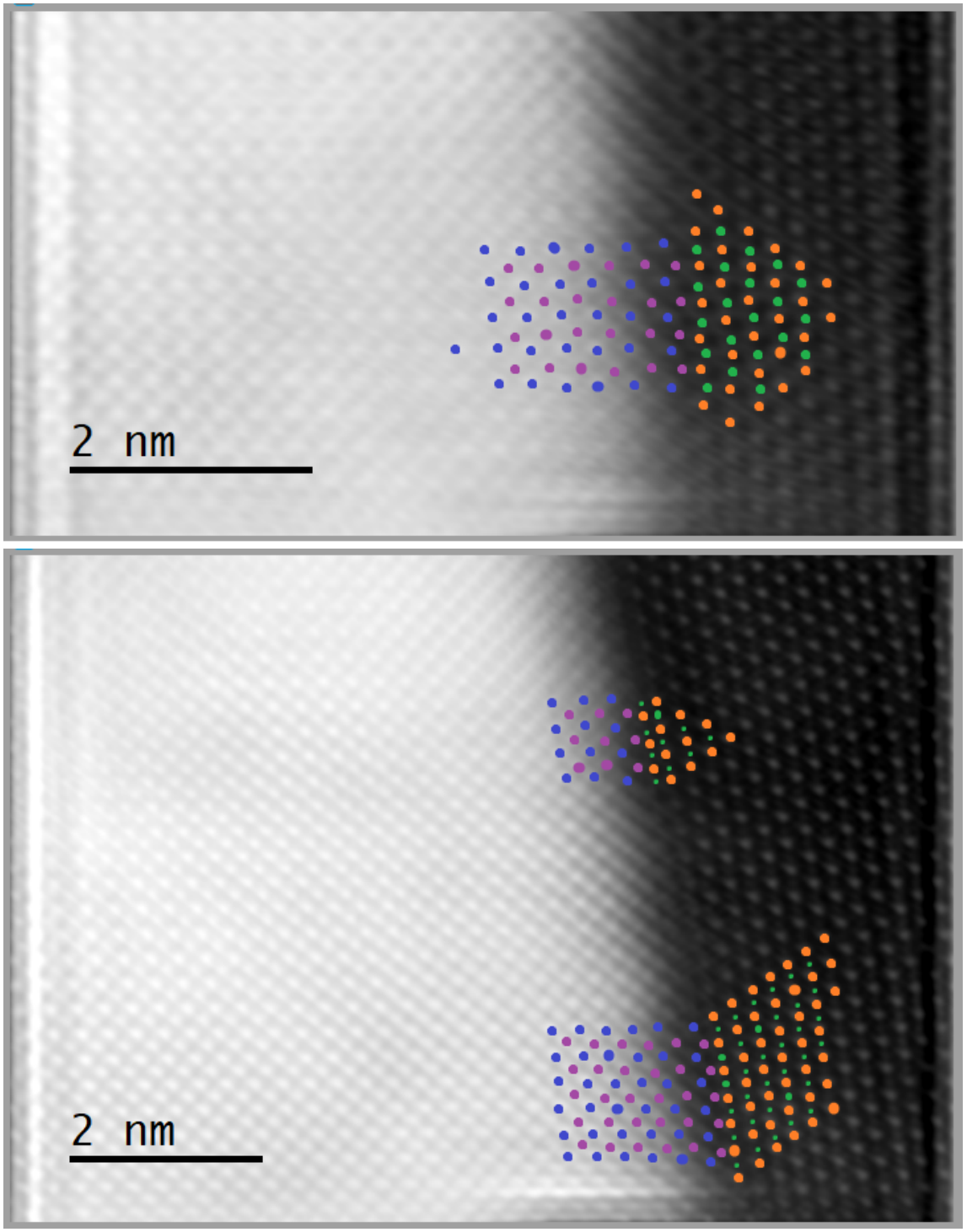

Figure 105: Results for the interfaces on both investigated images. The colour code for the atom site placements is Mg orange, O green, Co blue, Mn/Si purple, the dots have been placed manually. All three investigated regions on two images give the same result, Co binds to O and Mn/Si to Mg.

3.7.2 Micromagnetic simulations

Micromagnetic simulations with Mumax [62] have been performed with the following settings: Mesh size $512 \times 512 \times 1$ cells with cell size of $1 \cdot 10^{-9} \times 1 \cdot 10^{-9} \times 5 \cdot 10^{-9}$ m. Four regions have been defined: 3 nm MgO (nonmagnetic), 10 nm Co_2MnSi, 2 nm MgO tunneling barrier (nonmagnetic) and 15 nm Co_2MnSi. For the material parameters the saturation magnetization Msat has been set to Co_2FeSi: Msat $= 881 \cdot 10^3$ A/m [88] [86], the exchange stiffness to Aex $= 23.5 \cdot 10^{-12}$ J/m [89] and the 1st order uniaxial anisotropy constant to Ku1 $= 2.89 \cdot 10^3$ J/m^3 [88].
At simulation start the magnetic Co_2MnSi layers have been set to random magnetization and the system has been relaxed to the minimum energy state using the `relax()` method of Mumax. The simulation results have been imported into Gatan GMS where the magnetic induction and the phase image have been calculated by the earlier mentioned DM scripts by Cushley and Waclawski from the University of Glasgow. For the magnetization in all three components the results are shown in fig.106 top row: In x direction the magnetization changes periodically, in y direction both sections where both layers are magnetized in the same direction and in different directions are apparent and in z direction only a few parts are magnetized. The regions of the same magnetization are about twice the width of the layer system. Calculating the integrated magnetic induction and the phase (fig.106 central row) it shows that the parts of the idealized lamella where both layers are magnetized in the same way increase their presence in the phase far into the space next to it. This could have effects on the DPC images as any other signal would be superimposed by this signal that extends into the space next to the lamella.

Additional micromagnetic simulations using Micromagus [65] have been supplied by A. Hütten for both the thick TMR stack and the TMR stack. The thick TMR stack system has been divided in subsystems for reduced computing effort: 40 nm Co_2MnSi = 16 nm + 16 nm + 8 nm (layer thickness < demagnetization length). The other system has not been divided into subsystems because of the layer thickness already small enough. The hysteresis has been calculated from equilibrating the system in an external field of 0 T $\rightarrow$ 0.5 T $\rightarrow$ 0.5 T $\rightarrow -0.5$ T $\rightarrow -0.5$ T $\rightarrow$ 0 T. The material parameters are the saturation magnetization Msat=881 kA/m [88], the anisotropy constant $K1 = 28900$ erg/cm^3 [88], the exchange coupling $A = 23.5$ pJ/m $= 2.35 \cdot 10^{-6}$ erg/cm [88]. $L_{spm} = 18.432$ nm, the exchange length is given by $l_{exch} = 90.175$ nm and the demagnetization length by $l_{dem} = 17.4$ nm. The saturation magnetization has been replaced by an effective saturation magnetization where the MgO barrier is included:

$$M_{s,eff}(\text{TMR1}) = \frac{M_s \cdot 10 \text{ nm} + M_s \cdot 15 \text{ nm}}{10 \text{ nm} + 15 \text{ nm} + 1.7 \text{ nm}} = 824.906 \text{ kA/m}$$

$$M_{s,eff}(\text{TMR2}) = \frac{M_s \cdot 40 \text{ nm} + M_s \cdot 40 \text{ nm}}{40 \text{ nm} + 20 \text{ nm} + 40 \text{ nm}} = 708.4 \text{ kA/m}$$

The simulation results are shown in fig.107: In the selection of magnetic states from the simulation it can be seen that both layers do not switch at the same time, this is more evident in the TMR stack where one layer is 1.5 times the thickness of the other layer, in the thick version both Co_2MnSi layers are of equal thickness. Looking at the hystereses, the simulated ones agree with the measured ones well but there still are differences. The

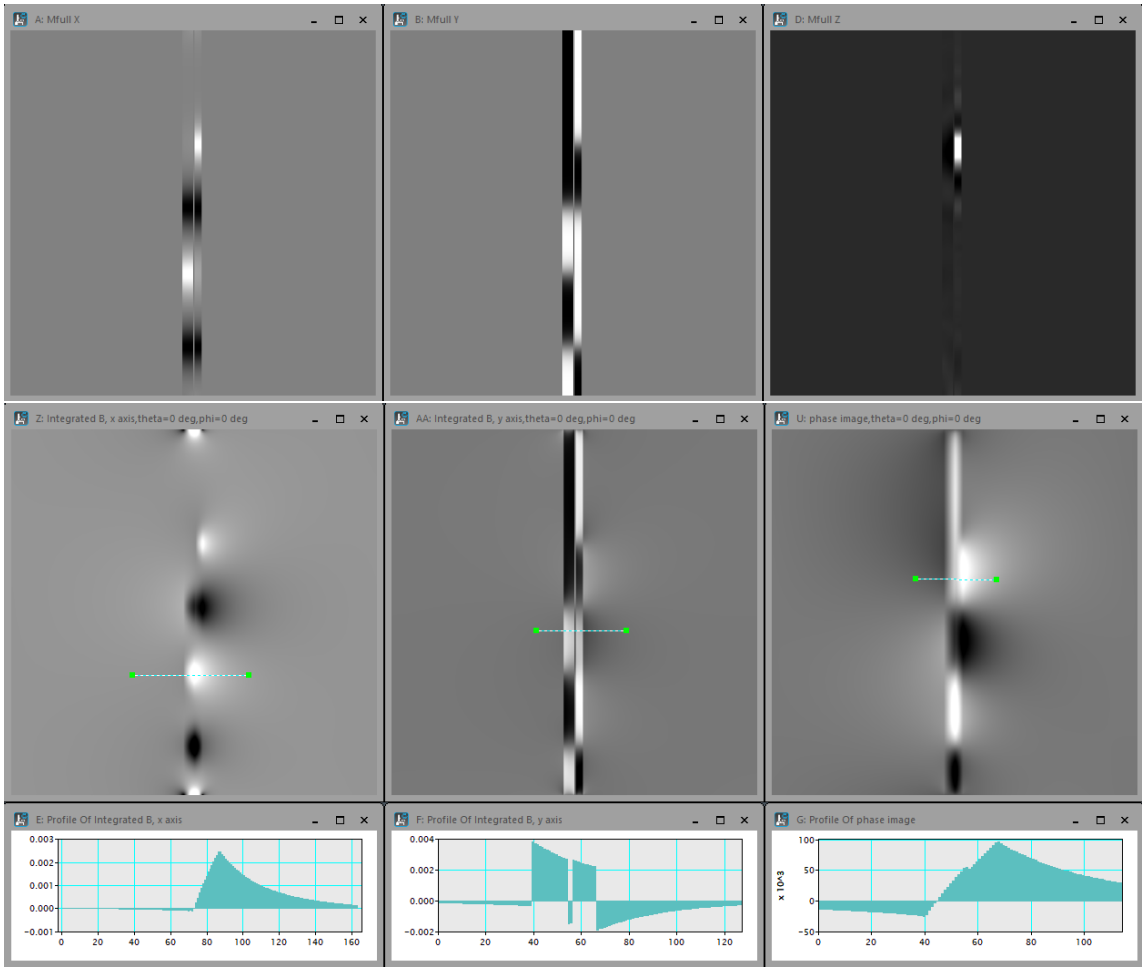

Figure 106: Top row: Simulated magnetization for the x, y and z direction for the TMR stack sample using Mumax. Different domains are visible. Center row: calculated integrated magnetic induction in x and y direction and phase image. Bottom row: Line profiles across parts of the induction and phase images to show the qualitative shape across the sample.

measured coercitivity is narrower than the simulated one: $0.15 < 2.14$ kA/m (TMR) and $0.69 < 2.71$ kA/m (TMR thick). Differences appear in the saturation magnetization, it is measured 6.1% higher than the simulated for the TMR stack and 34.4% lower for the thick TMR stack. The bulges in the hysteresis of the thick TMR stack are reproduced qualitatively.

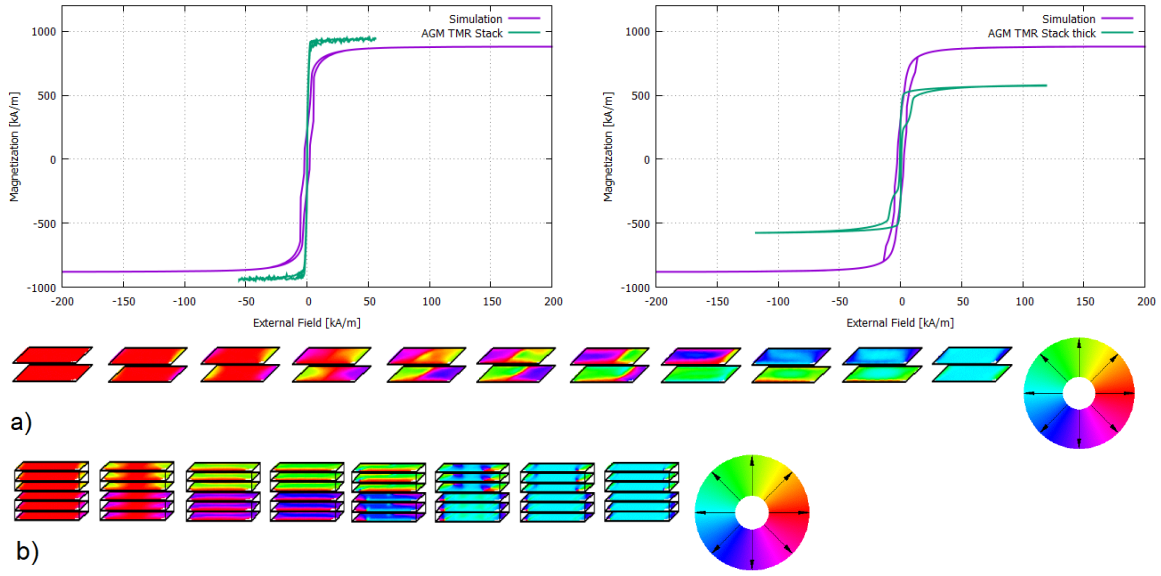

Figure 107: The hysteresis simulated with Micromagus (purple) compared to the AGM measurement for the TMR stack (left) and thick TMR stack (right) sample (green). Below the hystereses several magnetic states from the simulation are shown for (a) the TMR stack and (b) the thick TMR stack, colour wheel for directions on the right. The different switching behaviour is more evident in the TMR stack where one layer is 1.5 times the thickness of the other layer. Simulation and graphics courtesy to A. Hütten.

3.7.3 EMCD measurements

EMCD measurements have been performed on a piece of Co_2MnSi that has more area to tilt on than the TMR stack due to failure of the measurements on the original lamella after also strong oxidation occurred. The thickness of this lamella has been measured to 55-70 nm via EELS zero loss mapping. Due to this huge thickness only a weak EMCD signal can be expected. The measurements have been conducted in STEM Mode using the script from Appendix 6.13.4 with the following parameters: 200 kV, exposure time 20 sec, dispersion 0.5 eV/channel, STEM aperture 10 μm, camera length 4 cm to obtain separated diffraction discs. The discs (fig.108) have been moved out to the right side of the spectrometer entrance aperture because of the present very weak diffraction discs on the right of the systematic row.

A set of measurements has been acquired in a linescan with a point-to-point distance of

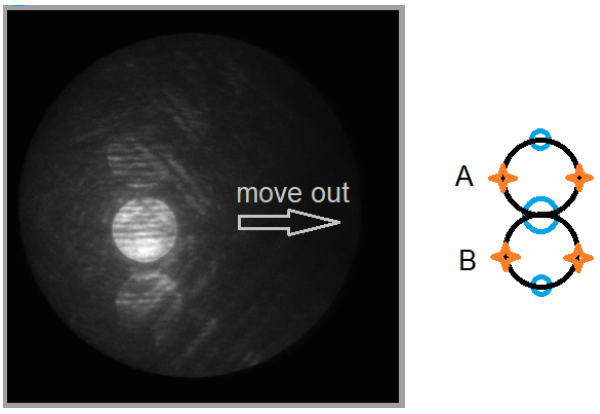

Figure 108: Left: Systematic row of diffraction discs aligned in the spectrometer entrance aperture. Right: Schematic of the systematic row, the Thales circles and the used EMCD positions.

5 nm. Two sets of three neighbouring points have been summed under the assumption thickness and crystal orientation do not change notably between these points to increase the signal to noise ratio. The spectra have been extracted manually on the EMCD positions A and B and evaluated on the Mn edge (L3 at 640 eV, L2 at 651 eV) and Co edge (L3 at 779 eV, L2 at 794 eV) by background subtraction and overlay spectrum A over spectrum B, if necessary aligning post-edge by integral. The results are shown in fig.109.

The Mn results are noisier although they seem to contain more counts, this is a result of aligning post-edge by integral and not real. Also the amount of Mn is only half of the amount of Co in this alloy. The two measurements on Mn are not in good agreement, the Mn 1 measurement shows a notable difference in the L3 edge and a small difference of the same sign in the L2 edge. The L2 difference is of the magnitude of the noise. The Mn 2 measurement shows a small effect on the L3 edge of the order of the noise but with a splitted peak and an opposite sign notable effect on the L2 edge. For comparison XMCD measurements on Mn in $Ga_{1-x}Mn_xP$ [123] show for Mn a huge XMCD effect on the L3 edge and a very small two-peaked opposite sign effect on the L2 edge, which might not be clearly distinguishable in EMCD. The Mn 1 measurement is in agreement with this

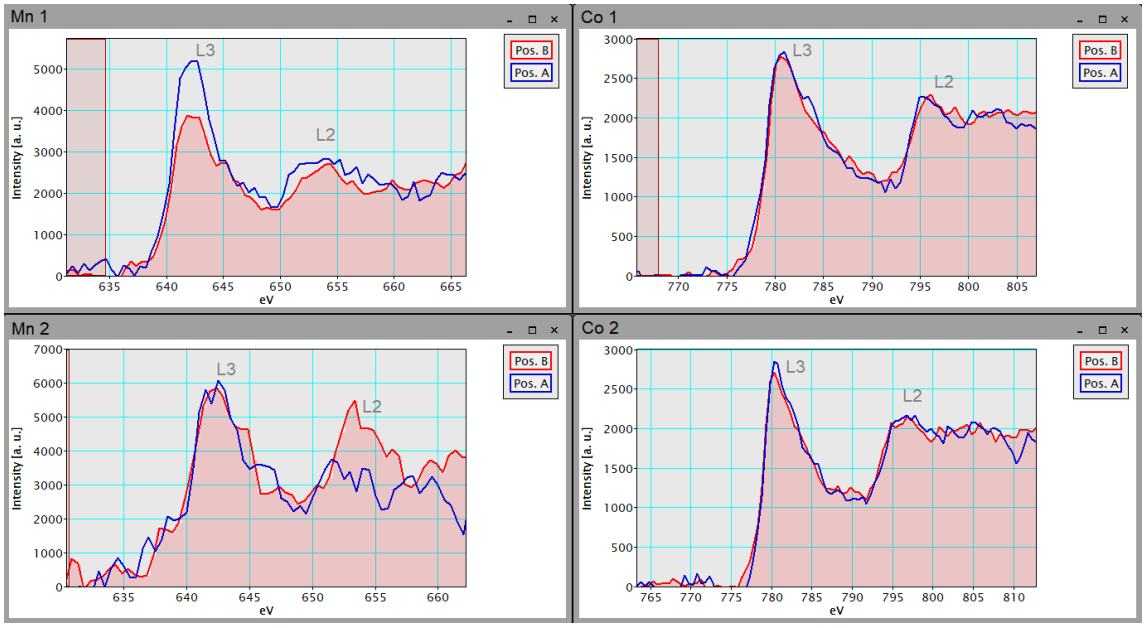

Figure 109: EMCD measuerments on Co_2MnSi: Left column two measurements on Mn, right column two measurements on Co.

XMCD measurement, even in the magnitude, also it is the better measurement because of the smaller noise and better off-edge agreement of the two measurement positions. Also it is in agreement with EMCD measurements of W. Hetaba on Ni_2MnSn([73] fig. 6.10). The two measurements on Co are comparable and show a small effect on the L3 edge and small opposite sign effect on the L2 edge that is comparable to the noise level. Measurements on Co by Rubino et.al [124] show a very similar result. The increased noise on the measurements presented here results from the specimen thickness that lies in the range that is disadvantageous for EMCD measurements. It can be stated that even at a thickness greater than 50 nm EMCD measurements are possible. The magnitude of the measured EMCD effects is presented in table 12.

Measurement	L3	L2
Mn 1	$14.53 \pm 4.41\%$	$1.98 \pm 7.19\%$
Mn 2	$4.77 \pm 5.08\%$	$20.33 \pm 6.87\%$
Co 1	$1.16 \pm 1.43\%$	$0.66 \pm 1.76\%$
Co 2	$2.54 \pm 2.16\%$	$0.58 \pm 2.78\%$

Table 12: Quantitative EMCD results for the measurements shown in fig.109.

3.7.4 DPC measurements

Differential phase contrast measurements have been carried out using both segmented and pixelated DPC to measure magnetic properties of the TMR Stack. As in previous measurements it has been tried to change the magnetization direction by applying an external magnetic field using the objective lens and tilting the specimen to ±25°. This corresponds again to a field of ±0.0423 T. It is not clear yet if the magnetization direction could be reversed. The segmented DPC data (fig.110) has been processed to find the rotation angle corresponding to minimum contrast in one component trying to contain the magnetic signal in the other component. The rotation angle is for the first two datasets 107°, for dataset 3-6 87°.

A line profile starting at the MgO substrate/Co_2MnSi interface with 100 pixels integration

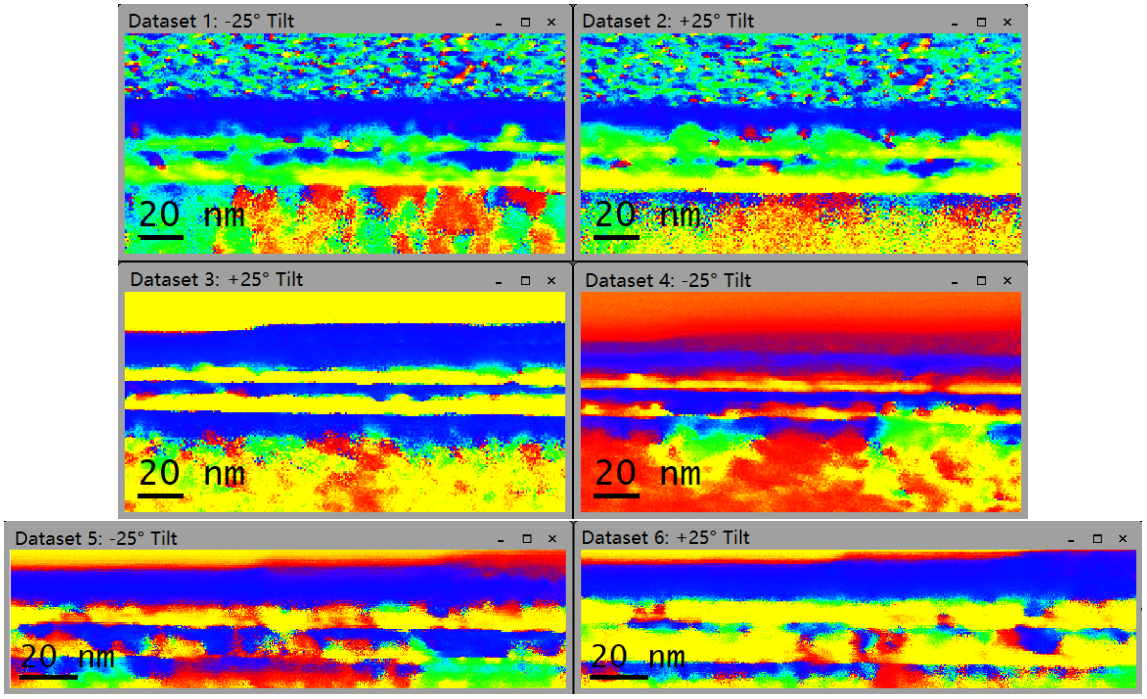

Figure 110: Segmented DPC colour images after processing including normalization on the MgO substrate and rotation of the components. It is not yet clear if the reversal of magnetization by an external field has been successful.

width has been drawn across the layer system for both component images. The results for each dataset are corrected for the thickness using the second linear function of table 11 as the measurements have been conducted in Glasgow before the second thinning of the lamella. The results are shown in fig.111 for the six datasets individually and a combined result for the two components is shown in fig.112. Especially when looking at the components separately it becomes obvious that in Component 1 no signal is reversed with external field reversal so no part of the signal in there can be of magnetic origin. So the description as magnetic induction is technically wrong. Since there are several possible reasons for beam deflections another explanation has to be sought.

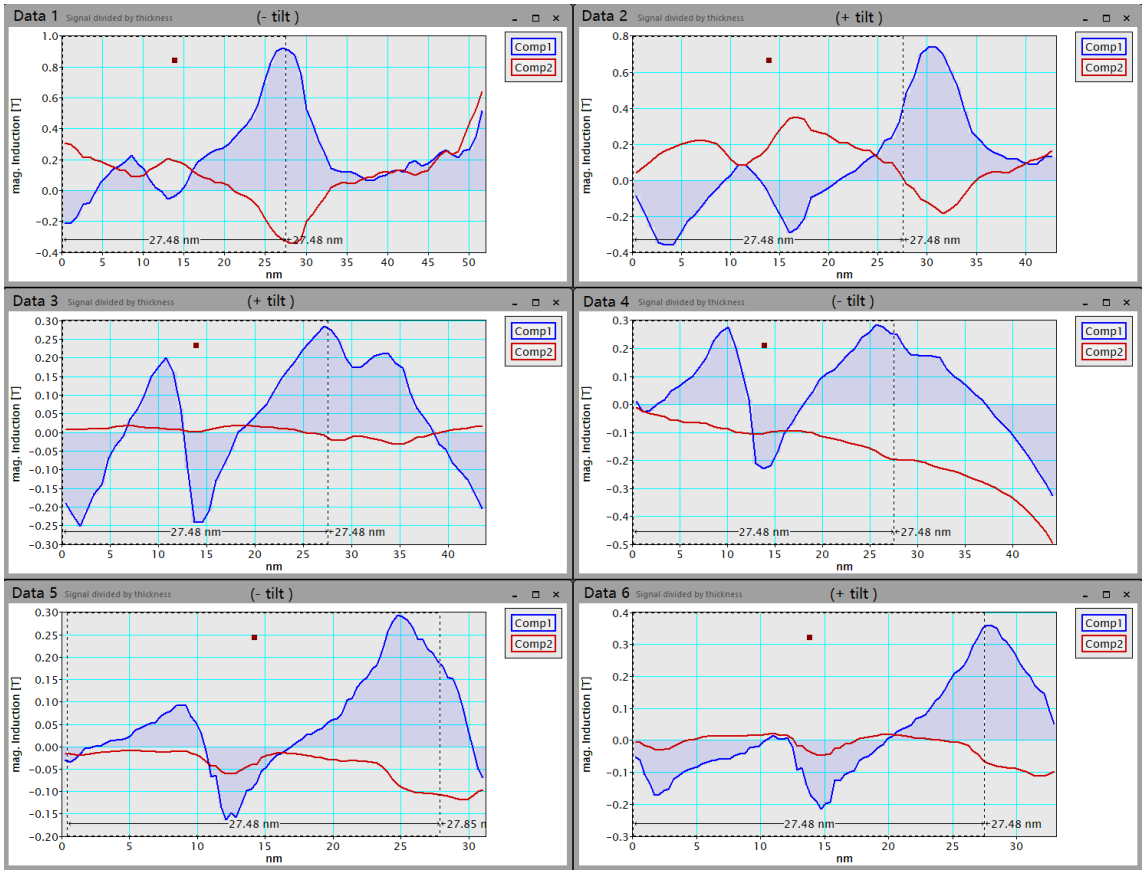

Figure 111: Segmented DPC results for the six TMR stack datasets, the $Co_2MnSi/MgO/Co_2MnSi$ part is indicated by a ROI. Starting point for the line profile is always the MgO substrate/Co_2MnSi interface (left end of each plot). Shown are the two perpendicular components after rotation and processing for the specimen thickness.

Looking at the mean inner potential of MgO and of Co_2MnSi reveals a possible source of this signal: The MIP of MgO is 13.01 ± 0.08 V [94] [95], the MIP of Co_2MnSi is again calculated of its elements using 29.5 V for pure Co [97], 9.26 ± 0.08 V for Si [95] and the value for Mn should be comparable to its neighbouring elements Fe (22 V) [47] [96] and Cr (23.6 V) [47] So the intermediate value of 22.8 V is used to model the MIP for Mn. The FIB-Pt is modelled with 25 V again [98]. For Co_2MnSi the MIP is calculated according to

$$2/4{\cdot}V_0(\mathrm{Co})+1/4{\cdot}V_0(\mathrm{Mn})+1/4{\cdot}V_0(\mathrm{Si}) = 2/4{\cdot}29.5\ \mathrm{V}+1/4{\cdot}22.8\ \mathrm{V}+1/4{\cdot}9.26\ \mathrm{V} = 22.765\ \mathrm{V} \approx 22.8\ \mathrm{V}.$$

A MgO protection layer has been applied to protect the second Co_2MnSi layer below, later the FIB-Pt has been added during the preparation of the lamella. This has been considered by modelling the system with and without a thin layer of MgO MIP. The change in MIP is inducing the deflection signals, therefore the first derivative of the model should represent the measured signal in a qualitative way. The result of this model approach is shown in fig.113. Considering the line profiles start on the MgO/Co_2MnSi interface and the signal

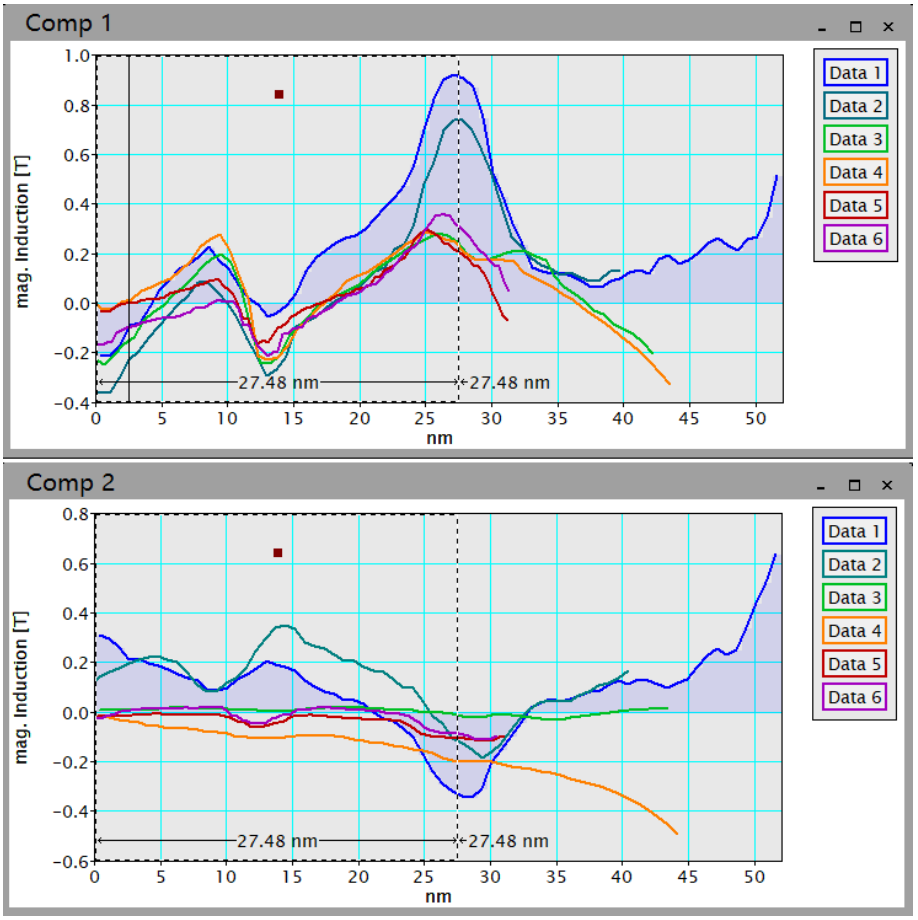

Figure 112: The two perpendicular components proposed to contain the magnetic induction of the TMR stack specimen. In component 1 no switching due to the external magnetic field can be seen, in component 2 differing behaviour can be observed but it is not in agreement with the tilt directions.

has been processed and rotated a qualitative agreement can be seen, although the direction is reversed, a positive change of the MIP corresponds to a negative deflection/signal in the induction profile. A weakness of this model is that only the qualitative change is modelled but no two dimensional landscape containing directions. At both interfaces of one layer the MIP induced deflection has opposite sign, the same is observed in the data for component 1, this is a reason to consider it being a result of the MIP change.

Component 2 shows a different behaviour, the two peaks correspond roughly with the Co_2MnSi layers instead of with the interfaces and two datasets (1 and 2) show these peaks, the other four close to flat behaviour. According to the tilt and corresponding external magnetic field direction the datasets 1, 4 and 5 should show a similar behaviour opposite to 2, 3 and 6. This can not be observed.
Segmented DPC is not a suitable tool to explore the magnetism of this system because of the huge MIP differences and the thin layers that have the MIP differences separated

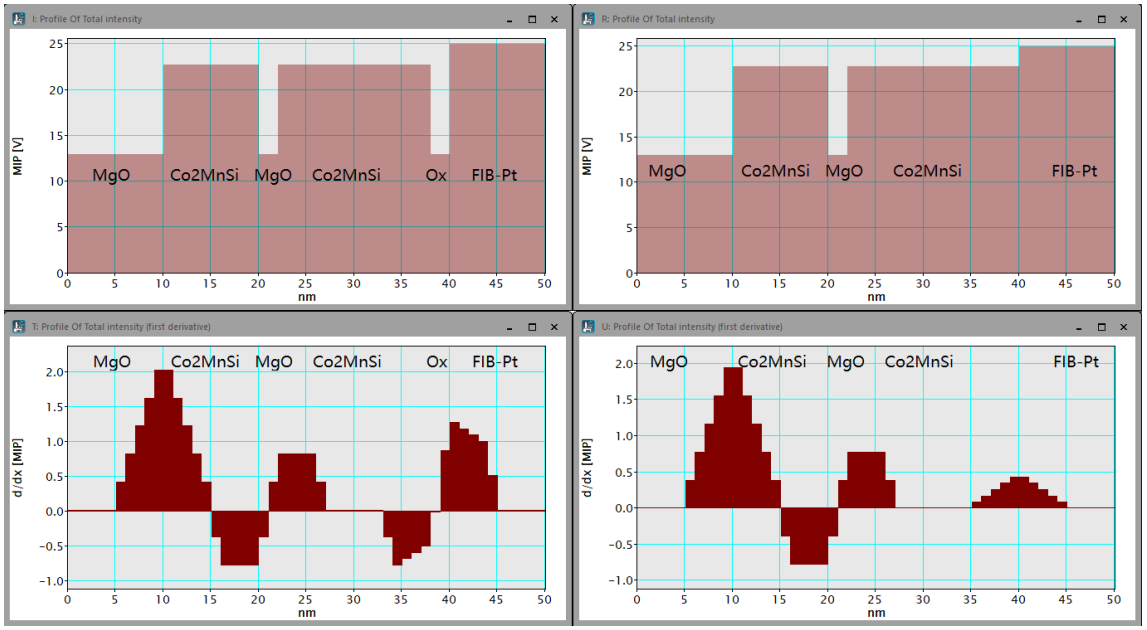

Figure 113: Models for the mean inner potential: left with MgO/Oxidation layer between Co_2MnSi and FIB-Pt, right without this layer. Below is the derivative of the MIP model showing where contrasts arise in the layer system due to a change in the MIP.

by only very few nanometers in distance. A possible solution is a similar specimen with increased layer thickness so in the central part of the layers the magnetic signal is not overlapped by signals arising from the interfaces. Pixelated DPC is at least less prone to contrast effects in phase correlation processing, the MIP induced effects remain.

Five pixelated datasets have been acquired with tilts of −25°, +25°, +25°, +25° and −25°, the last two datasets at a different magnification. The results for the first three datasets already processed for the thickness using thickness function 2 of tab. 11 are shown in fig.114 where the Y component is intended to be contrastless and the X component to contain the magnetic information. Therefore the raw data has been rotated by 68° (1), 68° (2) and 66° (3) to achieve this. Dataset 1 should show different behaviour than the datasets 2 and 3 and the magnetic induction should be negative if the signal is of magnetic origin, this is not the case.

The datasets 4 and 5 have been exposed to the external magnetic field in opposite

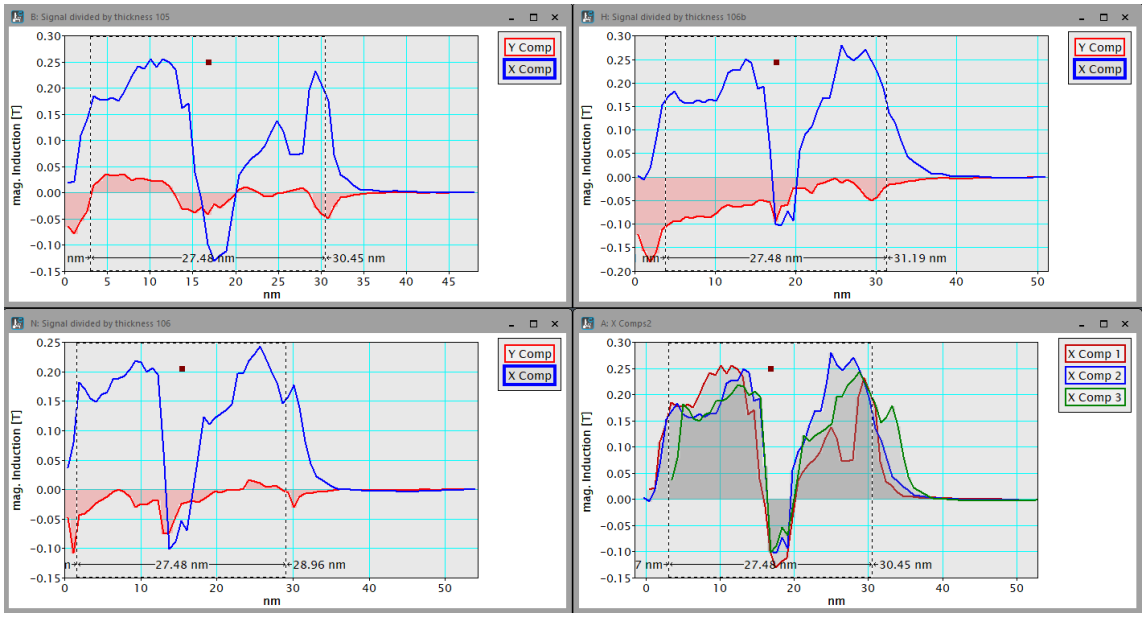

Figure 114: Pixelated DPC results for the datasets 1-3 and an overlay of the X-components (bottom left). No reaction to the external magnetic field, which points in a different direction for dataset 1, can be observed. The signal is localized on the Co_2MnSi layers. The declaration as magnetic induction is made only due to technical reasons since magnetic signal cannot be verified.

directions with a rotation angle to achieve minimum contrast in the Y- component of 61° and 60°. The results in fig.116 show a partially reversed signal in the X-component with probably magnetic origin. The beam deflections by the change in the MIP are superimposed. Details to the pixelated DPC results can be found in Appendix 6.8 with colour images and histograms for each dataset. The results for the magnetic induction are measured over the whole layer width and the central part of the layer (tab.13). As can be seen in fig.116 the 10 nm Co_2MnSi shows deflection in opposite directions, the 15 nm Co_2MnSi layer not. There the signal changes in the central layer, decreasing the result measured over the whole layer, the result from the central part shows a difference but both signals have the same sign. Therefore it is difficult to state if the signal is a true magnetic signal, although according to the AGM measurements a magnetic DPC signal can be expected. The phase image from the Mumax simulations suggests that in the case

where both layers are magnetized in the same direction the signal extends into regions away from the lamella which could explain the shown slope in the deflection and magnetic induction signal visible in measurement 4 and 5 (fig.114). The difference between the magnetic signals in both directions gives 0.55±0.38 T for the 10 nm layer and 0.21±0.34 T for the 15 nm layer measured over the whole layer and 0.75±0.14 T for the 10 nm layer and 0.11±0.09 T for the 15 nm layer measured only in the center of the layer. The signal is not symmetric enough to give a reliable statement about the magnetic interface properties, also a mismatch between the two component images cannot be fully excluded. The starting point has always been set to the interface to the MgO substrate but accuracy lies at up to several pixels. Therefore an overlay of lineprofiles covering a part of the substrate and more of the FIB-Pt and vacuum has been done (fig.115). The alignment between the two datasets has been done on the Y component which has a characteristic structure in the center, so the X components linked to the Y components match as well as those. Due to including parts of the substrate the processing for the specimen thickness is not possible anymore, the signal is now given in the strength of the deflection. The overall behaviour does not change, especially in the 15 nm layer no statements about the magnetism are possible. It can be stated that the mismatch between the up and down pointing deflections is not a real mismatch effect.

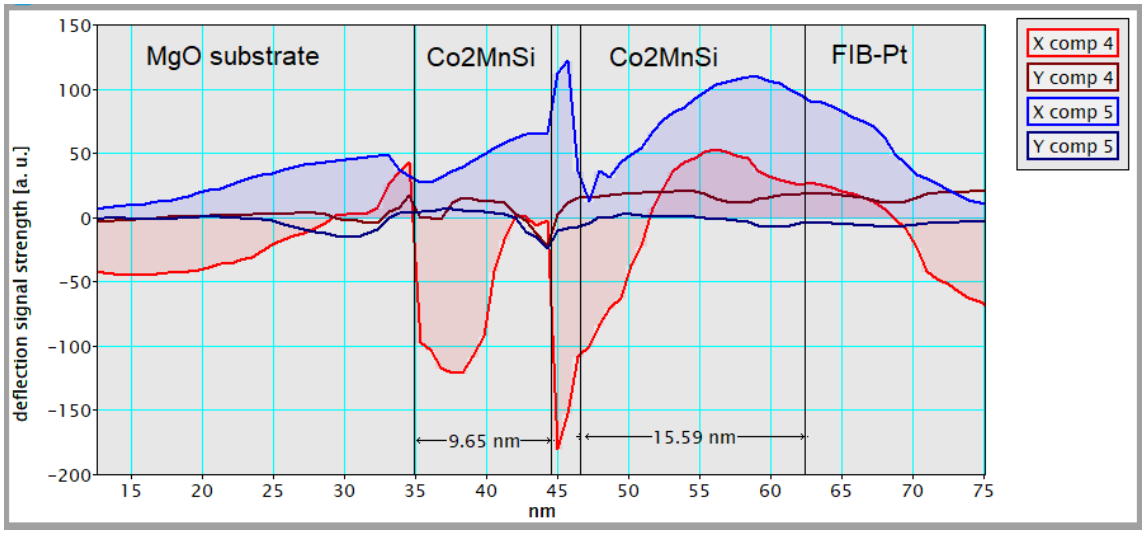

Figure 115: Overlay of both X and Y components of both datasets (4 and 5) aligned on the Y component, parts of the MgO substrate included for a better overview.

	10 nm Co_2MnSi	10 nm Co_2MnSi center	15 nm Co_2MnSi	15 nm Co_2MnSi center
Data 4	-0.34 ± 0.29 T	-0.60 ± 0.07 T	0.01 ± 0.20 T	0.15 ± 0.03 T
Data 5	0.21 ± 0.09 T	0.15 ± 0.07 T	0.22 ± 0.14 T	0.26 ± 0.06 T
Difference	0.55 ± 0.38 T	0.75 ± 0.14 T	0.21 ± 0.34 T	0.11 ± 0.09 T

Table 13: Results for the magnetic induction from the datasets 4 and 5, measured over the whole layer and only the central part omitting the interfaces. The measurement uncertainties are calculated from the standard deviations.

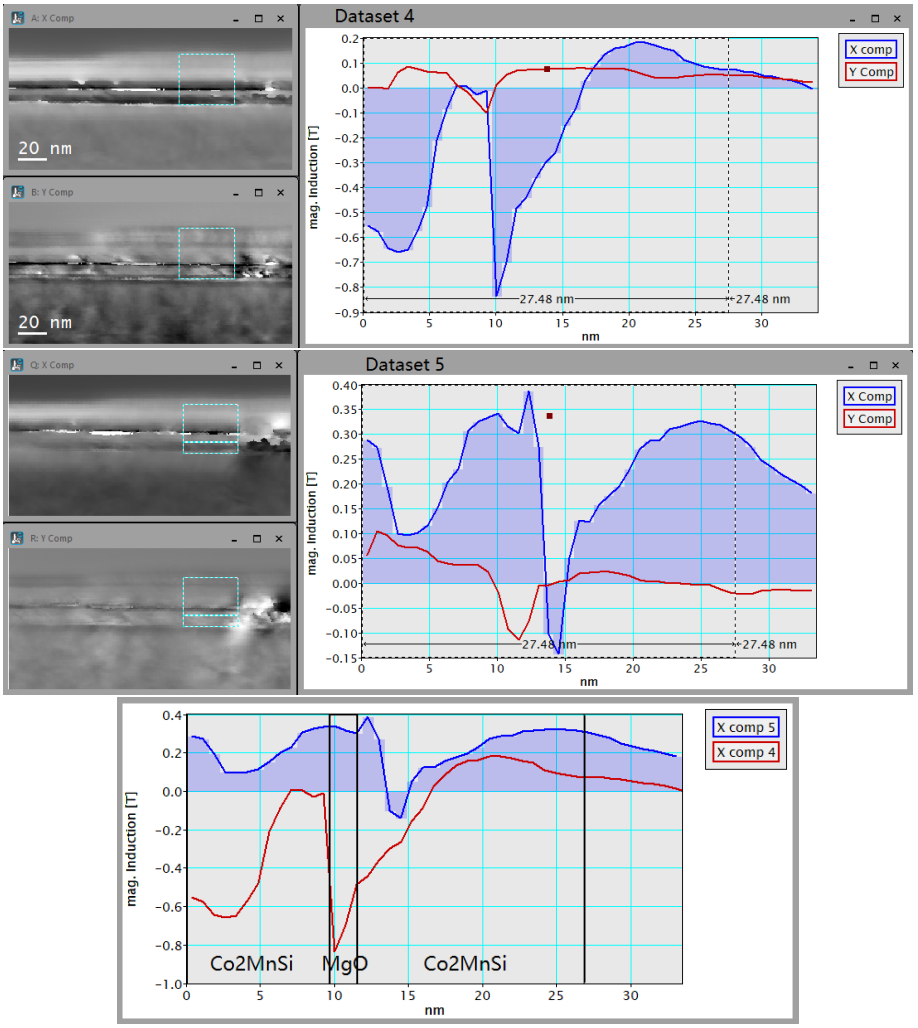

Figure 116: Pixelated DPC results for the datasets 4 and 5, which have been exposed to the external magnetic field in opposite directions, the layer system is indicated by a ROI (right). The component images are shown on the left. Substantial parts of the signal have been switched and are probably of magnetic origin. The deflections due to a change in the MIP at the interfaces is superimposed. Bottom: Both X-components superimposed.

3.7.5 Conclusions for the TMR Stack

The interface composition could be determined from FFT filtered HRSTEM HAADF images to consist of CoCo/O and MnSi/Mg on three investigated regions in two recorded images.
The specimen can be chemically separated in layers with sharp interfaces and interdiffusion can not be observed within the limits of the measurement conditions. The elemental composition matches the proportions for the intended composition Co_2MnSi. In these layers grains mostly of a size comparable to the layer thickness can be observed. The magnetic properties of the sample are in agreement with the simulations especially for the thin TMR stack, the domain walls and non-uniform magnetic states could not be observed in the TEM because of the fast switching behaviour. Considering the EMCD measurements both the Mn and the Co carry a magnetic moment although the need to measure on a different specimen of Co_2MnSi of a too large thickness makes accurate measurement and quantification difficult. In the DPC measurements the greatest effect is caused by the difference in the MIP between MgO and Co_2MnSi which combined with the closeness of the interfaces leads to a superposition of the deflections caused by the MIP difference and possibly magnetic signals of lower magnitude. Pixelated DPC has been able to measure a signal switched by the externally applied magnetic field of between 0.11 T and 0.75 T but with a large measurement uncertainty. Challenging on this specimen is the layer thickness of 10/15 nm which needs a high resolution to be able to detect any possible signal that could be assigned to its most likely origin. To obtain magnetic interface properties the interface region needs to be separated from the non-interface region by an increased layer thickness which leads to a overall non-functioning TMR Stack. This opens the door to investigate the properties of TMR stack on the nanoscale with up to atomic resolution with specially designed samples that allow access to desired properties without interference of other properties. For magnetic TEM investigations systems with lower MIP differences between the used materials are more suitable and are likely not to depend as much on the layer thickness and sample design.

3.8 The magnetic proximity effect

Spin currents play an increasingly important role in spintronics. Common detection techniques use a combination of a non-ferromagnetic with a ferromagnetic material where the inverse Spin-Hall effect [125] allows to convert the spin current into a transverse voltage in the non-ferromagnetic material. The use of nonmagnetic materials close to the stoner criterion can induce effects like the Hall effect or the Nernst effect based on proximity effects [126], which can introduce parasitic effects in measurements [127]. Magnetic proximity effects [128] are part of spintronic, superconducting, excitonic and topological phenomena [129] and thus of great importance in magnetic devices on the nanoscale. Materials close to the Stoner criterion are capable of showing such a magnetic proximity effect: The Stoner criterion explains how a system can become magnetic by lowering its energy with thus lower energy state corresponding to an imbalance in the number of spin-up and spin-down electrons in the electron shell of the atom, this creates an overall magnetic moment.

$$D_F U \geq 1$$

with D_F the density of states at the Fermi level and U the potential energy of the system. A short derivation of the Stoner criterion can be found in [130]. In the periodic system exist the well known ferromagnetic elements Fe, Co, Ni but also elements with a configuration that is very close to satisfying the Stoner criterion. These can become magnetic and satisfy the Stoner criterion by external influence of the ordered magnetic state close to the interface. For close-Stoner materials like Pd and Pt the magnetic proximity effect extends up to a few nanometers into the layer [131] [132] [133].

3.8.1 Possibilities to measure the magnetic proximity effect using electron microscopy

To measure the magnetic proximity in the TEM, the two magnetic measurement methods used in this thesis are capable with limitations. EMCD is the TEM/electron equivalent to XMCD which has been used for measuring the magnetic proximity effect often [128] [133] and is element-specific, in the TEM the EELS measurement is restricted to the range the spectrometer can measure and that is not superposed by the phonon interactions in the low loss region. This gives a measurable window of $\approx$ 200 eV to $\approx$ 1000 eV electron energy loss and the element to investigate needs to have a major EELS edge in this region. The ferromagnetic elements Co, Fe and Ni satisfy this condition, of the possible non-ferromagnetic candidates Pt (M_4 at 2202 eV, M_5 at 2122 eV)and Gd (M_4 at 1217 eV, M_5 at 1185 eV) are ruled out due to their edges being at too high energies. A possible candidate is vanadium with its major edges at 521 eV (L_2) 513 eV (L_3), where a proximity effect has already been measured using x-ray based methods [134] [135]. One issue of this material are possible edge overlaps with oxygen K (532 eV). An EMCD effect measured on the V edges would show the presence of a magnetic proximity effect.
Using magnetic DPC measurements to show the magnetic proximity effect is dependent on several conditions and may not be able to deliver the final proof: It is not element specific and especially at the interfaces sensitive to not only magnetic interactions but also to the change in the mean inner potential. The used materials therefore need to be very similar in their mean inner potentials and their contrast behaviour in the TEM. The best resolution of magnetic DPC is $\approx$ 1 nm in Low Mag mode with an additional

Lorentz lens, smaller magnetic structures cannot be resolved. The proximity effect needs to affect a certain amount of material apart from the interface to be measured using DPC, this requires a specimen with tailored properties. A multilayered specimen of alternating magnetic material and material that can show a magnetic proximity effect with different layer widths can allow to image the proximity effect by showing layers to be magnetic although their material is not ferromagnetic. The layer width needs to be up to two times the distance the proximity effect extends into the material from the interface and the chemical composition must be determined with high precision to exclude diffusion of the magnetic material as a source for the magnetism at that region. Excluding stray fields is manageable for external field sources but difficult for stray fields from the magnetic layers in the specimen itself.

3.8.2 Sample design and properties

A sample has been specially designed to consist of alternating layers of different thickness between a magnetic material inducing the proximity effect and a nonmagnetic element where a magnetic proximity effect should occur according to simulations. The thinnest layers should be about the width of the proximity effect in that material and fully magnetized by the magnetic layers next to it, the thicker layers should appear magnetically thinner than chemically, this measurements can be carried out using DPC. For an element-specific ability do detect a magnetic moment on this material with EMCD its EELS edges need to be in the well accessible range between low-loss and the noisier parts of the high loss, ideally between 200 and 800 eV.
The latter condition is fulfilled by vanadium, also there are simulations of a magnetic proximity effect in vanadium that reaches up to 1.9 nm into the layer [136] For the adjacent magnetic layers iron has been chosen. A layer system of Fe/V layers has been deposited by Co-sputter deposition by Dominik Graulich at room temperature on MgO substrate without additional cleaning. The base pressure has been $< 1 \cdot 10^{-8}$ mbar, the material has been sputtered from elemental targets for Fe (DC), Pt (DC) and V (RF) without a notable waiting time between the layers at 10 sccm Ar flow and 10 rpm substrate rotation. To obtain the correct layer thicknesses several gauge samples have been sputtered and evaluated before. The layer system consists of the following layers:
MgO substrate /(Fe(5 nm) / V(1 nm))x3 / (Fe(5 nm) / V(4 nm))x3 / (Fe(5 nm)/V(10 nm))x3 / Fe(5 nm) / Pt(10 nm, protection) which sums up to a total width of 105 nm for the layer system.

The 1 nm V layers should be fully magnetized, the 4 nm V layers nearly fully with a dip in the center and the 10 nm V layers should appear only $\approx$ 7 nm unmagnetized in DPC measurements. EMCD is needed to show that the V edge shows a magnetic moment to exclude that the DPC measures only stray fields from the iron. For evaluation of the measurements the chemical properties have to show if the layers are not mixed and how wide they are and the thickness profile of the lamella needs to be measured for the DPC data evaluation. The FIB lamella has been cut using the FEI Helios Dual Beam FIB including the second ion beam milling after thinning at 5 kV by Björn Büker. Thickness measurements have been performed by recording a zero-loss EELS mapping and evaluating it using the t/λ method. The calculated mean free path of iron (108.6 nm at 200 kV, $\beta = 8.333$ mrad) and vanadium (112.5 nm at 200 kV, $\beta = 8.333$ mrad) have been

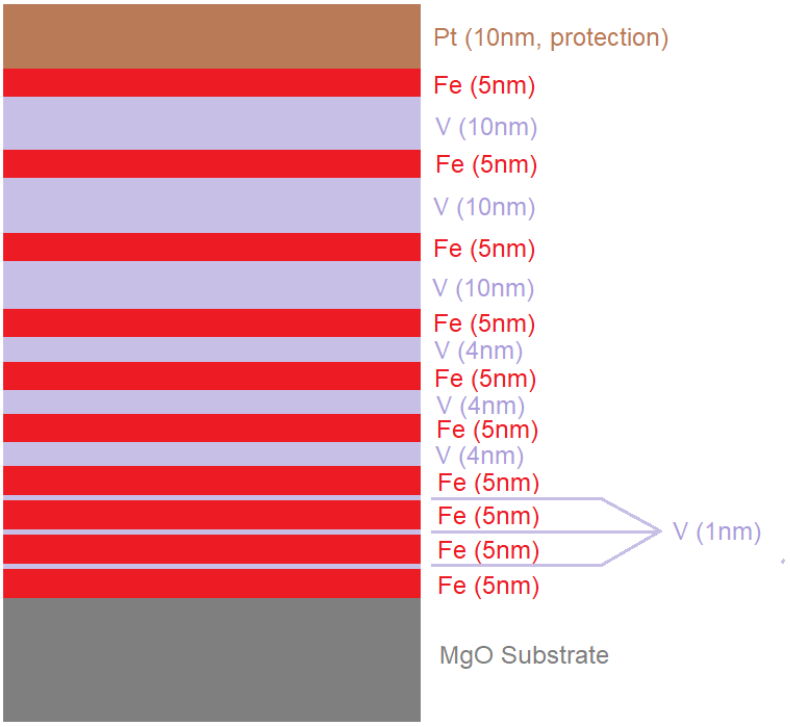

Figure 117: Design of the special sample for measuring the magnetic proximity effect of vanadium in the TEM.

used to convert the mapping into the specimen thickness. The result has been fitted by a quadratic function with the MgO/Fe interface as a starting point (fig.118):

$$-4.78766 \cdot 10^{-12}x^2 + 1.34349 \cdot 10^{-10}x + 1.1117 \cdot 10^{-7} \quad \text{(x in nm)}, \ \chi^2 = 15.64 \qquad (3.4)$$

The chemical properties have been measured by EELS, EDX and by a HAADF image, with EELS and EDX maps recorded back in Germany and the HAADF in Glasgow within days of the DPC measurements, so it most likely shows the properties of the specimen unchanged. While not in the TEM the specimen has been stored in a desiccator. Back in Germany months later another HAADF has been recorded so changes can be observed.
The quality of the layers needs to be determined, especially if diffusion or mixing of neighbouring layers of Fe and V occurred. Iron in the vanadium would lead to magnetic signal there and affect the DPC part of the proximity effect measurements.
As HAADF is sensitive to contrasts depending on the atomic number and only single elements have been used in this sample it should already indicate if the layers are not mixed. The HAADF results are shown in fig.119. The atomic number of vanadium is 23 and of iron 26, but the signal is $\sim Z^2$ so the layers can be distinguished.

The EELS results are shown in fig.120 and 121 with the first showing the whole layer system

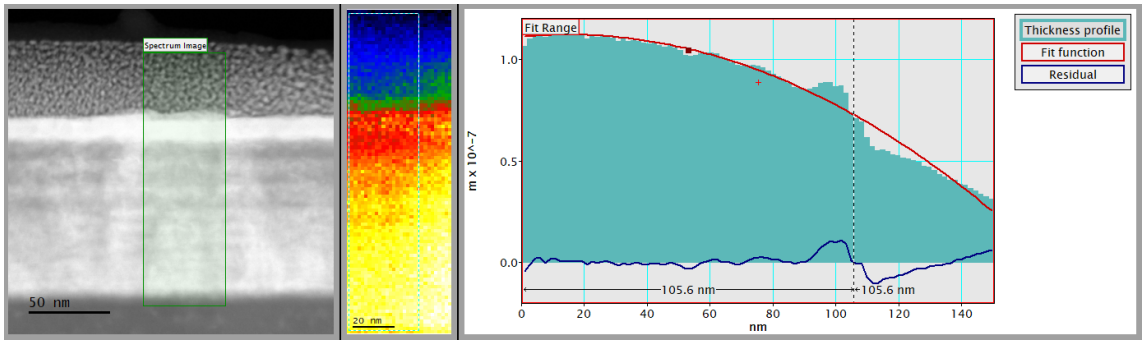

Figure 118: Left: Survey image for the thickness mapping. Center: thickness mapping (EELS, zero loss) with the region of the line profile indicated. Right: Thickness profile of the specimen with fitted quadratic function and fit residual, layer system indicated by ROI. The fit quality is given by $\chi^2 = 15.64$ arising mostly from the deviations at the transition between the layer system and the FIB-Pt.

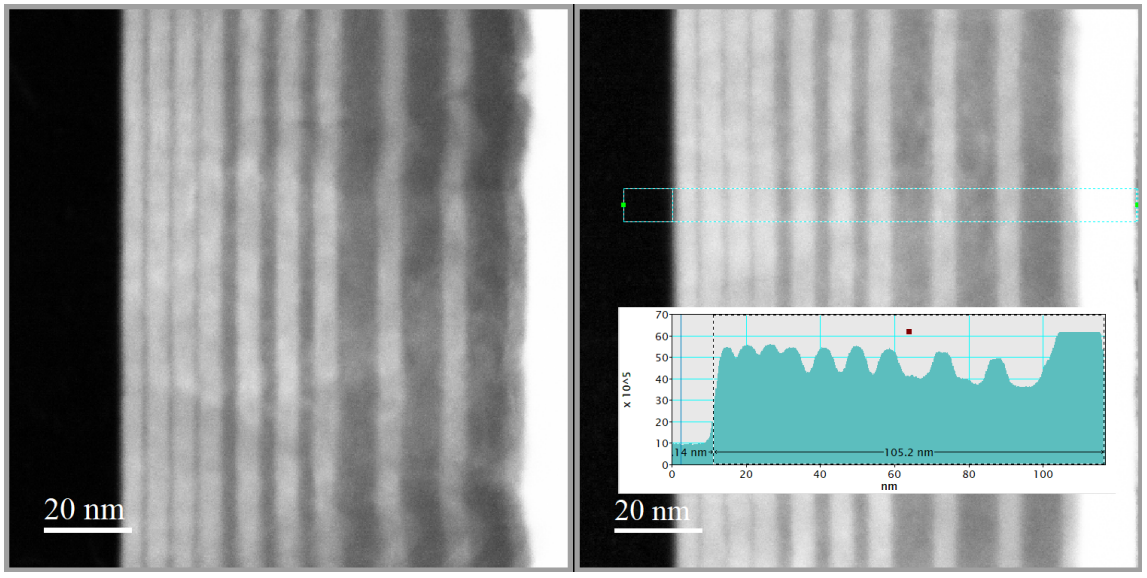

Figure 119: HAADF images of the V-Fe layer system recorded on the ARM200cF in Glasgow. Despite a difference in atomic number of only 3 between V(23) and Fe(26) the contrast allows to differentiate between both. On the right image a lineprofile is drawn across the layer system and included in the image, the ROI marks the layer system which is measured to 105.2 nm. The MgO substrate is on the left and the Pt protection layer on the right.

from MgO substrate to FIB-Pt and the second focuses especially on the thin vanadium layers of 1 nm and 4 nm thickness. It needs to be shown that no iron diffused into the vanadium. For the measurement the specimen has been tilted in (0, 0, 1) zone axis on the MgO substrate so the electron beam looks straight on the layer system. A simultaneous EELS/EDX mapping has been performed with the following parameters: 168×8 pixels at

0.1 sec exposure, 0.25 eV dispersion, $\beta = 41.67$ mrad, 5 mm entrance aperture, 320 V drift tube voltage, 1M magnification, 4 cm camera length. The elements iron (L edge at 708 eV), vanadium (L edge at 513 eV) and oxygen (K edge at 532 eV) have been mapped, shown below the elemental composition. Drift has been a major issue during acquisition and has been corrected post-acquisition. Then a line profile has been taken across the layer system, integrating over the whole maps.
The iron reaches zero between the 10 nm V layers and the 4 nm layers. The 1 nm V layers may contain iron, in this mapping they consist only up to 30% of vanadium. The step between each pixel is 0.72 nm so the 1 nm V layer is only hit by one scanning pixel or two pixels on the edges of the layer. Also the thickness of the specimen of ≈ 100 nm leads to electrons hitting the neighbouring layers if the specimen is not perfectly tilted, along with the broadening of the drop-shaped interaction volume of the electrons in the specimen below its surface, which leads to signal from a greater volume including the neighbouring layers especially in thick specimen. The 1 nm V layers are neighboured by 5 nm Fe layers, this in combination with the shape of the interaction volume can explain the high amount of Fe in the 1 nm V layers. This needs further investigation at higher resolution. The MgO substrate/Fe interface represented by O/Fe can be assumed sharp and act as an example for a sharp interface. The Fe never reaches 100% except in the topmost layer near the Pt protection layer (in the EELS result shown as a hole between Fe and O), so the Fe layers possibly contain a small amount of V. This might be due to altering in the V-containing specimen which also has been observed on the V/Co_2FeSi/V specimen (chapter 3.6.3). The EELS/EDX measurements could only be performed in Germany 5 months after the DPC/HAADF measurements in Glasgow because the image filter in Glasgow has been sent off for repair and the Covid pandemic prohibited access to the microscope in Germany. Differences in the specimen due to altering can only be estimated by analysis of the HAADF images because it is the only method available both in Glasgow with the DPC measurements and in Germany where finally EELS/EDX characterization has been performed. For the proximity effect it does not matter as the purity of the V layers is important for the DPC measurements and EMCD is element sensitive. Some oxidation occurred in the part of the specimen containing the 1 nm V layers, but it is not more than 10% at maximum and might result from overlap of the V and O edges instead of oxidation and insufficient separation since the O there coincides with the location of the V and oxidation is expected to affect thinner specimen parts stronger and there almost no oxidation can be measured. The reason to assume this is the coincident localization with the V and its increase, also it shows only where the V signal is not as strong.

To obtain more information on the thin V layers another mapping has been acquired focusing only on these part of the specimen with the following parameters: 200×9 pixels at 0.1 sec exposure, 0.25 eV dispersion, $\beta = 41.67$ mrad, 5 mm entrance aperture, 320 V drift tube voltage, 1.5M magnification, 4 cm camera length. The step width between two pixels is 0.41 nm. Again the elements Fe, V and O have been mapped. The results are shown in fig.121.
The decrease in stepsize and increase in resolution changes the amount of Fe in the 1 nm V layers from 70% to 50%. This allows the conjecture that even higher resolution might be able to show good quality V layers, but this measurement can only be conducted on a further thinned specimen. Between the 4 nm V layers the amount of Fe goes to zero for $\approx$2.5 nm. This shows the layers are separated from each other and no mixing occurs as

the effects on the interfaces between the layers are likely to result from specimen thickness and measurement parameters.

The EDX measurement is shown in fig.122 and includes the elements V, Fe, Mg, O and

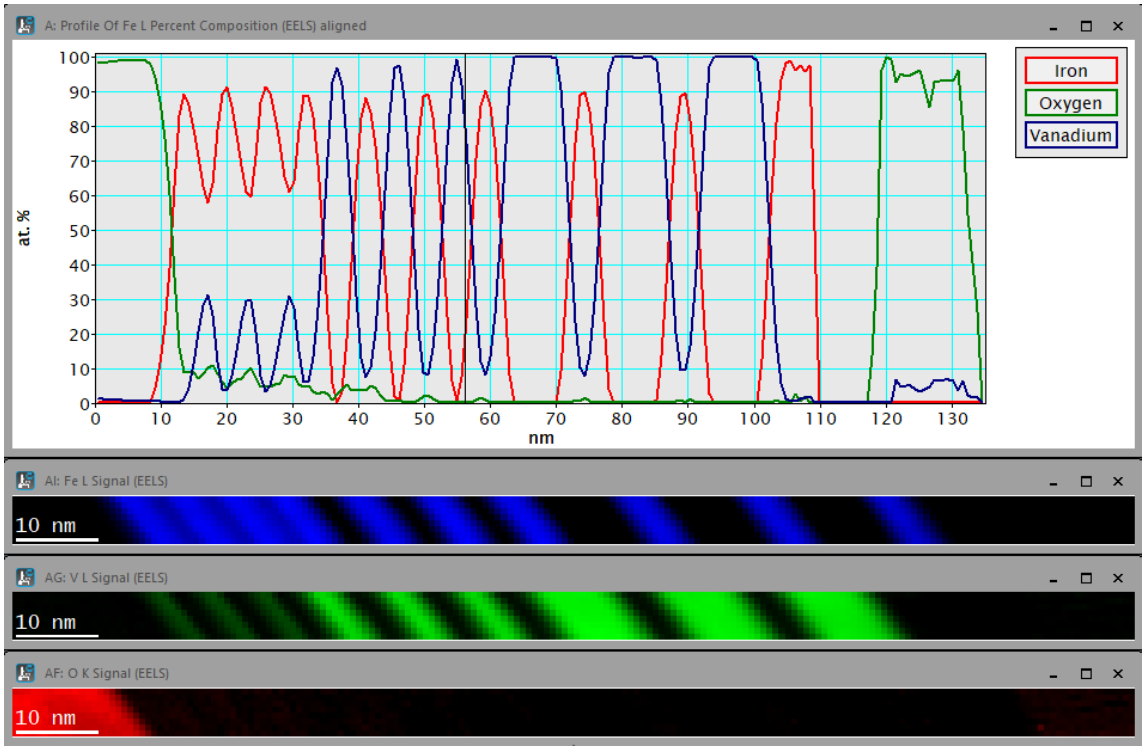

Figure 120: EELS result for the V-Fe layer system. Top to bottom: EELS result for the elemental composition, iron elemental map, vanadium elemental map and oxygen elemental map. The shown maps are not drift corrected. For the elemental composition the maps have been drift corrected. The MgO substrate is always on the left side.

Pt, so the protection layer of Pt is also visible. It has been acquired simultaneous with the first EELS map and contains far less counts: $\approx$ 37000 in 1040 pixels. The result is noisier and the 1 nm V layers can only barely distinguished, but the information about the chemical composition is consistent with the EELS measurement.

As the only measurement sensitive to chemical composition conducted both on the lamella in Glasgow and months later back in Germany is the HAADF image, it has been used to check if the specimen has changed notably during the time. Any alteration would change the slope of the contrast change at the interfaces. The Glasgow image has been acquired at 6 cm camera length, 1.5M magnification, 200 kV and 512×512 pixels image size, the Paderborn image at 4 cm camera length, 1.2M magnification and also 200 kV with an image size of 2048×2048 pixels on an JEOL ARM200F. The HAADF detector in Glasgow covers $90-370$ mrad at 6 cm camera length. In Paderborn the annular dark field detector has been used with a coverage of $140-550$ mrad at 4 cm camera length. The differences in the detectors and experimental conditions can lead to limited comparability of the measurements. On both images a line profile has been taken across the layers in an even region, both times with a width of 30 pixels, the region of the line profile is not the same in

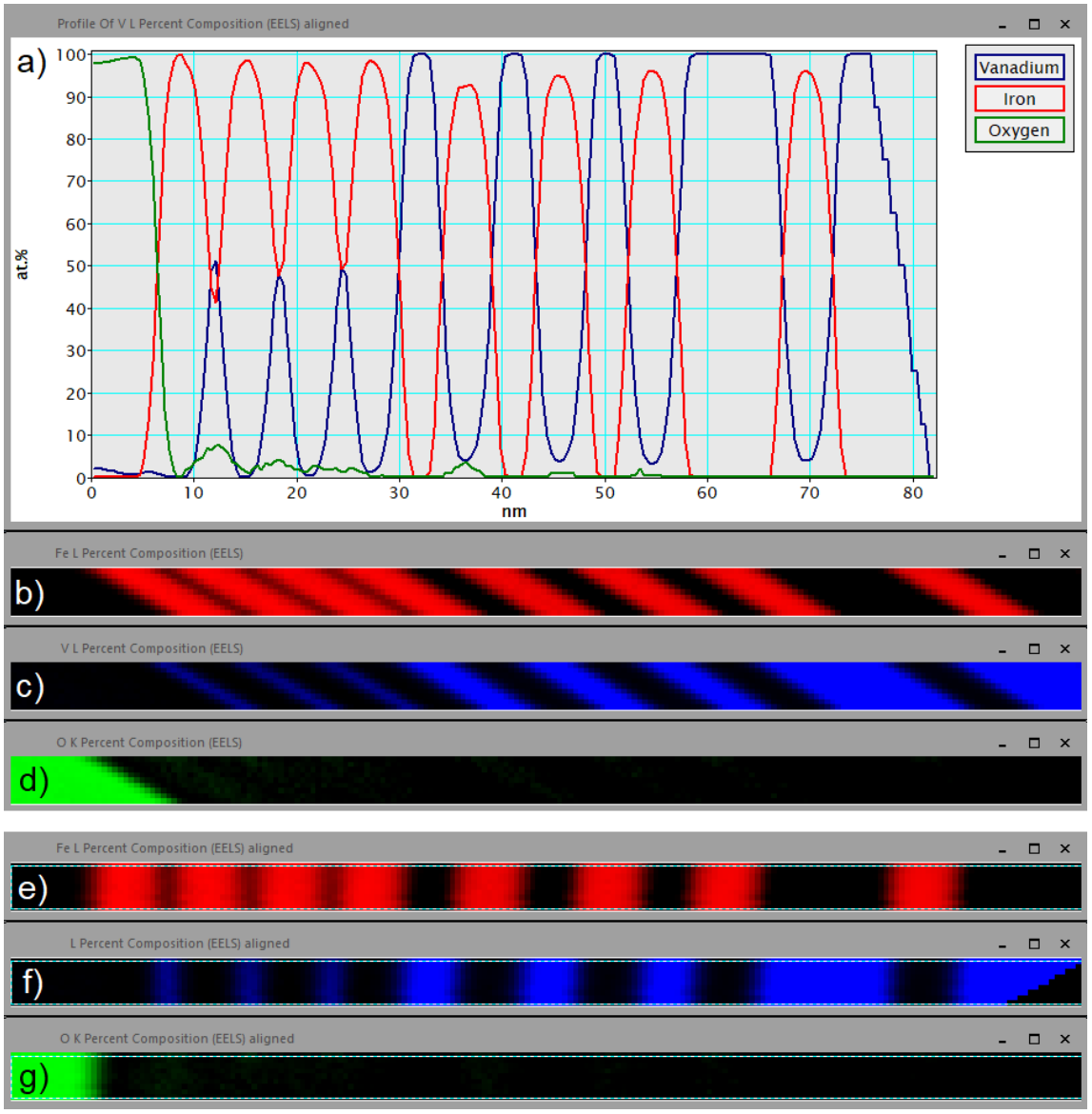

Figure 121: EELS result for the part of the V-Fe layer system containing the thin vanadium layers (a), MgO substrate always left. Below: (b-d) show the EELS maps for iron, vanadium and oxygen, (e-f) the post acquisition drift corrected iron, vanadium and oxygen EELS maps.

the two images. The maximum intensity in each profile has been used for normalization to 1. An overlay of both profiles has been created and both profiles aligned with each other, shown in fig.123. The protection layer consisting of the heavy element (Z=78) Pt shows the highest intensity. On the MgO substrate (right) the signal strength differs between the two measurements, for the Fe layers around the 1 nm V layers the difference is very small but increasing to about 20% of the signal strength in the region with the 20 nm V layers. If iron would have mixed with the vanadium, the Z-contrasts would mix and result

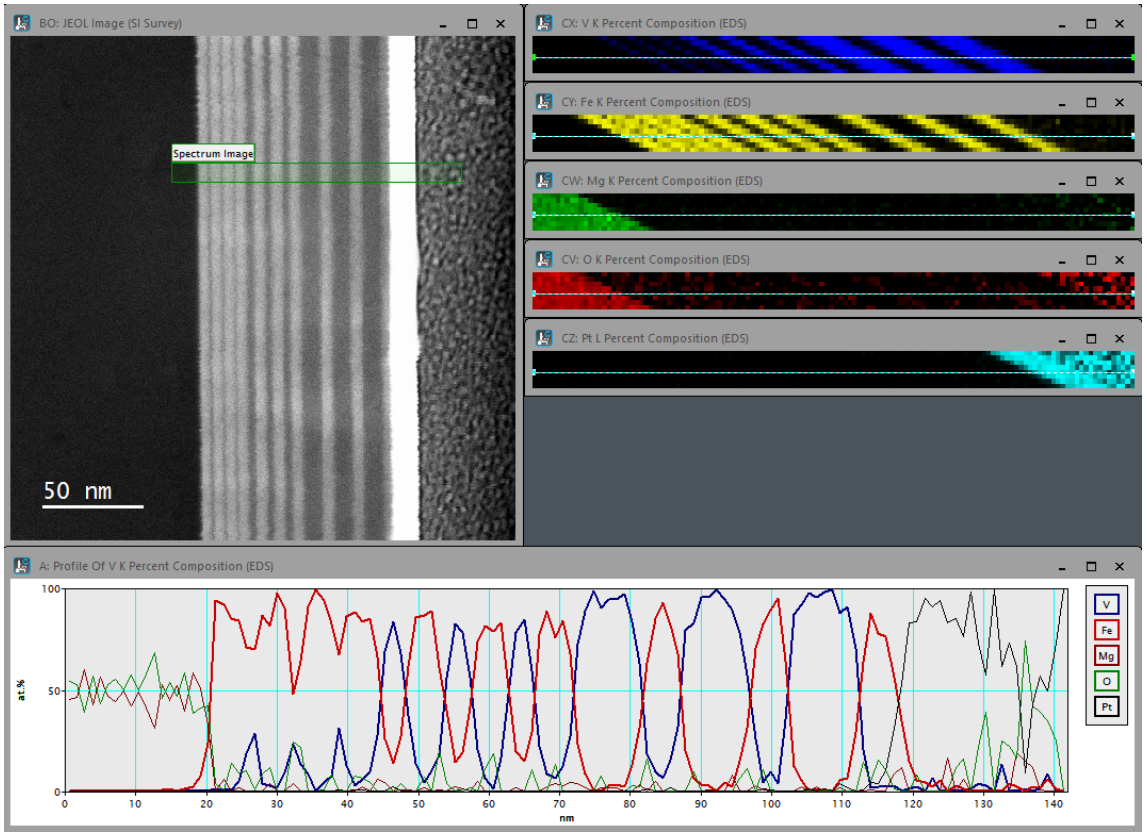

Figure 122: EDX results for the V-Fe layer system. Top left: Survey image with indicated region from where the SI has been recorded, top right: EDX elemental maps for the elements vanadium, iron, magnesium, oxygen and platinum, not drift corrected. Bottom: Elemental composition from a line profile overlay for the five elements, taken on the region indicated by the line in the elemental maps.

in a contrast between those of each element and the change in contrast at the interfaces would be smeared. But the slope on the interfaces is very comparable, showing no notable change of the specimen.

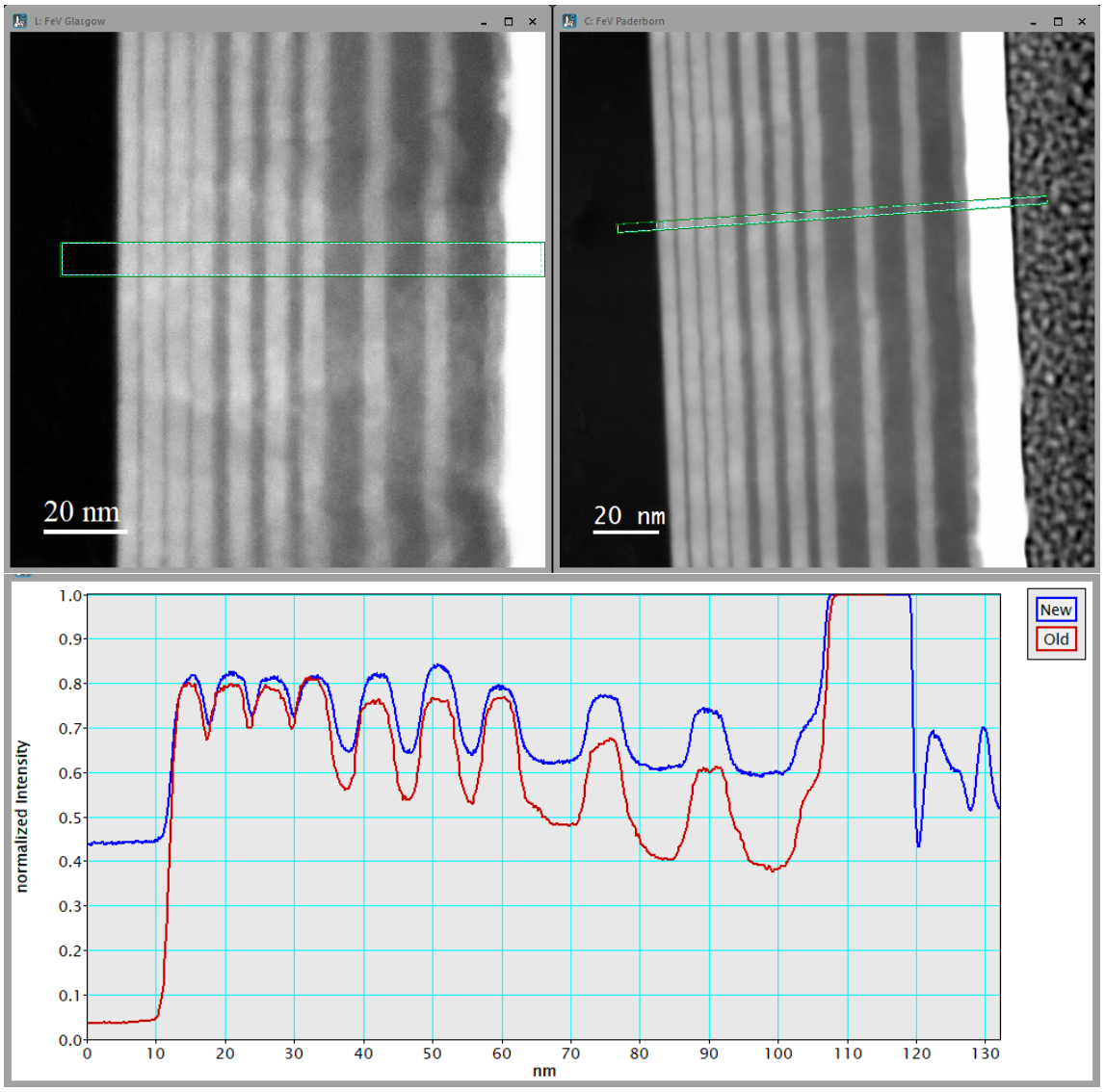

Figure 123: HAADF images of the V-Fe specimen recorded in Glasgow (top left) and five months later in Paderborn (top right). The region from which the line profile has been obtained is highlighted by a green rectangle. Bottom: overlay of both line profiles with normalized intensity.

3.8.3 DPC results

DPC measurements have been carried out in Glasgow on the ARM200cF using the 8-fold segmented detector system and the Medipix3 pixelated detector in Low Mag mode. To apply an in-plane magnetic component, the specimen has been tilted with the objective lens switched on to 0500 which corresponds to ≈ 0.1 T with maximal tilting angles of $\pm 25°$ giving a maximum external field of ± 0.0423 T which is enough to switch iron layers of 50 nm in a lamella. The measurement itself has been obtained after tilting back to 0°. A series of measurements has been acquired in different magnetic states including sections of Fe layers magnetized in opposite direction and domain walls in Fe layers (fig.124), due to magnetic hysteresis more measurements at one magnetization direction have been acquired than at the other. The magnification of these measurements ranges between 250kx and 1.2Mx, corresponding to a pixel distance of 1.48 nm to 0.31 nm. The maximum resolution of the probe in this Low Mag STEM mode is ≈ 1 nm, therefore at higher magnifications there is an overlap of the area scanned by the beam disc, still it is considered a new pixel. In this case it corresponds to up to three times averaging out noise and artifacts. The pixelated DPC results are omitted in this analysis because their resolution (step size between pixels) is not sufficient for this analysis to show proximity effects.

The measurements at lower magnification have been sufficient for a first idea of the

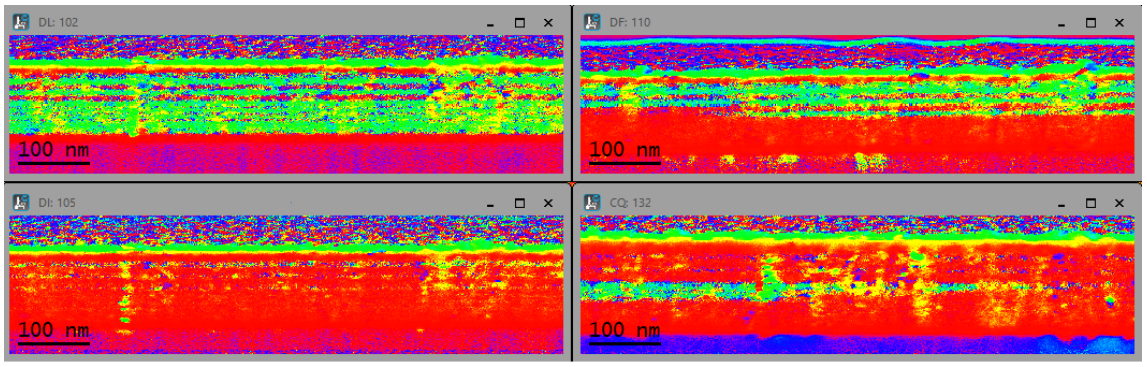

Figure 124: Selection of unprocessed segmented DPC colour images (MgO substrate at the bottom) at lower magnification (250kx) depicting the different magnetic states. Magnetic domain walls can be observed in both images on the right where one layer switches between green and red.

properties of this multilayer system, for detailed analysis a large set of 512×512 pixel datasets has been acquired at 1.2M magnification where 1 pixel represents 0.31 nm. A selection containing different magnetic states has been used for analysis (fig.124 bottom). Again the procedure of rotating the results to minimum contrast in one component has been applied. The rotation angle for the first collection of datasets is 71°, for the second collection $80-81°$. Using lineprofiles it has been ensured that the signal is accumulated in comp1 and comp2 is close to zero, then a line profile with 100 pixels integration width has been obtained from all used datasets on a region where approximately no grains or defects have been visible with the MgO/Fe interface as the starting point (fig.126). The result for the deflection has been processed according to eq. 2.39 using the thickness function eq.

3.4 to obtain the integrated magnetic induction.

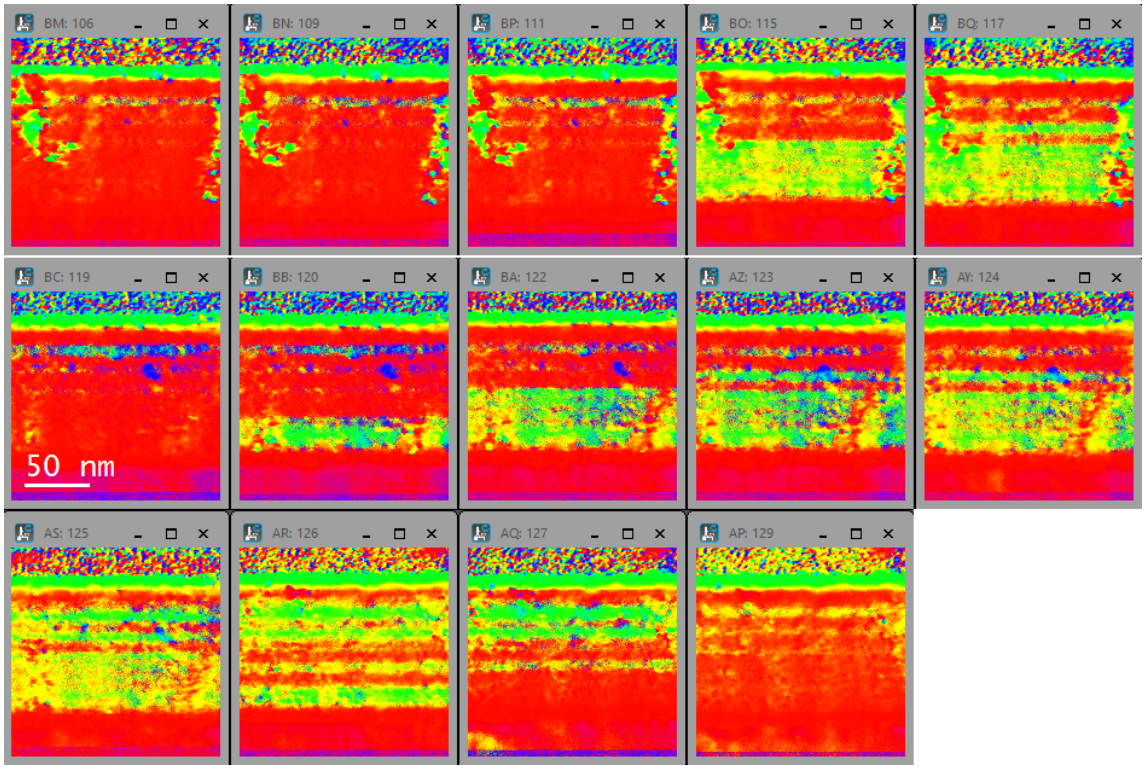

Figure 125: colour images from the selected datasets: Top row set 1 (5 datasets), both rows below set 2 (9 datasets).

The results for the deflection and the calculated magnetic induction are shown in fig.127 with the magnified section of the layer system without the peaks induced by the interfaces MgO/Fe and Fe/Pt shown at the bottom. The difference of the magnetic induction is calculated by subtracting one dataset that is at least in parts magnetized in the opposite direction from the other from another and dividing the resulting signal by two and shown in fig.128.
In set 1 only part of the layers have been switched magnetically so no total opposite magnetization data is available. The part including the 4 nm and 1 nm layers has been switched. In set 2 the system has been fully magnetized in both directions and states in between where only parts of the specimen have been switched occurred and have been included. The thin 1 nm V layers are not visible in the magnetic signal, the reasons are the layer thickness is comparable to the resolution in this mode, also a small tilt away from the perfect zone axis orientation of the specimen is enough that with the specimen thickness of $\approx$ 100 nm the beam crosses already the neighbouring Fe layers and shows magnetic deflection. The 4 nm V layers are different, in the case of a magnetic proximity effect they should also be magnetized in the same direction as the Fe and with the $\approx$ 1 nm resolution the layer should appear as magnetized. This can be observed, the decrease of 11.1% (measured over 2.48 nm on the difference signal, the difference between the two

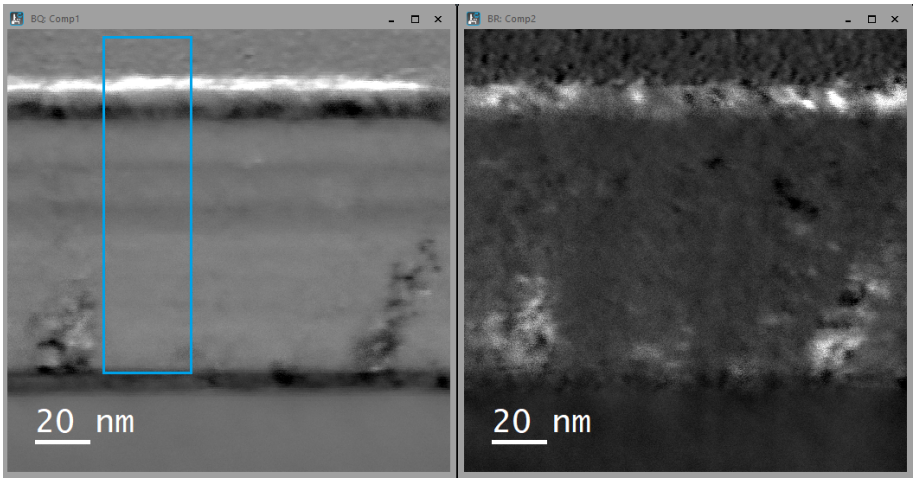

Figure 126: Comp1 (left) with the region highlighted from where the lineprofile has been obtained and comp2 (right) of one of the datasets, MgO substrate at the bottom. The contrast is accumulated in comp1, comp2 shows no visible layer system contrast. The grains and defects are visible in both components.

positions on peak and between two peaks has been calculated) in magnetization is notable but small. Therefore the 4 nm V layers can be considered to be magnetic, the proximity effect can reach up to 2 nm±1 nm into the V layer.
In the 10 nm V layers between 5 nm Fe the magnetic induction reaches approximately zero in the center of the layer, to determine what can considered to be zero magnetic induction the difference between two datasets of the same magnetization direction is obtained from the region of the layer system where it has the greatest values. This gives a value of ±0.041 T from the datasets 125-123 and ±0.068 T from the datasets 122-129, below the signal is considered to be zero. The zero condition is fulfilled for the central 4.95 nm of the 10 nm V layer, giving a magnetically influenced region of up to 2.5 nm next to the Fe layers of which 1.5±1.0 nm show a magnetic deflection of more than half of the maximum value and can be considered to show a magnetic proximity effect.
Because of the limited resolution and the DPC method being not element specific this results can only show a strong hint of a magnetic proximity effect in vanadium. Comparing these results to a similar layer system where vanadium is replaced by a material far away from the Stoner criterion that cannot be magnetically influenced but still is of similar contrast in the TEM could give further insights, this needs additional research. To prove the proximity effect, additionally measurements of the XMCD/EMCD type are necessary.

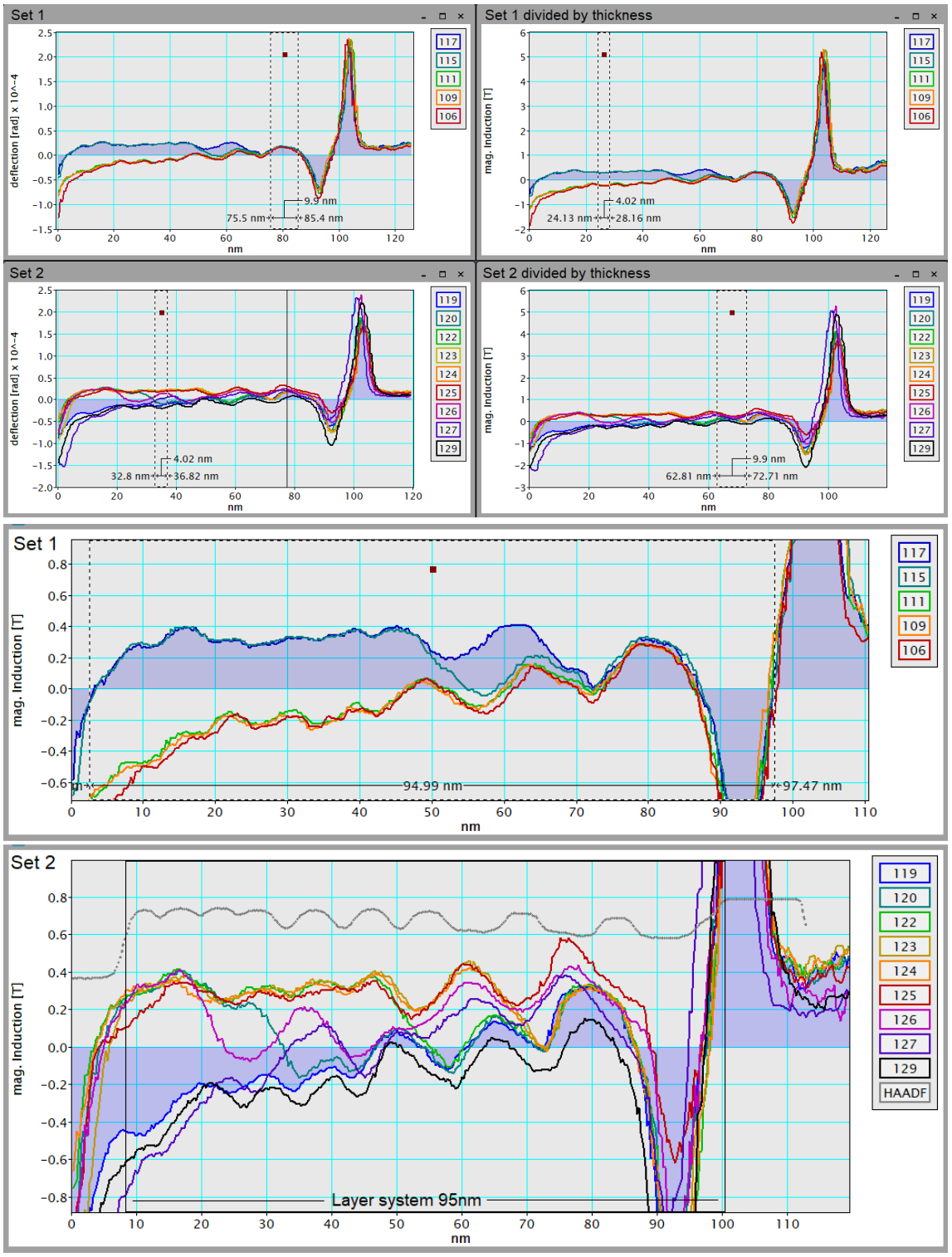

Figure 127: Top: Deflections and magnetic induction for the Collection of datasets set 1 and set 2. Bottom: Magnetic induction for set 1 and 2 with special emphasis to the Fe/V multilayer part, for set 2 overlaid with the rescaled intensity profile of the HAADF image.

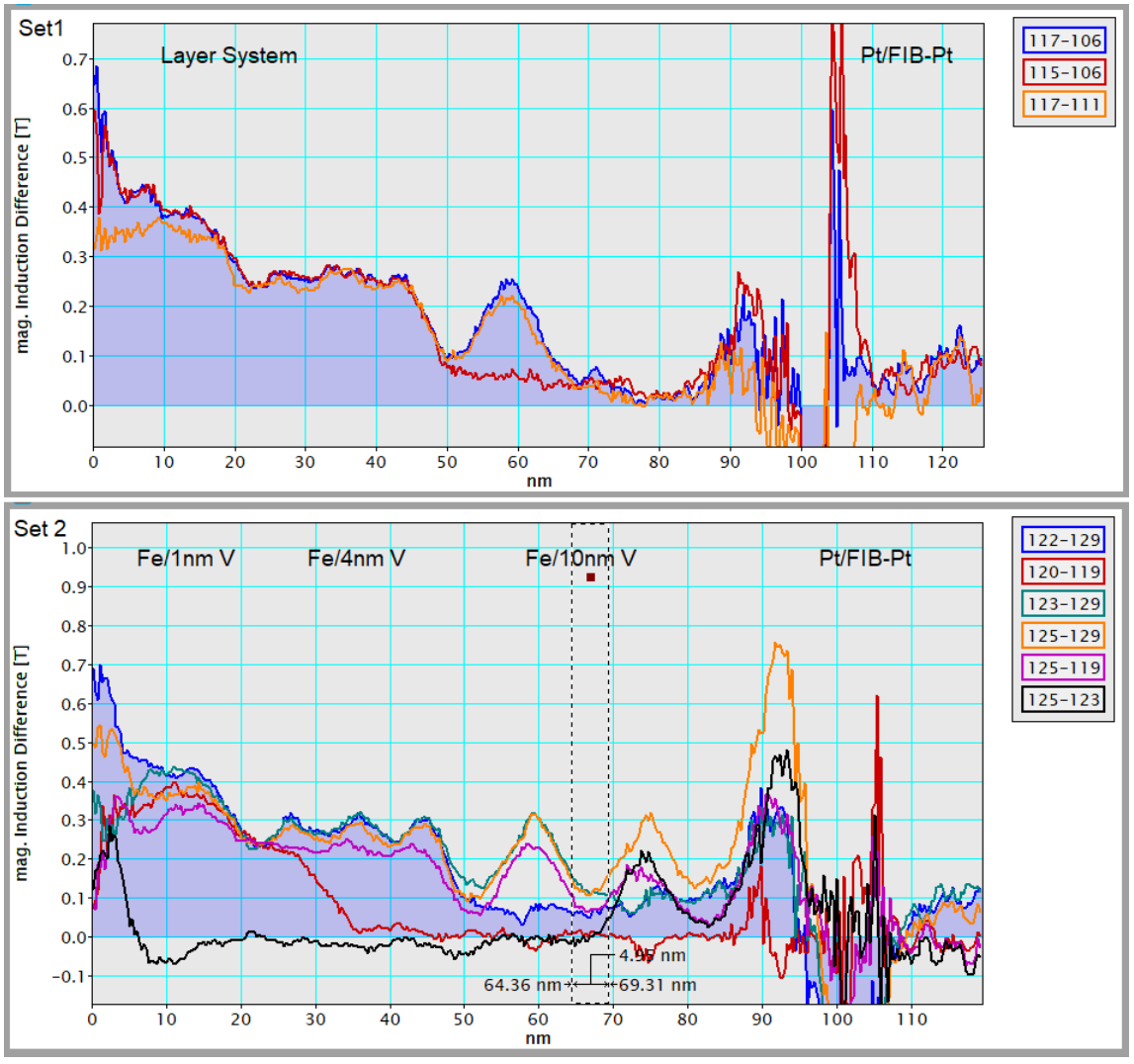

Figure 128: Difference signal results of the magnetic induction for parts of the datasets of set 1 (top) and set 2 (bottom), the numbers of the used datasets are noted in the legend. One part where the signal is considered to be zero is highlighted by a line profile. The blue line indicates zero in the 10 nm V layer part because the original datasets 122 and 129 have been magnetized in the same direction in this part.

3.8.4 EMCD results

EMCD measurements have first been performed in TEM Mode while illuminating the whole layer system. The measurement shows element specific if there is a magnetic moment. The specimen has been thinned further for later measurements only so its thickness is around 100 nm, which is very thick for EMCD measurements and not suitable for STEM EMCD. The rethinned thickness has been measured via EELS zero loss mapping (ARM200F, 200 kV, $\beta = 13.9$ mrad which gives a mfp of 101.9 nm for V and 98.3 nm for Fe using the Malis method [32]) and is shown in fig.129. The region of the EMCD linescan ranges between $\approx$ 30 nm and $\approx$ 60 nm in thickness, start of the linescan is on the thinner end according to the survey image (fig.3.8.4).

The crystal lattice of V and Fe is for both a bcc lattice with the lattice parameter of 0.2868

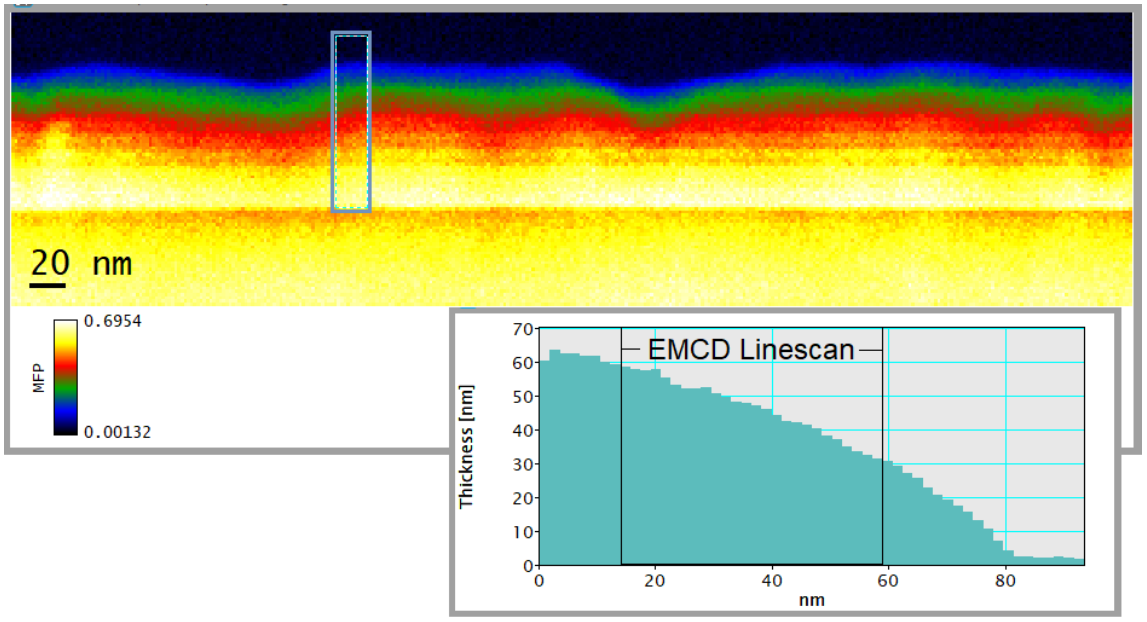

Figure 129: Thickness map of the rethinned part of the Fe/V multilayer lamella with the calculated thickness across a line profile on the EMCD position shown bottom right.

nm for Fe [137] and 0.30267 nm for V [138]. The lattice mismatch is $\approx$ 5.5% which leads to strain at the interfaces but should allow epitaxial growth of at least large crystallites up to the dimension of the whole layer system. For EMCD there is the advantage that the orientation of the reflexes are expected not to change their direction and therefore allowing linescans across the alternating V/Fe layers. The reflexes usable for the systematic row are (2,0,0), (-2,0,0) or (1,-1,0), (-1,1,0) for both V and Fe, the used reflexes are the (1,-1,0), (-1,1,0).

As visible in the HAADF image (fig.123) the layer system is not monocrystalline and the grains reach the width of the whole layer system. Therefore the crystal orientation changes with the position, which has to be taken into account for any EMCD measurements. During the tilting and measurement process for EMCD it could be observed that most of the grains/layer system has grown in a similar orientation and shows a systematic row if tilted into this condition on one part of the layer system. One measurement has been

conducted mostly or only on one grain.
The TEM mode EMCD measurements have been acquired consecutively and cover the four possible EMCD positions nearest to the central beam and have been measured in the order indicated in fig.130 left.

It has to be considered how much EMCD effect of the theoretical total value can be

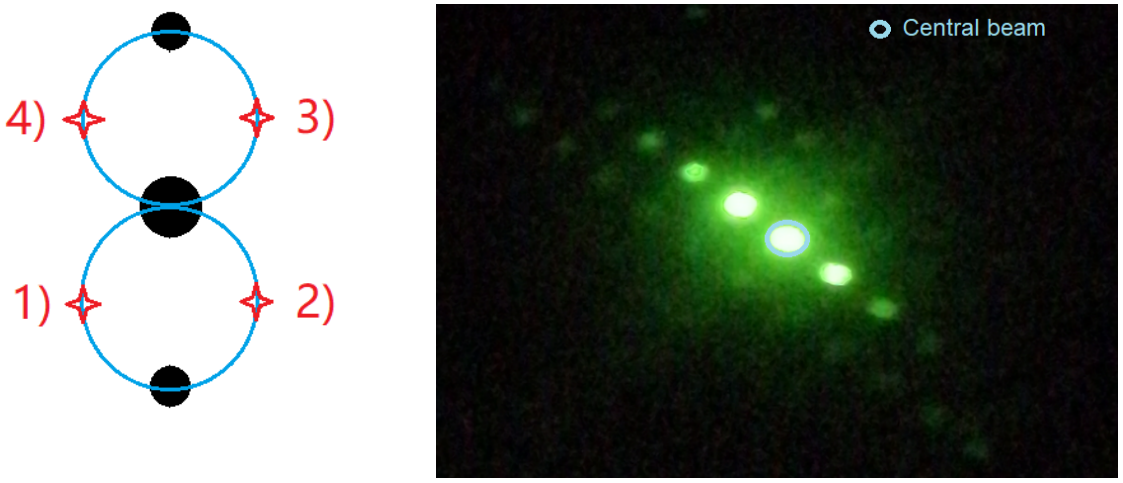

Figure 130: Left:Sequence of the TEM EMCD measurements and their position on the two Thales circles with respect to the systematic row. Right: phone image of the viewing screen showing a tilt already close to the used systematic row on this V/Fe multilayer system, the central beam is encircled.

measured by illuminating the whole layer system. This is estimated by calculating which amount of the vanadium shows a proximity effect and contributes to the EMCD effect. For a proximity effect (PE) reach of 0.5 nm, 1.0 nm, 1.5 nm and 2.0 nm the relation of contributing vanadium to total vanadium is calculated (tab.14):

	PE 0.5 nm	PE 1.0 nm	PE 1.5 nm	PE 2.0 nm
1 nm V layer	1.0 nm / 15 nm	1.0 nm / 15 nm	1.0 nm / 15 nm	1.0 nm / 15 nm
4 nm V layer	1.0 nm / 15 nm	2.0 nm / 15 nm	3.0 nm / 15 nm	4.0 nm / 15 nm
10 nm V layer	1.0 nm / 15 nm	2.0 nm / 15 nm	3.0 nm / 15 nm	4.0 / 15 nm
Total	$\frac{3}{15} = 20\%$	$\frac{5}{15} = 33\%$	$\frac{7}{15} = 47\%$	$\frac{9}{15} = 60\%$

Table 14: Fraction of the vanadium showing the proximity effect, the EMCD effect on vanadium is reduced to 20% to 60% depending on the reach into the vanadium layer from the V/Fe interface.

The parameters used for the TEM mode measurements are 200 kV, 600kx magnification, 10 sec exposure time, Gatan Quantum ER post-column image filter, selected area aperture 10 μm, diffraction mode: 60 cm camera length, 5 mm spectrometer entrance aperture, dispersion 0.25 eV/channel, drift tube voltage 350 V. The specimen has been tilted into a

systematic row condition on the V/Fe layer system (fig.130 right). The two reflections next to the transmitted beam have been used for measuring EMCD with the positions according to those shown in fig.130 left. The first position spectrum always contained more counts than the subsequent ones and on position 4 far less counts until the elemental edges are barely recognizable. From before the second thinning of the lamella one measurement containing all four positions is shown and one measurement where only position 2 and 3 could be evaluated. According to XMCD measurements the shape of the dichroic signal

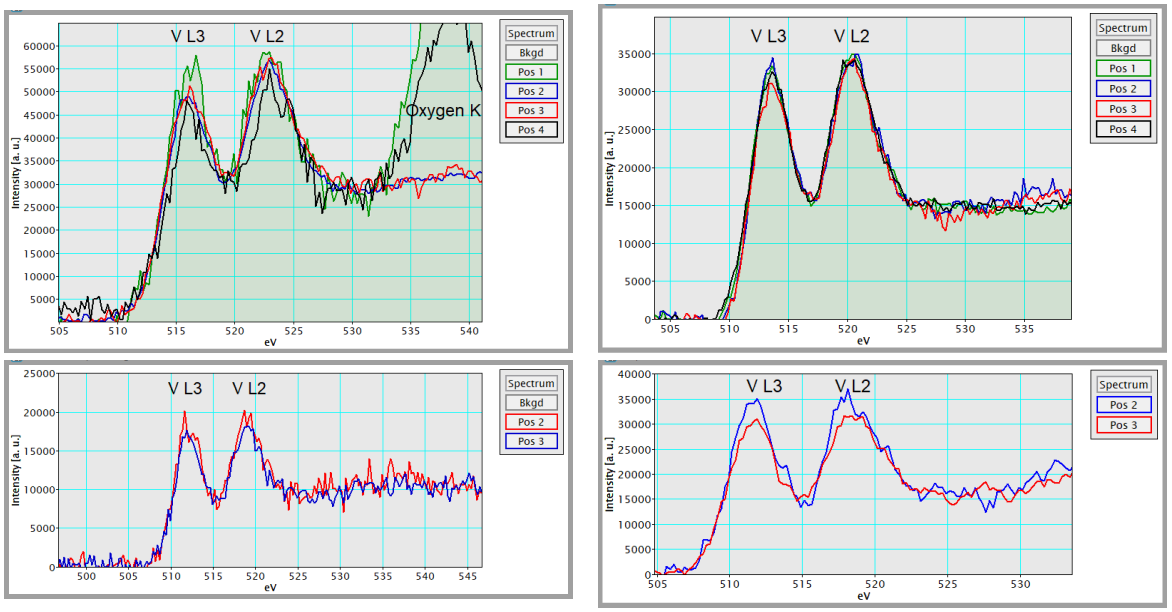

Figure 131: EMCD results for the V/Fe multilayer system before (left) and after (right) the second thinning. EELS spectra on the V $L_{2,3}$ edge have been obtained from up to four EMCD positions. Top: all four EMCD positions. Bottom: Position 2 and 3.

on vanadium has the same sign on both the L3 and L2 edge [135]. The EMCD effect on the measurements shown in fig.131 has been calculated in tab15: The effect is in

	Measurement thick			Measurement thin	
Position	V L3	V L2		V L3	V L2
Pos. 1-2 (1)	$7.6 \pm 2.1\%$	$1.3 \pm 1.8\%$		$-1.6 \pm 2.4\%$	$0 \pm 2.3\%$
Pos. 2-3 (1)	$-1.6 \pm 1.9\%$	$-0.6 \pm 1.7\%$		$5.0 \pm 1.8\%$	$1.0 \pm 1.6\%$
Pos. 3-4 (1)	$3.4 \pm 3.0\%$	$2.2 \pm 2.6\%$		$-2.4 \pm 2.0\%$	$0.1 \pm 1.9\%$
Pos. 4-1 (1)	$-9.4 \pm 2.2\%$	$-2.9 \pm 2.2\%$		$1.1 \pm 1.7\%$	$-1.2 \pm 1.6\%$
Pos. 2-3 (2)	$6.3 \pm 3.2\%$	$4.9 \pm 3.5\%$		$6.1 \pm 3.7\%$	$7.7 \pm 3.6\%$

Table 15: Results of two TEM EMCD measurements illuminating the full V/Fe multilayer system. Thick measurement on the lamella with thickness function 3.4 (ref. fig.131 left), thin measurement on the rethinned lamella (ref. fig.131 right). In both cases an aditional measurement on position 2 to 3 (2).

many cases comparable to the error calculated from the noise on the spectra before the edge after background subtraction, which gives the uncertainty of the measurement. The measurement of position 2 to 3 shows in 3 of four cases a stable effect of $\approx 5 - 7\%$ with

the uncertainty measuring approximately half of the result. This is an indication for a real EMCD effect that proves a magnetic moment on the vanadium. The presence of oxygen on the surface of the lamella gives the oxygen K peak at 532 eV that has an effect on the behaviour of the higher losses as they can not be considered to be related only to the vanadium. This limits the space for aligning the spectra in the case of a difference in counts to the region post-edge of vanadium that is pre-edge to oxygen. The count rate lowers with time and at each following position less counts may occur due to increasing damaging of the specimen. For at least comparable experimental conditions STEM-EMCD is a convenient choice.

STEM-EMCD measurements have been performed on the V/Fe multilayer system using a 16 point linescan using the EMCD positions 2 and 3. The parameters for the STEM measurements are 200 kV, 800 kx magnification, 4 cm camera length, 10 μm aperture to obtain at least at most separated diffraction discs, spot size 4C, 15 sec exposure time, Gatan Quantum ER post-column image filter, 5 mm spectrometer entrance aperture, dispersion 0.5 eV/channel, drift tube voltage 400 V. Several series of these EMCD linescan measurements have been acquired on different areas of the specimen, those showing altering in the diffraction conditions where additional diffraction spots than those of the systematic row have been excited are discarded. The measurements presented here have the transmitted beam/central spot always at almost the same place in the spectrum, nearly no drift or descan occurred (fig.3.8.4 bottom right). Therefore evaluation for EMCD has been possible using fixed positions to extract the spectra on the two EMCD positions, the script for automated data analysis from Appendix 6.13 has been simplified and used.

The linescan has been drawn across the central part of the lamella where especially the 4 nm V layers are present and reaches into both neighbouring regions with 10 nm and 1 nm V layers. The step size is 2.8 nm between two points. In all acquired spectra both V and Fe edges are present but with different intensity. This results from the tilting of the specimen ($\beta = -1.8°$ with the layer system parallel to the α direction), the beam always crosses both types of layer. The EMCD signal is shown as an overlay of all 16 points in fig.133. A shift on the Y axis is not possible without destroying the information about the zero point which is important for EMCD. One spectrum is shown to get the impression of where the V edges are. According to the earlier mentioned XMCD measurements [134] [135] the EMCD signal has the same sign on both V edges. A small signal above the noise can already be seen in this overlay and will be evaluated in detail for each point.
An effect could be calculated from the data for 15 of 16 points. On 5 points the signal has a different sign, also the uncertainty is very large. The possibility of opposite sign effects in a specimen like this would need very detailed simulations, as the external field of the objective lens that helps creating a specimen with spin polarization has not been changed, signal of both signs are unlikely. Therefore only the positive EMCD signals are considered to be real, which is supported by the better signal to noise ratio. The linescan positions are related to the position on the lamella and the chemical information in fig.135. Most of the linescan crosses the thin 1 nm V layers that are expected to show a proximity effect through the layer. The specimen tilt makes accurate relation of position and chemical composition difficult, the point with no effect at position 6 can still be in agreement with the center of the 4 nm V layer that shows no proximity effect. The other points are on the Fe and cross parts of the V layers due the tilt so a proximity and thus EMCD effect

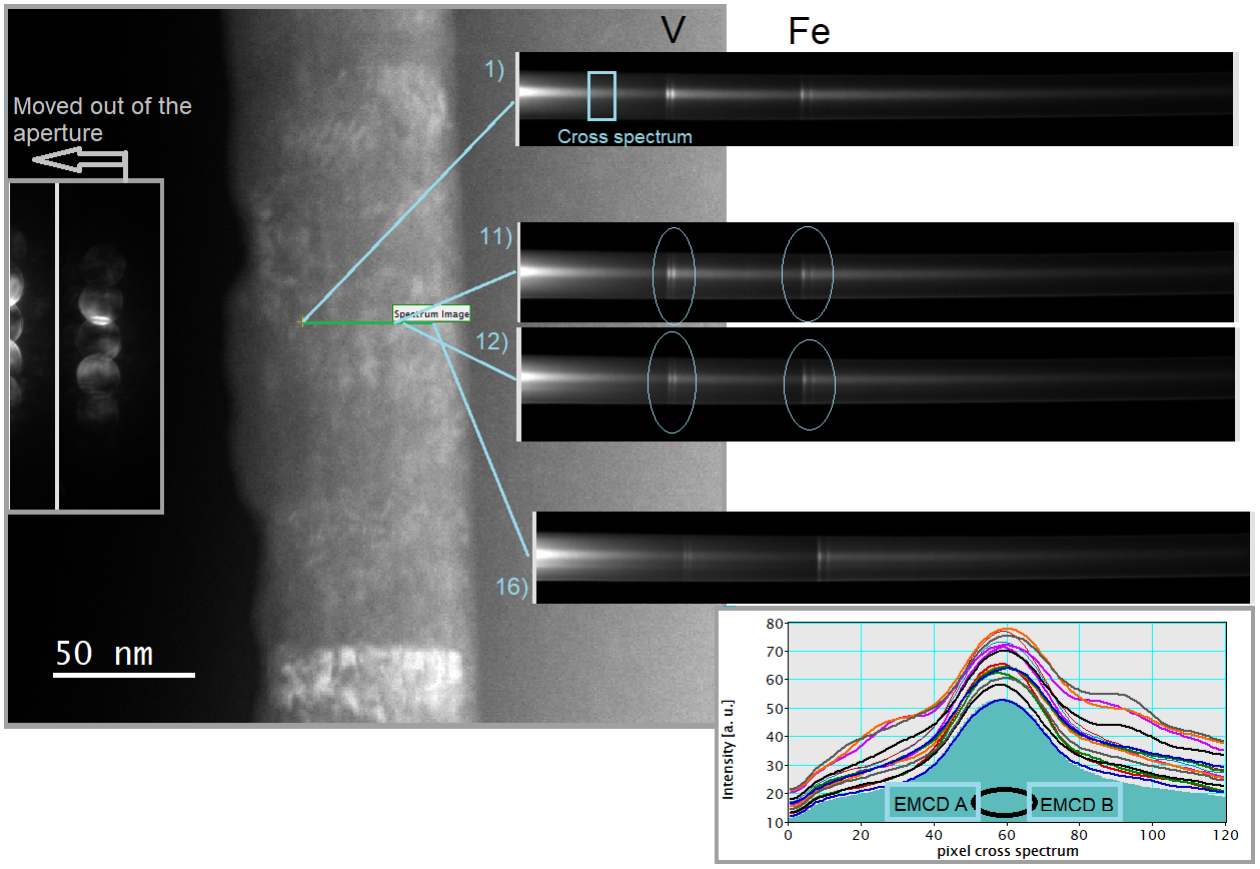

Figure 132: Selection of the measured STEM EMCD data on the survey image. Of the 16 datapoints of the linescan the first and last are shown, also the data of point 11 and 12. Between these two a change in intensity on both V and Fe edges indicates the crossing of an interface from a V rich region to a Fe rich region (layer). In the bottom right corner an overlay of all cross spectra is shown with indicated positions where to obtain the EMCD spectra. The peak caused by the central beam disc does not drift or show descan.

is likely to be expected, which is in agreement with the measurement.

3.8.5 Conclusion for the V/Fe multilayer system with respect to the magnetic proximity effect

The V/Fe multilayer sample has been designed with respect to the possibility to show the magnetic proximity effect on the vanadium. To achieve this, the layers have to be well separated chemically without diffusion. This could be shown for the 10 nm and 4 nm vanadium layers and reasonably concluded even for the 1 nm vanadium layers. The magnetic DPC measurements are in good agreement with expectations of a proximity effect of $\approx 0.5 - 1.5$ nm into the vanadium. The element specific EMCD results show the presence of the effect but do not have the point resolution to show how far the proximity

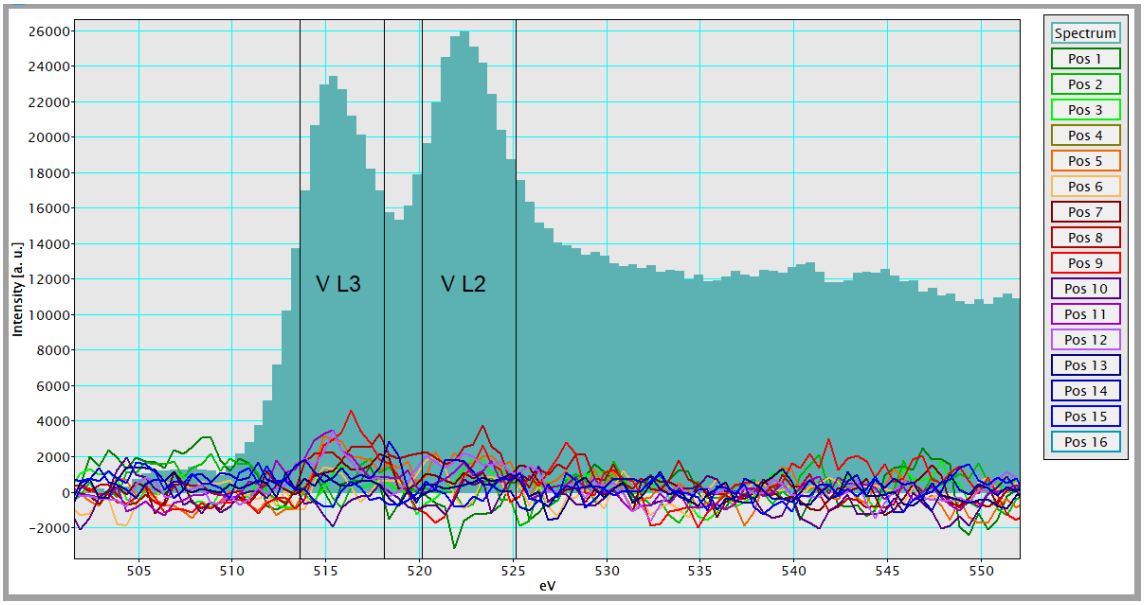

Figure 133: Overlay of the EMCD difference spectra for vanadium in the V/Fe multilayer system for all 16 linescan points. One V spectrum shown for orientation, the regions of the V edges where EMCD signal is to be expected are indicated by markers.

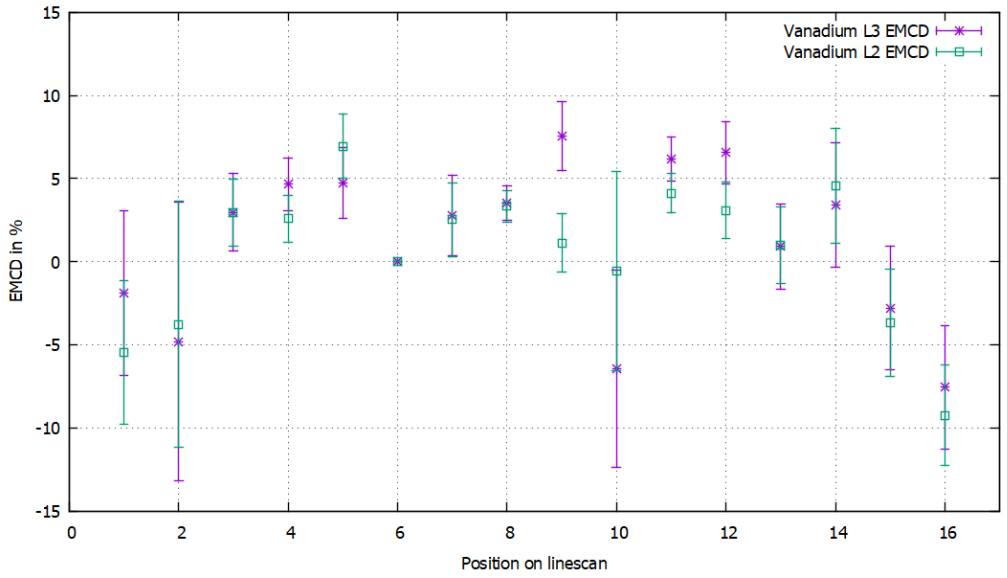

Figure 134: EMCD signal from the linescan on both vanadium L3 and L2 edges with respect to the linescan position. Data in table 16. MgO substrate on the right.

effect reaches into the vanadium. On the thin vanadium layers the signal is stable enough to state the presence of the proximity effects there, further investigations are needed to measure the effect more detailed.

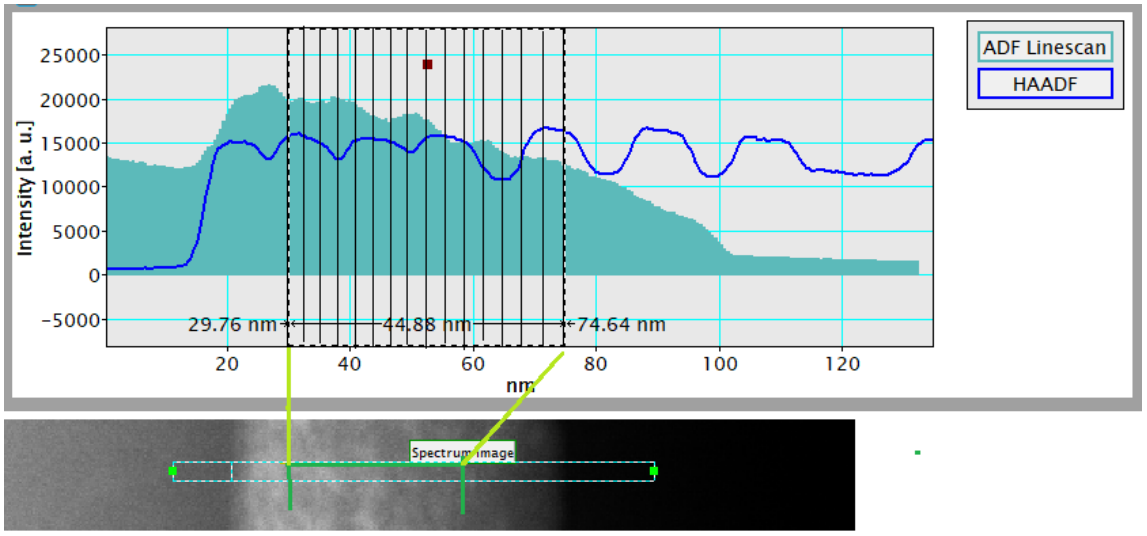

Figure 135: Position of the 16 points of the linescan on the lamella with respect to the layer system shown by the HAADF line profile overlaid over the intensity profile of the survey image. From point 5 on the signal is from the 4 nm V layer, start of the linescan and MgO substrate on the left.

Position	V L3	V L2
Pos. 1	$-1.9 \pm 4.9\%$	$-5.5 \pm 4.3\%$
Pos. 2	$-4.8 \pm 8.4\%$	$-3.8 \pm 7.4\%$
Pos. 3	$3.0 \pm 2.3\%$	$3.0 \pm 2.0\%$
Pos. 4	$4.7 \pm 1.6\%$	$2.6 \pm 1.4\%$
Pos. 5	$4.7 \pm 2.1\%$	$6.9 \pm 1.9\%$
Pos. 6	0	0
Pos. 7	$2.8 \pm 2.4\%$	$2.5 \pm 2.2\%$
Pos. 8	$3.5 \pm 1.0\%$	$3.3 \pm 0.9\%$
Pos. 9	$7.6 \pm 2.1\%$	$1.1 \pm 1.8\%$
Pos. 10	$-6.4 \pm 5.9\%$	$-0.6 \pm 6.0\%$
Pos. 11	$6.2 \pm 1.3\%$	$4.1 \pm 1.2\%$
Pos. 12	$6.6 \pm 1.9\%$	$3.1 \pm 1.7\%$
Pos. 13	$0.9 \pm 2.5\%$	$1.0 \pm 2.3\%$
Pos. 14	$3.4 \pm 3.7\%$	$4.6 \pm 3.5\%$
Pos. 15	$-2.8 \pm 3.7\%$	$-3.7 \pm 3.2\%$
Pos. 16	$-7.5 \pm 3.7\%$	$-9.2 \pm 3.0\%$

Table 16: EMCD results on the vanadium L3 and L2 edge on each position of the linescan. The uncertainty is calculated from the noise level compared to the difference signal. Lines for better readability.

4 The "Checkerboard"- an extraordinary sample

This sample has not been planned for this work, it is a great example for discovering something unexpected in science and investigate it further. NiCoMnAl is a Heusler shape memory alloy used for thin film devices and magnetocaloric applications [139] [140]. The large thermal hysteresis is a disadvantage for ferroic cooling applications as a narrow thermal hysteresis is needed [141] [142]. The sample was produced by Andreas Becker with the aim of reducing the hysteresis of the material for ferroic cooling applications. He inserted martensitic intercalation layers as seed layers into an austenitic film of NiCoMnAl to reduce the formation energy of the martensitic nucleation and thus reducing the width of the hysteresis.
On a (001) MgO substrate and a 30 nm vanadium buffer layer a system of austenite / martensite layers is grown in a magnetron co-sputter deposition chamber from 3″ pure elemental targets. Used were Ni (DC-source), Mn (DC-source), Al (DC-source) and Co (RF-source) at a base pressure $< 10^{-9}$ mbar with a distance between target and substrate of 21 cm. The substrate has been kept on the temperature of 450° C after the pre-cleaning process (ultrasonic bath: 10 min acetone, 10 min ethanol, 5 min DI Water, heating in the sputter chamber to 700° C for 30 min followed by a cool down phase to 450° C of 30 min). By varying the composition slightly between $C_1 = Ni_{43}Co_7Mn_{31}Al_{19}$ ($T_M = 232\ K$, $T_A = 248\ K$) and $C_2 = Ni_{47}Co_3Mn_{33}Al_{17}$ ($T_M = 308\ K$, $T_A = 343\ K$) by changing the energy on the target sources the different layers are realized: the first composition has a martensite/austenite transition below room temperature and the second composition above room temperature. In between the transition temperatures, thus also at room temperature, alternating martensite/austenite layers exist. T_M is the martensitic transition temperature and T_A the austenitic transition temperature. They are not equal because of thermal hysteresis which has been measured by A. Becker from XRD data (fig.136).
Samples with 0,2,3,4,7 and 13 martensitic intercalations were prepared with the thickness of the austenitic layers decreasing, of the martensitic intercalations always 30 nm. A 2 nm ruthenium layer on top protects the sample against oxidation.
Also magnetic measurements of all samples have been conducted by A. Becker. Here the VSM measurement in dependence of the temperature is shown with the data provided by A. Becker (fig.137). The sample has been cooled down from room temperature to 50 K and heated up again, a magnetic hysteresis can only be observed at temperatures between 280 K to 250 K, 240 K to 230 K and 180 K to 130 K. In all other temperature ranges up to room temperature the sample can be considered nonmagnetic.

The austenite can be described as a cubic B2 structure, the martensite as a 14M modulated $L2_1$ structure [143]. Both structures have random site placements of the atoms according to their abundance: On a lattice space sits either a Ni or a Co atom, the same goes for Mn and Al. The probabilities are the following:
C_1: Ni (0.86) Co (0.14) / Mn (0.62) Al (0.38)
C_2: Ni (0.96) Co (0.06) / Mn (0.66) Al (0.34)
An example for both structures including the random atom placement can be seen in fig.139, where the crystal structure has been modelled using QSTEM [144], the model building package allows to construct complicated models that include regions and random atom placement. The 14M structure can occur as "an adaptive phase constructed from tetragonal building blocks" [143] "to obtain an almost exact interface to the austenite and

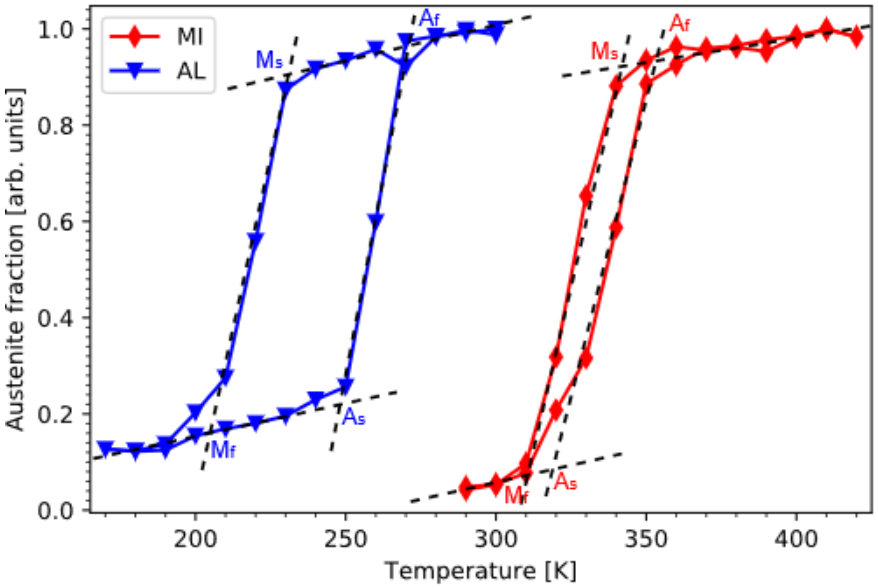

Figure 136: Thermal hysteresis of the austenite/martensite transition measured for the austenite layers (AL) and the martensitic intercalation layers (MI), measurement and graphics by A. Becker.

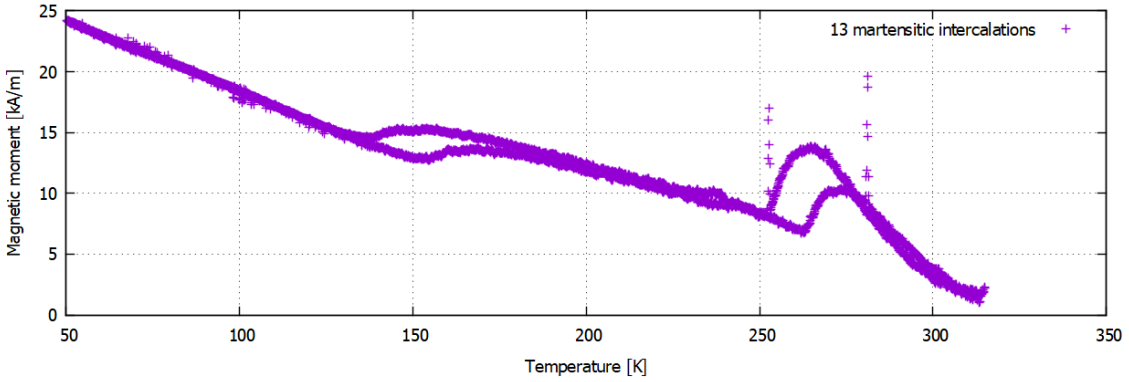

Figure 137: Magnetic hysteresis in dependence of the temperature for the 13 martensitic intercalation sample from VSM measurements, data reproduced with permission from A. Becker.

the MgO substrate." [143][[145] [146]]. Because of the creation of layers of either austenite or martensite type in this specimen, the adaptive phase occurs only if the presence of the interface allows and does not favor a different configuration, this will be subject of the following analysis.

A cross-section specimen was prepared by FIB milling at 45° to the substrate edge with 30 kV and polishing with 5 kV of the samples with 2,4,7 and 13 martensitic intercalations

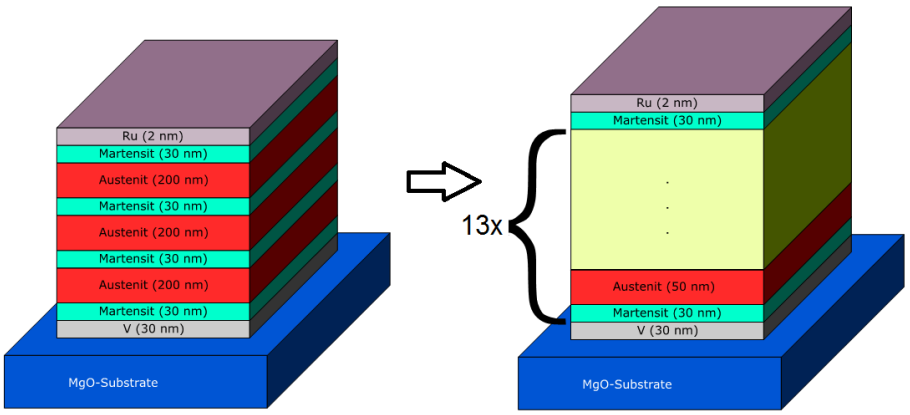

Figure 138: Structure of the system built from martensitic intercalations and austenitic layers, their width decreasing with increasing number of intercalations [graphic used with permission from Andreas Becker, modified].

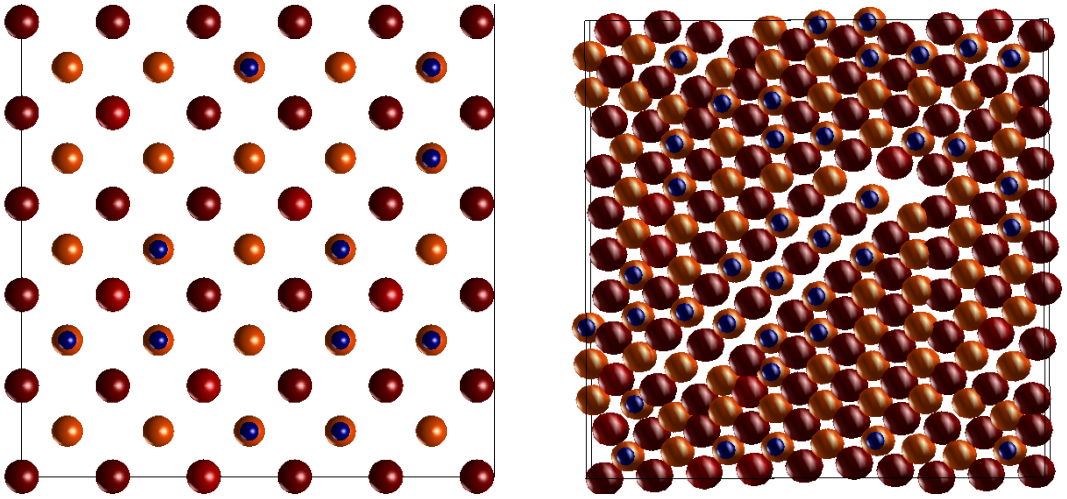

Figure 139: Models of the austenite and martensite structures built with QSTEM. To show the random atomic site placement more than one unit cell has been modelled. Left: Austenite structure, right: Martensite structure. The atom colours are fixed according to their position in the periodic table: Dark red: Ni, Medium red: Co, Orange: Mn, Blue: Al.

by Björn Büker using a FEI Helios FIB. TEM investigations were performed to check for the layer structure, crystallinity and chemical diffusion. On the specimen with 13 intercalations the formation of a checkerboard pattern could be observed:

The checkerboard pattern consists of three types of fields: big quadratic dark fields, smaller quadratic dark fields and in between slightly rectangular brighter fields. It is oriented at

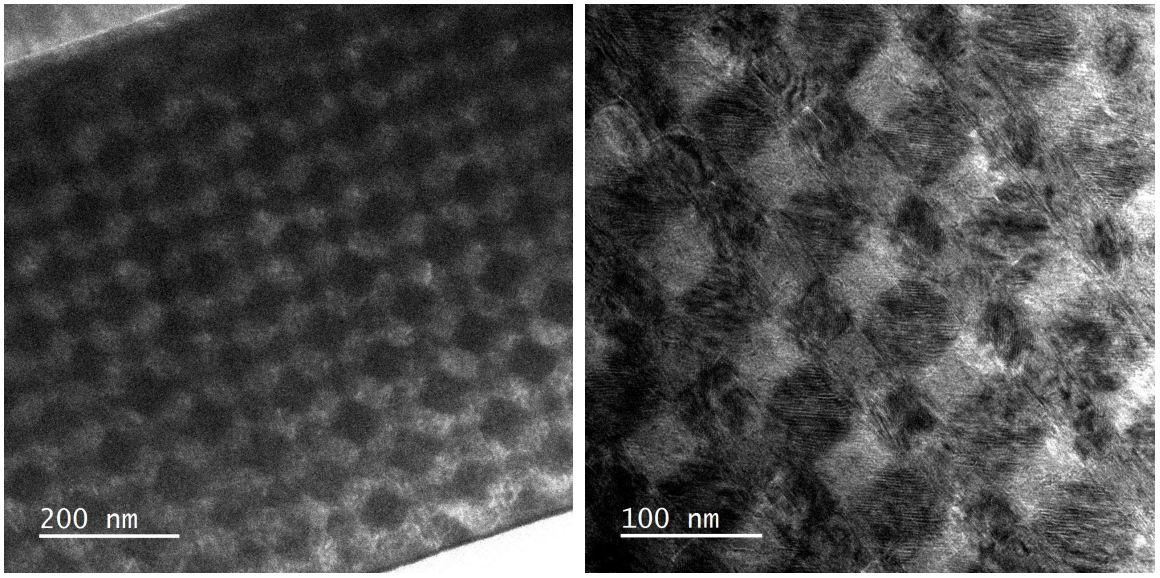

Figure 140: Left: The checkerboard structure as it appeared in the TEM, MgO substrate top left. Right: Close up of the checkerboard region, three types of fields are visible, greater and smaller quadratic dark fields and rectangular bright fields in between.

an angle of $45 \pm 2°$ to the substrate. The larger dark fields measure $\approx 60 \pm 5$ nm, the smaller dark fields $\approx 35 \pm 3$ nm, the brighter fields $\approx 60 \pm 5$ nm $\times \approx 35 \pm 3$ nm.

A relative thickness map was recorded using energy filtered TEM on the 2200FS with in-column filter. It is obtained by using the t/λ method in EFTEM mode. Two measurements with an energy window of 30 eV and 25 eV showed no relevant patterned thickness variations that could explain the pattern (fig.142).

The thickness of the lamella is at most at 1.5-2.1 mean free path. Calculating the mean free paths for both compositions using the Malis method [32] in the Mitchell DM script [83] at 200 kV with $\beta = 22$ mrad gives 92.67 nm (C_1) and 92.35 nm (C_2). This results in a maximum thickness of the checkerboard part of the lamella of up to 200 nm, which makes it a very thick specimen with the thickest parts being less electron transparent. Therefore the specimen has been rethinned by an additional FIB milling before analysing it further.

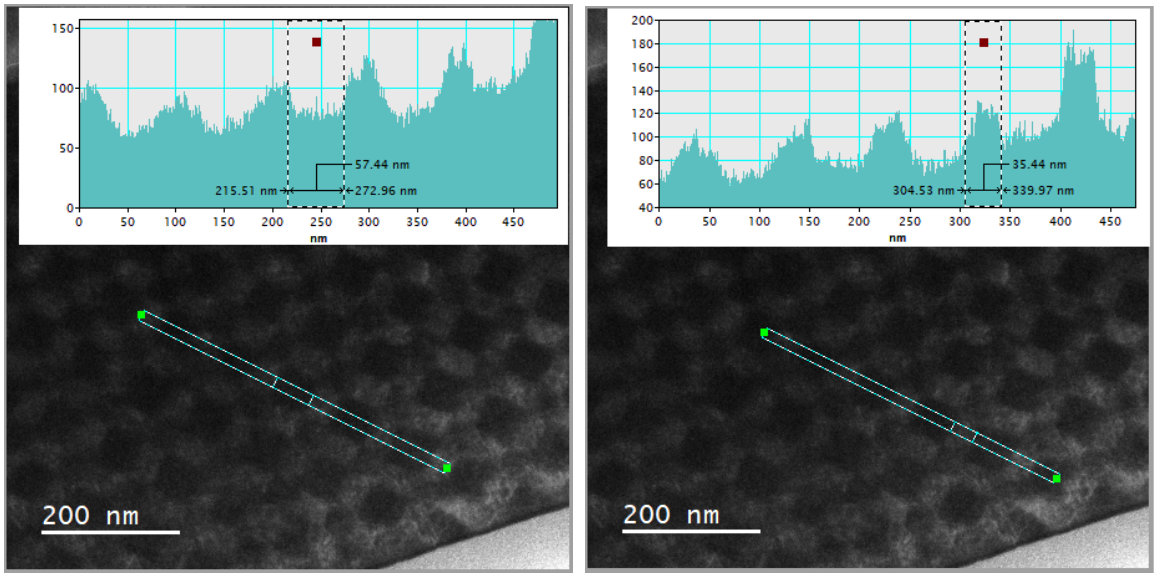

Figure 141: Left: Line profile measurement of the larger dark fields of the checkerboard pattern. Right: Line profile measurement of the bright fields (short side of the rectangle, corresponding also to the size of the small dark fields).

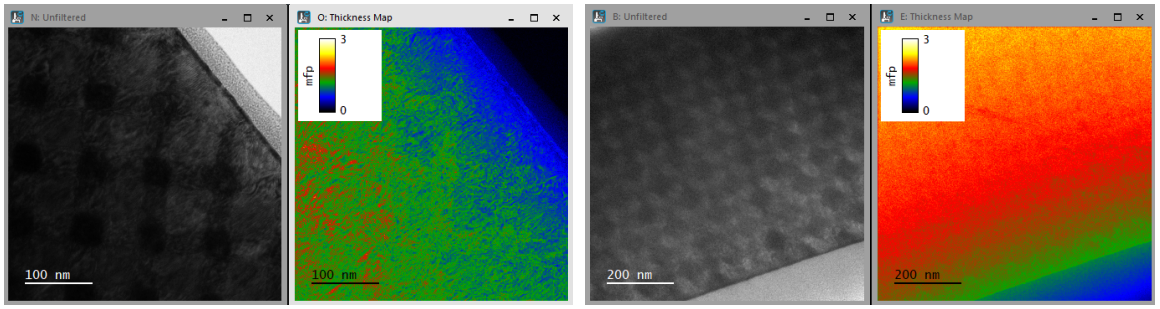

Figure 142: Left: Thickness map, filter window 25 eV. Right: Thickness map, filter window 30 eV.

4.1 Structural properties

4.1.1 Simulation of the crystal lattice and diffraction images

The crystal lattice of NiCoMnAl is known to be the B2 structure for austenite and the $L2_1$ structure for martensite with a 14M modulation [143]. Depending on the concentration of each element random site placement takes place. A TEM image simulation software that can build models and realize also random site placement is QSTEM with its program gbmaker [144]. The input file describing the properties of the unit cell uses the CFG format. From the unit cell a supercell has been built using gbmaker where the atoms are placed according to their site placement probability of either the austenite alloy or the martensite alloy as mentioned above. A TEM image and diffraction image simulation has been done for both and also for combinations of both on top of each other and a sandwich structure of austenite/martensite/austenite and martensite/austenite/martensite. The multislice simulation has been carried out with one slice per row of atoms and a potential offset in z to center the atoms in the slices as far as possible. For a TEM experiment the exit waves and diffraction images have been simulated at 200 kV acceleration voltage, a temperature of 300 K, Defocus of -60 nm and with and without TDS runs, which is used to add atom displacement according to the temperature. The detector has been set to cover the range between 0 mrad and 40 mrad. For the base materials of the checkerboard sample, martensite and austenite, the results are the following and shown in fig.143:

To resemble the proposed structure of regions of austenite and martensite on top of

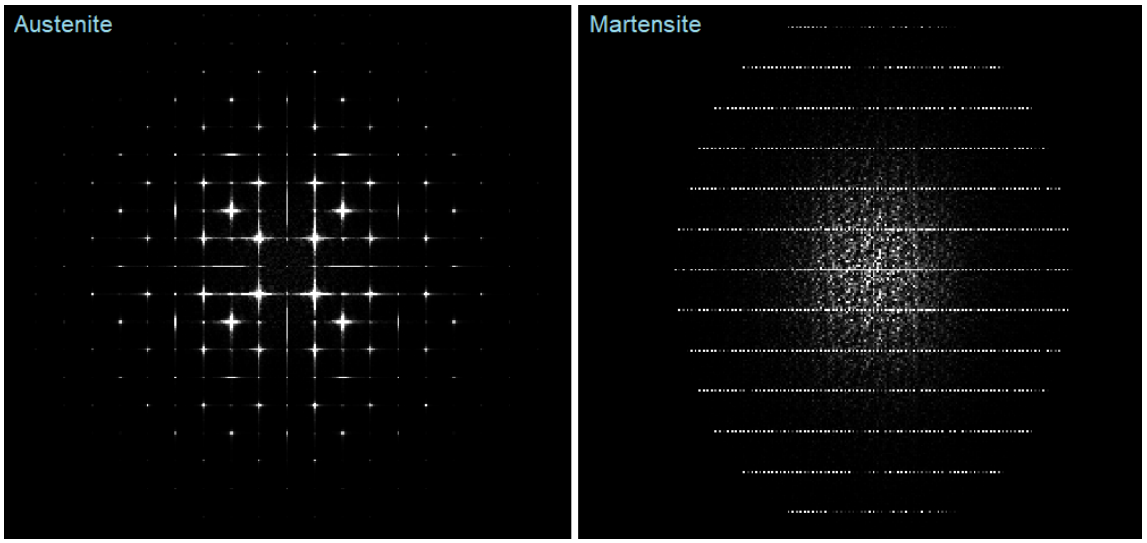

Figure 143: Simulated diffraction patterns of austenite (left) and martensite (right) of NiCoMnAl.

each other a reduced model of 10 nm austenite / 10 nm martensite / 10 nm austenite and 10 nm martensite / 10 nm austenite / 10 nm martensite has been built, again with random site placement and the element ratios C_1 (austenite) and C_2 (martensite). The diffraction images have been simulated again using QSTEM with the settings above, the results are shown in fig.144. The behaviour of the sputtered system has been simulated by a reduced

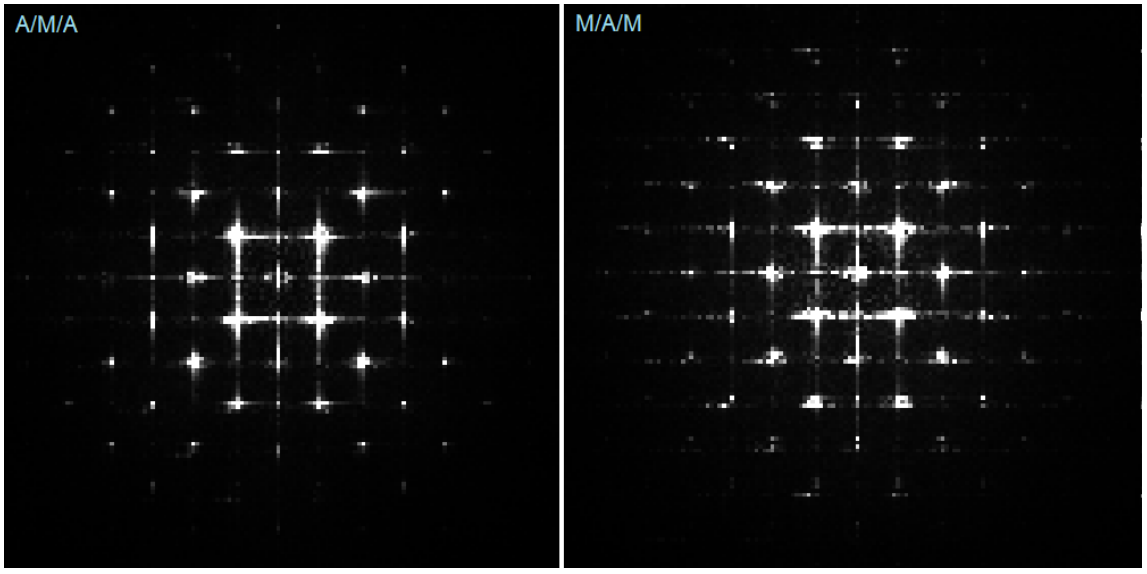

Figure 144: Simulated diffraction patterns of the austenite / 10 nm martensite / 10 nm austenite sandwich (left) and the 10 nm martensite / 10 nm austenite / 10 nm martensite sandwich (right).

system by a factor of 10 with martensite on top of austenite: a) 3 nm martensite on top of 1 nm austenite, b) 3 nm martensite on top of 3 nm austenite and 3 nm martensite on top of 5 nm austenite. The results are shown in fig.145 and fig.146.

It can be stated that the diffraction of the autenite resembles its cubic structure where the martensite only allows a different class of reflexes to be excited resulting in an unordered superposition in the center with lines of diffraction spots. Placing these two configurations of the material on top of each other leads to the pattern of austenite acting as a base with added reflexes from martensite around the excited austenite reflexes with increasing amount of martensite. More reflexes are visible on the austenite reflexes in the preferred scattering direction of the martensite, less in the perpendicular direction. As the amount of martensite on top of the austenite increases the number and intensity of the martensitic reflexes increase also. Not all of the reflexes shown in the simulation are strong enough to be visible in the TEM, depending on the specimen thickness and all contained crystal structures the electron wave has to cross only a subset of the reflexes is excited.

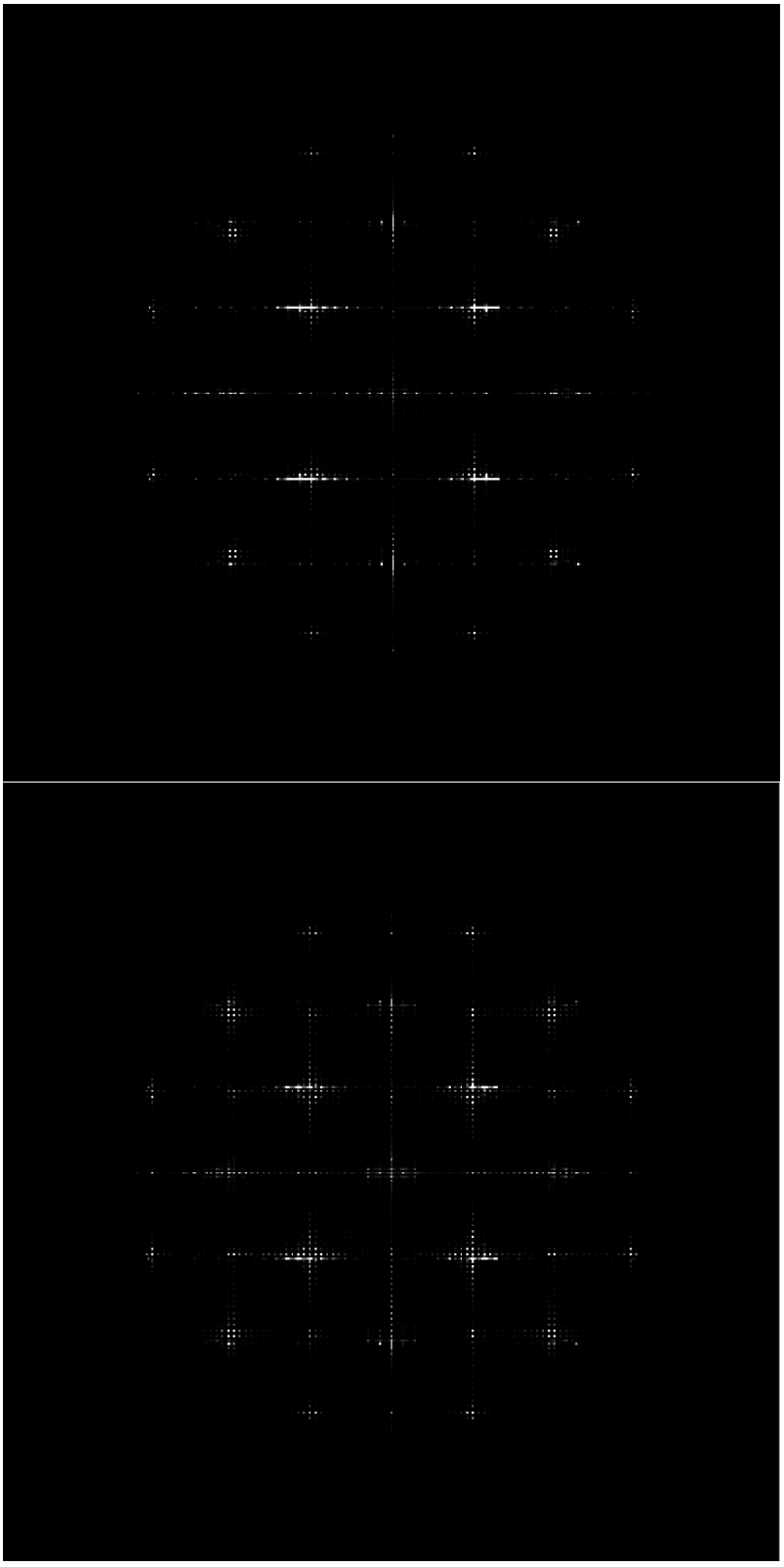

Figure 145: Simulation results of 3 nm martensite on top of 1 nm austenite (top) and 3 nm austenite (bottom).

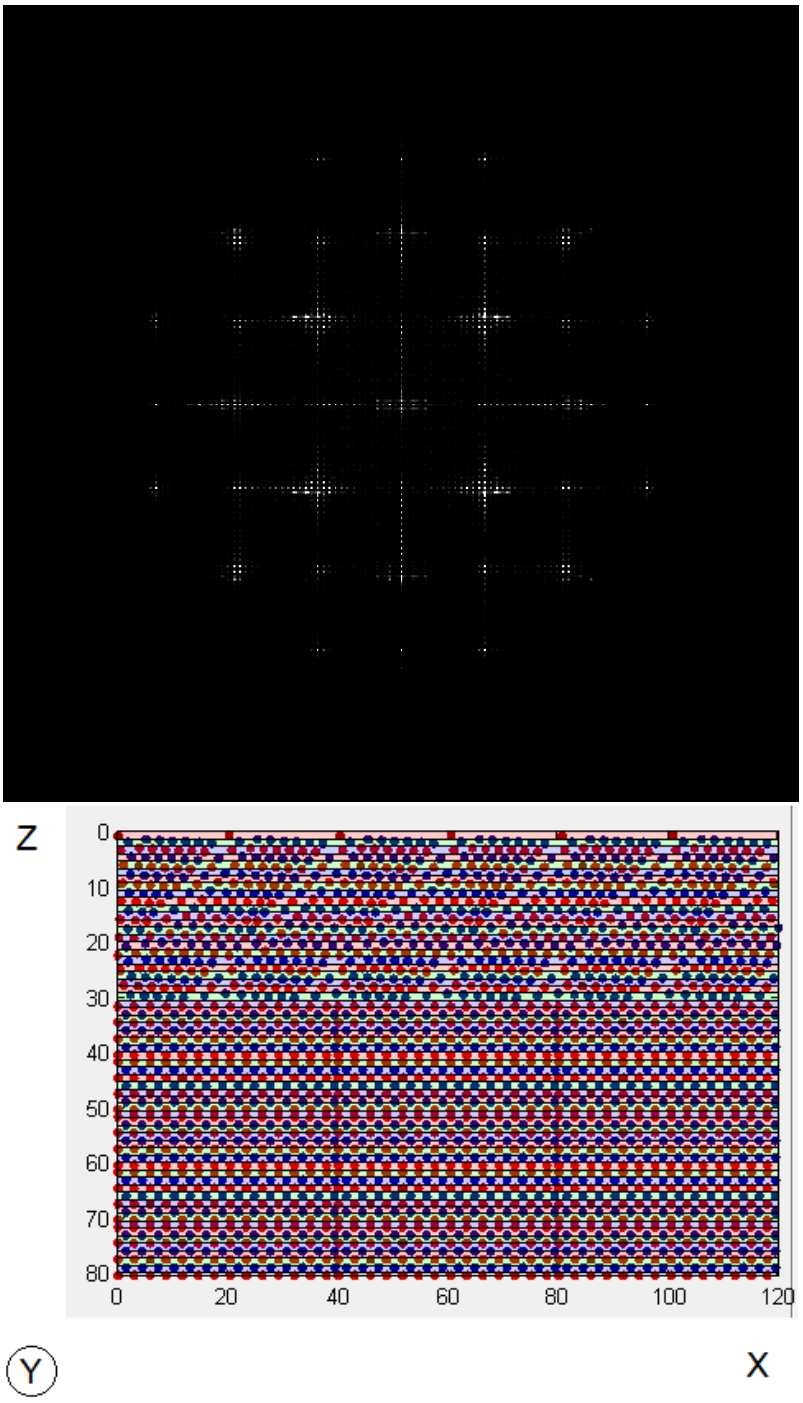

Figure 146: Simulation results of 5 nm martensite on top of 1 nm austenite (top) and the lattice configuration for the simulation in front view (bottom), units are Angstrom. The atom colours are fixed according to their position in the periodic table: Dark red: Ni, Medium red: Co, Orange: Mn, Blue: Al.

Using FFT on the simulated diffraction images gives a possible HRTEM image that still depends on parameters like defocus and camera length. Transforming the simulated diffraction pattern for austenite and martensite gives insights in the structure. The 14M modulation of the martensite is visible indirectly in the shown structure (fig.147 right). Processing the simulated diffraction pattern of martensite on austenite (fig.147 bottom) reveals the origin of the observed Moirè patterns in the dark checkerboard fields, it is most likely a result of martensite and austenite structures on top of each other. The direction of the Moirè patterns gives information about the orientation of the martensite cell, where the transition between two martensite cells marks the Moirè stripe in Y direction (directions as in fig.146 bottom), perpendicular to the surface of the austenite (Z direction) and to the X direction. The periodicity of the Moirè pattern in the simulation is measured to 2.01 nm.

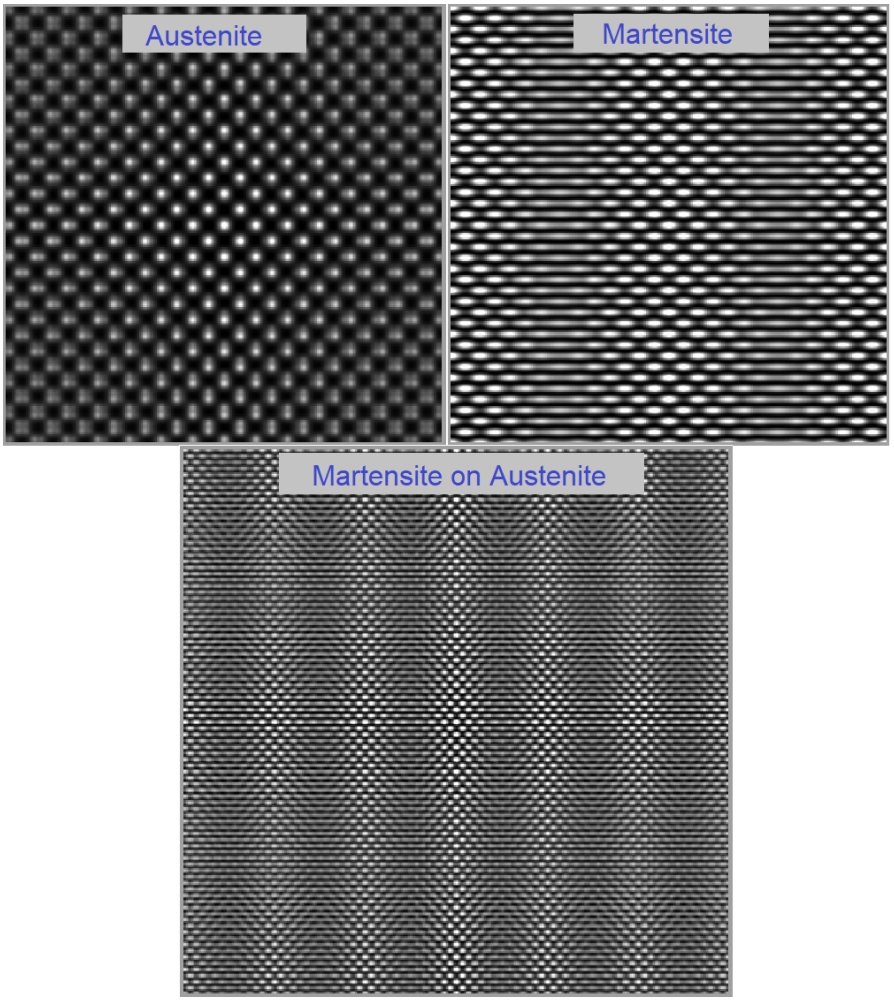

Figure 147: Top: FFT of the simulated austenite (left) and martensite (right) diffraction pattern. Bottom: FFT of the simulated martensite on austenite diffraction pattern with Moirè visible resulting from the superposition of the two different lattices.

4.1.2 Measurement of the crystal lattice and diffraction images

To measure the structural properties of the checkerboard specimen both diffraction and HRTEM images have been acquired on both microscopes (ARM200F, 2200FS). The HRTEM images allow to investigate a certain region more specifically by using the FFT, the selected area aperture in the microscopes is so large the region observed in diffraction measures about 100 nm in diameter. Also Moirè patterns could be observed and will be measured in this chapter.
A recorded diffraction pattern is shown in fig.148 together with another recorded diffraction pattern and a FFT diffraction pattern to show comparability. The diffraction pattern (recorded on the 2200FS with the OneView camera at 30 cm camera length) shows a very weak martensite structure overlaid over the clearly visible reflexes that are considered to result from the austenite. Those reflexes consist of at least three reflexes which can result from the martensite part but can also result from other mechanisms. In the FFT thestructure likely to result from the martensite becomes more clear, it is likely only the strongest excited reflexes can be observed in the diffraction pattern because of the dynamic range of the camera.
The distance d between the transmitted beam and the central one of the triple reflexes is measured to 0.5169 1/nm corresponding to a distance of 1.935 nm in the real space. The distance e is measured to 0.3633 1/nm corresponding to 2.753 nm in real space.

For further investigation FFT diffraction patterns are used, which are obtained from different regions of the checkerboard pattern. The images have been recorded slightly off a zone axis. Figure 149 and 150 show two HRTEM images and such FFT diffraction patterns from special regions. In fig.149 the different types of checkerboard fields (dark1, dark2 and bright) are shown with their diffraction patterns. The Moirè on the two dark fields is rotated by 90° and both show martensitic reflexes which are also rotated by 90° between the two fields. In the bright field no martensitic reflexes can be observed as far as this data allows, which is restricted by the presence of noise.
The distance between the rows of martensitic reflexes is measured to 3.803 1/nm (0.263 nm, A) and 3.663 1/nm (0.273 nm, B). The distance between two of the martensitic reflexes in a row correspond to 0.609 1/nm (1.64 nm, A) 1.104 1/nm (0.906 nm, B). The circled reflexes in C correspond to 3.438 1/nm (0.201 nm). Additional information and a partly measured real diffraction pattern can be found in Appendix 6.9.

A more detailed investigation is shown in fig.150 where a HRTEM showing a bright checkerboard field surrounded by different types of dark fields has been evaluated using FFT. Again the areas from where the FFTs have been obtained are highlighted by a coloured box and a number connects the region with the FFT. It can be stated that fields with the same Moirè direction show a similar FFT diffraction image with the martenstic reflexes in the same direction. These are present also in the numbers 1 and 3 but can be observed less clearly as in 2 and 4. In the central bright field no martensitic reflexes can be observed.
The angle between two overlaid perpendicular Moirè patterns from the same HRTEM image is measured via FFT (fig.151). The result is $91.1° \pm 1.5°$ which is in agreement with 90°.

In another HRTEM image that contains different types of checkerboard fields one of the

fields shows a Moirè pattern of which the FFT shows two martensite lattices rotated at an angle to each other of $\approx 140°$ (fig.152) with the angles measured to $138.1 \pm 2.0°$ and $141.8 \pm 2.0°$. The Moirè pattern itself has been measured to a distance of periodicity of 1.819 nm (fig.153 top) which is less than the simulated value.
The left Moirè pattern in the HRTEM image in fig.151 has been measured to a peak-to-peak distance in the lineprofile of 2.053 nm (fig.153 bottom), which is in good agreement with the value obtained from simulation for martensite on austenite.
The disagreement between these two values results from the presence of two lattices that cause the first mentioned Moirè pattern. Other Moirè patterns which occur mostly on the large dark fields and to some extent on the small dark fields have also been measured. The results are varying in the same field and also between the fields. Some values for the measured peak to peak distance in a lineprofile across the Moirè are: 1.412 nm, 1.757 nm, 1.374 nm, 1.669 nm, 1.97 nm. Additional Moirè pattern measurements can be found in Appendix 6.9. Because of the variation it is not possible to extract more information on the lattice structure from this data as usual from Moirè patterns. The martensite (14M structure) itself is expected to show a Moirè pattern as shown in the simulation, another lattice overlaid at an angle can be proved by diffraction or the FFT diffraction image. The Moirè is influenced not only by the lattice which can be affected by strain and also by the thickness and the number of lattices on top of each other, which is not clear for the checkerboard. What can be stated is that in some dark checkerboard fields at least two martensite directions are present, in the dark fields in general at least one martensite lattice and the bright fields do not show Moirè and their diffraction pattern is in agreement with austenite.
Not only TEM images give information about the structure, STEM/HRSTEM also adds information. The checkerboard pattern is visible even more clearly in STEM images and corresponding pairs of BF / DF images have been recorded in parallel on the ARM200F (fig.154, magnification 150kx, 12 cm camera length, 20 μs dwell time, DF detector coverage 45-180 mrad).
The fields change in their size because these images have been recorded in 2020 when the specimen already had changed notably and these images show the progress of the process. A more detailed set of images at higher magnification (fig.155, magnification 500kx, 4 cm camera length, 20 μs dwell time, DF detector coverage 140-550 mrad) allows to measure the fields to 64 ± 3 nm for the great quadratic dark fields and the long side of the bright rectangular fields, 35 ± 3 nm for the short side of the bright rectangular fields and 38 ± 3 nm for the small dark quadratic fields. The visibility in both BF and DF images indicates that the fields have a different scattering behaviour with the bright (in BF images) fields scattering weaker than the darker fields. In the DF image it can be observed that the small dark fields show also different scattering behaviour from the big dark fields, they are bright in the BF image and dark or the darkest parts of the image in the DF image. The rectangular fields appear to form lines with the small dark fields being the crossings. A lattice similar to the rectangular fields but overlaid at 90° in the crossings would explain the Moirè but also the scattering behaviour that leads to a dark appearance in TEM images.
Also from the region where the checkerboard pattern is not visible anymore STEM images have been recorded (fig.156 top, magnification 100kx, 12 cm camera length, 20 μs dwell time, DF detector coverage 45-180 mrad). Visible is a layer structure of the following dimensions: MgO substrate / 30 nm vanadium buffer layer / 60 nm layer / 30 nm layer /

50 nm layer / 28 nm layer / 44 nm layer / 28 nm layer / 42 nm layer / 24 nm layer / 40 nm layer / 28 nm layer / 42 nm layer / 28 nm layer / 40 nm layer / 26 nm layer / ≈ 100 nm layer to the vacuum. This structure is already in good agreement with the intended structure of the layer system.
An overlay with the EDX result (fig.156 bottom) for cobalt shows good agreement between the low-Co martensite layers and the intensity increase of the thinner layers in the no-checkerboard part. A line drawn on such a layer in the DF image in fig.156 connects it with the center of the dark checkerboard fields. Therefore it is reasonable to conclude the following:
The checkerboard pattern originates of the alternating austenite and martensite layers with the martensite acting as a seed layer. The assumption it that it is a favoured state that the austenite around changes its form to martensite, which grows at an 45° angle in at twinned form, but is based on an austenite unit cell stretched in one direction. From the opposite interface from the martensite to an austenite layer the growth direction of the martensite is reversed. With the martensite acting as seed the transition is going out from the martensite and stops when the next martensite layer is reached, probably because of incompatible crystal orientation, here it is assumed that the top part of the martensite cell is not equal to the bottom, which can already be observed in the model in fig.146 bottom. With increased austenite layer thickness it would be possible to transform everything to martensite and no austenite would be left in between, in the given configuration austenite is left in between forming the bright fields. The checkerboard appears at some layer thicknesses because the grown 3D diamonds of martensite form a stable structure.

Also in STEM mode the Moirè could be observed and it has been analysed in one DF image (recorded at 1.2Mx magnification, 20 cm camera length, 20 μs dwell time, DF detector coverage 27-110 mrad). It measures 1.74 nm in the big quadratic field and 1.59 nm in the small dark field (fig.157). Again a variation in width is visible (even more in the not measured big field below measurement B) that makes evaluation difficult.

In STEM atomic resolution images have been recorded, some covering parts of two checkerboard fields (fig.159, 12Mx magnification, 20 cm camera length, 20 μs dwell time, DF detector coverage 27-110 mrad). They show a slightly different FFT diffraction pattern with additional weak reflexes in the dark part, the distance has been measured and is denoted in the FFT. The cubic reflexes denote a distance of 5.13 1/nm which corresponds to 0.195 nm, the additional reflexes give 3.47 1/nm (0.288 nm) and the reflexes far away give 19.35 1/nm and 25.27 1/nm, which corresponds to a distance of 0.052 nm and less, it is most likely a reflex corresponding to a different lattice plane. This is supported by the next atomic resolution STEM image (fig.158, 12Mx magnification, 20 cm camera length, 20 μs dwell time, DF detector coverage 27-110 mrad) which shows the cubic reflexes repeated above and below the original reflexes at a distance that does not correspond to a lattice parameter. The two reflexes from the bright part of the previous image do not appear. The important distance here is more accurately measured because of less noise 4.872 1/nm corresponding to 0.205 nm. This is the distance in the cubic primitive austenite cell, the cell parameter of the unit cell is therefore 0.41 nm. A more detailed analysis is not possible because of the too high specimen thickness of at least 70 nm where these images have been recorded.

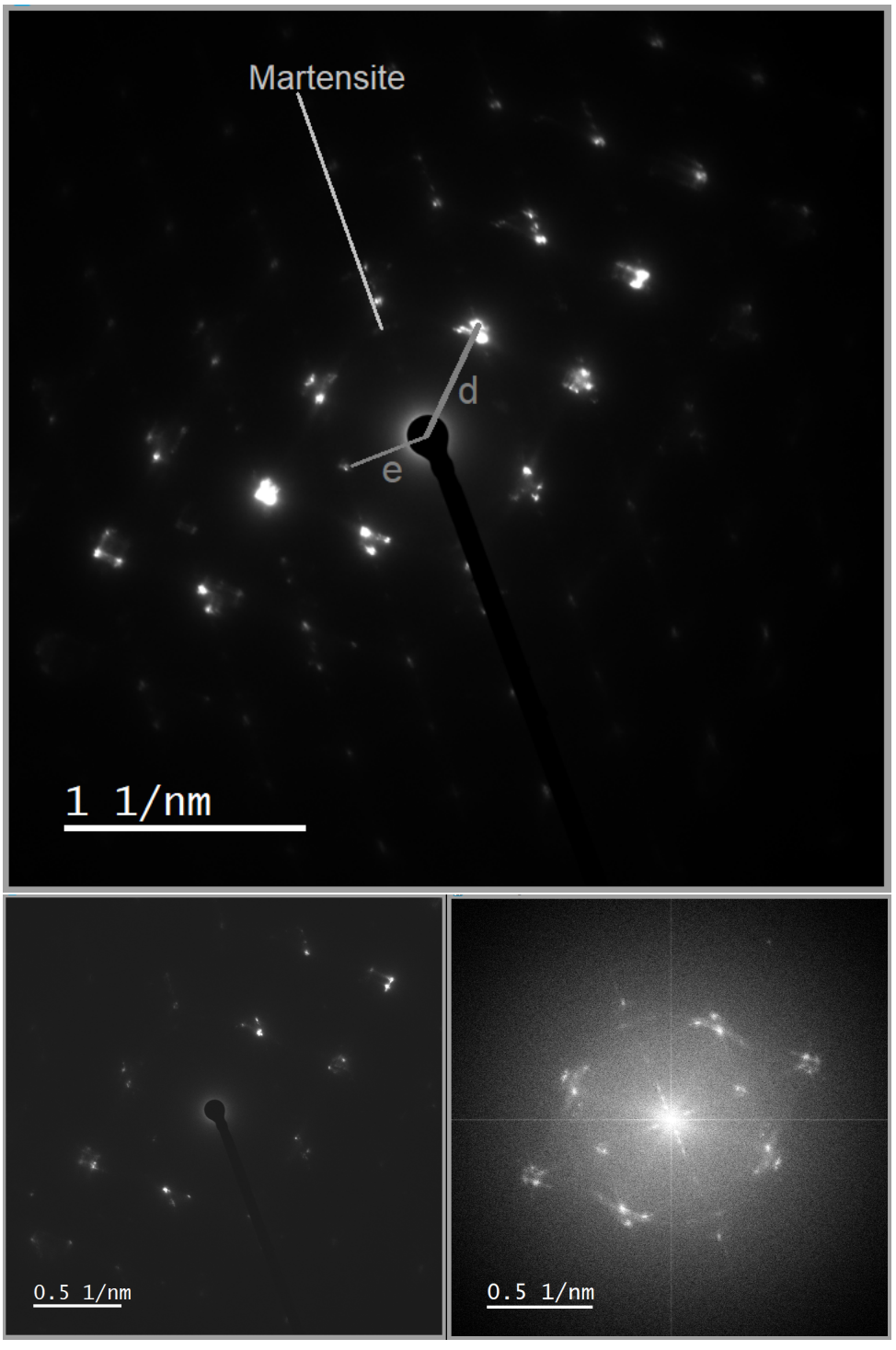

Figure 148: Top: Diffraction image of the checkerboard specimen recorded at 30 cm camera length. Bottom left: Diffraction image recorded at 50 cm camera length. Bottom right: FFT diffraction image of a HRTEM image recorded at 400kx magnification with an exposure time of 0.6384 sec. Images at the bottom adjusted for contrast. All images recorded on the 2200FS with the OneView camera.

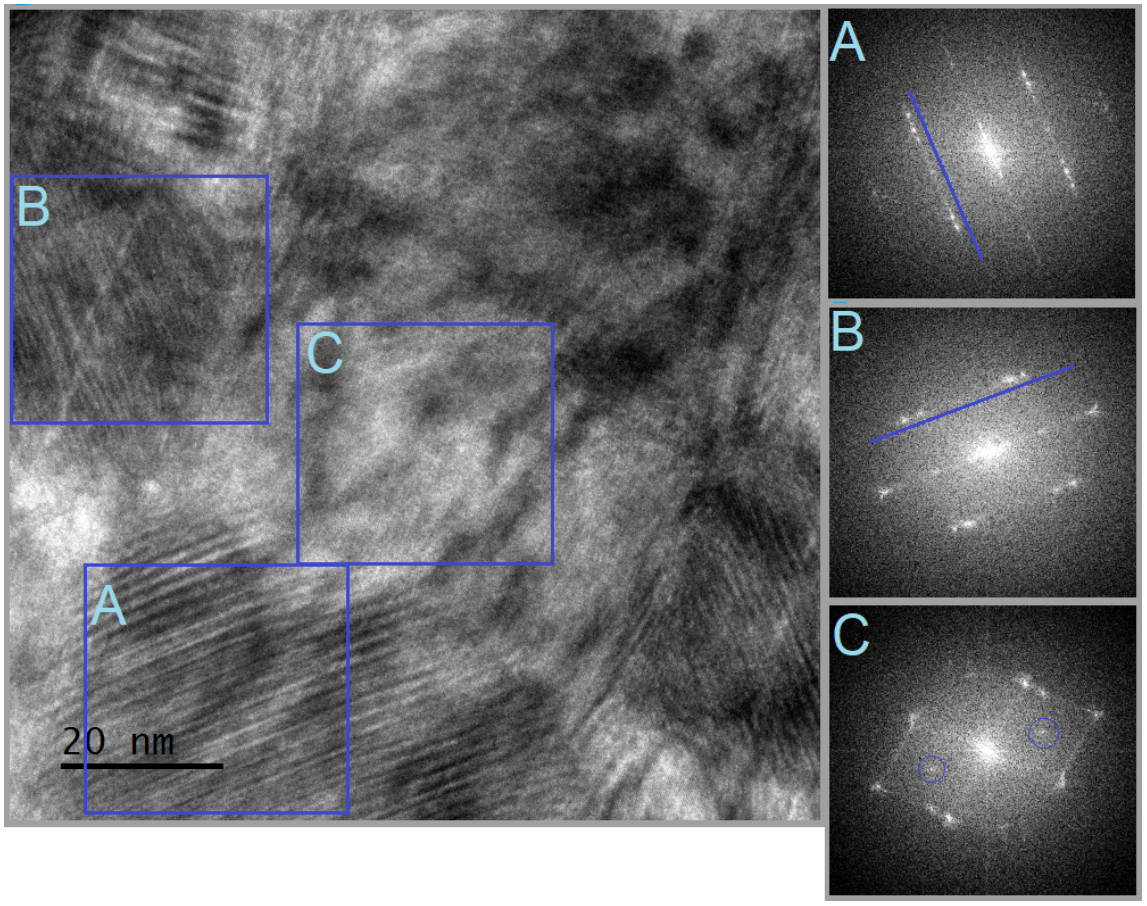

Figure 149: Left: HRTEM image of the checkerboard specimen recorded on the 2200FS with the OneView at 400kx magnification with an exposure time of 0.6384 sec. The regions from which FFT diffraction images have been obtained are indicated by the blue boxes and the letter connects them with the shown FFT on the right (contrast adjusted). The direction of the martensitic reflexes is highlighted by a line parallel to them and two reflexes probably resulting from austenite are highlighted by circles in C) as they also could be observed in the cooling experiment.

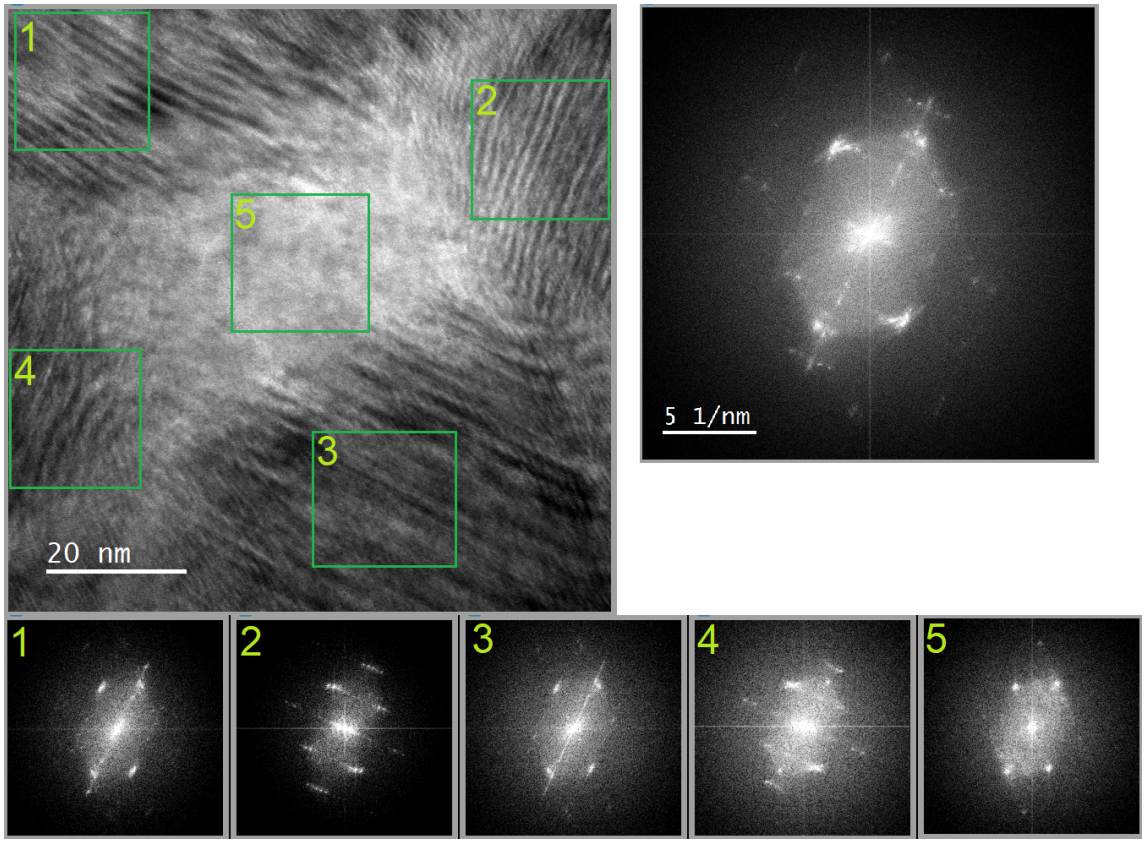

Figure 150: Left: HRTEM image of the checkerboard specimen recorded on the 2200FS with the OneView at 500kx magnification with an exposure time of 1.2768 sec. The regions from which FFT diffraction images have been obtained are indicated by the green boxes and the number connects them with the shown FFT at the bottom (contrast adjusted). Right: FFT diffraction image of the whole HRTEM image, contrast adjusted.

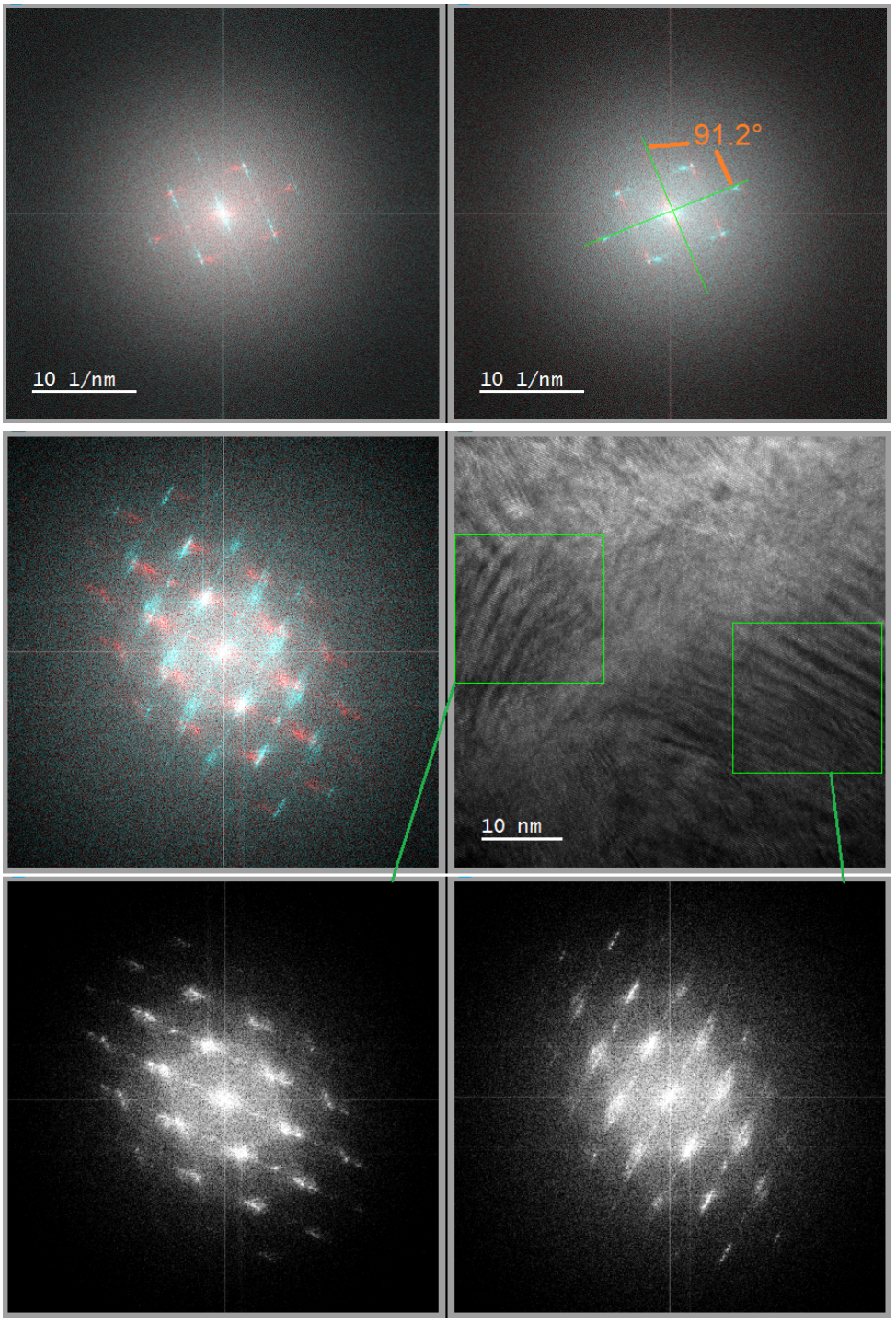

Figure 151: Top row: Two overlays of the same FFTs from two regions with perpendicular Moirè from one HRTEM image. The colours have been reversed between the left and the right image because the red is difficult to see and blue/green are very similar. Between the green lines the angle is measured. Center: HRTEM image with indicated regions for the FFTs on the right, RGB overlay of both FFTs on the left. Bottom: FFTs of the two indicated regions.

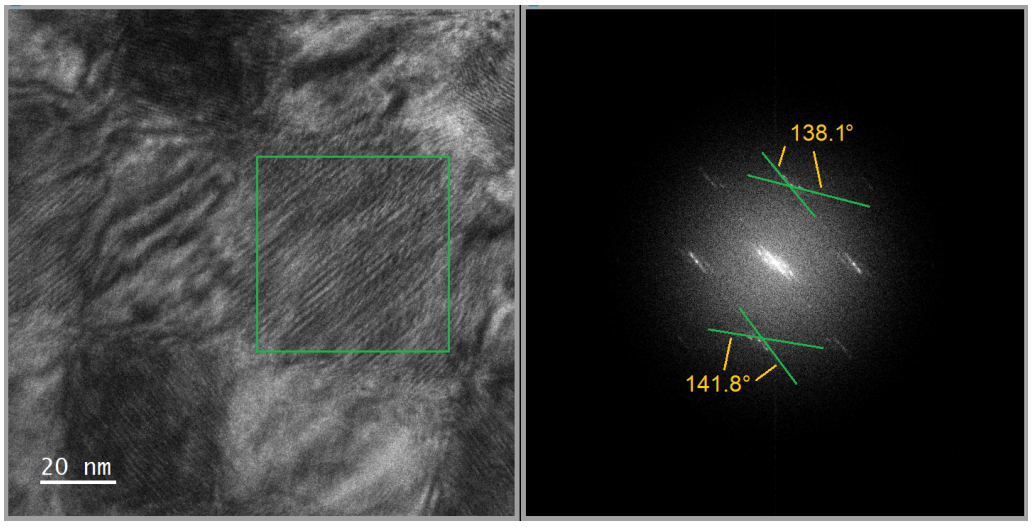

Figure 152: Left: A dark checkerboard field with strong Moirè patterns visible. The FFT is shown on the right with the measured angles between the two overlaid diffraction patterns which agree with an angle of 140°.

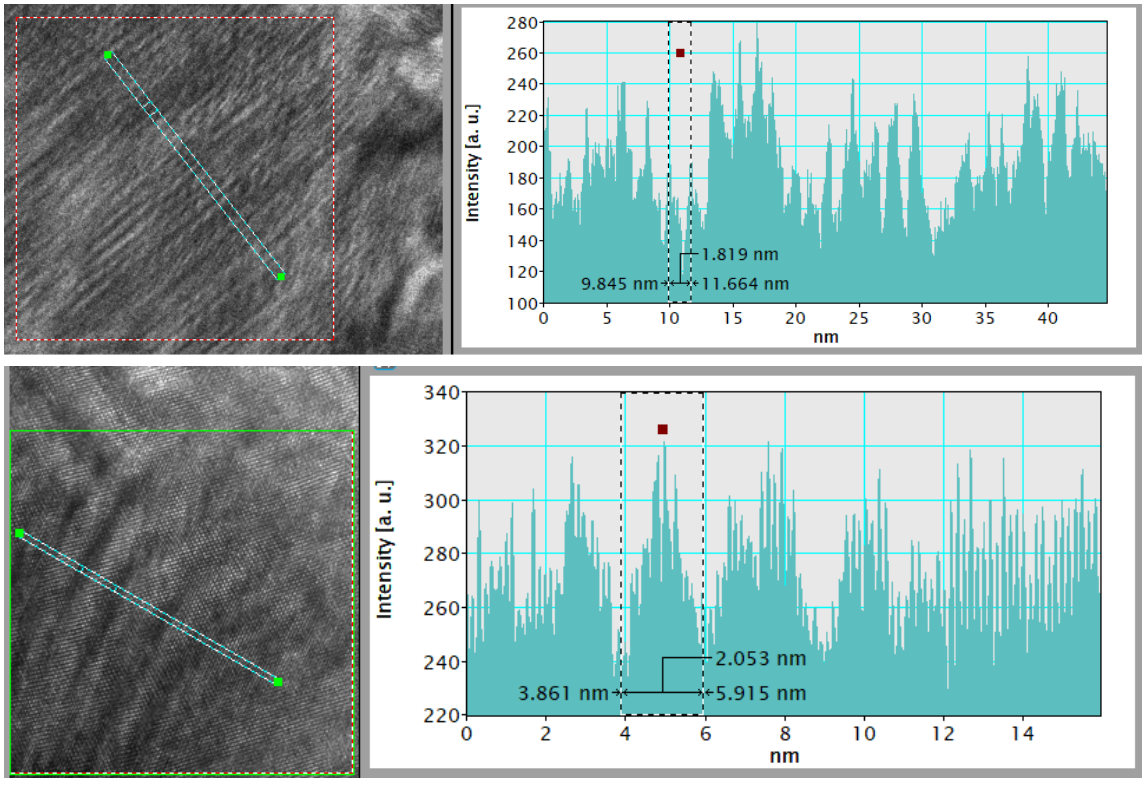

Figure 153: Measurements of Moirè patterns with the part of the TEM image shown on the left with the lineprofile on it and the lineprofile with the measured distance on the right.

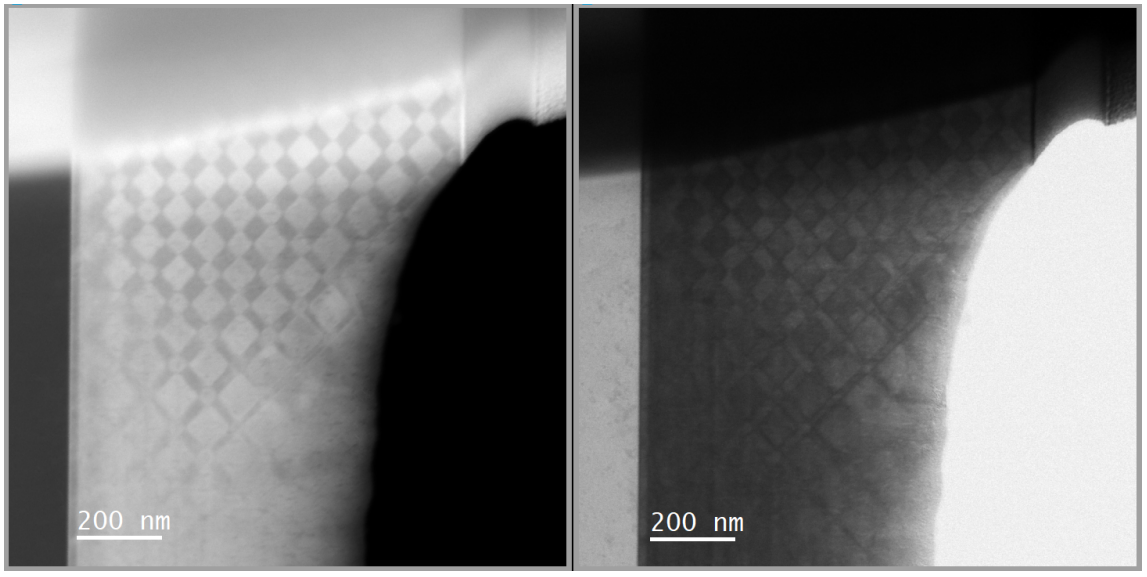

Figure 154: A set of BF (left) and DF (right) images of the checkerboard specimen recorded in parallel on the ARM200F.

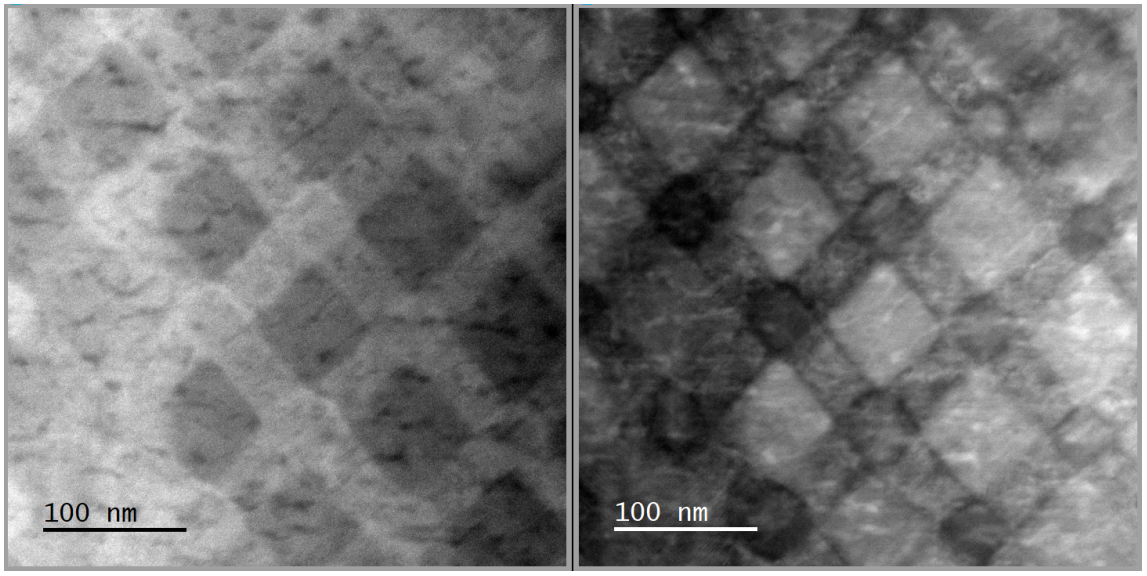

Figure 155: A set of BF (left) and DF (right) images of the checkerboard pattern recorded in parallel on the ARM200F.

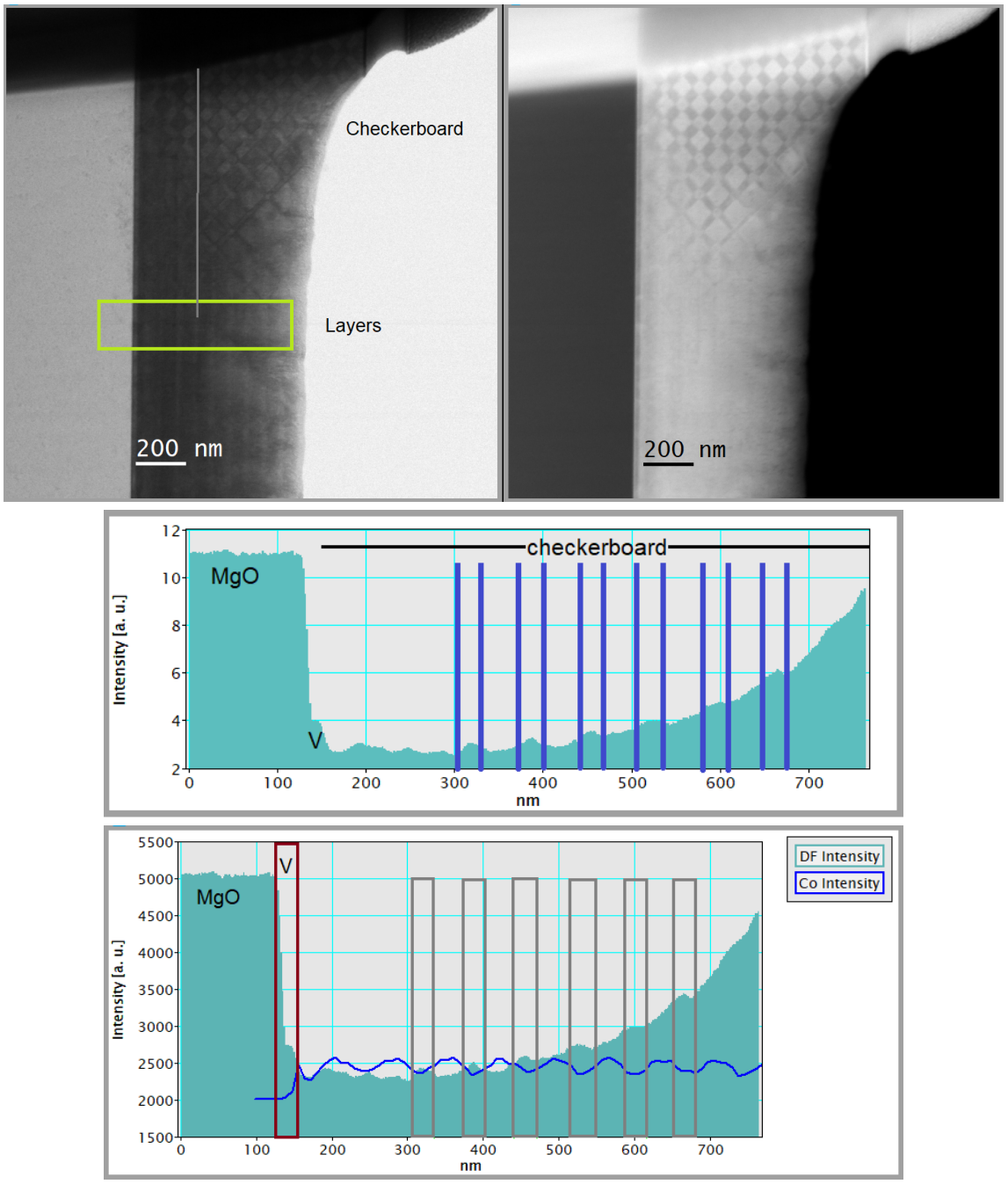

Figure 156: Top: DF (left) and BF (right) image of the checkerboard region and the region of the specimen where the checkerboard has vanished. Region of the lineprofile indicated by the box. MgO substrate on the left. Center: Lineprofile across the checkerboard-free part of the lamella. The layers that could be resolved clearly have been marked, MgO substrate on the left. Bottom: Overlay of the DF intensity profile from the center image with the Co EDX result.

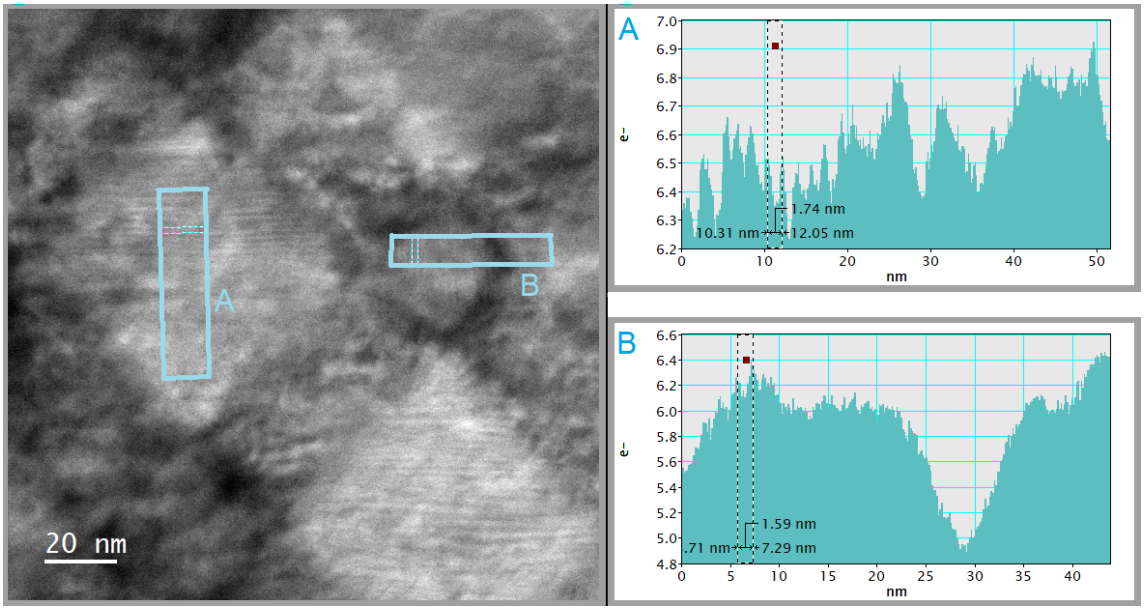

Figure 157: STEM DF image showing Moirè patterns in the checkerboard fields. The locations of the two lineprofiles used for measuring the distance have been highlighted.

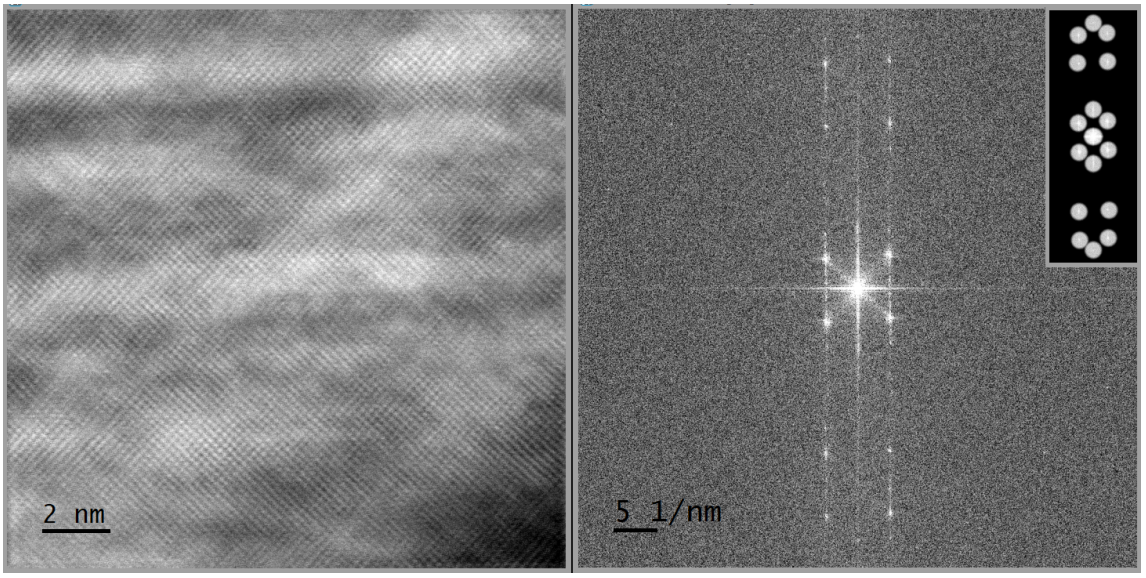

Figure 158: Atomic resolution STEM image of the checkerboard pattern. A FFT filtering has been applied by using the FFT, masking the reflexes and transforming back, the result and the original image have been added. The FFT is shown on the right and the mask top right.

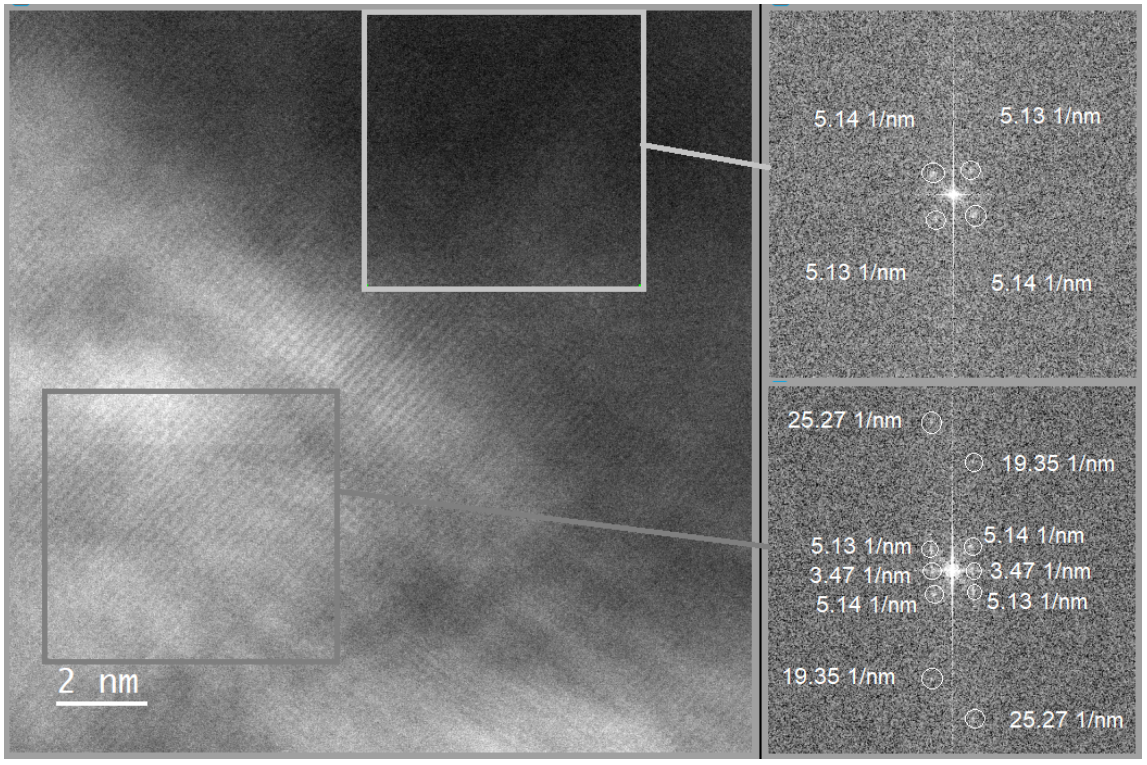

Figure 159: Atomic resolution STEM image of the checkerboard pattern covering two fields. The regions from which the FFT diffraction images have been obtained are highlighted and the reflexes encircled and their distance to the center of the pattern measured.

4.1.3 Dark Field TEM

A sequence of dark field TEM images has been recorded at both the ARM200F and the 2200FS TEM, using several different diffraction spots. At the ARM200F it was not possible to record the used spot due to high intensity on the camera, but at the 2200FS the camera filming the viewing screen could be used. Four types of checkerboard-fields can be characterised in agreement with the diffraction analysis: The larger dark fields and the smaller dark fields are oriented at 90° to each other but contain a common component. The brighter rectangular fields with their longer side pointing in the same direction consist of the same components, those brighter fields rotated by 90° are also in their structure rotated by 90° and have no common component with the other type of brighter fields (fig.161). The reflexes used in fig.160 b) and fig.161 a) and b) correspond to the rectangular checkerboard fields that can be considered to be austenite. Martensitic reflexes are harder to uncover because in a superimposed lattice they are superimposed with austenitic reflexes and provide additional reflexes. Fig.161 c) is such a reflex. Also martensite is an austenite cell stretched in one lattice vector direction and the 14M structure is a composition of these stretched cells.

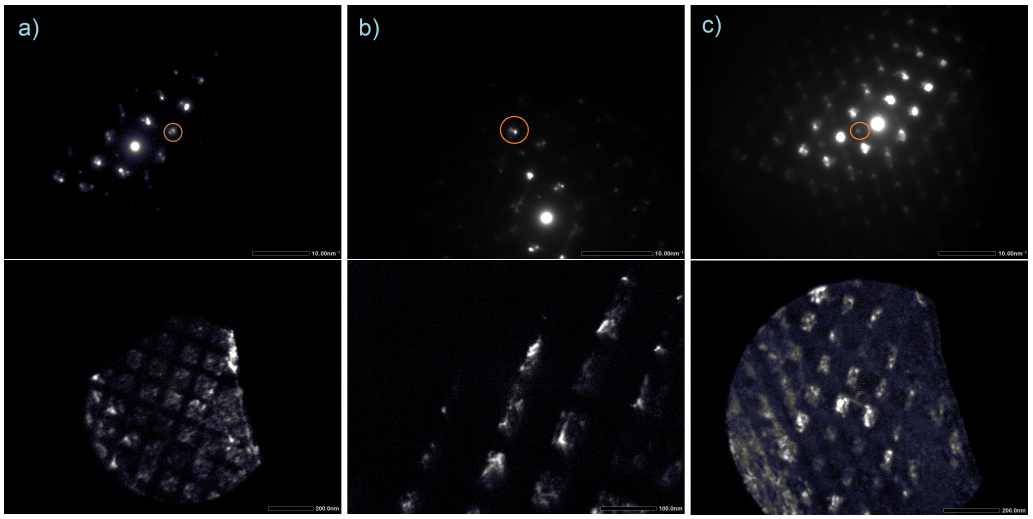

Figure 160: Examples of dark field images of the checkerboard recorded with the viewing screen camera on the 2200FS. It covers a larger area than the CCD camera and the images are only qualitative. The chosen diffraction spot is highlighted with a circle in the upper image.

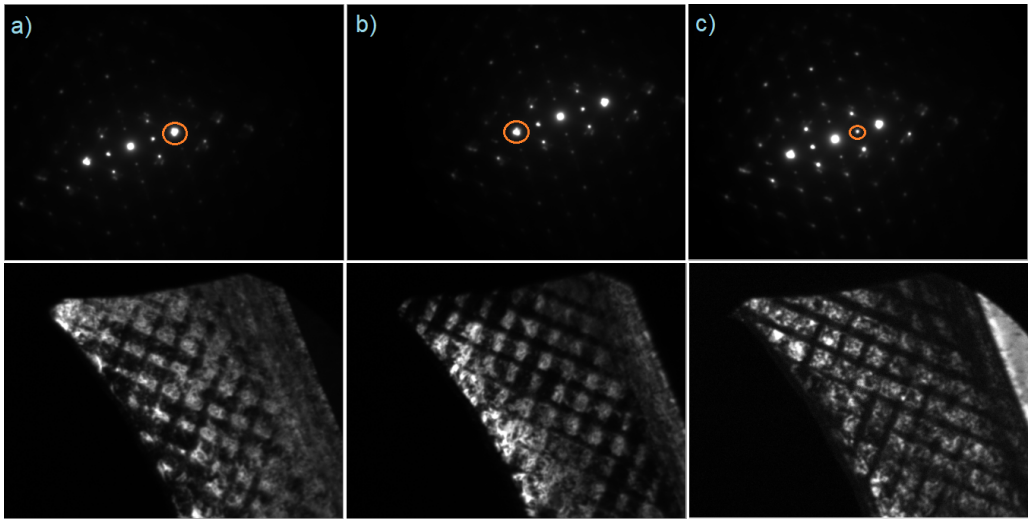

Figure 161: Examples of dark field images of the checkerboard recorded with the viewing screen camera on the 2200FS, chosen diffraction spot highlighted by an orange circle. The two most excited diffraction spots next to the central spot correspond to checkerboard fields rotated by 9°, a less strongly excited spot to all the greater dark fields.

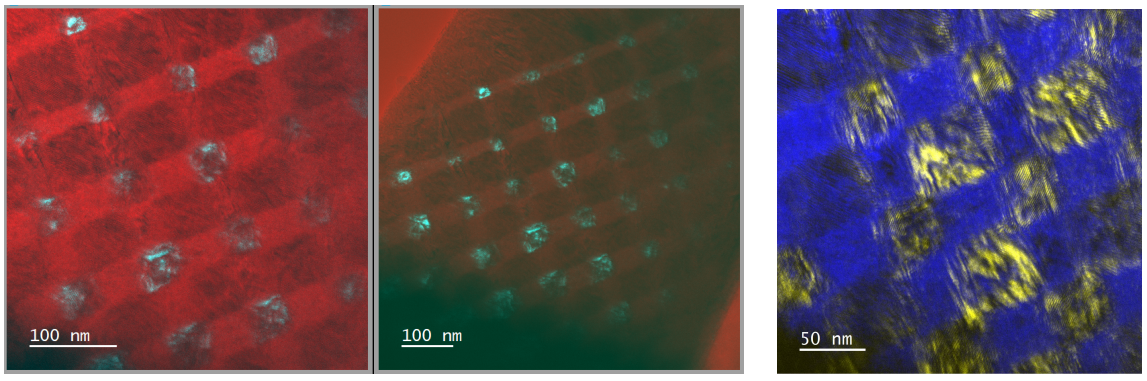

Figure 162: Overlay of BF and DF images of the same region: Left and center show the DF image using a reflex from only the small dark fields, right overlay of another BF and DF image with only a very small offset, the highlighted fields are of the big and small quadratic dark type, the non-highlighted fields of the brighter rectangle type. Images recorded on the ARM200F.

4.1.4 Tomography of the checkerboard

A tomography series has been recorded on the 2200FS TEM in steps of 1° ranging from 49.5° to −60.3°. At higher/lower angles the specimen shadowed itself.

From 49.5° to 36.3° degrees the checkerboard pattern is nearly not visible. Moirè

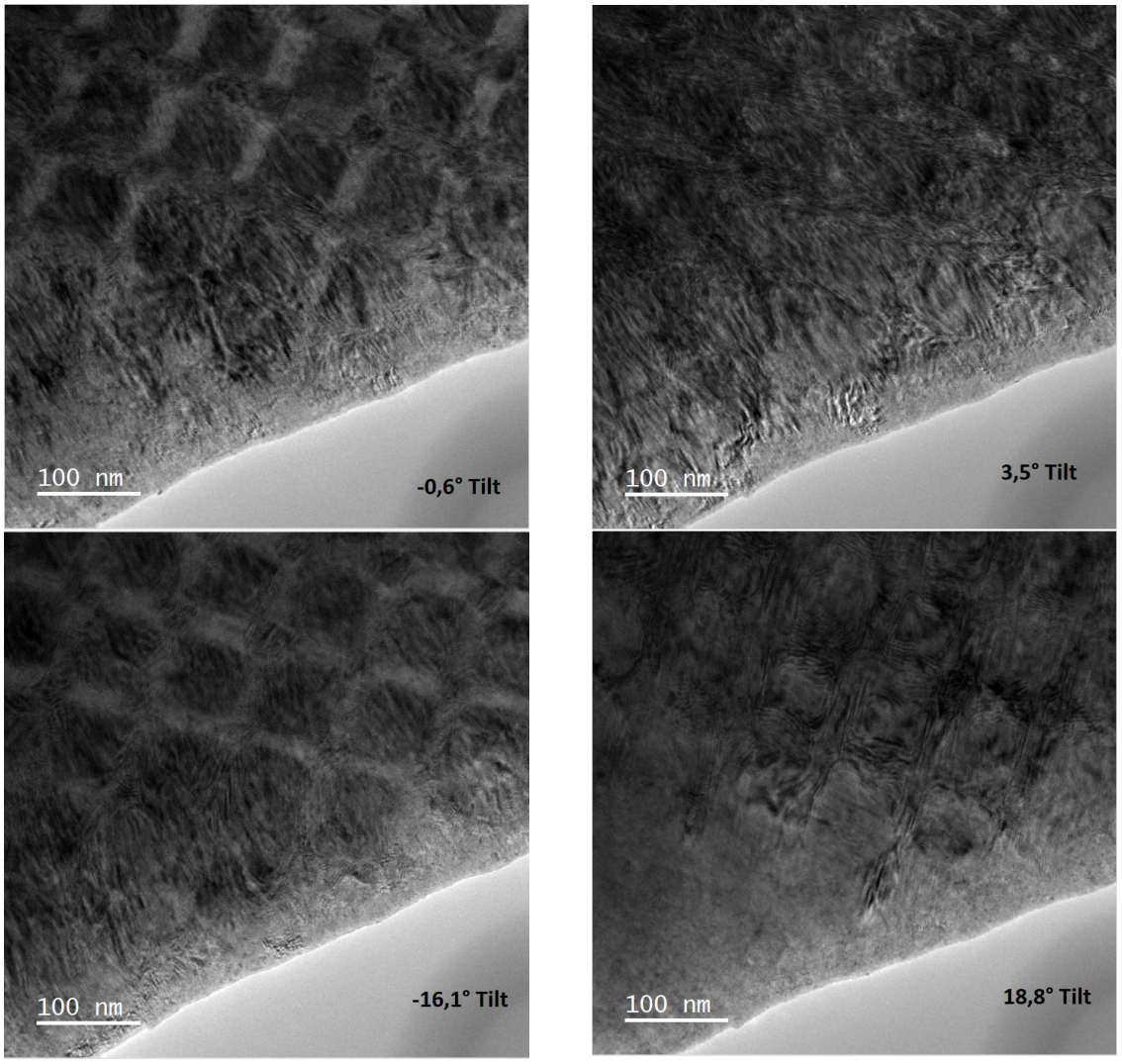

Figure 163: Examples of the tomography series of the checkerboard for image contrast (left) and Moirè contrast (right) at different tilting angles.

patterns in the form of the checkerboard emerge from 35.3° to 28.0° Tilt. From 27.0° to 24.0° a contrast difference and the checkerboard pattern becomes visible. 24.0° to 20.0° this vanishes and from 19.0° the Moirè becomes visible again, vanishing at 15.7°. From 8.6° on the checkerboard with higher contrast starts to become visible, vanishing into Moirè patterns at 4.5° degrees and re-emerging at 1.5°. At −3.6° again strong Moirè visible, at −5.8° the checkerboard fields re-emerge. Between −6.8° and −7.9° the brighter rectangular fields switch contrast, one gets brighter and those perpendicular get darker in contrast. At −8.9° part of this changes back and at −9.9° Moirè patterns become

the main characteristics again until −14.0° where it changes back to the checkerboard contrast pattern but the smaller darker fields show still less contrast but Moirè at first. At −18.2° the pattern becomes invisible again, at −21.3° the Moirè only starts until −29.4°. Then the contrast difference checkerboard energes again but with low contrast until −36.5°. At higher angles the Moirè checkerboard pattern becomes visible but from −40.6° on the contrast in either way becomes really low and a kind of pattern becomes barely recognizable. From −46.9° the amount of specimen to be crossed by the electron beam because of the tilt gets too high to make any statements, no pattern or else is visible as is between 49.5° and 36.3°.

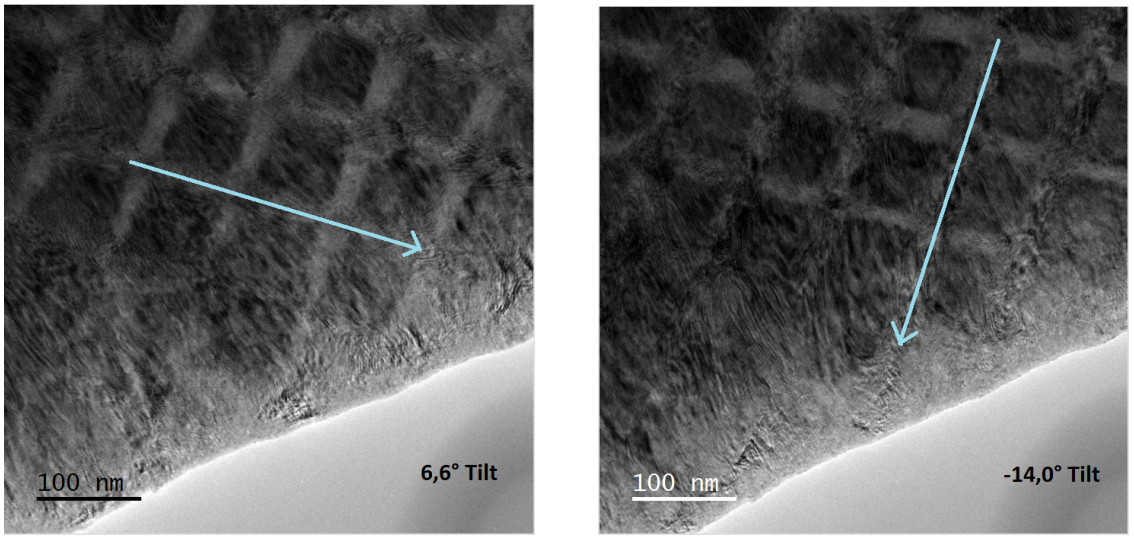

Figure 164: By tilting in the opposite direction, the fields changing to Moirè contrast change to the by 90° rotated ones.

The complete tilt series is shown in appendix 6.10. The pattern is changing with diffraction conditions, showing Moirè at tilt angles where the austenitic and martensitic sublattices superpose. The Moirè patterns still follow a checkerboard pattern. This supports that the checkerboard pattern is of crystallographic origin.
Usually a tomography tilt series is recorded for a reconstruction of the object. It also has been tried with this data but had to fail due to changing diffraction contrast and lack of contrast in combination with always present moire fringes. A reconstruction program needs a contrast clear enough in the input images it can identify it in every image. The change in contrast is only ≈ 7% between a brighter field and a darker field and reduces to ≈ 2%, these values are already obtained be taking a line profile integrated about 150 pixels (fig.165 left). Between single pixels or those of a rebinned image it is not possible for a program to discriminate reliably between a change in contrast that marks a feature and a contrast change inside a feature.

Although the contrast difference is weak, it is still a tool that allows to characterize the specimen properties angle-dependent. A line profile integrating over 200 pixels has been drawn across several checkerboard fields (fig. 165 right) and the overlays indicate if there is a difference between bright and dark checkerboard fields (peaks arise where

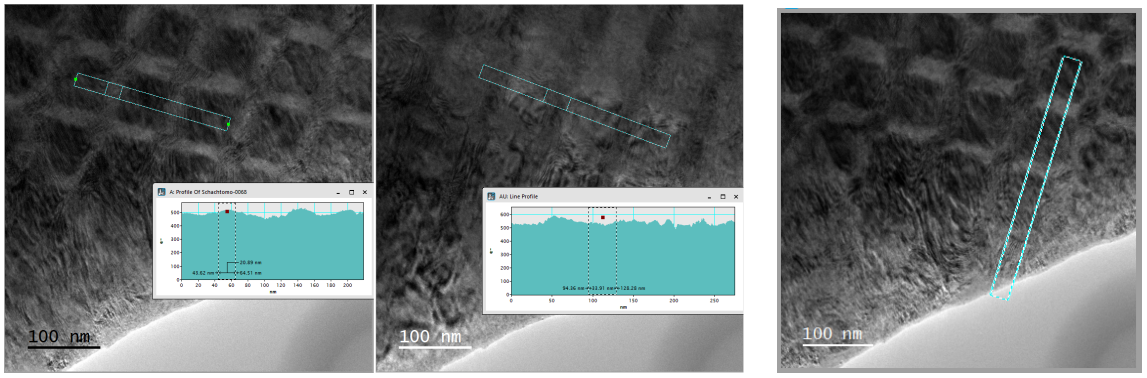

Figure 165: Left, center: Contrast differences in different images of the tilt series. Right: Line profile for contrast measurements.

the brighter fields are) or no contrast visible (the contrast resembles a line). The edge of the specimen to the vacuum has been used for aligning the line profiles, these are shown in Appendix 6.11. The contrast difference measured over a certain distance that contains at least two different checkerboard fields can be plotted against the tilt angle. To eliminate the effect of a changed condenser lens excitation between a tilt of -46.9° and -47.9° to adjust for brightness and contrast in the image a normalized contrast is used: $C_{\text{norm}} = (\text{Bright} - \text{Dark})/(\text{Bright} + \text{Dark})$. The chosen area contains four dark parts and three bright ones (fig.165 right). In fig.4.1.4 the result is shown:

The changes in contrast indicate the appearance of the checkerboard rectangles, which

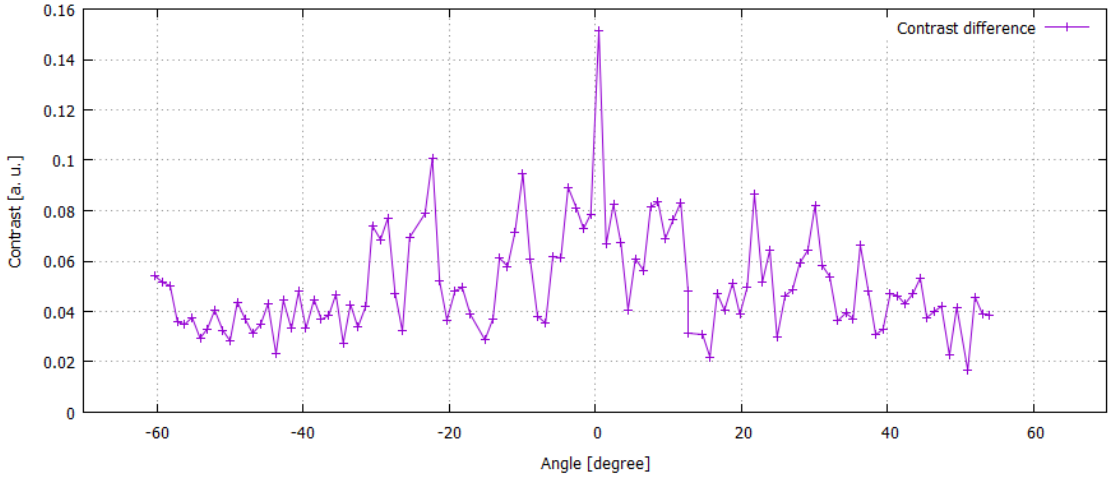

Figure 166: The contrast difference C_n of a ≈ 50 nm wide region in the line profiles that covers a bright and a dark field is plotted against the tilt angle.

takes place between $\approx -35°$ tilt and $\approx +38°$ tilt. At higher tilt angles the amount of specimen that has to be interpenetrated by the electron beam is much greater than at the almost direct way without external tilt, this makes contrast measurements more challenging. Also the thickness of the lamella varies, leading to a brightness gradient. For

this reasons all contrast measurements have been performed on the region containing the bright field farthest away from the vacuum in the depicted line profile (fig.165 right). The region used covers a distance of ≈ 50 nm. Tilt angles where the checkerboard pattern appears are −31° to −27°, −25° to −21°, −13° to −9°, −6° to +3°, +6° to +13°, +20° to +24°, +27° to +32° and a small peak from +35° to +37°. At other tilt angles there is no notable contrast difference, a possible explanation are the diffraction conditions of regions containing different crystal lattices of which several are crossed by the electron beam. More or less electrons are allowed through depending on the properties of the combined lattice structure, allowing the appearance of brighter and less bright fields. This would support a crystallographic origin of the checkerboard pattern.

4.1.5 Stability over time

The stability over time is of great importance if this alloy is used in any applications. From TEM investigations it is possible to give statements because the original lamella has been stored and investigated on several occasions over time. A second lamella has also been cut from the original sample, it has been thinned properly to ≈ 50 nm and lost the ckeckerboard pattern within about 3 months. The original lamella has been cut at the end of 2017 and stored in the FIB vacuum chamber until the first TEM investigation on Jan. 4th 2018, when the checkerboard pattern has been discovered. In the following week it has been rethinned by FIB milling and since then stored most of the time on air or in a vacuum bag. The base pressure in there is at maximum of the order of 10^{-3}to10^{-4} bar. This is not enough to exclude oxygen, but it keeps the specimen safe from humidity. The change over time is documented in fig.167 which shows overview images taken on several investigations between Jan. 4th 2018 and Sept. 7th 2020. The rethinning lead to beam damage in the thinner part of the lamella close to the vacuum where the checkerboard pattern disappeared (May, June 2018). In the image from June 12th it is already visible that the greater dark fields close to the disappearance region stretch out and the brighter rectangular fields in between become narrower until everything is dark and without pattern. This increases over time until the checkerboard pattern is only prsent in the thickest parts of the lamella close to the FIB-Pt attachment. The process is very slow and probably stoppable by keeping the material thick enough. Over 2.5 years mainly on air storage most FIB lamella alter their composition and appearance within weeks. This lamella has been used in the heating and cooling experiments still returning to the checkerboard pattern shape and the chemical properties did not change apart from some oxidation (chapter 4.2 "Chemical properties").

The increasing of the great dark and decreasing of the bright fields has been measured using line profiles integrating over approximately half of the field width in the center of the fields. The number of fields measured depends on the field of view and the state of the specimen. To make them comparable, only the last four fields go into the analysis, although this does not guarantee the same fields are measured. The images are not all of the same end of the lamella, the first 2018 image from a central part and an increasing amount of the lamella has altered so the last field is located more inwards. The results are shown in tab.17 with the last four measured widths plotted in fig.169. The change to greater dark/narrower bright fields towards the disappearance is visible. For measuring the rate of change the data spreads too much, showing great differences in width already

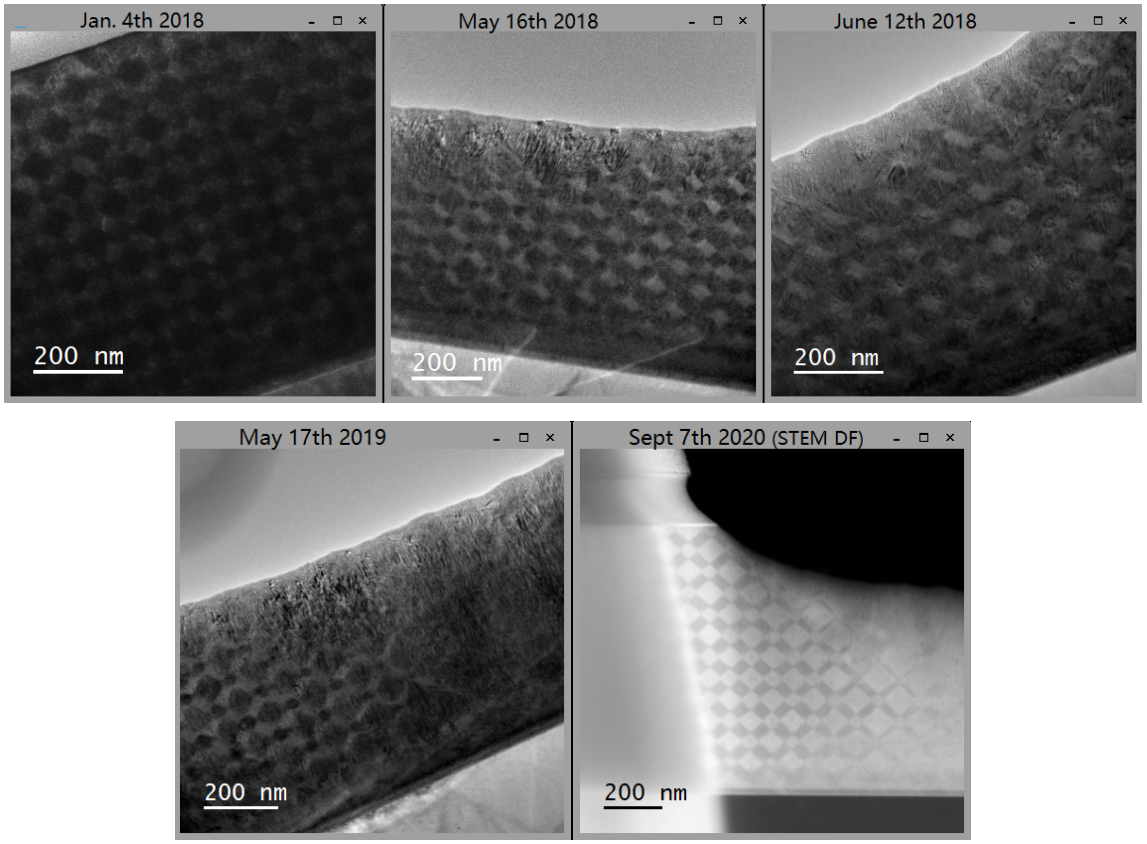

Figure 167: Time series of the checkerboard specimen from Jan. 4th 2018 to Sept. 7th 2020. Substrate always at the bottom. Four of the images are BF TEM images, the fifth from Sept. 7th 2020 is a DF STEM image because it shows the state more clearly than TEM images.

in 2018 but to obtain a distance the specific place of the field has to be known and the measured outer fields are not the same.

This analysis allows to describe the altering process in a qualitative way as for the

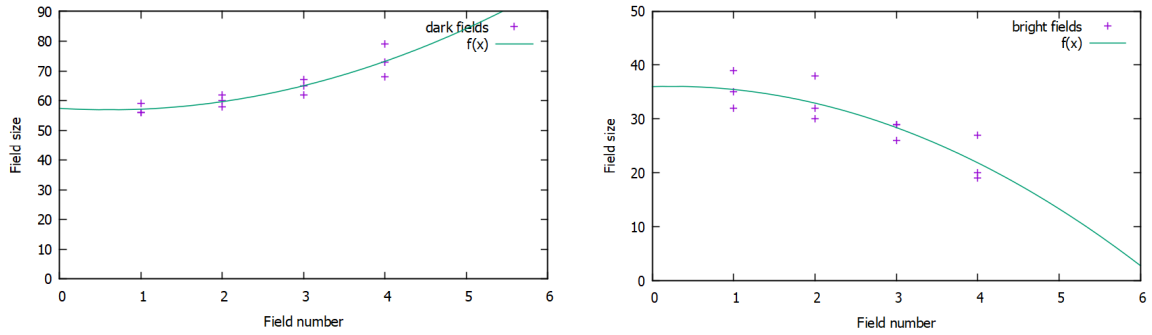

Figure 168: Quadratic fit for the size of last four fields before the checkerboard pattern vanishes. The three datasets from 12.6.2018, 17.5.2019 and 7.9.2020 have been used.

4.1.2018		16.5.2018		12.6.2018		17.5.2019		7.9.2020	
Dark	Bright	Dark	Bright	Dark	Bright	Dark	Bright	Dark	Bright
55 nm	36 nm	58 nm	33 nm	62 nm	29 nm	55 nm	35 nm	56 nm	41 nm
55 nm	35 nm	57 nm	32 nm	59 nm	28 nm	56 nm	32 nm	55 nm	40 nm
53 nm	39 nm	57 nm	33 nm	58 nm	29 nm	58 nm	29 nm	56 nm	41 nm
56 nm	35 nm	54 nm	36 nm	58 nm	32 nm	62 nm	27 nm	60 nm	39 nm
55 nm	35 nm	54 nm	35 nm	54 nm	32 nm	68 nm		67 nm	38 nm
58 nm	36 nm	60 nm	31 nm	59 nm	30 nm			79 nm	29 nm
56 nm	35 nm	61 nm	27 nm	62 nm	26 nm				20 nm
54 nm	37 nm	62 nm		65 nm	19 nm				
54 nm				73 nm					

Table 17: Measured checkerboard field widths of great dark and adjacent bright fields over time: from Jan 4th 2018 to Sept. 7th 2020. Measurement uncertainty 2nm.

outermost fields that are affected by the altering process an equation can be derived. For this analysis only the three newest datasets have been considered because of their common behaviour and because the altering process has to be in process. A quadratic function, an exponential function and a power function have been used in the fitting process with the quadratic function $f = a \cdot x^2 + b \cdot x + c$ describing the data most accurately (fig.168). The fit parameters have been calculated to $a = 1.41667 \pm 0.9034$, $b = -1.71667 \pm 4.589$ and $c = 57.4167 \pm 5.03$ for the dark fields and $a = -1.0 \pm 0.9832$, $b = 0.466667 \pm 4.994$ and $c = 36.0 \pm 5.474$ for the bright fields. A quadratic grow/decrease of the fields hints to a dependence on the surface of the sections that appear as the checkerboard fields but are three-dimensional as can be seen in the tomography series.

One possibility to obtain a change rate is the comparison of the distance where the checkerboard disappeared on measurements from different times. The difficulty is to measure approximately on the same region of the lamella. This gives a checkerboard-free distance of:
71.9 nm (16.5.2018)
77.2 nm (12.6.2018)
137.6 nm (17.5.2019)
230.6 nm (7.9.2020)
with a change of 5.3 nm/27 days, 60.4 nm/339 days and 93 nm/479 days, resulting in 0.196 nm/day, 0.178 nm/day and 0.194 nm/day with a mean of 0.190 ± 0.0099 nm/day, approximately 2 Angstrom per day. This is on the level of atomic rearranging at a lattice interface to minimize the energy at this interface. The assumption is that under the influence of non-zero temperature the lattice rearranges locally, supported by the boundary conditions of the thinness, presumably supported by introduced oxygen, in thicker material it is assumed the different phases stabilize each other.

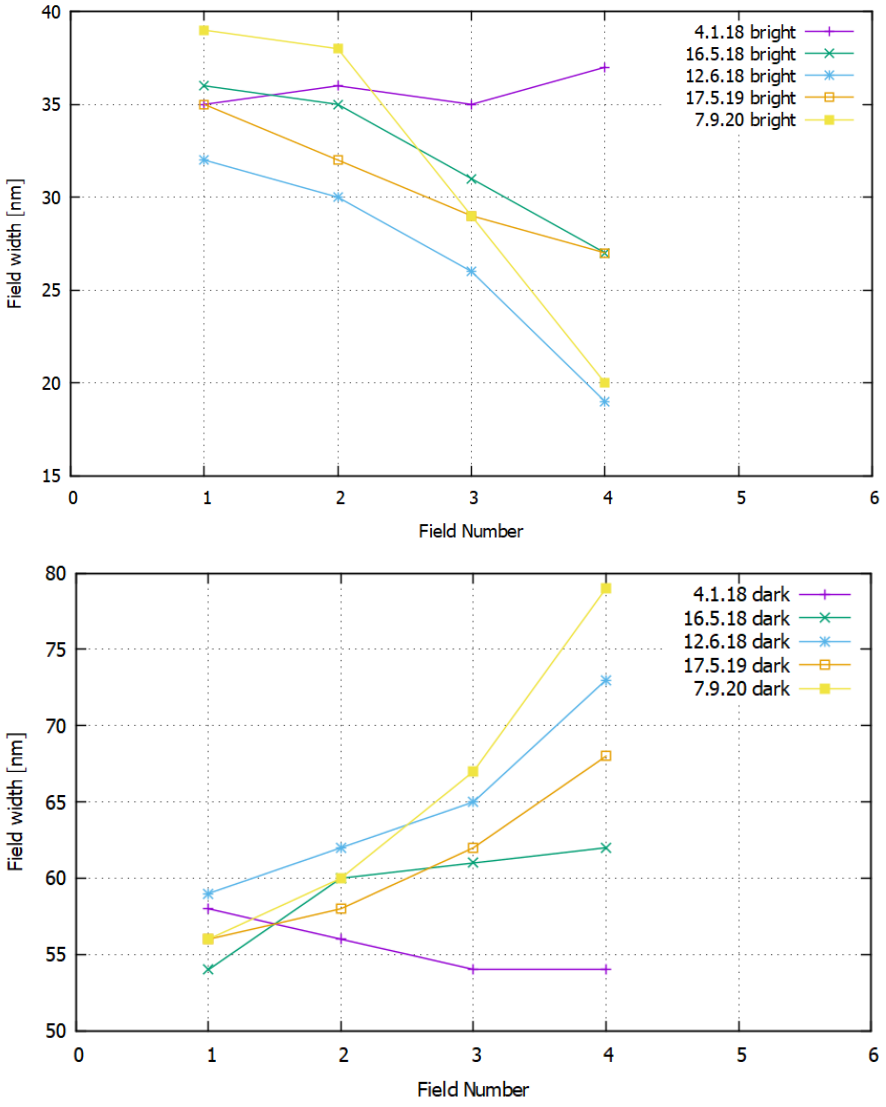

Figure 169: Plot of the width of the last four bright/dark fields of the checkerboard before they disappear in the direction of the vacuum end of the lamella for each of the five dated measurements. Top: bright field widths, bottom dark field widths.

4.2 Chemical properties

The chemical properties of the specimen have been evaluated by EDX on the JEOL 2200FS during the first investigation in 2018 and by simultaneous EELS and EDX on the ARM200F (Gatan Quantum ER post column image filter) in 2020. Because no notable change occurred only the 2020 measurements are presented here, they also have the advantage of investigating an area where the checkerboard pattern is present and another area where it is not present anymore (survey images of both in fig.170). On both regions a 105×5 pixel 2D array spectrum image has been acquired with a exposure time of 1.0 sec in STEM mode, 150kx magnification at 200 kV. The DigiScan device used software-syncronization, no drift correction has been applied during the measurement. The EELS data has been acquired by summing sub-frames of 0.1 sec, gain normalized and with Gatan´s high quality dark correction. The 5 mm spectrometer entrance aperture has been used, $\alpha = 70$ mrad, $\beta = 13.89$ mrad. The drift tube has been set to 430 V, the dispersion to 0.25 eV/channel. The EDX data has been acquired with a pixel time of 1.0 sec on a windowless SDD detector at an elevation angle of 40°, the system has 2048 channels and a dispersion of 10 eV/channel, capable of detecting X-ray photons between 0 eV and 20.48 keV.

The elemental maps have been drift corrected post acquisition using the V layer as

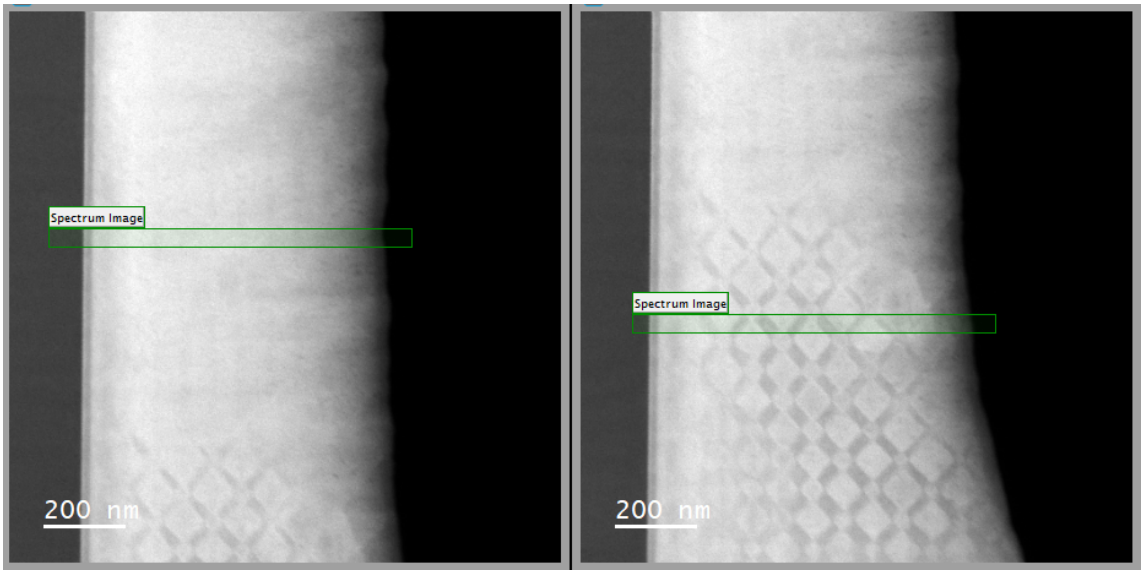

Figure 170: STEM-dark field survey images for the EELS/EDX measurements. Left: the measured region is on the part that does not show the checkerboard pattern anymore but layers instead. Right: the measured region lies across the checkerboard part of the lamella.

a feature. For the general chemical result line profiles have been obtained on all drift corrected elemental maps integrating over 4 pixels, integrating over the available 5 pixels gives rise for boundary effects in GMS and gives wrong results. The results are shown in fig.172 and fig.173. The EELS signal has been very weak and noisy on a large background resulting from the thickness of the lamella, which gives ≈ 80 nm in the thinnest part near

vacuum and rises towards the substrate. The EDX result suffers less from this conditions, the spectra contain few counts but also a low background. The V seed layer is not measured propery in EELS, the V content should approach 100%, because the edge (L_2 = 521 eV) overlaps with the O K-edge (532 eV) which could not be deconvolved properly due to the noisy character of the spectra. All results show the O from the MgO substrate and a sharp interface to the V seed layer. At the end of the lamella towards the vacuum oxidation of the sample occurred. The EDX results show the variation in the Co content used to create two similar compositions with different transition temperatures for the martensite/austenite transition, the EELS results are too noisy but still show variations. It is not possible to link the Co content variation to a variation in Al, which power has been reduced slightly during the sputter process, instead all three other elements, Ni, Mn and Al show irregular variations that sum up to compensate the Co variation. The elemental composition is measured by integrating over 255.3 nm in the central area of the layer system, giving the following results (tab.18), where another EDX measurement performed on the checkerboard pattern present on the other end of the lamella has been added (e) because it has a similar O content to measurement (d, off the checkerboard pattern) but has been measured on the checkerboard pattern. The error results are given by the standard deviation in the percent composition over the measured area. A more thorough discussion of the measurement uncertainty cannot be given as no proper standard to compare to is present for this sample. Comparison within these results is possible, they all have been measured on the same system. The accuracy of the results can be assumed to about 10% for the EELS measurements and about 5% for the EDX measurements in general [20].

	Ni	Co	Mn	Al	O
EELS (a)	48.2±2.1%	5.6±1.5%	46.2±1.5%	x	0%
EELS (b)	46.3±2.2%	5.2±2.2%	48.5±2.2%	x	0%
EDX (c)	57.9±0.9%	5.1±0.8%	25.9±1.0%	9.5±1.0%	1.3±0.7%
EDX (d)	48.4±1.5%	4.2±0.7%	21.7±0.8%	16.5±1.1%	8.9±1.4%
EDX (e)	47.7±0.8%	4.3±0.7%	22.6±0.7%	17.8±1.0%	7.4±1.2%

Table 18: Average composition of the checkerboard specimen measured by integration over an 255.3 nm wide area in the central part in the line profiles. The Al content could not be measured in EELS, the O content differs notably between the EDX measurements and is not measurable in the EELS data.

To resolve the differences between the martensite/austenite layers the elemental composition is measured both on a Co peak and a Co low over a narrow area of 24.7 nm that is smaller than the martensite layer extent of ≈ 30 nm in the EDX results (tab.19). Within the same measurement the Co content varies by ≈ 2%, the measurement on the checkerboard shows a constant Ni content and Both Mn and Al varying slightly by < 1%, in the second measurement the Al content varies by 2.7%. The oxidation differs by 1.3%/2.0%. Off the checkerboard pattern all elements show a variation, for Ni 3.7%, for Mn 0.7%, for Al 1.6% and the oxidation varies by 1.0%. It is not clear if the increased amount of oxygen leads to the disappearance of the checkerboard pattern or if it is only a result of the longevity of the lamella stored on air contact. The amount of oxygen in the measurement from the other end of the lamella is comparable to the amount measured off the checkerboard. The

thickness increases towards the ends of the lamella which are the only regions still showing the checkerboard pattern. There the relation between oxygen-influenced surface and the rest of the layer system material is different from the thinner part of the lamella where the checkerboard pattern is gone, but this can not explain measurement e). Therefore oxygen has been excluded and the results have been analysed for only the main components Ni, Co, Mn and Al, shown in tab.19 bottom part. The Ni content becomes more comparable but varies with the measurement location. In Co only small changes in the results can be observed and the $\approx 2\%$ difference between the layers is present again. The Mn content is very similar throughout all measurements and the Al content comparable between the off check and on check2 measurements. The first on check measurement from the opposite end of the lamella differs in Ni and Al, with seemingly the Ni part being replaced by Al in the other measurements. If this is a real effect is not clear, from the lamella being a very small part of the sputtered sample that should be homogeneous it is not expected.
Within the same measurement the results are comparable because the same systematic errors occur. Between measurements it is difficult to estimate the measurement uncertainty, statistical methods can be used on a set of measurements but they eliminate the differences between the regions. Therefore the results are given without an error value, the evaluation has been carried out using the Gatan GMS3 STEM SI toolbox.

The Co content is important for the different phase transition temperatures of the alloy.

	Ni	Co	Mn	Al	O
On Check, Co high	58.4±1.0%	6.0±0.2%	26.2±0.5%	8.9±0.7%	0.3±0.4%
On Check, Co low	58.4±0.5%	4.0±0.5%	27.6±0.6%	8.3±0.3%	1.6±0.3%
Off Check, Co high	45.7±1.4%	5.3±0.1%	21.1±0.7%	17.5±1.3%	10.3±0.8%
Off Check, Co low	49.4±1.4%	3.4±0.1%	21.8±0.2%	15.9±0.6%	9.3±1.1%
On Check 2, Co high	47.5±1.1%	5.0±0.2%	21.8±0.7%	19.2±0.5%	6.4±0.8%
On Check 2, Co low	48.3±0.3%	3.7±0.3%	22.9±0.5%	16.5±0.2%	8.4±1.0%
Without oxygen:					
On Check, Co high	58.6±1.0%	6.0±0.3%	26.5±0.7%	9.0±0.6%	
On Check, Co low	58.9±0.4%	4.5±0.2%	26.9±0.9%	9.7±0.8%	
Off Check, Co high	54.0±0.4%	5.5±0.4%	23.1±0.1%	17.3±0.6%	
Off Check, Co low	54.7±1.6%	3.6±0.1%	24.3±0.4%	17.5±1.7%	
On Check 2, Co high	50.7±0.9%	5.3±0.3%	23.6±1.1%	20.3±0.1%	
On Check 2, Co low	51.5±0.8%	3.6±0.1%	25.0±0.5%	19.9±0.9%	

Table 19: Averaged composition of a 24.7 nm wide region covering a Co peak or Co low within the same measurement (On check: c), off check: d), on check 2: e)). The evaluation has been carried out including oxygen (top) and excluding it (bottom). The EDX measurements on the checkerboard pattern and off the pattern have been used. The Co difference is comparable, the role of the other elements can not be fully explained. The O content differs by a great amount between these two measurements. Taking the oxygen out of consideration changes the proportions on Ni and raises the Mn content, Al remains comparable and Co changes only by very small amounts. The error is given by the standard deviation from the used datapoints.

The Co data has been separated from the EELS and EDX measurements and found to form layers that differ in their Co content by $\approx 2\%$ (fig.171). The layers with higher Co

content are found to be 49.4 ± 8.2 nm, those with less Co content 32.9 ± 8.2 nm. These layers can be separated in the EDX measurements, the EELS measurements are very noisy and some layers can only be guessed to be there.

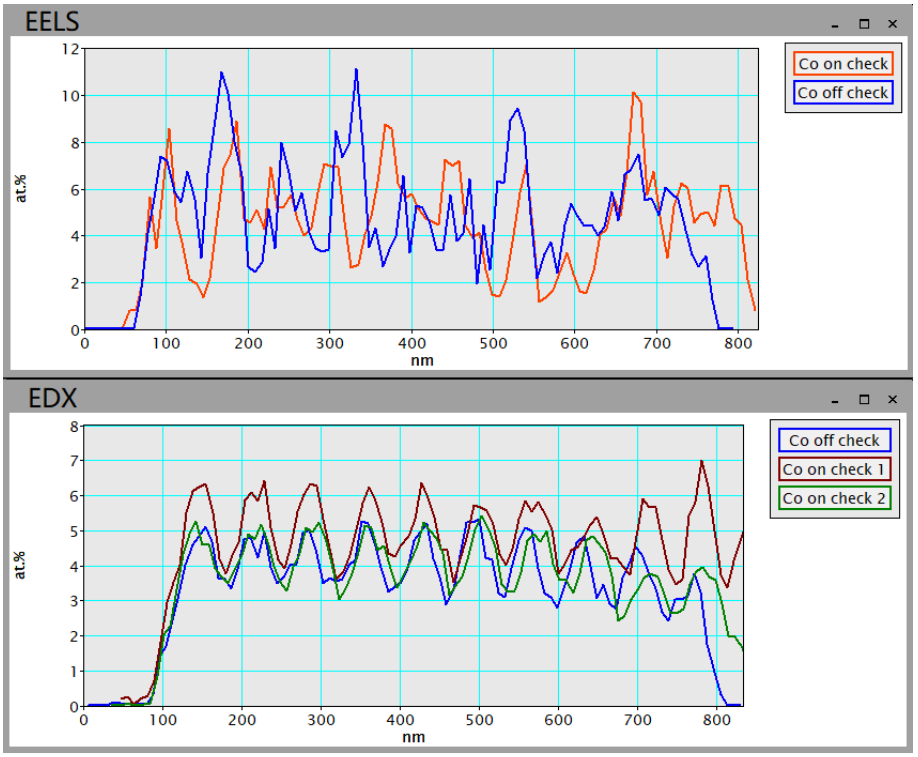

Figure 171: Top: Co result from the EELS measurements, the layers could not be clearly resolved because of he noisy spectra. Bottom: Co result from the EDX measurements from both ends of the lamella still containing the checkerboard pattern and a region where the pattern has disappeared. The layers of varying Co content can be resolved clearly.

To exclude modulation in different directions, one 60x15 pixel map has been acquired of a region containing several checkerboard fields and checked using line profiles in different directions. The Co modulation is the only relevant composition change and it follows the sputtered layers. The elemental maps can be found in Appendix 6.12, the layer modulation in the Co is clearly visible. Post-acquisition drift correction has been omitted because no feature is in any of the maps that can be used to align on.

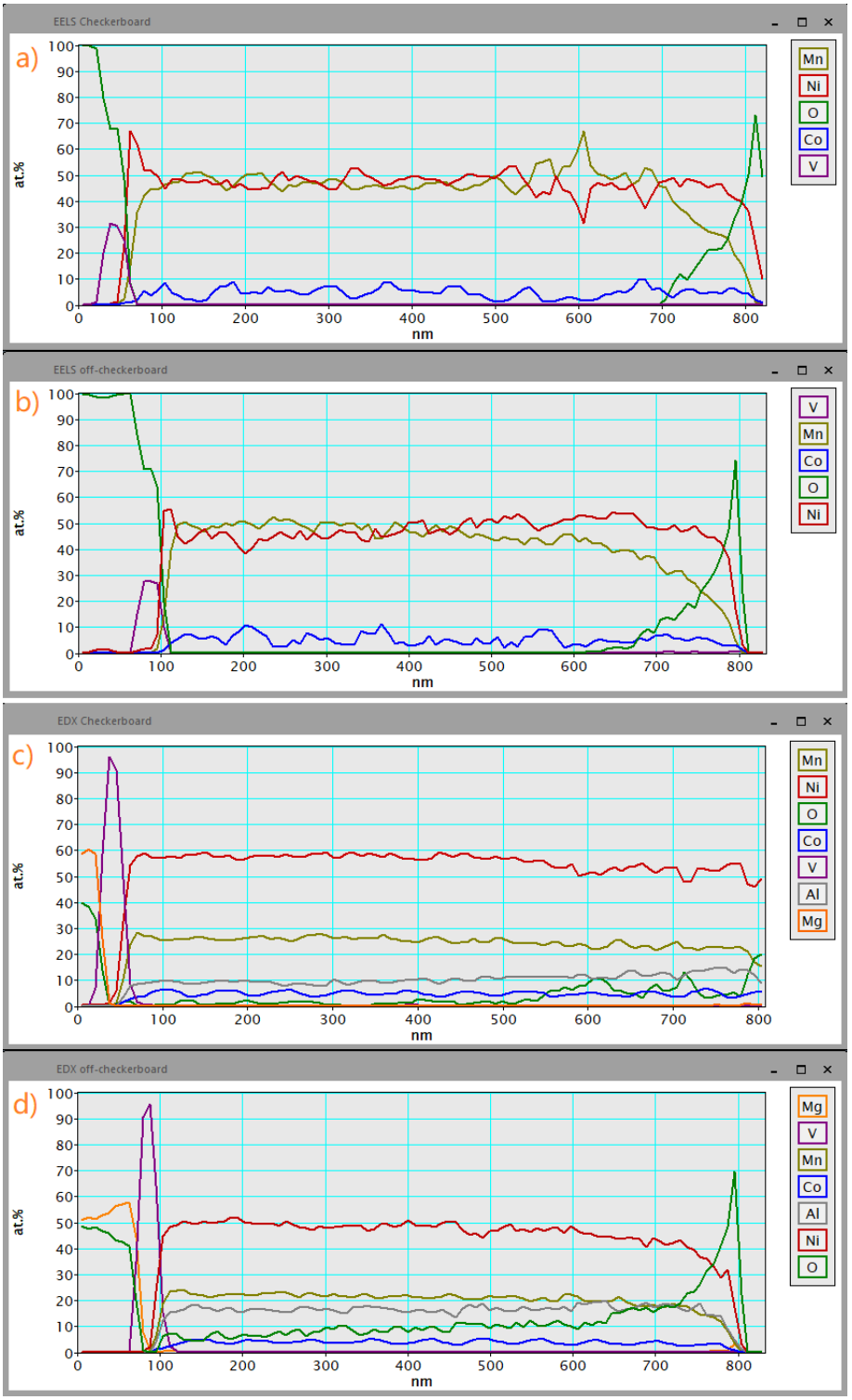

Figure 172: Chemical results of the checkerboard: a) EELS measurement on the checkerboard region, b) EELS measurement on the region without checkerboard, c) EDX measurement on the checkerboard region, d) EDX measurement on the region without checkerboard. In the EDX measurements the varying Co content of the martensite/austenite layers is clearly visible. MgO substrate always on the left.

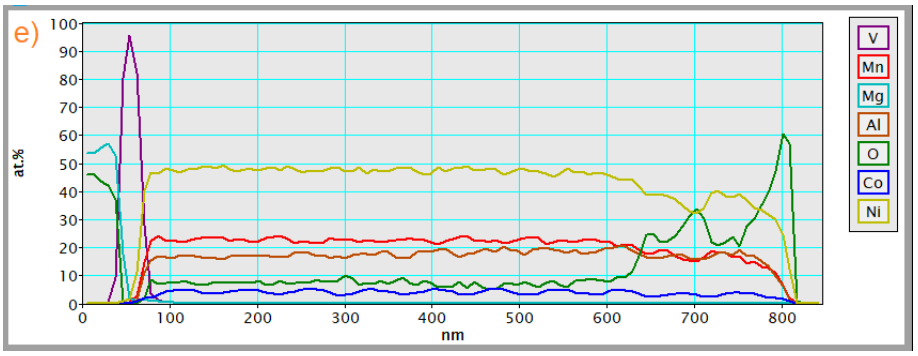

Figure 173: EDX result e) of the opposite end of the lamella where the checkerboard is also still present. Oxidation of the near-vacuum part (right) occurs over ≈180 nm.

4.3 Reproduction

None of the three other specimen made from the four samples selected for TEM investigation showed a checkerboard pattern. However the sample that has a number of intercalations of 7 which is closest to the one of the checkerboard sample with 13 intercalations shows some regions that could be regarded as a preliminary stage of the checkerboard (fig.174).

In this sample sequence the thickness of the austenitic layers is decreasing while the

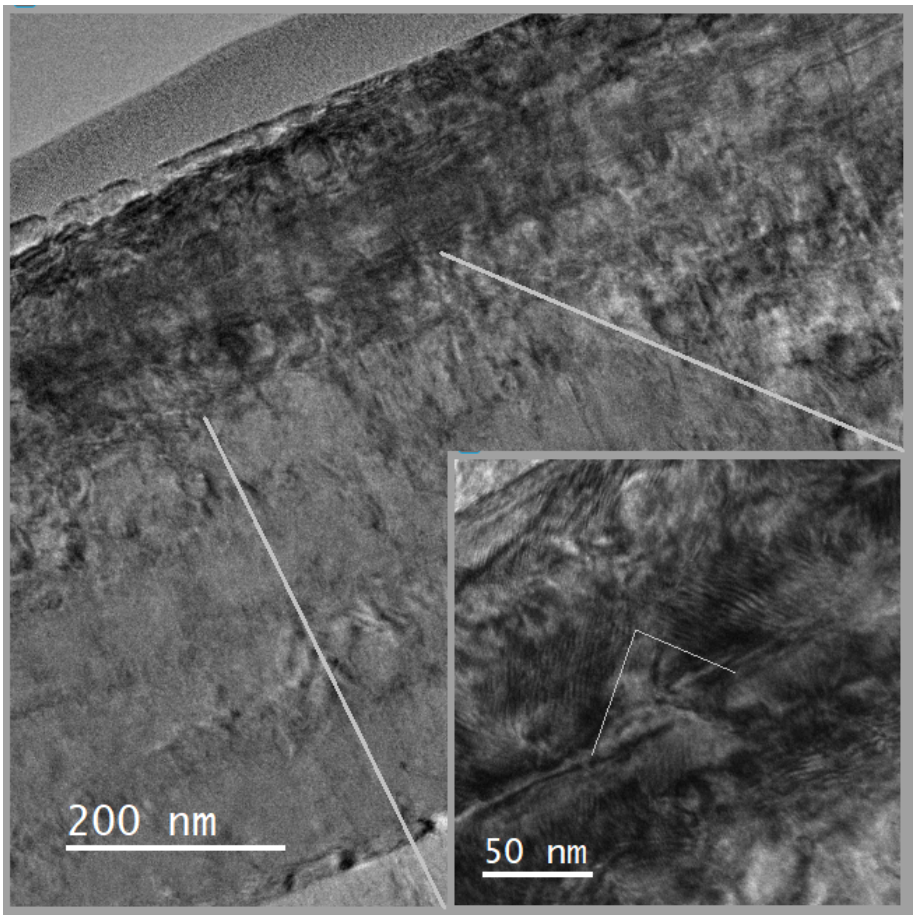

Figure 174: The sample with 7 martensitic intercalations shows regions of nearly rectangular shape with the by 90° to each other oriented Moiré patterns of neighbouring regions that are a characteristic of the checkerboard. Apart from a few regions only layers are visible. MgO substrate at the bottom of the image.

thickness of the martensitic intercalations is always the same, their number is rising. The sample showing the checkerboard pattern is the one with the most intercalations. This leads to the conjecture that the thickness of the layers plays a role in the formation of the checkerboard. When the thickness of the austenitic layer approaches the thickness of the martensitic intercalations, formation of a checkboard pattern can be observed.

To check this conjecture three samples have been prepared by Andreas Becker with the same sputter parameters as before on MgO substrate with a 30 nm V seed layer but different layer thicknesses with alternating layers of:

A) 6× martensite (10 nm)/ 5× austenite (30 nm)
B) 6× martensite (30 nm)/ 5× austenite (30 nm)
C) 6× martensite (30 nm)/ 5× austenite (50 nm).

The lamellas prepared out of sample B and C show a checkerboard pattern at an angle of 45° to the MgO substrate (fig.176), although it is not as perfect as the one from the original sample. A possible reason is that this first lamella has been cut very thick compared to the better thinned from the reproduced samples, and the structure is three-dimensional. The measured dimensions of the pattern are:
Specimen B: 47 ± 5 nm for the greater dark fields, 23 ± 3 nm for the smaller dark fields, the rectangular brighter fields are in between, measuring 47 ± 5 nm at the long side and 23 ± 3 nm at the short side.
Specimen C: 60 ± 5 nm for the greater fields, 40 ± 5 nm for the small dark fields, the transition regions measure 60 ± 5 nm at the long side and 40 ± 5 nm at the short side. The small fields are the darkest fields, this might be because of a non-perfect tilt angle, the specimen is not tilted to zone-axis. Specimen A does not show the checkerboard pattern. The existence of the structure has been proved by a bright field STEM image which shows the quadratic and rectangular cells:

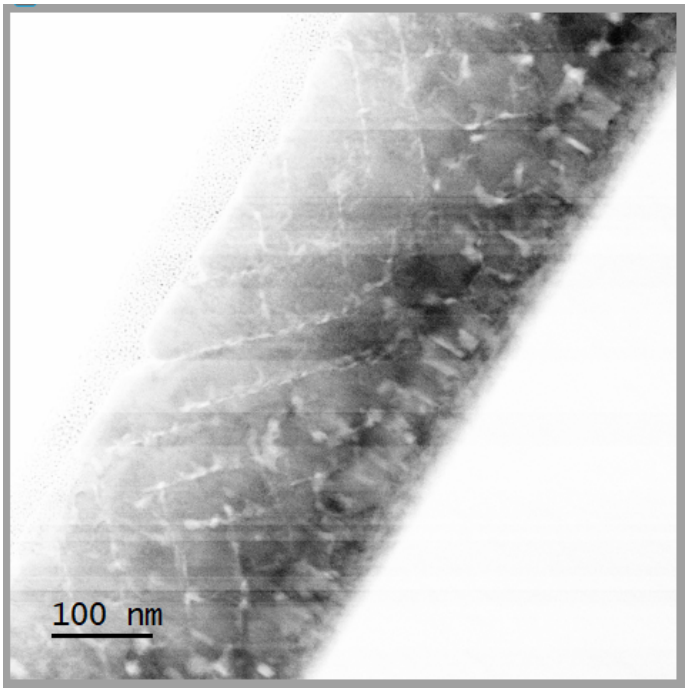

Figure 175: Bright field STEM image of reproduction specimen B showing a rectangular structure at an angle of $\approx 45°$ to the substrate resembling a checkerboard pattern. Substrate bottom right.

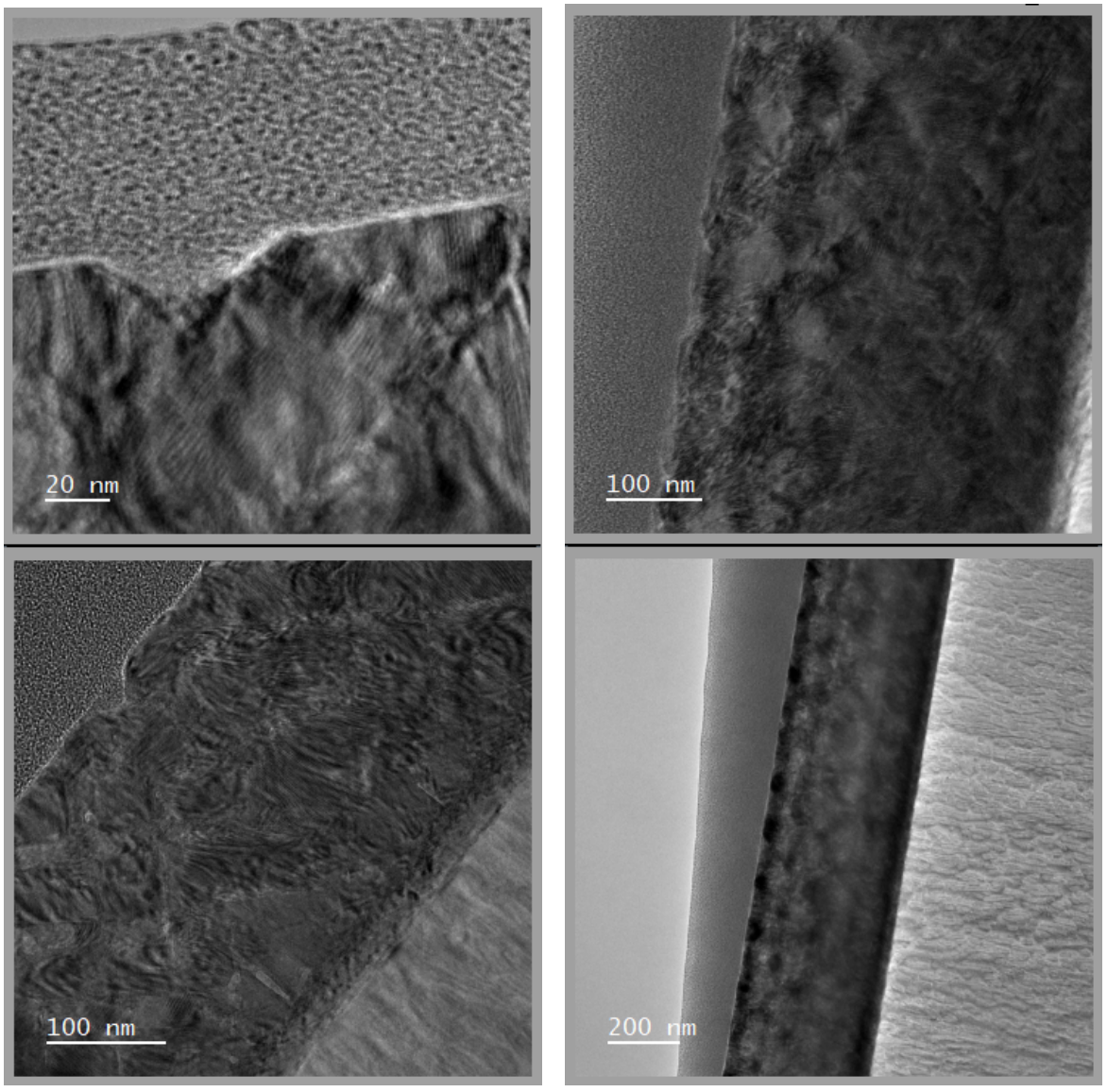

Figure 176: Left: Result of reproduction sample B, substrate bottom right. Right: Result of reproduction sample C, substrate on the right. Lamella overview at the bottom, higher magnification image in the top row.

4.4 Temperature dependence: heating and cooling

Heating experiments have been performed on the JEOL 2200-FS using the JEOL EM-31670SHTH heating specimen holder. From room temperature the specimen has been heated to 30° C, from there to 140° C in steps of 10° C. During the cooldown time measurements have been obtained at the temperatures of 115° C, 105° C, 95° C, 85° C and 75° C. After reaching the target temperature there has been a waiting time for stabilization of 10-15 min before obtaining any measurement. If any notable specimen drift occurred the waiting time has been extended. At each temperature several TEM images have been acquired, providing an overview and going up to HRTEM images of the structure. The change of the checkerboard structure is visible, it starts to vanish at 80° C and is mostly gone at 120° C. Two series of images is shown in fig.178 with the first series depicting an overview of the lamella and the second series focusing on a part containing several fields of the ckeckerboard.

The temperature of this phase transition can be measured to lie in between $\approx 110°$ C$-130°$ C from the TEM images. After cooling down the fields are present as before heating the specimen. During the measurements in the cooldown phase where the depicted temperature has been set as target temperature on the heater a thermionic hysteresis could be observed, at 75° C the checkerboard pattern started to reappear slightly, which can be seen in fig.179 (top). This thermionic hysteresis is difficult to measure from TEM images, but as the phase transition involves a contrast change from a notable difference between brighter and darker fields to no field structure observable the present contrast difference across fields can be used as an observable. A visualization of this can be seen in fig.179 (bottom) where for all measured temperatures the contrast across three bright and in between two dark fields ($\approx$ 220 nm) has been measured by a line profile with an integration width of 400 pixels, which corresponds to the central part of the row of fields without the edges to neighbouring ones. The data is shown according to the temperature where it has been measured, starting from the bottom with 30° C, going up to 140° C and further back down to 75° C. The contrast arising from the fields is gone at 110° C, at 130° C the contrast is totally flat, indicating that the transition has ended after the checkerboard fields have vanished. During cooling down the contrast reached at 75° C is not comparable to 70° C or 80° C but to 120° C, proving the thermal hysteresis.
A measurable quantity is the difference between the minimum and maximum values of a line profile, providing a contrast measurement for the deviation from a line defined by the low values of the line profile. This method can be affected by a change in illumination conditions like a different excitation of the condensor lens but can act as a guideline. This contrast measurement is shown against the temperature in fig.177 where a hysteresis can be seen. The rapid change indicates the change in the illumination conditions made during the lower temperatures to optimize the image on the camera.

The TEM also allows a closer look at the structural change by performing HRTEM measurements. At each temperature an image is chosen in a way it contains similar content and parts of both types of field. Acquisition parameters are magnification 600kx in TEM mode, 200 kV acceleration voltage, exposure 0.1596 sec on the Gatan OneView camera, 4069×4096 pixels. The images have been transformed into a diffraction pattern using

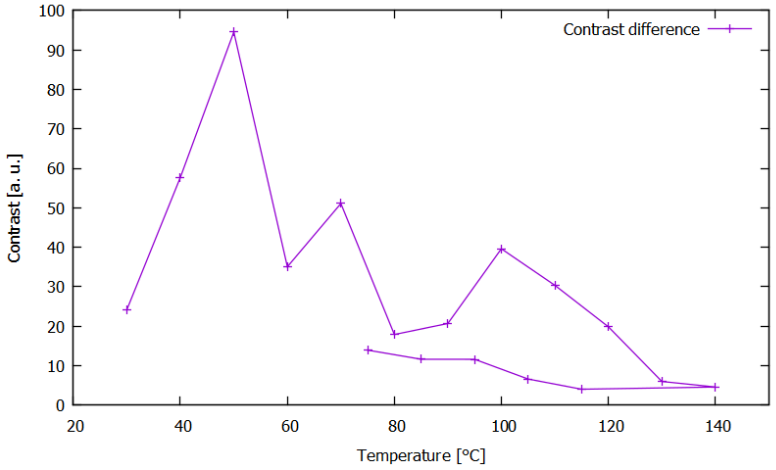

Figure 177: Here the contrast change is shown against the measurement temperature, indicating the presence of a thermionic hysteresis.

FFT. An overlay of these FFT diffraction patterns at the temperatures of 40° C, 80° C, 100° C and 130° C (fig. central image) shows the change occuring by increasing the temperature. The specimen has not been tilted perfectly to a specific zone axis, this limits the information that can be obtained. The small spots from the martensite which are visible especially at 40° C and 50° C vanish with increasing temperature, only austenite is present from 110° C on.

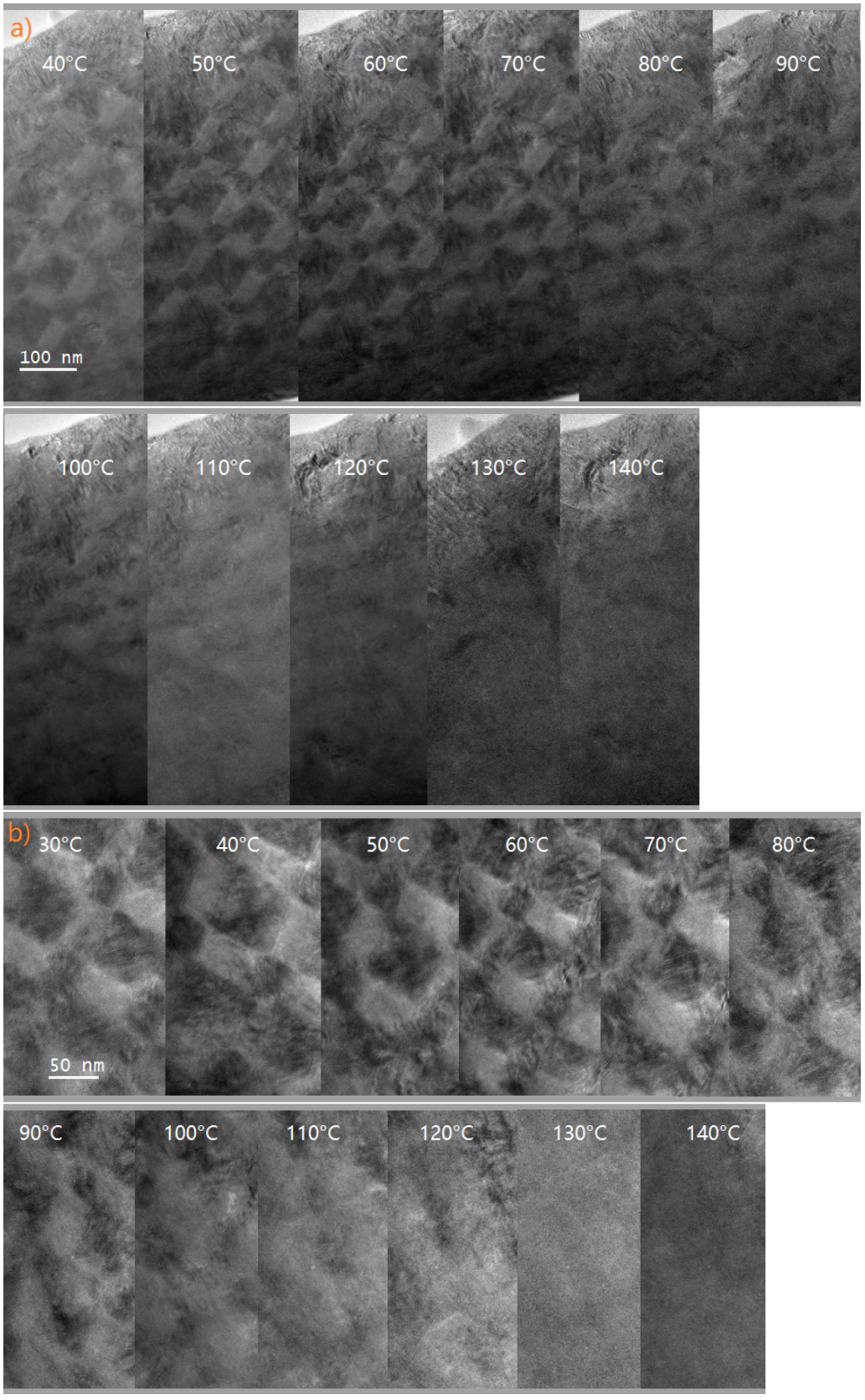

Figure 178: Temperature series of the checkerboard specimen from 30° C to 140° C. The upper series (a) shows an overview of the specimen, the lower series (b) focuses on a section of checkerboard fields and their temperature evolution.

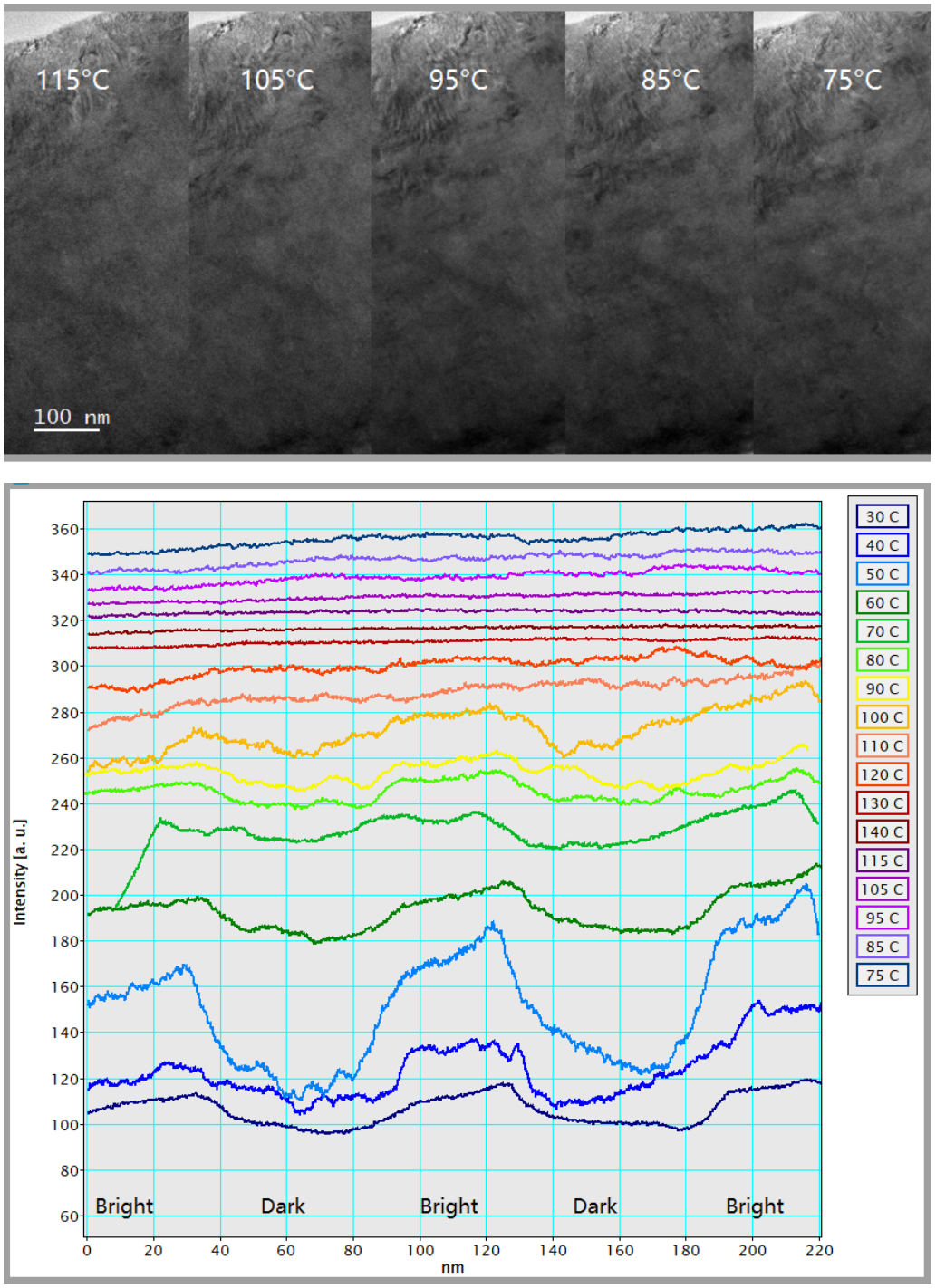

Figure 179: Top: Temperature series of the checkerboard at five temperatures during the cooldown phase. The checkerboard starts to reappear at a different temperature than it did vanish. Bottom: The lineprofiles taken across a series of dark and bright fields are used to measure the contrast and thus the state of the specimen in the transition. The intensity value is of no importance, the data has been shifted on the y-axis for better accessibility. Differences like the step-like behaviour at low temperatures or the contrastless lines at 140° C show the state of the specimen.

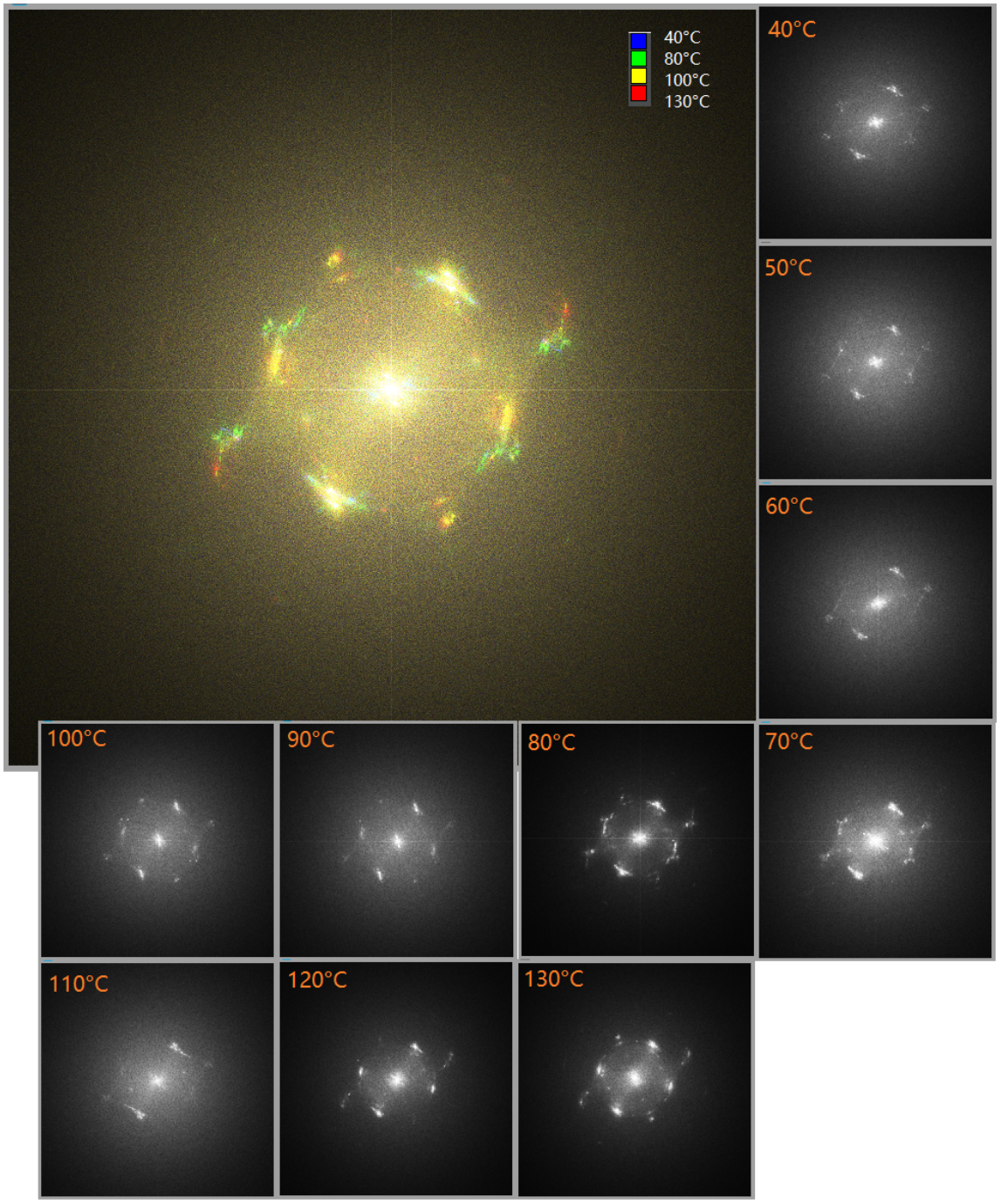

Figure 180: Central part: overlay of four FFT diffraction images acquired at 40° C, 80° C, 100° C and 130° C. The green and blue parts are only present in the phase containing the checkerboard pattern and originate from martensitic parts in the specimen, the yellow and red parts are on/above the phase transition and show only austenite The FFT diffraction images for the temperatures from 40° C to 130° C are grouped around.

A cooling experiment has been performed using the cryo transfer holder system of Fischione on the JEOL 2200FS. The system has been cooled to -170° C (103.15 K) using liquid nitrogen and after reaching this temperature a waiting time of 15 min has been kept for the specimen to stabilize. Before and after the cooling experiment TEM and HRTEM images have been acquired. At room temperature both austenitic and martensitic fields have been there (fig.181).

At -170° C TEM images and diffraction patterns have been acquired (fig.182). The TEM

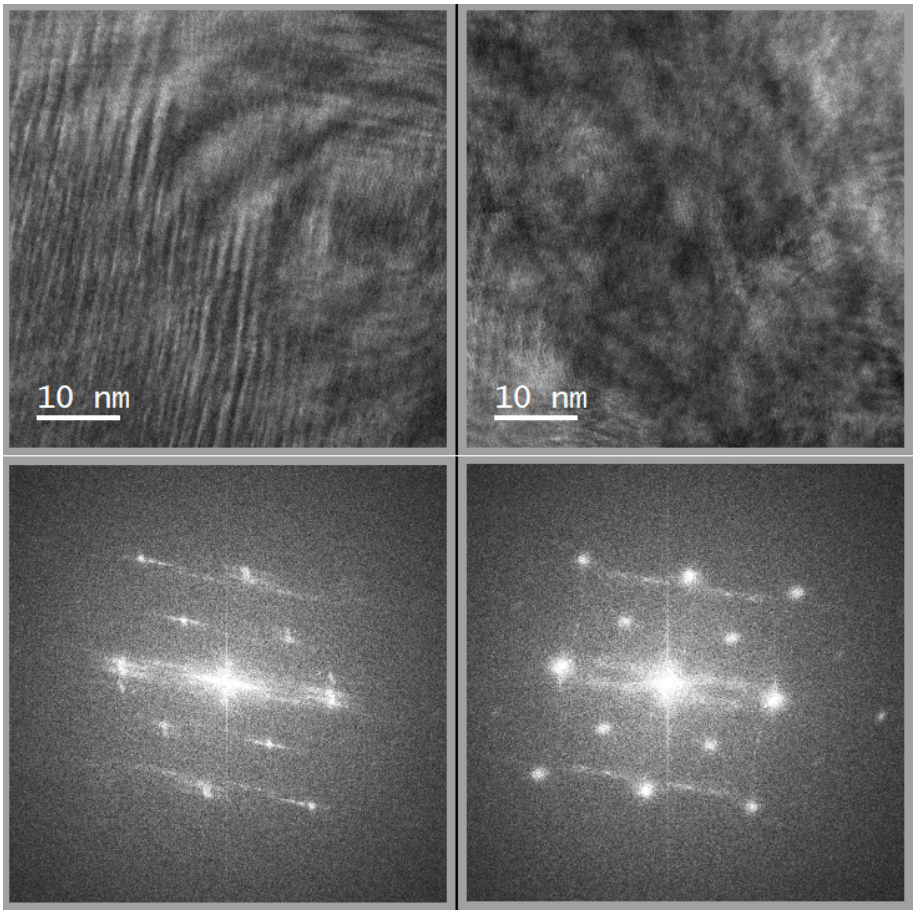

Figure 181: Martensite (left) and austenite (right) parts of the checkerboard specimen before the cooling experiment. The two images at the top are the HRTEM images, below the diffraction pattern obtained by FFT. The presence of martensite in the left image is confirmed by the additional martensitic diffraction spots.

image shows Moiré patterns in quadratic forms or at least perpendicular to those of the next region. This is probably a preliminary stage and source of the checkerboard pattern where the quadratic regions become part of the checkerboard fields. Apart from the Moiré no other noteworthy contrasts are visible. The diffraction pattern has been recorded at a camera length of 25 cm on the Gatan OneView camera after positioning the 10 μm selected area aperture on the specimen. The beam stopper to exclude the transmitted beam with its high intensity is visible in the image. Visible in the diffraction pattern are a set of rows

of reflexes with a distance between two parallel rows of 0.467 1/nm and a second set of rows perpendicular to the first set separated again by 0.467 1/nm. The rows of reflexes are in agreement with the simulation for the martensite diffraction pattern, here two types of martensite perpendicular to each other can explain the two sets of rows.
At the temperature of this measurement the specimen should have undergone the phase transition to martensite, the lower martensite transition temperature of the two material compositions lies at $T_M = 232\ \mathrm{K} > T_{measurement} = 103\ \mathrm{K}$. Some reflexes close to the edges of the squares are brighter, these are also excited at higher temperature like room temperature when the specimen consists only partly of martensite.
In the center of the squares formed by the two sets of rows a single weak reflex is present at a distance of 0.126 1/nm from the transmitted beam or the next crossing of two rows. It corresponds to a distance of 3.065 nm and can be observed in a detailed view to have neighbouring weaker reflexes with which it forms a row similar to the observed strongly excited rows of reflexes caused by martensite. A possible source is the structure superposition that leads to the appearance of the Moiré pattern or an underlying martensite structure similar to the observed one but shifted.

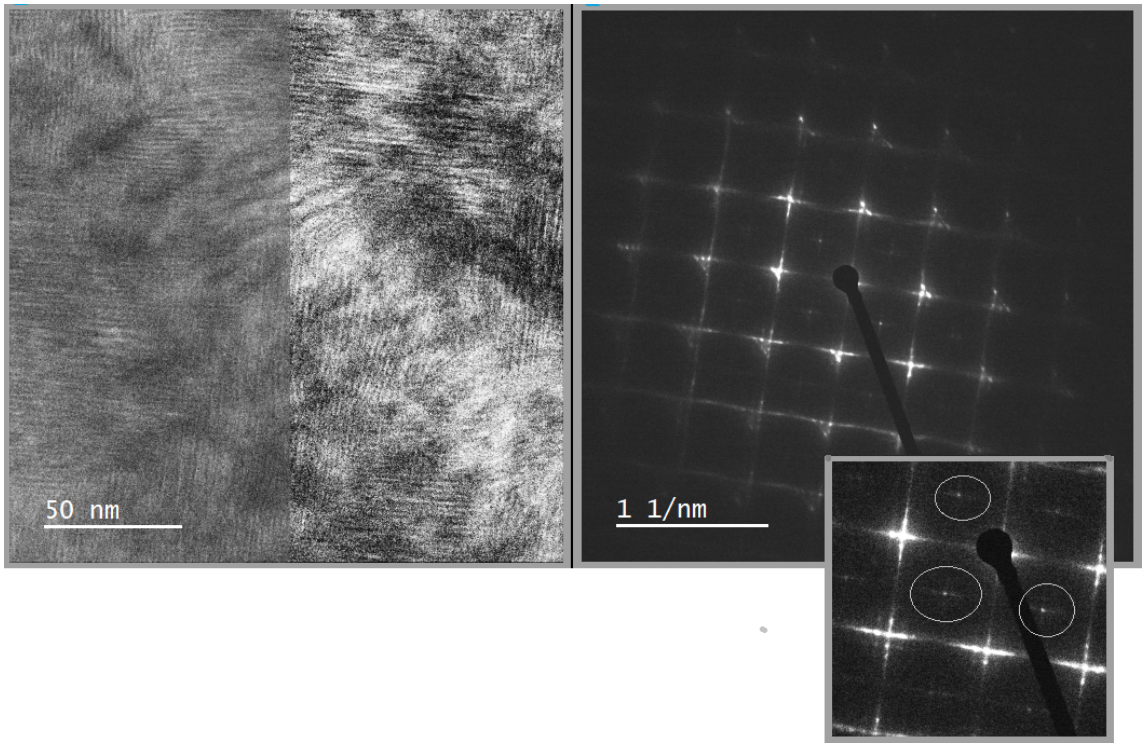

Figure 182: Left: TEM image of the specimen at -170° C, the right half of the image has been enhanced in contrast to make the Moiré and its directions more visible. Right: Diffraction pattern recorded at the same temperature.

4.5 Magnetic properties: DPC and EMCD

To obtain information on the magnetic properties of this specimen, DPC and EMCD measurements have been performed:

4.5.1 Differential phase contrast measurement of the magnetic properties of the checkerboard

Segmented differential phase contrast measurements have been obtained on the ARM200F in Padernorn in low mag mode (200 kV, alpha 2, 1500 cm camera length, 20 μm aperture). To obtain also magnetic information the beam has been centered accurately with special emphasis on the four outer segments. To obtain possible magnetic signal, the specimen has been tilted to $\pm 25°$ in the field of the objective lens set to 0500, corresponding to 0.1 T, therefore the in-plane external field at $\pm 25°$ corresponds to a field strength of ± 0.0423 T. The measurements have been performed after tilting back to 0° after the OL field has been turned to zero again and an additional waiting time of 15 sec to avoid influences of the external field on the specimen magnetization during tilting back. Several datasets have been recorded: before applying an external field and after applying the external field in both directions with an overview dataset and a close-up dataset of the checkerboard fields. The corresponding colour images can be seen in fig.183, they show qualitatively comparable information and the checkerboard pattern is visible even in terms of direction and strength of the beam deflection.

The component images have been calculated from the eight segment images with a

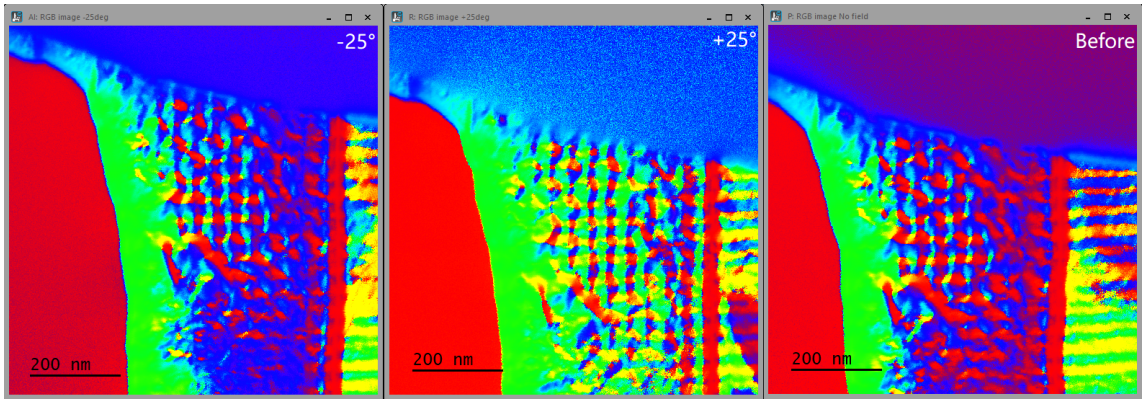

Figure 183: RGB images of the overview datasets, from left to right: after tilting to $-25°$ in the OL field, after tilting to $+25°$ in the external field and before application of the external field.

normalization on the MgO substrate. To try to separate the component signal a rotation of 85° has been applied in an attempt to minimize the contrast in one component. Line profiles have been drawn across the specimen in different orientations with an integration width of 10 pixels to be able to detect properties of the size of the checkerboard fields: Across several fields, parallel and perpendicular to the substrate (fig.184).

The line profiles have been overlaid for both tilting directions to detect any magnetic

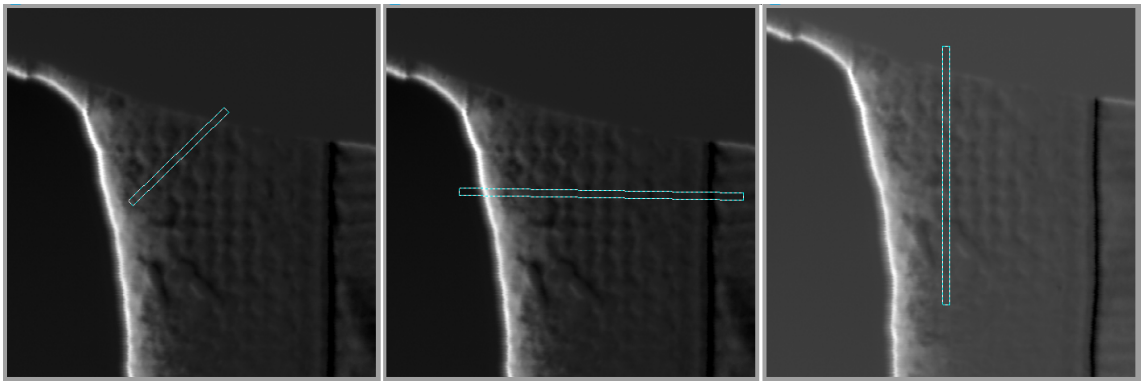

Figure 184: Position of the line profiles on the lamella: Across several checkerboard fields (45° angle), perpendicular to the substrate and parallel to the substrate.

signal that would be switched by the external field. The results for all three line profiles are displayed in fig.186. For both external field orientations the results in each component show the same behaviour, the absolute value differs slightly. For a better visibility component 1 is always displayed in blue/bluegreen and component 2 in red/orange. In the case of magnetic signal being present a reversal within one component could be seen, this is not the case. Apart from magnetic signal the specimen shows location-dependent properties: Measuring the deflection across a row of fields results in alternating deflections depending on the fields, the dark/big fields show small up to negative deflection in component 1 (comp1) and positive deflection up to $0.2 \cdot 10^{-4}$ rad in component 2 (comp2). The fields in between show a peak in comp1 and an opposite peak in comp2. It allows to detect the checkerboard fields by their deflection, on the interfaces between fields the change is continuous without extra peaks that would show a sharp interface between materials with different mean inner potential, from this data a gradual change can be assumed. Using FWHM especially of the comp2 signal it is possible to measure the dark fields to 55 ± 3 nm and the smaller fields to 34 ± 3 nm.
Measuring the deflection signal perpendicular to the substrate gives a result similar to the Co EDX signal resembling the layer structure. It is more apparent in comp1 but also present in comp2 which results from the rotation not being able to separate the two components. Again no magnetically switched signal could be observed. The peak-to-peak distance is measured to 75.4 ± 5.2 nm, using again a FWHM approach it is possible to separate alternating regions of 52 ± 3 nm and 29 ± 3 nm which is in agreement with the sputtered austenite/martensite layer thickness but ≈ 75 nm also with the checkerboard fields at a 45° angle, smaller regions if the line profile crosses only parts of fields. If the origin of this modulation are the layers, it should also be present where the checkerboard is not present anymore. This is not the case, comp1 shows only a slightly modulated deflection up to $-0.2 \cdot 10^{-4}$ rad, comp2 a flat signal at $-0.24 \cdot 10^{-4}$ rad. The modulation in the checkerboard area lies close to $\pm 0.5 \cdot 10^{-4}$ rad. Therefore most of the modulation originates from the checkerboard fields alone respective of the properties of the interface between the fields.
Parallel to the substrate the signal is more complicated. The line profile has been drawn from the end of the lamella across the checkerboard pattern into the region where the

checkerboard is not visible anymore. Comp1 and comp2 appear to be a mirror of each other, apart from a small offset. The checkerboard fields are oriented at 45° to the line profile and it crosses the fields through their center. Peaks in comp1 measure approximately between 70 nm and 80 nm, this is in agreement with the diagonal of quadratic fields with a size of $50 - 55$ nm. In comp2 the region covered by a peak in comp1 shows a transition between two peaks from positive to negative deflection with a substructure of two small peaks before going down further, similar a saw profile, marking three subregions of approximately equal size. The origin of this structure needs to be covered by future research.
If the line profile is dragged across the field of view it changes in a regular manner for both the profiles parallel and perpendicular to the substrate. This can not be shown in one graphic but it is in accordance with dragging a line profile that measures the intensity at a 45° angle over a checkerboard where dark fields have a different intensity than bright fields.
The close-up images can be processed only without post-acquisition normalization because in one image is no nonmagnetic feature that is not structured and has no varying thickness. To create the radius and theta images the python script for segmented DPC processing provided by the Glasgow group has been used in addition, the histogram allows a centering that acts as normalization. A rotation of 155° has been applied. As for the pixelated DPC data the X and Y components have been imported in Digital Micrograph and evaluated using lineprofiles. The results are the same as for the overview image with additional details in the line profile across the fields (fig.185). The fields are not represented by a peak or

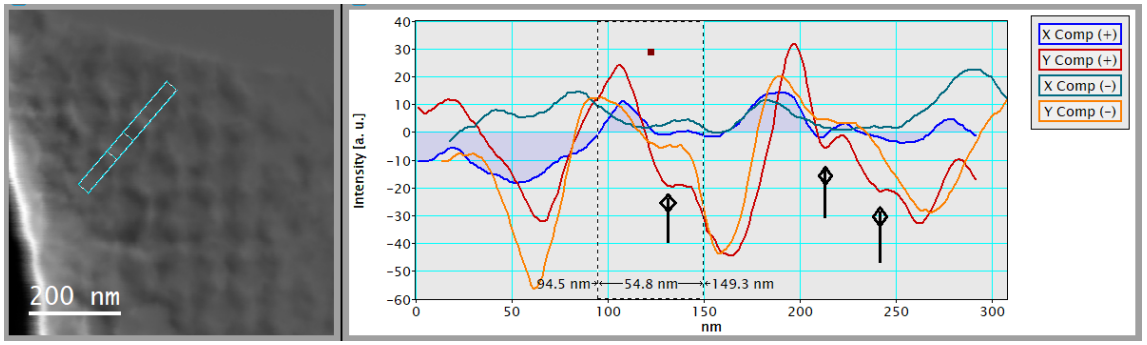

Figure 185: Left: Y component with indicated line profile position. Right: Line profile integrating over 20 pixels across a series of checkerboard fields on both X and Y component after tilting to $+25°$ and $-25°$ in the external field.

low but by a transition in the Y component with peaks of opposite directions marking the transition to the next, different field. This can be an indication for a change in the mean inner potential that takes place on the border between the fields. The X component also shows transitional behaviour. The substructure of one or two additional smaller peaks in the Y component becomes more clear, although the reason for their appearance needs still further investigation.
From the results shown in fig.187 again no reversal corresponding to magnetic signal can be observed. This is in accordance with the magnetic measurements showing a magnetic hysteresis below room temperature. Both histograms in fig.187 bottom are centered

on zero deflection with only one center and no notable substructure, underlining that there is no magnetic signal. The checkerboard field structure is apparent and in the theta(r) image that combines deflection signal strength and direction strong deflection in opposite directions is apparent at the opposite boundaries of a checkerboard field. As the mean inner potential is dependent on the crystal lattice structure a periodic change in structure, for example between martensite and austenite, could cause this structure in deflection. The difference in MIP could not be too high, otherwise the deflection signal would show larger peaks at the interfaces between two fields that would overwhelm the other signal as it can be seen on the TMR stack specimen. A great change in MIP between martensite and austenite is also unlikely because only the crystal lattice changes, the elemental composition is nearly the same. The DPC measurement therefore supports the assumption that the checkerboard fields consist of martensite or austenite. A three-dimensional extent could be a possible explanation for the substructure in the fields in the DPC measurements: if the fields do not form a perfect column with respect to the MgO underlying field interfaces in checkerboard cuboids below the surface ones may cause a small deflection.

It can be stated that the checkerboard fields leave a non-magnetic mark in the DPC signal in agreement with the magnetic VSM measures (fig.137) and the fields have a different quality in at least two dimensions. A change in the mean inner potential is a possible source, in any case further research and detailed modelling has to be carried out.

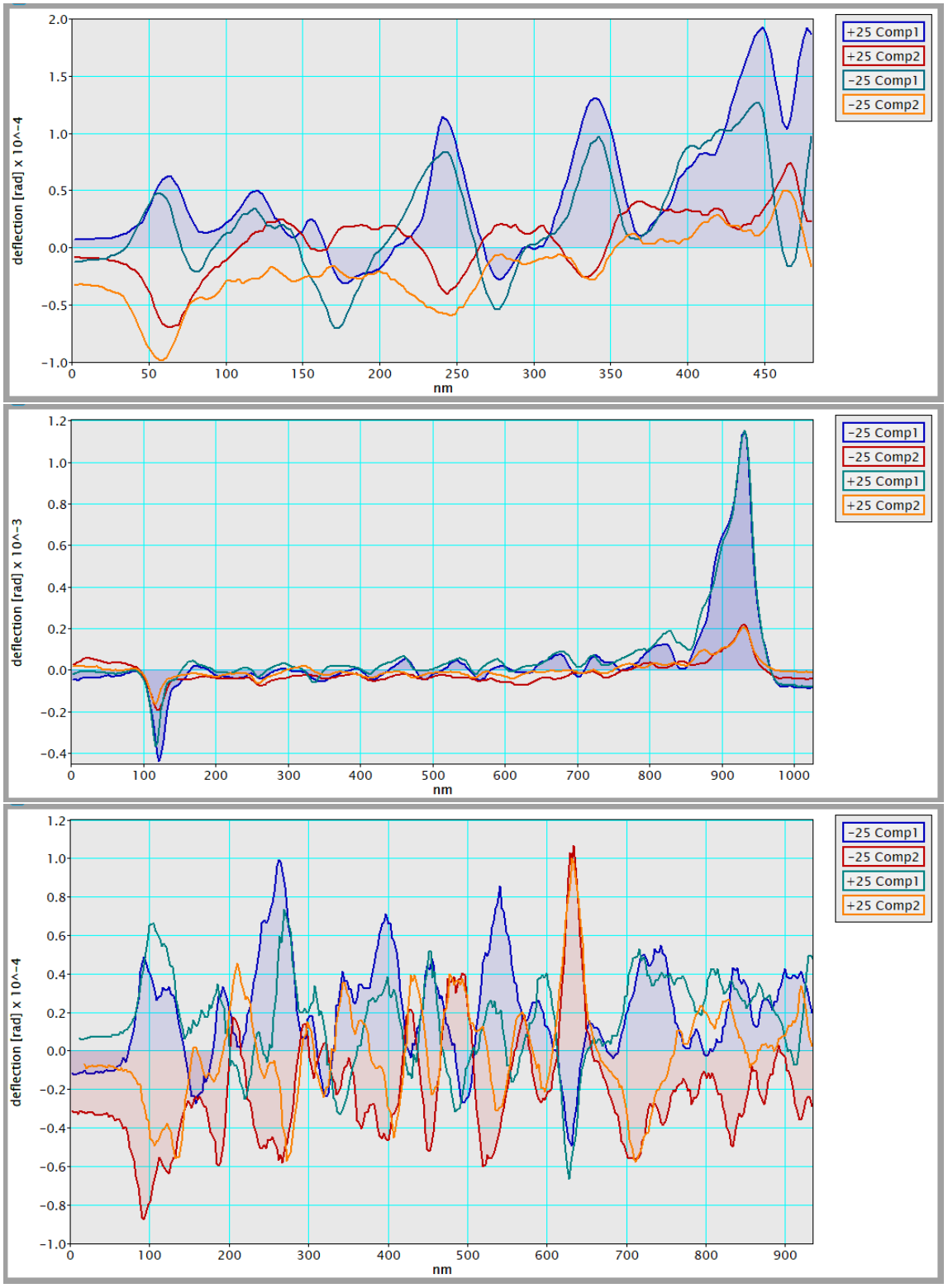

Figure 186: Line profiles on both DPC components across checkerboard fields (top, end of lamella on the right), perpendicular to the substrate (center, substrate on the left) and parallel to the substrate (bottom, end of lamella on the left) show the beam deflection.

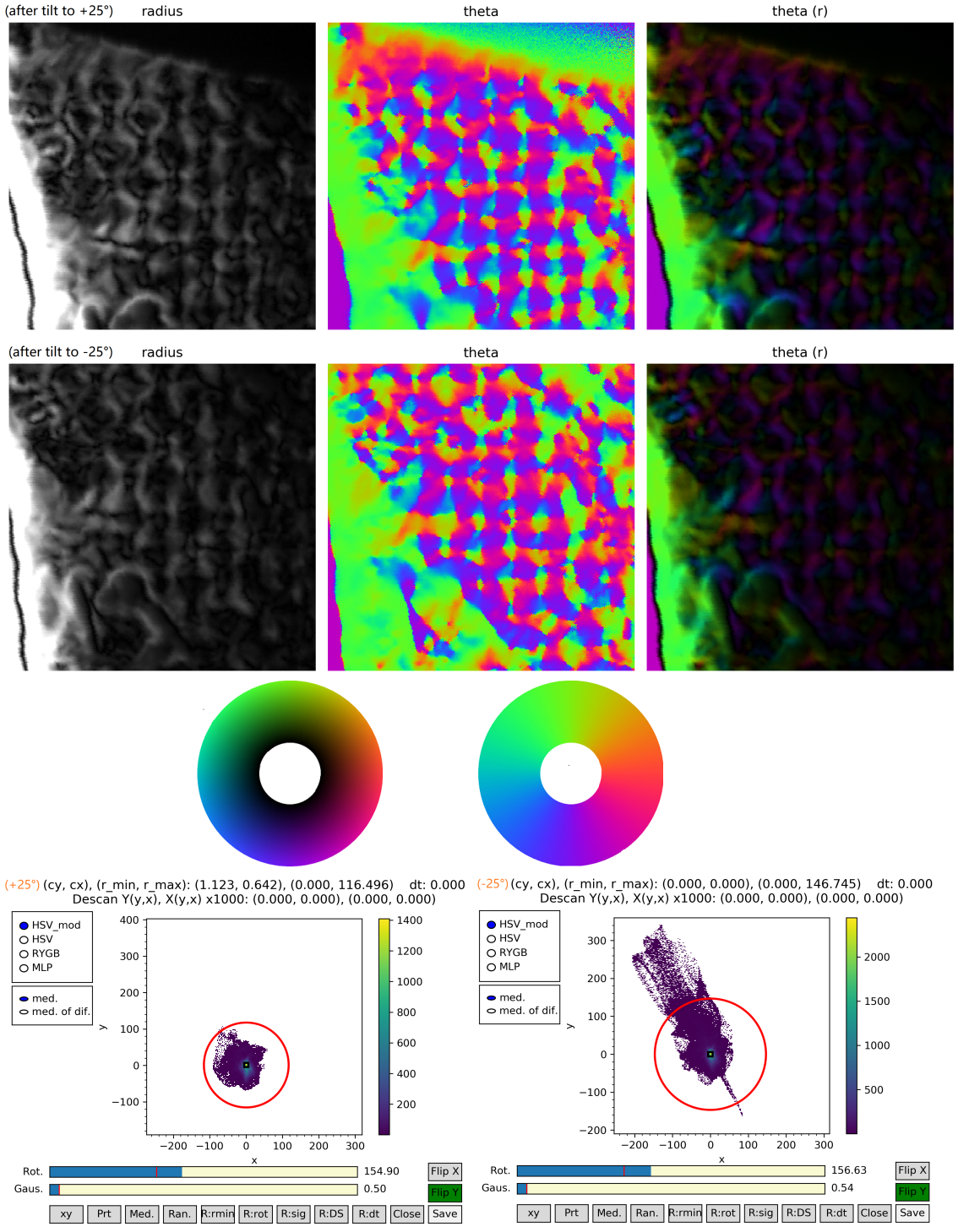

Figure 187: Radius, theta angle and combined deflection results for the checkerboard close up image after tilting to +25° (top) and −25° (center), colour wheels below with the left wheel showing direction and strength of the deflection and the right wheel only the colour coded directions. No difference that could result from magnetic signal (opposite orientation in both datasets) is visible. Bottom: Histograms for both datasets.

4.5.2 EMCD measurements on the checkerboard and comparison samples

EMCD measurements have been performed in STEM mode on the ARM200F. A series of 10 spectra has been acquired with the following parameters: exposure 50 sec, 5 mm spectrometer entrance aperture, dispersion 0.25 eV/channel, drift tube 550 V, 500kx magnification, 12 cm camera length, 10 μm aperture, spot size 4C.
The linescan has been acquired on an area near the vacuum where the specimen is relatively thin and crosses three checkerboard fields (fig.188 left). The thickness has been measured by a zero loss linescan recorded previously. Looking at the survey image of the linescan the checkerboard fields are not properly visible, this results from the way of acquiring this image, it is neither a BF or DF image but recorded of the electrons that are not excluded by the apertures and detectors below the spectrometer entrance aperture measure only the electrons from the edge of the diffraction discs. The contrast formed by such a setting is very complicated and can only be used for orientation on the specimen, not for analysis. On the points of the linescan an EMCD effect could be measured on both Mn and Ni, the Co edge is too narrow and barely distinguishable from noise because of the low Co content and Al does not have an EELS edge in the well accessible range. The specific reflexes used in the systematic row could not be determined because of the complicated crystal structure, this limits the amount of information that can be obtained. A result for Mn is shown in fig.188 right, the effect is clearly visible but on the noise level.

All EMCD spectra have been evaluated manually by finding the positions A and B,

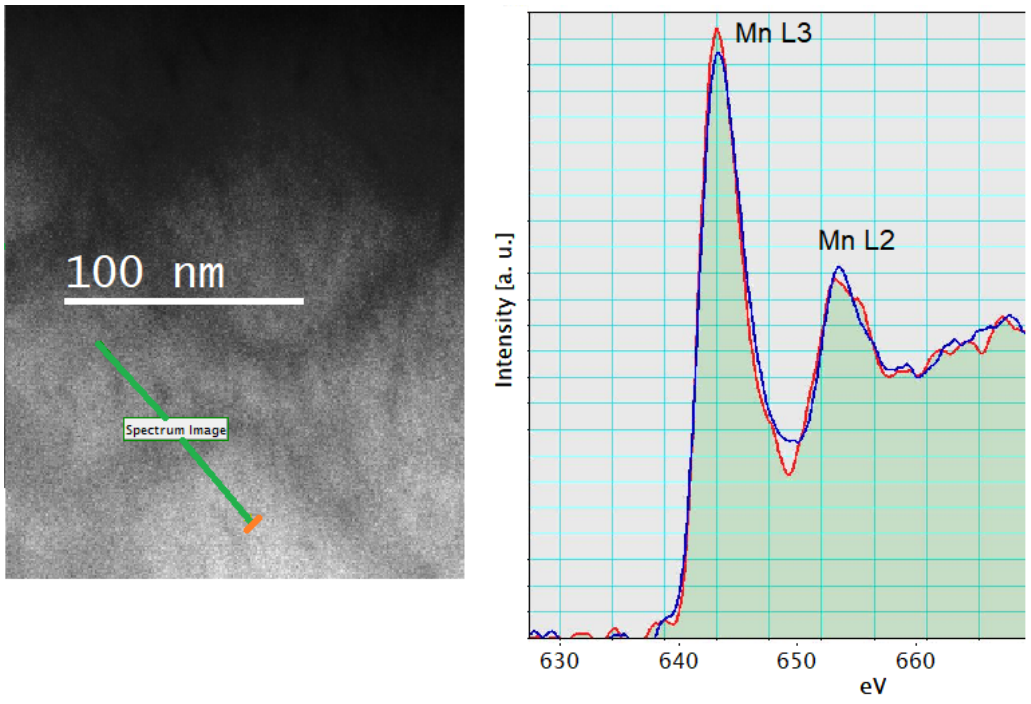

Figure 188: Left: Part of the survey image with the marked linescan (starting point orange). Right: Example of a datapoint showing an EMCD effect on the Mn L3 and L2 edges.

extracting spectra integrated over 30 pixels on those positions, performing background

subtraction, laying spectrum A over spectrum B and if necessary aligning by integral post edge, both for Mn and Ni. The EMCD effect has been measured by the peak height difference: $(A-B)/(A+B)$. For the thickness the result is ≈ 70 nm to ≈ 95 nm, which is huge for EMCD measurements. The resulting EMCD measurements have been plotted both against the specimen thickness (fig.189) and the distance on the linescan to measure possible differences in the magnetic properties between the checkerboard fields (fig.190).

Measuring the EMCD effect with respect to the specimen thickness did not show any

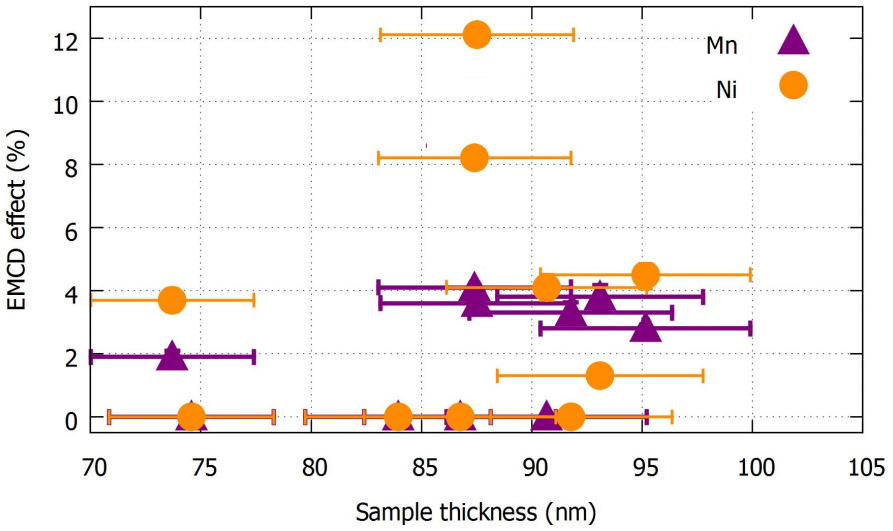

Figure 189: EMCD results plotted against the specimen thickness. For a clearer presentation only the errorbars on the thickness are shown.

usable information. The thickness dependence is influenced by the Pendellösung and the EMCD effect decreases with increasing specimen thickness. Although large effects on Ni of $\approx 12\%$ and $\approx 8\%$ have been measured. The Mn results are all on a similar level which increases their credibility. But it can not even be stated that the specimen has the same or comparable properties on every datapoint, therefore the data is shown against the linescan position and a relation to the checkerboard fields has been tried.

The distance on the linescan can be determined with an accuracy of ≈ 1 nm. Notable are the linescan points with no EMCD effect covering ≈ 30 nm, the region can be identified with the rectangular checkerboard field in the survey image. On each side of this region the highest EMCD effects on Ni and on Mn have been measured. This can result from either magnetic interface effects or the contributing specimen part is thinner than the total specimen thickness because of the tilt to achieve the systematic row.

The other EMCD effects have also been measured on the big quadratic checkerboard fields next to the rectangular one. These fields can be considered to have some magnetic properties, although the data is still very limited and some datapoints show zero effect on at least one element.

A simulation of the effects that can be expected would be very complicated because of the mixture of austenite and martensite and the random site placement, a martensite unit cell

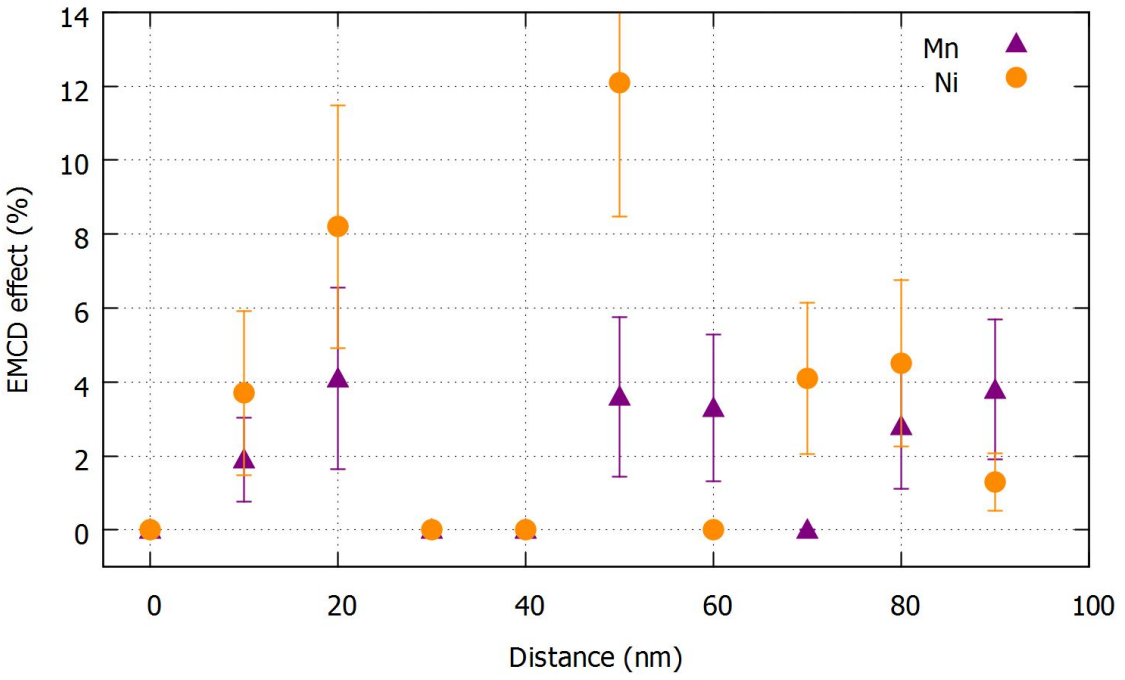

Figure 190: EMCD results with respect to the location on the linescan. Since the location could be determined with good accuracy, only the errorbars for the EMCD effect are shown.

contains 98 atoms, therefore no simulation has been done.

It is important to note that the EMCD effect and the corresponding magnetic moment seems to appear on the atoms but no overall magnetic signal could be observed at room temperature in both VSM and DPC measurements. Therefore the EMCD measurements refer to very local effects.

4.6 Conclusion for the checkerboard

The checkerboard is a highly interesting sample where three types of fields, the big quadratic, the small quadratic and the rectangular fields have been found. The rectangular fields have two subtypes and are perpendicular to each other oriented. Chemically the sample still consists of the intended layers of slightly varying composition, the varying Co content could be proven and the layer structure is present both in regions where the checkerboard pattern exists and where it has vanished.
The HRTEM investigations also support that both martensite and austenite are present with hints that the big quadratic fields consist mainly of martensite, the rectangular fields of austenite and the small rectangular fields show both martensite signs in the FFT diffraction but are similar to the rectangular fields in STEM images, which also hint that these fields consist of an overlay of both directions of the rectangular fields. This could

also explain the Moirè patterns and these the FFT diffraction patterns. Therefore it is not totally clear which patterns result from martensite and which are influenced by Moirè or a combination, this needs further investigations.
Depending on the chosen reflex dark field TEM imaging is able to show only certain types of the checkerboard fields which supports a crystallographic origin of this pattern. Also in STEM and HAADF imaging the pattern is clearly visible with the contrasts giving more information on the types of fields. Also it shows a layer structure of better visibility where the checkerboard pattern has vanished and a clear correspondence of the layers with the checkerboard pattern. Careful measurements of these layers allow to assign them to the intended austenite and martensite layers. Martensite grows at an angle of 45° to austenite consistent with these observations.
In tomography exist tilt angles where special substructures are highlighted or no checkerboard contrast is visible.
At low temperatures the whole sample is martensitic and at high temperatures austenitic, this could be proven. The phase transition to austenitic behaviour is related to vanishing of the checkerboard pattern and could be measured to lie between 110° C and 130° C. A thermionic hysteresis could be measured from the TEM images during the heating/cooling process, the hysteresis is correlated with the disappearance/appearance of the checkerboard fields. The used method of contrast difference measurements can be applied to all compositions where changes in the lattice lead to changes in contrast. Also the phase transition to martensite at low temperatures could be shown but not measured in detail due to limits in the cooling system. Again the checkerboard is gone but regular Moirè structures are still present parts of which are likely to form the checkerboard after backtransformation to austenite.
No magnetic contrast but an EMCD effect could be observed. The checkerboard pattern leads to a change in the mean inner potential, this vanishes when the checkerboard has vanished.
The stability over time is very good because even the cut TEM lamella is after 2.5 years still in a condition for TEM investigations although the checkerboard pattern slowly vanishes from the thinnest parts of the lamella onwards. The rate of change is about 2 Angstrom per day which is at the level of lattice recombinations at interfaces. It can be assumed that thicker samples are even more stable which makes this a very good material for any applications.
With appropriate layer thickness relations the checkerboard could be reproduced, an interesting investigation in the future would be if other materials that exist in martensite and austenite show a similar behaviour.
This sample shows a highly interesting interplay between martensite and austenite together with a thermal hysteresis and a possibility for ferroic cooling applications. The regularity can help to keep desired properties more stable and make this NiCoMnAl a very promising material.

5 Summary and Conclusion

In this thesis a set of highly interesting samples has been thoroughly investigated. The need to characterize the specimen in many ways in the TEM and partially with external methods to be able to give a statement about the magnetic properties becomes obvious and the combination of DPC and EMCD allows deeper insights in the magnetism of the specimen. Although not everything occurred as planned and specimen altered due to time and oxidation a set of interesting and important new insights could be achieved. The pitfalls of EMCD measurements used as a tool on samples of interest instead of good samples for the development of this method have shown themselves and could be treated in a way to achieve results on both types of electron microscope, although the TEM with a post-column filter is to be preferred for EMCD measurements because of the more stable properties of the dispersion.

The dependence of the EMCD signal of the specimen thickness because of the Pendellösung has been shown on CoFe on the Fe L3 edge and the Co L3 edge although the data is still very noisy. To improve this a measurement of the thickness with the unrestricted beam via zero loss map before the EMCD measurement could lead to more accuracy. The EMCD spectra could be improved only by an improved specimen preparation which is difficult because these FIB lamella have been very well prepared, and a microscope equipped with descan coils.

The two samples with Co_2FeSi in a sandwich between iron and vanadium were intended to complement each other as iron is magnetic and vanadium not. In the sample sandwiched by iron the Co_2FeSi could be shown to act as a magnetic bridge, the only other possibility is the magnetic moment points in the same direction as the field of the objective lens, which would show how easily Co_2FeSi can be influenced by external fields and how soft-magnetic it is. The changing structure and chemical composition towards more iron-rich alloys could not be shown to affect the magnetic properties which is a good signal for production of any magnetic sensors containing this material. The EMCD measurements indicate a strong magnetic moment on the Co atoms near the interface, the magnetic induction in DPC is strongly influenced by the iron and extends up to $\approx$ 13 nm into the Co_2FeSi layer. By application of an external magnetic field inducing in-plane components into the specimen switching of the polarization direction of the magnetic layers and creation of domain walls has been possible, the domain walls prefer to appear on defects or grain boundaries and are of the Neel type.
Although in the iron sandwich no magnetic signal purely attached to the Co_2FeSi could be measured this has been possible in the vanadium Co_2FeSi sandwich even though on this sample damage occurred by oxidation. The vanadium has been shown to diffuse into the Co_2FeSi layer which most likely altered its magnetic behaviour. With the increased sensitivity of the pixelated detector beam disc shifts corresponding to a magnetic induction of 0.018 T have been measured which proves the applicability of DPC even for very small magnetic signals. The alteration of the specimen prevented EMCD measurements unfortunately, a future experiment also measuring EMCD on the vanadium could give more insights into this system. The interfacial magnetic behaviour has been shielded by the shifts caused by the mean inner potential, for DPC investigations directly on the interface of two materials a difference in the mean inner potential of both materials as

close as possible to zero or a very accurate modelling of the MIP is needed. The form of the magnetic and MIP signal suggests a magnetism up to the interfaces with a Gaussian decay of the stray field into the vanadium.

In the TMR stack the MIP is of even greater importance as it consumes the magnetic signal. A different kind of TMR stack with a small MIP difference between magnetic material and barrier would be better for TEM investigations. A possibly magnetic signal in this specimen has a very special shape as only one of the Co_2MnSi layers could be clearly switched by the external field. Chemically the sample could be characterized and it consists of chemically separated layers and a mostly epitaxial crystalline growth. The interface between MgO and Co_2MnSi could be characterized on HAADF images by the extensive use of the lineprofile tool, the by the material preferred bindings are CoCo/O and MnSi/Mg, which allows tailoring of the electronic transport and spincaloric properties. EMCD effects have been measured on Co and Mn on a new lamella of an increased layer thickness with large uncertainties but allowing to state the presence of magnetic moments in both parts of the Co_2MnSi alloy, the Si edges are not in the accessible EELS range for EMCD.

With a specially tailored layer system of Fe and V the presence of the magnetic proximity effect could be underlined by DPC and shown by additional spatially resolved EMCD measurements on the V edges. EMCD turns out to be a useful tool for showing the presence of magnetic moments with high spatial resolution even if the noise on the data does not allow for a precise determination of the spin to orbital magnetic moment. The DPC data is very interesting and allows for more interesting results with the presence of magnetic domain walls and a different reaction of the Fe layers to the externally applied magnetic field. The growth of the material is grainy but inside a grain surprisingly ordered, having a layer of multimaterial nano-crystallites.

The so called checkerboard specimen is a material full of surprises to uncover as has been done in this work using the TEM and complementary by using various other methods in the dissertation of A. Becker. The growth of martensite is regularized when bounded by the layer geometry and thickness, leading not only to the very unusual checkerboard pattern while chemically still consisting of layers of slightly varying composition but also allowing to form a stable material with a narrow thermal hysteresis promising for magnetocaloric applications. The found structural properties give rise to the assumption of a similar behaviour of alloys that consist also of a martensitic and an austenitic phase at different temperatures controllable by the exact composition. A cycle of transitions appears possible, this material seems to have allowed to produce a material that even if it consists of only one of the two possible phases at very high or very low temperatures the other phase is embedded as information in the crystal lattice.

6 Appendix

6.1 Additional information on the CoFe EMCD datasets

Here the crossprofiles, thickness profiles and linescan survey images for the CoFe EMCD datasets are shown. The crossprofiles increase in intensity with the linescan position because the linescan starting point has always been set close to the vacuum and the specimen thickness increases also with linescan position.
The following additional data for the used EMCD linescan datasets show the survey image with the linescan position highlighted in green top left, the EFTEM thickness map with the region of the lineprofile highlighted top right and the thickness lineprofile in mean free path at the bottom. The extent of the linescan is marked by a ROI in the thickness line profile.

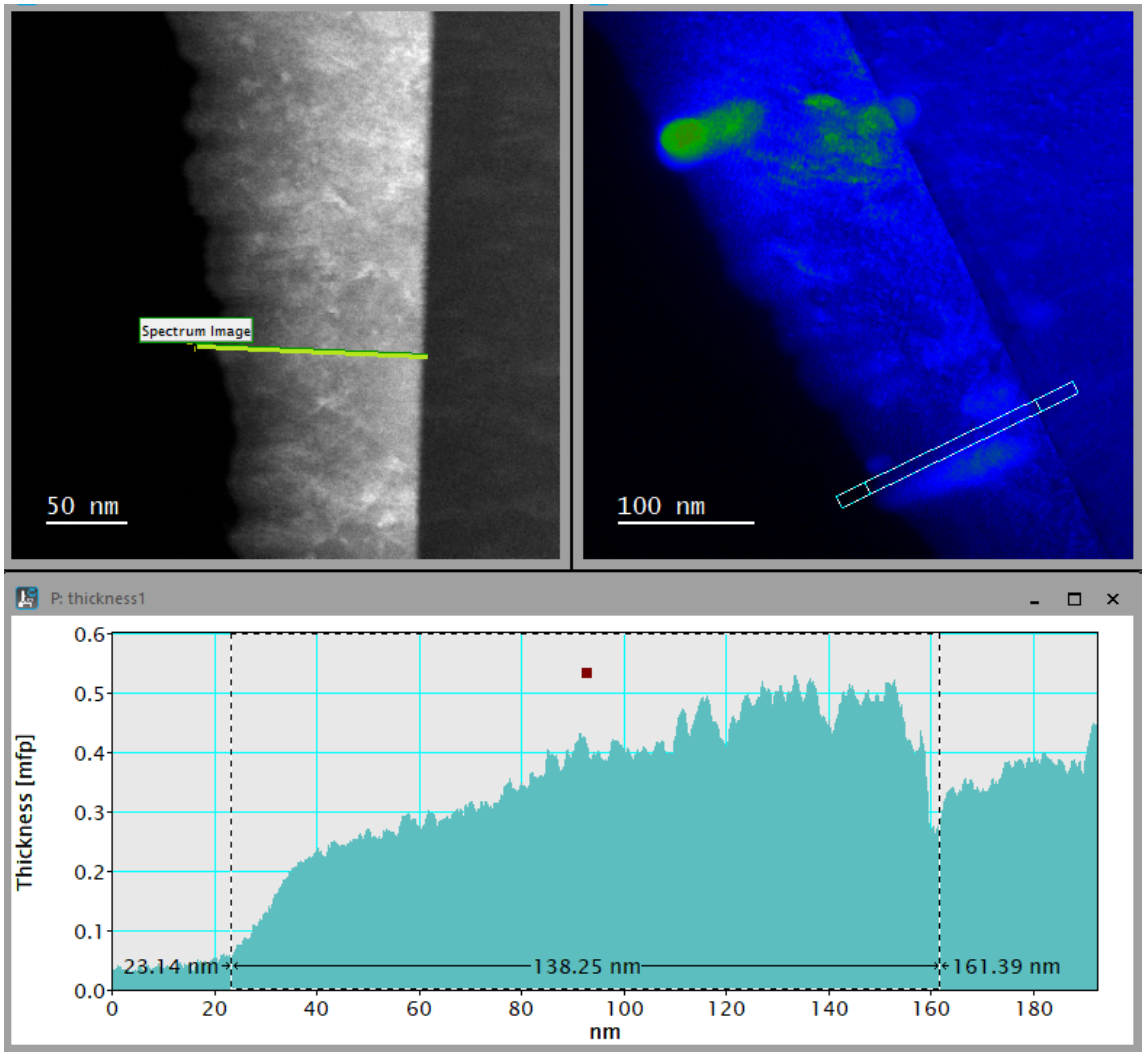

Figure 191: Additional data for the EMCD linescan dataset 1 on the CoFe wedge.

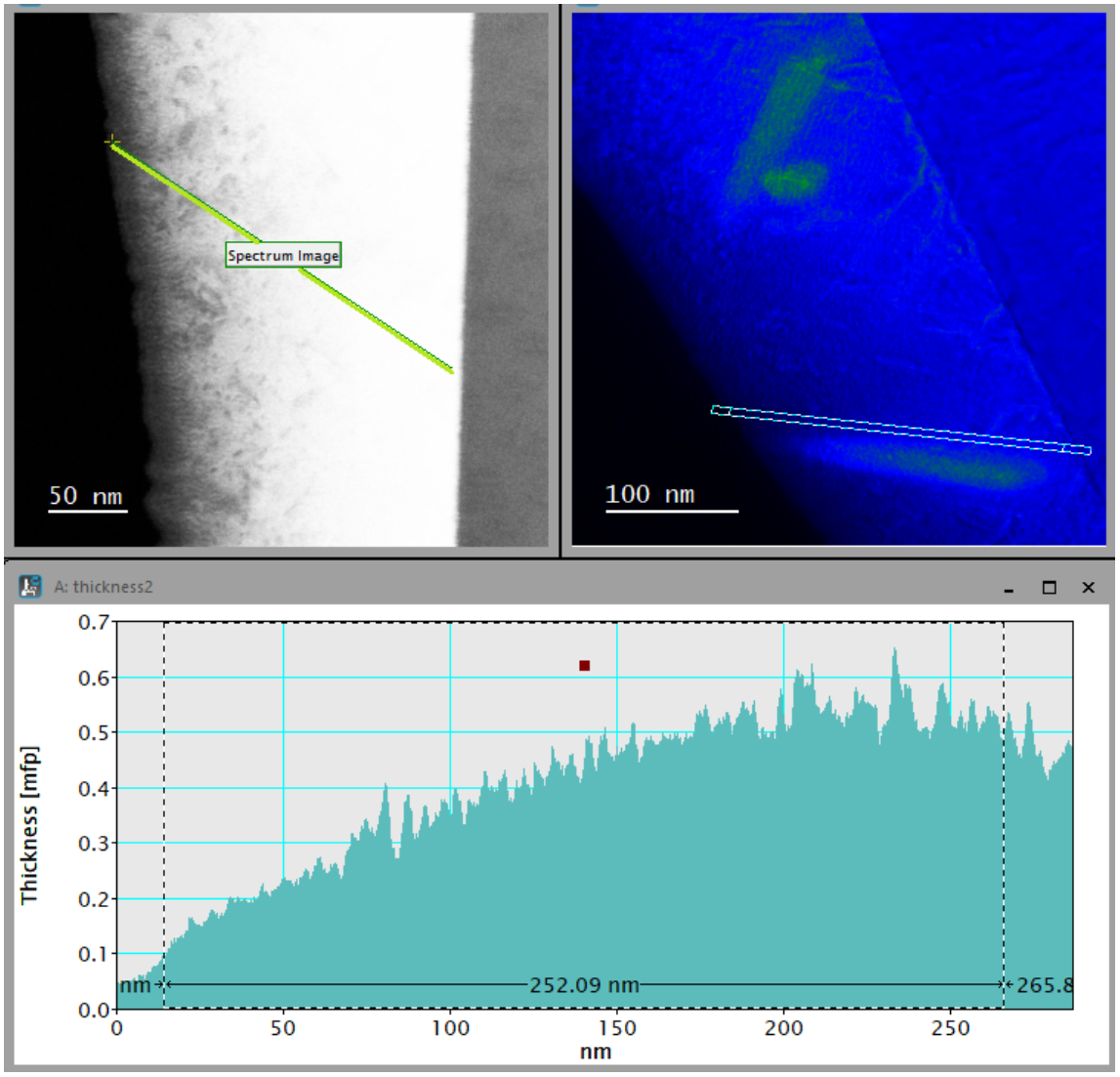

Figure 192: Additional data for the EMCD linescan dataset 2 on the CoFe wedge.

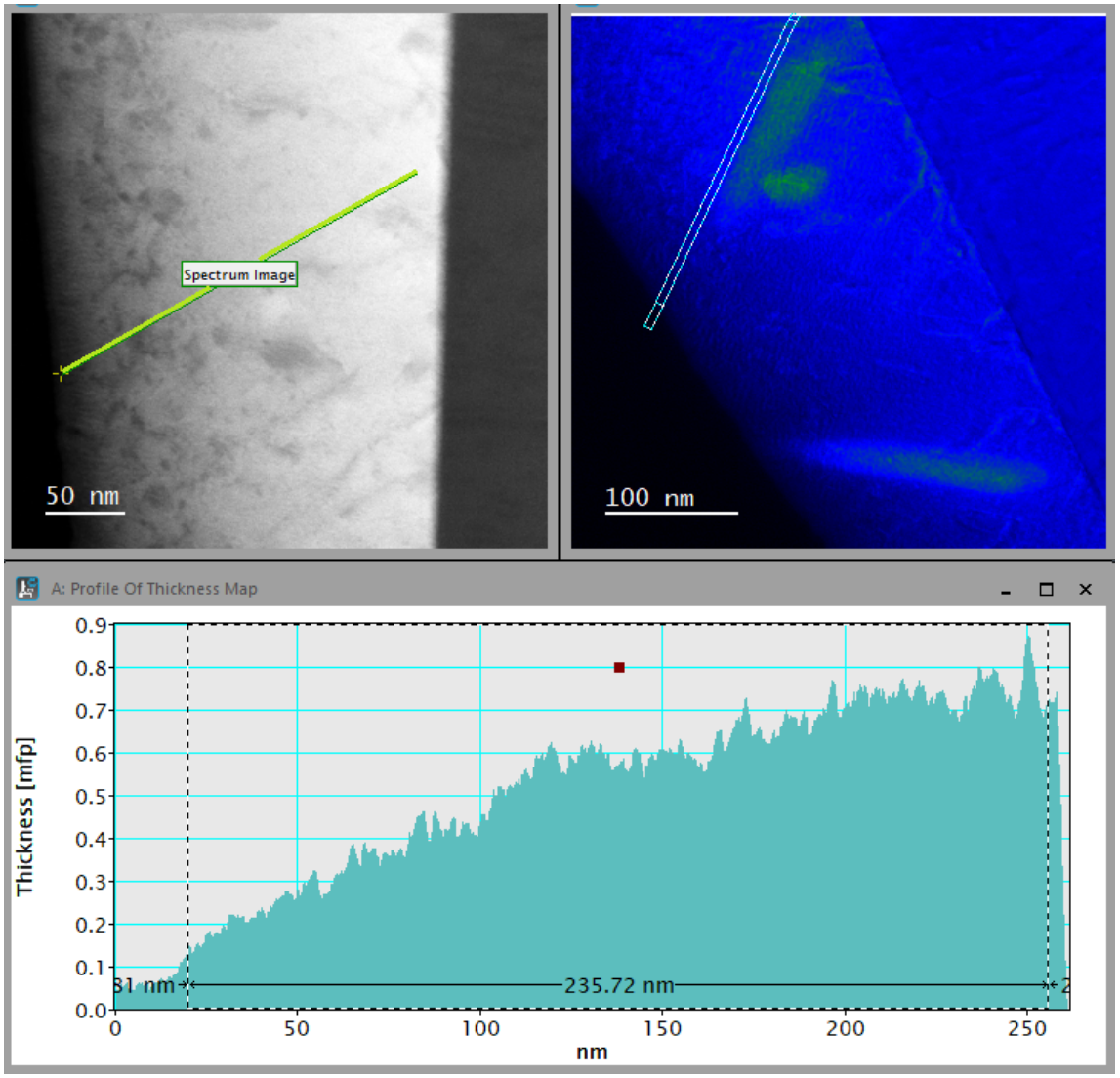

Figure 193: Additional data for the EMCD linescan dataset 3 on the CoFe wedge.

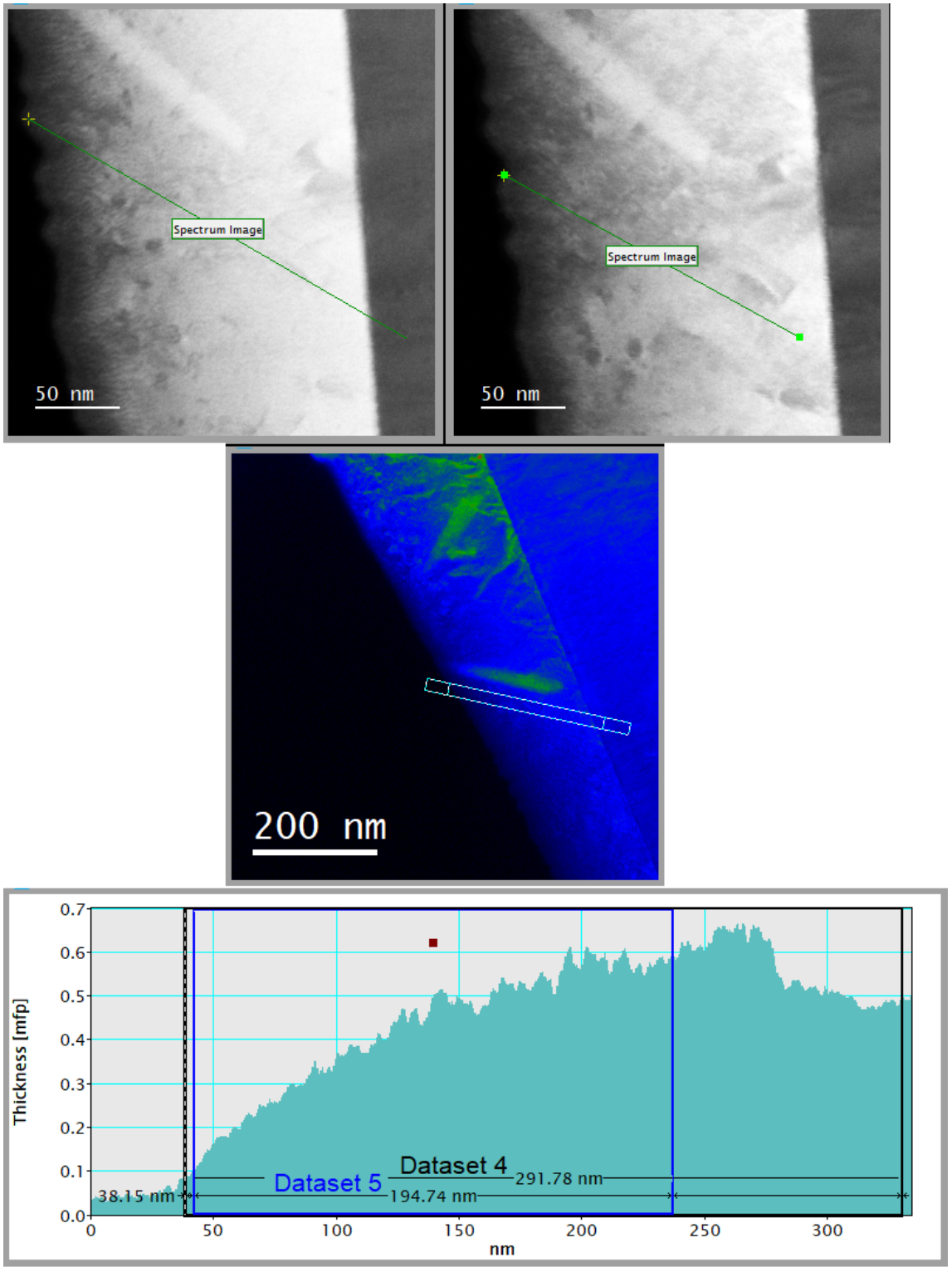

Figure 194: Additional data for the EMCD linescan dataset 4 and 5 on the CoFe wedge. The lines have been drawn close to each other and the thickness line profile has been obtained from the region in between.

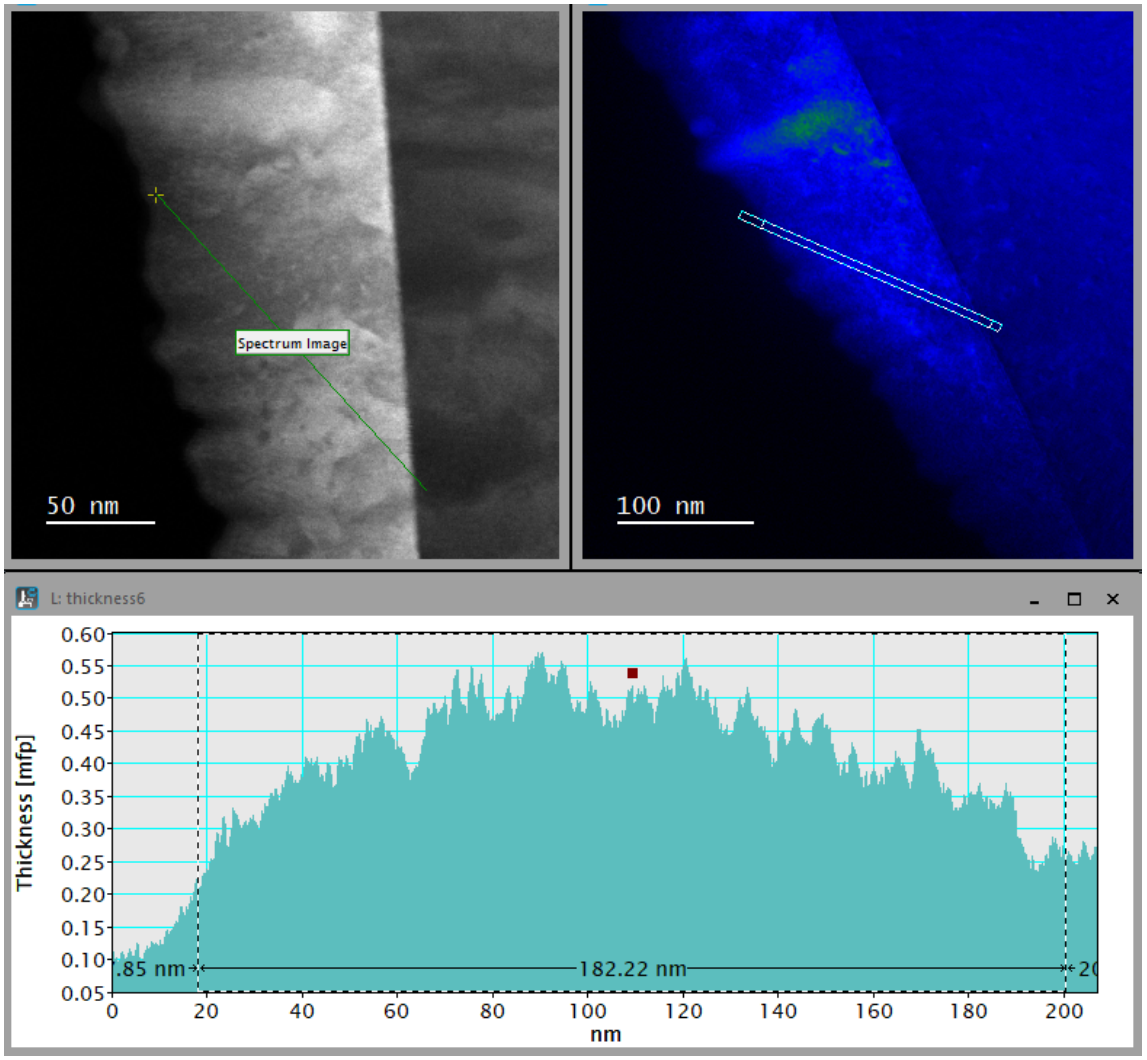

Figure 195: Additional data for the EMCD linescan dataset 6 on the CoFe wedge.

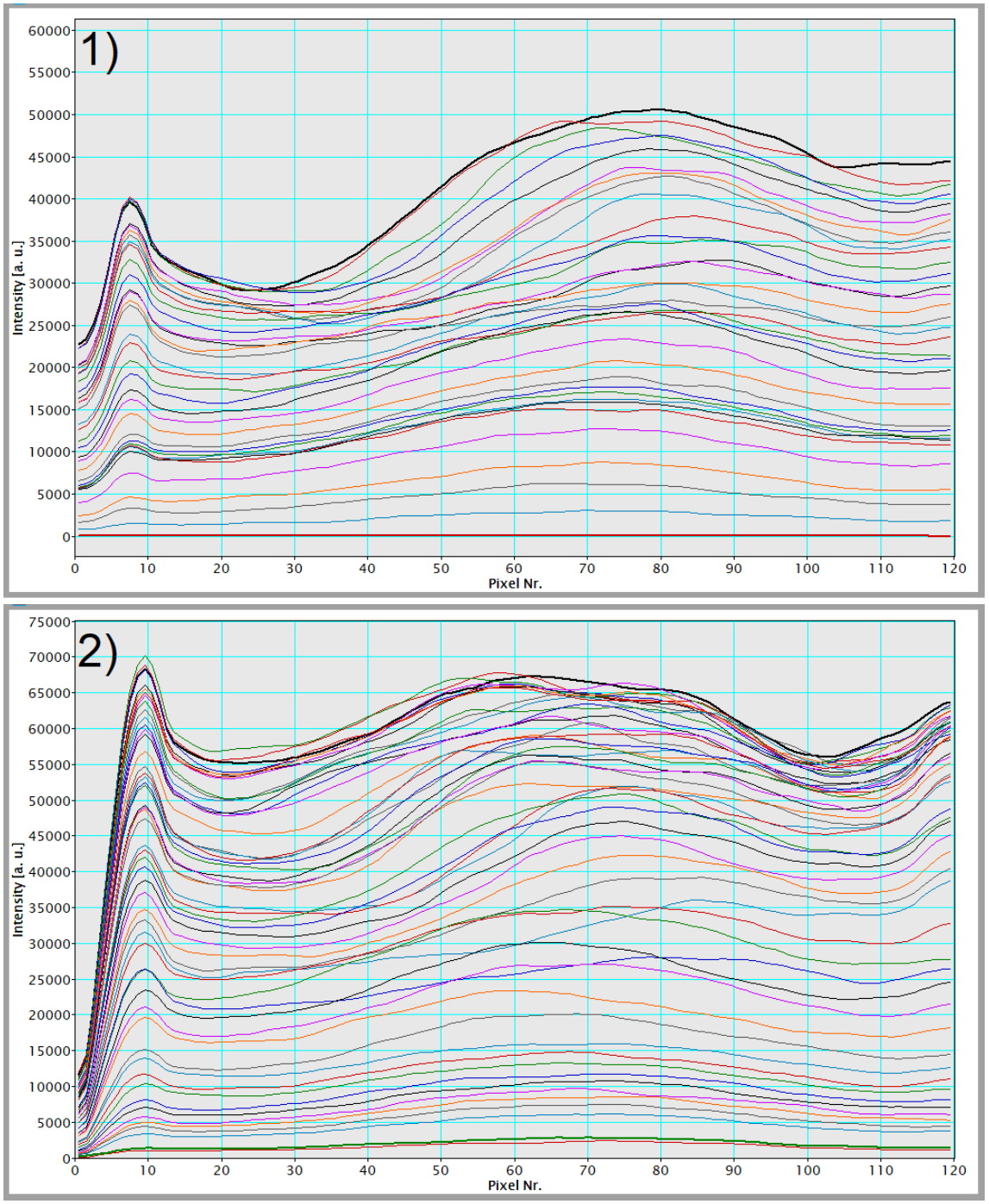

Figure 196: Crossprofiles for dataset 1 (top) and dataset 2 (bottom). The profile of the first (red, green) and last (black) datapoint of the linescan are shown with increased thickness. Only weak beam movement or drift is visible and more in dataset 2 than in dataset 1, the position of the central diffraction disc can be considered stable.

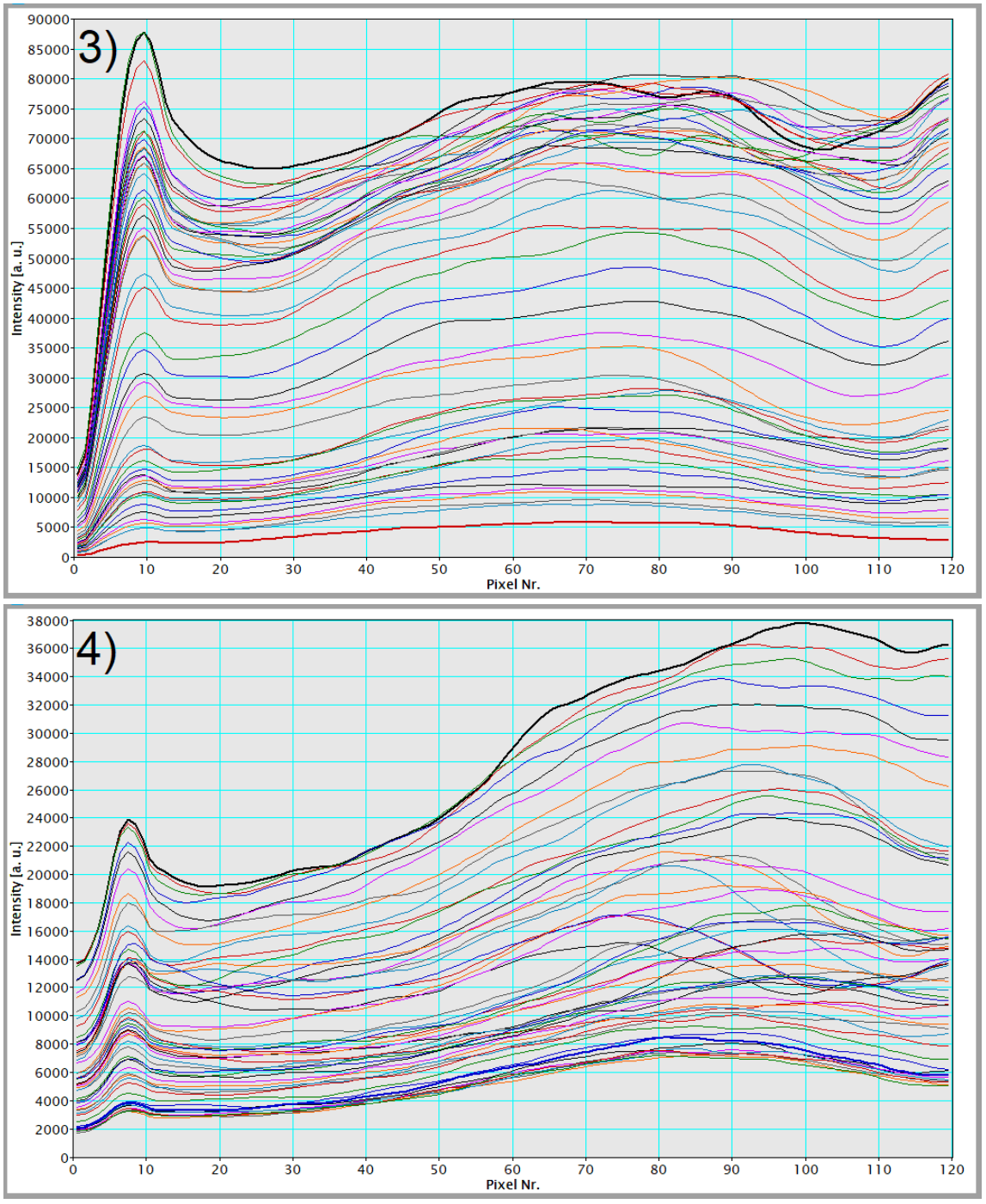

Figure 197: Crossprofiles for dataset 3 (top) and dataset 4 (bottom). The profile of the first (red, blue) and last (black) datapoint of the linescan are shown with increased thickness. In dataset 3 the central diffraction disc position is mostly stable with exceptions closer to the end of the linescan, in dataset 4 it lies closer to the bottom of the raw spectrum (right of the crossprofile) with a few exceptions in the middle of the linescan.

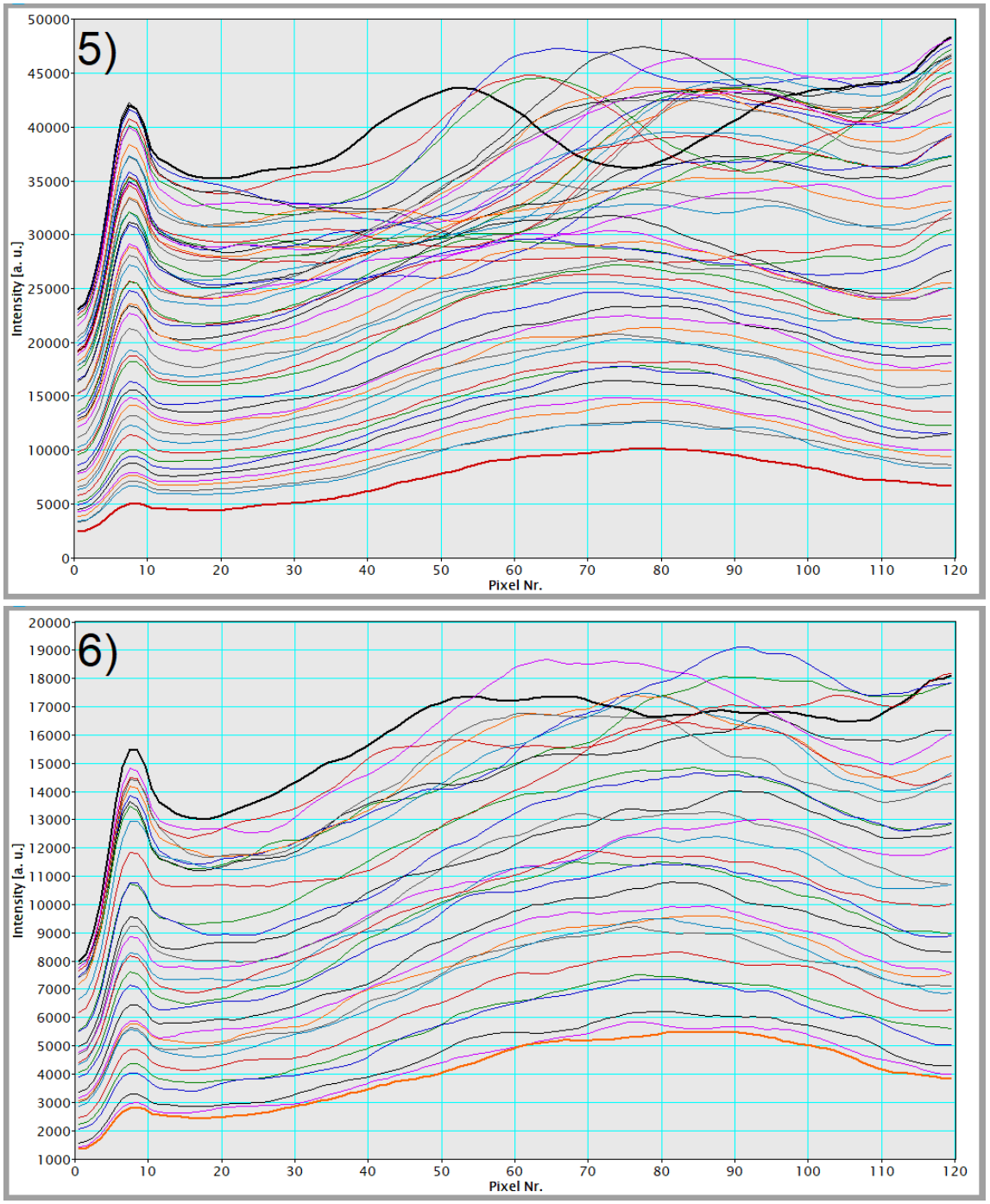

Figure 198: Crossprofiles for dataset 5 (top) and dataset 6 (bottom). The profile of the first (red) and last (black) datapoint of the linescan are shown with increased thickness. Notable beam movement is visible in dataset 5 so the evaluation needs to be done separately for datapoints with a similar central diffraction disc position. In dataset 6 only a few datapoints need separate evaluation.

6.2 Pixelated DPC datasets of the Fe/Co_2FeSi/Fe system

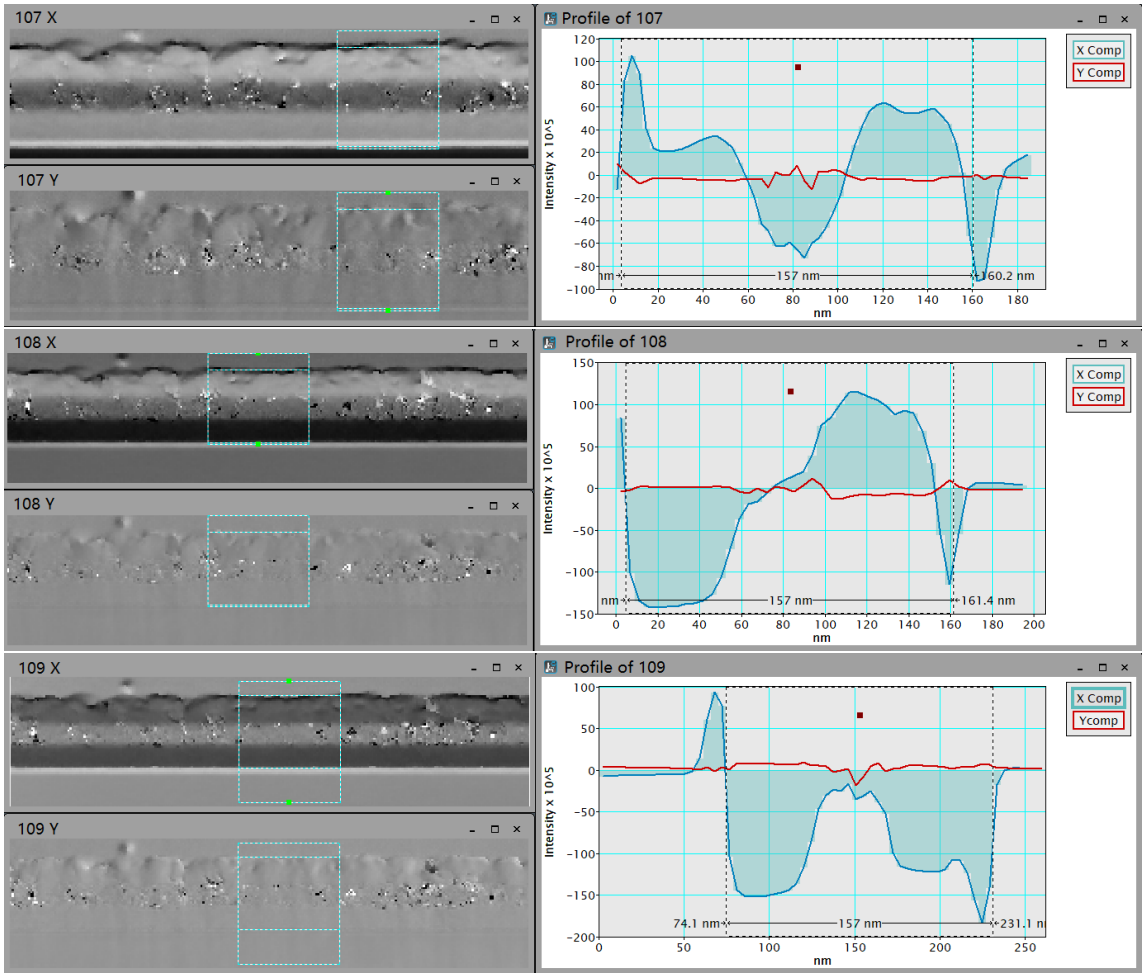

Figure 199: Processed pixelated DPC datasets with the X component shown top left, the Y component bottom left and the intensity profile on the right for all three datasets. Top to bottom: Dataset 107, 108 and 109.

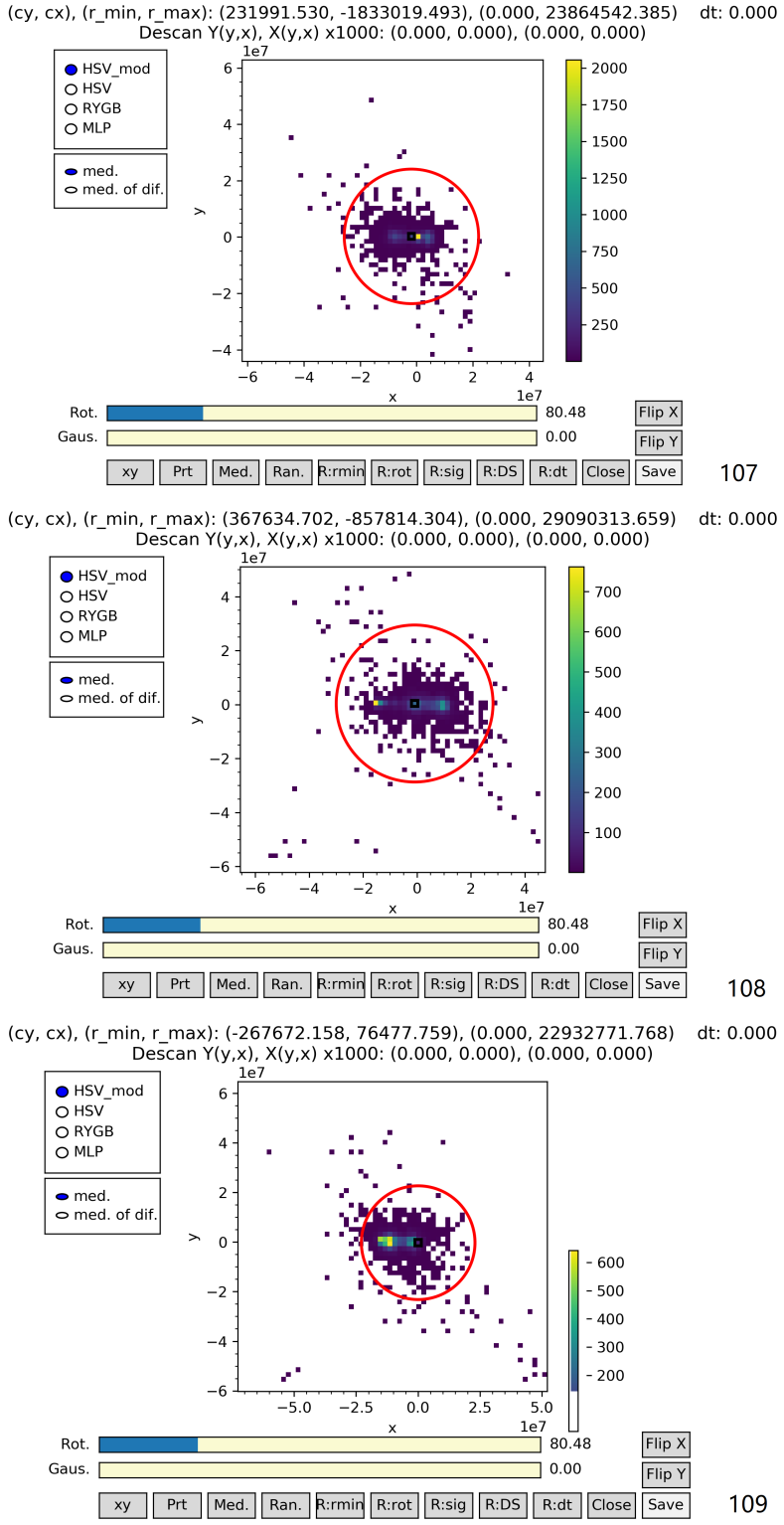

Figure 200: Evaluation of the pixelated DPC datasets: Positions of the center of the central diffraction disc. The red circle indicates which range has been taken into account. The center is set so that it marks the center which is determined only from the MgO data, serving as normalization. Then the data only from the layer system is taken into account to determine the range of the red circle. Big shifts not resulting from the layer system are therefore excluded.

6.3 Chemical results of the Fe/Co_2FeSi/Fe interfaces

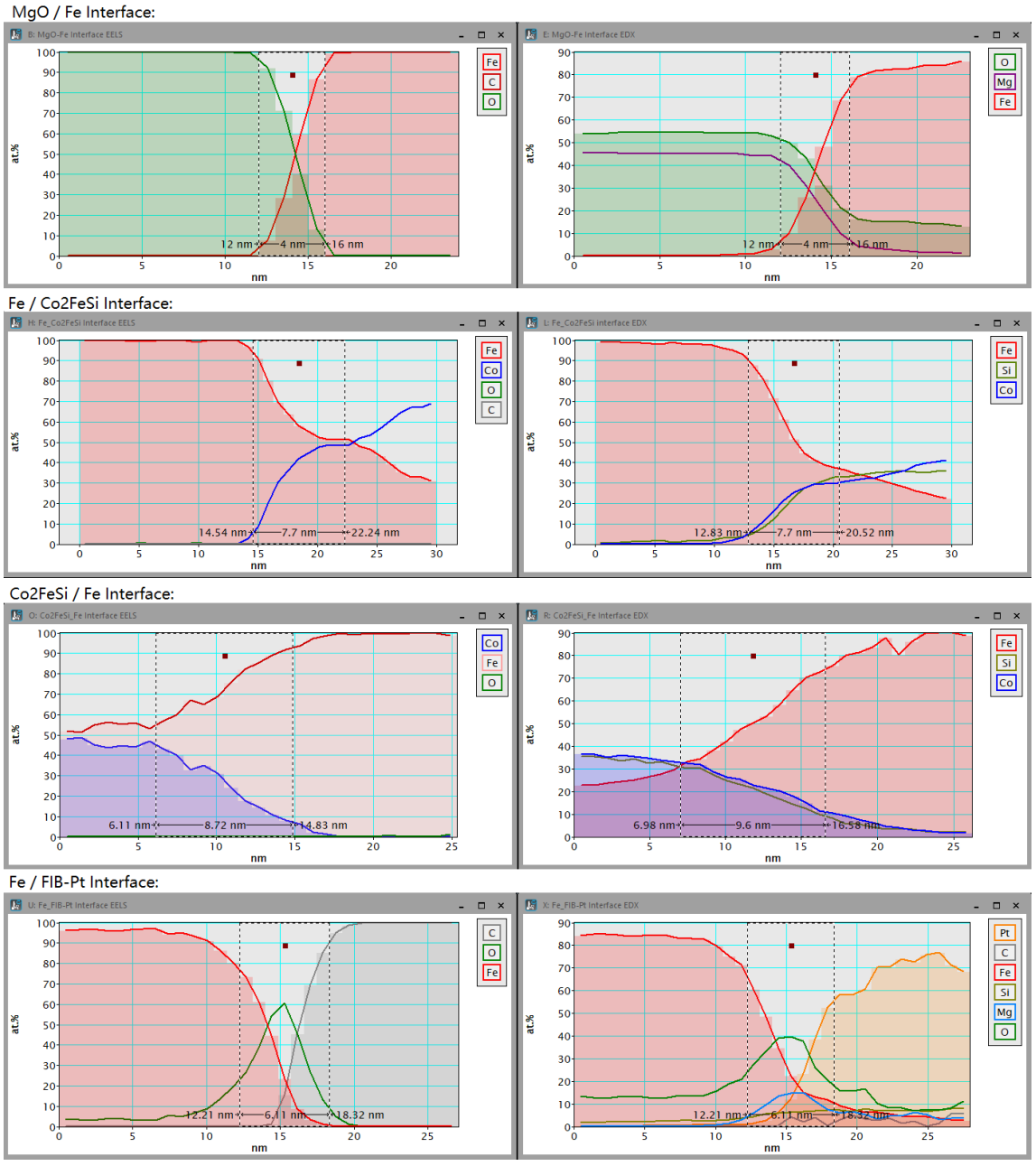

Figure 201: EELS (left) and EDX (right) results acquired on the interfaces between two layers, fro top to bottom: MgO/Fe interface, Fe/Co_2FeSi interface, Co_2FeSi/Fe interface and Fe/FIB-Pt interface. The different quality of both Heusler/Fe interfaces can be seen in more detail, the Co_2FeSi/Fe interface shows the broadening and change of the composition in two steps that allows the creation of different and more Fe-rich alloys than intended.

6.4 V/Co_2FeSi/V Peak shift data and Spectrum Image extracts

Data showing the described results of the peak shift mapping for the V/Co_2FeSi/V specimen.

6.4.1 Peak shifts of the overview dataset:

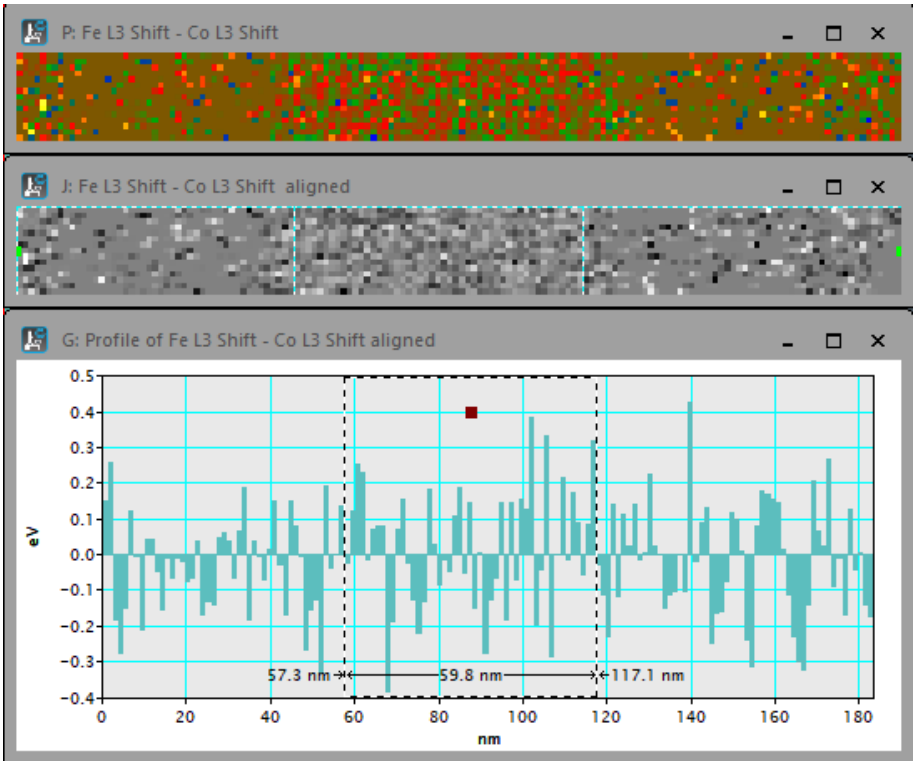

Figure 202: Peak shifts of the difference between Fe L3 and Co L3 edges mapped across the layer system. Any signal disappears in the noise.

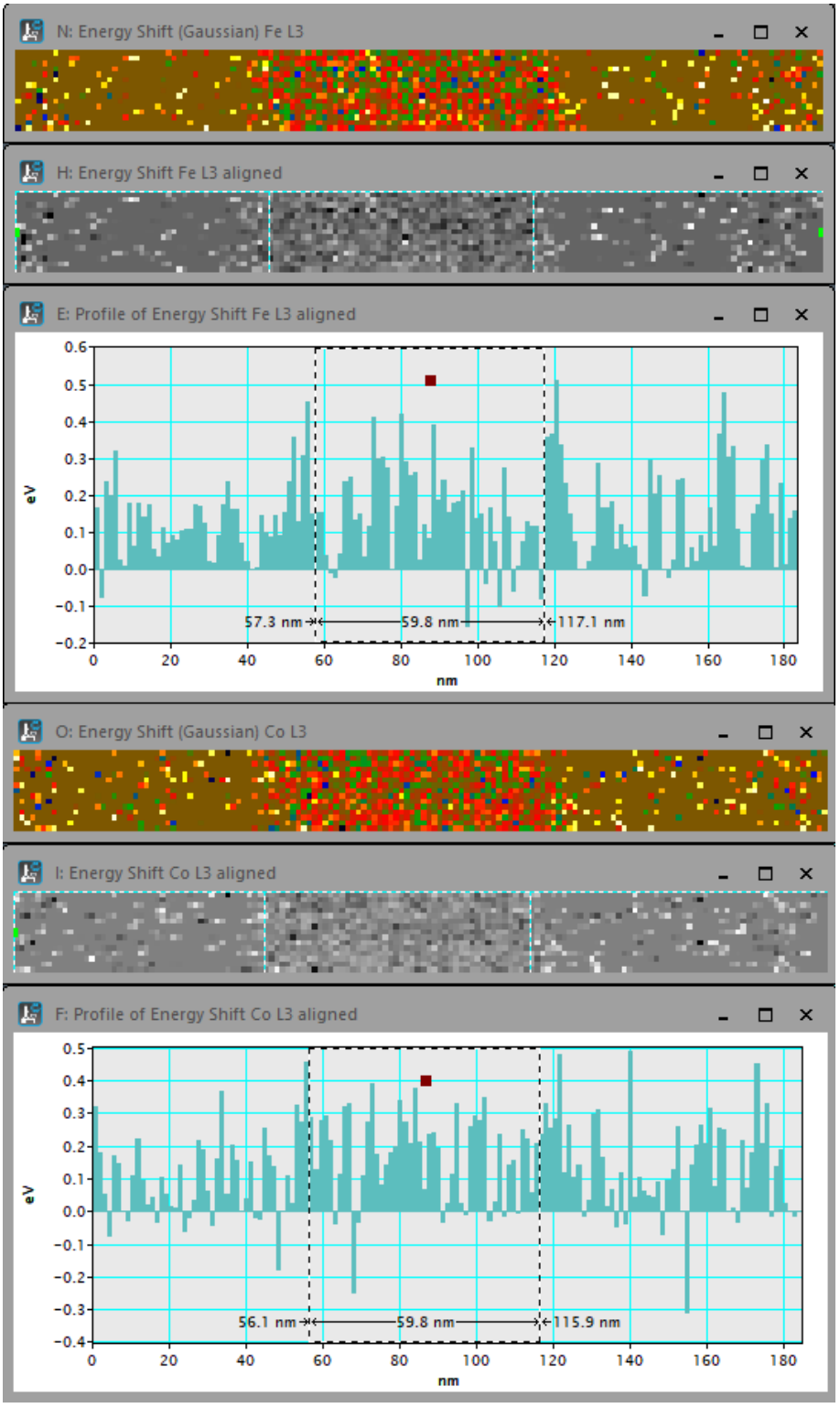

Figure 203: Peak shifts of the Fe L3 (top) and Co L3 (bottom) edges mapped across the layer system. The data is noisy and in the Co any peak shifts disappear in the noise.

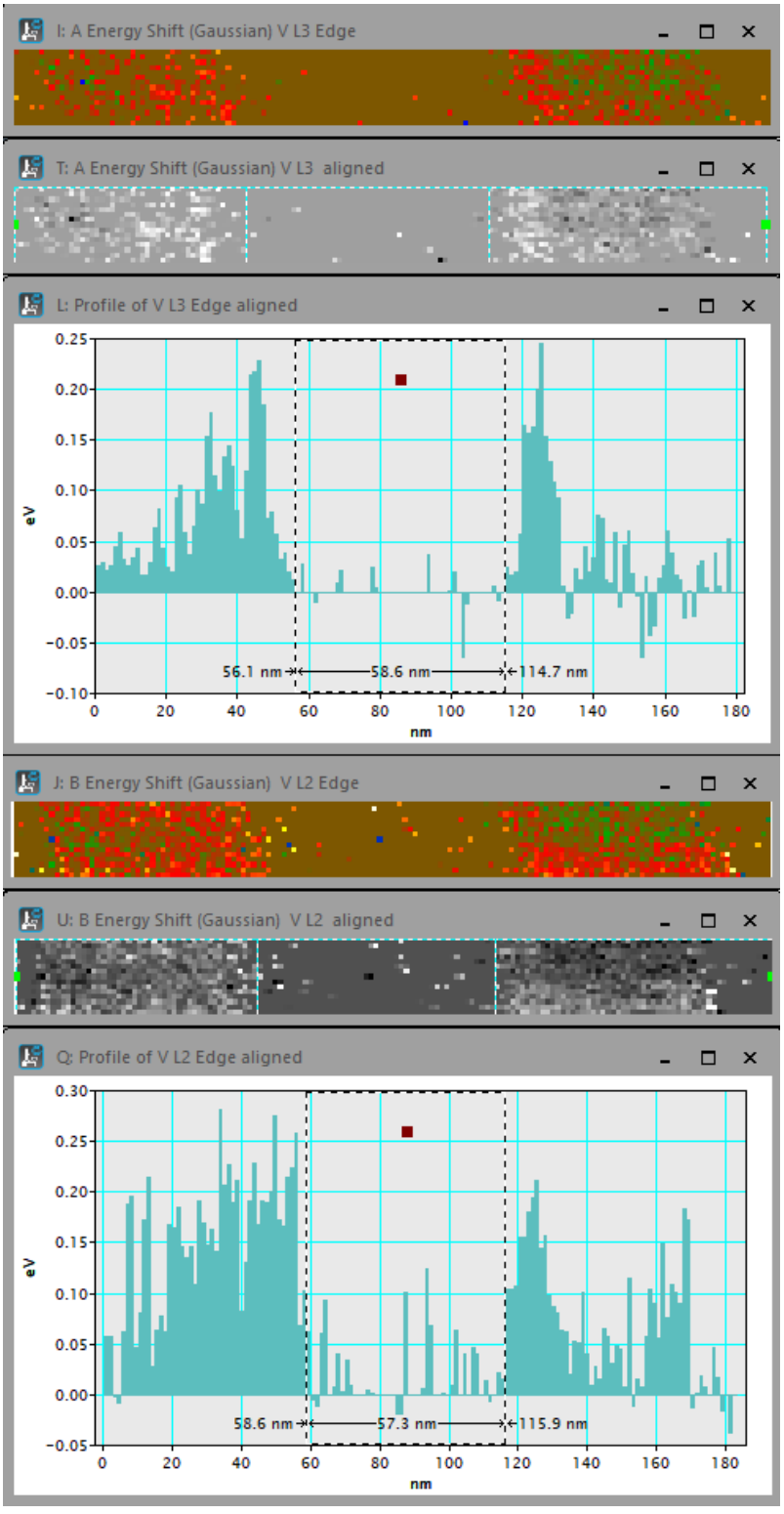

Figure 204: Peak shifts of the V L3 (top) and V L2 (bottom) edges mapped across the layer system. They show that the V layers are of different quality, the 2nd one showing high shifts only near the Co_2FeSi/ interface.

6.4.2 Peak shifts of the MgO/V interface region:

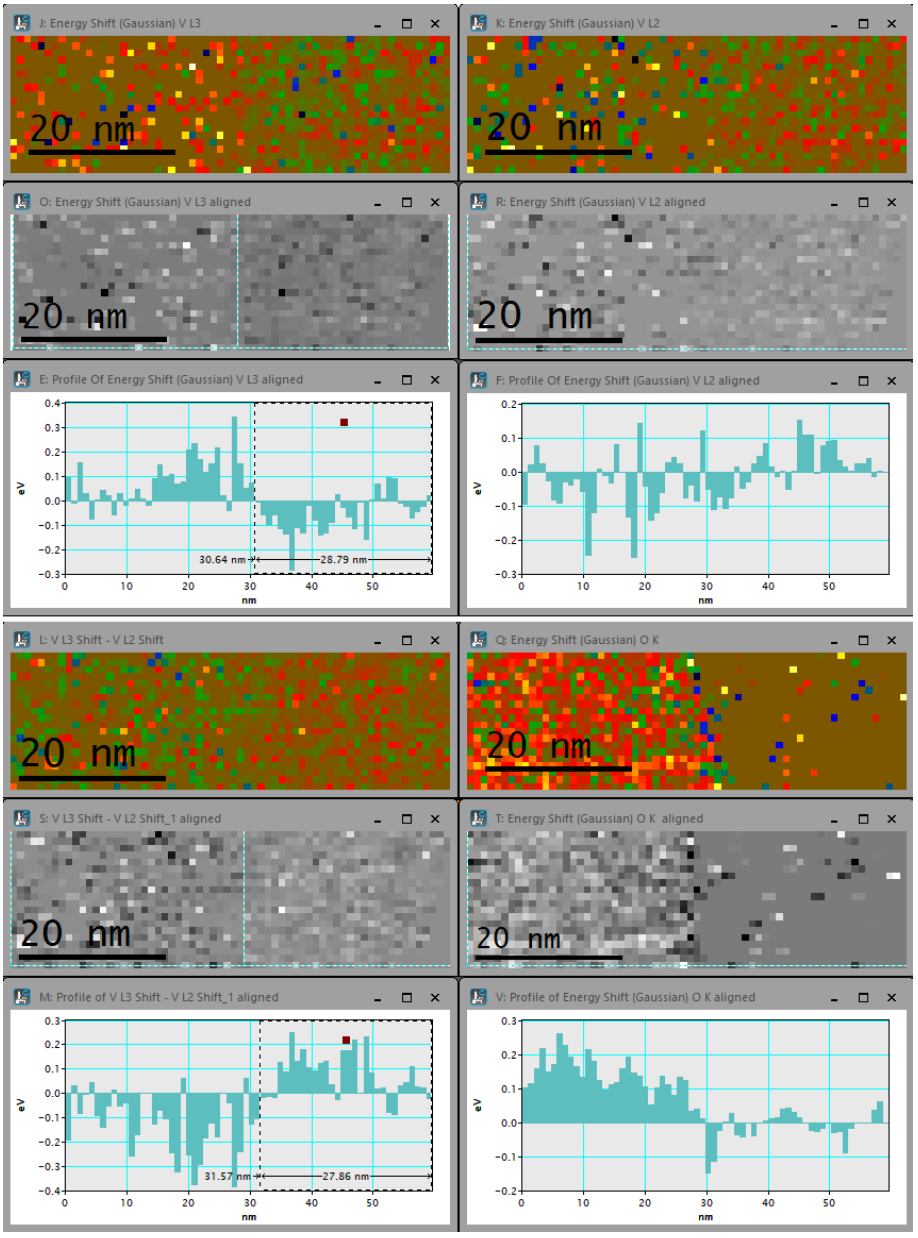

Figure 205: Peak shifts of the V L3 (top left) and V L2 (top right) edges mapped across the MgO/V interface, their difference (bottom left) and the shifts on the O K edge. The V L3 edge shows a change in the interface region, but the data is very noisy. The oxygen shows a change in shifts towards the interface.

6.4.3 Peak shifts of the V/Co_2FeSi interface region:

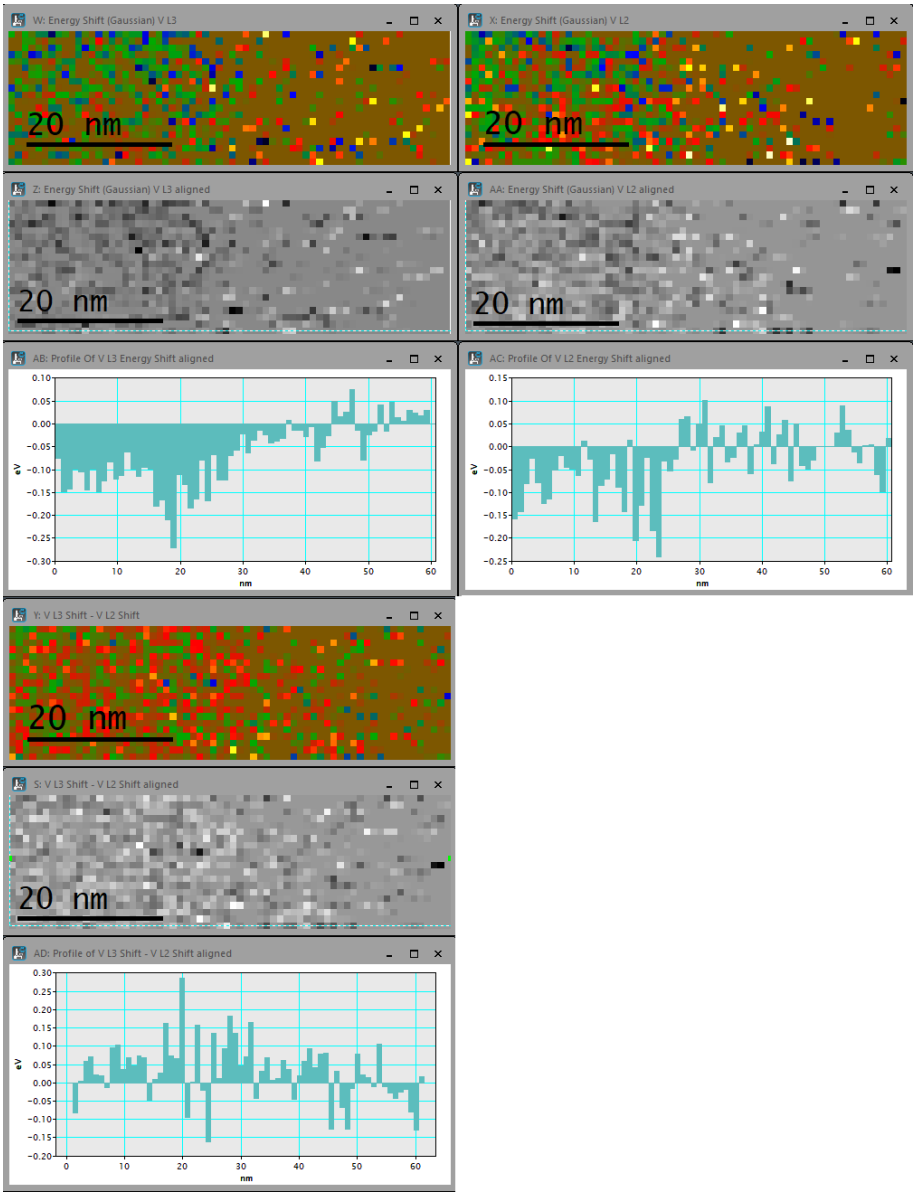

Figure 206: Peak shifts of V L3 (top left) and L2 (top right) edges across the V/Co_2FeSi interface and the difference between the shifts (bottom). In the L3 edge no shifts are visible, in the L2 edge they are increasing from noise across the interface but cannot be properly distinguished from the noise.

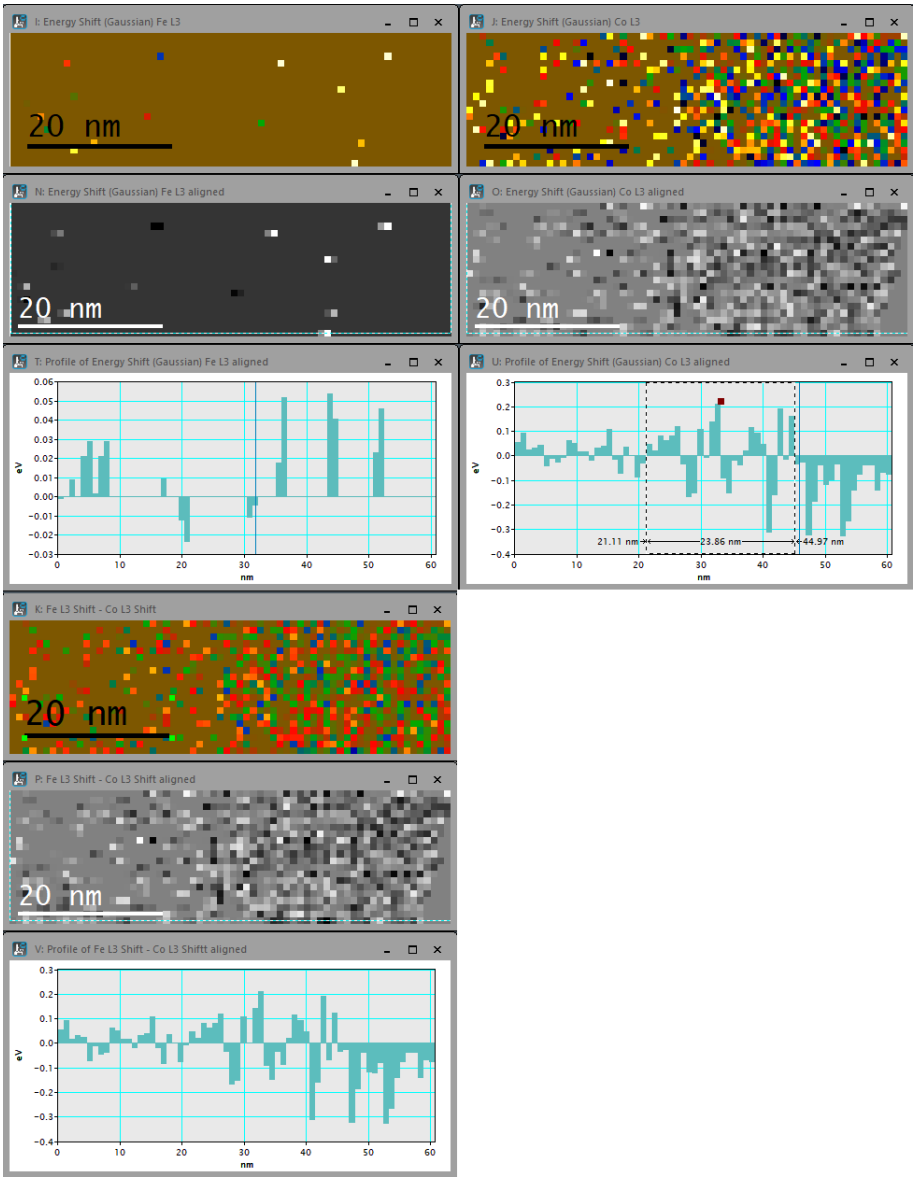

Figure 207: Peak shifts of Fe L3 (top left) and Co L3 (top right) edges across the V/Co_2FeSi interface and the difference between the shifts (bottom). In the L2 edge the interface is visible, in the L3 edge it is smeared. The difference of the shifts has no signal distinguishable from the noise.

6.4.4 Peak shifts of the Co_2FeSi/V interface region:

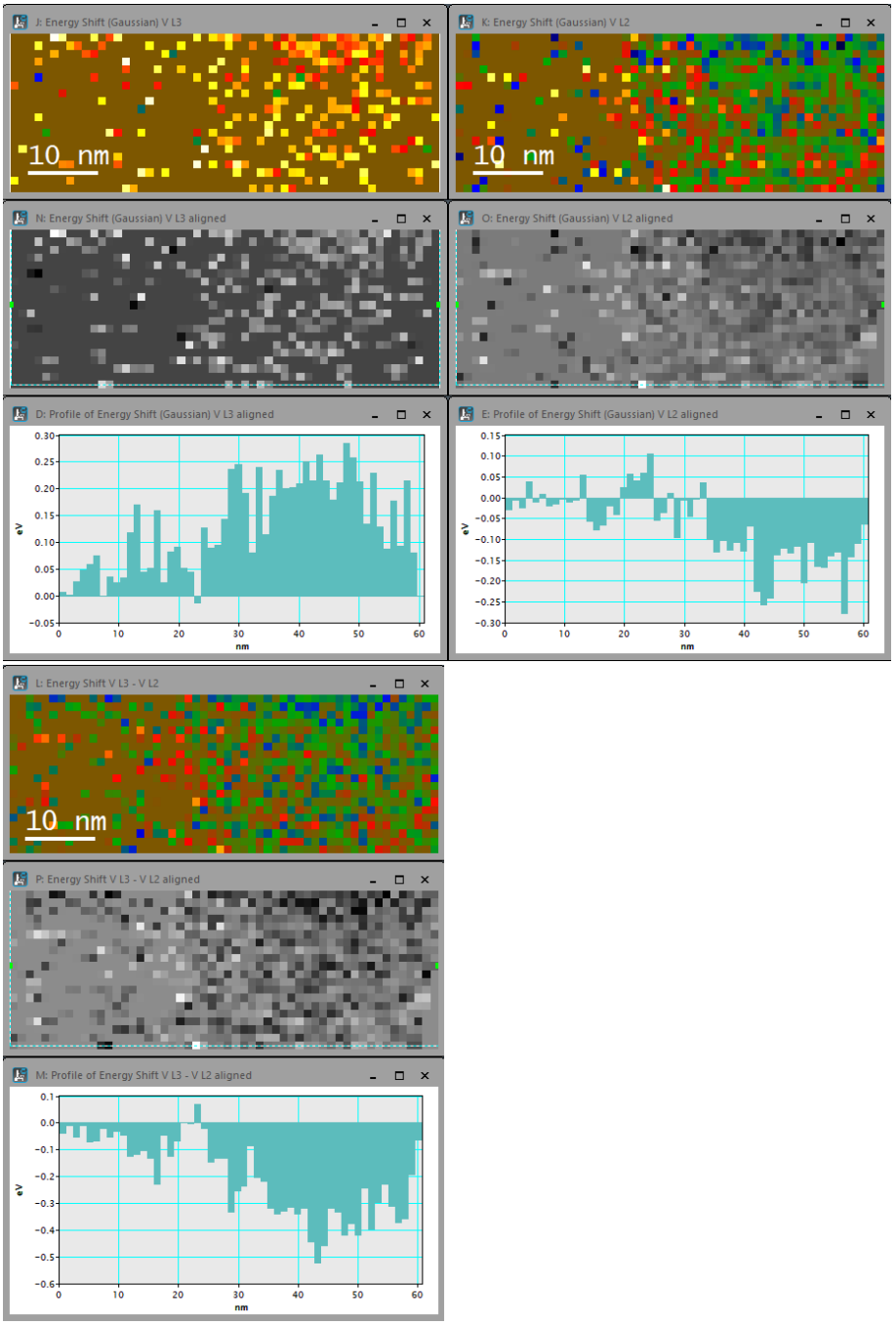

Figure 208: Peak shifts of V L3 (top left) and L2 (top right) edges across the Co_2FeSi/V interface and the difference between the shifts (bottom). There is a change in the shifts at the interface but the data is too noisy to determine the exact width of it as there is also noise in the Heusler region.

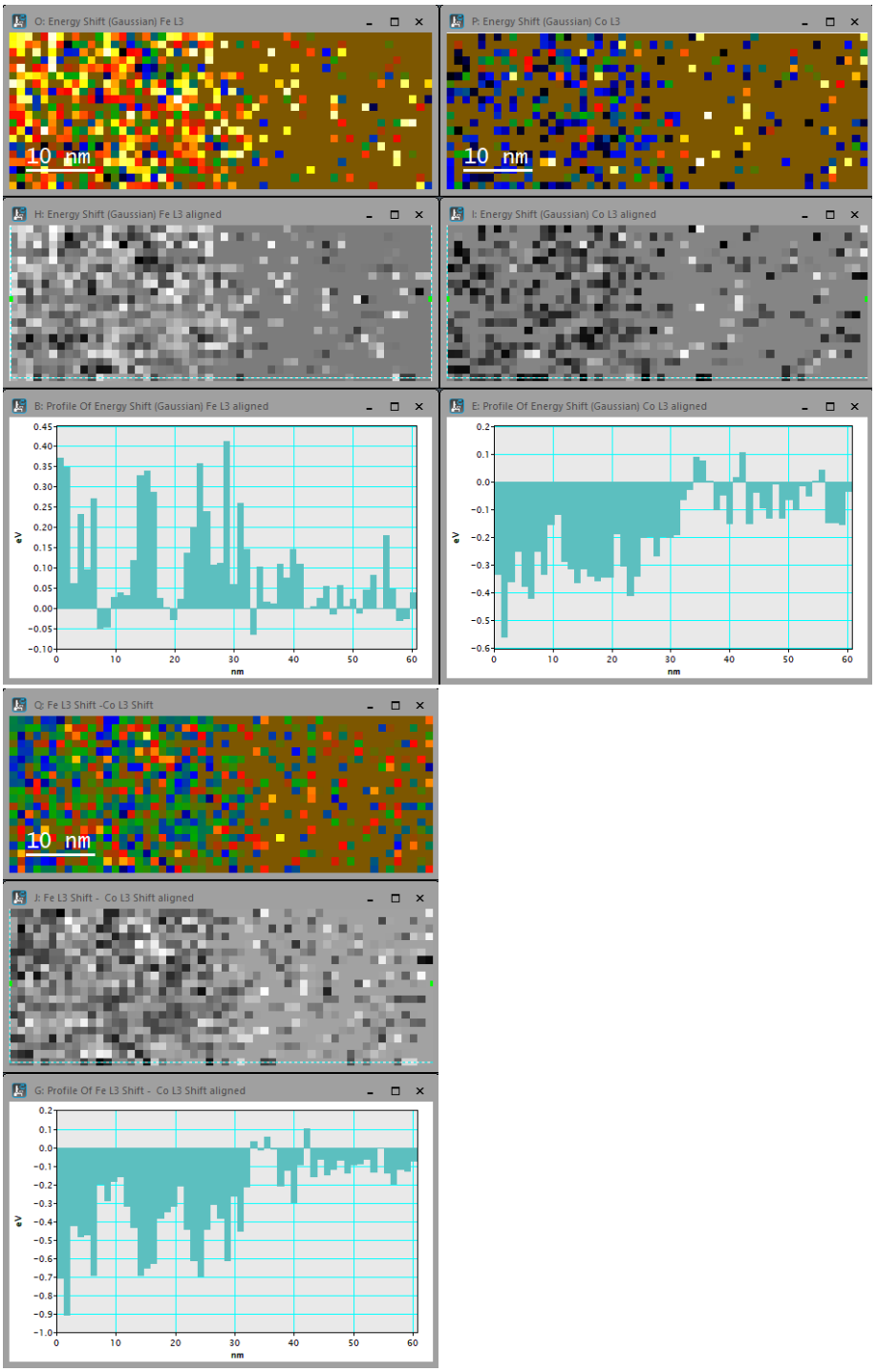

Figure 209: Peak shifts of Fe L3 (top left) and Co L3 (top right) edges across the Co_2FeSi/V interface and the difference between the shifts (bottom). Only in the cobalt the region between the Heusler and the vanadium, which contains no cobalt, is visible. The Fe shift data is very noisy and allows only qualitative estimation of the interface width and no details about the chemical properties in that region.

6.4.5 Spectrum image extracts of the interfacial regions

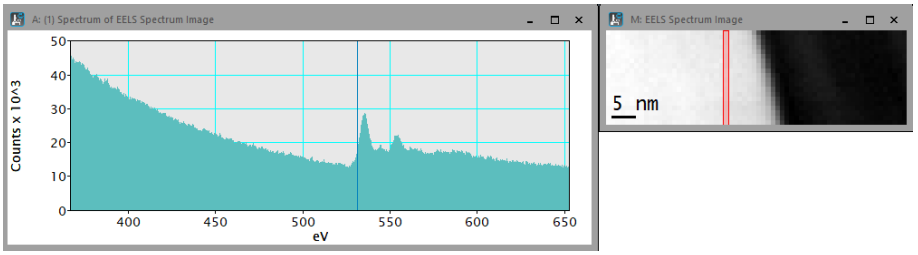

Figure 210: Extract of the spectrum image of the MgO/V interface, the red region in the SI on the right is where the spectrum on the left is taken from via summation over all included pixels. In this spectrum the blue line indicates the O edge (532 eV), no V edge (513/521 eV) is visible above the noise level. The spectrum image is not drift corrected.

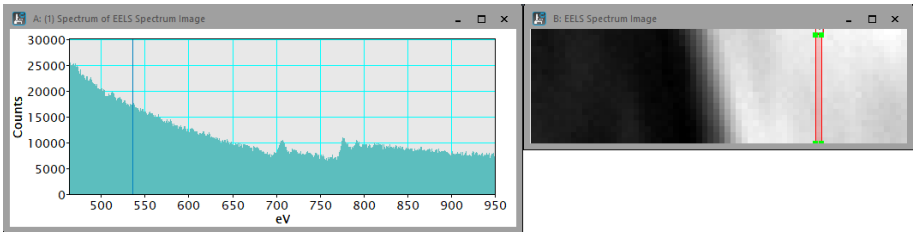

Figure 211: Extract of the spectrum image of the V/Co_2FeSi interface, the red region in the SI on the right is where the spectrum on the left is taken from (summation over all included pixels). The blue line in the extracted spectrum indicates the O edge (532 eV) where no edge is visible above the noise level, also no V edge (513/521 eV) is visible. The spectrum image is not drift corrected.

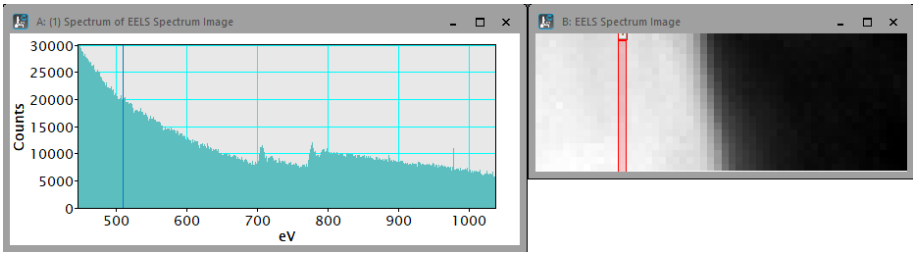

Figure 212: Extract of the spectrum image of the Co_2FeSi/V interface, the red region in the SI on the right is where the spectrum on the left is taken from (summation over all included pixels). The blue line in the extracted spectrum indicates the V edge (513 eV), where no edge is visible above the noise level. The spectrum image is not drift corrected.

6.5 Pixelated DPC datasets of the VCo_2FeSi/V specimen

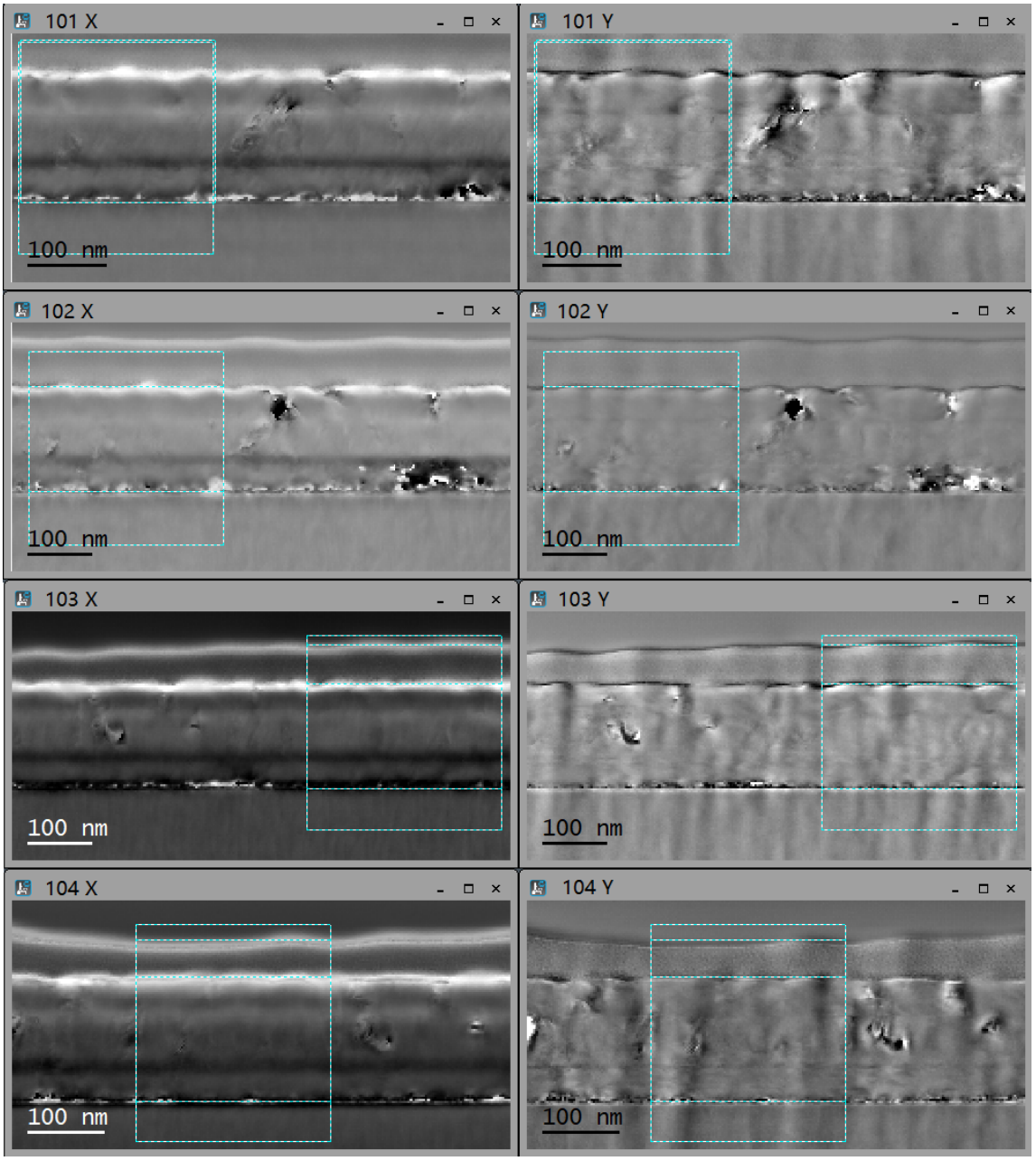

Figure 213: X and Y components of the four pixelated DPC datasets. Rotation angles to separate possible magnetic contrast between the components are 63° (101), 65° (102), 63° (103) and 60° (104). Left column shows the X components, right column the Y components, the regions from where the line profiles have been obtained are indicated by the rectangles.

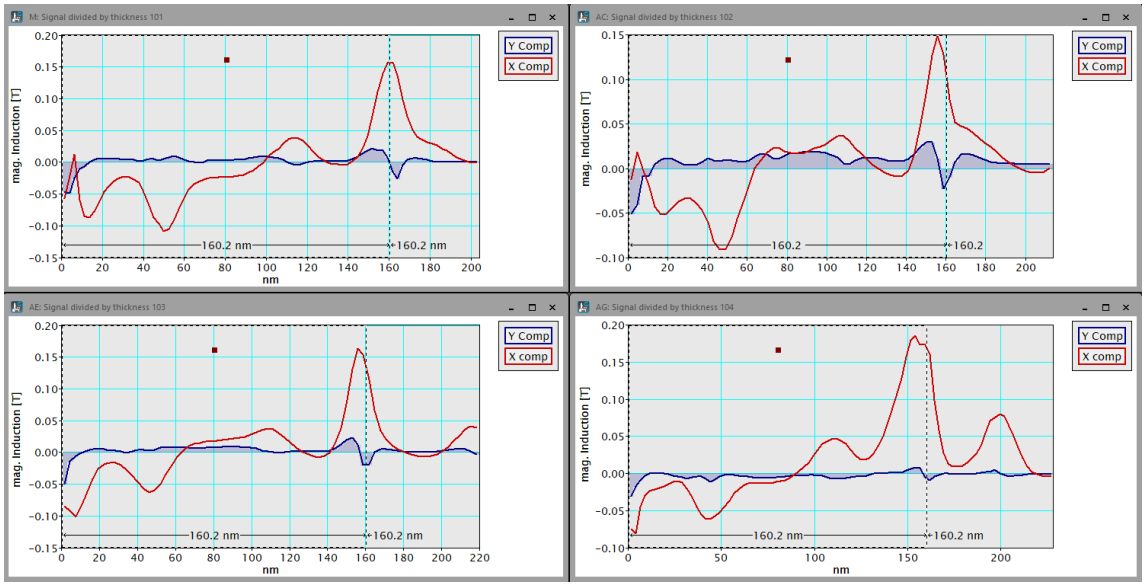

Figure 214: Overlay of the line profiles of the thickness-corrected signal starting at the MgO/V interface. The layer system is indicated by the ROIs. The X component (red) shows probably magnetic signal as it could be switched.

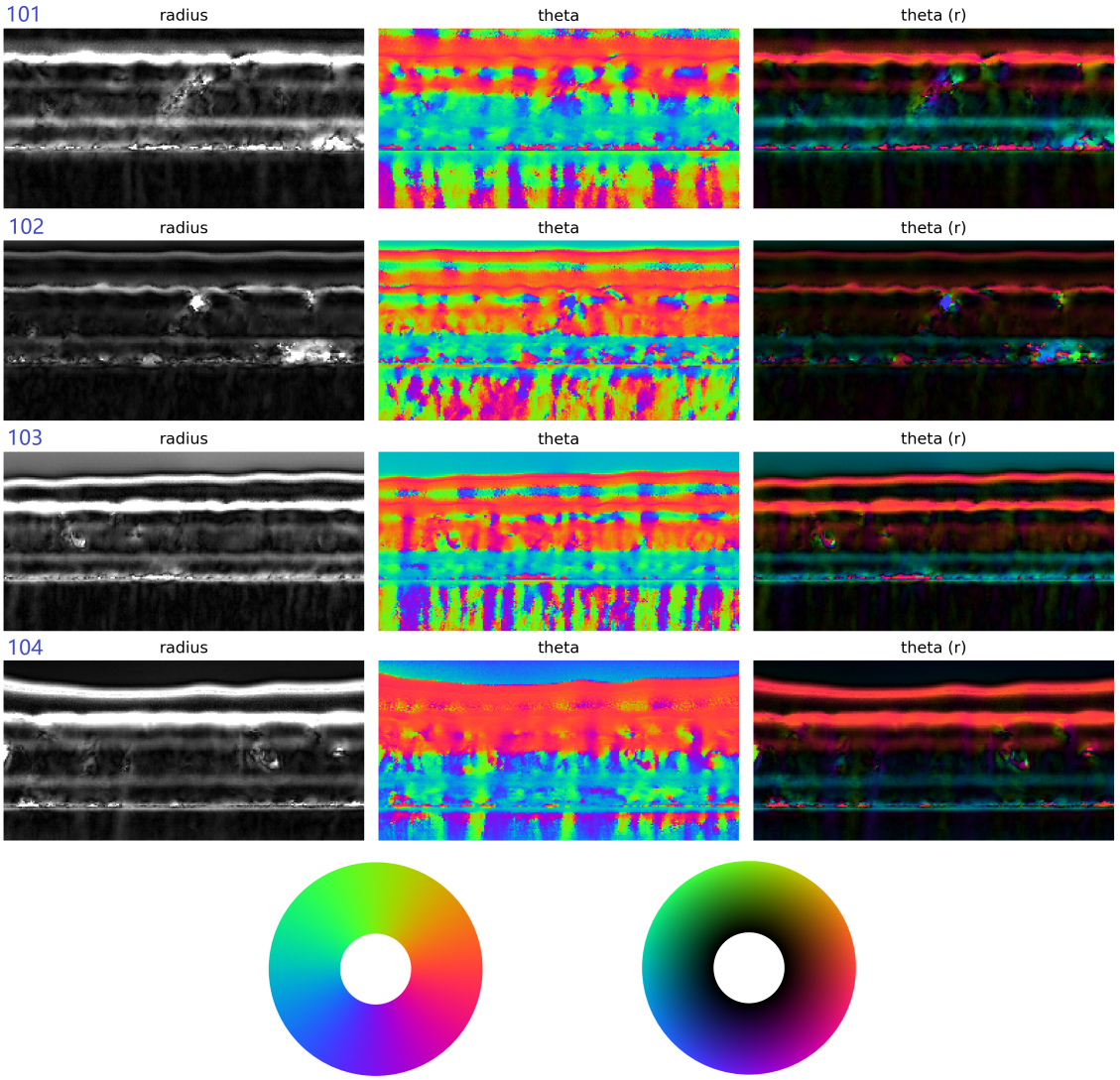

Figure 215: Pixelated DPC results for the four datasets:left column shows the deflection distance (radius), central column the deflection angle (theta) and the right column the combination theta(r). Colour wheels to indicate strength and position below. The maximum theta is limited by the red circle in the histogram (fig.216).

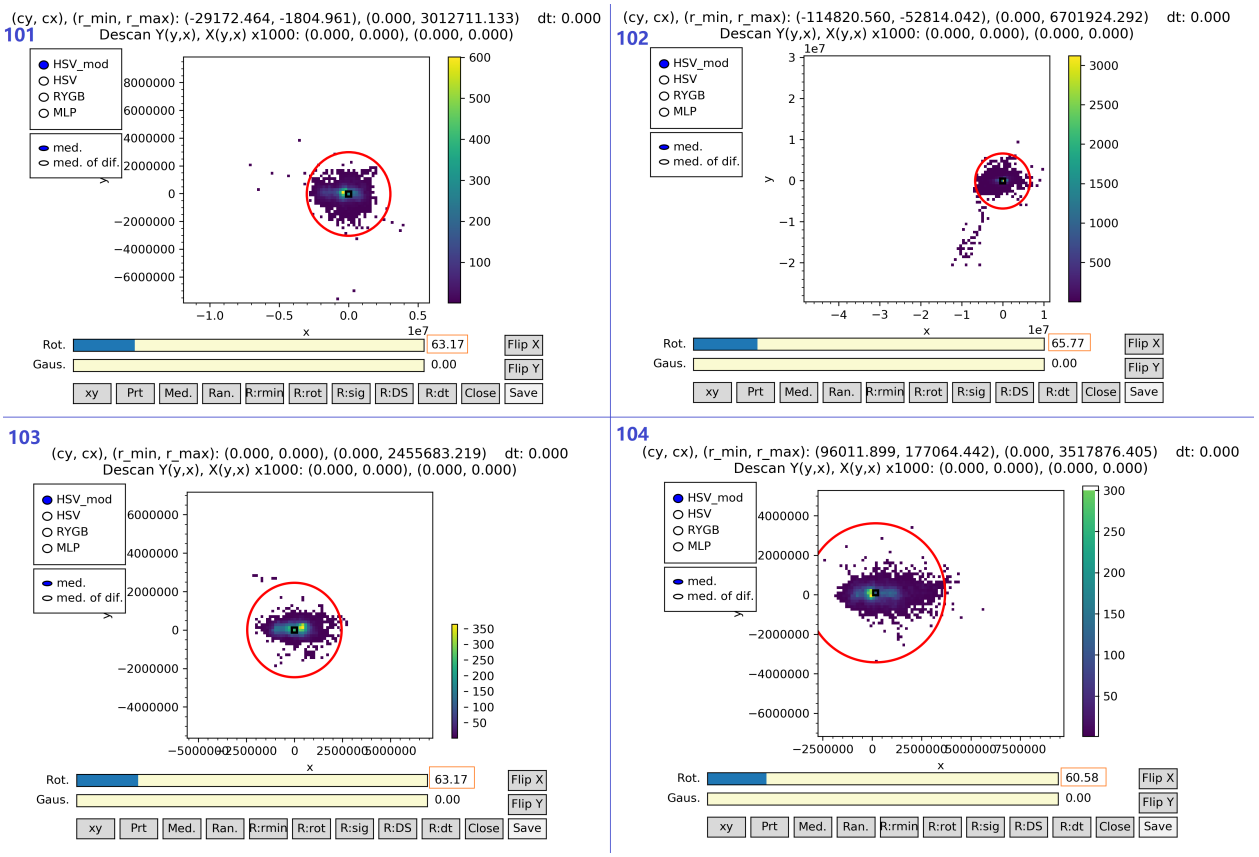

Figure 216: Positions of the center of the central diffraction disc. The red circle indicates the used range of positions, its center is set on the MgO central position for normalization. Other high intensity regions that represent a certain shift possibly contain magnetic signal. Units are arbitrary and the displaying routine still contains bugs, the intensity bar right of the histogram indicates how many pixels with a circle of the shown deflection has been found.

6.6 Thickness estimation of the TMR stack lamella: before and after 2nd thinning

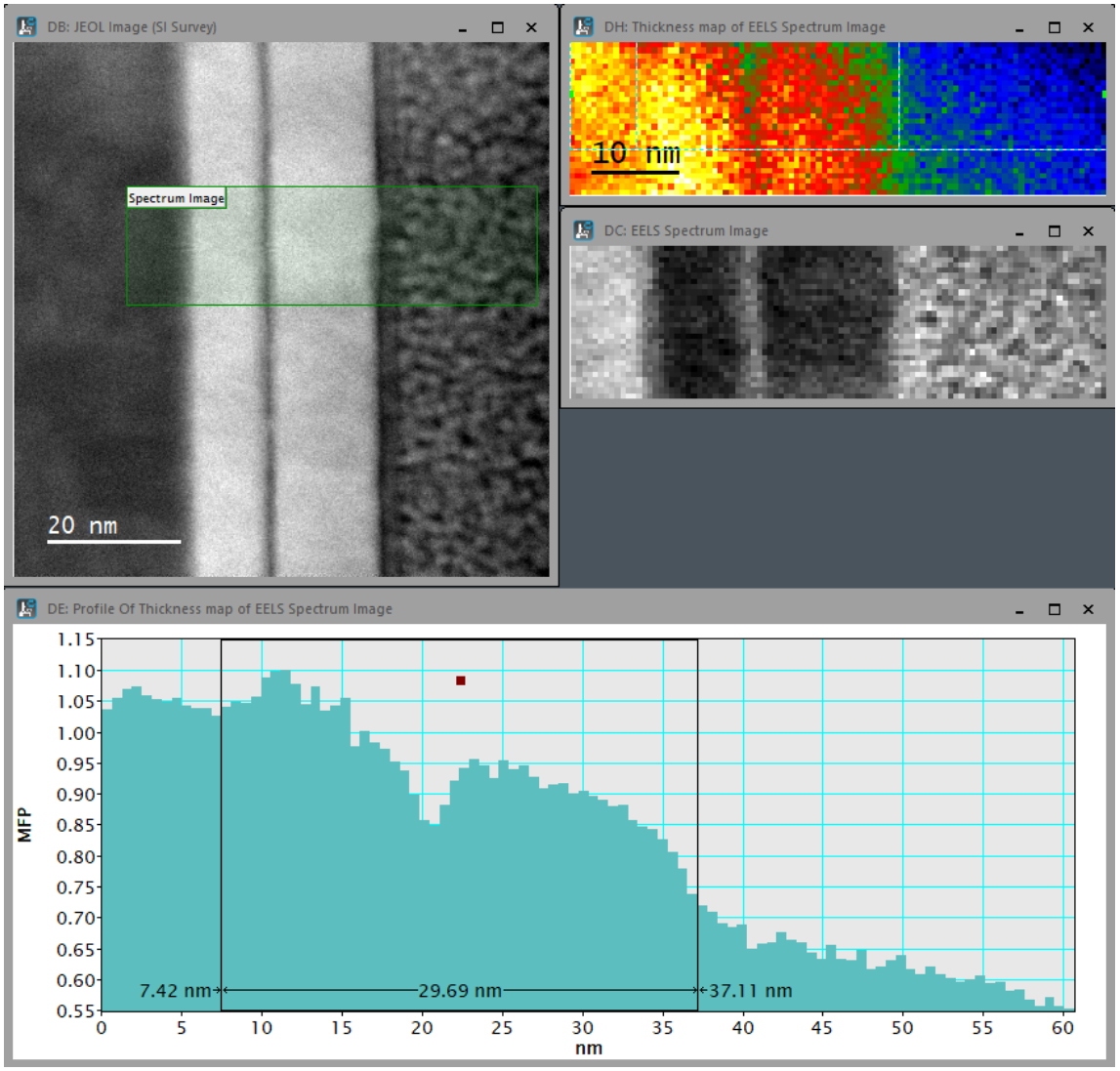

Figure 217: Thickness mapping of the TMR stack lamella before thinning on a thicker part, FIB-Pt present in a thick layer. Top right: STEM survey image with indicated area of the thickness mapping, substrate on the left and FIB-Pt on the right of the layer system. Top right: Thickness map with thickness in mfp colour coded, area of the line profile shown by marking. Below the spectrum image that shows a bright field image calculated from the total intensity. Bottom: Line profile across the thickness map showing the thickness in the unit of mean free path measured using the t/λ method. The layer system is indicated by the black rectangle.

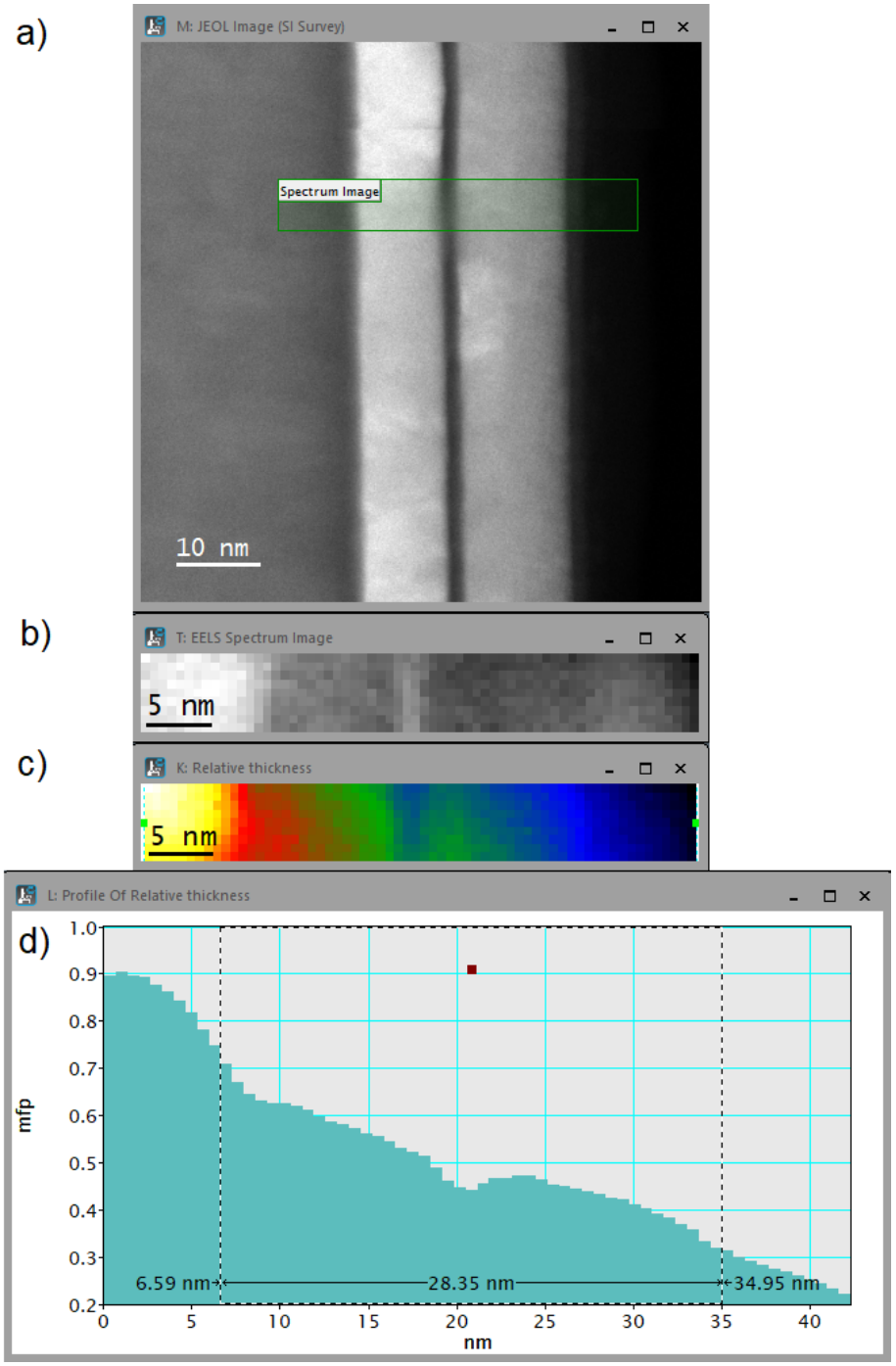

Figure 218: Thickness mapping of the TMR stack lamella before thinning on a thin part without FIB-Pt present. From Top to bottom: a) STEM survey image with the region of the thickness mapping indicated by the green rectangle, b) zero loss spectrum image showing a bright field image calculated from the total intensity, c) thickness mapping calculated from the zero loss spectrum image with the thickness in mean free path colour coded and d) line profile across the thickness map with the thickness shown in units of mean free path. The layer system is indicated by the ROI.

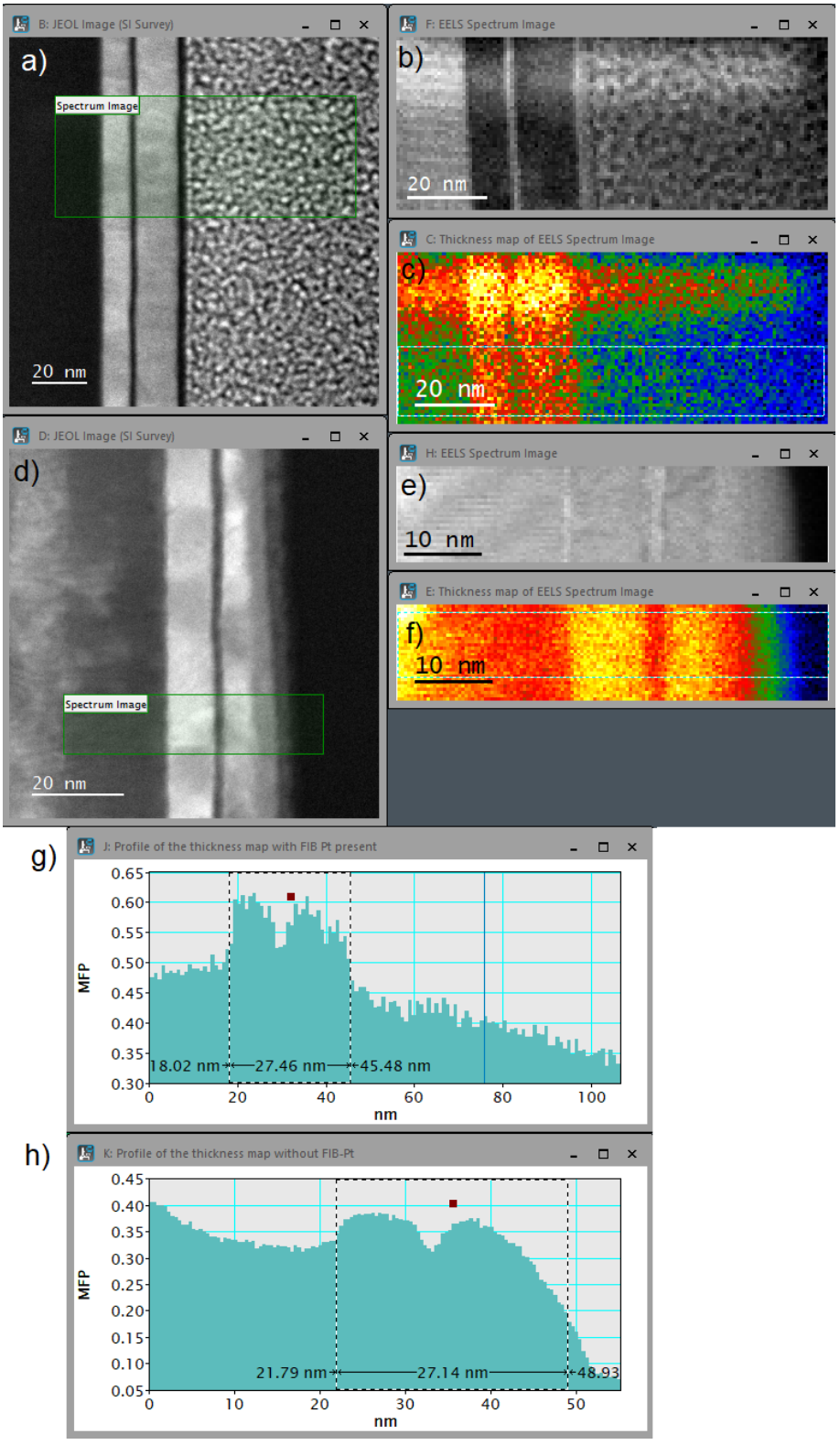

Figure 219: The lamella after the second thinning: a) Survey image of the thick part, b) zero loss spectrum image, c) thickness map with visible contamination from a linescan before. d) shows the survey image of a thin part with e) the zero loss spectrum image and f) the thickness map. Across both thickness maps a lineprofile has been obtained to indicate the thickness in mfp: g) for the thick part and h) for the thin part of the lamella.

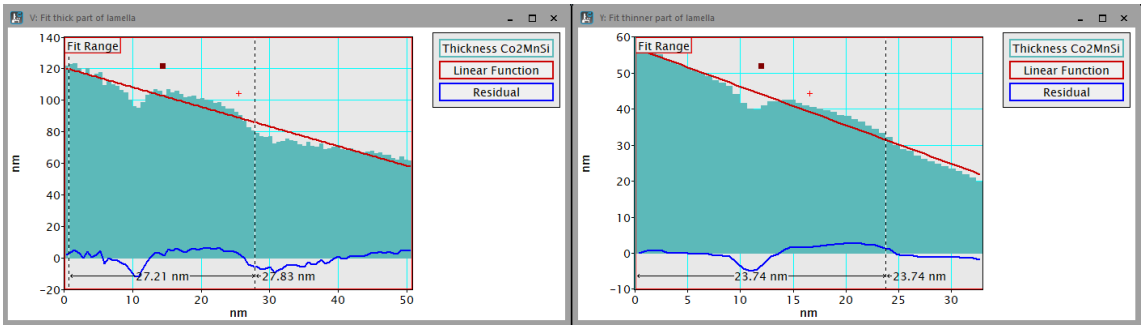

Figure 220: Left: thick part of the lamella before thinning. Right: thin part of the lamella before thinning. Shown are thickness profiles across the layer system obtained by multiplying the data in mfp with the mean free path for Co_2MnSi. The MgO part is neglected this way but the fit is carried out starting from the MgO/Co_2MnSi interface and the MgO barrier and protection layer are very narrow and the chosen window for the fit is drawn over only the two Co_2MnSi layers with the MgO barrier in the center. The fit results are $f(x) = -1.24887 \cdot x + 120.357$ (left) and $f(x) = -1.0729 \cdot x + 56.6188$ (right).

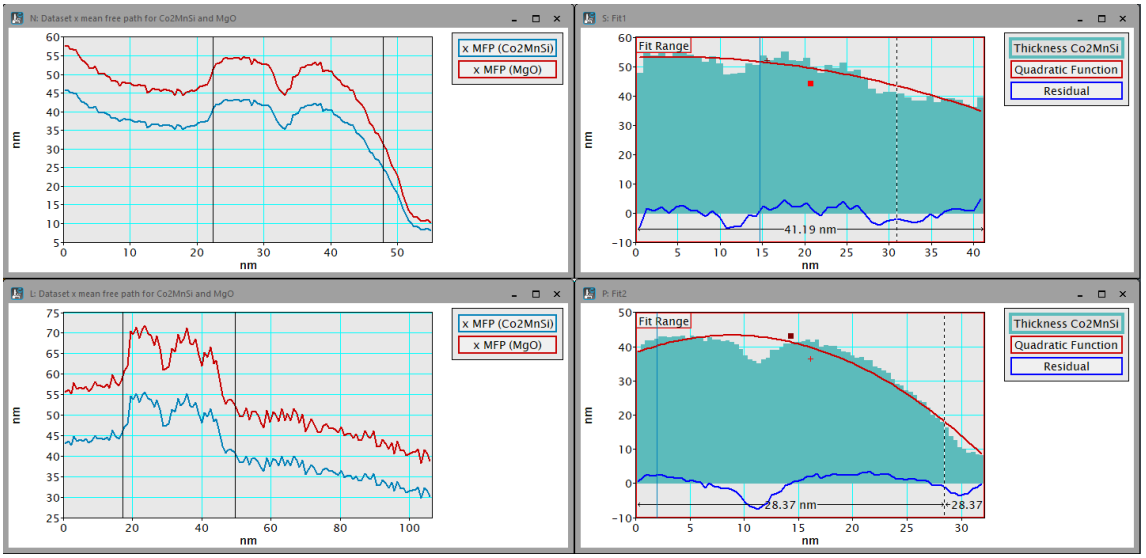

Figure 221: Thickness after the 2nd thinning: Right: Thickness profiles across the layer system for the thick (top) and thin (bottom) part of the lamella, each with a fitted quadratic function and the fit residual shown. The fit results are $f(x) = -0.0137211 \cdot x^2 + 0.0102797 \cdot x + 53.0034$ (thick part, top right) and $f(x) = -0.0653795 \cdot x^2 + 1.12328 \cdot x + 38.5144$ (thin part, bottom right). For the fit the thickness profile in mfp has been multiplied with the mean free path for Co_2MnSi as done before (fig.220). On the left the results are shown for the thickness profiles multiplied with the mfp values for both MgO and Co_2MnSi with the layer system indicated by the black lines.

6.7 Chemical analysis of the TMR stack

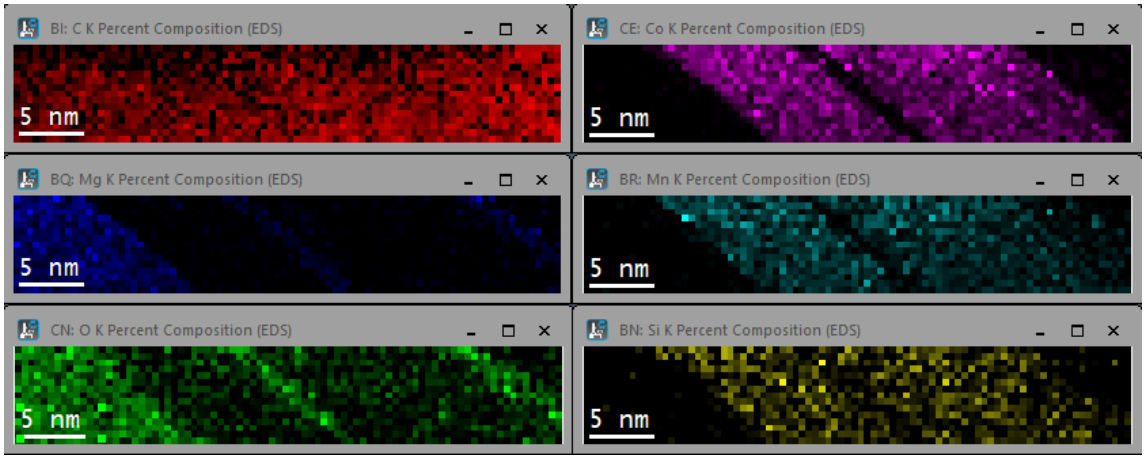

Figure 222: EDX mapping of the chemical composition of the TMR stack for the elements C, Mg, O (left) and Co, Mn, Si (right), showing the percent composition, not drift corrected. Acquisition time 0.2 sec, 2.5M magnification, 20 cm camera length. The increasing C contamination is visible in the C map, scan start has been top left of the map. All other layers are sharp, the MgO barrier visible and mostly clear of any other elemental contributions, some oxidation occurred to the Co_2MnSi layers.

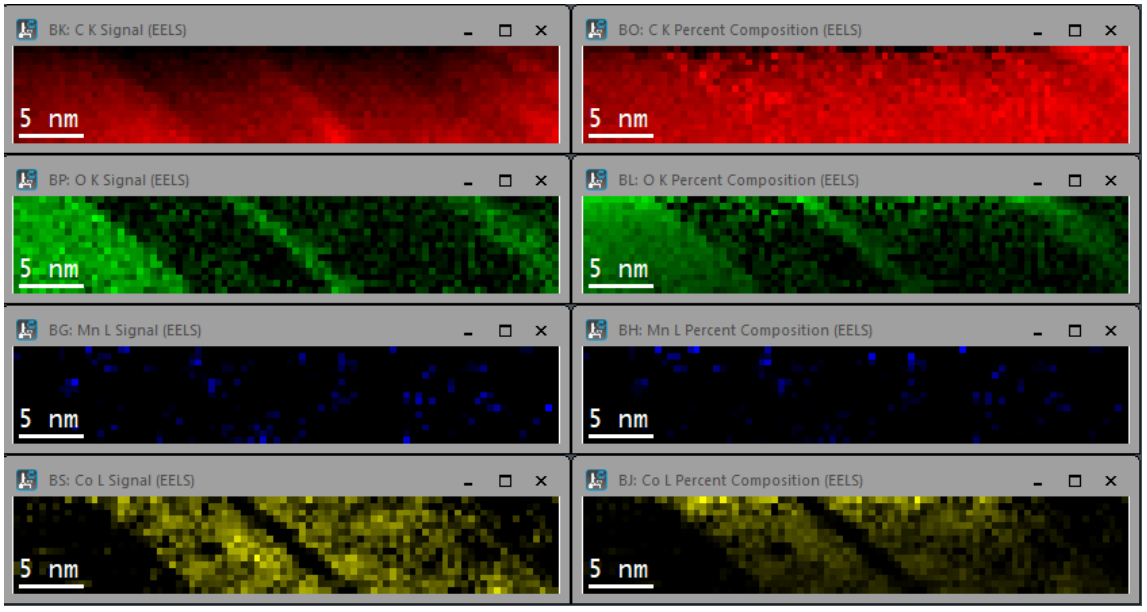

Figure 223: EELS mapping of the chemical composition of the TMR stack for the elements C, O, Mn and Co with the left column showing the signal strength in counts and the right column the percent composition. This mapping has been acquired simultaneous with the EDX mapping in fig.222. The increasing C contamination is visible in the C map. The Co signal shows the Heusler layers clearly, the Mn signal is only noise and would have needed a longer exposure time and the O map shows the MgO substrate and barrier clearly but also some oxidation in the layer system. Clear Mn signal is available from the EDX map.

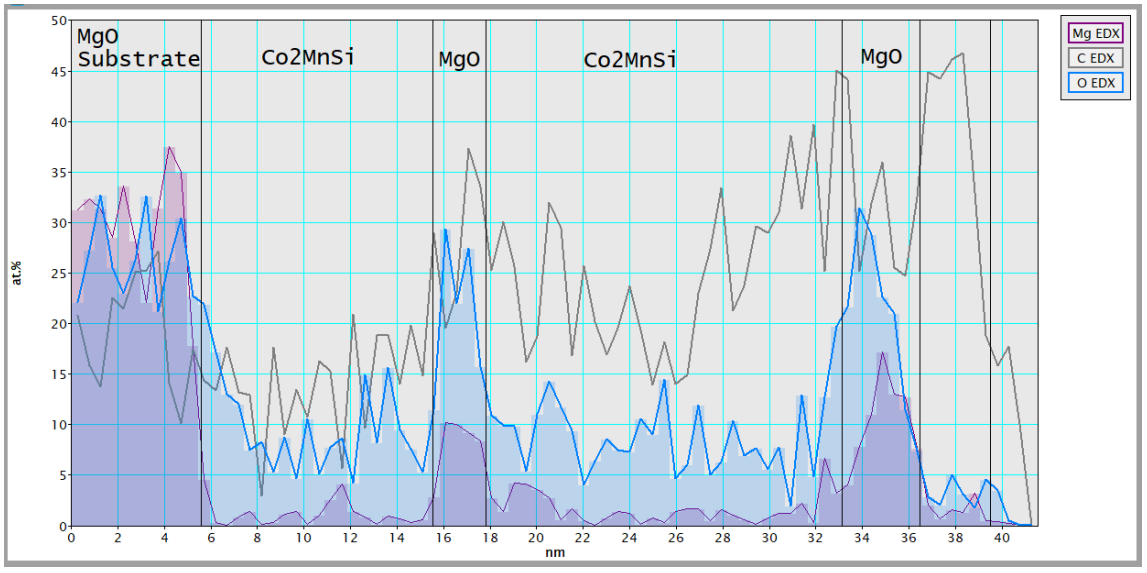

Figure 224: The elemental composition for Mg, C and O obtained from line profiles across the drift corrected maps.

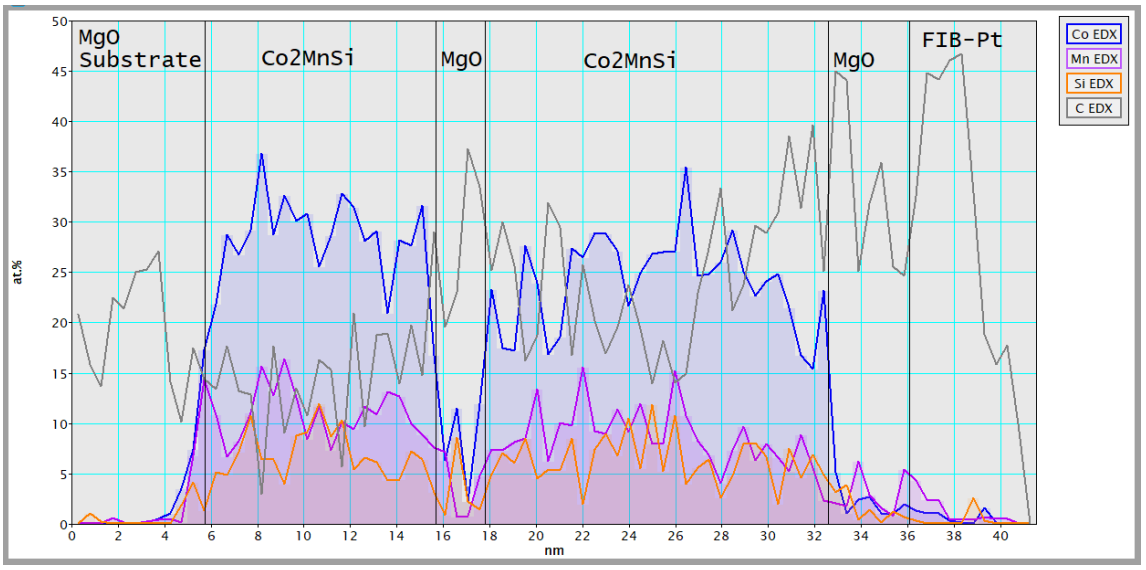

Figure 225: The elemental composition for the relevant elements of the Heusler allay, Co, Mn and Si obtained from line profiles across the drift corrected maps, C added for comparison with fig.224.

6.8 Pixelated DPC of the TMR stack

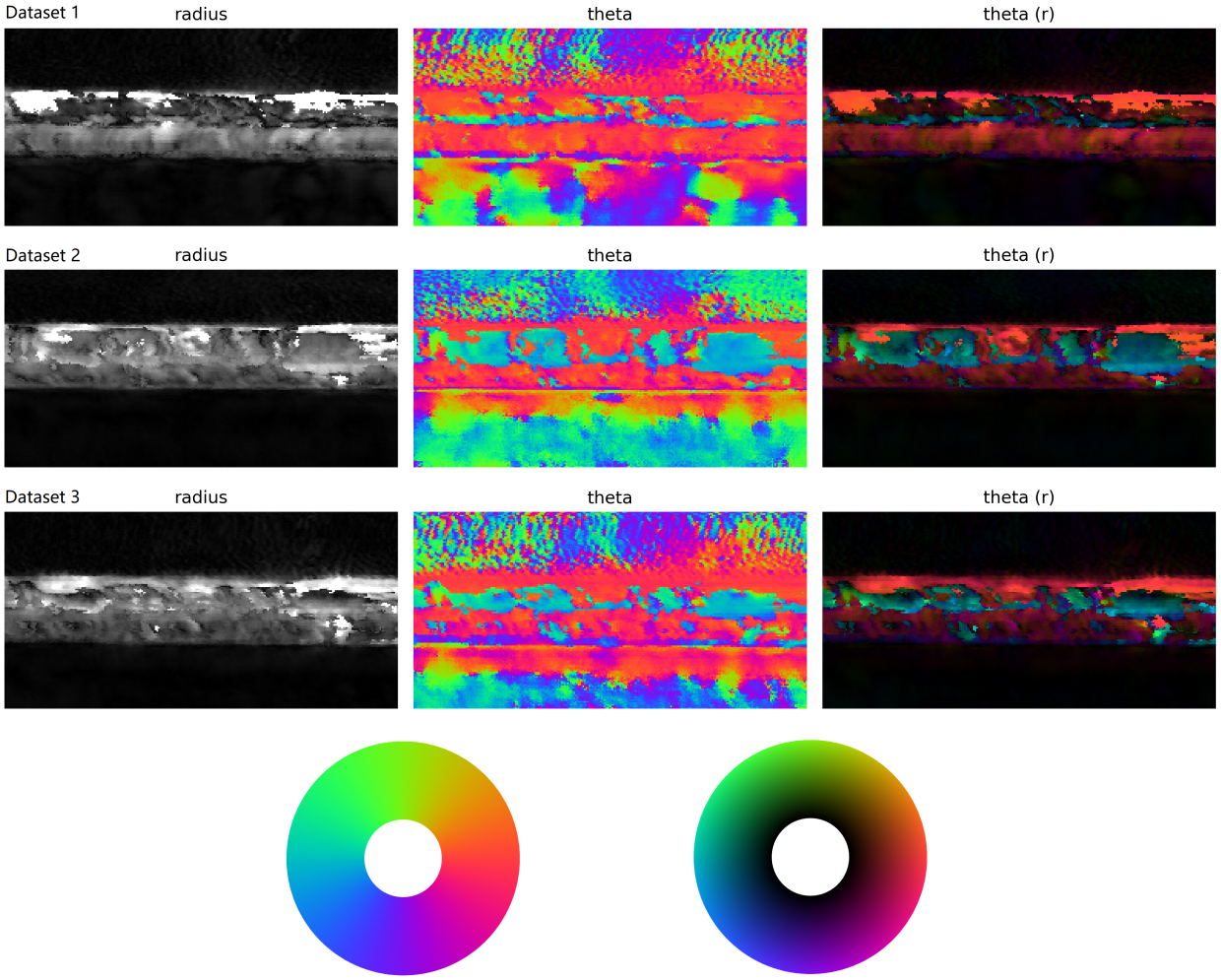

Figure 226: Pixelated DPC results for the first three of five TMR datasets (Tilt direction $-, +, +, +, -$): the left column shows the deflection distance (radius), the central column the deflection angle (theta) and the right column the combination theta(r). Colour wheels to indicate strength and position below. The maximum theta is limited by the red circle in the histogram (fig.228).

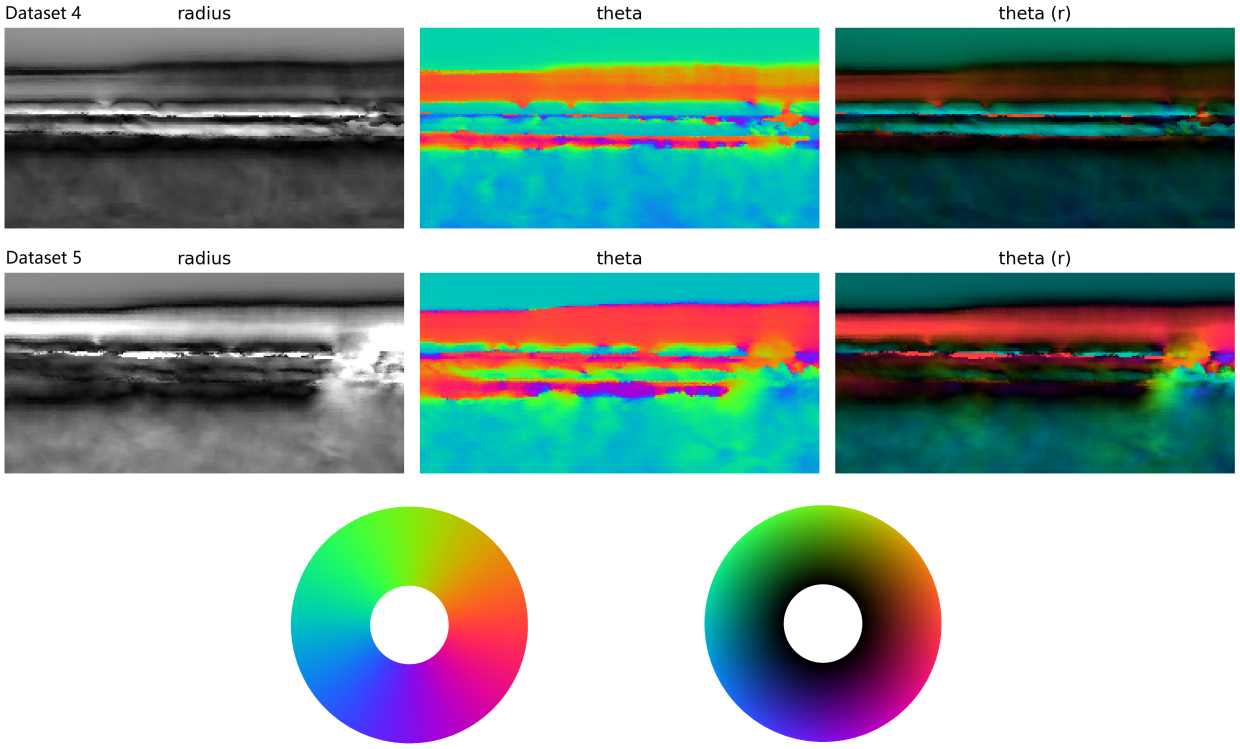

Figure 227: Pixelated DPC results for the last two of five TMR datasets (Tilt direction $-, +, +, +, -$): the left column shows the deflection distance (radius), the central column the deflection angle (theta) and the right column the combination theta(r). Colour wheels to indicate strength and position below. The maximum theta is limited by the red circle in the histogram (fig.228).

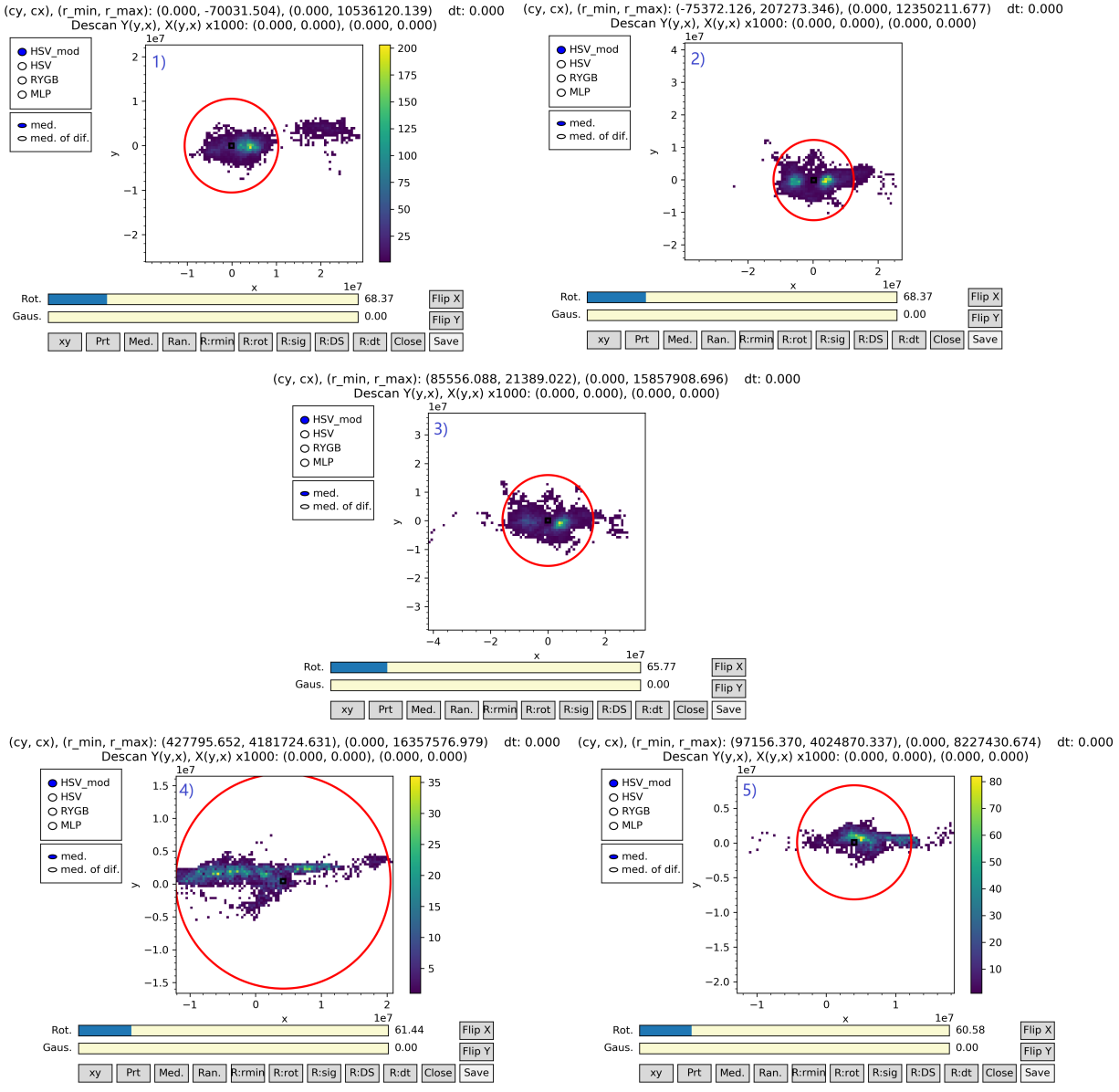

Figure 228: Positions of the center of the central diffraction disc. The red circle indicates the used range of positions, its center is set on the MgO central position for normalization. Other high intensity regions that represent a certain shift possibly contain magnetic signal. Units are arbitrary, the intensity bar right of the histogram indicates how many pixels with a circle of the shown deflection has been found. The rotation angle for the datasets to achieve one component with minimum contrast is always between 60° and 70°: 68°, 68°, 66°, 61° and 60°.

6.9 Additional structural information on the checkerboard

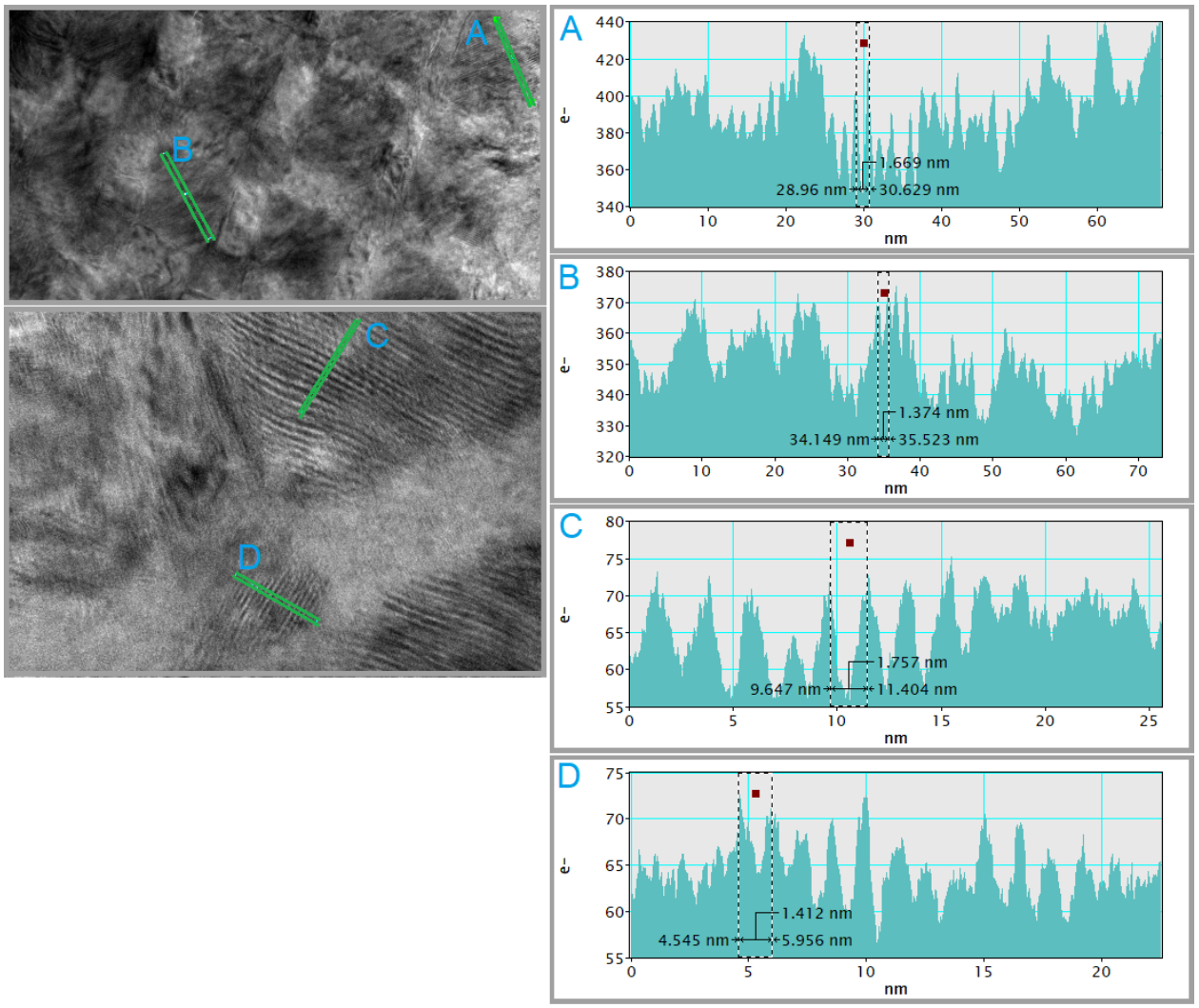

Figure 229: Measured Moirè patterns on checkerboard fields, the lineprofiles are shown in green on the excerpt of the TEM image and the letter connects lineprofile and region. The values are A: 1.669 nm, B: 1.374 nm, C: 1.757 nm, D: 1.412 nm. This distance varies over the lineprofiles, the measured distance is the most often appearing / most regular value.

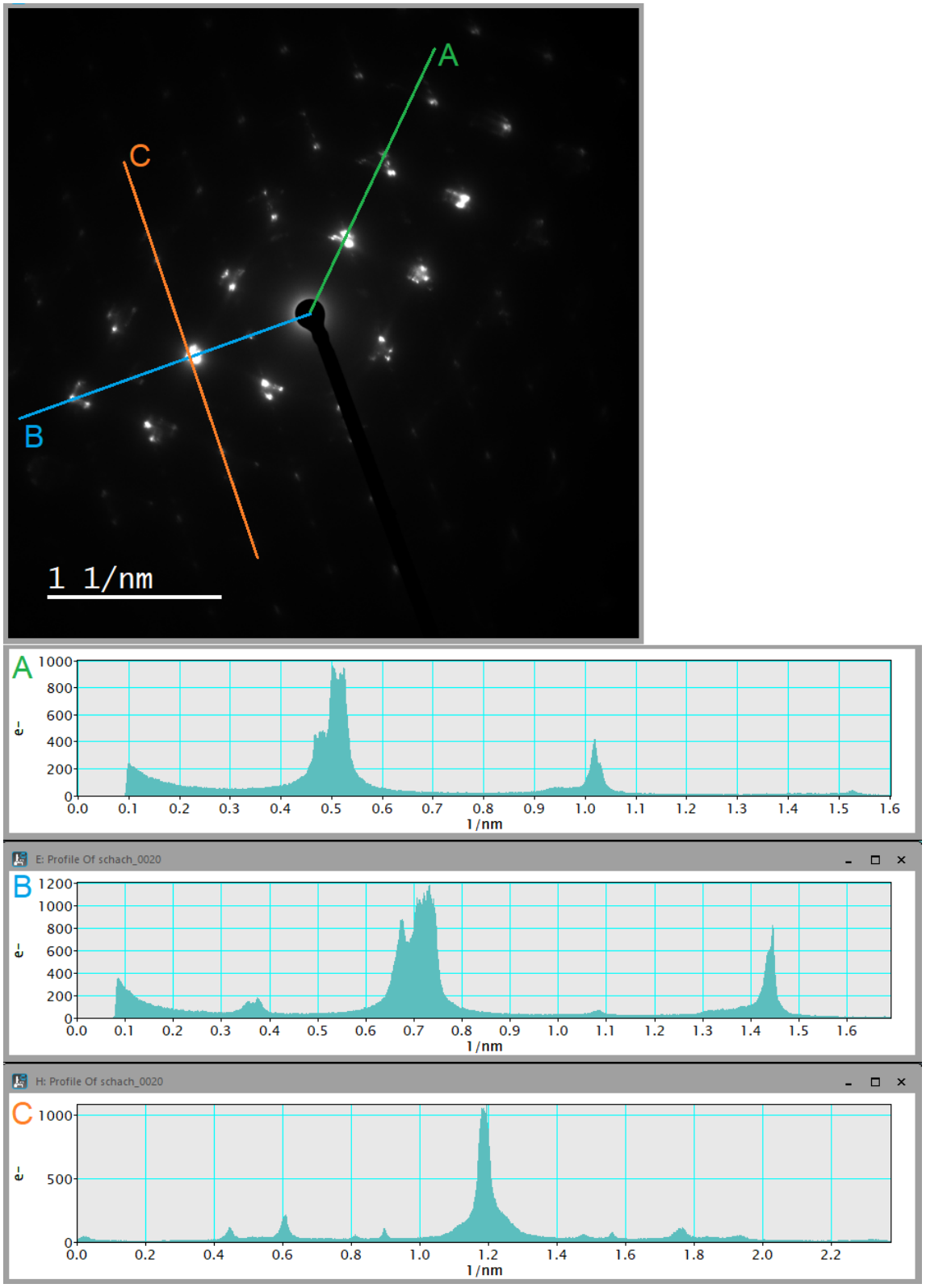

Figure 230: The diffraction image (top) has been measured via lineprofiles through several reflexes which are shown below.

6.10 Data of the checkerboard tomography series

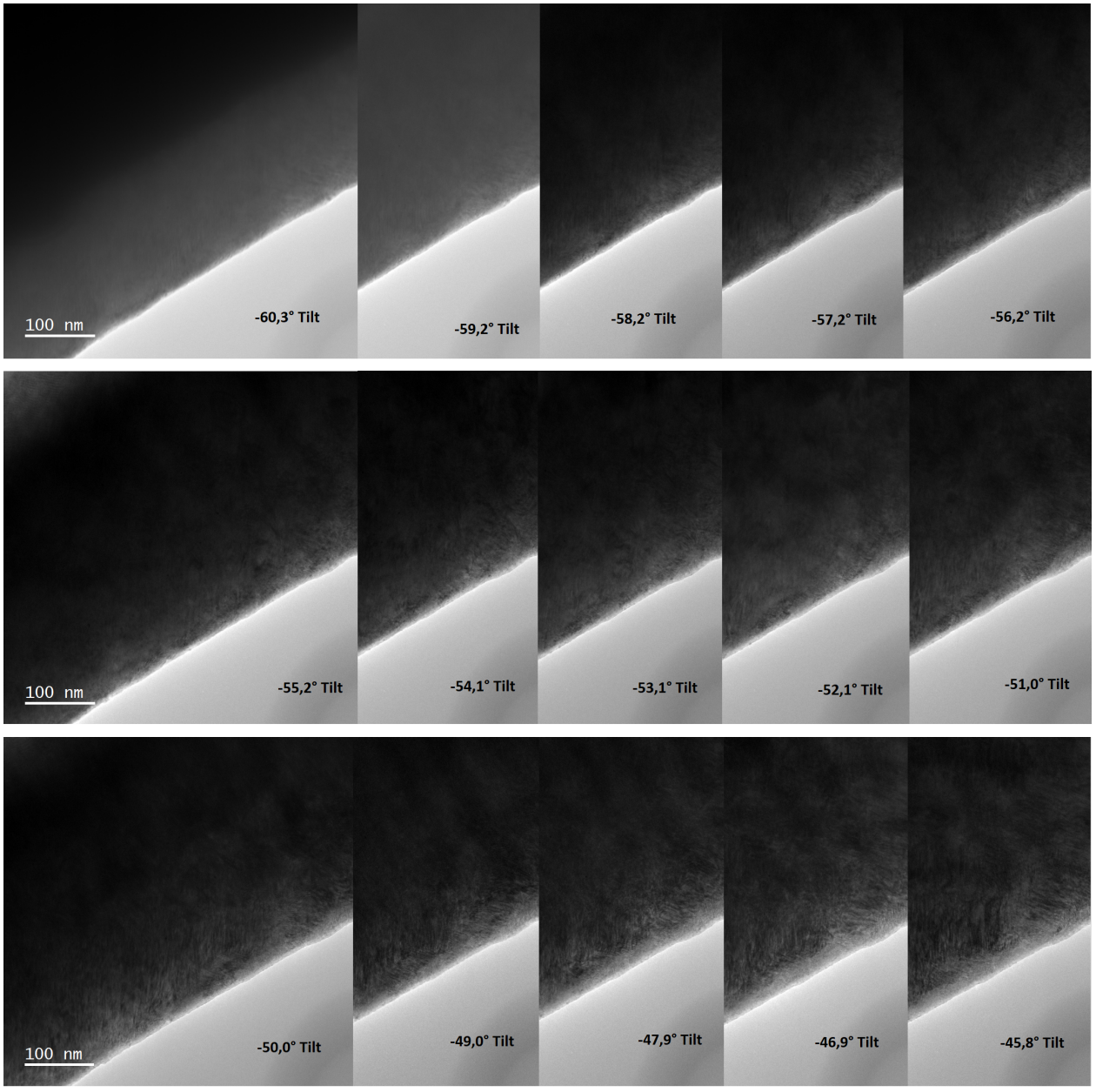

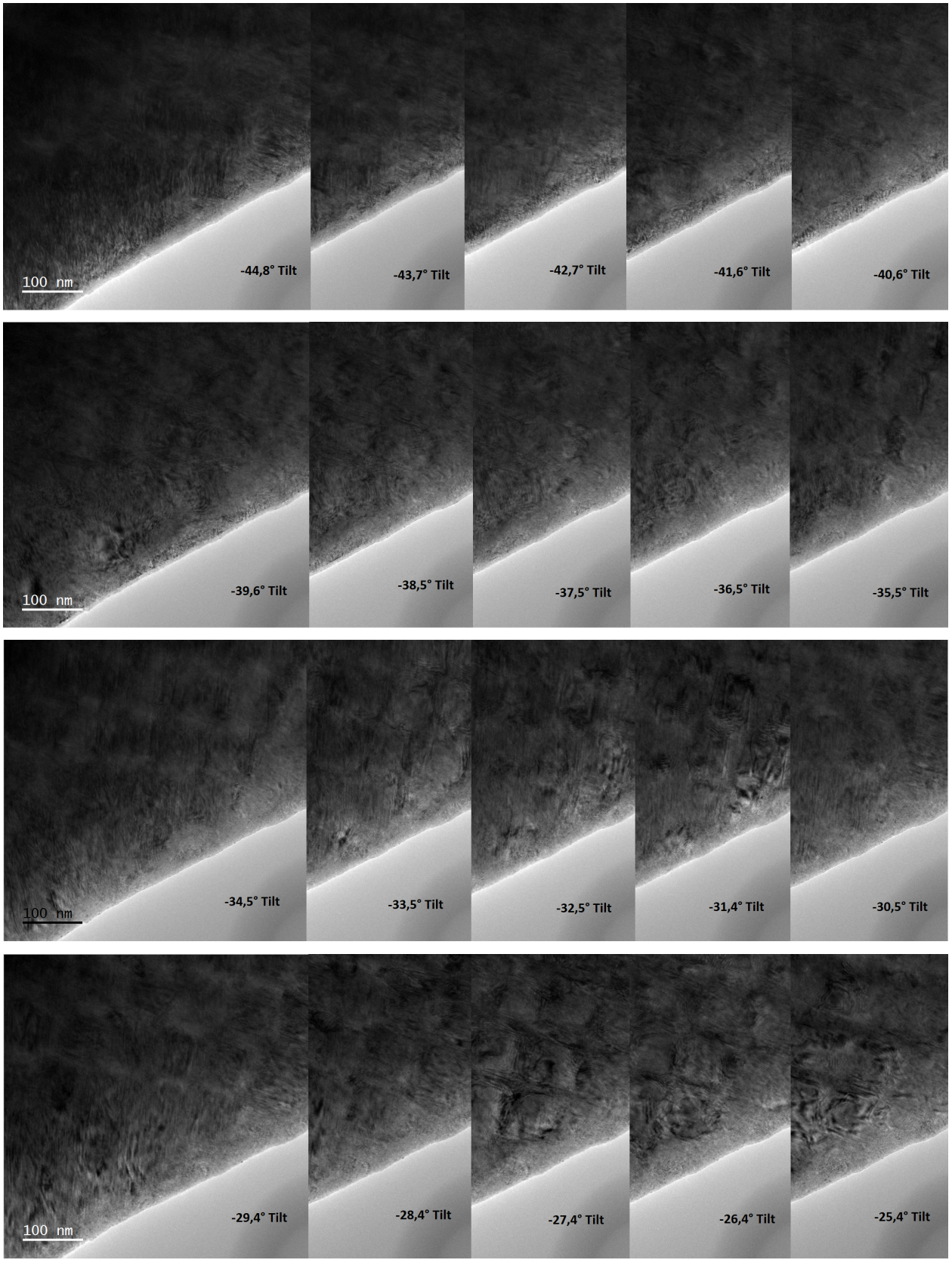
100 nm
-44,8° Tilt
-43,7° Tilt
-42,7° Tilt
-41,6° Tilt
-40,6° Tilt
100 nm
-39,6° Tilt
-38,5° Tilt
-37,5° Tilt
-36,5° Tilt
-35,5° Tilt
100 nm
-34,5° Tilt
-33,5° Tilt
-32,5° Tilt
-31,4° Tilt
-30,5° Tilt
100 nm
-29,4° Tilt
-28,4° Tilt
-27,4° Tilt
-26,4° Tilt
-25,4° Tilt

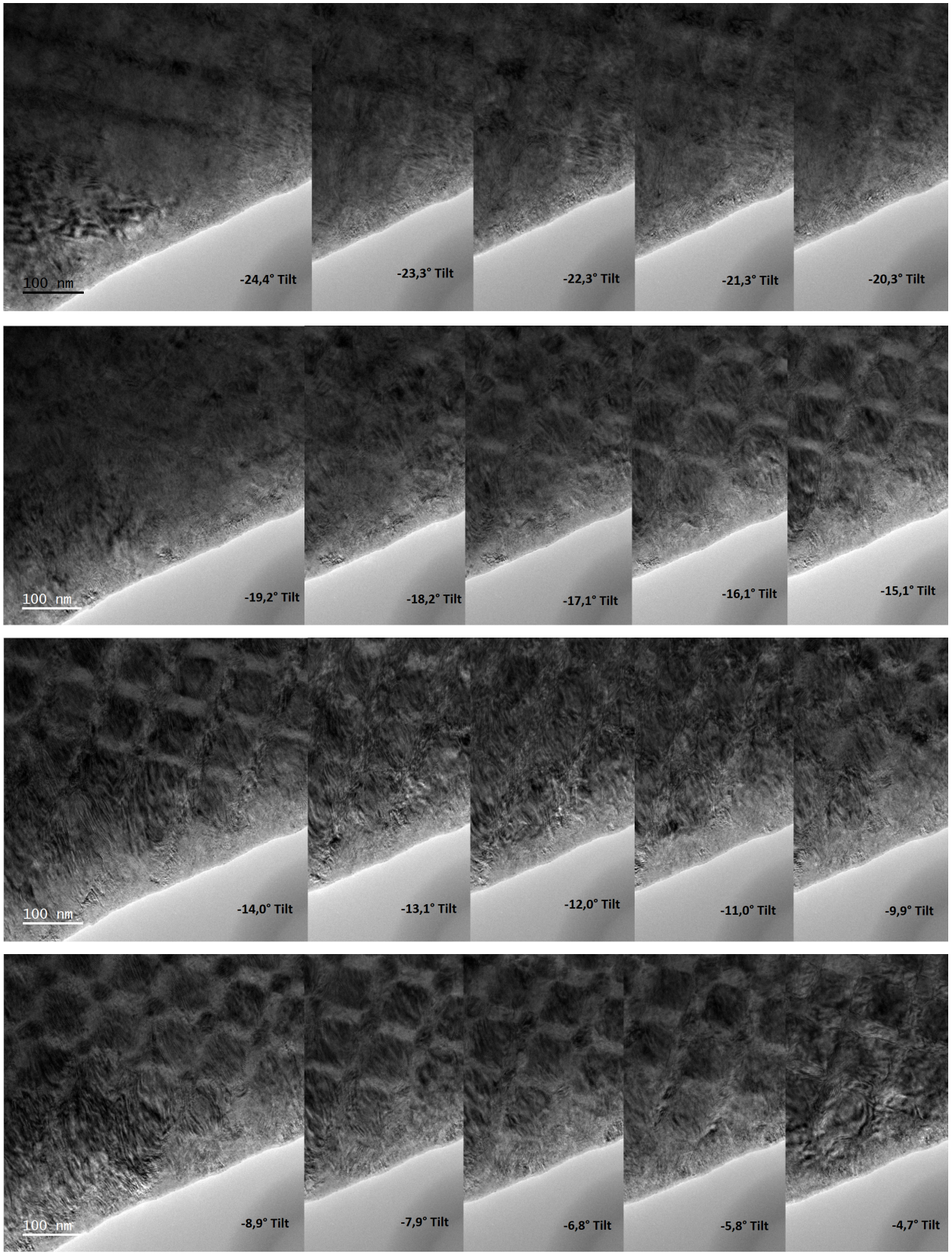
100 nm
-24,4° Tilt
-23,3° Tilt
-22,3° Tilt
-21,3° Tilt
-20,3° Tilt
100 nm
-19,2° Tilt
-18,2° Tilt
-17,1° Tilt
-16,1° Tilt
-15,1° Tilt
100 nm
-14,0° Tilt
-13,1° Tilt
-12,0° Tilt
-11,0° Tilt
-9,9° Tilt
100 nm
-8,9° Tilt
-7,9° Tilt
-6,8° Tilt
-5,8° Tilt
-4,7° Tilt

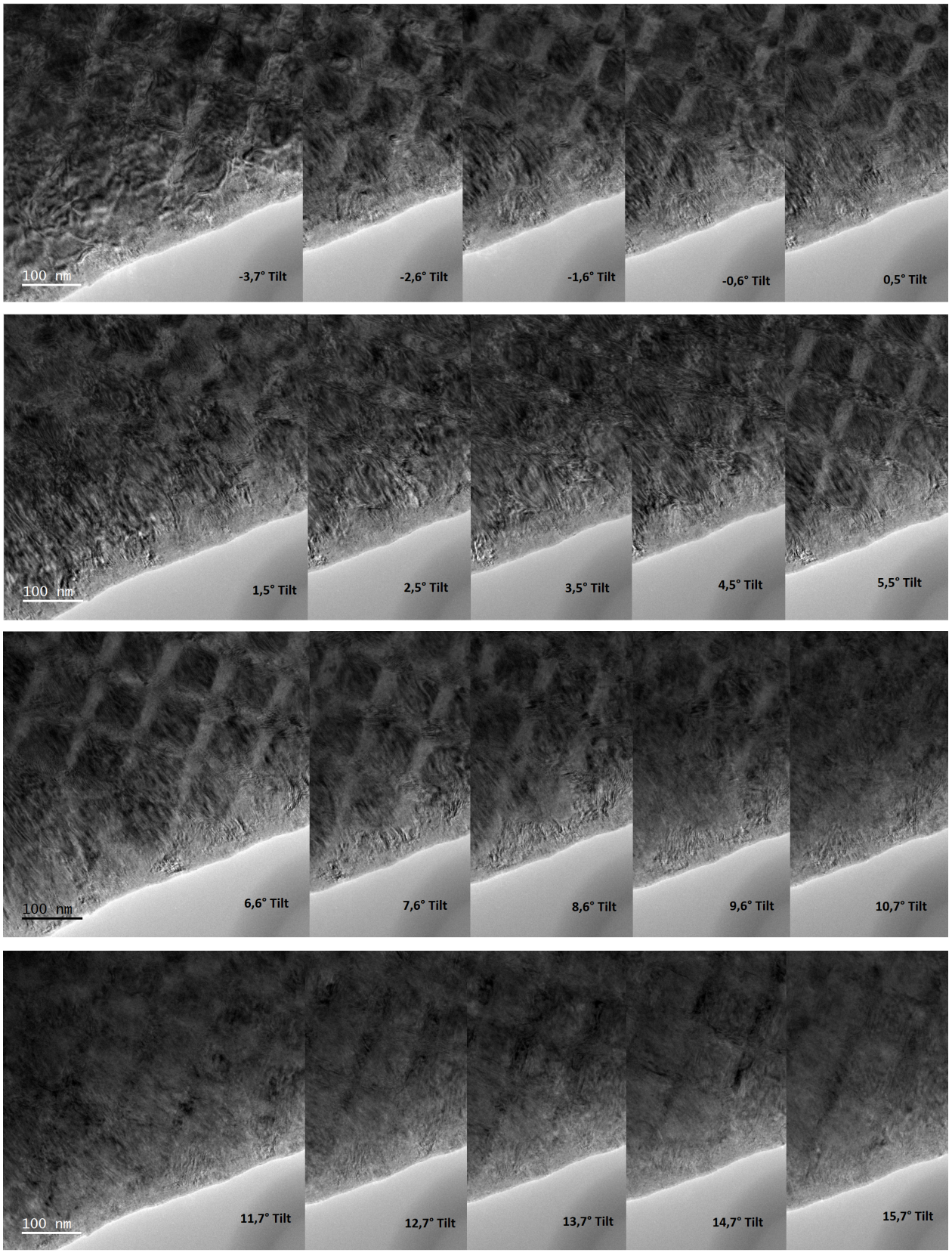
100 nm
-3,7° Tilt
-2,6° Tilt
-1,6° Tilt
-0,6° Tilt
0,5° Tilt
100 nm
1,5° Tilt
2,5° Tilt
3,5° Tilt
4,5° Tilt
5,5° Tilt
100 nm
6,6° Tilt
7,6° Tilt
8,6° Tilt
9,6° Tilt
10,7° Tilt
100 nm
11,7° Tilt
12,7° Tilt
13,7° Tilt
14,7° Tilt
15,7° Tilt

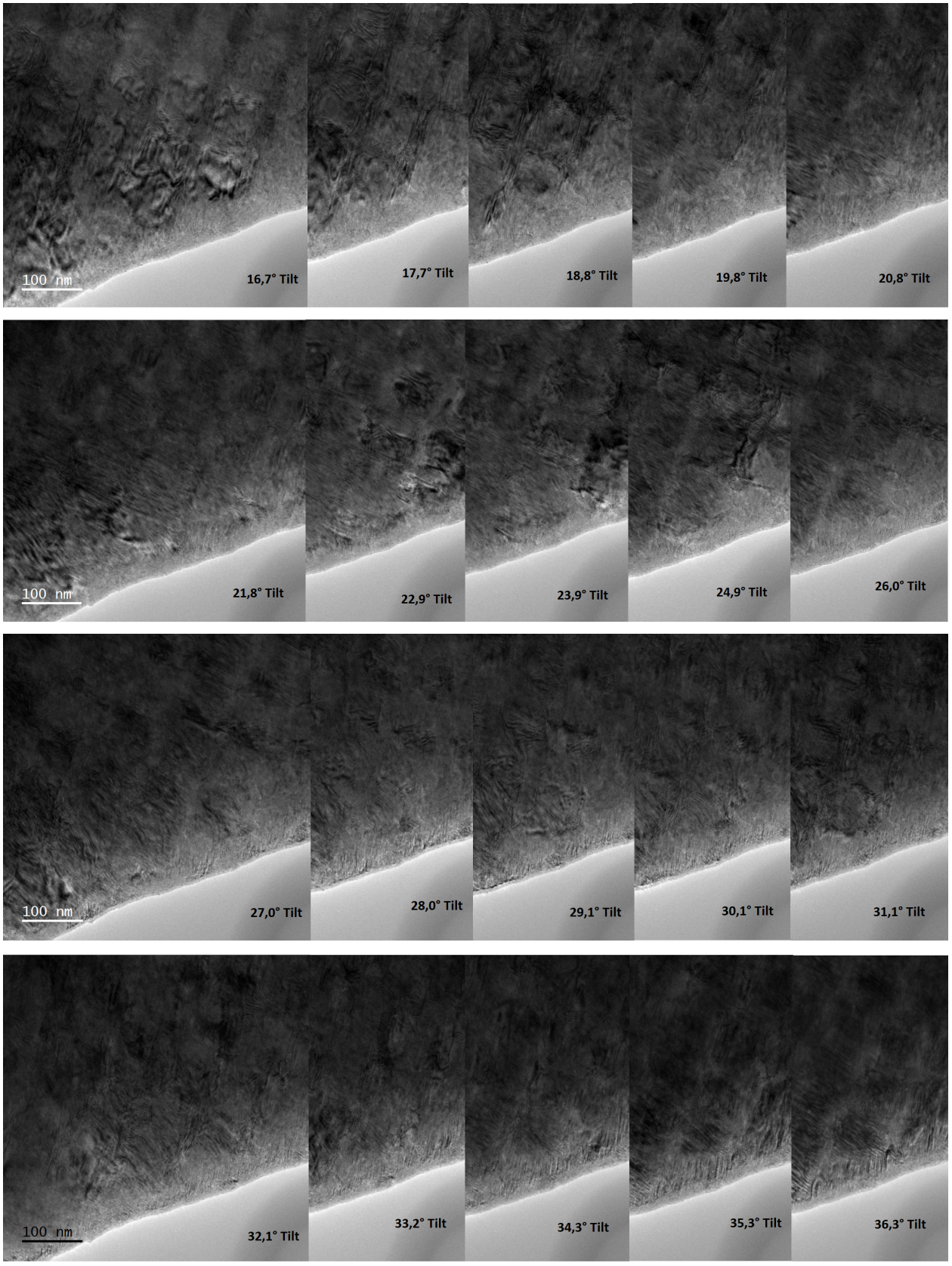
100 nm
16,7° Tilt
17,7° Tilt
18,8° Tilt
19,8° Tilt
20,8° Tilt
100 nm
21,8° Tilt
22,9° Tilt
23,9° Tilt
24,9° Tilt
26,0° Tilt
100 nm
27,0° Tilt
28,0° Tilt
29,1° Tilt
30,1° Tilt
31,1° Tilt
100 nm
32,1° Tilt
33,2° Tilt
34,3° Tilt
35,3° Tilt
36,3° Tilt

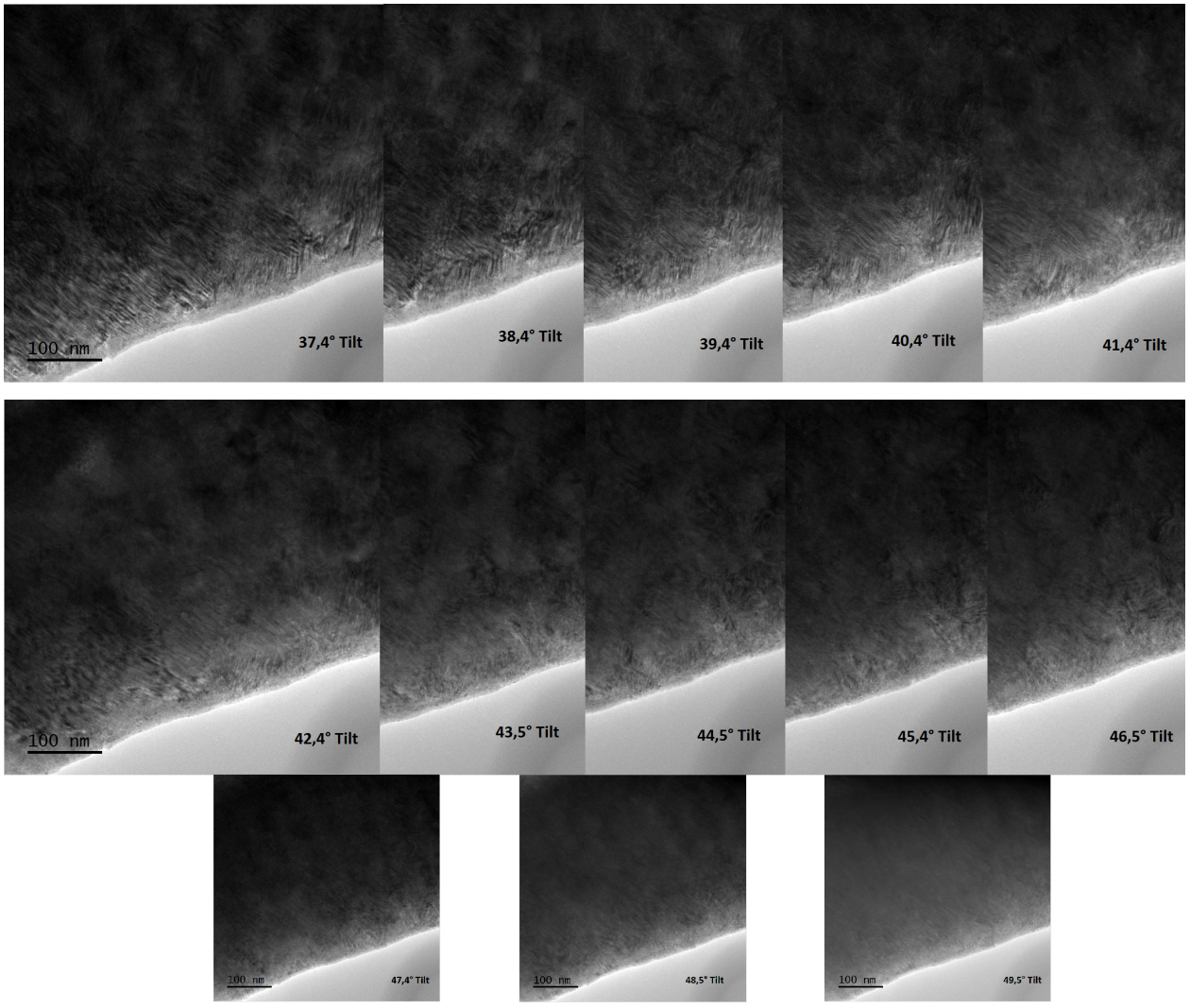
100 nm
37,4° Tilt
38,4° Tilt
39,4° Tilt
40,4° Tilt
41,4° Tilt
100 nm
42,4° Tilt
43,5° Tilt
44,5° Tilt
45,4° Tilt
46,5° Tilt
100 nm
47,4° Tilt
100 nm
48,5° Tilt
100 nm
49,5° Tilt

6.11 Checkerboard contrast plots

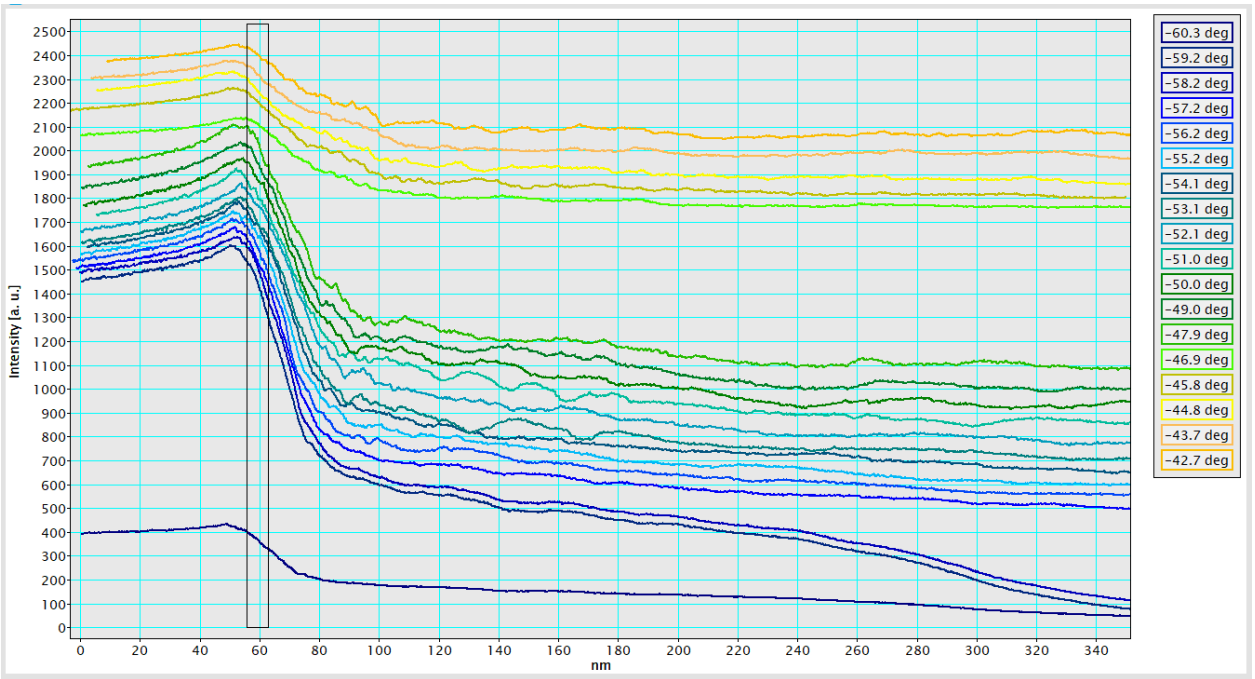

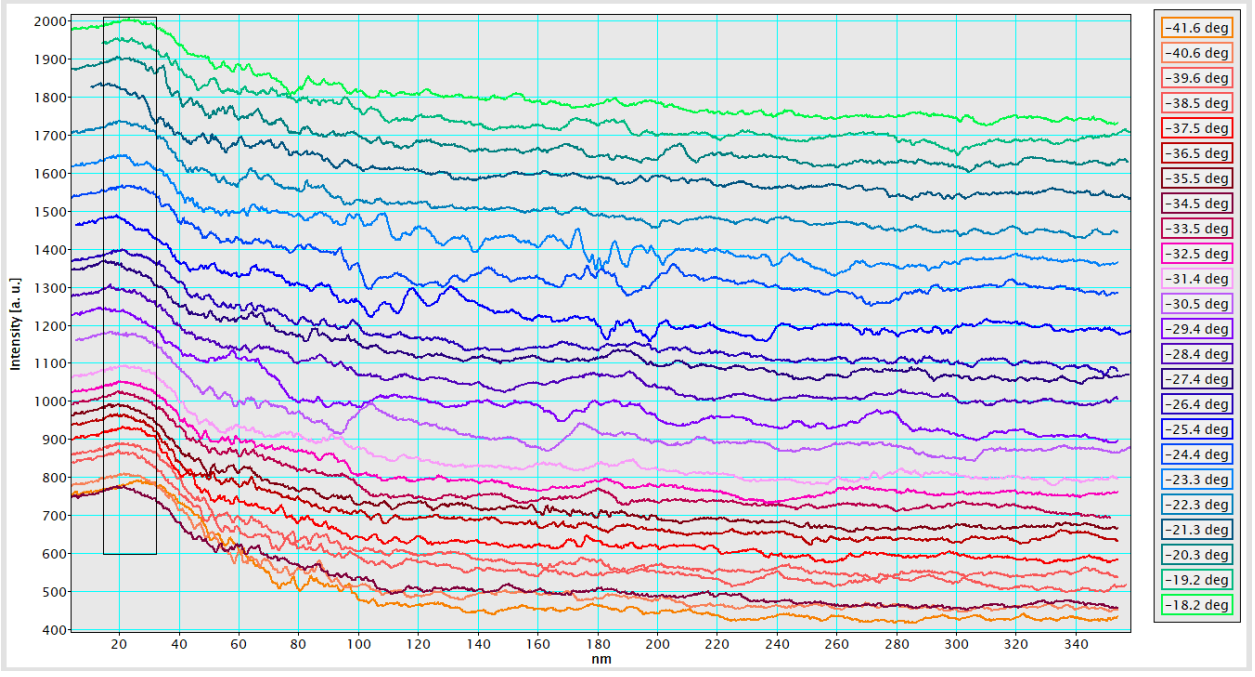

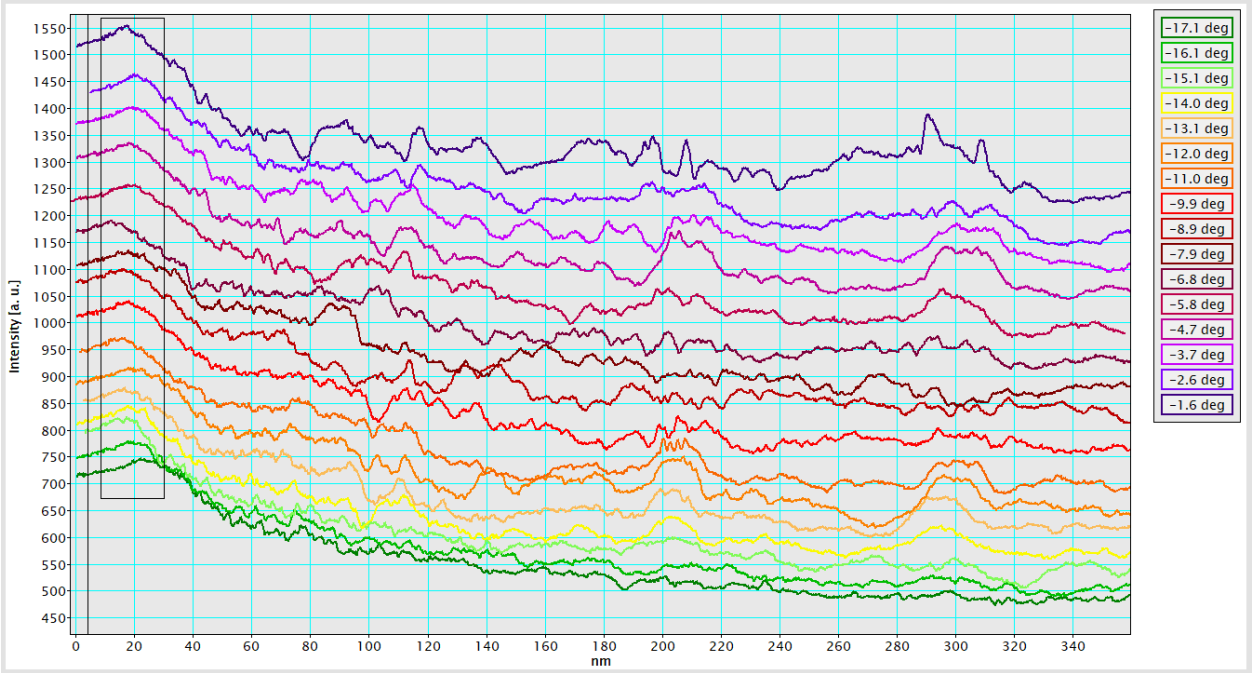
Intensity [a. u.]
nm
-17.1 deg
-16.1 deg
-15.1 deg
-14.0 deg
-13.1 deg
-12.0 deg
-11.0 deg
-9.9 deg
-8.9 deg
-7.9 deg
-6.8 deg
-5.8 deg
-4.7 deg
-3.7 deg
-2.6 deg
-1.6 deg

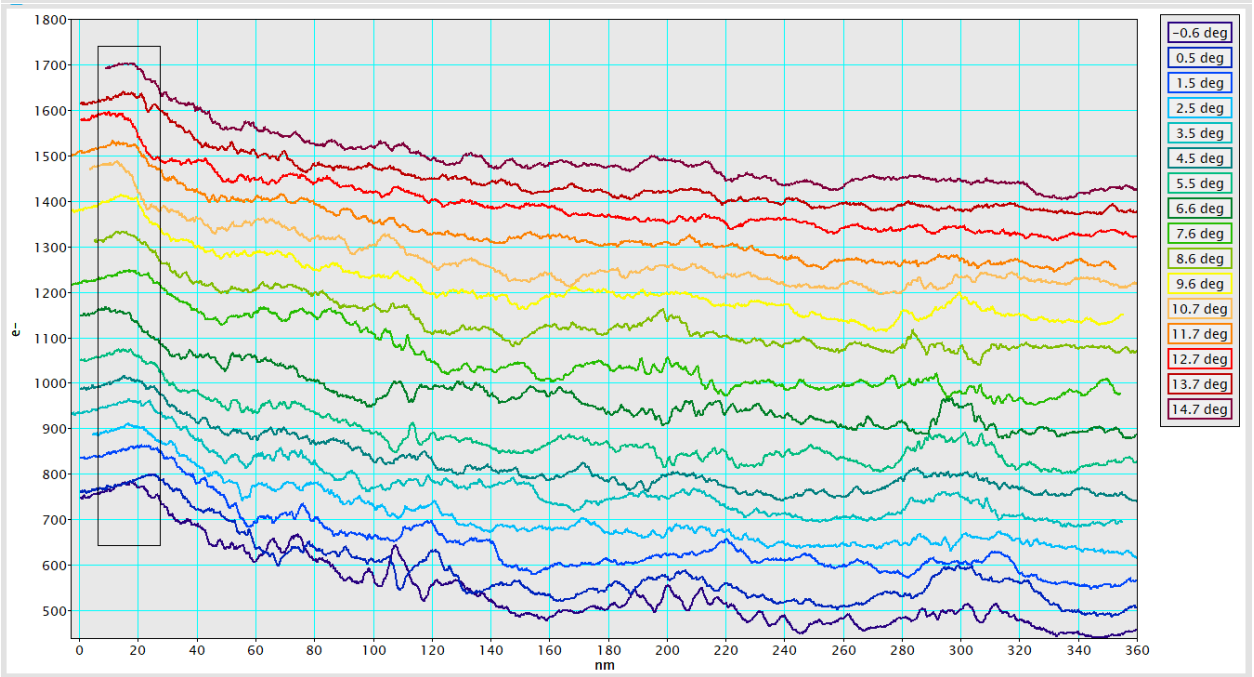
e-
nm
-0.6 deg
0.5 deg
1.5 deg
2.5 deg
3.5 deg
4.5 deg
5.5 deg
6.6 deg
7.6 deg
8.6 deg
9.6 deg
10.7 deg
11.7 deg
12.7 deg
13.7 deg
14.7 deg

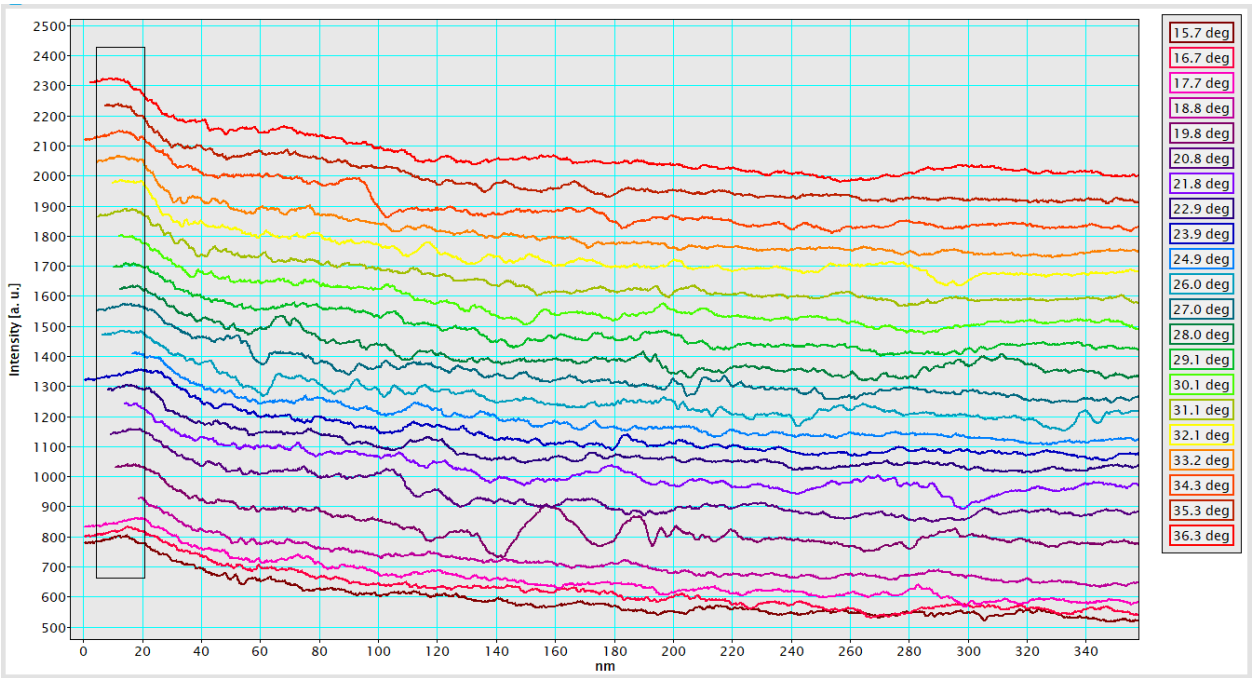
Intensity [a. u.]
nm
15.7 deg
16.7 deg
17.7 deg
18.8 deg
19.8 deg
20.8 deg
21.8 deg
22.9 deg
23.9 deg
24.9 deg
26.0 deg
27.0 deg
28.0 deg
29.1 deg
30.1 deg
31.1 deg
32.1 deg
33.2 deg
34.3 deg
35.3 deg
36.3 deg

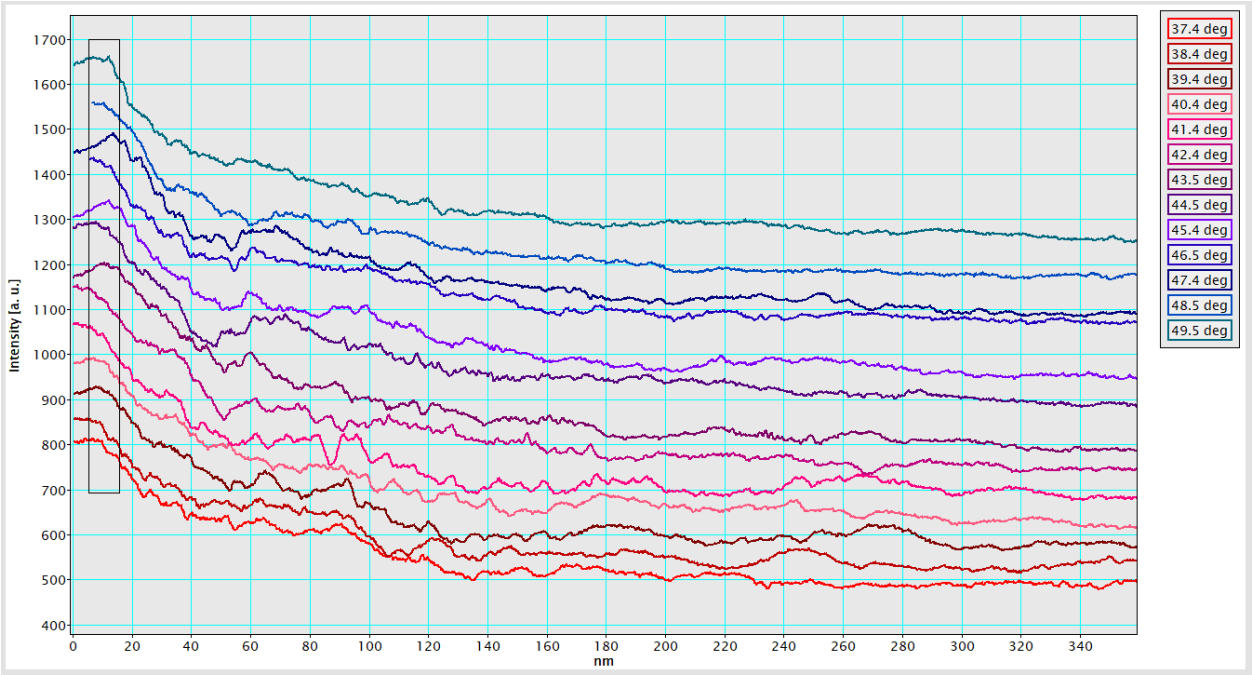
Intensity [a. u.]
nm
37.4 deg
38.4 deg
39.4 deg
40.4 deg
41.4 deg
42.4 deg
43.5 deg
44.5 deg
45.4 deg
46.5 deg
47.4 deg
48.5 deg
49.5 deg

6.12 Elemental maps of the checkerboard

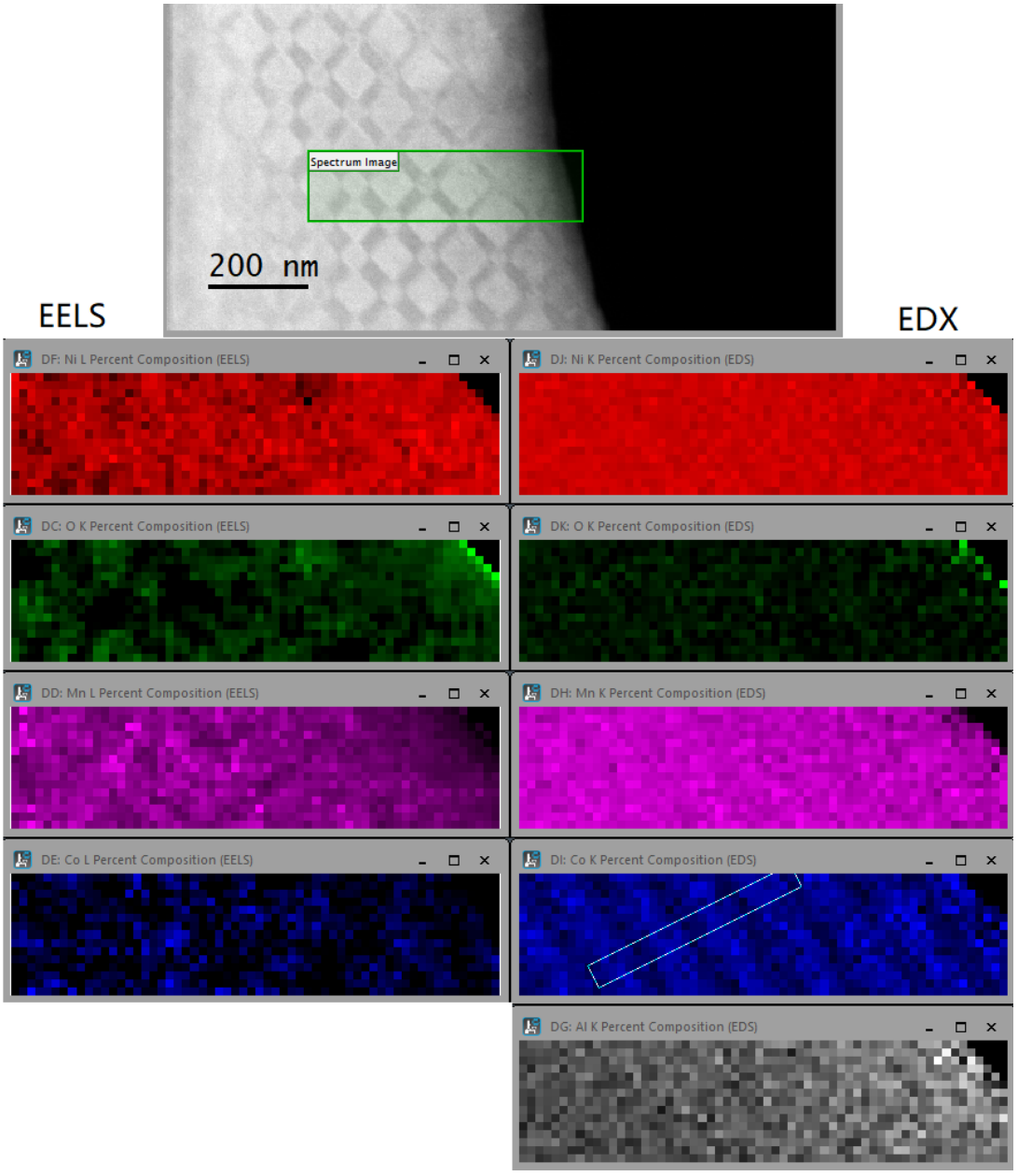

Figure 231: Survey image indicating the measured region and EELS (left column) and EDX (right column) elemental maps of the checkerboard specimen, not drift corrected.

6.13 DM scripts for EMCD evaluation

6.13.1 Script for automated EMCD data analysis:

This script takes in an image, takes a crossspectrum across it to determine the maximum position where the central beam has been, searches to both sides for a EMCD spectrum pair by creating spectra and comparing the background, then gives the best match pair of positions and spectra background subtracted. The set values are from the Fe edge of the Fe/Co_2FeSi/Fe system and need to be replaced for different data, what to do can be read from the comments. Used scripts: Savitzky Golay Spectral Filter [81], Create Spectrum from Image [147], Double Atan EELS background [148] by D. Mitchell and Batch Folder readin [82] by B. Schaffer.

```
// based on  scripts from Dave Mitchell for Savitzky Golay filtering, making a // spectrum

void linearregression(image xdata, image ydata, number &a, number &b)
{
  number xsize, ysize
  getsize(xdata, xsize, ysize)

  image xsqrd=xdata**2
  image xtimesy=xdata*ydata

  number sumofy, sumofx, sumofxtimesy, sumofxsqrd

  sumofy=sum(ydata)
  sumofx=sum(xdata)
  sumofxtimesy=sum(xtimesy)
  sumofxsqrd=sum(xsqrd)

  number denominator=xsize*sumofxsqrd-sumofx**2

  a=((sumofy*sumofxsqrd)-(sumofx*sumofxtimesy))/denominator
  b=((xsize*sumofxtimesy)-(sumofx*sumofy))/denominator
}

image fiteelsbackground(image spectrum, number roistart, number roiend,
number &a, number &b)
{
  number origin, scale, fitrange
  fitrange=roiend-roistart
  string units
  spectrum.imagegetdimensioncalibration(0,origin, scale, units, 0)
  // Set up the log data of the intensity on the region defined by the ROI
  image fitregionintensity=spectrum[0,roistart, 1, roiend]
  ImageSetDimensionCalibration(fitregionintensity,0,origin-roistart,
  scale, "eV",1)
  fitregionintensity=log(fitregionintensity)
  // Set up the log data of the energy scale on the region defined by the ROI
  image fitregioninx=fitregionintensity*0
  fitregioninx=(icol-origin+roistart)*scale
  // Call the above function to fit a straight line to the log-log plot
  // since the coefficients are passed in by reference into the
  //FitEEELSBackground function
  // the parameters (as well as the background fit) can be
  //obtained from the calling function
```

```
  linearregression(fitregioninx, fitregionintensity, a, b)
  // On the basis of the above fit, compute the backgroud fit
  image background=spectrum*0
  background=a+b*(icol-origin)*scale // A.E**-r
  background=exp(background)
  background[0,0,1,roistart]=0
  return background
  }

image ComputeSavitzkyGolayCoefficients(number points, number polynomialorder)
{
  polynomialorder=round(polynomialorder)
  if(polynomialorder<2) polynomialorder=2
  if(polynomialorder>3) polynomialorder=3

  points=round(points)
  if(mod(points,2)==0) points=points+1
  if(points<3) points=3
  if(points>99) points=99

  image designmatrix=realimage("",4,polynomialorder+1,points)

  designmatrix[0,0,points,1]=1

  number halfsize=((points-1)/2)*-1
  number i

  for(i=0; i<points; i++)
    {
      designmatrix[i,1,i+1,2]=halfsize
      halfsize=halfsize+1
    }

  designmatrix[0,2,points,3]=designmatrix[0,1,points,2]**2
  // polynomial order 2
  if(polynomialorder==3)designmatrix[0,3,points,4]=designmatrix
  [0,2,points,3]**2 // polynomial order 3

  image matrixtranspose=matrixtranspose(designmatrix)
  image matproduct=matrixmultiply(matrixtranspose, designmatrix)

  image inversematrix=matrixinverse(matproduct)
  image coeffmatrix=matrixmultiply(inversematrix, matrixtranspose)

  return coeffmatrix
}

image SavitzkyGolay (image front)
{
number points=15 // the width of the window for fitting (3-99)
// must be odd
number polyorder=2
// the polynomial order 2 (for 1D plots) to 3 (for derivatives)

  polyorder=round(polyorder)
  if(polyorder<2) polyorder=2
  if(polyorder>3) polyorder=3
```

```
  points=round(points)
  if(mod(points,2)==0) points=points+1
  if(points<3) points=3
  if(points>99) points=99

  image sgcoeffs=ComputeSavitzkyGolayCoefficients(points, polyorder)

  number xsize, ysize, i
  getsize(front, xsize, ysize)
  string imgname=getname(front)

  if(ysize!=1)
    {
      showalert("Ensure a 1D spectrum is shown front-most",2)
      exit(0)
    }

  image smooth=imageclone(front)*0
  taggroup fronttags=front.imagegettaggroup()
  taggroup smoothtags=smooth.imagegettaggroup()
  taggroupcopytagsfrom(smoothtags, fronttags)
  imagecopycalibrationfrom(smooth, front)

  image paddedimg=realimage("", 4, xsize+(points-1), ysize)
  number half=(points-1)/2

  image windowimg=front[0,0,1,half]
  image reversewindowimg=imageclone(windowimg)*0
  reversewindowimg=windowimg[half-icol, irow]
  paddedimg[0,0,1,half]=reversewindowimg

  paddedimg[0,half, 1, xsize+half]=front

  windowimg=front[0,xsize-half, 1, xsize]
  reversewindowimg=windowimg[half-icol, irow]
  paddedimg[0,xsize+half, 1, xsize+(half*2)]=reversewindowimg
  number padxsize, padysize
  getsize(paddedimg, padxsize, padysize)

  image window
  number halfsize=(points-1)/2

  for(i=0; i<padxsize-(half*2); i++)
  {
    window=paddedimg[0,i, 1, i+points]
    number smoothvalue=sum(window*sgcoeffs[0,0,1,points])
    // top row contains smoothing coefficients
    setpixel(smooth, i, 0, smoothvalue)
  }

  setname(smooth, imgname+" (Smooth Sav-Golay w "+points+" po "+polyorder+")")
  return(smooth)
}

image MakeSpectrum  (image front, string namead)
  {
  // Make Spectra: Variables
  number width, height, maxval
```

```
  number scalex, scaley, originx, originy
  string imgname

  getname(front, imgname)
  getsize(front, width, height)

  getscale(front, scalex, scaley)
  getorigin(front, originx, originy)
  maxval=max(front)

  // Create a spectrum from the image
  image projection = realimage(imgname+" "+namead, 4, width, 1)
  projection = 0
  projection[icol,0]+=front
  setname(projection, imgname+" "+namead)

  // Copy all the tags from the foremost image to the spectrum
  TagGroup sourcetags=imagegettaggroup(front)
  TagGroup targettags=imagegettaggroup(projection)
  taggroupcopytagsfrom(targettags,sourcetags)
  projection.ImageGetTagGroup().TagGroupSetTagAsString( "Meta Data:Format",
   "Spectrum" )
  projection.ImageGetTagGroup().TagGroupSetTagAsString( "Meta Data:Signal",
   "EELS" )

  // Calibrate and annotate the spectrum
  ImageSetDimensionCalibration( projection, 0, originx, scalex, "eV", 1 )
  ImageSetIntensityUnitInfo( projection, "e-", 1 )

  return projection
  }


void PerformBatchAction( image img )

{
//WATCH OUT! Cross Profile needs an accessible maximum in between,
// otherwise wont work
image emcda, emcdb, bpeaka, bpeakb, pedgea, pedgeb, subimage

number xdim, ydim, top1, top2, left, bottom, right, xcentre, ycentre
number beforepeak, beforepeaka, beforepeakb
number integraldiff, integrala, integralb, storetop1, storetop2,
number xaligna, xalignb, xalign, xalignw
number intstart, intdifftot, intwidth
number maxvalue, maxstorex, maxstorey, minval1, minval2,
number minstore1x, minstore1y, minstore2x, minstore2y,
number topstart, topend, xstart, xend

string imgname=getname(img)
imagedisplay imgdisp = img.ImageGetImageDisplay(0)

// Settng the important numbers:
xalign=1202 // just before the edge starts in pixel
intstart=1332 // start of post edge integration in pixel
intwidth=80

//number intstart2, intwidth2
```

```
//intstart2=1030   //second post edge integration
//intwidth2=300

topstart=942
//area limits for the cross profile, integrating over 60 pixels
// at the moment to receive a smooth profile
topend=1062
xstart=560
xend=610

ydim=30  // width for EMCD spectrum integration, here 30 pixel

//getnumber("Enter Width of ROI",0,ydim)

xdim=2048
left=0
beforepeaka=0
beforepeakb=0
integrala=0
integralb=0
intdifftot=sum(img)

//from here working on image

subimage=img[topstart, xstart, topend, xend]
image trans=img[0,0,(xend-xstart),(topend-topstart)]
trans=trans*0
trans = subimage[irow,icol]

string subname="Crossspec"
image projections=MakeSpectrum(trans, subname)
//ShowImage(projections)

//Now Savitzky filtering for cross spectrum
image smoothsavc=SavitzkyGolay(projections)
setname(smoothsavc, imgname+" Cross Sav-Gol")
ShowImage(smoothsavc)

//get xvalue of maximum, use it for further processing
maxvalue=max(smoothsavc, maxstorex, maxstorey)
result("\n Maximum:"+maxvalue)
result("\n Mx:"+maxstorex)
number topmaximum=maxstorex+topstart


for(number top1=945; top1<topmaximum; top1++) {
  for(top2=topmaximum; top2<1040; top2++) {
    if(top2-top1>(ydim-1))
      {
// This positions the ROI Image by on the basis of its top left position
bottom=top1+ydim
right=left+xdim
xcentre=left+((right-left)/2)
ycentre=top1+((bottom-top1)/2)
emcda=img[top1, left, bottom, right]

bottom=top2+ydim
right=left+xdim
```

```
xcentre=left+((right-left)/2)
ycentre=top2+((bottom-top2)/2)
emcdb=img[top2, left, bottom, right]

//Roi for Integrals before the peak:
number bottomi, xcentrei, ycentrei

bottomi=top1+ydim
xcentrei=xalign+(((xalign+30)-xalign)/2)
ycentrei=top1+((bottom-top1)/2)
bpeaka=img[top1, xalign, bottomi, (xalign+30)]
beforepeaka=sum(bpeaka)/30

bottomi=top2+ydim
xcentrei=xalign+(((xalign+30)-xalign)/2)
ycentrei=top2+((bottom-top2)/2)
bpeakb=img[top2, xalign, bottomi, (xalign+30)]
beforepeakb=sum(bpeakb)/30

//Spectrum A
string SpecAname="SpA"
image projectiona=MakeSpectrum(emcda, SpecAname)

//Spectrum B
string SpecBname="SpB"
image projectionb=MakeSpectrum(emcdb, SpecBname)

//Alignment of the spectra before the peak so they match as good as possible
beforepeak=beforepeaka/beforepeakb
projectionb=projectionb*beforepeak

//Comparison of the post-edge Integral to determine quality of the spectra
number bottomk, xcentrek, ycentrek

bottomk=top1+ydim
xcentrek=intstart+(((intstart+intwidth)-intstart)/2)
ycentrek=top1+((bottom-top1)/2)
pedgea=img[top1, intstart, bottomk, (intstart+intwidth)]
integrala=sum(pedgea)

bottomk=top2+ydim
xcentrek=intstart+(((intstart+intwidth)-intstart)/2)
ycentrek=top2+((bottom-top2)/2)
pedgeb=img[top2, intstart, bottomk, (intstart+intwidth)]
integralb=sum(pedgeb)*beforepeak

//Optional: Integral 2 post all edges, weighted to half of the first
//integral (weighted sum, 2*Diff post edge*Diff post all edges,
// easier way is to just use one integral), important is that the
// result gets bigger with mismatch between the spectra
/*image postedgea, postedgeb
number integrala2, integralb2

bottomk=top1+ydim
xcentrek=intstart2+(((intstart2+intwidth2)-intstart2)/2)
ycentrek=top1+((bottom-top1)/2)
postedgea=img[top1, intstart2, bottomk, (intstart2+intwidth2)]
integrala2=sum(postedgea)
```

```
bottomk=top2+ydim
xcentrek=intstart2+(((intstart2+intwidth2)-intstart2)/2)
ycentrek=top2+((bottom-top2)/2)
postedgeb=img[top2, intstart2, bottomk, (intstart2+intwidth2)]
integralb2=sum(postedgeb)*beforepeak

integraldiff=2*(abs(integrala-integralb))*(abs(integrala2-integralb2))
*/

integraldiff=abs(integrala-integralb)
//result("\t Integraldiff:"+integraldiff)

if(integraldiff<intdifftot)
    {
      intdifftot=integraldiff
      storetop1=top1
      storetop2=top2
      }
    }
  }
}

// get the stored "good" position values to create the two spectra

bottom=storetop1+ydim
right=left+xdim
xcentre=left+((right-left)/2)
ycentre=storetop1+((bottom-storetop1)/2)
emcda=img[storetop1, left, bottom, right]

bottom=storetop2+ydim
right=left+xdim
xcentre=left+((right-left)/2)
ycentre=storetop2+((bottom-storetop2)/2)
emcdb=img[storetop2, left, bottom, right]

//Roi for Integral:
number bottomi, xcentrei, ycentrei

bottomi=storetop1+ydim
xcentrei=xalign+(((xalign+30)-xalign)/2)
ycentrei=storetop1+((bottom-top1)/2)
bpeaka=img[storetop1, xalign, bottomi, (xalign+30)]
beforepeaka=sum(bpeaka)/30

bottomi=storetop2+ydim
xcentrei=xalign+(((xalign+30)-xalign)/2)
ycentrei=storetop2+((bottom-top2)/2)
bpeakb=img[storetop2, xalign, bottomi, (xalign+30)]
beforepeakb=sum(bpeakb)/30

//Spectrum A
string SpecAname="SpA"
image fprojectiona=MakeSpectrum(emcda, SpecAname)

/* Display and position the spectrum
showimage(fprojectiona)
```

```
setwindowposition(fprojectiona, 142,24)
setwindowsize(fprojectiona, 880, 455)
updateimage(fprojectiona)
*/

//start (and end) of background subtraction for your currend edge
number start, end
start=1025
end=1200

//BACKGROUND Subtraction
number A, r
// Pass in the spectrum and calculate the background
image background=fiteelsbackground(fprojectiona, start, end, A, r)
// Strip out the edge and add it to the display
image edgeimga=fprojectiona-background
edgeimga[0,0,1,start]=0
// sets all channels in the spectrum before start to zero
showimage(edgeimga)
edgeimga.ImageGetTagGroup().TagGroupSetTagAsString( "Meta Data:Format",
 "Spectrum" )
edgeimga.ImageGetTagGroup().TagGroupSetTagAsString( "Meta Data:Signal",
 "EELS" )
imagedisplay edgedispa = edgeimga.ImageGetImageDisplay(0)
edgedispa.imagedisplayaddimage(edgeimga, "SpA")
edgedispa.lineplotimagedisplaysetlegendshown(1)
setname(edgeimga, imgname+" ("+start+" to "+end+")")

//Now Savitzky filtering for SpecA
image smoothspecA=SavitzkyGolay(fprojectiona)
setname(smoothspecA, imgname+" Sav-Gol SpA")
ShowImage(smoothspecA)

//Now spectrum B

//Spectrum B
string SpecBname="SpB"
image fprojectionb=MakeSpectrum(emcdb, SpecBname)

beforepeak=beforepeaka/beforepeakb
fprojectionb=fprojectionb*beforepeak

/* Display and position the spectrum
showimage(fprojectionb)
setwindowposition(fprojectionb, 142,24)
setwindowsize(fprojectionb, 880, 455)
updateimage(fprojectionb)
*/

// Pass in the spectrum and calculate the background
background=fiteelsbackground(fprojectionb, start, end, A, r)
// Strip out the edge and add it to the display
image edgeimgb=fprojectionb-background
edgeimgb[0,0,1,start]=0
/ sets all channels in the spectrum before start to zero
showimage(edgeimgb)
edgeimgb.ImageGetTagGroup().TagGroupSetTagAsString( "Meta Data:Format",
 "Spectrum" )
```

```
edgeimgb.ImageGetTagGroup().TagGroupSetTagAsString( "Meta Data:Signal",
"EELS" )
edgedispa.imagedisplayaddimage(edgeimgb, "SpB")
//setname(edgeimgb, imgname+" (SpB"+start+" to "+end+")")


//Now Savitzky filtering for SpecA
image smoothspecB=SavitzkyGolay(fprojectionb)
setname(smoothspecB, imgname+" Sav-Gol SpB")
ShowImage(smoothspecB)

image EMCDdiff
EMCDdiff=fprojectiona-fprojectionb
setname(EMCDdiff, imgname+" EMCDdiff")
showimage(EMCDdiff)

image EMCDdiffSav
EMCDdiffSav=smoothspecA-smoothspecB
setname(EMCDdiffSav, imgname+" EMCDdiff of Sav-Golay")
showimage(EMCDdiffSav)

result("\ntop1 = "+storetop1+"\t")
result("\ntop2 = "+storetop2+"\n")
}

// Function converts a string to lower-case characters
string ToLowerCase( string in )
{
 string out = ""
 for( number c = 0 ; c < len( in ) ; c++ )
 {
         string letter = mid( in , c , 1 )
         number n = asc( letter )
         if ( ( n > 64 ) && ( n < 91 ) )        letter = chr( n + 32 )
         out += letter
         }
 return out
}


// Function to create a list of file entries with full path
TagGroup CreateFileList( string folder )
{

 TagGroup filesTG = GetFilesInDirectory( folder , 1 )
// 1 = Get files, 2 = Get folders, 3 = Get both
 TagGroup fileList = NewTagList()

 for (number i = 0; i < filesTG.TagGroupCountTags() ; i++ )
 {
   TagGroup entryTG
   if ( filesTG.TagGroupGetIndexedTagAsTagGroup( i , entryTG ) )
   {
       string fileName
          if ( entryTG.TagGroupGetTagAsString( "Name" , fileName ) )
           {
               filelist.TagGroupInsertTagAsString( fileList.TagGroupCountTags
               () , folder + fileName )
```

```
            }
    }
 }
 return fileList
}


// Function removes entries not matching in suffix
TagGroup FilterFilesList( TagGroup list, string suffix )
{
 TagGroup outList = NewTagList()
 suffix = ToLowerCase( suffix )
 for ( number i = 0 ; i < list.TagGroupCountTags() ; i++ )
 {
    string origstr
    if ( list.TagGroupGetIndexedTagAsString( i , origstr ) )
      {
         string str = ToLowerCase( origstr )
         number matches = 1
         if ( len( str ) >= len( suffix ) )
         // Ensure that the suffix isn't longer than the whole string
           {
             if ( suffix == right( str , len( suffix ) ) )
             // Compare suffix to end of original string
                {
                   outList.TagGroupInsertTagAsString
                   (outList.TagGroupCountTags() , origstr)
                   // Copy if matching
                     }
             }
    }
 }
 return outList
}



// Open and process all files in a given fileList
void BatchProcessList( TagGroup fileList , string name )
{
 number nEntries = fileList.TagGroupCountTags()
 if ( nEntries > 0 )
         result( "Processing file list <" + name + "> with " + nEntries + " files.\n" )
 else
         result( "File list <" + name + "> does not contain any files.\n" )
 for ( number i = 0 ; i < nEntries ; i++ )
 {
         string str
         if ( fileList.TagGroupGetIndexedTagAsString( i , str ) )
         {
                 result( "\t open: " + str + "\t" )
                 image img := OpenImage( str )
                 if ( img.ImageIsValid() )
                 {
                         // Actual batch-action
                         result( "process... \n" )
                         PerformBatchAction( img )
                 }
```

```
                else
                        result( "skipped... \n" )
        }
 }
}


// Main routine. Processes all dm3/dm4 files in a directory
void BatchProcessFilesInFolder()
{
 string folder , outputFolder
 if ( !GetDirectoryDialog( "Select folder" , "" , folder ) )
        return

 TagGroup fileList = CreateFileList( folder )
 TagGroup fileListDM3 = FilterFilesList( fileList , ".dm3" )
 BatchProcessList( fileListDM3 , "DM3 list" )
 TagGroup fileListDM4 = FilterFilesList( fileList , ".dm4" )
 BatchProcessList( fileListDM4 , "DM4 list" )
}

BatchProcessFilesInFolder()
```

6.13.2 Setting the EMCD positions manually, working on front image

```
// based on  scripts from Dave Mitchell for Savitzky Golay filtering,
//making a spectrum from an image, background subtraction from a spectrum

//Takes in an EMCD image, asks for the regions beside the maximum,
//makes two spectra on the sides of the maximum
//and returns them background subtracted and Savitzky-Golay filtered

void linearregression(image xdata, image ydata, number &a, number &b)
  {
    number xsize, ysize
    getsize(xdata, xsize, ysize)

    image xsqrd=xdata**2
    image xtimesy=xdata*ydata

    number sumofy, sumofx, sumofxtimesy, sumofxsqrd

    sumofy=sum(ydata)
    sumofx=sum(xdata)
    sumofxtimesy=sum(xtimesy)
    sumofxsqrd=sum(xsqrd)

    number denominator=xsize*sumofxsqrd-sumofx**2

    a=((sumofy*sumofxsqrd)-(sumofx*sumofxtimesy))/denominator
    b=((xsize*sumofxtimesy)-(sumofx*sumofy))/denominator
  }

image fiteelsbackground(image spectrum, number roistart, number roiend,
 number &a, number &b)
  {
```

```
  number origin, scale, fitrange
  fitrange=roiend-roistart
  string units
  spectrum.imagegetdimensioncalibration(0,origin, scale, units, 0)
  // Set up the log data of the intensity on the region
  //defined by the ROI
  image fitregionintensity=spectrum[0,roistart, 1, roiend]
  ImageSetDimensionCalibration(fitregionintensity,0,origin-roistart,
  scale, "eV",1)
  fitregionintensity=log(fitregionintensity)
  // Set up the log data of the energy scale on the region
  //defined by the ROI
  image fitregioninx=fitregionintensity*0
  fitregioninx=(icol-origin+roistart)*scale
  // Call the above function to fit a straight line to the log-log plot
  // since the coefficients are passed in by reference into the
  FitEEELSBackground function
  // the parameters (as well as the background fit) can be obtained
  from the calling function
  linearregression(fitregioninx, fitregionintensity, a, b)
  // On the basis of the above fit, compute the backgroud fit
  image background=spectrum*0
  background=a+b*(icol-origin)*scale // A.E**-r
  background=exp(background)
  background[0,0,1,roistart]=0
  return background
  }

image ComputeSavitzkyGolayCoefficients(number points, number polynomialorder)
  {
  polynomialorder=round(polynomialorder)
  if(polynomialorder<2) polynomialorder=2
  if(polynomialorder>3) polynomialorder=3

  points=round(points)
  if(mod(points,2)==0) points=points+1
  if(points<3) points=3
  if(points>99) points=99

  image designmatrix=realimage("",4,polynomialorder+1,points)

  designmatrix[0,0,points,1]=1

  number halfsize=((points-1)/2)*-1
  number i

  for(i=0; i<points; i++)
    {
      designmatrix[i,1,i+1,2]=halfsize
      halfsize=halfsize+1
    }

  designmatrix[0,2,points,3]=designmatrix[0,1,points,2]**2
  // polynomial order 2
  if(polynomialorder==3)designmatrix[0,3,points,4]=designmatrix
  [0,2,points,3]**2  // polynomial order 3

  image matrixtranspose=matrixtranspose(designmatrix)
```

```
  image matproduct=matrixmultiply(matrixtranspose, designmatrix)

  image inversematrix=matrixinverse(matproduct)
  image coeffmatrix=matrixmultiply(inversematrix, matrixtranspose)

  return coeffmatrix
  }

image SavitzkyGolay (image front)
{
  number points=15 // the width of the window for fitting (3-99)
  // must be odd
  number polyorder=2
  // the polynomial order 2 (for 1D plots) to 3 (for derivatives)

  polyorder=round(polyorder)
  if(polyorder<2) polyorder=2
  if(polyorder>3) polyorder=3

  points=round(points)
  if(mod(points,2)==0) points=points+1
  if(points<3) points=3
  if(points>99) points=99

  image sgcoeffs=ComputeSavitzkyGolayCoefficients(points, polyorder)

  number xsize, ysize, i
  getsize(front, xsize, ysize)
  string imgname=getname(front)

  if(ysize!=1)
    {
    showalert("Ensure a 1D spectrum is shown front-most",2)
    exit(0)
    }

  image smooth=imageclone(front)*0
  taggroup fronttags=front.imagegettaggroup()
  taggroup smoothtags=smooth.imagegettaggroup()
  taggroupcopytagsfrom(smoothtags, fronttags)
  imagecopycalibrationfrom(smooth, front)

  image paddedimg=realimage("", 4, xsize+(points-1), ysize)
  number half=(points-1)/2

  image windowimg=front[0,0,1,half]
  image reversewindowimg=imageclone(windowimg)*0
  reversewindowimg=windowimg[half-icol, irow]
  paddedimg[0,0,1,half]=reversewindowimg

  paddedimg[0,half, 1, xsize+half]=front

  windowimg=front[0,xsize-half, 1, xsize]
  reversewindowimg=windowimg[half-icol, irow]
  paddedimg[0,xsize+half, 1, xsize+(half*2)]=reversewindowimg
  number padxsize, padysize
  getsize(paddedimg, padxsize, padysize)
```

```
  image window
  number halfsize=(points-1)/2

  for(i=0; i<padxsize-(half*2); i++)
    {
    window=paddedimg[0,i, 1, i+points]
    number smoothvalue=sum(window*sgcoeffs[0,0,1,points])
    // top row contains smoothing coefficients
    setpixel(smooth, i, 0, smoothvalue)
    }

  setname(smooth, imgname+" (Smooth Sav-Golay w "+points+" po
  "+polyorder+")")
  return(smooth)
}

image MakeSpectrum  (image front, string namead)
  {
  // Make Spectra: Variables
  number width, height, maxval
  number scalex, scaley, originx, originy
  string imgname

  getname(front, imgname)
  getsize(front, width, height)

  getscale(front, scalex, scaley)
  getorigin(front, originx, originy)
  maxval=max(front)

  // Create a spectrum from the image
  image projection = realimage(imgname+" "+namead, 4, width, 1)
  projection = 0
  projection[icol,0]+=front
  setname(projection, imgname+" "+namead)

  // Copy all the tags from the foremost image to the spectrum
  TagGroup sourcetags=imagegettaggroup(front)
  TagGroup targettags=imagegettaggroup(projection)
  taggroupcopytagsfrom(targettags,sourcetags)
  projection.ImageGetTagGroup().TagGroupSetTagAsString( "Meta Data:
  Format", "Spectrum" )
  projection.ImageGetTagGroup().TagGroupSetTagAsString( "Meta Data:
  Signal", "EELS" )

  // Calibrate and annotate the spectrum
  ImageSetDimensionCalibration( projection, 0, originx, scalex,
  "eV", 1 )
  ImageSetIntensityUnitInfo( projection, "e-", 1 )

  return projection
  }

image img:=getfrontimage()
image emcda, emcdb, bpeaka, bpeakb, pedgea, pedgeb, subimage

number xdim, ydim, top1, top2, left, bottom, right, xcentre, ycentre
number beforepeak, beforepeaka, beforepeakb
```

```
number integraldiff, integrala, integralb, storetop1, storetop2,
xaligna, xalignb, xalign, xalignw
number intstart, intdifftot, intwidth
number maxvalue, maxstorex, maxstorey, topstart, topend, xstart, xend

string imgname=getname(img)
imagedisplay imgdisp = img.ImageGetImageDisplay(0)

// Settng the important numbers: pre Edge position first
xalign=1209

topstart=942    //area limits for the cross profile, integrating over 60
pixels at the moment to receive a smooth profile, use edge position!
topend=1062
xstart=750
xend=810

//start (and end) of background subtraction for your current edge in pixels
number start, end
start=1025
end=1200

ydim=30  // width for EMCD spectrum integration, here 30 pixel

xdim=2048
left=0

//from here working on image

subimage=img[topstart, xstart, topend, xend]
image trans=img[0,0,(xend-xstart),(topend-topstart)]
trans=trans*0
trans = subimage[irow,icol]

string subname="Crossspec"
image projections=MakeSpectrum(trans, subname)

//Now Savitzky filtering for cross spectrum
image smoothsavc=SavitzkyGolay(projections)
setname(smoothsavc, imgname+" Cross Sav-Gol")
ShowImage(smoothsavc)

//get xvalue of maximum, use it for further processing
maxvalue=max(smoothsavc, maxstorex, maxstorey)
result("\n Maximum:"+maxvalue)
result("\n Mx:"+maxstorex)
number topmaximum=maxstorex+topstart

number center1, center2
getnumber("Enter Top1 center position of ROI",0,center1)
getnumber("Enter Top2 center position of ROI",0,center2)
top1=center1-15
top2=center2-15
storetop1=topstart+top1-ydim
storetop2=topstart+top2

result("\n Top2n:"+storetop2)
result("\n Top1n:"+storetop1)
```

```
// get the position values to create the two spectra

bottom=storetop1+ydim
right=left+xdim
xcentre=left+((right-left)/2)
ycentre=storetop1+((bottom-storetop1)/2)
emcda=img[storetop1, left, bottom, right]

bottom=storetop2+ydim
right=left+xdim
xcentre=left+((right-left)/2)
ycentre=storetop2+((bottom-storetop2)/2)
emcdb=img[storetop2, left, bottom, right]

//Roi for Integral:
number bottomi, xcentrei, ycentrei

bottomi=storetop1+ydim
xcentrei=xalign+(((xalign+30)-xalign)/2)
ycentrei=storetop1+((bottom-top1)/2)
bpeaka=img[storetop1, xalign, bottomi, (xalign+30)]
beforepeaka=sum(bpeaka)/30

bottomi=storetop2+ydim
xcentrei=xalign+(((xalign+30)-xalign)/2)
ycentrei=storetop2+((bottom-top2)/2)
bpeakb=img[storetop2, xalign, bottomi, (xalign+30)]
beforepeakb=sum(bpeakb)/30

//Spectrum A
string SpecAname="SpA"
image fprojectiona=MakeSpectrum(emcda, SpecAname)
setname(fprojectiona, imgname+" SpA")

//BACKGROUND Subtraction
number A, r
// Pass in the spectrum and calculate the background
image background=fiteelsbackground(fprojectiona, start, end, A, r)
// Strip out the edge and add it to the display
image edgeimga=fprojectiona-background
edgeimga[0,0,1,start]=0
//sets all channels in the spectrum before start to zero
showimage(edgeimga)
setname(edgeimga, imgname+" Spec")
edgeimga.ImageGetTagGroup().TagGroupSetTagAsString( "Meta Data:Format",
 "Spectrum" )
edgeimga.ImageGetTagGroup().TagGroupSetTagAsString( "Meta Data:Signal",
"EELS" )
imagedisplay edgedispa = edgeimga.ImageGetImageDisplay(0)
edgedispa.imagedisplayaddimage(edgeimga, "SpA")
edgedispa.lineplotimagedisplaysetlegendshown(1)

//Now Savitzky filtering for SpecA
image smoothspecA=SavitzkyGolay(fprojectiona)
setname(smoothspecA, imgname+" Sav-Gol SpA")

// Pass in the spectrum and calculate the background
```

```
background=fiteelsbackground(smoothspecA, start, end, A, r)
// Strip out the edge and add it to the display
image edgesavA=smoothspecA-background
edgesavA[0,0,1,start]=0
//sets all channels in the spectrum before start to zero
showimage(edgesavA)
setname(edgesavA, imgname+" Sav-Golay Spec")
edgesavA.ImageGetTagGroup().TagGroupSetTagAsString( "Meta Data:Format",
 "Spectrum" )
edgesavA.ImageGetTagGroup().TagGroupSetTagAsString( "Meta Data:Signal",
"EELS" )
imagedisplay edgedispsavA = edgesavA.ImageGetImageDisplay(0)
edgedispsavA.imagedisplayaddimage(edgesavA, "SpA F")
edgedispsavA.lineplotimagedisplaysetlegendshown(1)

//Now spectrum B
string SpecBname="SpB"
image fprojectionb=MakeSpectrum(emcdb, SpecBname)

beforepeak=beforepeaka/beforepeakb
fprojectionb=fprojectionb*beforepeak
setname(fprojectionb, imgname+" SpB")

// Pass in the spectrum and calculate the background
background=fiteelsbackground(fprojectionb, start, end, A, r)
// Strip out the edge and add it to the display
image edgeimgb=fprojectionb-background
edgeimgb[0,0,1,start]=0
// sets all channels in the spectrum before start to zero
edgeimgb.ImageGetTagGroup().TagGroupSetTagAsString( "Meta Data:Format",
 "Spectrum" )
edgeimgb.ImageGetTagGroup().TagGroupSetTagAsString( "Meta Data:Signal",
"EELS" )
edgedispa.imagedisplayaddimage(edgeimgb, "SpB")

//Now Savitzky filtering for SpecB
image smoothspecB=SavitzkyGolay(fprojectionb)
setname(smoothspecB, imgname+" Sav-Gol SpB")

// Pass in the spectrum and calculate the background
background=fiteelsbackground(smoothspecB, start, end, A, r)
// Strip out the edge and add it to the display
image edgesavB=smoothspecB-background
edgesavB[0,0,1,start]=0
//sets all channels in the spectrum before start to zero
edgesavB.ImageGetTagGroup().TagGroupSetTagAsString( "Meta Data:Format",
"Spectrum" )
edgesavB.ImageGetTagGroup().TagGroupSetTagAsString( "Meta Data:Signal",
"EELS" )
edgedispsavA.imagedisplayaddimage(edgesavB, "SpB F")

//Can compute the difference but does not take care of a difference
of a few pixels in position so better use another script afterwards
/*
image EMCDdiff
EMCDdiff=fprojectiona-fprojectionb
setname(EMCDdiff, imgname+" EMCDdiff")
showimage(EMCDdiff)
```

```
image EMCDdiffSav
EMCDdiffSav=smoothspecA-smoothspecB
setname(EMCDdiffSav, imgname+" EMCDdiff of Sav-Golay")
showimage(EMCDdiffSav)
*/
```

6.13.3 Shifting one spectrum with respect to the other and calculate the difference

```
image img:=getfrontimage()
string imgname=getname(img)
imagedisplay imgdisp = img.ImageGetImageDisplay(0)
number left, right

TagGroup DLG, DLGItems
DLG = DLGCreateDialog( "Please enter value around 100", DLGItems )

TagGroup val1tg
DLGitems.DLGAddElement( DLGCreateRealField( "First value  :", val1tg, 101,
8, 3 ) )
if ( !Alloc( UIframe ).Init( DLG ).Pose() )
 Throw( "User abort." )

left=val1tg.DLGGetValue()
Result( "First value: " + val1tg.DLGGetValue() + "\n" )

right=left+1900
object sliceid=imgdisp.imagedisplaygetsliceidbyindex(1)
object sliceid2=imgdisp.imagedisplaygetsliceidbyindex(2)

image region=img{1}[0, 100, 1, 2000]
setname(region, "Sp A")
// Copy all the tags from the foremost image to the spectrum
TagGroup sourcetags=imagegettaggroup(img)
TagGroup targettags=imagegettaggroup(region)
taggroupcopytagsfrom(targettags,sourcetags)
region.ImageGetTagGroup().TagGroupSetTagAsString( "Meta Data:Format",
"Spectrum" )
region.ImageGetTagGroup().TagGroupSetTagAsString( "Meta Data:Signal",
"EELS" )
setname(region, imgname+" EMCD")
ShowImage(region)

image region2:=Imageclone(img{2}[0, left, 1, right])
TagGroup sourcetags2=imagegettaggroup(img)
TagGroup targettags2=imagegettaggroup(region2)
taggroupcopytagsfrom(targettags2,sourcetags2)
region2.ImageGetTagGroup().TagGroupSetTagAsString( "Meta Data:Format",
 "Spectrum" )
region2.ImageGetTagGroup().TagGroupSetTagAsString( "Meta Data:Signal",
"EELS" )

imagedisplay regiondisp = region.ImageGetImageDisplay(0)
regiondisp.lineplotimagedisplaysetlegendshown(1)
regiondisp.imagedisplayaddimage(region2, "Sp B")

//align by integral add!
```

```
image Difference
Difference=region-region2
regiondisp.imagedisplayaddimage(Difference, "Difference")
```

6.13.4 Hook-Up Script for EMCD spectrum acquisition

```
void Emcd ()
{
number camID = CameraGetActiveCameraID( )
number exposure = 40
// exposure time in seconds, change to desired value before installation
image img1
CameraPrepareForAcquire( camID )
img1 := CameraAcquire( camID, exposure )
ShowImage( img1 )
}
```

6.14 Mumax input scripts for the simulations

For each of the investigated samples an example input script is shown. The starting conditions can differ depending on the setting, simulations have been performed both for a random starting configuration and a configuration induced by an external magnetic field in X and in Y direction. Depending on results and configuration the system has been driven through a part of a hysteresis curve by a slowly increasing and then decreasing external magnetic field.

6.14.1 Mumax input script for Fe/Co_2FeSi/Fe

This simulation starts from Fe layers magnetized in opposite directions and a random magnetization in the Co_2FeSi layer. The system is driven through the half of a hysteresis by increasing the external magnetic field up to 0.006 T in Y direction and down to zero again and minimizing the system energy using the minimize() function. The mesh size has been chosen as large as possible to reduce the computational effort.

```
SetMesh(512, 512, 1, 5e-09, 5e-09, 10e-09, 0, 0, 0)
SetGeom(Cuboid(150e-09, 2000e-9, 10e-09))

defregion(1, xrange(25e-9, 75e-9))
defregion(2, xrange(-25e-9, 25e-9))
defregion(3, xrange(-75e-9, -25e-9))
save(regions)

Msat.SetRegion(1, 1710e3)
tableAdd(m.Region(1))
Msat.SetRegion(2, 881e3)
tableAdd(m.Region(2))
Msat.SetRegion(3, 1710e3)
tableAdd(m.Region(3))
Aex.SetRegion(1, 25e-12)
Aex.SetRegion(2, 23.5e-12)
Aex.SetRegion(3, 25e-12)
Ku1.SetRegion(1, 4.81e4)
Ku1.SetRegion(2, 2.89e3)
Ku1.SetRegion(3, 4.81e4)
```

```
alpha = 0.5

m.SetRegion(1, uniform(0, 1, 0))
m.SetRegion(2, RandomMag())
m.SetRegion(3, uniform(0, -1, 0))

saveas(m, "ramdommag")
OutputFormat = OVF1_Text
saveas(Msat, "Saturation_Magnetisation.ovf")
cc := 1
vol_name := sprintf("TestMag")
Bmax := 6.0e-3
Bstep := 2.0e-3
MinimizerStop = 1e-6

TableAdd(B_ext)
TableAdd(m.Comp(0))
TableAdd(m.Comp(1))
TableAdd(m.Comp(2))
TableAdd(m_full.region(1))
TableAdd(m_full.region(2))
TableAdd(m_full.region(3))
TableAdd(E_total)

for B := 0.0; B <= Bmax; B += Bstep {
  B_ext = vector(0, B, 0)
  minimize()
  tablesave()
  vol_Name_X := sprintf("Mfull_x_", cc)
  vol_Name_Y := sprintf("Mfull_y_", cc)
  vol_Name_Z := sprintf("Mfull_z_", cc)
  saveas(m_full.Comp(0), vol_Name_X)
  saveas(m_full.Comp(1), vol_Name_Y)
  saveas(m_full.Comp(2), vol_Name_Z)
  cc = cc + 1
}

for B := Bmax; B >= 0; B -= Bstep {
  B_ext = vector(0, B, 0)
  minimize()
  tablesave()
  vol_Name_X := sprintf("Mfull_x_", cc)
  vol_Name_Y := sprintf("Mfull_y_", cc)
  vol_Name_Z := sprintf("Mfull_z_", cc)
  saveas(m_full.Comp(0), vol_Name_X)
  saveas(m_full.Comp(1), vol_Name_Y)
  saveas(m_full.Comp(2), vol_Name_Z)
  cc = cc + 1
}
```

6.14.2 Mumax input script for V/Co_2FeSi/V

This simulation starts from random magnetization on three layers of 50 nm thickness, the central layer is the Co_2FeSi layer, the outer layers consist of vanadium which is nonmagnetic.

```
SetMesh(512, 512, 1, 5e-09, 5e-09, 10e-09, 0, 0, 0)
SetGeom(Cuboid(150e-09, 2000e-9, 10e-09))

defregion(1, xrange(25e-9, 75e-9))
defregion(2, xrange(-25e-9, 25e-9))
defregion(3, xrange(-75e-9, -25e-9))
save(regions)

Msat.SetRegion(1, 0)
tableAdd(m.Region(1))
Msat.SetRegion(2, 881e3)
tableAdd(m.Region(2))
Msat.SetRegion(3, 0)
tableAdd(m.Region(3))
Aex.SetRegion(1, 0)
Aex.SetRegion(2, 23.5e-12)
Aex.SetRegion(3, 0)
Ku1.SetRegion(1, 0)
Ku1.SetRegion(2, 2.89e3)
Ku1.SetRegion(3, 0)

alpha = 0.3
m.SetRegion(2, RandomMag())
saveas(m, "ramdommag")
B_ext = vector(0, 0, 0)

OutputFormat = OVF1_Text
save(m.Comp(0))
save(m.Comp(1))
save(m.Comp(2))
TableAdd(E_total)
tableAdd(m.Region(1))
tableAdd(m.Region(2))
tableAdd(m.Region(3))
saveas(Msat, "Saturation_Magnetisation.ovf")
vol_name := sprintf("TestMag")
TableAdd(B_ext)
TableAdd(m.Comp(0))
TableAdd(m.Comp(1))
TableAdd(m.Comp(2))
TableAdd(m_full.region(1))
TableAdd(m_full.region(2))
TableAdd(m_full.region(3))
TableAdd(E_total)

vol_Name_X := sprintf("Mfull_x_")
vol_Name_Y := sprintf("Mfull_y_")
vol_Name_Z := sprintf("Mfull_z_")
saveas(m_full.Comp(0), vol_Name_X)
saveas(m_full.Comp(1), vol_Name_Y)
saveas(m_full.Comp(2), vol_Name_Z)

relax()
tablesave()
```

6.14.3 Mumax input script for the TMR stack

The simulation starts from random magnetization and uses the relax() method to minimize the energy. The mesh size is chosen so the very small MgO layers can be included. Further refinement would increase the computational effort.

```
SetMesh(512, 512, 1, 1e-09, 1e-09, 5e-09, 0, 0, 0)
SetGeom(Cuboid(30e-09, 2000e-9, 10e-09))

defregion(1, xrange(12e-9, 15e-9))
defregion(2, xrange(2e-9, 12e-9))
defregion(3, xrange(0e-9, 2e-9))
defregion(4, xrange(-15e-9, 0e-9))
save(regions)

Msat.SetRegion(1, 0)
tableAdd(m.Region(1))
Msat.SetRegion(2, 881e3)
tableAdd(m.Region(2))
Msat.SetRegion(3, 0)
tableAdd(m.Region(3))
Msat.SetRegion(4, 881e3)
tableAdd(m.Region(4))

Aex.SetRegion(1, 0)
Aex.SetRegion(2, 31.5e-12)
Aex.SetRegion(3, 0)
Aex.SetRegion(4, 31.5e-12)

Ku1.SetRegion(1, 0)
Ku1.SetRegion(2, 2.89e3)
Ku1.SetRegion(3, 0)
Ku1.SetRegion(4, 2.89e3)

alpha = 0.5
m.SetRegion(2, RandomMag())
m.SetRegion(4, RandomMag())
saveas(m, "ramdommag")

OutputFormat = OVF1_Text
saveas(Msat, "Saturation_Magnetisation.ovf")
vol_name := sprintf("TestMag")

TableAdd(B_ext)
TableAdd(m.Comp(0))
TableAdd(m.Comp(1))
TableAdd(m.Comp(2))
TableAdd(m_full.region(1))
TableAdd(m_full.region(2))
TableAdd(m_full.region(3))
TableAdd(E_total)

relax()
vol_Name_X := sprintf("Mfull_x_")
vol_Name_Y := sprintf("Mfull_y_")
vol_Name_Z := sprintf("Mfull_z_")
saveas(m_full.Comp(0), vol_Name_X)
```

```
saveas(m_full.Comp(1), vol_Name_Y)
saveas(m_full.Comp(2), vol_Name_Z)
```

6.15 QSTEM model examples

6.15.1 CFG file for austenite

The example file in the .cfg format for a austenite crystal. This model has been created earlier for a slightly different composition and later has been adapted qualitatively for comparison with the checkerboard specimen. For adapting it quantitatively the structure of the checkerboard could not be resolved in all needed details because of the nested structures in different directions.
First the lattice parameters are specified. For each used atom the positions are given by the first three coordinates (in fractional coordinates) and the probability in case of random site placement by the 5th entry per line. The 4th entry is the Debye Waller factor which is not used in this example and therefore set to 1.0.

```
Number of particles = 4
A = 1.0 Angstrom
H0(1,1) = 5.771 A
H0(1,2) = 0 A
H0(1,3) = 0 A
H0(2,1) = 0 A
H0(2,2) = 5.771 A
H0(2,3) = 0 A
H0(3,1) = 0 A
H0(3,2) = 0 A
H0(3,3) = 5.771 A
.NO_VELOCITY.
entry_count = 5
59
Ni
0.0 0.0 0.0 1.0 0.86
59
Co
0.0 0.0 0.0 1.0 0.14
55
Mn
0.5 0.5 0.5 1.0 0.62
27
Al
0.5 0.5 0.5 1.0 0.38
```

6.15.2 CFG file for martensite

The example file in the .cfg format for the martensite crystal.

```
Number of particles = 196   # Number of atoms per unit cell
 A = 1.0 Angstrom
H0(1,1) = 20.149 A
H0(1,2) = 0 A
H0(1,3) = 0 A
```

```
H0(2,1) = 0 A
H0(2,2) = 2.735 A
H0(2,3) = 0 A
H0(3,1) = 0 A
H0(3,2) = 0 A
H0(3,3) = 21.726 A
.NO_VELOCITY.     # Keep this line if you do not want to do MD with this config.
entry_count = 5
59
Ni
0   0 0   1.0 86
0.00977 0 0.15046 1.0 86
0.01955 0 0.30092 1.0 86
0.02933 0 0.45139 1.0 86
0.0391  0 0.60185 1.0 86
0.04888 0 0.75232 1.0 86
0.02444 0 0.87616 1.0 86
0.16134 0 0.01818 1.0 86
0.14526 0 0.14319 1.0 86
0.15465 0 0.29368 1.0 86
0.16403 0 0.44416 1.0 86
0.17342 0 0.59465 1.0 86
0.1828  0 0.74514 1.0 86
0.19219 0 0.89563 1.0 86
0.32269 0 0.03631 1.0 86
0.28879 0 0.16231 1.0 86
0.2549  0 0.28831 1.0 86
0.28171 0 0.43786 1.0 86
0.29109 0 0.58835 1.0 86
0.30047 0 0.73883 1.0 86
0.30986 0 0.88932 1.0 86
0.45816 0 0.02905 1.0 86
0.59362 0 0.02179 1.0 86
0.72908 0 0.01453 1.0 86
0.86454 0 0.00726 1.0 86
0.46793 0 0.17952 1.0 86
0.60339 0 0.17225 1.0 86
0.73886 0 0.16499 1.0 86
0.87432 0 0.15772 1.0 86
0.43404 0 0.30551 1.0 86
0.61317 0 0.32272 1.0 86
0.74863 0 0.31546 1.0 86
0.88409 0 0.30819 1.0 86
0.3824  0 0.43156 1.0 86
0.57041 0 0.44874 1.0 86
0.75841 0 0.46592 1.0 86
0.89387 0 0.45866 1.0 86
0.40851 0 0.58204 1.0 86
0.52592 0 0.57574 1.0 86
0.71392 0 0.59292 1.0 86
0.90192 0 0.6101  1.0 86
0.41815 0 0.73253 1.0 86
0.53583 0 0.72623 1.0 86
0.6535  0 0.71992 1.0 86
0.8415  0 0.7371  1.0 86
0.42754 0 0.88302 1.0 86
0.54521 0 0.87672 1.0 86
0.66289 0 0.87041 1.0 86
```

```
0.78056 0 0.86411 1.0 86
59
Co
0   0   0 1.0 14
0.00977 0 0.15046 1.0 14
0.01955 0 0.30092 1.0 14
0.02933 0 0.45139 1.0 14
0.0391  0 0.60185 1.0 14
0.04888 0 0.75232 1.0 14
0.02444 0 0.87616 1.0 14
0.16134 0 0.01818 1.0 14
0.14526 0 0.14319 1.0 14
0.15465 0 0.29368 1.0 14
0.16403 0 0.44416 1.0 14
0.17342 0 0.59465 1.0 14
0.1828  0 0.74514 1.0 14
0.19219 0 0.89563 1.0 14
0.32269 0 0.03631 1.0 14
0.28879 0 0.16231 1.0 14
0.2549  0 0.28831 1.0 14
0.28171 0 0.43786 1.0 14
0.29109 0 0.58835 1.0 14
0.30047 0 0.73883 1.0 14
0.30986 0 0.88932 1.0 14
0.45816 0 0.02905 1.0 14
0.59362 0 0.02179 1.0 14
0.72908 0 0.01453 1.0 14
0.86454 0 0.00726 1.0 14
0.46793 0 0.17952 1.0 14
0.60339 0 0.17225 1.0 14
0.73886 0 0.16499 1.0 14
0.87432 0 0.15772 1.0 14
0.43404 0 0.30551 1.0 14
0.61317 0 0.32272 1.0 14
0.74863 0 0.31546 1.0 14
0.88409 0 0.30819 1.0 14
0.3824  0 0.43156 1.0 14
0.57041 0 0.44874 1.0 14
0.75841 0 0.46592 1.0 14
0.89387 0 0.45866 1.0 14
0.40851 0 0.58204 1.0 14
0.52592 0 0.57574 1.0 14
0.71392 0 0.59292 1.0 14
0.90192 0 0.6101  1.0 14
0.41815 0 0.73253 1.0 14
0.53583 0 0.72623 1.0 14
0.6535  0 0.71992 1.0 14
0.8415  0 0.7371  1.0 14
0.42754 0 0.88302 1.0 14
0.54521 0 0.87672 1.0 14
0.66289 0 0.87041 1.0 14
0.78056 0 0.86411 1.0 14
55
Mn
0.07263 0.5 0.0716  1.0 62
0.24202 0.5 0.09931 1.0 62
0.39531 0.5 0.10792 1.0 62
0.52589 0.5 0.10429 1.0 62
```

```
0.66135 0.5 0.09702 1.0 62
0.79681 0.5 0.08976 1.0 62
0.93227 0.5 0.0825  1.0 62
0.0871  0.5 0.22207 1.0 62
0.20008 0.5 0.21475 1.0 62
0.36142 0.5 0.23392 1.0 62
0.54055 0.5 0.25112 1.0 62
0.67601 0.5 0.24386 1.0 62
0.81147 0.5 0.23659 1.0 62
0.94694 0.5 0.22933 1.0 62
0.09199 0.5 0.37255 1.0 62
0.21818 0.5 0.36577 1.0 62
0.31865 0.5 0.35994 1.0 62
0.50222 0.5 0.37713 1.0 62
0.68579 0.5 0.39432 1.0 62
0.82125 0.5 0.38706 1.0 62
0.9616  0.5 0.37616 1.0 62
0.10138 0.5 0.52303 1.0 62
0.22757 0.5 0.51626 1.0 62
0.34511 0.5 0.50995 1.0 62
0.45416 0.5 0.50365 1.0 62
0.64216 0.5 0.52083 1.0 62
0.83017 0.5 0.53801 1.0 62
0.97627 0.5 0.523 1.0 62
0.11096 0.5 0.6735  1.0 62
0.23695 0.5 0.66675 1.0 62
0.35462 0.5 0.66044 1.0 62
0.47217 0.5 0.65414 1.0 62
0.58971 0.5 0.64783 1.0 62
0.77771 0.5 0.66501 1.0 62
0.96571 0.5 0.68219 1.0 62
0.12054 0.5 0.82398 1.0 62
0.24634 0.5 0.81724 1.0 62
0.36401 0.5 0.81093 1.0 62
0.48168 0.5 0.80462 1.0 62
0.59936 0.5 0.79832 1.0 62
0.71703 0.5 0.79201 1.0 62
0.90503 0.5 0.8092  1.0 62
0.09291 0.5 0.94717 1.0 62
0.25572 0.5 0.96772 1.0 62
0.37339 0.5 0.96142 1.0 62
0.49107 0.5 0.95511 1.0 62
0.60874 0.5 0.94881 1.0 62
0.72641 0.5 0.94250 1.0 62
0.84435 0.5 0.93619 1.0 62
27
Al
0.07263 0.5 0.0716  1.0 38
0.24202 0.5 0.09931 1.0 38
0.39531 0.5 0.10792 1.0 38
0.52589 0.5 0.10429 1.0 38
0.66135 0.5 0.09702 1.0 38
0.79681 0.5 0.08976 1.0 38
0.93227 0.5 0.0825  1.0 38
0.0871  0.5 0.22207 1.0 38
0.20008 0.5 0.21475 1.0 38
0.36142 0.5 0.23392 1.0 38
0.54055 0.5 0.25112 1.0 38
```

```
0.67601 0.5 0.24386 1.0 38
0.81147 0.5 0.23659 1.0 38
0.94694 0.5 0.22933 1.0 38
0.09199 0.5 0.37255 1.0 38
0.21818 0.5 0.36577 1.0 38
0.31865 0.5 0.35994 1.0 38
0.50222 0.5 0.37713 1.0 38
0.68579 0.5 0.39432 1.0 38
0.82125 0.5 0.38706 1.0 38
0.9616  0.5 0.37616 1.0 38
0.10138 0.5 0.52303 1.0 38
0.22757 0.5 0.51626 1.0 38
0.34511 0.5 0.50995 1.0 38
0.45416 0.5 0.50365 1.0 38
0.64216 0.5 0.52083 1.0 38
0.83017 0.5 0.53801 1.0 38
0.97627 0.5 0.523 1.0 38
0.11096 0.5 0.6735  1.0 38
0.23695 0.5 0.66675 1.0 38
0.35462 0.5 0.66044 1.0 38
0.47217 0.5 0.65414 1.0 38
0.58971 0.5 0.64783 1.0 38
0.77771 0.5 0.66501 1.0 38
0.96571 0.5 0.68219 1.0 38
0.12054 0.5 0.82398 1.0 38
0.24634 0.5 0.81724 1.0 38
0.36401 0.5 0.81093 1.0 38
0.48168 0.5 0.80462 1.0 38
0.59936 0.5 0.79832 1.0 38
0.71703 0.5 0.79201 1.0 38
0.90503 0.5 0.8092  1.0 38
0.09291 0.5 0.94717 1.0 38
0.25572 0.5 0.96772 1.0 38
0.37339 0.5 0.96142 1.0 38
0.49107 0.5 0.95511 1.0 38
0.60874 0.5 0.94881 1.0 38
0.72641 0.5 0.94250 1.0 38
0.84435 0.5 0.93619 1.0 38
```

6.15.3 File for use with GBMaker to build a layer sandwich

This file creates cubes of 30 nm x 30 nm x 30 nm filled with austenite / martensite / austenite on top of each other. Saved with the ending .gbm and called from the command line the tool GBMaker which is part of QSTEM creates the desired crystal composition including random site placement according to the given probability.

```
box: 300 300 900  % Size of rectangular bounding box in A

crystal: Substrate TestAustenit30nm.cfg % first cystal

tilt: 0 0 0 degree
translation: 0 0 0

plane: 0 0 600 0 1 0  1 0 0
```

```
plane: 0 0 900 1 0 0 0 1 0

crystal: Martensite martensite2.cfg % second cystal

tilt: 0 0 0 degree
translation: 0 0 0

plane: 0 0 300 0 1 0  1 0 0
plane: 0 0 600 1 0 0 0 1 0

crystal: Substrate TestAustenit30nm.cfg % third cystal

tilt: 0 0 0 degree
translation: 0 0 0

plane: 0 0 0 0 1 0  1 0 0
plane: 0 0 300 1 0 0 0 1 0
```

References

[1] W. Rössler, J. Zimmer, T. Bever, K. Prügl, W. Granig, D. Hammerschmidt, and E. Katzmaier. *Advanced Microsystems for Automotive Applications. Integrated giant magneto resistors: A new sensor technology for automotive applications.* Springer, Berlin, 2006.

[2] C. Giebeler, T. Kuiper, J.B.A.D. van Zon, M. Doescher, G. Schulz, and D. Oelgeschlaeger. Robust GMR Sensors for Automotive Applications. *Tech. Mess.*, 2001.

[3] U. Hartmann. *Magnetic Multilayers and Giant Magnetoresistance - Fundamentals and Industrial Applications.* Springer Verlag, Berlin, 2000.

[4] S.S.P. Parkin. Giant magnetoresistance in magnetic nanostructures. *Annu. Rev. Mater. Sci.*, 25:357–388, 1995.

[5] V.D. Krishna, K. Wu, A.M. Perez, and J.-P. Wang. Giant magnetoresistance-based biosensor for detection of influenza A virus. *Front. Microbiol.*, 7, 2016.

[6] M. Wu and S. Huang. Magnetic nanoparticles in cancer diagnosis, drug delivery and treatment. *Molecular and Clinical Oncology*, 7:738–746, 2017.

[7] C. Felser and A. Hirohata, editors. *Heusler Alloys, Properties, growth, applications*, volume 222. Springer, 2016.

[8] S. J. Calloriv, K. Chao, B. Nagy, L. F. Kiss, L. Bottyan, K. Lin, and F. Klose. The Structures and Magnetism of Fe/FeO/Fe/FeV Characterized by Magnetometry and Polarized Neutron Reflectometry. In *2016 International Conference of Asian Union of Magnetics Societies (ICAUMS)*, 2016.

[9] C. Wang, A. Kohn, S. G. Wang, L. Y. Chang, S.-Y. Choi, A. I. Kirkland, A. K. Petford-Long, and R. C. C. Ward. Structural characterization of interfaces in epitaxial Fe/MgO/Fe magnetic tunnel junctions by transmission electron microscopy. *Phys. Rev. B*, 82:024428, Jul 2010.

[10] M. Knoll and E. Ruska. Das Elektronenmikroskop. *Zeitschrift für Physik*, 78:318–339, 1932.

[11] G. Dehm, J.M. Howe, and J. Zweck. *In-situ Electron Microscopy: Applications in Physics, Chemistry and Materials Science.* Wiley, 2012.

[12] Jeol. *Instructions JEM-ARM200F.* Jeol Japan, 1-2, Musashino 3-chome, Akishima, Tokyo 196-8558 Japan, 2012.

[13] Y. Liao. Practical electron microscopy and database. https://www.globalsino.com/EM/page4531.html, 2018.

[14] A. Gubbens, M. Barfels, C. Trevor, R. Twesten, P. Mooney, P. Thomas, N. Menon, B. Kraus, C. Mao, and B. McGinn. The GIF Quantum, a next generation post-column imaging energy filter. *Ultramicroscopy*, 110(8):962 – 970, 2010. Proceedings of the international workshop on enhanced data generated by electrons.

[15] Jeol. *Instruction Manual JEM FS-2200.* Jeol Japan, 1-2, Musashino 3-chome, Akishima, Tokyo 196-8558 Japan.

[16] J. Lindner and et. al. Owl-ac Ausrüstung. https://www.owl-ac.de/forschung/ausruestung/, 2016.

[17] D. Henry. Electron-sample interactions. https://serc.carleton.edu/research_education/geochemsheets/electroninteractions.html.

[18] Gatan Corporation. Eels.info. https://eels.info/about/techniques/eels-0, 2016.

[19] D.B. Williams and C.B. Carter. *Transmission Electron Microscopy.* Springer, 2009.

[20] R. F. Egerton. *Electron Energy-Loss Spectroscopy in the Electron Microscope.* Springer US, 3rd edition, 2011.

[21] C. R. Brundle, C. A. Evans, and S. Wilson, editors. *Encyclopedia of Materials Characterization.* Butterworth-Heinemann, 1992.

[22] F. Lenz. Zur Streuung mittelschneller Elektronen in kleinste Winkel. *Z. Naturforsch.*, 9A:185–204, 1954.

[23] T. I. Morrison, M. B. Brodsky, N. J. Zaluzec, and L. R. Sill. Iron d-band occupancy in amorphous Fe_x Ge_{1-x}. *Phys. Rev. B*, 32:3107–3111, Sep 1985.

[24] M. Isaacson. *Microbeam Analysis in Biology.* Academic Press, 1979.

[25] T. Mizoguchi, I. Tanaka, M. Mizuno, H. Adachi, T. Hashimoto, H. Inui, and M. Yamaguchi. Defect and electronic structure of TiSi2 thin films produced by co-sputterings.: Part II: Chemical bonding and electron energy-loss near-edge structures. *Acta Materialia*, 49(12):2321 – 2328, 2001.

[26] H. Adachi, T. Mukoyama, and J. Kawai. *Hartree-Fock-Slater Method for Materials Science.* Springer, 01 2006.

[27] B.G. Mendis, M. MacKenzie, and A.J. Craven. A new analytical method for characterising the bonding environment at rough interfaces in high-k gate stacks using electron energy loss spectroscopy. *Ultramicroscopy*, 110(2):105 – 117, 2010.

[28] R. D. Leapman and C. R. Swyt. Separation of overlapping core edges in electron energy loss spectra by multiple-least-squares fitting. *Ultramicroscopy*, 26:393–404, 1988.

[29] T. Manoubi, M. Tence, M. G. Walls, and C. Colliex. Curve fitting methods for quantiative analysis in electron energy loss spectroscopy. *Microanal. Microstruct.*, 1:23–39, 1990.

[30] J. Verbeeck and S. Van Aert. Model based quantification of eels spectra. *Ultramicroscopy*, 101:207–214, 2004.

[31] P.J. Thomas and R.D. Twesten. A Simple, Model Based Approach for Robust Quantification of EELS Spectra and Spectrum-Images. *Microscopy and Microanalysis*, 18(S2):968–969, 2012.

[32] T. Malis, S. C. Cheng, and R. F. Egerton. EELS log-ratio technique for specimen-thickness measurement in the TEM. *Journal of Electron Microscopy Technique*, 8(2):193–200, 1988.

[33] G. Schütz, W. Wagner, W. Wilhelm, P. Kienle, R. Zeller, R. Frahm, and G. Materlik. Absorption of circularly polarized x-rays in iron. *Phys. Rev. Lett.*, 58:737–740, Feb 1987.

[34] C. T. Chen, Y. U. Idzerda, H.-J. Lin, N. V. Smith, G. Meigs, E. Chaban, G. H. Ho, E. Pellegrin, and F. Sette. Experimental Confirmation of the X-Ray Magnetic Circular Dichroism Sum Rules for Iron and Cobalt. *Phys. Rev. Lett.*, 75:152–155, Jul 1995.

[35] C. Hébert and P. Schattschneider. A proposal for dichroic experiments in the electron microscope. *Ultramicroscopy*, 96(3):463 – 468, 2003. Proceedings of the International Workshop on Strategies and Advances in Atomic Level Spectroscopy and Analysis.

[36] P. Schattschneider, M. Stöger-Pollach, S. Rubino, M. Sperl, C. Hurm, J. Zweck, and J. Rusz. Detection of magnetic circular dichroism on the two-nanometer scale. *Phys. Rev. B*, 78:104413, Sep 2008.

[37] J. Rusz, S. Muto, J. Spiegelberg, R. Adam, K. Tatsumi, D. E. Bürgler, P. M. Oppeneer, and Schneider C. M. Magnetic measurements with atomic-plane resolution. *Nature Communications*, 2016.

[38] M. Nelhiebel, P. Schattschneider, and B. Jouffrey. Observation of Ionization in a Crystal Interferometer. *Phys. Rev. Lett.*, 85:1847–1850, Aug 2000.

[39] L. Calmels, F. Houdellier, B. Warot-Fonrose, C. Gatel, M. J. Hÿtch, V. Serin, E. Snoeck, and P. Schattschneider. Experimental application of sum rules for electron energy loss magnetic chiral dichroism. *Phys. Rev. B*, 76:060409, Aug 2007.

[40] C. Hébert, P. Schattschneider, S. Rubino, P. Novak, J. Rusz, and M. Stöger-Pollach. Magnetic circular dichroism in electron energy loss spectrometry. *Ultramicroscopy*, 108(3):277 – 284, 2008.

[41] J. Rusz, S. Rubino, and P. Schattschneider. First-principles theory of chiral dichroism in electron microscopy applied to 3*d* ferromagnets. *Phys. Rev. B*, 75:214425, Jun 2007.

[42] P. Schattschneider. *Linear and Chiral Dichroism in the Electron Microscope*. Pan Stanford Publishing, 2012.

[43] N. Yao and Z.L. Wang, editors. *Handbook of Microscopy for Nanotechnology*, chapter 22, page 687. Springer, 2005.

[44] J. N. Chapman and M. R. Scheinfein. Transmission electron microscopies of magnetic microstructures. *Journal of Magnetism and Magnetic Materials*, 200(1):729 – 740, 1999.

[45] S. McVitie and M. Cushley. Quantitative fresnel lorentz microscopy and the transport of intensity equation. *Ultramicroscopy*, 106(4):423 – 431, 2006.

[46] R. E. Dunin-Borkowski. The development of Fresnel contrast analysis, and the interpretation of mean inner potential profiles at interfaces. *Ultramicroscopy*, 83:193–216, 2000.

[47] A. Sanchez and M.A. Ochando. Calculation of the mean inner potential. *Journal of Physics C: Solid State Physics*, 18(1):33–41, jan 1985.

[48] I. Lazić, E. G. T. Bosch, and Lazar S. Phase contrast stem for thin samples: Integrated differential phase contrast. *Ultramicroscopy*, 160:265 – 280, 2016.

[49] S. McVitie and G.S. White. Imaging Amperian currents by Lorentz microscopy. *Journal of Physics D: Applied Physics*, 37(2):280–288, dec 2003.

[50] Y. Aharonov and D. Bohm. Significance of Electromagnetic Potentials in the Quantum Theory. *Phys. Rev.*, 115:485–491, Aug 1959.

[51] J. N. Chapman, I. R. McFadyen, and S. McVitie. Modified differential phase contrast lorentz microscopy for improved imaging of magnetic structures. In *1990 IEEE International Magnetics Conference (INTERMAG)*, pages 1506–1511, 1990.

[52] E. N. Gimenez, R. Ballabriga, G. Blaj, M. Campbell, I. Dolbnya, E. Frodjh, I. Horswell, X. Llopart, J. Marchal, J. McGrath, D. Omar, R. Plackett, K. Sawhney, and N. Tartoni. Medipix3RX: Characterizing the Medipix3 redesign with synchrotron radiation. *IEEE Transactions on Nuclear Science*, 62(3):1413–1421, 2015.

[53] J.A. Mir, R. Plackett, I. Shipsey, and J.M.F. dos Santos. Using the medipix3 detector for direct electron imaging in the range 60 keV to 200 keV in electron microscopy. *Journal of Instrumentation*, 12(11):C11015–C11015, nov 2017.

[54] FPD: Fast pixelated detector data storage, analysis and visualisation. https://gitlab.com/fpdpy/fpd. Accessed on September 14th 2020.

[55] D. McGrouther and G. Paterson. 4D STEM DPC Processing. UofG MCMP private communications, 2019. Jupyter notebook.

[56] R. O. Duda and P. E. Hart. Use of the Hough Transformation to Detect Lines and Curves in Pictures. *Commun. ACM*, 15(1):11–15, jan 1972.

[57] J. Illingworth and J. Kittler. The adaptive hough transform. *IEEE transactions on pattern analysis and machine intelligence*, page 690–698, 1987.

[58] M. Sjödahl and L. R. Benckert. Electronic speckle photography: analysis of an algorithm giving the displacement with subpixel accuracy. *Appl. Opt.*, 32(13):2278–2284, May 1993.

[59] J.O. III Smith. Generalized Hamming window family. Accessed on September 14th, 2020.

[60] M.A. Fischler and R.C. Bolles. Random sample consensus:A paradigm for model fitting with applications to image analysis and automated cartography. Technical report, SRI International, 1980.

[61] S. Löffler and P. Schattschneider. A software package for the simulation of energy-loss magnetic chiral dichroism. *Ultramicroscopy*, 110(7):831 – 835, 2010.

[62] A. Vansteenkiste, J. Leliaert, M. Dvornik1, M. Helsen, F. Garcia-Sanchez, and B. Van Waeyenberge1. The design and verification of MuMax3. *AIP Advances*, 4(107133), 2014.

[63] Wikipedia. List of Runge–Kutta methods. https://en.wikipedia.org/wiki/List_of_Runge%E2%80%93Kutta_methods, 12 2019.

[64] M. Mansuripur. Computation of electron diffraction patterns in lorentz electron microscopy of thin magnetic films. *Journal of Applied Physics*, 69(4):2455–2464, 1991.

[65] D. Berkov. MicroMagus - software for micromagnetic simulation. *ResearchGate*, 01 2008.

[66] M. Song and K. Furuya. Fabrication and characterization of nanostructures on insulator substrates by electron-beam-induced deposition. *Science and Technology of Advanced Materials*, 9(2):023002, 2008.

[67] K. Furuya. Nanofabrication by advanced electron microscopy using intense and focused beam*. *Science and Technology of Advanced Materials*, 9(1):014110, 2008.

[68] Micro to Nano. Micro to nano shop. https://www.microtonano.com/de/EMR-Kohlenstoff-Carbon-Support-Traegerfilme-fuer-TEM.php, 2020.

[69] J. Wingbermühle. Transportphänomene in magnetischen Tunnelkontakten unter besonderer Berücksichtigung der Ionenstrahlsputterdeposition. Technical report, FZ Jülich, Institut für Festkörperforschung, 2002.

[70] W. Hetaba and M. Stöger-Pollach. *EMCD investigation of the Verwey-transition in magnetite*, pages 1086–1087. American Cancer Society, 2016.

[71] M. Stöger-Pollach, C.D. Treiber, G.P. Resch, D.A. Keays, and I. Ennen. EMCD real space maps of Magnetospirillum magnetotacticum. *Micron*, 42(5):456 – 460, 2011.

[72] T. Koide, T. Shidara, K. Ymaguchi, A. Fujimori, H. Fukutani, N. Kimizuka, and S. Kimura. Core-level magnetic circular dichroism in Fe3O4 and CoFe2O4. *Journal of Electron Spectroscopy and Related Phenomena*, 78:275 – 278, 1996.

[73] W. Hetaba. *The theory and application of inelastic coherence in the electron microscope*. PhD thesis, Technische Universität Wien, 2015.

[74] A. Moskaltsova, J. Krieft, D. Graulich, T. Matalla-Wagner, and T. Kuschel. Impact of the magnetic proximity effect in pt on the total magnetic moment of Pt/Co/Ta trilayers studied by x-ray resonant magnetic reflectivity. *AIP Advances*, 10(1):015154, 2020.

[75] T. Kuschel and D. Graulich. Private communications about the magnetic proximity effect in vanadium. XRMR measurements, 2019.

[76] P. Schattschneider, M. Stöger-Pollach, S. Rubino, M. Sperl, Ch. Hurm, J. Zweck, and J. Rusz. Detection of magnetic circular dichroism on the two-nanometer scale. *Phys. Rev. B*, 78:104413, Sep 2008.

[77] P. Stadelmann. JEMS-Swiss, JEMS java version V4. www.jems-swiss.ch, 2020.

[78] B. Warot-Fonrose, C. Gatel, L. Calmels, V. Serin, E. Snoeck, and S. Cherifi. Magnetic properties of FeCo alloys measured by energy-loss magnetic chiral dichroism. *Journal of Applied Physics*, 107(9):09D301, 2010.

[79] Y. Lee, J. Lee, C.J. Bae, J.-G. Park, H.-J. Noh, J.-H. Park, and T. Hyeon. Large-Scale Synthesis of Uniform and Crystalline Magnetite Nanoparticles Using Reverse Micelles as Nanoreactors under Reflux Conditions. *Advanced Functional Materials*, 15(3):503–509, 2005.

[80] C. Taake. Optimierung von EMCD Messungen an einem Transmissionselektronenmikroskop mit in-column Filter. Master thesis, Bielefeld University, 2019.

[81] D.R.G. Mitchell. Savitzky Golay Spectral Filter. http://www.dmscripting.com/savitzky-golay_spectral_filter.html, 2016.

[82] B. Schaffer. *How to Script... Digital Micrograph Scripting Handbook*. Selfpublished, contact how.to.dms@tavernmaker.de, 2019.

[83] D.R.G. Mitchell. Mean free path estimator. http://www.dmscripting.com/meanfreepathestimator.html.

[84] S. Löffler and W. Hetaba. Convergent-beam EMCD: benefits, pitfalls and applications. *Microscopy*, 67(suppl_1):i60–i71, Jan 2018.

[85] J. M. D. Coey. *Magnetism and Magnetic Materials*. Cambridge University Press, 2010.

[86] W. Zhu, D. Wu, B. Zhao, Z. Zhu, X. Yang, Z. Zhang, and Q. Y. Jin. Correlations Between Structural and Magnetic Properties of Co_2FeSi Heusler-Alloy Thin Films. *Phys. Rev. Applied*, 8:034012, Sep 2017.

[87] Y. Liao. Practical electron microscopy and database on sample thickness determination methods using eels. https://www.globalsino.com/EM/page4621.html, 2020.

[88] S. Kämmerer, A. Thomas, A. Hütten, and G. Reiss. Co2MnSi Heusler alloy as magnetic electrodes in magnetic tunnel junctions. *Applied Physics Letters*, 85(1):79–81, 2004.

[89] T. Kubota, J. Hamrle, Y. Sakuraba, O. Gaier, M. Oogane, A. Sakuma, B. Hillebrands, K. Takanashi, and Y. Ando. Structure, exchange stiffness, and magnetic anisotropy of $Co2MnAl_x$ Si_{1-x} Heusler compounds. *Journal of Applied Physics*, 106(11):113907, 2009.

[90] S. Mankovsky, D. Ködderitzsch, G. Woltersdorf, and H. Ebert. First-principles calculation of the Gilbert damping parameter via the linear response formalism with application to magnetic transition metals and alloys. *Phys. Rev. B*, 87:014430, Jan 2013.

[91] A. Yadav and S. Chaudhary. Effect of growth temperature on the electronic transport and anomalous Hall effect response in co-sputtered Co2FeSi thin films. *Journal of Applied Physics*, 118(19):193902, 2015.

[92] D. McGrouther. Dpc_component_rotate. DM script, Provided by the group of Stephen McVitie, University of Glasgow, 2006.

[93] V. Asvini, G. Saravanan, and R.K. et al. Kalaiezhily. Effect of Substrate Temperature on Structural, Morphological, Magnetic, and Electrical Properties of Fe2CoSi Heusler Alloy Thin Films for Spin-Based Device Applications. *J. Supercond. Nov. Magn.*, 32:2247–2257, 2019.

[94] A.I. Kirkland and S.J. Haigh, editors. *Nanocharacterisation*. Nanoscience & Nanotechnology Series. The Royal Society of Chemistry, 2015.

[95] M. Gajdardziska-Josifovska, M.R. McCartney, W.J. de Ruijter, D.J. Smith, J.K. Weiss, and J.M. Zuo. Accurate measurements of mean inner potential of crystal wedges using digital electron holograms. *Ultramicroscopy*, 50(3):285 – 299, 1993.

[96] R. I. Anishchenko. Calculation of the mean inner potential of a crystal in the statistical theory. *physica status solidi (b)*, 18(2):923–928, 1966.

[97] R. E. Dunin-Borkowski, M. R. McCartney, D. J. Smith, and S. S. P. Parkin. Towards quantitative electron holography of magnetic thin films using in situ magnetization reversal. *Ultramicroscopy*, 74:61–73, 1998.

[98] S. Ichikawa, T. Akita, K. Okazaki, M. Okumura, K. Tanaka, and M. Kohyama. Mean Inner Potential of Nanostructured Noble Metal Catalysts - Pt/TiO2 Catalyst. *MRS Proceedings*, 788:L8.21, 2003.

[99] S. McVitie, D. McGrouther, S. McFadzean, D. A. MacLaren, K. J. O'Shea, and M. J. Benitez. Aberration corrected lorentz scanning transmission electron microscopy. *Ultramicroscopy*, 152:57–62, 2015.

[100] R. C. O'Handley. *Modern Magnetic Materials, Principles and applications*. Wiley, 1999.

[101] V. Niculescu, J.I. Budnick, W.A. Hines, K. Raj, S. Pickart, and S. Skalski. Relating structural, magnetic moment, and hyperfine field behavior to a local environment model in $Fe_{3-x}Co_xSi$ alloys. *Phys. Rev. B*, 19:452–464, 1979.

[102] M. Hashimoto, J. Herfort, H.-P. Schönherr, and K. H. Ploog. Epitaxial Heusler alloy Co2FeSi/GaAs(001) hybrid structures. *Applied Physics Letters*, 87(10):102506, 2005.

[103] D.R.G. Mitchell. SI Tools. http://www.dmscripting.com/sitools.html, 2016. version:20160903, v4.0.

[104] O. Gaier, J. Hamrle, S. Trudel, B. Hillebrands, H. Schneider, and G. Jakob. Exchange stiffness in the Co2FeSi heusler compound. *Journal of Physics D: Applied Physics*, 42(23):232001, nov 2009.

[105] K. Persson. Materials data on V (SG:229) by materials project, 11 2014. Computed materials data using density functional theory calculations. These calculations determine the electronic structure of bulk materials by solving approximations to the Schrodinger equation. For more information, see https://materialsproject.org/docs/calculations.

[106] C.W. Tucker, A.U. Seybolt, and H.T. Sumsion. The location of oxygen atoms in vanadium-oxygen alloys by means of neutron diffraction. *Acta Metallurgica*, 1:390–393, 1953. via Crystallography Open Database.

[107] J. S. Moodera, Lisa R. Kinder, Terrilyn M. Wong, and R. Meservey. Large Magnetoresistance at Room Temperature in Ferromagnetic Thin Film Tunnel Junctions. *Phys. Rev. Lett.*, 74:3273–3276, Apr 1995.

[108] C. Felser and H.H. Fecher, editors. *Spintronics – From Materials to Devices*, volume 1. Springer, 2013.

[109] Y. Miura, K. Abe, and M. Shirai. Half-metallic behavior of Co2MnSi/Co2MnAl/MgO interface and its coherent tunneling conductance. *Journal of Physics: Conference Series*, 200(5):052016, Jan 2010.

[110] J. M. D. Coey and M. Venkatesan. Half-metallic ferromagnetism: Example of CrO2 (invited). *Journal of Applied Physics*, 91(10):8345–8350, 2002.

[111] M. Julliere. Tunneling between ferromagnetic films. *Physics Letters A*, 54(3):225 – 226, 1975.

[112] D. Ebke. *Cobalt-based Heusler compounds in magnetic tunnel junctions*. PhD thesis, Bielefeld University, 2010.

[113] Y. Sakuraba, M. Hattori, M. Oogane, Y. Ando, H. Kato, A. Sakuma, T. Miyazaki, and H. Kubota. Giant tunneling magnetoresistance in Co2MnSi/Al–O/Co2MnSi magnetic tunnel junctions. *Applied Physics Letters*, 88(19):192508, 2006.

[114] T. Ishikawa, T. Marukame, H. Kijima, K.-I. Matsuda, T. Uemura, M. Arita, and M. Yamamoto. Spin-dependent tunneling characteristics of fully epitaxial magnetic tunneling junctions with a full-heusler alloy Co2MnSi thin film and a MgO tunnel barrier. *Applied Physics Letters*, 89(19):192505, 2006.

[115] M. Yamamoto, T. Ishikawa, T. Taira, G. Li, K. Matsuda, and T. Uemura. Effect of defects in heusler alloy thin films on spin-dependent tunnelling characteristics of Co2MnSi/MgO/Co2MnSi and Co2MnGe/MgO/Co2MnGe magnetic tunnel junctions. *Journal of Physics: Condensed Matter*, 22(16):164212, mar 2010.

[116] S. Tsunegi, Y. Sakuraba, M. Oogane, K. Takanashi, and Y. Ando. Large tunnel magnetoresistance in magnetic tunnel junctions using a Co2MnSi heusler alloy electrode and a MgO barrier. *Applied Physics Letters*, 93(11):112506, 2008.

[117] T. Ishikawa, H. Liu, T. Taira, K. Matsuda, T. Uemura, and M. Yamamoto. Influence of film composition in Co2MnSi electrodes on tunnel magnetoresistance characteristics of Co2MnSi/MgO/Co2MnSi magnetic tunnel junctions. *Applied Physics Letters*, 95(23):232512, 2009.

[118] B. Geisler and P. Kratzer. Spincaloric properties of epitaxial Co2MnSi/MgO/Co2MnSi magnetic tunnel junctions. *Phys. Rev. B*, 92:144418, Oct 2015.

[119] S. Sasaki, K. Fujino, and Y. Takeuchi. X-ray determination of electron-density distributions in oxides, MgO, MnO, CoO, and NiO, and atomic scattering factors of their constituent atoms. *Proceedings of the Japan Academy, Series B*, 55(2):43–48, 1979.

[120] S. Fujii, S. Ishida, and S. Asano. Electronic and magnetic properties of $X_2Mn_{1-x}V_xSi$ ($X = Fe$ and Co). *Journal of the Physical Society of Japan*, 63(5):1881–1888, 1994.

[121] S. Gražulis, D. Chateigner, R. T. Downs, A. F. T. Yokochi, M. Quirós, L. Lutterotti, E. Manakova, J. Butkus, P. Moeck, and A. Le Bail. Crystallography Open Database – an open-access collection of crystal structures. *Journal of Applied Crystallography*, 42(4):726–729, Aug 2009.

[122] K. Momma and F. Izumi. Vesta 3. https://jp-minerals.org/vesta/en.doc.html, 2019. Software for three dimensional crystal viisualization.

[123] P. R. Stone, M. A. Scarpulla, R. Farshchi, I. D. Sharp, E. E. Haller, O. D. Dubon, K. M. Yu, J. W. Beeman, E. Arenholz, J. D. Denlinger, and H. Ohldag. Mn $L_{3,2}$ x-ray absorption and magnetic circular dichroism in ferromagnetic $Ga_{1-x}Mn_xP$. *Applied Physics Letters*, 89(1):012504, 2006.

[124] S. Rubino, P. Schattschneider, M. Stöger-Pollach, C. Hébert, J. Rusz, L. Calmels, B. Warot-Fonrose, F. Houdellier, V. Serin, P. Novak, and et al. Energy-loss magnetic chiral dichroism (emcd): Magnetic chiral dichroism in the electron microscope. *Journal of Materials Research*, 23(10):2582–2590, 2008.

[125] E. Saitoh, M. Ueda, H. Miyajima, and G. Tatara. Conversion of spin current into charge current at room temperature: Inverse spin-hall effect. *Applied Physics Letters*, 88(18):182509, 2006.

[126] S. Y. Huang, X. Fan, D. Qu, Y. P. Chen, W. G. Wang, J. Wu, T. Y. Chen, J. Q. Xiao, and C. L. Chien. Transport magnetic proximity effects in platinum. *Phys. Rev. Lett.*, 109:107204, Sep 2012.

[127] T. Kuschel, C. Klewe, J.-M. Schmalhorst, F. Bertram, O. Kuschel, T. Schemme, J. Wollschläger, S. Francoual, J. Strempfer, A. Gupta, M. Meinert, G. Götz, D. Meier, and G. Reiss. Static magnetic proximity effect in Pt/$NiFe_2$ O_4 and Pt/Fe bilayers investigated by x-ray resonant magnetic reflectivity. *Phys. Rev. Lett.*, 115:097401, Aug 2015.

[128] P .K. Mann and S. M. Yusuf. Two interface effects: Exchange bias and magnetic proximity. *Physics Reports*, 535(2):61 – 99, 2014. Two interface effects: Exchange bias and magnetic proximity.

[129] D. Zhong, K. L. Seyler, X. Linpeng, N. P. Wilson, T. Taniguchi, M. A. Watanabe, K.and McGuire, K. C. Fu, D. Xiao, W. Yao, and X. Xu. Layer-resolved magnetic proximity effect in van der Waals heterostructures. *Nature Nanotechnology*, 15:187–191, 2020.

[130] A. Rustagi. Stoner Ferromagnetism. http://www.phys.ufl.edu/∼avinash/Notes/Stoner_Ferromagnetism/Stoner_FM.pdf, 2018.

[131] L. Cheng, Z. Altounian, D. H. Ryan, J. O. Ström-Olsen, M. Sutton, and Z. Tun. Pd polarization and interfacial moments in Pd-Fe multilayers. *Phys. Rev. B*, 69:144403, Apr 2004.

[132] W. L. Lim, N. Ebrahim-Zadeh, J. C. Owens, H. G. E. Hentschel, and S. Urazhdin. Temperature-dependent proximity magnetism in Pt. *Applied Physics Letters*, 102(16):162404, 2013.

[133] F. Wilhelm, P. Poulopoulos, G. Ceballos, H. Wende, K. Baberschke, P. Srivastava, D. Benea, H. Ebert, M. Angelakeris, N. K. Flevaris, D. Niarchos, A. Rogalev, and N. B. Brookes. Layer-resolved magnetic moments in Ni/Pt multilayers. *Phys. Rev. Lett.*, 85:413–416, Jul 2000.

[134] M. Schwickert and R. Coehoorn. Magnetic moments, coupling, and interface interdiffusion in Fe/V(001) superlattices. *Physical Review B, Condensed Matter and Materials*, 57:13681–13691, 1998.

[135] M. A. Tomaz, W. J. Antel, W. L. O'Brien, and G. R. Harp. Induced V moments in Fe/V(100), (211), and (110) superlattices studied using x-ray magnetic circular dichroism. *Journal of Physics: Condensed Matter*, 9(11):L179–L184, mar 1997.

[136] D. Graulich and T. Kuschel. Private communications on the range of the magnetic proximity effect in V. From recent measurement fits., 2020.

[137] ChemSpider. Chemical structure of Fe. *ChemSpider*, 2020. CSID:22368.

[138] B. Pokroy, J. S. Fieramosca, R. B. Von Dreele, A. N. Fitch, E. N. Caspi, and E. Zolotoyabko. Atomic structure of biogenic aragonite. *Chemistry of Materials*, 19(13):3244–3251, 2007.

[139] P. Neibecker, M. E. Gruner, X. Xu, R. Kainuma, W. Petry, R. Pentcheva, and M. Leitner. Ordering tendencies and electronic properties in quaternary Heusler derivatives. *Phys. Rev. B*, 96:165131, Oct 2017.

[140] X. Xu, W. Ito, M. Tokunaga, T. Kihara, K. Oka, R.Y. Umetsu, T. Kanomata, and R. Kainuma. The Thermal Transformation Arrest Phenomenon in NiCoMnAl Heusler Alloys. *Metals*, 2013.

[141] B. Weise, B. Dutta, N. Teichert, A. Hütten, T. Hickel, and A. Waske. Role of disorder when upscaling magnetocaloric Ni-Co-Mn-Al heusler alloys from thin films to ribbons. *Scientific Reports*, 8(9147):2045–2322, 2018.

[142] A. Diestel, P. Chekhonin, R. Niemann, W. Skrotzki, K. Nielsch, and S. Fähler. Reducing thermal hysteresis in epitaxial Ni-Mn-Ga-Co films by transformation cycling. *physica status solidi (b)*, 255(2), 2018.

[143] N. Teichert. *Shape memory Heusler alloys for thin film applications.* PhD thesis, Bielefeld University, 2016.

[144] C. Koch. *Determination of core structure periodicity and point defect density along dislocations.* PhD thesis, Arizona State University, 2002.

[145] S. Kaufmann, U. K. Rößler, O. Heczko, M. Wuttig, J. Buschbeck, L. Schultz, and S. Fähler. Adaptive modulations of martensites. *Physical Review Letters*, 104, 2010.

[146] A. Khachaturyan, S. Shapiro, and S. Semenovskaya. Adaptive phaseformation in martensitic transformation. *Physical Review B*, 43, 1991.

[147] D. R. G. Mitchell. Create spectrum from image. http://www.dmscripting.com/create_spectrum_from_image.html, 2004.

[148] D. R. G. Mitchell. Double atan eels background. http://www.dmscripting.com/double_atan_eels_background.html, 2015.

Statement of Authorship

Except where reference is made in the text of this thesis, this thesis contains no material published elsewhere or extracted in whole or in part from a thesis presented by me for another degree or diploma. No other persons work has been used without due acknowledgement in the main text of the thesis. This thesis has not been submitted for the award of any other degree or diploma in any other tertiary institution.

Bielefeld, December 16, 2020 _____

Signature